UNIVERSITY OF CALIFORNIA, SAN DIEGO

Vibration-Based Health Monitoring and Mechanics-Based Nonlinear Finite Element Model Updating of Civil Structures

A dissertation submitted in partial satisfaction of the requirements for the degree

Doctor of Philosophy

in

Structural Engineering

by

Rodrigo Astroza

Committee in charge:

Professor Joel P. Conte, Chair
Professor William S. Hodgkiss
Professor J. Enrique Luco
Professor José I. Restrepo
Professor Michael D. Todd

2015

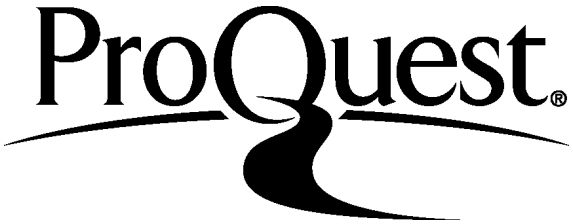

The dissertation of Rodrigo Astroza is approved, and it is acceptable in quality and form for publication on microfilm and electronically:

_____

_____

_____

_____

_____

Chair

University of California, San Diego

2015

DEDICATION

To my family, Dayana and Little Piri,

and my parents, Ximena and Maximiliano

TABLE OF CONTENTS

LIST OF FIGURES

LIST OF TABLES

ACKNOWLEDGEMENTS

I would like to express my deepest appreciation and sincere gratitude to my Ph.D. advisor, Professor Joel P. Conte. His expertise, encouragement, dedication, meticulousness, and guidance have been a great support during my doctoral studies. It has been a great experience working with and learning from him. I am very thankful to him for being always available, for spending a lot of time in meetings and discussions, and for providing me the opportunity to conduct my research at the University of California, San Diego (UC San Diego).

I would like to thank all the members of my doctoral committee, Professors William S. Hodgkiss, J. Enrique Luco, José I. Restrepo, and Michael D. Todd, for their inspiring courses, interest in my research work, and constructive suggestions and comments to improve my research work.

I would also like to thank Professor G. Rodolfo Saragoni from the University of Chile for being my research supervisor and engineering boss for many years before I came to UC San Diego. Your support, encouragement, and wise words were fundamental to come to UC San Diego and to follow a career focused on research and academia. Your time and suggestions are greatly appreciated.

I would like to express my gratitude to the Fulbright Commission and the National Commission for Scientific and Technological Research (CONICYT) for the graduate fellowship (BIO Equal Opportunities Scholarship) that supported the first four years of my doctoral studies. I am also grateful for the financial support provided by the

UCSD Academic Senate (RN091G-Conte) and by the Department of Structural Engineering at UC San Diego during my last year of studies.

The experimental data used in this dissertation were collected from experiments conducted at the Englekirk Structural Engineering Center of the UC San Diego. I am very grateful to all the staff members in the laboratory, especially Dan Radulescu, for their technical support and valuable help. I also thank Professors Tara C. Hutchinson, Joel P. Conte, and José I. Restrepo for providing me the opportunity to participate and collaborate in the BNCS project conducted at the shake table facility.

I am grateful to Mr. Hamed Ebrahimian for his collaboration on nonlinear system identification of civil structures. My research on this topic benefited from working with him. I also would like to acknowledge Dr. Yong Li, Mr. Xiang Wang, and Ms. Michelle Chen, Yujia Liu, and Elide Pantoli for giving me the opportunity to conduct research with them in a friendly and collaborative environment.

I would like to acknowledge all friends and colleagues I had the opportunity to meet in San Diego: Professors André Barbosa and Andreas Stavridis; Drs. Maurizio Gobbato, Yong Li, Juan Murcia-Delso, and Giovanni de Francesco; and Mr./Ms. Rodrigo Carreño, Michelle Chen, David Duck, Hamed Ebrahimian, Elias Espino, Artem Korobenko, Andreas Koutras, Yujia Li, Koorosh Lotfizadeh, Marios Mavros, Giovanni Montefusco, Arpit Nema, Elide Pantoli, Vasileios Papadopoulos, Alireza Sarebanha, and Xiang Wang.

I would like to thank my parents Ximena and Maximiliano for their support, encouragements, and efforts for providing me a good education. Last but not least, I want to express my deepest gratitude to my family, Dayana and Little Piri. The support,

courage, advices, generosity, patient, and love of my wonderful wife Dayana Takahashi are without a doubt what made this journey possible. I will be always in debt with you for supporting and encouraging me during these five years.

Chapter 3 of this dissertation contains the material that has been submitted for publication "Influence of the construction process and nonstructural components on the modal properties of a five-story building" in *Earthquake Engineering & Structural Dynamics*, Astroza, Rodrigo; Ebrahimian, H., and Conte, J.P., Restrepo, J.I., and Hutchinson, T.C. The dissertation author was the primary investigator and author of this paper.

Chapter 4 is largely a reprint of the material that has been submitted for publication "System identification of a full-scale five-story reinforced concrete building tested on the NEES-UCSD shake table" in *Structural Control and Health Monitoring*, Astroza, Rodrigo; Ebrahimian, H., and Conte, J.P., Restrepo, J.I., and Hutchinson, T.C. The dissertation author was the primary investigator and author of this paper.

Part of Chapter 5 is a reprint of the material that is currently being prepared for submission for publication "Seismic response analyses and modal identification of a full-scale five-story base-isolated building tested on a shake table" in *ASCE Journal of Structural Engineering*, Astroza, Rodrigo; Ebrahimian, H.; Conte, J.P.; Restrepo, J.I.; and Hutchinson, T.C. The dissertation author was the primary investigator and author of this paper.

Part of Chapter 6 is a reprint of the material that is currently being prepared for submission for publication "Statistical analysis of the modal properties of a five-story reinforced concrete seismically-damaged building identified using ambient vibrations" in

Engineering Structures, Astroza, Rodrigo; Ebrahimian, H.; Conte, J.P.; Restrepo, J.I.; and Hutchinson, T.C. The dissertation author was the primary investigator and author of this paper.

Chapter 7, in full, is a reprint of the material as it appears in "Material parameter identification in distributed plasticity FE models of frame-type structures using nonlinear stochastic filtering" in *ASCE Journal of Engineering Mechanics* (2015), Astroza, Rodrigo; Ebrahimian, H., and Conte, J.P. The dissertation author was the primary investigator and author of this paper.

Chapter 8 is a reprint of the material that is currently being prepared for submission for publication "Nonlinear system identification for health monitoring of civil structures" in *Computers & Structures*, Astroza, Rodrigo; Ebrahimian, H.; and Conte, J.P. The dissertation author was the primary investigator and author of this paper.

Part of Chapter 9 is a reprint of the material that is currently being prepared for submission for publication "Performance comparison of Kalman−based filters for nonlinear structural finite element model updating" in *Structural Health Monitoring*, Astroza, Rodrigo; Ebrahimian, H.; and Conte, J.P. The dissertation author was the primary investigator and author of this paper.

Part of Chapter 10 is a reprint of the material that is currently being prepared for submission for publication "Bayesian nonlinear structural FE model updating for damage identification of civil structures subjected to unknown inputs" in *Structural Safety*, Astroza, Rodrigo; Ebrahimian, H.; and Conte, J.P. The dissertation author was the primary investigator and author of this paper.

VITA

2005	Bachelor of Science in Civil Engineering, University of Chile, Chile.
2007	Professional Degree in Civil Engineering, University of Chile, Chile.
2007	Master of Science in Earthquake Engineering, University of Chile, Chile.
2015	Doctor of Philosophy in Structural Engineering, University of California, San Diego, USA.

PUBLICATIONS

Astroza, M., Ruiz, S., and **Astroza, R.** (2012). "Damage assessment and seismic intensity analysis of the 2010 (Mw 8.8) Maule Earthquake." *Earthquake Spectra*, 28(S1), S145-S164. http://dx.doi.org/10.1193/1.4000027.

Astroza, R., Pantoli, E., Selva, F., Restrepo, J.I., Hutchinson, T.C., and Conte, J.P. (2015). "Experimental evaluation of the seismic response of a roof-top mounted cooling tower." *Earthquake Spectra*, In press. http://dx.doi.org/10.1193/071513EQS205M

Astroza, R., Ebrahimian, H., and Conte, J.P. (2015). "Material parameter identification in distributed plasticity FE models of frame-type structures using nonlinear stochastic filtering." *ASCE Journal of Engineering Mechanics*, 141(5), 04014149. http://ascelibrary.org/doi/abs/10.1061/(ASCE)EM.1943-7889.0000851

Ebrahimian, H., **Astroza, R.**, and Conte, J.P. (2015). "Extended Kalman filter for material parameter estimation in nonlinear structural finite element models using direct differentiation method." *Earthquake Engineering & Structural Dynamics*, 44(10), 1495–1522. http://onlinelibrary.wiley.com/doi/10.1002/eqe.2532/full

Wang, X., **Astroza, R.**, Hutchinson, T.C., Conte, J.P., and Restrepo, J.I. (2015). "Dynamic characteristics and seismic behavior of prefabricated steel stairs in a full-scale five-story building shake table test program." *Earthquake Engineering & Structural Dynamics*, In press. http://onlinelibrary.wiley.com/doi/10.1002/eqe.2595/full

Astroza, R., Ebrahimian, H., Conte, J.P., Restrepo, J.I., and Hutchinson, T.C. (2015). "System identification of a full-scale five-story reinforced concrete building tested on the NEES-UCSD shake table." Accepted in *Structural Control and Health Monitoring.*

Chen, M.C., Pantoli, E., Wang, X., **Astroza, R.**, Ebrahimian, H., Hutchinson, T.C., Conte, J.P., Restrepo, J.I., Marin, C., Walsh, K., Bachman, R., Hoehler, M., Englekirk, R., and Faghihi, M. (2015). "Full-scale structural and nonstructural building system performance during earthquakes: Part I – Specimen description, test protocol, and structural response." Accepted for publication in *Earthquake Spectra*.

Pantoli, E., Chen, M.C., Wang, X., **Astroza, R.**, Ebrahimian, H., Hutchinson, T.C., Conte, J.P., Restrepo, J.I., Marin, C., Walsh, K., Bachman, R., Hoehler, M., Englekirk, R., and Faghihi, M. (2015). "Full-scale structural and nonstructural building system performance during earthquakes: Part II – NCS damage states." Accepted for publication in *Earthquake Spectra*.

Pantoli, E., Chen, M.C., Hutchinson, T.C., **Astroza, R.**, Conte, J.P., Ebrahimian, H., Restrepo, J.I., and Wang, X. (2015). "Landmark dataset from the building nonstructural components and systems (BNCS) project." Accepted for publication in *Earthquake Spectra*.

Astroza, R., Ebrahimian, H., Conte, J.P., Restrepo, J.I., and Hutchinson, T.C. "Influence of the construction process and nonstructural components on the modal properties of a five-story building." Submitted to *Earthquake Engineering & Structural Dynamics.*

Ebrahimian, H., **Astroza, R.**, Conte, J.P., and de Callafon, R.A. "Nonlinear finite element model updating for damage identification of civil structures using batch Bayesian estimation." Submitted to *Mechanical Systems and Signal Processing*.

ABSTRACT OF THE DISSERTATION

Vibration-Based Health Monitoring and Mechanics-Based Nonlinear Finite Element Model Updating of Civil Structures

by

Rodrigo Astroza

Doctor of Philosophy in Structural Engineering

University of California, San Diego, 2015

Professor Joel P. Conte, Chair

Aging, man-made and natural hazards (e.g., earthquakes and hurricanes) may induce significant damage or even cause the collapse of civil structures. Such damage and failures imply life and economic losses, and function disruption of critical facilities;

however, these devastating consequences can be reduced by means of accurate and timely risk mitigation decisions taken before and after the damage-inducing event. Structural health monitoring (SHM) has emerged as an attractive technology for the research and engineering communities to provide tools and protocols aiming to inform and prioritize the decision-making process and, therefore, has been accepted as a critical tool to achieve sustainable and resilient communities. Condition-based inspection and monitoring strategies to assess the residual life, detect any damage and safety threat at the earliest possible stage, and prioritize the repair or replacement of critical infrastructure are crucial preventive and proactive actions that can be facilitated by the use of advanced SHM methodologies. Because of recent advances in computational resources and cost reductions in sensor technologies, nowadays, dense and sophisticated sensor networks have been deployed and are collecting data for different types of civil structures throughout the world. However, current methods and practices in SHM are not achieving the goal of supporting the decision-making process. In this regard, two major hurdles are: (1) there is still a need to validate current state-of-the-art system identification (SID) and damage identification (DID) methods using data recorded from large and complex civil structures subjected to real or realistic damage-inducing events (e.g., man-made or natural hazards such as earthquakes), and (2) there is a disconnect between the advances made in the subfields of SHM and mechanics-based modeling and simulation of structures. This dissertation contributes to overcome these two hurdles by (1) analyzing vibration data recorded from a full-scale five-story reinforced concrete (RC) building fully outfitted with nonstructural components and systems, which was seismically tested and subjected to progressive damage on the NEES@UCSD shake table, and (2) developing and validating a novel and advanced SHM and DID framework that integrates high-fidelity mechanics-based nonlinear finite element (FE) structural modeling and analysis with state-of-the-art Bayesian inference methods.

The first part of this dissertation focuses on SID and dynamic characterization of the full-scale five-story RC building specimen. Dynamic data for different sources of excitation, including ambient vibration as well as free and forced vibration tests, are used to investigate the evolution of the modal properties during construction of the building.

Variations of the modal properties of the building, under both fixed-base and base-isolated configurations, due to the effects of nonstructural components, seismic-induced damage, and environmental conditions are explored comprehensively. In the second part of the dissertation, a novel framework is developed for system and damage identification of nonlinear structural systems subjected to known or unknown inputs. The proposed framework is validated using homogeneous and heterogeneous sensor data simulated from realistic nonlinear FE models of structures of increasing complexity, including 2D and 3D steel and RC frame structures, subjected to seismic excitation. Stochastic (Bayesian) filtering methods, including the Unscented Kalman filter and the Extended Kalman filter, are used to estimate unknown parameters of the FE model, unknown input base excitations, and their estimation uncertainties using spatially-sparse noisy measurements. By employing the estimated model parameters and input excitations, the updated nonlinear FE model can be interrogated to detect, localize, classify, and assess the damage in the structure, and can also be used for damage prognosis purposes.

CHAPTER 1

INTRODUCTION

1.1. Background and motivation

During the last twenty years, the civil engineering community has paid increasing attention to developing and adopting solutions for inspection, monitoring, and maintenance of civil infrastructure systems. Important life safety and economic benefits can be attained by providing information about the condition of a structure after it has been exposed to natural or man-made hazards as well as aging and by identifying potential damage at the earliest possible stage. The process of implementing damage identification methodologies for civil, aerospace, and mechanical structures is known as Structural Health Monitoring (SHM) and has been the object of significant efforts in research and engineering practice (Balageas et al. 2006, Brownjohn 2007, Farrar and Worden 2012). The importance of detecting damage at an early stage has been emphasized by major structural collapses in recent years, such as the I-35W Mississippi River Bridge in Minnesota, USA, in 2007 (Figure 1.1a), the Loncomilla Bridge in Chile in 2004 (Figure 1.1b), and a wind turbine at the Foote Creek Rim wind energy facility near Arlington, in Wyoming, USA, in 2010 (Figure 1.2). The consequences of failure and

collapse of such civil structures are associated with life safety, economic losses, and function disruption, e.g., the collapse of the I-35W Mississippi River bridge caused thirteen fatalities, many injured people (French et al. 2011), and resulted in a daily economic loss of US$71,000 to US$220,000 (Xie and Levinson 2011). The I-35W St. Anthony Falls Bridge was constructed to replace the collapsed I-35W Mississippi River bridge. Because of the interest in implementing SHM systems after the collapse, more than 500 sensors were installed in the new bridge (French et al. 2011).

Figure 1.1: (a) Collapse of the I-35W Mississippi River bridge in Minnesota, USA, in 2007, (b) Collapse of the Loncomilla bridge in Chile in 2004.

Figure 1.2: Collapse of a wind turbine at the Foote Creek Rim wind energy facility near Arlington, in Wyoming, USA, in 2010.

Function disruption or collapse of civil infrastructures, such as bridges, dams, power generation plants, and emergency-response buildings, have devastating economic and life-safety effects (DHS 2014). Given that the vulnerability of civil infrastructures represents a significant threat to the safety, health, and economic development of a country, many national agencies and professional associations have made a priority to survey and report on the health of civil infrastructures. For example, in 2013, the American Society of Civil Engineers (ASCE) in the latest Report Card for America's Infrastructure (ASCE 2013) graded the health of the infrastructure in the United States with an overall D+ (poor), requiring an estimated investment of 3.6 trillion dollars to upgrade it. In particular, the health of the bridges was graded with a C+ (mediocre). Different criteria were considered in the evaluations, such as physical condition, safety, resilience, and needed investments for improvement. According to the Federal Highway Administration of the US Department of Transportation, a large number of deficient bridges are associated with high safety and economic risk (FHWA 2012). For example, in 2012, 24.9% of the bridges in the US were classified as structurally deficient or obsolete (Figure 1.3).

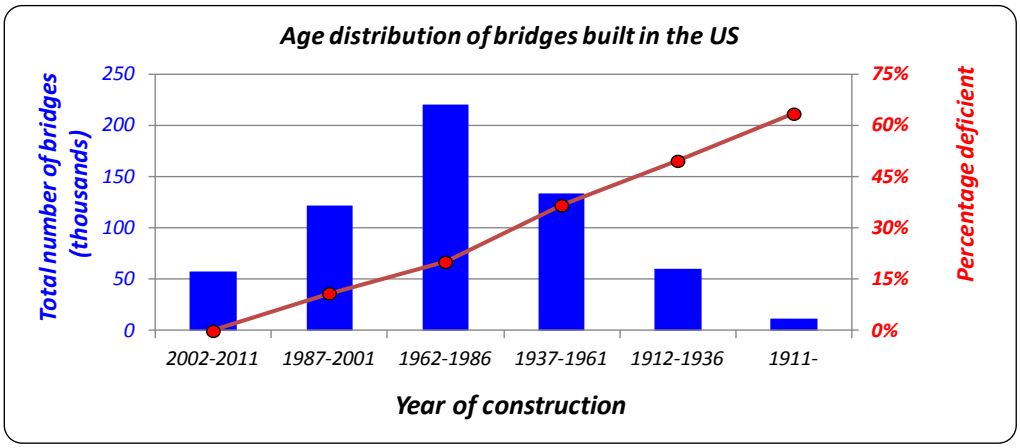

Figure 1.3: Count, age, and deficiency of bridges in the US (FHWA 2012).

Other countries have also emphasized the risk associated to old and aged infrastructure. In Canada, more than 40% of the bridges currently in use were built before 1977 and a large portion of them require urgent rehabilitation or need to be replaced (ISIS 2007). The cost for rehabilitating the infrastructure in Canada was estimated in more than US$700 billion (ISIS 2007). In Australia, a large percentage of the 50,000 public brides are 30 to 40 years old and require strengthening. About US$170 million are spent each year on bridge maintenance and it is estimated that the infrastructure in Australia is deteriorating at a rate of US$270 million a year (Sumitomo 2009). In Japan, bridges were mainly built in the 1970s, and many of them have shown aging problems, including fracture of steel members (Fujino and Siringoringo 2008).

Renovation and retrofit of these infrastructures require extensive time, labor, and financial resources. Therefore, crucial preventive and proactive actions need to be pursued and are required to inform and prioritize the decision-making process, including efficient condition-based inspection and monitoring strategies to assess the residual life, detecting any damage and safety threat at the earliest possible stage, and prioritizing the repair or replacement of the critical infrastructure. SHM has been widely accepted in the US and around the world as a critical tool for the management of sustainable and resilient critical infrastructure (Pasman and Kirillov 2007, Gopalakrishnan and Peeta 2010).

Disastrous events such as earthquakes are known to potentially induce structural damage to civil infrastructures. While more significant and serious effects are expected in deficient and old structures, new or retrofitted structures are also vulnerable to performance losses during such events. Damage initiation and progression cannot always be detected through visual screening and thus sometimes detailed, costly, and invasive

post-event inspection and evaluation are required to detect various damages (e.g., connection failures in steel moment-frame buildings during the 1994 Northridge earthquake). The hidden onset of damage can propagate and result in degradation of structural performance and a threat to life safety, which are of particular concern following catastrophic events. For example, hidden damage was detected in many steel buildings following the Northridge 1994 (Chen and Yamaguchi 1996, Fairweather 1996, FEMA 2000a) and Kobe 1995 earthquakes (FEMA 2000b).

Potential impacts of earthquakes as well as other natural and man-made hazards on urban societies can be reduced through accurate and timely risk mitigation decisions after the catastrophic event. The mitigation decisions can be supported and facilitated by the use of advanced SHM methods to help assess the damage in and the residual strength of the civil infrastructure.

1.2. Research objectives and scope

Developing and implementing advanced SHM and damage identification methodologies for civil infrastructure requires three significant steps, key to attain a disaster-resilient nation (CNER 2011): (1) monitor their performance during normal operation and extreme loads, (2) diagnose the incidence, location, type and extent of damage after catastrophic events, and (3) predict their future functionality and remaining useful life. These steps can be realized by deploying a sensor network on the structure of interest, collecting continuous data from the sensing systems, extracting information from these data through advanced system and damage identification methods, and using the knowledge to support the decision-making for maintenance and inspections, emergency

response, and post-disaster rehabilitation (Figure 1.4). Recent advances in computing power and cost reductions in sensor technology (Ansari 2005, Mukhopadhyay 2011) offer a great opportunity to develop and implement system and damage identification techniques for SHM of civil structures. These techniques also need to integrate state-of-the-art high-fidelity mechanics-based computational tools used to model and simulate the complex behavior of civil structures.

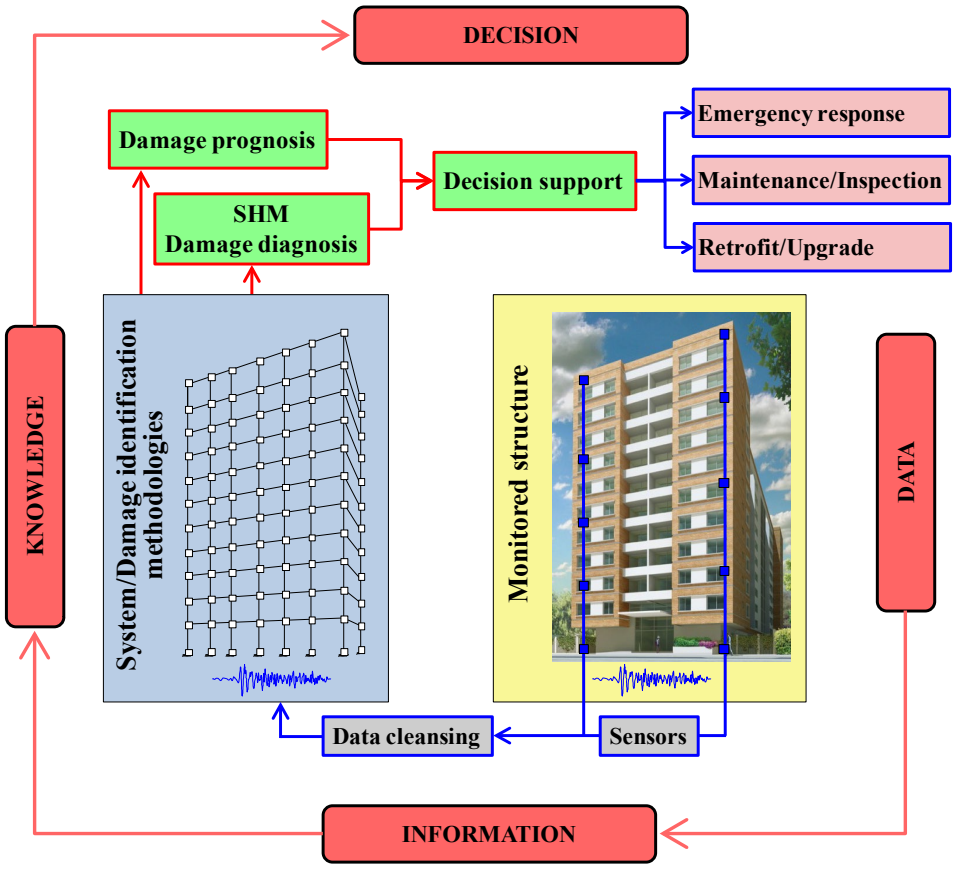

Figure 1.4: SHM-based decision support.

Advances in sensor technology developed within other engineering disciplines have also been integrated and used for SHM purposes in the civil engineering community. Nowadays, dense and sophisticated sensor networks have been deployed and are collecting data from different types of civil structures throughout the world (Lee and

Shin 1997, Wong 2004, Koh et al. 2005a, Koh et al. 2005b, Fujino and Siringoringo 2008, Habel 2009, Ou and Li 2010, Ni and Wong 2012, Catbas et al. 2013). However, current methods and practices in SHM are not achieving the goal of supporting the decision-making process for emergency management, condition-based maintenance and inspections, and structural retrofit or upgrade, which are critical and both extremely costly and time consuming tasks for large and complex civil structures in the real-world.

First, there is a need to validate current state-of-the-art system and damage identification methods using data recorded from large and complex civil structures subjected to ambient, service and damage-inducing extreme loads. To date, most system and damage identification studies have been widely and successfully applied to simplified numerical structural models (i.e., numerically simulated dynamic response data) and small-scale physical structural models tested dynamically in laboratory conditions. Because of the scarcity of densely instrumented and significantly damaged structures, the high cost, operational requirements, and complexity of conducting tests on full-scale structures, availability of data recorded from real structures undergoing real damage and degradation processes has been extremely limited. Most of the full-scale tests have been conducted on in-situ bridge structures condemned for demolition, in which artificial damage was induced during the demolition process. For building structures, studies on full-scale structures subjected to damage are even more limited.

In this dissertation, comprehensive system identification (SID) and dynamic characterization of a full-scale five-story reinforced concrete (RC) building tested on the Large High-Performance Outdoor Shake Table (NEES@UCSD) are conducted. Vibration data generated from different sources of excitation (ambient vibration as well as free and

forced vibration tests) are employed to investigate the evolution of the modal properties during the construction of the structure and to study the effects of nonstructural components, seismic-induced damage, and environmental conditions on the identified dynamic characteristics of the building, for both fixed-base and base-isolated configurations of the test specimen.

Secondly, there is a disconnect between the advances made in the subfields of SHM and computational mechanics-based modeling and simulation of structures. In particular, all system and damage identification studies on nonlinear structures have been conducted using simple nonlinear structural models (e.g., single degree-of-freedom, chain-like multi-degree-of-freedom systems, and shear building models) or small scale physical specimens tested in laboratories. In this dissertation, a new framework for system and damage identification of nonlinear structural systems is developed and validated. The proposed framework integrates high-fidelity mechanics-based nonlinear finite element (FE) structural modeling and analysis with Bayesian inference techniques. The methodology can be employed for rapid damage identification. Civil structures subjected to earthquake excitation are the focus in this dissertation.

1.3. Outline of the dissertation

Chapter 2 presents a review of the fundamental aspects of system and damage identification in SHM reported in the literature, and summarizes some of the most relevant experimental studies and real-world application examples in these research areas.

The first part of the dissertation, Chapters 3 through 6, focuses on the system identification and dynamic characterization of a full-scale five-story reinforced concrete building (BNCS building) tested on the NEES@UCSD shake table. The second part of the dissertation, Chapters 7 through 10, presents a novel framework for system and damage identification of civil structures which integrates high-fidelity mechanics-based nonlinear FE structural modeling and analysis with nonlinear Bayesian inference methods.

Chapter 3 investigates the influence of the construction process and effects of nonstructural components and systems (NCSs) on the modal properties of the BNCS building. Ambient vibration (AV) data were recorded daily and shock (free vibration) and forced vibration tests (low-amplitude white noise base excitations) were conducted on the building at different stages of construction. Different state-of-the-art system identification methods, including three output-only and two input-output, are used to estimate the modal properties of the building. The obtained results are used to investigate the effects of the construction process and NCSs on the dynamic properties of this building system and to compare the modal properties obtained from different methods, as well as the performance of these methods.

Chapter 4 describes the effects of amplitude of excitation and structural as well as nonstructural damage in the modal properties of the BNCS building in its fixed-base configuration. While fixed to the shake table platen, the building was subjected to a suite of six earthquake motions designed and applied to progressively damage the structure and NCSs. Between seismic tests, ambient vibration response was recorded, and, in addition, low-amplitude white noise (WN) base excitation tests were conducted at key stages

during the test protocol. Using the vibration data recorded, different system identification methods are used to estimate the modal properties of an equivalent viscously-damped linear elastic time-invariant model of the building at different levels of damage and their results are compared. Furthermore, the correlation between actual damage (from visual inspections performed between the seismic tests) and the identified modal parameters is analyzed. The identified natural frequencies are used to determine the progressive loss of apparent global stiffness of the building, and the state-space models identified using WN base excitation test data are employed to investigate the relative modal contributions to the measured building response at different damage states. This research provides a unique opportunity to investigate the performance of different SID methods when applied to vibration data recorded from a real building subjected to progressive damage, which was induced by a realistic source of earthquake excitation.

In Chapter 5, the BNCS building with seismic isolation at its base is investigated. In this configuration, the building was subjected to a sequence of seven seismic tests, which progressively increased the seismic demand on the structure and NCSs. Using WN and seismic test data, the effects of the isolation system in elongating the predominant period of the building, concentrating the deformation in the isolation layer, and augmenting the energy dissipation capacity of the building system are explored. The effectiveness of the isolation in reducing the floor acceleration and interstory drift demands is demonstrated. Before and after each seismic test, low-amplitude WN base excitation tests were conducted and AV data were recorded continuously for approximately sixteen days. Using these data, the modal parameters of an equivalent viscously-damped linear elastic time invariant model are estimated.

Chapter 6 presents a comprehensive statistical analysis of the identified modal properties of the BNCS building in its fixed-base configuration using AV data recorded continuously for about fifteen days and including different damage states. Two state-of-the-art methods of operational modal analysis are used to automatically identify the modal properties of the fixed-base building at different damage states using the recorded AV data. A statistical analysis of the identified modal parameters is performed to investigate the statistical variability and accuracy of the system identification results. The variability of the identified modal parameters due to environmental conditions is also investigated.

Chapter 7 introduces a novel framework that combines high-fidelity mechanics-based nonlinear (hysteretic) FE models and nonlinear stochastic filtering methods to estimate unknown material parameters in frame-type structures. The proposed framework updates nonlinear FE models using spatially limited noisy measurement data, and it can be directly used for damage identification purposes. Numerically simulated data of a cantilever steel column, representing a bridge pier, and a two-dimensional steel frame subjected to earthquake ground motions of varying intensities are used to validate the effectiveness, robustness, and accuracy of the framework.

Chapter 8 extends the framework presented in Chapter 7 and analyzes the performance and robustness of the methodology using numerically simulated data from a three-dimensional 5-story 2-by-1 bay RC frame building subjected to bi-directional earthquake excitations. The case of acceleration response data measured at a limited number of locations is studied and the benefits of using heterogeneous sensor arrays on the identifiability of the modeling parameters and updating of the nonlinear FE model are

also investigated. Damping parameters, in addition to parameters characterizing the nonlinear material constitutive laws, are also considered in the estimation process. Three non-sequential updating approaches are presented and analyzed to alleviate the computational burden. An adaptive filtering approach is proposed to estimate the measurement noise covariance matrix in addition to the time-invariant modeling parameters. Effects of the input measurement noise on the estimation results are also analyzed.

In Chapter 9, the performance of three different Kalman−based filters, namely the Unscented Kalman filter (UKF), Extended Kalman filter (EKF) and Iterated-EKF (IEFK), for nonlinear structural finite element model updating is investigated. Comparison of the performance of these different filters in terms of convergence, accuracy, robustness, and computational requirements is conducted. Numerically simulated data from a three-dimensional 5-story 2-by-1 bay RC frame building subjected to bi-directional earthquake excitation is used as an application example.

Chapter 10 presents a methodology to update mechanics-based nonlinear structural FE models subjected to unknown input excitation(s). The approach can estimate unknown time-invariant parameters of a nonlinear FE model of the structure and the unknown time-histories of the input excitations, using spatially-sparse output response measurements recorded during a damage-inducing event. Using the estimated model parameters and input excitations, the updated nonlinear FE model can be interrogated to detect, localize, classify, and assess the damage in the structure. The effects of using heterogeneous sensor arrays and high intensity levels of output measurement noise are investigated. Numerically simulated response data of a three-

dimensional 4-story 2-by-1 bay steel frame building with six unknown modeling parameters, subjected to unknown bi-directional seismic excitation; and a three-dimensional 5-story 2-by-1 bay RC frame building with nine unknown modeling parameters and subjected to unknown bi-directional seismic excitation are used to validate the proposed methodologies.

Chapter 11 presents the summary and conclusions of this dissertation as well as recommendations for future related research.

References

American Society of Civil Engineers (ASCE). (2013). *2013 Report card for America's infrastructure*. http://www.infrastructurereportcard.org. (Accessed 05/2014).

Ansari, F. (Ed.) (2005). *Sensing issues in civil structural health monitoring*. Springer, Dordrecht, The Netherlands.

Balageas, D., Fritzen, C.P., and Guemes, A. (Eds.) (2006). *Structural health monitoring*. ISTE Ltd., London, UK.

Brownjohn, J.M.W. (2007). "Structural health monitoring of civil infrastructure." *Philosophical Transactions of the Royal Society A: Mathematical, Physical and Engineering Sciences*, 365, 589–622.

Catbas, F.N., Kijewski-Correa, T., and Aktan, A.E. (2013). *Structural identification of constructed systems: Approaches, methods, and technologies for effective practice of St-Id*. American Society of Civil Engineers, Reston, VA.

Chen, W.F. and Yamaguchi, E. (1996). "Spotlight on steel moment frames." *ASCE Civil Engineering*, 66(3), 44–46.

Committee on National Earthquake Resilience (CNER) (2011). *National earthquake resilience: Research, implementation, and outreach*. The National Academies Press, Washington, D.C.

Department of Homeland Security (DHS). (2014). http://www.dhs.gov. (Accessed 05/2015).

Fairweather, V. (1996). "Seismic solutions for steel frame buildings." *ASCE Civil Engineering*, 66(3), 40–43.

Farrar, C.R. and Worden, K. (2012). *Structural health monitoring: A Machine learning perspective*. John Wiley & Sons, Ltd., West Sussex, UK.

Federal Highway Administration (FHWA). 2012. National bridge inventory NBI. www.fhwa.dot.gov/bridge/nbi.htm. (Accessed 12/2013).

FEMA (2000a). *Recommended post-earthquake evaluation and repair criteria for welded steel moment frame buildings*. FEMA-352, Washington, DC.

FEMA (2000b). *A policy guide to steel moment-frame construction*. FEMA-354, Washington, DC.

French, C.E., Hedegaard, B., Shield, C.K., and Stolarski, H. (2011). "I35W collapse, rebuild, and structural health monitoring - Challenges associated with structural health monitoring of bridge systems." In *Review of progress in quantitative nondestructive evaluation*, AIP Conference Proceedings 1335, 9, San Diego, CA.

Fujino, Y. and Siringoringo, D.M. (2008). "Structural health monitoring of bridges in Japan: An overview of the current trend." *4th International Conference on FRP Composites in Civil Engineering* (*CICE*), Zurich, Switzerland.

Gopalakrishnan, K. and Peeta, S. (2010). *Sustainable and resilient critical infrastructure systems: Simulation, modeling, and intelligent engineering*. Springer, Berlin.

Habel, W.R. (2009). *Structural health monitoring research in Europe: Trends and applications*. In Structural Health Monitoring of Civil Infrastructure Systems. Woodhead Publishing, Cambridge, UK.

Intelligent Sensing for Innovative Structures (ISIS). (2007). *Reinforcing concrete structures with fibre-reinforced polymers*. ISIS Canada Research Network, Design Manual No.3, University of Manitoba, Manitoba, Canada.

Koh, H.M., Choo, J.F., Kim, S., and Kil, H.B. (2005). "Applications and researches in bridge health monitoring systems and intelligent infrastructures in Korea." In *Structural health monitoring and intelligent infrastructure*, Taylor & Francis.

Koh, H.M., Kim, S., and Choo, J.F. (2005). "Recent development of bridge health monitoring system in Korea." In S*ensing issues in civil structural health monitoring*. Springer, Dordrecht, The Netherlands.

Lee, W.H. and Shin, T.C. (1997). "Real time seismic monitoring of buildings and bridges in Taiwan." In *Structural health monitoring*. Technomic Pub Co., Lancaster, PA.

Mukhopadhyay, S. (Ed.) (2011). *New developments in sensing technology for structural health monitoring*. Springer, Berlin, Germany.

Ni, Y.Q. and Wong, K.Y. (2012). "Integrating bridge structural health monitoring and condition-based maintenance management." *4th Civil Structural Health Monitoring Workshop*, Berlin, Germany.

Ou, J. and Li, H. (2010). "Structural health monitoring in mainland China: Review and future trends." *Structural Health Monitoring*, 9(3), 219–231.

Pasman, H. and Kirillov, I. (Eds.) (2007). *Resilience of cities to terrorist and other threats*. Springer, Dordrecht, The Netherlands.

Sumitomo Australia Pty Ltd. (2009). *Bridge repair market statistics*. www.iceng.com.au/files/link/Bridge-market-statistics.pdf. (Accessed 04/2015).

Wong, K. (2004). "Instrumentation and health monitoring of cable-supported bridges." *Structural Control and Health Monitoring*, 11(2), 91–124.

Xie, F. and Levinson, D. (2011). "Evaluating the Effects of I-35W bridge collapse on road-users in the Twin Cities metropolitan region." *Transportation Planning and Technology*, 34(7), 691–703.

CHAPTER 2

STRUCTURAL HEALTH MONITORING: A LITERATURE REVIEW

2.1. Introduction

The need and importance of implementing accurate and robust system identification (SID) and damage identification (DID) strategies for civil structures has attracted significant attention to structural health monitoring (SHM) within the structural engineering community over the last forty years. Structural monitoring can be useful and necessary in different cases and applications, such as: modifications/retrofit of existing structures, monitoring during demolition, structures subjected to aggressive environments or degradation of materials, fatigue damage assessment, in-situ characterization of loads, to assist structural maintenance, to support emergency response, quality control of construction, post-event damage assessment, etc. In particular, for Damage Identification (DID), the research community has developed and adopted a hierarchical organizational scheme to assess the condition of a structure. This scheme includes five different levels of damage identification (Rytter 1993, Worden and Dulieu-Barton 2004), namely, Level

1: Detection (existence of damage), Level 2: Localization (location of damage), Level 3: Classification (type of damage), Level 4: Assessment (extent of damage), and Level 5: Prediction/Prognosis (estimation of remaining useful life).

System and damage identification methodologies can be classified based on different criteria, such as:

- Model-based versus signal processing (model-free) based methods,
- Methods assuming linear versus nonlinear response of the system,
- Domain of the method (time, frequency, modal, or time-frequency domain methods),
- Input-output (single input-single output or SISO, single input-multiple output or SIMO, multiple input-single output or MISO, multiple input-multiple output or MIMO) versus output-only methods,
- Type of applications used to validate and verify the methods (numerically simulated data from simplified models, numerically simulated data from realistic models of large and complex structures, data collected from small scale physical laboratory experiments, data collected from large/full-scale experiments, data recorded from structures in the field).

The remainder of this chapter focuses on a literature review based on the assumption of linear or nonlinear response of the structural system. In addition, special emphasis is given to the type of applications used to verify the different methodologies.

2.2. Linear system and damage identification

Estimation of the linear dynamic characteristics of structures has been a subject of great importance for many decades. The design and analysis of civil structures subjected to dynamic loads, such as winds or earthquakes, requires the knowledge of the dynamic properties of the structure of interest. From the 1930's, many field tests have been conducted to propose simplified expressions to relate the number of stories or height of buildings to their natural periods of vibration, which are required to estimate the dynamic loads imposed on the structure, and also to verify the results of analytical models. One of the first and most extensive studies focused on the identification of the dynamic properties of building structures was conducted following the 1933 Long Beach earthquake; Carder (1936) reported the fundamental period of 212 buildings and 37 tank towers located in California, the former estimated from ambient vibrations and the latter using free vibrations. In 1934, Jacobsen and Blume built a mechanical shaker at Stanford University, and used it to conduct forced vibration tests in order to estimate the dynamic properties of buildings, dams, bridges, and soils. Some of these resu1ts are summarized in Blume (1936), giving special emphasis to the estimation of the natural periods of vibration. Later on, significant efforts were made to investigate the response of civil structures subjected to different types of dynamic excitation, such as mechanical shakers, free-vibration tests, induced ground motions (e.g., nuclear blast), seismic events, and ambient vibrations (e.g., Kanai and Yoshigawa 1951, Alford and Housner 1952, Hudson 1960, Hudson 1964, Cherry and Brady 1965, Clough et al. 1965, Nielsen 1966, Kuroiwa 1967, Rea et al. 1971, Jennings et al. 1971, Trifunac 1972, Blume 1972, Hart and Ibanez

1973, Hart et al. 1973, Shah and Kircher 1973, Udwadia and Trifunac 1973, Foutch 1976).

The use of the identified dynamic properties of structures and quantities derived therefrom (e.g., modal curvatures) has been later extended to other applications, one being damage identification, a research areas that has attracted significant attention from the structural engineering community. Methods based on linear SID, with modal parameter identification being the most popular in this group, have been proposed for DID purposes for many years. DID based on changes in the identified modal properties of an equivalent linear-elastic viscously-damped model of the structure has been undoubtedly one of the most popular approaches. This approach assumes that low-amplitude dynamic input-output or output-only data are available before and after the structure has suffered damage. Its premise is that by analyzing the changes in the identified modal properties or quantities derived therefrom, which depend on the physical characteristics of the structure (i.e., mass, stiffness, and energy dissipation mechanisms), damage in the structure can be identified (Doebling et al. 1996, Housner et al. 1997, Carden and Fanning 2004, Fan and Qiao 2011). Important research efforts within modal identification-based methods for DID are:

- Methods based on changes in identified natural frequencies (Loland and Dodds 1976, Idichandy and Ganapathy 1990, Salawu 1997, Bicanic and Chen 1997, Chassiakos et al. 2007), used mostly for damage detection.
- Methods based on changes in mode shapes (Mayes 1992, Zhou et al. 2005, Siddique et al. 2006).
- Methods based on mode shape curvatures (Pandey et al. 1991, Maeck and De

Roeck 1999, Abel Wahab and De Roeck 1999).

- Methods based on changes in flexibility (Raghavendrachar and Aktan 1992, Pandey and Biswas 1994, Pandey and Biswas 1995, Catbas and Aktan 2000, Bernal 2002, Bernal and Gunes 2004).
- Methods based on changes in stiffness matrix (Salawu and Williams 1993, Maeck et al. 2000, Maeck el al. 2001, Lus et al. 2004).
- Methods based on changes in frequency response function (Lew 1995, Sampaio et al. 1999).
- Methods based on modal strain energy (Stubbs et al. 1995, Stubbs and Kim 1996, Shi et al. 1998, Shi et al. 2000).
- Methods based on residual forces (Ricles and Kosmatka 1992, Kosmatka and Ricles 1999, Zimmerman et al. 2001).

DID based on changes in identified modal parameters has been widely and successfully applied to simplified numerical structural models (i.e., numerically simulated dynamic response data) and small-scale physical structural models tested dynamically in laboratory condition (Brownjohn 2007). However, because of the scarcity of densely instrumented and significantly damaged structures, along with the high cost, operational requirements, and complexity of conducting tests on full-scale structures, availability of data recorded from real structures undergoing real damage and degradation processes has been extremely limited. Most of full-scale tests have been conducted on in-situ bridge structures condemned for demolition (Farrar et al. 2000, Peeters and De Roeck 2001, Huth et al. 2005, Lauzon and DeWolf 2006, Dilena et al. 2011, Siringoringo et al. 2013), in which artificial damage was induced during the demolition process (e.g.,

partial saw cuts in steel I beams, partial cuts of post-tensioning tendons). However, this kind of artificial damage is not representative of real damage caused by natural loads or aging. For building structures, shake table tests have provided unique data to assess the modal parameters of buildings at different states of damage (Moaveni et al. 2010, Ji et al. 2011, Hien and Mita 2011, Moaveni et al. 2011, Moaveni et al. 2013, Astroza et al. 2013, Belleri et al. 2014). Other structures such as dams (Darbre and Proulx 2002), wind turbines (Prowell et al. 2011, Adams et al. 2011), and offshore platforms (Vandiver 1975, Campbell and Vandiver 1980, Shahrivar and Bouwkamp 1986, Brincker et al. 1995) have also been studied using this approach.

To make use of more realistic structural models in SHM, finite element (FE) model updating, a model-based method introduced in the 1970s for linear structures (Berman and Flannelly 1971), has emerged as a powerful methodology (Housner et al. 1997, Friswell and Mottershead 1995, Marwala 2010). FE model updating can be defined as the process of calibrating or tuning a FE model to minimize the discrepancies between the FE predicted and measured responses of the real structure of interest. This process can be conducted in the frequency, time, time-frequency, or modal domains and can be formulated for deterministic or stochastic structural models. A probabilistic formulation is desirable, since it incorporates uncertainties in the measurements and model predictions, which in turn allow the assessment of the uncertainty in the estimated parameters as part of the FE model updating procedure (Beck and Katafygiotis 1998). Several methods for FE model updating have been proposed in the literature and most of them have been used in conjunction with linear FE structural models (Mottershead and Friswell 1993, Friswell and Mottershead 1995, Marwala 2010), including applications to

full-scale structural specimens (Alvin 1997, Fritzen et al. 1998, Cobb and Liebst 1997, Brownjohn et al. 2001, Teughels and De Roeck 2004, Teughels and De Roeck 2005, Lam et al. 2004, Jaishi and Ren 2005, Jaishi and Ren 2006, Moaveni et al. 2010, Mottershead et al. 2011, Simoen et al. 2013, Sipple and Sanayei 2014). However, when using linear FE models updated based on input-output or output-only data obtained from low-amplitude excitation, the damage is estimated as a loss of effective stiffness, which makes it difficult or impossible to accomplish Levels 3 (classification) and 4 (assessment) and disallow Level 5 (prognosis) of DID.

Other approaches have also been used for DID assuming linear elastic structural response. Methods based on neural networks and genetic algorithms (Hao and Xia 2002, Adeli and Jiang 2006, Marano et al. 2010, Meruane and Heylen 2011, Chen and Nagarajaiah 2011), principal component analysis and blind source separation (Poncelet et al. 2007, Li et al. 2012, Yang and Nagarajaiah 2013a, Abazarsa et al. 2013, Antoni and Chuahan 2013, Yang and Nagarajaiah 2013b), Bayesian inference (Sohn and Law 1997, Sohn and Law 2000, Ching and Beck 2004, Yuen et al. 2006, Yuen and Kuok 2011) have been investigated.

DID based on linear elastic response of structures and, in particular, methods based on changes in modal properties have been objected primarily because (i) linearity is an idealization of the response behavior of real structures which are intrinsically nonlinear from the onset of loading (Kerschen et al. 2006), i.e., even when subjected to low amplitude excitations (Moaveni et al. 2011, Astroza et al. 2013), (ii) modal parameters and derived quantities (e.g., curvature mode shapes, modal strain energy) are global properties of the structure and often are not sensitive enough to local damage at

the component or sub-component level (Zheng and Mita 2008, Gopalakrishnan et al. 2011), and (iii) low-amplitude (e.g., ambient) vibrations used for modal identification provide information about loss of effective stiffness, but do not contain information about loss of strength, the most important form of structural damage, and the history of inelastic deformations and related damage experienced by the structure.

2.3. Nonlinear system and damage identification

To overcome the limitations of linear (e.g., modal-based) damage identification methods, several model-free or signal processing based methods have been proposed and investigated for nonlinear structural systems. Their application has been limited to simulated data from simple nonlinear structural models and to small scale physical specimens and the results have shown limited success, because these methods cannot accurately classify and assess the damage. Moreover, they have not been successfully applied to real structures. Among these methods, we can mention the restoring force surface method (Masri and Caughey 1979, Masri et al. 1982), wavelet decompositions (Staszewski 1998, Kijewski and Kareem 2003, Yan et al. 2006, Aguirre et al. 2013, Guo and Kareem 2015), Empirical Mode Decomposition combined with the Hilbert-Huang Transform (Huang et al. 1998, Yang and Lin 2004a, Feldman 2011), Volterra and Wiener series (Worden and Tomlinson 2001), modal analysis for nonlinear systems (Rosenberg 1962, Vakakis et al. 1996, Vakakis 1997), and the Wigner-Ville distribution (Feldman and Braun 1995, Bradford et al. 2006).

More recently, batch and sequential estimation techniques, such as the minimum mean-square error (MMSE) estimation and adaptive least squares (ALS) estimation, as

well as Bayesian methods such as maximum a posteriori (MAP) estimation, the extended Kalman filter (EKF), the unscented Kalman filter (UKF), and particle filters (PF), have been used in model-based methods for parametric identification of nonlinear structural models (Hoshiya and Saito 1984, Chassiakos et al. 1998, Smyth et al. 1999, Yang and Lin 2004b, Corigliano and Mariani 2004, Ghanem and Ferro 2006, Wu and Smyth 2007, Chatzi and Smyth 2009, Ching et al. 2006a, Ching et al. 2006b, Muto and Beck 2008, Huang et al. 2010).

A special mention must be given to the pioneering work of Distefano and co-workers in the 1970's (Distefano and Rath 1975a, Distefano and Rath 1975, Distefano and Pena-Pardo 1976). They proposed batch (optimization-based) and filtering approaches to estimate states and parameters of nonlinear hysteretic structural systems, including SDOF and shear-type building structures.

Applications of the abovementioned estimation methods have been limited to simulated data from highly idealized nonlinear structural models, such as single degree-of-freedom (DOF), chain-like multi-DOF systems and shear building models, which are not suitable for accurate and reliable nonlinear response prediction of actual civil structures with real-world complexities.

In recent years, a limited number of studies have focused on deterministic and probabilistic (Bayesian) methods for nonlinear FE model updating of civil structures subjected to static and dynamic loadings (Nasrellah and Manohar 2011, Song and Dyke 2013, Song et al. 2013, Liu and Au 2013, Omrani et al. 2013, Yang et al. 2014). However, in the case of nonlinear hysteretic FE model updating of structures subjected to dynamic excitation, previous studies used simplified structural models with lumped

nonlinearities (e.g., plastic hinges) described using empirical nonlinear models, such as the Bouc-Wen model (Ismail et al. 2009). These simplified and empirical models are not capable to properly represent the actual nonlinear behavior of structures and, consequently, are not typically employed in state-of-the-art mechanics-based structural FE models in analysis and design of nonlinear structures (Filippou and Fenves 2004).

The FE method, originally introduced in the 1950's (Argyris 1954, Turner et al. 1956) remains an active area of research aiming at high-fidelity nonlinear response simulation of structures up to incipient collapse and beyond. Different types of FEs (e.g., 1D beam-column elements, 2D plate/shell elements, 3D continuum/brick elements) with different formulations (e.g., displacement-based, force/stress-based, mixed/hybrid) and various kinds of nonlinear material constitutive models (e.g., pseudo-elasticity, plasticity, coupled damage-plasticity, smeared crack) were and are still being developed for this purpose. Also, the increase in computational power permits the use of nonlinear structural models of increasing complexity and fidelity.

Recently, methodologies for model updating of state-of-the-art nonlinear FE models using input-output data recorded during damage-inducing events, i.e., loading events strong enough to force the structure into its nonlinear range of behavior, have been proposed in the literature. This approach represents an important progress in the field of SHM of civil structures, as it will potentially provide a methodology for rapid post-earthquake performance assessment of structural safety from the updated nonlinear mechanics-based FE structural model. In addition, damage prognosis can also be conducted using the updated FE model and possible future loading scenarios. Using numerically simulated response data from a two-dimensional 1-story 1-bay steel frame

with distributed-plasticity subjected to a harmonic lateral force excitation, Shahidi and Pakzad (2014) used the response surface method to update two parameters of a bilinear material constitutive law (modulus of elasticity and post yielding stiffness ratio), which was utilized to model the fibers of the frame structural members. Astroza et al. (2015) and Ebrahimian et al. (2015) used the UKF and EKF, respectively, to estimate time-invariant parameters describing the nonlinear material constitutive models of simple but realistic steel structures. Their application examples used numerically simulated response data of a cantilever steel pier and a two- dimensional 3-story 3-bay steel frame and involved the estimation of three to eight parameters. The methodologies proposed by Astroza et al. (2015) and Ebrahimian et al. (2015) represent the first comprehensive effort to integrate high-fidelity mechanics-based nonlinear FE modeling and response simulation of civil structures with advanced Bayesian inference methods for SHM. They are paving the way to real-world applications and will result in significant progress in the areas of SHM, disaster management, risk mitigation, and public safety.

References

Abazarsa, F., Ghahari, S.F., Nateghi, F., and Taciroglu, E. (2013). "Response-only modal identification of structures using limited sensors." *Structural Control and Health Monitoring*, 20(6), 987–1006.

Abdel Wahab, M.M. and De Roeck, G. (1999). "Damage detection in bridges using modal curvatures: Application to a real damage scenario." *Journal of Sound and Vibration*, 226(2), 217–235.

Adams, D., White, J., Rumsey, M., and Farrar, C.R. (2011). "Structural health monitoring of wind turbines: Method and application to a HAWT." *Wind Energy*, 14(4), 603–623.

Adeli, H. and Jiang, X. (2006). "Dynamic fuzzy wavelet neural network model for structural system identification." *ASCE Journal of Structural Engineering*, 132(1), 102–111.

Aguirre, D.A., Gaviria, C.A., and Montejo, L.A. (2013). "Wavelet-based damage detection in reinforced concrete structures subjected to seismic excitations." *Journal of Earthquake Engineering*, 17(8), 1103–1125.

Alford, A.L. and Housner, G.W. (1952). "A dynamic test of a four-story reinforced concrete building." *Bulletin of the Seismological Society of America*, 43(1), 7–16.

Alvin, K.F. (1997). "Finite element model update via Bayesian estimation and minimization of dynamic residuals." *AIAA Journal*, 35(5), 879–886.

Antoni, J. and Chuahan, S.A. (2013). "Study and extension of second-order blind source separation to operational modal analysis." *Journal of Sound and Vibration*, 332(4), 1079–1106.

Argyris, J.H. (1954). "Energy theorems and structural analysis, Part 1." *Aircraft Engineering*, 26, 383–394.

Astroza, R., Ebrahimian, H., Conte, J.P., Restrepo, J.L, and Hutchinson, T.C. (2013). "Modal identification of 5-story RC building tested on NEES-UCSD shake table." *31st International Modal Analysis Conference* (*IMAC XXXI*), Garden Grove, CA.

Astroza, R., Ebrahimian, H., and Conte, J.P. (2015). "Material parameter identification in distributed plasticity FE models of frame-type structures using nonlinear stochastic filtering." *ASCE Journal of Engineering Mechanics*, 141(5), 04014149.

Beck, J.L. and Katafygiotis, L. (1998). "Updating models and their uncertainties. I: Bayesian statistical framework." *ASCE Journal of Engineering Mechanics*, 124(4), 455–461.

Belleri, A, Moaveni, B., and Restrepo, J.I. (2014). "Damage assessment through structural identification of a large-scale three-story precast concrete structure." *Earthquake Engineering & Structural Dynamics*, 43(1), 61–76.

Berman, A. and Flannelly, W. (1971). "Theory of incomplete models of dynamic structures." *AIAA Journal*, 9(8), 1481–1487.

Bernal, D. (2002). "Load vectors for damage localization." *ASCE Journal of Engineering Mechanics*, 128(1), 7–14.

Bernal, D. and Gunes, B. (2004). "Flexibility based approach for damage characterization: Benchmark application." *ASCE Journal of Engineering Mechanics*, 130(1), 61–70.

Bicanic, N. and Chen, H. P. (1997). "Damage identification in framed structures using natural frequencies." *International Journal for Numerical Methods in Engineering*, 40(23), 4451–4468.

Blume, J.A. (1936). The building and ground vibrator. Chapter 7 in *Earthquake investigations in California: 1934–1935*. US Coast and Geodetic Survey, Special publication No. 201. Washington D.C.

Blume, J.A. (l972). "Highrise building characteristics and responses determined from nuclear seismology." *Bulletin of the Seismological Society of America*, 62(2), 519–540.

Bradford, S.C., Yang, J., and Heaton, T. (2006). "Variations in the dynamic properties of structures: The Wigner-Ville distribution." *8th U.S. National Conference on Earthquake Engineering*, San Francisco, CA.

Brincker, R., Kirkegaard, P.H., Andersen, P., and Martínez, M.E. (1995). "Damage detection in an offshore structure." *13th International Modal Analysis Conference* (*IMAC XIII*), Nashville, TN.

Brownjohn, J.M.W., Xia, P.Q., Hao, H., and Xia, Y. (2001). "Civil structure condition assessment by finite element model updating: Methodology and case studies." *Finite Elements in Analysis and Design*, 37(10), 761–775.

Brownjohn, J.M.W. (2007). "Structural health monitoring of civil infrastructure." *Philosophical Transactions of the Royal Society A: Mathematical, Physical and Engineering Sciences*, 365(1851), 589–622.

Campbell, R.B. and Vandiver, J.K. (1980). "The estimation of natural frequencies and damping ratios of offshore structures." *Offshore Technology Conference*, Houston, TX.

Carden, E.P. and Fanning, P. (2004). "Vibration based condition monitoring: A review." *Structural Health Monitoring*, 3(4), 355–377.

Carder, D.S. (1936). Vibration observations. Chapter 5 in *Earthquake investigations in California: 1934–1935*. US Coast and Geodetic Survey, Special publication No. 201. Washington D.C.

Catbas, F. N. and Aktan, A. E. (2000). "Modal analysis as a bridge health monitoring tool." *14th Analysis and Computational Specialty Conference*, Chicago, IL.

Chassiakos, A.G., Masri, S.F., Nayeri, R.O., Caffrey, J.P., Tzong, G., and Chen, H.P. (2007). "Use of vibration monitoring data to track structural changes in a retrofitted building." *Structural Control and Health Monitoring*, 14(2), 218–238.

Chassiakos, A.G., Masri, S.F., Smyth, A.W., and Caughey, T.K. (1998). "On-line identification of hysteretic systems." *Journal of Applied Mechanics*, 65(1), 194–203.

Chatzi, E.N. and Srnyth, A.W. (2009). "The Unscented Kalman filter and particle filter methods for nonlinear structural system identification with non-collocated heterogeneous sensing." *Structural Control and Health Monitoring*, 16(1), 99–123.

Chen, B. and Nagarajaiah, S. (2011). "Observer-based structural damage detection using genetic algorithm." *Structural Control and Health Monitoring*, 20(4), 520–531.

Cherry, S. and Brady, A.O. (1965). "Determination of the structural dynamic properties by statistical analysis of random vibrations." *3rd World Conference on Earthquake Engineering*, New Zealand .

Ching, J. and Beck, J.L. (2004). "Bayesian analysis of the Phase II IASC-ASCE structural health monitoring experimental benchmark data." *ASCE Journal of Engineering Mechanics*, 130(10), 1233–1244.

Ching, J., Beck, J.L., and Porter, K.A. (2006a). "Bayesian state and parameter estimation of uncertain dynamical systems." *Probabilistic Engineering Mechanics*, 21(1), 81–96.

Ching, J., Beck, J.L., Porter, K.A., and Shaikhutdinov, R. (2006b). "Bayesian state estimation method for nonlinear systems and its application to recorded seismic response." *ASCE Journal of Engineering Mechanics*, 132(4), 396–410.

Clough, R.W., Benuska, K.L., and Wilson, E.L. (1965). "Inelastic earthquake response of tall buildings." *3rd World Conference on Earthquake Engineering*, New Zealand.

Cobb, R.G. and Liebst, B.S. (1997). "Sensor placement and structural damage identification from minimal sensor information." *AIAA Journal*, 35(2), 369–374.

Corigliano, A. and Mariani, S. (2004). "Parameter identification in explicit structural dynamics: Performance of the extended Kalman filter." *Computer Methods in Applied Mechanics and Engineering*, 193(36–38), 3807–3835.

Darbre, G.R. and Proulx, J. (2002). "Continuous ambient-vibration monitoring of the arch darn of Mauvosin." *Earthquake Engineering & Structural Dynamics*, 31(2), 475–480.

Dilena, M., Morassi, A., and Perin, M. (2011). "Dynamic identification of a reinforced concrete damaged bridge." *Mechanical Systems and Signal Processing*, 25(8), 2990–3009.

Distefano, N. and Pena-Pardo, B. (1976). "System identification of frames under seismic loads." *Journal of the Engineering Mechanics Division*, 102(EM2), 313–330.

Distefano, N. and Rath, A. (1975a). "System identification in nonlinear structural seismic dynamics." *Computer Methods in Applied Mechanics and Engineering*, 5(3), 353–372.

Distefano, N. and Rath, A. (l975b). "Sequential identification of hysteretic and viscous models in structural seismic dynamics." *Computer Methods in Applied Mechanics and Engineering*, 6(2), 219–232.

Doebling, S.W., Farrar, C.R., Prime, M.B., and Shevitz, D.W. (1996). *Damage identification and health monitoring of structural and mechanical systems from changes in their vibration characteristics: A literature review*. Report No. LA–1 3070– MS, Los Alamos National Laboratory, Los Alamos, NM.

Ebrahimian, H., Astroza, R., and Conte, J.P. (2015). "Extended Kalman filter for material parameter estimation in nonlinear structural finite element models using direct differentiation method." Accepted for publication in *Earthquake Engineering & Structural Dynamics*.

Fan, W. and Qiao, P. (2011). "Vibration-based damage identification methods: A review and comparative study." *Structural Health Monitoring*, 10(1), 83–111.

Farrar, C.R., Cornwell, P.J., Doebling, S.W., and Prime, M.B. (2000). *Structural health monitoring studies of the Alamosa Canyon and I-40 Bridges*. Report LA-13635–MS. Los Alamos National Laboratory, Los Alamos, NM.

Feldman, M. (2011). "Hilbert transform in vibration analysis." *Mechanical Systems and Signal Processing*, 25(3), 735–780.

Feldman, M. and Braun, S. (1995). "Identification of non-linear system parameters via the instantaneous frequency: Application of the Hilbert transform and Wigner-Ville technique." *13th international Modal Analysis Conference* (*IMAC XIII*), Nashville, TN.

Filippou, F.C. and Fenves, G.L. (2004). "Methods of analysis for earthquake-resistant structures." In *Earthquake Engineering: From Engineering Seismology to Performance-based Engineering*, Boca Raton, FL, CRC Press.

Foutch, D.A. (1976). "Recent advances in dynamic testing of full-scale structures." *ASCE/EMD Specialty Conference*, Dynamic response of structures, UCLA.

Friswell, M.I. and Mottershead, J.E. (1995). *Finite Element Model Updating in Structural Dynamics*. Kluwer Academic Publishers, Boston, USA.

Fritzen, C-P., Jennewein, D., and Kiefer, T. (1998). "Damage detection based on model updating methods." *Mechanical Systems and Signal Processing*, 12(1), 163–186.

Ghanem, R. and Ferro, G. (2006). "Health monitoring for strongly non-linear systems using the ensemble Kalman filter." *Structural Control and Health Monitoring*, 13(1), 245–259.

Gopalakrishnan, S., Ruzzene, M., and Hanagud, S. (2011). *Computational techniques for structural health monitoring*. Springer Series in Reliability Engineering, Heidelberg, Germany.

Guo, Y. and Kareem, A. (2015). "System identification through non-stationary response: Wavelet and transformed singular value decomposition-based approach." *ASCE Journal of Engineering Mechanics*, 141(7), 04015013.

Hao, H. and Xia, Y. (2002). "Vibration-based damage detection of structures by genetic algorithm." *ASCE Journal of Computing in Civil Engineering*, 16(3), 222–229.

Hart, G.C. and Ibanez, P. (1973). "Experimental determination of damping in nuclear power plants structures and equipment." *Nuclear Engineering and Design*, 25(1), 112–125.

Hart, G.C., Lew, M., and DiJulio, R.M. (1973). "High-rise building response: Damping and period nonlinearities." *5th World Conference on Earthquake Engineering*, Rome, Italy.

Hien, H. and Mita, A. (2011). "Damage identification of full scale four-story steel building using multi-input multi-output models." *SPIE Sensors and Smart Structures Technologies for Civil Mechanical, and Aerospace Systems*, vol. 7981, San Diego, CA.

Hoshiya, M. and Saito, E. (1984). "Structural identification by extended Kalman filter." *ASCE Journal of Engineering Mechanics*, 110(12), 1757–1770.

Housner, G.W., Bergman, L., Caughey, T., Chassiakos, A., Claus, R., Masri, S., Skelton, R., Soong, T.T., Spencer, B., and Yao, J. (1997). "Structural control: Past, present, and future." *ASCE Journal of Engineering Mechanics*, 123(9), 897–971.

Huang, H., Yang., J.N., and Zhou, L. (2010). "Adaptive quadratic sum-squares error with unknown inputs for damage identification of structures." *Structural Control and Health Monitoring*, 17(4), 404–426.

Huang, N.E., Shen, Z., Long, S.R., Wu, M.C., Shih, H.H., Zheng, Q., Yen, N.C., Tung, C.C., and Liu, H.H. (1998). "The empirical mode decomposition and the Hilbert spectrum for nonlinear and non-stationary time series analysis." *Proceedings of the Royal Society A Mathematical Physical and Engineering Sciences*, 454(1971), 903–995.

Hudson, D.E. (1960). "A comparison of theoretical and experimental determination of building response to earthquakes." *2nd World Conference on Earthquake Engineering*, Tokyo, Japan.

Hudson, D.E. (1964). "Resonance testing of full-scale structures." *Journal of the Engineering Mechanics Division ASCE*, 90(EM3), 1–19.

Huth, O., Feltrin, G., Maeck, J., Kilic, N., anq Motavalli, M. (2005). "Damage identification using modal data: Experiences on a prestressed concrete bridge." *ASCE Journal of Structural Engineering*, 131(12), 1898–1910.

Idichandy, V.G. and Ganapathy, C. (1990). "Modal parameters for structural integrity monitoring of fixed offshore platforms." *Experimental Mechanics*, 30(4), 382–391.

Ismail, M., Ikhouane, F., and Rodellar, J. (2009). "The hysteresis Bouc-Wen model, A survey." *Archives of Computational Methods in Engineering*, 16(2), 161–188.

Jaishi, B. and Ren, W. X. (2005). "Structural finite element model updating using ambient vibration test results." *ASCE Journal of Structural Engineering*, 131(4), 617–628.

Jaishi, B. and Ren, W. X. (2006). "Damage detection by finite element model updating using modal flexibility residual." *Journal of Sound and Vibration*, 290 (1–2), 369–387.

Jennings, P.C., Matthiesen, R.B., and Hoerner, J. (1971). *Forced vibration test of a 22-story steel frame building*. Report EERL 71–01, California Institute of Technology, Pasadena, CA.

Ji, X., Fenves, G., Kajiwara, K., and Nakashima, M. (2011). "Seismic damage detection of a full-scale shaking table test structure." *ASCE Journal of Structural Engineering*, 137(1), 14–21.

Kanai, K. and Yoshigawa, S. (1951). "On the damping of vibration of actual buildings. I." *Bulletin of the Earthquake Research Institute*, Tokyo University, 30, 121–126.

Kerschen, G., Worden, K., Vakakis, A.F., and Golinval, J.C. (2006). "Past, present and future of nonlinear system identification in structural dynamics." *Mechanical Systems and Signal Processing*, 20(3), 505–592.

Kijewski, T. and Kareem, A. (2003). "Wavelet transforms for system identification in civil engineering." *Computer-Aided Civil and Infrastructure Engineering*, 18(5), 339–355.

Kosmatka, J. B. and Ricles, J. M. (1999). "Damage detection in structures by modal vibration characterization." *ASCE Journal of Structural Engineering*, 125(12), 1384–1392.

Kuroiwa, J.H. (1967). *Vibration test of a multistory building*. Report EERL 67–03, California Institute of Technology, Pasadena, CA.

Lam, H.F., Katafygiotis, L.S., and Mickleborough, N.C. (2004). "Application of a statistical model updating approach on Phase I of the IASC-ASCE structural health monitoring benchmark study." *ASCE Journal of Engineering Mechanics*, 130(1), 34–48.

Lauzon, R. and DeWolf, J. (2006). "Ambient vibration monitoring of a highway bridge undergoing a destructive test." *ASCE Journal of Bridge Engineering*, 11(5), 602–610.

Lew, J.S. (1995). "Using transfer function parameter changes for damage detection of structures." *AIAA Journal*, 33(11), 2189–2193.

Li, W-M., Zhu, H-P., Ding, L-Y., and Luo, H-B. (2012). "Structural damage recognition by grouped data based on Principal Component Analysis theory." *Automation in Construction*, 22, 258–270.

Liu, P. and Au, S-K. (2013). "Bayesian parameter identification of hysteretic behavior of composite walls." *Probabilistic Engineering Mechanics*, 34, 101–109.

Loland, O. and Dodds, J.C. (1976). "Experience in developing and operating integrity monitoring system in North sea." *8th Annual Offshore Technology Conference*, 313–319.

Lus, H., Betti, R., Yu, J., and De Angelis, M. (2004). "Investigation of a system identification methodology in the context of the ASCE benchmark problem." *ASCE Journal of Engineering Mechanics*, 130(1), 71–84.

Maeck, J., Abdel Wahab, M., Peeters, B., De Roeck, G., Visscher, J., Wilde, W.P., Ndambi, J.M., and Vantomme, J. (2000). "Damage identification in reinforced concrete structures by dynamic stiffness determination." *Engineering Structures*, 22(10), 1339–1349.

Maeck, J., Peeters, B.,and De Roeck, G. (2001). "Damage Identification on the Z24 bridge using vibration monitoring." *Smart Materials and Structures*, 10(3), 512–517.

Maeck, J. and De Roeck, G. (1999). "Damage detection on a prestressed concrete bridge and RC beams using dynamic system identification." *Key Engineering Materials*, 167–168, 320–327.

Marano, G.C., Quaranta, G., and Monti, G. (2010). "Modified genetic algorithm for the dynamic identification of structural systems using incomplete measurements." *Computer-Aided Civil and Infrastructure Engineering*, 26(2), 92–110.

Marwala, T. (2010). *Finite element model updating using computational intelligence techniques: Applications to structural dynamics*. Springer, Heidelberg, Germany.

Masri, S.F. and Caughey. T.K. (1979). "A nonparametric identification technique for nonlinear dynamic problems." *Journal of Applied Mechanics*, 46(2), 433–447.

Masri, S.F., Caughey, T.K., and Sassi, H. (1982). "A nonparametric identification of nearly arbitrary nonlinear systems." *Journal of Applied Mechanics*, 49(3), 619–628.

Mayes, R.L. (1992). "Error localization using mode shapes - An application to a two link robot arm." *10th International Modal Analysis Conference* (*IMAC X*), San Diego, CA.

Meruane, V. and Heylen, W. (2011). "An hybrid real genetic algorithm to detect structural damage using modal properties." *Mechanical Systems and Signal Processing*, 25(5), 1559–1573.

Moaveni, B., He, X., Conte, J.P., and Restrepo, J.I. (2010). "Damage identification study of a seven-story full-scale building slice tested on the UCSD-NEES shake table." *Structural Safety*, 32(5), 347–356.

Moaveni, B., He, X., Conte, J.P., Restrepo, J.I., and Panagiotou, M. (2011). "System identification study of a 7-story full-scale building slice tested on the UCSD-NEES shake table." *ASCE Journal of Structural Engineering*, 137(6), 705–717.

Moaveni, B., Stavridis, A., Lombaert, G., Conte, J.P., and Shing, P.B. (2013). "Finite-element model updating for assessment of progressive damage in a 3-story infilled RC frame." *ASCE Journal of Structural Engineering*, 139, SPECIAL ISSUE: Real-World Applications for Structural Identification and Health Monitoring Methodologies, 1665–1674.

Mottershead, J.E. and Friswell, M.I. (1993). "Model updating in structural dynamics: A survey." *Journal of Sound and Vibration*, 167(2), 347–375.

Mottershead, J.E., Link, M., and Friswell, M.I. (2011). "The sensitivity method in finite element model updating: A tutorial." *Mechanical Systems and Signal Processing*, 25(7), 2275–2296.

Muto, M. and Beck, J.L. (2008). "Bayesian updating and model class selection for hysteretic structural models using stochastic simulation." *Journal of Vibration and Control*, 14(1–2), 7–34.

Nasrellah, H.A. and Manohar, C.S. (2011). "Finite element method based Monte Carlo filters for structural system identification." *Probabilistic Engineering Mechanics*, 26(2), 294–307.

Nielsen, N.N. (1966). "Vibration tests of a nine-story steel frame building." *Journal of the Engineering Mechanics Division ASCE*, 92(1), 81–110.

Omrani, R., Hudson, R., and Taciroglu, E. (2013). "Parametric identification of non-degrading hysteresis in a laterally-torsionally coupled building using an unscented Kalman filter." *ASCE Journal of Engineering Mechanics*, 139(4), 452–468.

Pandey, A.K. and Biswas, M. (1994). "Damage detection in structures using changes in flexibility." *Journal of Sound and Vibration*, 169(1), 3–17.

Pandey, A.K. and Biswas, M. (1995). "Damage diagnosis of truss structures by estimation of flexibility change." *Modal analysis: The International Journal of Analytical and Experimental Modal Analysis*, 10(2), 104–117.

Pandey, A.K., Biswas, M., and Samman, M.M. (1991). "Damage detection from changes in curvature mode shapes." *Journal of Sound and Vibration*, 145(2), 321–332.

Peeters, B. and De Roeck, G. (2001). "One-year monitoring of the Z24-bridge: Environmental effects versus damage events." *Earthquake Engineering & Structural Dynamics*, 30(2), 149–171.

Poncelet, F., Kerschen, G., Golinval, J-C., and Verhelst, D. (2007). "Output-only modal analysis using blind source separation techniques." *Mechanical Systems and Signal Processing*, 21(6), 2335–2358.

Prowell, I., Uang, C.M., Elgamal, A., Luco, J.E., and Guo, L. (2011). "Shake table testing of a utility scale wind turbine." *ASCE Journal of Engineering Mechanics*, 138(7), 900–909.

Raghavendrachar, M. and Aktan, A. (1992). "Flexibility by multi-reference impact testing for bridge diagnostics." *ASCE Journal of Structural Engineering*, 118(8), 2186–2203.

Rea, D., Shah, A.A., and Bouwkarnp, J.G. (1971). *Dynamic behavior of a high-rise diagonally braced steel building*. Report EERC 71–5, U.C. Berkeley, CA.

Ricles, J. M. and Kosmatka, J. B. (1992). "Damage detection in elastic structures using vibratory residual forces and weighted sensitivity." *AIAA Journal*, 30(9), 2310–2316.

Rosenberg, R.M. (1962). "The normal modes of nonlinear N-degree-of-freedom systems." *Journal of Applied Mechanics*, 29(1), 7–14.

Rytter, A. (1993). *Vibration based inspection of civil engineering structures*. PhD Thesis, Department of Building Technology and Structural Engineering, University of Aalborg, Denmark.

Salawu, O.S. (1997). "Detection of structural damage through changes in frequency: A review." *Engineering Structures*, 19(9), 718–723.

Salawu, O.S. and Williams, C. (1993). "Structural damage detection using experimental modal analysis -A comparison of some methods." *11th International Modal Analysis Conference* (*IMAC XI*), Kissimmee, FL.

Sampaio, R.P.C., Maia, N.M.M., and Silva, J.M.M. (1999). "Damage detection using the frequency-response-function curvature method." *Journal of Sound and Vibration*, 226(5), 1029–1042.

Shah, A.A. and Kircher, C.A. (1973). "Measurements and statistical evaluation of dynamic characteristics of full scale structures." *5th World Conference on Earthquake Engineering*, Rome, Italy.

Shahidi, S. and Pakzad, S. (2014). "Generalized response surface model updating using time domain data." *ASCE Journal of Structural Engineering*, 140, SPECIAL ISSUE: Computational Simulation in Structural Engineering, A4014001.

Shahrivar, F. and Bouwkamp, J.G. (1986). "Damage detection in offshore platforms using vibration information." *Journal of Energy Resources Technology*, 108(2), 97–106.

Shi, Z.Y., Law, S.S., and Zhang, L.M. (2000). "Structural damage detection from modal strain energy change." *ASCE Journal of Engineering Mechanics*, 126(12), 1216–1223.

Shi, Z.Y., Law, S.S., and Zhang, L.M. (1998). "Structural damage localization from modal strain energy change." *Journal of Sound and Vibration*, 218(5), 825–844.

Siddique, A.B., Wegner, L.D., Sparling, B.F. (2006). "Identifying damage on a bridge deck using vibration-based damage indices derived from limited measurements." *SPIE Conference on Nondestructive Evaluation and Health Monitoring of Aerospace Materials, Composites, and Civil Infrastructure V*, San Diego, CA.

Simoen, E., Moaveni, B., Conte, J.P., and Lombaert, G. (2013). "Uncertainty quantification in the assessment of progressive damage in a seven-story full-scale building slice." *ASCE Journal of Engineering Mechanics*, 139(12), 1818–1830.

Sipple, J.D. and Sanayei, M. (2014). "Finite element model updating using frequency response functions and numerical sensitivities." *Structural Control and Health Monitoring*, 21(5), 784–802.

Siringoringo, D., Fujino, Y., and Nagayama, T. (2013). "Dynamic characteristics of an overpass bridge in a full-scale destructive test." *ASCE Journal of Engineering Mechanics*, 139, SPECIAL ISSUE: Dynamics and Analysis of Large-Scale Structures, 691–701.

Smyth, A.W., Masri, S.F., Chassiakos, A.G., and Caughey, T.K. (1999). "On-line parametric identification of MDOF nonlinear hysteretic systems." *ASCE Journal of Engineering Mechanics*, 125(2), 133–142.

Sohn, H. and Law, K.H. (1997). "Bayesian probabilistic approach for structure damage detection." *Earthquake Engineering & Structural Dynamics*, 26(12), 1259–1281.

Sohn, H. and Law, K.H. (2000). "Bayesian probabilistic damage detection of a reinforced concrete bridge column." *Earthquake Engineering & Structural Dynamics*, 29(8), 1131–1152.

Song, W. and Dyke, S.J. (2013). "Real-time dynamic model updating of a hysteretic structural system." *ASCE Journal of Structural Engineering*, 140(3), 04013082.

Song, W., Dyke, S.J., and Harmon, T. (2013). "Application of nonlinear model updating for a reinforced concrete (RC) shear wall." *ASCE Journal of Engineering Mechanics*, 139(5), 635–649.

Staszewski, W.J. (1998). "Identification of non-linear systems using multi-scale ridges and skeletons of the wavelet transform." *Journal of Sound and Vibration*, 214(4), 639–658 .

Stubbs, N. and Kim, J.T. (1996). "Damage localization in structures without baseline modal parameters." *AIAA Journal*, 34(8), 210–218.

Stubbs, N., Kim, J.T., and Farrar, C.R. (1995). "Field verification of a nondestructive damage localization and severity estimation algorithm." *13th International Modal Analysis Conference* (*IMAC XIII*), Nashville, TN.

Teughels, A. and De Roeck, G. (2004). "Structural damage identification of the bridge Z24 by FE model updating." *Journal of Sound and Vibration*, 278(3), 589–610.

Teughels, A. and De Roeck, G. (2005). "Damage detection and parameter identification by finite element model updating." *Archives of Computational Methods in Engineering*, 12(2), 123–164.

Trifunac, M.D. (1972). "Comparison between ambient and forced vibration experiments." *Earthquake Engineering and Structural Dynamics*, 1(2), 133–150.

Tumer, M.J., Clough, R.W., Martín, H.C., and Topp, L.J. (1956). "Stiffness and deflection analysis of complex structures." *Journal of Aeronautical Science*, 23(9), 805–823.

Udwadia, F.E. and Trifunac, M.D. (1973). "Ambient vibration test of full scale structures." *5th World Conference on Earthquake Engineering*, Rome, Italy.

Vakakis, A.F. (1997). "Non-linear normal modes and their applications in vibration theory: An overview." *Mechanical Systems and Signal Processing*, 11(1), 3–22.

Vakakis, A.F., Manevitch, L.I., Mikhlin, Y.V., Pilipchuk, V.N. and Zevin, A.A (1996). *Normal modes and localization in nonlinear systems*. Wiley, New York, NY.

Vandiver, J.K. (1975). "Detection of structural failure on fixed platforms by measurements of dynamic response." *Offshore Technology Conference*, Houston, TX.

Worden, K. and Dulieu-Barton, J.M. (2004). "An overview of intelligent fault detection in systems and structures." *Structural Health Monitoring*, 3(1), 85–98.

Worden, K. and Tomlinson, G.R. (2001). *Nonlinearity in structural dynamics: Detection, identification and modeling*. Institute of Physics Publishing , Bristol, UK.

Wu, M. and Smyth, A.W. (2007). "Application of the Unscented Kalman filter for real-time nonlinear structural system identification." *Structural Control and Health Monitoring*, 14(7), 971–990.

Yan, B. F., Miyamoto, A., and Bruhwiler, E. (2006). "Wavelet transform-based modal parameter identification considering uncertainty." *Journal of Sound and Vibration*, 291(1–2), 285–301.

Yang, J.N, Xia, Y., and Loh, C.H. (2014). "Damage detection of hysteretic structures with pinching effect." *ASCE Journal of Engineering Mechanics*, 140(3), 462–472.

Yang, J.N. and Lin, S. (2004a). "Hilbert-Huang based approach for structural damage detection." *ASCE Journal of Engineering Mechanics*, 130(1), 85–95.

Yang, J.N. and Lin, S. (2004b). "On-line identification of non-linear hysteretic structures using an adaptive tracking technique." *International Journal of Non-Linear Mechanics*, 39(9), 1481–1491.

Yang, Y and Nagarajaiah, S. (2013a). "Time-frequency blind source separation using independent component analysis for output-only modal identification of highly-damped structures." *ASCE Journal of Structural Engineering*, 139(10), 1780–1793.

Yang, Y. and Nagarajaiah, S. (2013b). "Blind identification of modal parameters in time domain based on complexity pursuit." *Earthquake Engineering & Structural Dynamics*, 42(13), 1885–1905.

Yuen, K-V. and Kuok, S-C. (2011). "Bayesian methods for updating dynamic models." *Applied Mechanics Review*, 64(1), 010802.

Yuen, K-V., Beck, J.L., and Katafygiotis, L. (2006) "Unified probabilistic approach for model updating and damage detection." *Journal of Applied Mechanics*, 73(4), 555–564.

Zheng, H. and Mita, A. (2008). "Damage indicator defined as distance between ARMA models for structural health monitoring." *Structural Control and Health Monitoring*, 15(7), 992–1005.

Zhou, Z., Sparling, B.F., Wegner, L.D. (2005). "Damage detection on a steel-free bridge deck using random vibration." *SPIE Conference on Nondestructive Evaluation and*

Health Monitoring of Aerospace Materials, Composites, and Civil Infrastructure IV, Bellingham, WA.

Zimmerman, D. C., Kim, H. M., Bartkowicz, T. J., and Kaouk, M. (2001). "Damage detection using expanded dynamic residuals." *Journal of Dynamic Systems, Measurement, and Control*, 123(4), 699–705.

CHAPTER 3

INFLUENCE OF THE CONSTRUCTION PROCESS AND NONSTRUCTURAL COMPONENTS ON THE MODAL PROPERTIES OF A FIVE-STORY BUILDING

3.1. Introduction

Development of finite element (FE) modeling and analysis tools and the advent of powerful and affordable computers have had a significant impact in the fields of structural and earthquake engineering. Nowadays, it is common and almost required in practice to analyze civil structures under different load cases using refined, albeit linear, three-dimensional FE models. However, professional judgment and experience of the engineers are not sufficient to ensure that the FE structural models developed are able to capture the actual behavior of the structure of interest when subjected to different types of loading, particularly earthquakes. Parameter and modeling uncertainties (e.g., material and geometric parameters, energy dissipation mechanisms) exist and affect the accuracy of the FE models developed to analyze structures subjected to dynamic loads.

Health monitoring and particularly system identification of civil structures has become an important field filling the gap between numerical models and actual behavior of structures. Estimation of the dynamic properties of structures using vibration data recorded in the field or from large-scale structural specimens in the laboratory under realistic conditions allows to calibrate numerical models of these structures (e.g., Brownjohn 2003, Ogiyama and Sato 2004, Jaishi and Ren 2005, Skolnik et al. 2006, Nayeri et al. 2008, Kanazawa et al. 2008, Moaveni et al. 2011). Moreover, results of structural identification can be used to (i) detect, locate, and quantify structural damage induced by extreme events (e.g., Farrar et al. 2001, Ramos et al. 2010, Moaveni et al. 2010,2011), (ii) design or analyze retrofit strategies (e.g., Mendoza et al. 1991, Kanazawa 2005, Lorenz 2006, Niousha and Motosaka 2007, Soyoz et al 2013,, and (iii) study the effects of environmental conditions on the dynamic properties of structures (e.g., Cornwell et al. 1999, Peeters and De Roeck 2001a, Sohn 2003, He at al. 2007).

Experimental modal analysis and operational modal analysis are the main procedures to identify the modal parameters (natural frequencies, equivalent damping ratios, and mode shapes) from recorded structural vibration data, information that can be used to improve and update numerical models of the structure of interest. Most of the studies conducted in this area were based on data collected from completed structures (e.g., Brownjohn 2003, Skolnik et al. 2006, Hong et al. 2009), while only a few have analyzed the variation of the dynamic properties of buildings during construction (e.g., Ventura and Schuster 1996, Memari et al. 1999, Ni et al. 2011, Nunez et al. 2013) and the effects of nonstructural components and systems (NCSs) on the dynamic properties (e.g., Kanazawa et al. 2008, Su et al. 2005, But and Omenzetter 2014, Devin and Fanning

2012). Based on previous studies, by following the construction process of a building, it is possible to validate numerical structural models used for design purposes and to control the quality of the construction. Furthermore, it has been shown that the effects of the NCSs should not be neglected because their dynamic interaction with the structure can influence significantly the dynamic properties of the complete (coupled structural and nonstructural) building system.

Most of the studies investigating the effect of the construction process and NCSs on the modal properties of structures have been conducted on real buildings; consequently, it was not possible to closely follow the construction process in order to disaggregate the effects of the construction process and NCSs on the "final" dynamic characteristics of the buildings. Also, these studies only considered output-only methods to estimate the modal properties, because it is difficult and expensive to perform forced vibration tests on real structures. As a result, previous studies have not been able to analyze in detail the effect of the amplitude of the excitation (or structural response) on the identified modal parameters. This is an important factor influencing the dynamic interaction between the structure and the NCSs. This interaction depends significantly on the level of kinematic and inertia interaction between the structure and the NCSs, which is directly related to the amplitude of the input excitation.

A shake table test program on a fully furnished full-scale building offers the unique opportunity to follow the construction process in detail and also to consider different sources and amplitudes of input excitations in the test protocol. This chapter focuses on a full-scale five-story reinforced concrete (RC) building specimen equipped with a wide range of NCSs and tested on the NEES-UCSD shake table in the period

August 2011 - May 2012. Structural responses from (i) daily ambient vibrations, (ii) free vibrations induced by impacts on the structure, and (iii) white noise base excitation tests performed at different amplitudes were recorded at different stages of construction and installation of the NCSs. The recorded output-only and input-output data were used to identify the dynamic characteristics (i.e., natural frequencies, equivalent damping ratios, and mode shapes) of the test specimen. A detailed supervision of the construction process and installation of the NCSs together with a comprehensive set of experimental data allows to study the evolution of the modal properties of the building specimen during construction and analyze the effect of NCSs on the modal properties of the system. The study presented in this chapter investigates the disaggregated effects of different construction activities and several NCSs on the natural frequencies, damping ratios, and mode shapes of the building specimen obtained from low-intensity excitation.

3.2. Description of specimen and construction process

3.2.1. Specimen

The test structure was a full-scale five-story cast-in-place RC building. The building had two bays in the longitudinal direction (direction of shaking) and one bay in the transverse direction, with plan dimensions of 6.60×11.00 m, respectively. The building had a floor-to-floor height of 4.27 m, a total height (measured from the top of the foundation to the top of the roof slab) of 21.34 m, and an estimated total weight of 3010 kN for the bare building structure and 4420 kN for the structure with all the NCSs, with both weights excluding the foundation which weighed 1870 kN. The lateral load

resisting system was provided by two identical one-bay special RC moment resisting frames. These frames were oriented east-west (direction of shaking) with one on the north face of the building and the other on the south face. The beams had a 0.30×0.71 m cross-section and their reinforcement, especially at the beam-column connection, varied in details from floor to floor for performance comparison purposes. All 0.66×0.46 m columns were reinforced with 6 #6 and 4 #9 longitudinal bars and a prefabricated transverse reinforcement grid. The floor system consisted of a 0.2 m thick concrete slab at all levels. There were two main openings on each floor slab to accommodate a steel stair assembly and a functioning elevator, each of which ran the full height of the building. Two 0.15 m thick transverse RC shear walls provided the support for the elevator guiderails. Detailed information about the structural system, nonstructural components and their design considerations can be found in Chen et al. (2013). Figure 3.1 shows schematic elevation and plan views of the test building.

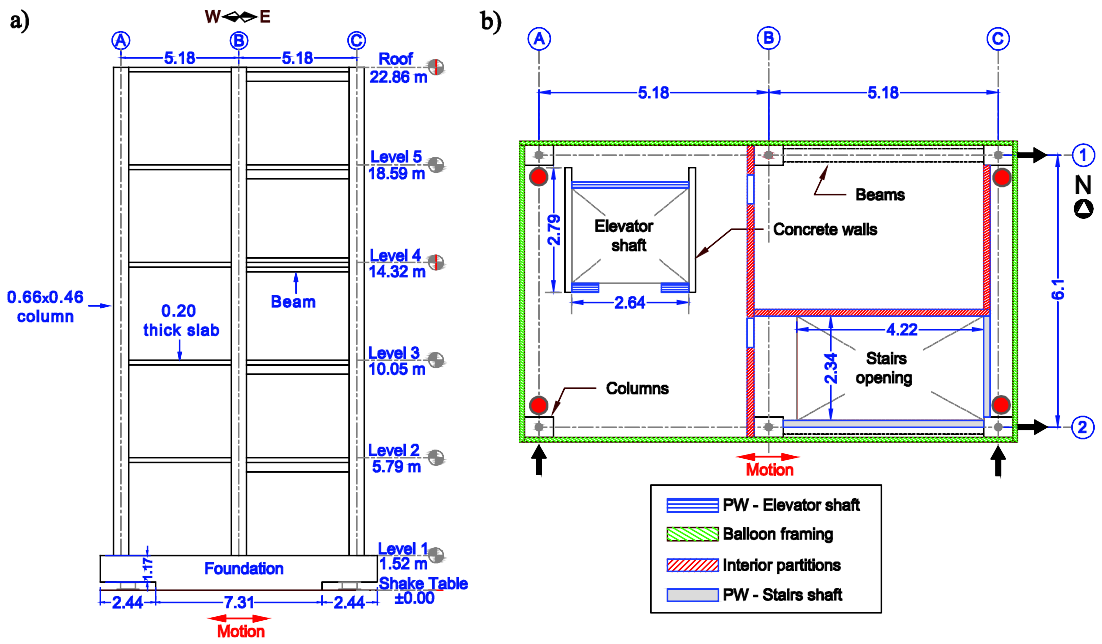

Figure 3.1: Test specimen: (a) South elevation, (b) Plan view of level 3 with temporary (black arrows) and final (red circles) accelerometer arrays (dimensions in m)

3.2.2. Construction process

The construction of the building began in May 2011 with the foundation. The foundation consisted of two 1.5 m thick post-tensioned beams running east-west connected with transverse beams and an interior slab. The foundation was completed in June 2011. Constructions proceed with the superstructure, which was built at a rate of one level every two to three weeks. The shoring system involved three adjacent floors, the main shoring was installed at the floor under construction, while reshores were placed at the two floors below and then removed five days after concrete was cast to allow sufficient strength gain. The bare building structure was completed on September 23, 2011. In parallel with the construction of the building, the installation of the stairs began on August 13 and was completed on October 11, 2011.

After completion of the bare building structure, installation of the NCSs started on October 13, 2011. Each level was equipped with special-purpose NCSs to support various types of occupancy. The first floor was designated as a utility floor, while the second floor was configured as a home office and a laboratory environment area, including anchored and unanchored equipments for seismic performance comparison purposes. The third floor housed two computer servers representing important electronic equipment commonly damaged during earthquakes. Levels four and five were designated as hospital floors, the fourth floor was configured as an intensive care unit (ICU) while the fifth floor represented a surgery suite. Also, partial mechanical, electrical, and plumbing subsystems were installed in the building. An electrical distribution system was required to support operation of the medical equipment, elevator, and lighting, while the plumbing system

supported the storm drain service, fire sprinklers, and HVAC (*heating, ventilation, and air conditioning*) unit. A fully-operational passenger elevator, a prefabricated steel stairs, a ceiling subsystem, and gypsum board partition walls were also installed in the building. The facade consisted of a light gauge metal stud balloon framing overlaid with synthetic stucco over the bottom three stories and precast concrete panels over the top two stories. Anchored to the roof were a penthouse, an air handling unit (AHU), and a water-filled cooling tower with a volume of approximately 1.25 m^3. The installation of all NCSs was completed on February 22, 2012. On March 2, 2012, four high-damping rubber isolators were installed below the four corners of the building, condition which remained until the end of the first phase of the seismic tests (May 1, 2012). Figure 3.2 shows the building specimen at different stages of construction.

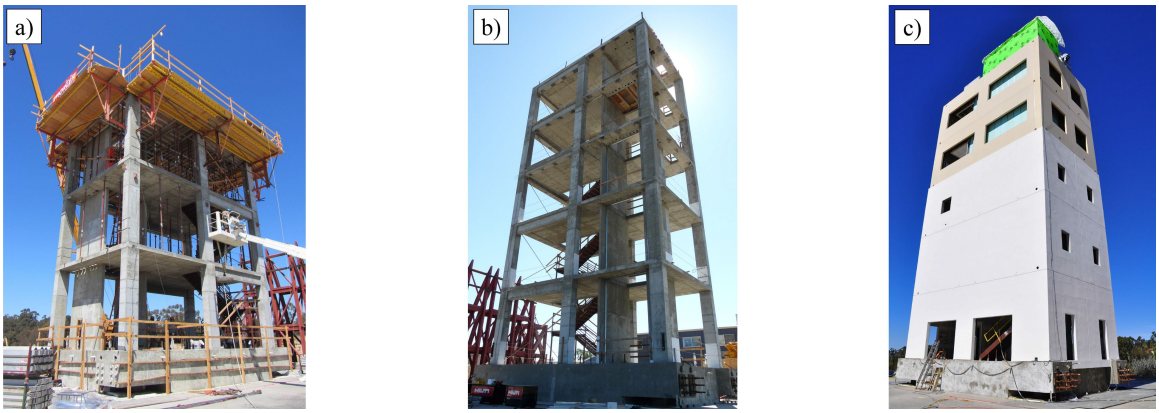

Figure 3.2: Test building at different stages during construction: (a) August 18, 2011 (SW corner), (b) October 12, 2011 (bare structure, NW corner), (c) February 23, 2012 (complete building, SE corner).

The installation of the exterior balloon framing (from Level 1 to Level 4, see Figure 3.1b) was performed between November 1 and December 7, 2011. This installation involved three phases: installation of vertical steel studs (November 1 to November 17, 2011), installation of angle clips (November 28 to November 30, 2011),

and installation of exterior wallboard (November 29 to December 7, 2011). The weight of the balloon framing was approximately 55 kN per story and the system consisted of continuous light gauge metal studs each connected with a clip, for lateral and vertical support, to each floor slab or beam over the bottom three stories. The exterior precast cladding covering the fourth and fifth stories was installed on December 19 and 20, 2011. The weight of each panel varied between 35 and 53 kN for a total weight of approximately 340 kN per story. The panels were connected to the building structure through a bearing plate at the bottom (for vertical support) and pin-connected to the slab or beam at the top by means of steel plates and horizontal steel rods (push-pull connections). Therefore, the precast cladding system was designed to have minimum contribution in the lateral stiffness of the building.

The main components of the elevator system contributing to the mass of the building were the counterweight and the cabin. The counterweight, which consisted of steel block weights, was gradually installed between January 17 and February 22, 2012, reaching a total weight of 16.2 kN. The cabin was installed on February 6 and 7, 2012, and it had a weight of 9.9 kN. The main roof-top mounted equipments, consisting of a cooling tower and an AHU, were installed on December 9 and December 13, 2011, respectively. The weight of the cooling tower, including its supporting system, was 18.1 kN (under empty condition) while the weight of the AHU was 6.7 kN. Also, a penthouse with a total weight of 25.5 kN (surrounding the roof slab stairs opening) was installed on the roof between November 18 and December 2, 2011.

The interior partition walls (PWs) were installed between December 5 and December 23, 2011, in the first three stories, and between January 9 and February 7,

2012, in the fourth and fifth stories. Vertical studs at top and bottom tracks were attached to the concrete with fasteners spaced at 0.61 m and the gypsum panels were attached to them using drilling screws also spaced at 0.61 m. The weight of the PW systems varied between 26 and 43 kN per floor. Figure 3.1b shows a plan view of Level 3 of the building. More information about the interior PWs is available in Wang et al. (2015).

3.3. Instrumentation array and dynamic tests

3.3.1. Instrumentation array

Before placing the concrete slab at the third level, a temporary accelerometer array was deployed in the structure on August 18, 2011, consisting of four translational sensors per floor (2 in the longitudinal and 2 in the transverse direction, see Figure 3.1b). The accelerometers were ±10 g MEMS Measurement Specialties model 4000A, with a frequency range DC–350 Hz and dynamic range of 76 dB. The data acquisition system consisted of 16-bit National Instruments PXI chassis (model SCXI 1520). Later, on April 9, 2012, a denser accelerometer array consisting of four triaxial accelerometers per floor (one at each corner) was deployed in the building. In addition, two triaxial accelerometers were installed on the platen of the shake table and one at the interior bottom of the foundation block (reaction mass) of the shake table. These accelerometers were force-balance Episensor, with amplitude range of ±4 g, frequency range DC–200 Hz and wide dynamic range of 155 dB. The data acquisition system consisted of Quanterra Q330 data loggers from Kinemetrics, Inc. Figure 3.1b shows the typical floor instrumentation for both accelerometer arrays. Also, linear potentiometers (~120), string potentiometers (~

50), strain gages (~50), load cells (~70), GPS antennas (5) and digital cameras (~87) were deployed in the test structure to record data during the seismic tests (Hutchinson et al. 2014).

In this study, to study the effects of the main construction activities and individual NCSs installed in the test specimen, the acceleration response of the building measured by the temporary accelerometer array was used to identify the modal dynamic properties of the test specimen at several stages of construction. The data were sampled at 240 Hz and the acceleration time series were detrended and filtered using a band-pass order 4 IIR Butterworth filter with cut-off frequencies at 0.25 and 25 Hz, frequency range containing all the vibration modes contributing noticeably to the dynamic response of the building.

3.3.2. Dynamic tests

Vibration data from more than 400 dynamic tests were recorded on the building during the period from August 2011 to May 2012. The dynamic tests consisted of ambient vibration, free vibration (shock-induced), and forced vibration tests (low-amplitude white noise, pulse-type, and seismic base excitations) using the NEES-UCSD shake table. During the construction of the specimen, 10 minutes of ambient vibration data were recorded daily and shock tests (using a truck tire) were performed on average once a week between August 18 and December 22, 2011. It is noted that the construction of the first two stories of the structure were completed prior to August 18, 2011, and no tests were performed during that period. Low-amplitude white noise base excitation tests were conducted at key stages of the construction process, i.e., on October 12, 2011 when the construction of the structural skeleton was finished (bare building structure), on

February 23, 2012 when the installation of all NCSs was completed (complete building), and on March 09, 2012 when the building was supported by seismic isolators. Also, before and after each seismic test, ambient vibration data were collected and white noise tests were conducted to investigate the effects of damage on the modal dynamic characteristics of the building system, which is the subject of another study (Astroza et al. 2015). Table 3.1 summarizes the recorded vibration data used in this study.

Table 3.1: Recorded vibration data used in this study.

Date	Description of the test	State of the system
Aug. 18 - Oct. 12, 2011	Daily 10min ambient vibrations	Under construction
Aug. 22 - Oct. 12, 2011	Weekly shock/impact tests	Under construction
Oct. 12, 2011	10min WN (1.0%g RMS) + 10min WN (1.5%g RMS)	Bare building structure
Oct. 13, 2011 - Feb. 23, 2012	Daily 10min ambient vibration	Installation of NCSs
Feb. 23, 2012	10min WN (1.0%g RMS) + 10min WN (1.5%g RMS)	Complete building

RMS: root-mean-

Figure 3.3 shows the time histories and Fourier amplitude spectra (FAS) of the total acceleration response recorded at the foundation and roof levels of the structure from ambient vibration, white noise, and shock tests conducted in October 2011. Regarding the shock tests, each time they were performed, different impact locations were considered in order to excite different modes. In general, the shocks were applied at two different heights (an intermediate and the highest constructed levels) of the specimen under construction and at four different locations in plan (center of north-south and east-west sides and south-east and south-west corners).

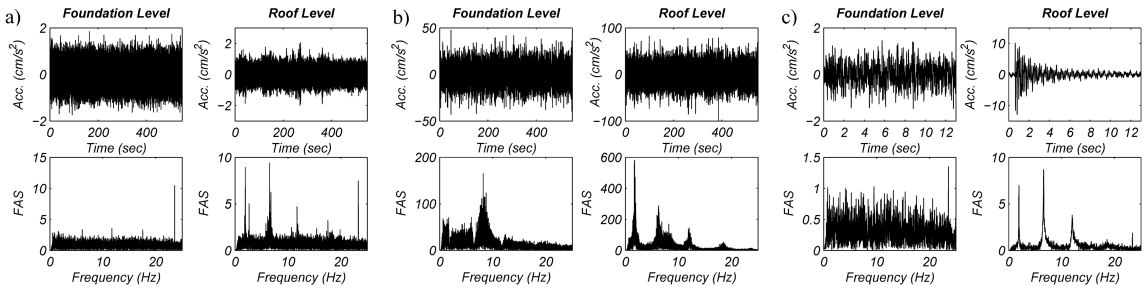

Figure 3.3: Time histories and Fourier amplitude spectra (FAS) of the total acceleration responses recorded at foundation and roof levels during (a) ambient vibration test (October 19, 2011), (b) white noise base excitation test (1.0%g RMS, October 12, 2012), and (c) shock-induced free vibration test (October 12, 2011).

The complete test protocol provided dynamic data to analyze the effects of the construction process, NCSs, and structural/non-structural damage on the modal dynamic properties of the building specimen. In the next sections, the system identification results obtained from the data collected between August 18, 2011 and February 23, 2012 are presented and analyzed to investigate the effects of the construction process and NCSs.

3.4. System identification methods used

To estimate the modal properties of the building specimen at different construction stages, three state-of-the-art output-only system identification methods, all assuming broad-band and uncorrelated random process excitation (i.e., input is a white noise process), were used with the ambient vibration data. The modal properties were identified using ten-minute long datasets of ambient vibration. The output-only methods used were the Data-Driven Stochastic Subspace Identification (SSI-DATA) (Van Overschee and De Moor 1996), the Multiple-Reference Natural Excitation Technique combined with Eigensystem Realization Algorithm (NExT-ERA) (Juang and Pappa 1985), and the Enhanced Frequency Domain Decomposition (EFDD) (Brinker et al.

2001a,b). For the low-amplitude white noise base excitation test data, in addition to the three abovementioned output-only methods, two input-output methods were employed. The input-output methods used were the Deterministic-Stochastic Subspace Identification (DSI) (Van Overschee and De Moor 1996) and the Observer/Kalman Filter Identification combined with Eigensystem Realization Algorithm (OKID-ERA) (Juang 1994). For each white noise base excitation test, one ten-minutes long dataset was used to estimate the modal parameters.

It is important to note that all the system identification methods used in this work assume a linear time-invariant dynamic model of the test specimen with all sources of energy dissipation represented by linear viscous damping, herein termed equivalent viscous damping. Consequently, the identified natural frequencies and damping ratios correspond to the modal parameters of an equivalent linear elastic model of the test structure. In the next sub-sections, a brief description of each method is provided.

3.4.1. Data-Driven Stochastic Subspace Identification (SSI-DATA)

SSI-DATA is a time-domain system identification method that extracts a linear state-space model (see Appendix A for details and derivations) of the system from output-only measurement data (Van Overschee and De Moor 1996). Contrary to the two-stage time-domain methods (such as SSI-COV or NExT-ERA), SSI-DATA does not require computing the covariance matrices of the data and it is numerically more robust because it does not need to square up the output data (Peeters and De Roeck 2001b). In addition, robust numerical techniques such as QR factorization, singular value decomposition, and least squares are involved in this method.

To reduce the computational demands of the identification process, the acceleration time series were resampled at 60 Hz. The output Hankel matrices were constructed using 25 block rows with the number of rows per block equal to the number of output channels (variable depending on the stage of construction) and 35,951 columns (making use of the entire 10 minutes of data decimated at 60 Hz). Stabilization diagrams were used for all system identification methods based on state-space representation (SSI-DATA, NExT-ERA, DSI, and OKID-ERA) to select the order of the identified model. Values suggested in the literature were used for the stability criteria of the modal parameters (e.g. Peeters and De Roeck 2001b):

$$\left|f_i - f_j\right| / f_j \le 1\% \qquad \left|\xi_i - \xi_j\right| / \xi_j \le 5\% \qquad \left(1\text{-}MAC_{\phi_i,\phi_j}\right)100 \le 2\% \qquad n_s \ge 6 \tag{3.1}$$

where f_i, ξ_i and f_j, ξ_j are the identified natural frequencies and damping ratios for models of consecutive orders, MAC_{ϕ_i,ϕ_j} is the modal assurance criterion (Allemang and Brown 1982) of a pair of corresponding modes shapes identified for models of consecutive orders, and ns denotes the number of consecutive times (as the model order is increased progressively by increments of 2) that an identified mode satisfies the triple stability criterion defined in Equation (3.1).

3.4.2. Multiple-Reference Natural Excitation Technique combined with Eigensystem Realization Algorithm (NExT-ERA)

The NExT is based on the fact that the theoretical cross-correlation function of the measured response along two different degrees of freedom of a structure subjected to broad-band excitation has the same analytical form as the free vibration response of the

structure (James et al. 1993). Once an estimation of the cross-correlation function is obtained for a given reference channel, the ERA method can be used to estimate the modal parameters. In order to avoid selecting a reference channel that may coincide with a modal node, a vector of reference channels can be used (He et al. 2009). In this study, the cross-correlation functions were computed through inverse Fourier transformation of the corresponding cross-power spectral density functions, which were estimated using Welch's method with a Hanning window of length 1/8 of the total length of the signal and 50% of overlap between windows. For the ERA method, the cross-correlation functions were downsampled to 60 Hz and used to construct Hankel matrices with 150 block rows (the number of rows per block was equal to the number of output channels, which varied depending on the stage of construction) and 150 columns (i.e., considering 150 time lag values).

3.4.3. Enhanced Frequency Domain Decomposition (EFDD)

The Frequency Domain Decomposition (FDD) method was introduced by Brincker et al. (2001a) and it corresponds to an extension of the peak-picking method. The EFDD method (Brinker et al. 2001b) estimates the modal properties of a system from the singular value decomposition of the cross-power spectral density matrix of the measured outputs, since the singular values can be interpreted as the auto-spectral densities of the modal coordinates and the singular vectors as the modes shapes. Taking the auto-spectral density back to the time domain by inverse Fourier transformation, the damping ratio and natural frequency can be determined from the resulting single-degree-of-freedom auto-correlation function (ACF). In the implementation of the EFDD method,

the measured acceleration time series were resampled at 80 Hz and the cross-power spectral density functions were estimated using Welch's method with a Hanning window of length 1/4 of the total length of the signal and 50% of overlap between windows.

3.4.4. Deterministic-Stochastic Subspace Identification (DSI)

The Deterministic-Stochastic Subspace Identification (DSI) method, a time-domain technique, was developed by Van Overschee and De Moor (1996). It considers a linear time-invariant dynamical system excited by external input and which includes both process and measurement noises. It extracts a linear state-space model of the system from a Hankel block matrix constructed from the input-output recorded data. Then, assuming that (i) the deterministic input and the process and measurement noises are uncorrelated, (ii) the deterministic input is persistently exciting, and (iii) the process and measurement noises are not identically zero, DSI estimates the matrices of the state-space model using the same numerical techniques as SSI DATA. In applying DSI to this study, the measured acceleration time histories were resampled at 60 Hz and the Hankel matrices were constructed using 15 block rows with 21 (1 input and 20 output channels) rows per block and 35,971 columns.

3.4.5. Observer/Kalman Filter Identification Combined with Eigensystem Realization Algorithm (OKID-ERA)

This time-domain method was developed by Juang et al. (1991). It introduces a feedback loop (observer) to make the identified system as stable as desired by introducing prescribed eigenvalues for the observer, in order to compute both the system

and observer Markov parameters from the input-output recorded data. Then, the state space model is estimated using the Markov parameters following the ERA method. Similarly to the previous method, the recorded acceleration time series were resampled at 60 Hz to reduce the computational burden. An output matrix of 20 (number of output channels) rows and 2000 columns (corresponding to 33 sec of data decimated at 60 Hz) and an input-output matrix of $r+(m+r)\,p=1+(20+1)250=5251$ rows (r = number of input channels, m = number of output channels, and p = integer such that $\mathbf{C}\bar{\mathbf{A}}^{k}\bar{\mathbf{B}}\approx\mathbf{0}$ for $k\geq p$, where $\bar{\mathbf{A}}$, $\bar{\mathbf{B}}$, and $\mathbf{C}$ denote the state, input, and output matrices of the system with the observer) and 2000 columns were constructed with the recorded input-output data of each white noise base excitation test.

3.5. Evolution of the Identified Modal Properties during Construction

Using the temporary accelerometer array showed in Figure 3.1a (black arrows), vibration response data of the building structure were recorded under ambient vibrations during its construction (August 18 – October 12, 2011) and under low-amplitude white noise base excitation tests performed on the building in its bare building structure condition (October 12, 2011). The effects of six main activities of the construction process (Table 3.2) were analyzed. The bottom row of Figure 3.4 shows the time evolution of the construction in terms of these six activities, while the first four rows of the same figure graph the temporal evolution of the natural frequencies and damping ratios of the first four modes of the structure identified using SSI-DATA, NExT-ERA, and EFDD during the construction process (August 18 to October 11, 2011). Clearly,

since the structure became more flexible as the construction progressed, the natural frequencies decreased with time.

Table 3.2: Main construction activities.

Name	Activity
A1	Formwork and shoring of slab
A2	Installation of steel reinforcement cage and placement of concrete slab
A3	Formwork of columns and walls
A4	Installation of steel reinforcement cage and placement of concrete walls and columns
A5	Shoring removal
A6	Installation of stairs

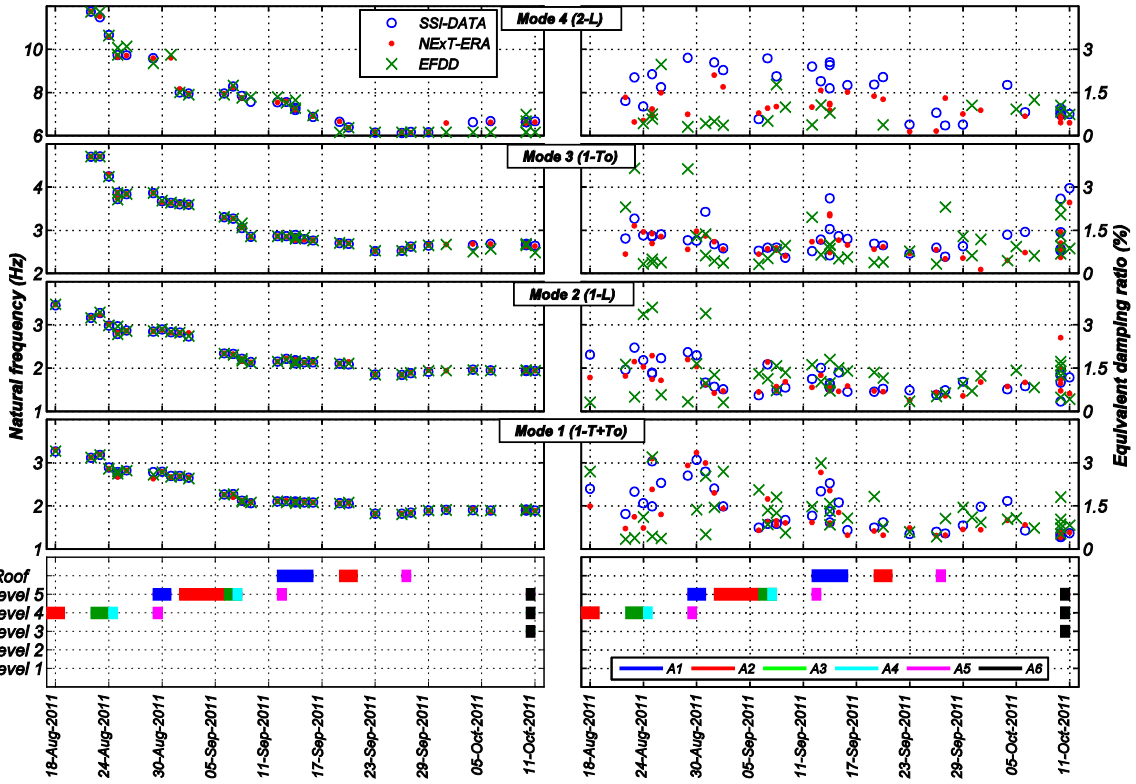

Figure 3.4: Temporal evolution of the natural frequencies and damping ratios of the first four modes identified with ambient vibration data during construction.

The actions inducing the most abrupt changes in the natural frequencies were the placement of concrete of the fifth floor and roof slabs (A2) (September 6 and September 22, 2011, respectively) and the placement of concrete of the columns and shear walls (A4) at levels four and five (August 24 and September 8, 2011, respectively). This is due

to the fact that both activities significantly increased the mass of the building without changing its lateral stiffness and therefore decreased the natural frequencies. The magnitude of the jumps in the variation of the natural frequencies due to placement of concrete reduces as construction progresses, since the added mass becomes progressively lower as compared to the total mass of the built portion of the building. On the other hand, as expected, the effect of formwork and shoring (A1 and A3) is negligible because their masses were negligible compared to the total mass of the structure and they did not contribute to the lateral stiffness of the building. Similarly, stair installation (A6) and shoring removal (A5) did not induce any noticeable change in the dynamic properties of the building due to the same reasons as for activities A1 and A3. Finally, it is observed that, from September 26 to October 10, 2011, the natural frequencies gradually increased (1.82 to 1.92, 1.84 to 1.94, 2.52 to 2.68, and 6.12 to 6.61 Hz for the first, second, third, and fourth modes, respectively), which is most likely due to the hardening of concrete (during the curing process) over time and corresponding stiffness gain. This effect has also been detected in previous studies (Kanazawa et al. 2008, Tian and Yi 2008). Table 3.3 summarizes the changes in natural frequencies due to each of the construction activities inducing important changes in the identified natural frequencies.

Regarding the equivalent damping ratios, their values mostly lie in the range 0.5-2.5% for all modes identified using ambient vibration data, which is consistent with previous studies (e.g., Skolnik et al. 2006, Nayeri et al. 2008, Moaveni et al. 2011). However, as well known, the scatter of the damping estimates is inherently significantly higher than that of the corresponding natural frequencies, thus making it difficult to draw any conclusions about the effect of the construction activities on the identified modal

damping ratios. Also, it is observed that the agreement between the damping ratios identified from different methods is better for the lower than for the higher modes. Furthermore, the damping ratios estimated by EFDD are most often lower than those identified using NExT-ERA and SSI-DATA, and more so for the modes with a relatively low contribution to the measured response (here higher modes), which is consistent with previous studies (e.g., He et al. 2009, Antonacci et al. 2011).

Table 3.3: Natural frequencies identified using SSI-DATA with ambient vibration data before and after major construction activities.

Activity	Date		Natural frequency (Hz)			
			Mode 1 1-T+To	Mode 2 1-L	Mode 3 1-To	Mode 4 2-L
Level 4 - Placement of concrete of columns and walls	08/23/11	Before	3.18	3.27	4.71	11.48
	08/25/11	After	2.74	2.80	3.73	9.63
Level 5 - Placement of concrete of slab	09/01/11	Before	2.69	2.82	3.60	8.00
	09/07/11	After	2.27	2.33	3.27	7.94
Level 5 - Placement of concrete of columns and walls	09/07/11	Before	2.27	2.33	3.27	7.94
	09/09/11	After	2.06	2.14	2.85	7.56
Roof - Placement of concrete of slab	09/16/11	Before	2.08	2.13	2.76	6.87
	09/23/11	After	1.82	1.85	2.51	6.14
Hardening of concrete	09/26/11	Before	1.82	1.84	2.52	6.12
	10/10/11	After	1.92	1.94	2.68	6.61

Figure 3.5 shows the evolution of the first four mode shapes identified using NExT-ERA with ambient vibration data after the concrete of slabs of the second, third, fourth, and roof levels was placed. During the entire construction process, the first, second, third, and fourth modes corresponded to the first transverse-torsional (1-T+To), first longitudinal (1-L), first torsional (1-To), and second longitudinal (2-L) modes, respectively. The identified modes remained basically with the same shapes and proportions during the construction process. Since the mode shapes identified with the system identification methods used in this work are complex-valued, the real-valued mode approximations were computed using the method proposed by Imregun and Ewins

(1993), which obtains a real-valued mode by maximizing the MAC value between the complex mode and its corresponding realized real mode.

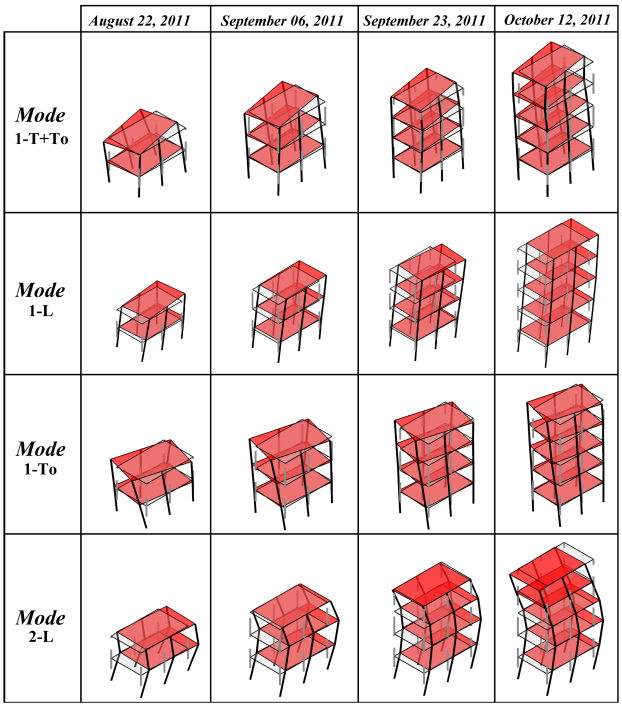

Figure 3.5: Evolution of the first four mode shapes identified using NExT-ERA with ambient vibration data during construction.

3.6. System Identification of the Bare Building Structure

A first set of dynamic tests was performed using the shake table on the building specimen in its bare condition on August 12, 2011. The low-amplitude banded (0.25 to 25 Hz) white noise acceleration consisted of two 10 minute long signals, with nominal root-mean-square (RMS) amplitudes of 1.0 and 1.5% g, respectively. The modal properties of the bare building structure were estimated using the output-only system identification methods described previously, i.e., SSI-DATA, NExT-ERA, and EFDD. The methods were applied to the vibration response data from white noise base excitation tests and ambient vibrations, the latter recorded before and after the shake table tests.

Additionally, modal parameters were also identified using the input-output methods with the vibration data from the white noise base excitation tests.

Table 3.4 reports the natural frequencies and equivalent damping ratios for ten modes of the bare building structure identified using five methods from the white noise base excitation test data with RMS = 1.0 and 1.5% g. Table 3.4 also provides the sample mean and coefficient-of-variation (c.o.v.) of the modal parameter estimates across the five methods. The natural frequencies identified by different methods for the same level of excitation are in very good agreement, with maximum and average relative differences of 4.3% and 0.9%, respectively. The identified damping ratios exhibit significantly higher method-to-method variability (which is consistent with previous studies, e.g., Ndambi et al. 2000, Moaveni et al. 2011), with maximum and average absolute relative differences of 121.3% and 31.3%, respectively. These relative differences are computed taking the mean value over all the SID methods as the reference value.

Using ambient vibration data, the identified first and second modes correspond to the 1-T+To and 1-L modes, respectively, while this order changes when using white noise base excitation test data. This mode-crossing phenomenon is caused by the reduction in stiffness of the building in its longitudinal direction (direction of shake table motion) during the white noise base excitation test. Therefore, the natural frequency of the first longitudinal mode to become lower than the natural frequency of the first coupled transverse-torsional mode. It is noticed that the input-output methods provide consistently lower estimates of damping than the output-only methods (excluding EFDD which typically produces low values of damping as observed earlier), especially for the first mode of vibration.

The relative differences (in %) between natural frequencies identified from vibration data due to white noise base excitation with RMS = 1.5% g and RMS = 1.0% g, as well as the sample means and coefficients of variation, are reported in Table 3.5 for the five system identification methods used. The identified natural frequencies decrease as the amplitude of the excitation increases from RMS = 1.0% g to RMS = 1.5% g. Despite these differences are not high (less than 3.5% on average), they clearly show the effect of concrete cracking and the consequent loss of stiffness during the white noise base excitation tests.

Table 3.4: Natural frequencies and damping ratios of the bare building structure identified from white noise base excitation test data.

		Natural frequency (Hz)							Equivalent damping ratio (%)						
	Mode	SSI-DATA	NExT-ERA	EFDD	DSI	OKID-ERA	Mean	c.o.v. (%)	SSI-DATA	NExT-ERA	EFDD	DSI	OKID-ERA	Mean	c.o.v. (%)
White Noise RMS = 1.0%g	1 (1-L)	1.82	1.83	1.84	1.87	1.86	1.84	1.0	5.16	5.80	2.22	1.13	3.36	3.53	49.5
	2 (1-T+To)	1.88	1.87	1.95	1.90	1.90	1.90	1.4	1.30	1.44	2.74	0.78	1.36	1.52	42.9
	3 (1-To)	2.63	2.63	2.64	2.63	2.63	2.63	0.2	0.93	1.02	0.44	0.97	1.42	0.96	32.8
	4 (2-L)	6.29	6.29	6.35	6.51	6.34	6.36	1.3	3.77	2.74	2.48	1.00	1.08	2.21	47.5
	5 (2-L+To)	6.43	6.32	6.80	-	6.53	6.52	2.7	1.11	0.94	2.42	-	1.07	1.38	43.3
	6 (2-To)	10.67	10.68	10.99	10.69	10.89	10.78	1.2	1.04	1.81	0.77	1.62	2.66	1.58	41.8
	7 (3-L)	12.22	12.20	12.15	12.00	12.00	12.11	0.8	1.52	1.70	1.28	1.03	1.04	1.31	20.1
	8 (3-To)	13.53	13.39	13.98	13.45	13.47	13.56	1.6	0.75	0.27	1.39	0.89	0.52	0.76	49.3
	9 (4-L)	18.59	18.64	18.82	18.49	18.64	18.64	0.6	2.34	2.02	2.18	1.64	1.45	1.93	17.3
	10 (5-L)	23.19	23.55	23.29	23.44	23.29	23.35	0.5	1.65	2.16	0.85	1.81	0.57	1.41	42.6
White Noise RMS = 1.5%g	1 (1-L)	1.75	1.73	1.76	1.83	1.83	1.78	2.4	6.32	3.76	5.15	1.39	3.47	4.02	41.5
	2 (1-T+To)	1.89	1.87	1.86	1.89	1.88	1.88	0.6	1.29	1.07	3.94	1.16	1.44	1.78	61.0
	3 (1-To)	2.60	2.62	2.62	2.61	2.60	2.61	0.3	1.06	1.33	0.59	1.10	1.30	1.08	24.8
	4 (2-L)	6.21	6.05	6.23	6.38	6.28	6.23	1.7	3.84	1.61	1.81	0.88	1.18	1.86	55.8
	5 (2-L+To)	6.40	6.17	6.36	6.45	6.42	6.36	1.6	0.77	2.82	2.45	0.99	0.59	1.52	60.6
	6 (2-To)	10.64	10.61	10.67	10.61	10.79	10.66	0.6	2.37	1.87	1.07	1.88	3.18	2.07	33.4
	7 (3-L)	12.11	12.12	12.39	11.79	11.93	12.07	1.7	2.70	2.87	1.26	2.33	2.06	2.24	25.4
	8 (3-To)	13.48	-	13.33	13.43	-	13.42	0.5	0.75	-	0.71	0.66	-	0.71	5.3
	9 (4-L)	18.46	18.51	18.70	18.25	18.29	18.44	0.9	2.13	1.59	2.97	1.61	1.63	1.99	26.8
	10 (5-L)	23.19	22.92	23.05	23.00	23.14	23.06	0.4	1.48	1.72	1.87	1.38	1.28	1.55	14.1

L: longitudinal / T: transverse / To: torsional

Table 3.5: Relative differences (in %) between natural frequencies of the bare building structure identified from white noise base excitation test data with RMS = 1.5% g and RMS = 1.0% g (used as reference).

Mode	SSI-DATA	NExT-ERA	EFDD	DSI	OKID-ERA	Mean (%)	c.o.v. (%)
1 (1-L)	-3.8	-5.5	-4.4	-2.1	-1.6	**-3.5**	**41.0**
2 (1-T+To)	0.5	0.0	-4.5	-0.5	-1.1	**-1.1**	**161.5**
3 (1-To)	-1.1	-0.4	-0.9	-0.9	-1.1	**-0.9**	**30.8**
4 (2-L)	-1.3	-3.8	-1.8	-2.0	-0.9	**-2.0**	**50.6**
5 (2-L+To)	-0.5	-2.4	-6.5	-	-1.7	**-2.7**	**82.0**
6 (2-To)	-0.3	-0.7	-2.9	-0.7	-0.9	**-1.1**	**84.8**
7 (3-L)	-0.9	-0.7	1.9	-1.7	-0.6	**-0.4**	**318.9**
8 (3-To)	-0.4	-	-4.6	-0.1	-	**-1.7**	**121.0**
9 (4-L)	-0.7	-0.7	-0.6	-1.3	-1.9	**-1.0**	**46.0**
10 (5-L)	-0.0	-2.7	-1.0	-1.9	-0.6	**-1.2**	**75.3**

The loss of stiffness during white noise base excitation tests is confirmed by comparing in Table 3.6 the natural frequencies identified from ambient vibration data recorded before and after the white noise tests. The natural frequencies identified using ambient vibrations before and after the white noise tests are practically the same, but are higher than their counterparts identified during the white noise base excitation tests. Additionally, the first two modes cross again, and the order of the modes identified before the white noise tests is recovered. This indicates that the concrete members cracked during the white noise tests; however, the amplitude of the ambient vibrations is small and not sufficient to re-open (a large majority of) the cracks, which remained closed due to gravity effects. Moreover, by comparing the damping ratios identified using ambient vibration and white noise base excitation data (Figure 3.6), it is observed that the identified damping ratios of the longitudinal modes (1-L and 2-L) increase as the amplitude of the excitation increases, while the identified damping ratios of other modes do not experience much variation. This is due to the fact that during the white noise base

excitation tests, more hysteretic energy dissipation is identified as equivalent damping ratios of the modes in the direction of the shake table excitation.

Table 3.6: Natural frequencies (Hz) of the bare building structure identified with ambient vibration data recorded before and after white noise base excitation tests.

Mode	Before white noise tests (October 12, 2011)			After white noise tests (October 13, 2011)		
	SSI-DATA	NExT-ERA	EFDD	SSI-DATA	NExT-ERA	EFDD
1 (1-L)	1.91	1.90	1.93	1.90	1.92	1.92
2 (1-T+To)	1.89	1.89	1.92	1.88	1.88	1.91
3 (1-To)	2.66	2.68	2.73	2.63	2.63	2.72
4 (2-L)	6.36	6.36	6.39	6.16	6.15	6.18
5 (2-L+To)	6.55	6.59	6.71	6.53	6.49	6.65
6 (2-To)	10.83	10.84	11.07	10.77	10.73	10.85
7 (3-L)	12.01	12.07	12.05	11.97	11.70	11.71
8 (3-To)	13.43	13.46	13.68	13.63	13.61	14.12
9 (4-L)	18.96	18.75	18.82	18.40	18.73	18.82
10 (5-L)	24.19	23.30	23.29	23.76	23.50	23.93

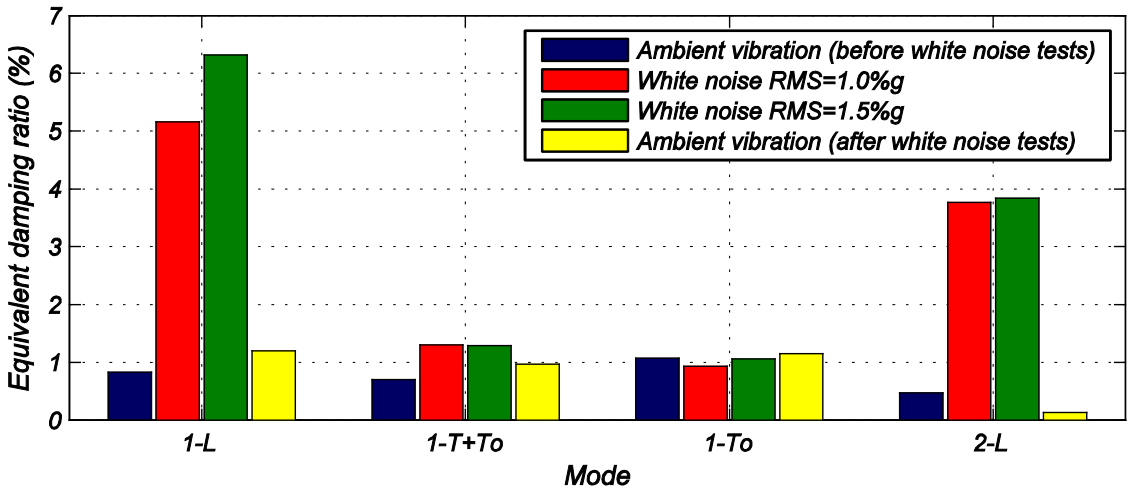

Figure 3.6: Equivalent damping ratios of the bare building structure identified using SSI-DATA with ambient vibration (recorded before and after white noise tests) and white noise base excitation data.

Figure 3.7 shows the mode shapes identified using NExT-ERA based on the first white noise base excitation test data (RMS = 1.0% g). These modes correspond to the first five longitudinal (1-L, 2-L, 3-L, 4-L, and 5-L), the first two coupled translational-torsional (1-T+To, 2-L+To), and the first three torsional (1-To, 2-To, and 3-To) modes.

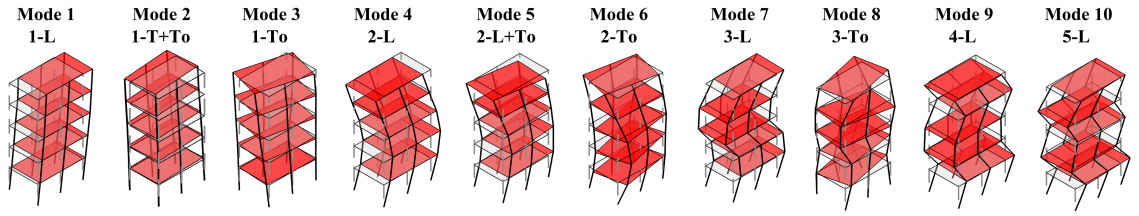

Figure 3.7: Mode shapes of the bare building structure identified from white noise base excitation test data (RMS = 1.0% g) using NExT-ERA.

The polar plot representation of the identified mode shapes (Figure 3.8) informs about the level of non-classical damping in the identified modes. Most of the identified modes are estimated as almost purely classically damped, since all the vectors in their polar plot are close to collinear. However, modes 1-T+To, 2-L+To, and 5-L are estimated with a significant level of non-classical damping. It is worth mentioning that estimation errors (due to measurement noise, modeling errors, etc.) can introduce non-classical damping characteristics in the identification of a classically damped mode.

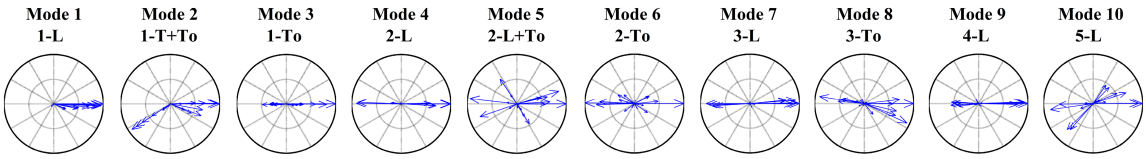

Figure 3.8: Polar plots of complex mode shapes of the bare building structure identified using OKID-ERA from RMS = 1.0% g white noise base excitation test data.

In order to compare the mode shapes identified using the five different methods, Figure 3.9 shows the MAC values between identified mode shapes. High MAC values (close to one) indicate that the mode shapes identified using different methods are in very good agreement. It is noticed that the MAC values between modes 4 (2-L) and 5 (2-L+To) are significant, reaching values around 0.5. This is most likely due to the fact that these two modes are dominated by their longitudinal components and they differ primarily in their torsional components (see Figure 3.7).

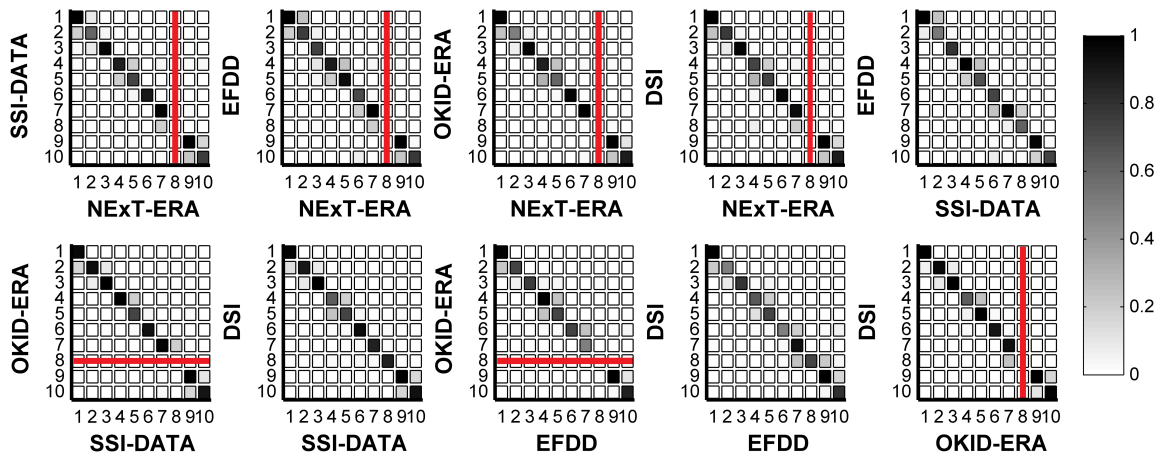

Figure 3.9: MAC values between the mode shapes of the bare building structure identified using five different methods from RMS = 1.5% g white noise base excitation test data.

The modal parameters were also estimated with the shock-induced free vibration data using the ERA method. As explained in Section 3.3.2, between eight and eighteen shocks tests were performed during each day of testing in order to excite as many modes as possible. Table 3.7 reports the natural frequencies and damping ratios of the bare building structure identified using the free vibration data recorded before the white noise base excitation tests. The natural frequencies are very similar to those identified using ambient vibration data (see Table 3.6), while the damping ratios are between the values estimated using ambient vibration and white noise base excitation test data (see Table 3.4 and Table 3.6). As observed from Figure 3.3, the amplitude of the shock-induced maximum acceleration response lies between the RMS amplitude of the acceleration response from the ambient vibration and WN base excitation tests, respectively.

Table 3.7: Natural frequencies and damping ratios of the bare building structure identified from shock-induced free vibration data.

Mode	Natural frequency (Hz)	Damping ratio (%)
1 (1-L)	1.92	4.15
2 (1-T+To)	1.89	1.07
3 (1-To)	2.64	1.65
4 (2-L)	6.37	0.77
5 (2-L+To)	6.63	1.12
6 (2-To)	10.93	1.75
7 (3-L)	12.00	1.08
8 (3-To)	13.51	2.21
9 (4-L)	18.38	1.93
10 (5-L)	24.14	1.56

3.7. Effects of Nonstructural Components

During the installation of the NCSs, daily ambient vibration data were recorded. Additionally, low-amplitude white noise base excitation tests were conducted when the building, including all the NCSs, was completed on February 23, 2012. Figure 3.10 presents the evolution of the natural frequencies and damping ratios of the first three modes of the building identified using the SSI-DATA, NExT-ERA, and EFDD methods and ambient vibration data during the period of installation of the NCSs, i.e., October 13, 2011, to February 22, 2012. The bottom panels show the Gantt chart with the activities regarding the installation of the main NCSs defined in Table 3.8.

Figure 3.10 shows that there is a good agreement between the natural frequencies identified using SSI-DATA, NExT-ERA, and EFDD, while the identified damping ratios, ranging between 0.4 and 2.0%, exhibit a much higher method-to-method variability. As already mentioned, the damping ratios estimated by EFDD are most often lower than those identified using NExT-ERA and SSI-DATA.

Table 3.8: Main NCSs installed in the building.

Name	NCSs	Name	NCSs
C1	Partition walls (elevator shaft)	C9	Precast cladding (levels 4 and 5)
C2	Partition walls (stair shaft: levels 1 to 3)	C10	Elevator counterweight and rails
C3	Partition walls (stair shaft: levels 4 and 5)	C11	Interior partitions (levels 4 and 5)
C4	Balloon framing	C12	Ceilings
C5	Penthouse	C13	Sprinkler system (level 5)
C6	Interior partitions (levels 1 to 3)	C14	Roof and gas pipes (level 4)
C7	Cooling tower	C15	Contents (levels 2, 4 and 5)
C8	AHU	C16	Elevator cabin

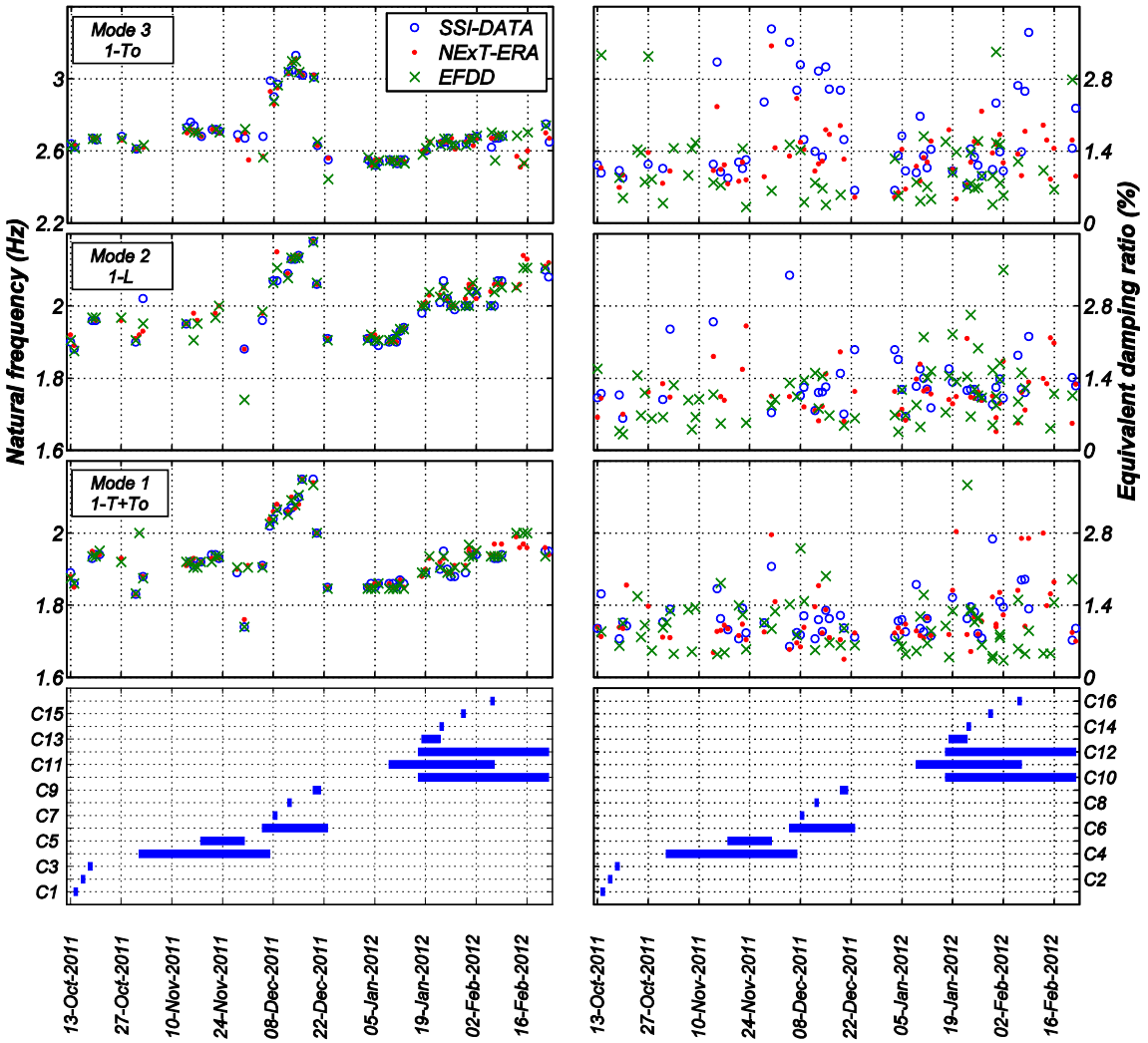

Figure 3.10: Evolution of the natural frequencies and damping ratios of the first three modes identified during installation of the main NCSs.

The influence of the partition walls on the lateral stiffness of the building can be observed from the variation of the identified modal frequencies during the installation of

NCSs. Due to the installation of partition walls around the elevator shaft (C1) and the stair shaft (C2 and C3) between October 13 and October 21, 2011, the first, second, and third identified natural frequencies increased from 1.88 to 1.94 Hz, 1.90 to 1.96 Hz, and 2.63 to 2.67 Hz, respectively. This indicates that C1 to C3 increase the initial lateral stiffness of the building by about 6%. Later, between December 5 and December 19, 2011, the natural frequencies of the first three modes increased from 1.91 to 2.10 Hz, 1.96 to 2.15 Hz, and 2.68 to 3.01 Hz, respectively, as a result of the installation of the interior partitions on the first, second, and third levels (C6). Within the same time window, the roof-mounted equipment, i.e., cooling tower (C7) and AHU (C8), was installed, but the added stiffness of the partition walls overshadowed the effect of the added mass due to the roof-mounted equipment and the partition walls, and the first three natural frequencies increased. This indicates that interior partition walls on the bottom three floors further increase the initial lateral stiffness of the building by approximately 20%. Finally, from January 10 to February 10, 2012, these natural frequencies gradually increased due to the installation of the partition walls on the fourth and fifth levels (C11). During this time window, the effect of the added mass contributed by the elevator counterweight and rails (C10), pipes (C14), new partition walls and building contents (C15) was more than compensated by the stiffening effect of the new partition walls. Furthermore, it appears from the RHS of Figure 3.10, with special attention to C1-C3, C6 and C11, that the partition walls also slightly increase the identified equivalent viscous damping ratios of the first three modes. Similar results have been reported in previous studies (e.g., Kanazawa et al. 2008, Devin and Fanning 2012). Comparison of the damping ratios identified for the bare structure (see RHS of Figure 3.4) and the complete

building (see RHS of Figure 3.10) indicates that the average damping ratios of the first three modes increased from 0% (1-To mode) to 40% (1-T+To mode) due to the NCSs. However, it is noteworthy that the modal damping coefficients $C_n = 2\xi_n \omega_n M_n$ also increase from the bare structure to the complete building through the increase of the modal mass M_n and natural frequency ω_n of the dominant modes.

Between December 19 and December 20, 2011, the first three modal frequencies decreased from 2.15 to 2.00 Hz, 2.18 to 2.06 Hz, and 3.01 to 2.63 Hz, respectively, due to the placement of the precast concrete cladding panels (C9) on the south and west faces of the building at the fourth and fifth levels. From December 20 to December 22, 2011, the same frequencies further decreased from 2.00 to 1.85 Hz, 2.06 to 1.91 Hz, and 2.63 to 2.55 Hz, respectively, when the precast concrete cladding panels (C9) on the north and east building facades were installed. As mentioned in Section 3.2.2, the precast concrete cladding panels mainly added mass to the building system. However, they did not contribute significantly to the lateral stiffness of the building due to their sliding connections (for in-plane motions) at the top. The system identification results also show that the addition of the balloon framing (C4) between November 2 and November 23, 2011, moderately increased the first three modes natural frequencies from 1.88 to 1.93 Hz, 1.93 to 2.00 Hz, and 2.62 to 2.70 Hz, respectively, thus indicating that the stiffening effect of the relatively light balloon framing dominated its inertial effect. Installation of the ceilings (C12), penthouse (C5), and elevator cabin (C16) did not induce any noticeable effects on the modal properties of the building or their effects were negligible compared to those induced by other NCSs installed at the same time.

As a general trend during the entire period of installation of the NCSs, it can be observed that the damping ratios tend to slightly increase over time, but this trend is hidden by the large variability (estimation uncertainty) of the identified damping ratios. Most of this additional source of damping is most likely produced by the kinematic interaction between some NCSs and the structural skeleton. It is worth recalling that since the underlying mathematical model of the structure assumed by the system identification methods used herein only considers linear viscous damping, all actual sources of energy dissipation of the building structure are identified as equivalent linear viscous damping ratios.

3.8. System Identification of the Complete Building

After all the NCSs were installed in the building (complete building), a second set of dynamic tests using the shake table was performed on February 23, 2012. The same sequence of two banded (0.25 to 25.00 Hz) white noise base excitation tests (RMS = 1.0% g and 1.5% g) was applied three times to the complete building considering different positions of the elevator cabin. In the first configuration, the elevator cabin and counterweight were located at the bottom and top levels of the building, respectively. In the second configuration, the cabin and counterweight were located at the same level (at mid-height of story 3) in order to concentrate the mass of the elevator system. Finally, in the third configuration, the cabin and counterweight were located at the top and bottom levels of the building, respectively. The modal parameters were estimated using the output-only and input-output methods with the recorded data obtained from the white

noise base excitation tests. Additionally, output-only methods were used with the ambient vibration data recorded before and after the shake table white noise tests.

Table 3.9 shows the natural frequencies and damping ratios for ten modes of the complete building structure with elevator under configuration 1 (counterweight at the top of the building) identified using the white noise base excitation test data. It is important to note that the identification results obtained for the other two configurations of the elevator system do not differ significantly from those for configuration 1, with differences less than 3% for the natural frequencies and less than 15% for the damping ratios. Consequently, it can be concluded that the position of the elevator does not have any important effect on the modal properties of the first ten modes of the complete building.

From Table 3.4 and Table 3.9, it is observed that the natural frequencies of modes 1-L, 1-T+To, 1-To, 2-To, 3-L, and 3-To decrease by 1% to 9% from the bare building structure to the complete building, while the reverse is true for modes 2-L, 2-L+To, 4-L, and 5-L as their natural frequencies increase by 1% to 18%. This observation applies for both levels of white noise base excitation (RMS = 1.0% g and 1.5% g). On the other hand, the estimated damping ratios increase from the bare building structure to the complete building for all the modes identified, with increments ranging from 15% to 191%. These results provide a near real-world example on the effects of the NCSs on the modal properties of a building. First, the additional stiffness and masses provided by the NCSs change, increasing or decreasing, the modal frequencies of the bare building structure, and second, the NCSs increase the equivalent modal damping ratios of the bare building structure, due to the additional sources of energy dissipation provided by the

NCSs themselves and the kinematic interaction between the NCSs and the supporting structure.

Table 3.9: Natural frequencies and damping ratios of the complete building (configuration 1) identified from white noise base excitation test data.

		Natural frequency (Hz)							Equivalent damping ratio (%)						
	Mode	SSI-DATA	NExT-ERA	EFDD	DSI	OKID-ERA	Mean	c.o.v. (%)	SSI-DATA	NExT-ERA	EFDD	DSI	OKID-ERA	Mean	c.o.v. (%)
White Noise RMS = 1.0%g	1 (1-L)	1.74	1.72	1.71	1.82	1.83	1.76	2.8	4.94	4.22	4.15	4.58	4.17	4.41	7.0
	2 (1-T+To)	1.85	1.90	1.86	1.86	1.89	1.87	1.1	3.55	1.54	4.24	3.04	3.73	3.22	28.7
	3 (1-To)	2.52	2.52	2.57	2.52	2.52	2.53	0.7	2.34	2.54	0.99	2.82	3.52	2.44	34.0
	4 (2-L)	6.93	7.04	7.08	7.00	6.98	7.01	0.7	7.75	0.76	1.63	4.35	4.62	3.82	64.6
	5 (2-L+To)	7.17	8.00	7.69	7.93	-	7.70	4.2	0.80	1.11	3.25	5.67	-	2.71	72.2
	6 (2-To)	10.38	10.11	-	-	-	10.25	1.3	2.30	2.39	-	-	-	2.35	1.9
	7 (3-L)	11.50	11.77	12.05	11.68	11.57	11.71	1.7	1.83	4.23	1.98	4.89	6.17	3.82	44.1
	8 (3-To)	12.52	12.76	-	12.62	-	12.63	0.8	1.08	0.77	-	1.62	-	1.16	30.4
	9 (4-L)	18.81	18.72	18.60	18.68	19.42	18.85	1.6	7.50	3.37	2.08	3.36	2.44	3.75	51.8
	10 (5-L)	23.60	23.62	24.00	23.69	24.44	23.87	1.3	5.23	6.51	1.06	3.63	0.52	3.39	68.4
White Noise RMS = 1.5%g	1 (1-L)	1.55	1.58	1.58	1.71	1.70	1.62	4.1	6.28	6.04	5.95	4.36	5.07	5.54	13.0
	2 (1-T+To)	1.81	1.81	1.82	1.81	1.83	1.82	0.4	4.17	3.38	4.66	3.81	1.19	3.44	34.9
	3 (1-To)	2.51	2.52	2.52	2.46	2.39	2.48	2.0	2.81	2.04	2.65	3.68	2.55	2.75	19.4
	4 (2-L)	6.68	6.81	6.75	6.74	6.79	6.75	0.7	2.28	1.13	2.46	4.13	4.90	2.98	45.5
	5 (2-L+To)	7.25	6.94	7.22	7.20	7.09	7.14	1.6	0.77	0.30	3.05	1.90	2.90	1.78	61.9
	6 (2-To)	9.82	-	-	9.94	9.99	9.92	0.7	2.50	-	-	3.76	0.88	2.38	49.5
	7 (3-L)	11.63	11.92	11.69	11.38	11.64	11.65	1.5	8.04	1.82	1.92	3.26	2.91	3.59	63.9
	8 (3-To)	12.66	12.62	-	12.56	12.35	12.55	1.0	0.85	0.20	-	0.81	0.67	0.63	40.9
	9 (4-L)	19.22	19.12	19.02	18.66	19.25	19.05	1.1	4.84	2.73	1.50	7.18	8.09	4.87	51.7
	10 (5-L)	23.52	23.50	23.59	23.31	23.59	23.50	0.4	3.71	4.21	1.98	3.37	1.91	3.04	30.7

L: longitudinal / T: transverse / To: torsional

Similar observations to those for the bare building structure can be made for the complete building. First, it is noticed that the identified natural frequencies decrease as the amplitude of the excitation increases from RMS = 1.0% g to 1.5% g as shown in Table 3.10 (analog of Table 3.5 for the bare building structure). The reduction is higher than for the bare building structure, reaching almost 8% for the first mode (on average), versus 3.5% for the bare building structure. This is due to both cracking in the concrete

and change in the significant stiffness contribution of the NCSs (due for example to slight relative motions between the structure and the partition walls).

Table 3.10: Relative differences (in %) between natural frequencies of the complete building identified from white noise base excitation test data with RMS = 1.5% g and RMS = 1.0% g (used as reference).

Mode	SSI-DATA	NExT-ERA	EFDD	DSI	OKID-ERA	Mean (%)	c.o.v. (%)
1 (1-L)	-10.92	-8.25	-7.60	-5.83	-7.10	**-7.94**	**21.3**
2 (1-T+To)	-2.16	-4.74	-2.15	-2.52	-3.17	**-2.95**	**32.9**
3 (1-To)	-0.40	0.00	-1.65	-2.37	-5.16	**-1.92**	**95.6**
4 (2-L)	-3.61	-3.27	-4.66	-3.71	-2.72	**-3.59**	**17.6**
5 (2-L+To)	1.12	-13.25	-6.14	-9.21	-	**-6.87**	**76.5**
6 (2-To)	-5.39	-	-	-	-	**-5.39**	**-**
7 (3-L)	1.13	1.27	-3.06	-2.57	0.61	**-0.52**	**360.5**
8 (3-To)	1.12	-1.10	-	-0.48	-	**-0.15**	**616.0**
9 (4-L)	2.18	2.14	2.23	-0.11	-0.88	**1.11**	**119.7**
10 (5-L)	-0.34	-0.51	-1.71	-1.60	-3.48	**-1.53**	**73.4**

Table 3.11 shows the first four modes natural frequencies identified using ambient vibration data recorded before and after the white noise base excitation tests of February 23, 2012. It is the analog of Table 3.6 for the bare building structure. It is observed that the first four modes natural frequencies remain almost unchanged, are higher than their counterparts for the bare building structure (see Table 3.6), and are higher than those identified from white noise base excitation test data for the complete building (see Table 3.9). Similar conclusions are drawn as for the bare building structure, i.e., the concrete cracked, and the connections between the structure and non-structural components (e.g., partition walls) started to loosen up during the white noise base excitation tests; however, this damage initiation appears to be "healed" under subsequent ambient vibrations due to gravity effects (preventing a large majority of the cracks to re-open) combined with very low amplitude of vibrations. The crossing of the first two modes is observed again. Under ambient vibrations, before and after application of the white noise base excitation tests to

the complete building, mode 1-T+To has the lowest frequency while during the white noise base excitation tests, mode 1-L has the lowest frequency. As explained earlier, this effect is due to the loss of stiffness experienced by the building in its longitudinal direction (direction of shake table motion) during the white noise base excitation tests. On the other hand, damping ratios identified from ambient vibration data are lower than those identified from white noise base excitation data (Figure 3.11), as explained in Section 3.6 for the bare building structure. However, for the complete building, the identified damping ratios of the modes with transverse and torsional components (1-T+To and 1-To) also increase with increasing amplitude of the excitation because of the additional sources of energy dissipation provided by the NCSs and their interaction with the supporting structure.

Table 3.11: Natural frequencies (Hz) of the complete building identified from ambient vibration data recorded before and after white noise base excitation tests.

Mode	Before white noise tests (February 23, 2012)			After white noise tests (February 24, 2012)		
	SSI-DATA	NExT-ERA	EFDD	SSI-DATA	NExT-ERA	EFDD
1 (1-L)	2.08	2.09	2.09	2.03	2.04	2.04
2 (1-T+To)	1.95	1.95	1.95	1.94	1.95	1.95
3 (1-To)	2.71	2.70	2.72	2.67	2.68	2.67
4 (2-L)	7.76	7.71	7.70	7.74	7.72	7.74

Figure 3.12 shows the mode shapes identified using DSI from the white noise base excitation test data with RMS = 1.5% g. The same mode shapes as those corresponding to the bare building structure (see Figure 3.7) are identified, i.e., the first to fifth longitudinal (1-L, 2-L, 3-L, 4-L, and 5-L), the first two coupled translational-torsional (1-T+To, 2-L+T) and the first three torsional (1-T, 2-T, and 3-T) modes. This indicates that the NCSs did not affect the mode shapes for this level of excitation.

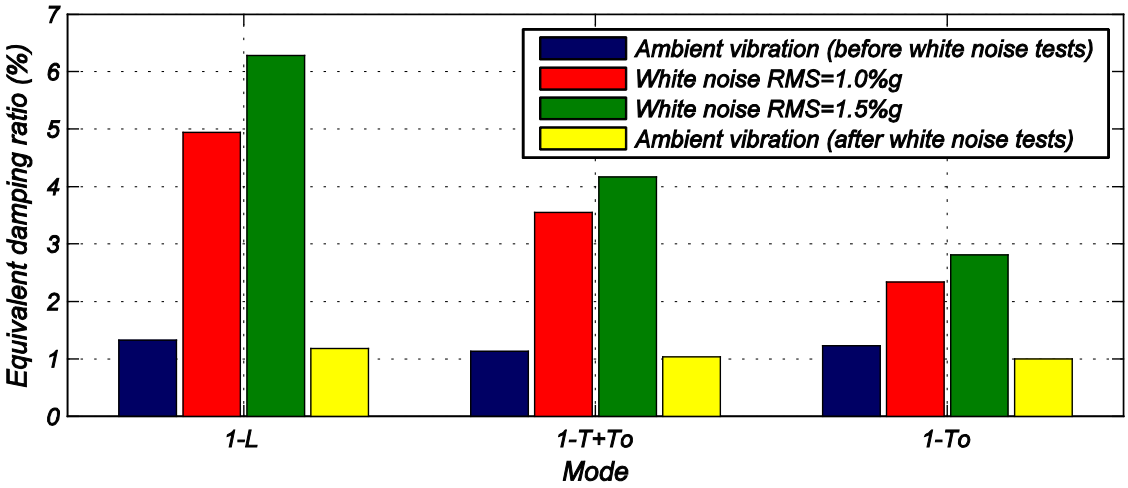

Figure 3.11: Equivalent damping ratios of the complete building identified using SSI-DATA with ambient vibration (recorded before and after white noise tests) and white noise base excitation data.

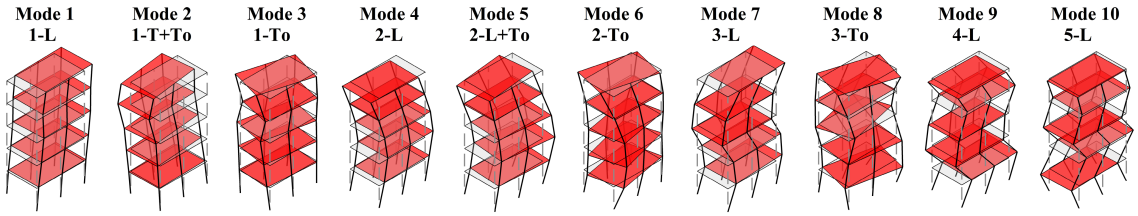

Figure 3.12: Mode shapes of the complete building identified using DSI from white noise base excitation test data (RMS = 1.5% g).

Additionally, the MAC values between the identified mode shapes for the different white noise base excitations (RMS = 1.0% g and 1.5% g) were compared for the complete building, and were found very close to unity for the corresponding modes. This implies that the change in amplitude of the white noise base excitation from RMS = 1.0% g to 1.5% g does not affect the (effective) mode shapes of the building.

The polar plot representation in Figure 3.13 of the mode shapes identified using DSI from the white noise base excitation test data (from RMS = 1.5% g) shows that modes 1-L, 1-To, and 2-L are estimated nearly as classically damped, while modes 1-T+To, 2-L+To, 2-To, 3-L, 3-To, 4-L, and 5-L are identified with some non-classical damping characteristics. As mentioned previously, non-classical damping characteristics

may partially be the product of estimation uncertainty (error); however, by comparing the polar plots in Figure 3.8 and Figure 3.13, it appears that the identified non-classical damping in the higher modes is more pronounced in the complete building than in the bare building structure, i.e., NCSs increase the level of identified non-classical damping in the higher modes.

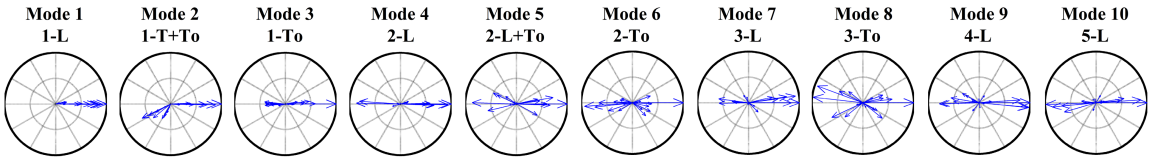

Figure 3.13: Polar plots of complex mode shapes of the complete building identified using DSI from white noise base excitation test data (RMS = 1.5%g).

Figure 3.14 portrays the MAC values between the mode shapes identified using different methods from white noise base excitation test data (RMS = 1.5%g). Similarly to the case of the bare building structure (Figure 3.9), the corresponding modes (diagonal entries) have high MAC values, indicating good agreement between corresponding mode shapes identified using different methods. It is observed that identified lower modes with main component in the direction of excitation, i.e., modes 1 (1-L), 4 (2-L), and 7 (3-L), show a very good agreement between the different methods (MAC close to one); however, some modes with transverse and torsional components, e.g. modes 2 (1-T+To) and 3 (1-To), show lower correlation between different methods. This suggests that the uncertainty in the identified mode shapes is higher for those modes with lower contribution to the total response of the building.

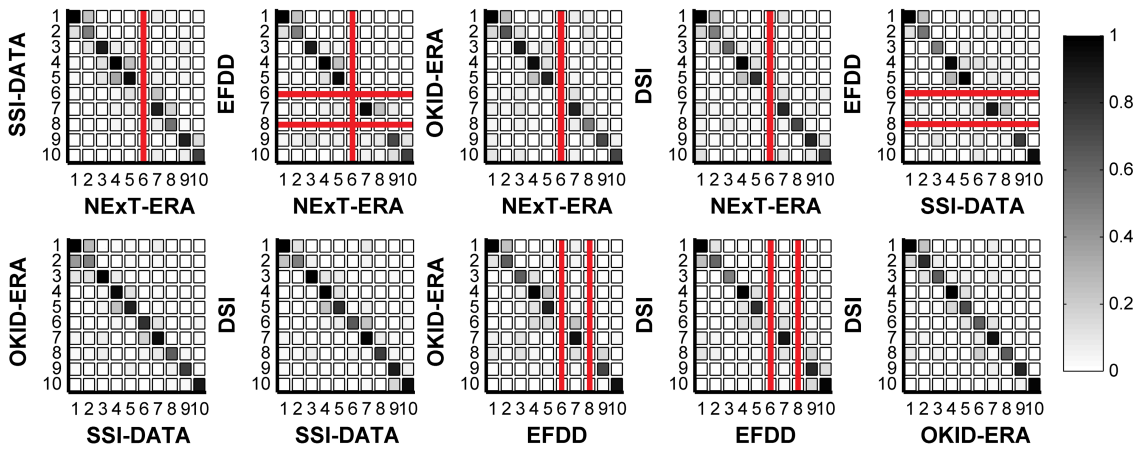

Figure 3.14: MAC values between the mode shapes of the complete building identified using five different methods from RMS = 1.5%g white noise base excitation test data.

3.9. Conclusions

A full scale five-story reinforced concrete building was built and tested, under base-isolated and fixed-based conditions, on the NEES-UCSD shake table in the period May 2011 – May 2012. Before conducting the seismic tests, a temporary accelerometer array was deployed on the fixed-base structure to study the evolution of its modal parameters during the construction process and the effects of the major non-structural components and systems (NCSs) on the dynamic properties of the building. A sequence of dynamic tests, including daily ambient vibration, weekly shock-induced free vibration, and some low-amplitude white noise base excitation tests, were performed on the structure at different stages of construction. Different state-of-the-art system identification methods, including three output-only (SSI-DATA, NExT-ERA and EFDD) and two input-output (OKID-ERA and DSI) methods, were used to estimate the modal properties of the structure (natural frequencies, damping ratios, and mode shapes) from the structural vibration data recorded through the accelerometer array. The natural

frequencies and mode shapes identified by different methods are found in very good and good agreement, respectively, whereas the identified damping ratios show much larger method-to-method variability than the natural frequencies and mode shapes. The effects of different construction activities on the modal properties of the building specimen under construction are analyzed. It is found that placement of concrete to build the main structural elements (slabs, columns, and walls) reduces the natural frequencies because of the additional mass (without stiffness) incorporated to the structure. Also, the effect of concrete hardening and corresponding stiffness gain during the curing process is detected through gradual increase in the natural frequencies. Some NCSs have a significant effect on the identified natural frequencies and damping ratios of the building. The precast cladding induces abrupt decreases in the natural frequencies due to their significant added mass (without significant added stiffness) to the building. The interior partition walls increase significantly the initial lateral stiffness of the building (e.g., the interior partition walls at the bottom three floors by about 20%) and consequently decrease its natural frequencies. Furthermore, they slightly increase the identified damping ratios of the building.

The effect of cracking in the concrete and corresponding loss of stiffness during the white noise base excitation tests performed on both the bare building structure and the complete building was clearly observed from the natural frequencies identified using the white noise base excitation test data. The installation of the NCSs decreased the natural frequency (identified from ambient vibration data) of some modes (by up to 9%) and increased that of others (by up to 18%), while the identified damping ratios increased by 15 to 191% for all the modes from the bare building structure to the complete building,

due to the additional sources of energy dissipation provided by the NCSs themselves and their interaction with the structural skeleton. Finally, it is observed that the low amplitude of structural vibration induced by ambient excitations is not sufficient to exercise (re-open) the majority of the cracks developed during the white noise base excitation tests performed (with RMS = 1.0%g and 1.5%g) and therefore to identify the corresponding loss of stiffness of the structure.

Modal properties identified for both the bare structure and complete building clearly evidence the effect of the amplitude of the excitation on the natural frequencies and damping ratios. In the case of the bare building structure, from ambient vibration (with a RMS acceleration of 0.03%g on the roof) to WN base excitation with RMS = 1.0%g (with a RMS acceleration of 1.85%g on the roof), the natural frequency of mode 1-L decreases by approximately 3% and the damping ratios of modes 1-L and 2-L increase by approximately 250%. From WN base excitation with RMS = 1.0%g to WN base excitation with RMS = 1.5%g (with a RMS acceleration of 1.95%g on the roof), the natural frequency of mode 1-L decreases by approximately 3.5% and the damping ratios increase by approximately 15% for most of the modes. In the case of the complete building, similar results are obtained. From ambient vibration (with a RMS acceleration 0.03%g on the roof) to WN base excitation with RMS = 1.0%g (with a RMS acceleration of 1.62%g on the roof), the natural frequency of mode 1-L decreases by approximately 15% and the damping ratios of the first four modes increase between 140 and 350%. From WN base excitation with RMS = 1.0%g to WN base excitation with RMS = 1.5%g (with a RMS acceleration of 1.75%g on the roof), the natural frequency of model 1-L

decreases by approximately 8% and the damping ratios slightly increase (by a few percent) for most of the modes.

The relatively dense instrumentation of the building specimen combined with the daily recorded vibration data and the detailed tracking of the construction process and installation of the NCSs enabled a comprehensive study of the individual and combined effects of different construction activities and NCSs on the modal properties of the building specimen.

3.10. Acknowledgements

Chapter 3 is largely a reprint of the material that has been submitted for publication "Influence of the construction process and nonstructural components on the modal properties of a five-story building" in *Earthquake Engineering & Structural Dynamics*, Astroza, Rodrigo; Ebrahimian, H.; and Conte, J.P., Restrepo, J.I., and Hutchinson, T.C. The dissertation author was the primary investigator and author of this paper.

References

Allemang, R. J. and Brown, D. L., 1982. "A correlation coefficient for modal vector analysis." *Proc.,1st Int. Modal Analysis Conf. (IMAC I)*, Orlando, FL, 110–116.

Antonacci, E., De Stefano, A., Gattulli, V., Lepidi, M., and Matta, E., 2011. "Comparative study of vibration-based parametric identification techniques for a three-dimensional frame structure." *Structural Control & Health Monitoring*, 19(5), 579–608.

Astroza, R., Ebrahimian, H., Conte, J.P., Restrepo, J.I., and Hutchinson, T.C. "System identification of a full-scale five-story reinforced concrete building tested on the NEES-UCSD shake table." Submitted to *Structural Control and Health Monitoring*.

Brincker, R., Ventura, C., and Andersen, P., 2001a. "Damping estimation by frequency domain decomposition" *19th Int. Modal Analysis Conf. (IMAC XIX)*, Bethel, CT, 698–703.

Brincker, R., Zhang, L., and Andersen, P., 2001b. "Modal identification of output-only systems using frequency domain decomposition." *Smart Materials and Structures*, 10(3), 441–445.

Brownjohn, J.M.W., 2003. "Ambient vibration studies for system identification of tall buildings." *Earthquake Engineering & Structural Dynamics*, 32(1), 71–95.

Butt, F. and Omenzetter, P., 2014. "Seismic response trends evaluation and finite element model calibration of an instrumented RC building considering soil–structure interaction and non-structural components." *Engineering Structures*, 65, 111–123.

Chen, M., Pantoli, E., Wang, X., Astroza, R., Ebrahimian, H., Mintz, S., Hutchinson, T.C., Conte, J.P., Restrepo, J.I., Meacham, B., Kim, J., and Park, H. *BNCS Report #1: Full-scale structural and nonstructural building system performance during earthquakes and post-earthquake fire - Specimen design, construction and test protocol*. Structural Systems Research Project Report Series, SSRP 13/09, University of California San Diego, La Jolla, CA, 2013.

Cornwell, P., Farrar, C.R., Doebling, S.W., and Sohn, H., 1999. "Environmental variability of modal properties." *Experimental Techniques*, 23(6), 45–48.

Devin A. and Fanning, P. J., 2012. "Impact of Nonstructural Components on Modal Response and Structural Damping." *30th Int. Modal Analysis Conf. (IMAC XXX)*, Jacksonville, FL, 415–421.

Farrar, C.R., Doebling, S.W., and Nix, D.A., 2001. "Vibration-based structural damage identification." *Philosophical Transactions of the Royal Society A*, 359(1778), 131–149.

He, X., Fraser, M., Conte J.P., and Elgamal, A., 2007. "Investigation of environmental effects on identified modal parameters of the Voigt Bridge." *18th Engineering Mechanics Division Conference ASCE*, Blacksburg, VA.

He, X., Moaveni, B., Conte, J. P., Elgamal, A., and Masri, S. F., 2009. "System identification of Alfred Zampa Memorial Bridge using dynamic field test data." *Journal of Structural Engineering ASCE*, 135(1), 54–66.

Hong, A.L., Betti, R., and Lin, C.C., 2009. "Identification of dynamic models of a building structure using multiple earthquake records." *Structural Control & Health Monitoring*, 16(2), 178–199.

Hutchinson, T.C., Restrepo, J.I., Conte, J.C., Pantoli, E., Chen, M.C., Wang, X., Astroza, R., and Ebrahimian, H. 2014. *Shake table testing of a five story building outfitted with NCSs (BNCS project)*. Network for Earthquake Engineering Simulation (distributor), Dataset.

Imregun, M. and Ewins, D.J., 1993. "Realization of Complex Mode Shapes." *11th Int. Modal Analysis Conf. (IMAC XI)*, Kissimmee-FL, 1303–1309.

Jaishi, B. and Ren, W.X., 2005. "Structural finite element model updating using ambient vibration test results." *Journal of Structural Engineering ASCE*, 131(4), 617–628.

James, G. H., Carne, T.G., and Lauffer, J.P., 1993. *The natural excitation technique (NExT) for modal parameter extraction from operating wind turbines*. Report SAND92-1666, Sandia National Laboratories, Sandia, NM.

Juang, J.N. and Pappa, R.S. 1985. "An Eigensystem Realization Algorithm for Modal Parameter Identification and Model Reduction." *Journal of Guidance, Control, and Dynamics*, 8(5), 620–627.

Juang, J.N., 1994. *Applied System Identification*. Prentice Hall, Upper Saddle River, N.J.

Juang, J.N., Phan, M., Horta, L.G., and Longman, R.W., 1991. *Identification of observer Kalman filter Markov parameters - Theory and experiments*. NASA Technical Report TM-104069, Hampton, VA.

Kanazawa, K., 2005. "Natural frequency transition of a building during seismic retrofitting works." *23th Int. Modal Analysis Conf. (IMAC XXIII),* Orlando, FL, paper 67.

Kanazawa, K., Kirita, F., Kitamura, H,. and Matsuoka, Y., 2008. "Health monitoring of 4-story steel moment frame before and after the collapse test." *14th World Conference on Earthquake Engineering (WCEE)*, Beijing, China.

Lorenz, W., 2006. "Iterative system identification for the assessment and retrofitting of a historic pre-stressed concrete bridge in Berlin*." 5th Int. Conf. on Structural Analysis of Historical Constructions*, New Delhi, India.

Memari, A.M., Aghakouchak, A.A., Ashtiany, M.G., and Tiv, M., 1999. "Full-scale dynamic testing of a steel frame building during construction." *Engineering Structures*, 21(12), 1115−1127.

Mendoza L., Reyes, A., and Luco, J.E., 1991. "Ambient vibration tests of the Mexicali General Hospital." *Earthquake Spectra*, 7(2), 281−300.

Moaveni, B., He, X., Conte, J.P., and Restrepo, J.I., 2010. "Damage identification study of a seven-story full-scale building slice tested on the UCSD-NEES shake table." *Structural Safety*, 32(5), 347−356.

Moaveni, B., He, X., Conte, J.P., Restrepo, J.I., and Panagiotou M., 2011. "System identification study of a seven-story full-scale building slice tested on the UCSD-NEES shake table." *Journal of Structural Engineering ASCE*, 137(6), 705−717.

Moaveni, B., Stavridis, A., Lombaert, G., Conte, J.P., and Shing, P.B., 2013. "Finite element model updating for assessment of progressive damage in a three-story infilled RC frame." *Journal of Structural Engineering ASCE*, 139, 1665−1674.

Nayeri, R.D., Masri, S.F., Ghanem, R.G., and Nigbor, R.L., 2008. "A novel approach for the structural identification and monitoring of a full-scale 17-storey building based on ambient vibration measurements." *Smart Materials and Structures*, 17, 025006, 1–19.

Ndambi, J.M., Peeters, B., Maeck, J., De Visscher, J., Wahab, M.A., Vantomme, J., De Roeck, G., and De Wilde, W.P., 2000. "Comparison of techniques for modal analysis of concrete structures." *Engineering Structures*, 22(9), 1159−1166.

Ni, Y.Q., Li, B., Lam, K.H., Zhu, D.P., Wang, Y., Lynch, J.P., and Law, K.H., 2011. "In-construction vibration monitoring of a super-tall structure using a long-range wireless sensing system." *Smart Structures and Systems*, 7(2), 83−102.

Niousha, A. and Motosaka, M., 2007. "System identification and damage assessment of an existing building before and after retrofit." *AIJ Journal of Structural Engineering*, 53B, 297–304.

Nunez, T., Boroschek, R., and Larrain, A., 2013. "Validation of a Construction Process using a Structural Health Monitoring Network." *Journal of Performance of Constructed Facilities ASCE*, 27(3), 270–282.

Ogiyama, K. and Sato, T., 2004. "Nonlinear structural system identification using shaking table test data of five-story model building." *Proc. SPIE 5394, Health Monitoring and Smart Nondestructive Evaluation of Structural and Biological Systems*, San Diego, CA, 475–484.

Peeters, B. and De Roeck, G., 2001a. "One-year monitoring of the Z24-Bridge: environmental effects versus damage events." *Earthquake Engineering & Structural Dynamics*, 30(2), 149–171.

Peeters, B. and De Roeck, G., 2001b. "Stochastic system identification for operational modal analysis: A review." *Journal of Dynamic Systems, Measurement, and Control*, 123(4), 659–666.

Ramos, L.F., De Roeck, G., Lourenço, P. B., and Campos-Costa, A., 2010. "Damage identification on arched masonry structures using ambient and random impact vibrations." *Engineering Structures*, 32(1), 146–162.

Skolnik, D., Lei, Y., Yu, E., and Wallace, J.W., 2006. "Identification, model updating, and response prediction of an instrumented 15-story steel-frame building." *Earthquake Spectra*, 22(3), 781–802.

Sohn, H., 2003. "Effects of environmental and operational variability on structural health monitoring." *Philosophical Transactions of the Royal Society A*, 365(1851), 539–560.

Soyoz, S., Taciroglu, E., Orakcal, K., Nigbor, R., Skolnik, D., Lus, H., and Safak, E., 2013. "Ambient and forced vibration testing of a reinforced concrete building before and after its seismic retrofitting." *Journal of Structural Engineering ASCE*, 139, 1741–1752.

Su, R. K. L., Chandler, A.M., Sheikh, M.N., and Lam, N.T.K., 2005. "Influence of non-structural components on lateral stiffness of tall buildings." *The Structural Design of Tall and Special Buildings*, 14(2), 143–164.

Tian, M. and Yi, W., 2008. "Dynamic behavior of reinforced concrete frame structure during construction." *Journal of Central South University of Technology*, 15(3), 418−422.

Van Overschee, P., De Moor, B., 1996. *Subspace Identification for Linear Systems: Theory, Implementation, Applications*. Kluwer Academic Publishers, Dordrecht, The Netherlands.

Ventura, C. E. and Schuster, N.D., 1996. "Structural dynamic properties of a reinforced concrete high-rise building during construction." *Canadian Journal of Civil Engineering*, 23(4), 950−972.

Wang, X., Pantoli, E., Hutchinson, T.C., Restrepo, J.I., Wood, R.L., Hoehler, M.S., Grzesik, P., and Sesma, F.H. (2015). "Seismic Performance of Cold-Formed Steel Wall Systems in a Full-Scale Building." *Journal of Structural Engineering ASCE*, In press, 04015014.

CHAPTER 4

SYSTEM IDENTIFICATION OF A FULL-SCALE FIVE-STORY REINFORCED CONCRETE BUILDING TESTED ON THE NEES-UCSD SHAKE TABLE

4.1. Introduction

The advances in structural health monitoring (SHM) over the last forty years have attracted significant attention from the structural engineering community as the need for implementing accurate and robust damage identification (DID) strategies for civil structures only increases. Undoubtedly, DID based on changes in the identified modal properties of an equivalent linear elastic viscously damped model of the structure has been one of the most popular approaches. This approach assumes that low-amplitude dynamic input-output or output-only data are available before and after the structure has suffered damage. Such damage can be detected and localized by analyzing changes in these modal properties or quantities derived therefrom (e.g., curvature mode shapes), which depend on the physical characteristics of the structure (i.e., mass, stiffness, and energy dissipation mechanisms). Experimental and operational modal analyses are the

main techniques to identify the modal parameters (natural frequencies, damping ratios, and mode shapes) from recorded structural vibration data. A comprehensive and detailed literature review on vibration-based DID can be found in Doebling et al. (1996) and Fan and Qiao (2011).

Most vibration-based DID studies have been conducted using idealized theoretical models and numerically simulated data, or using experimental data from small-scale tests of single structural components, subassemblies, and systems (e.g., Johnson et al. 2004, Bernal et al. 2002, Giraldo et al. 2009). Only a few studies have used experimental data obtained from real structures or large-scale shake table tests. Most full-scale damage-controlled tests have been conducted on bridge structures (Farrar et al. 2000, Peeters and De Roeck 2001, Huth et al. 2005, Lauzon and DeWolf 2006, Siringoringo et al. 2012, Dilena and Morassi 2012) by progressively inducing artificial damage (e.g., partial saw cuts in steel beams and/or partial cuts of post-tensioning tendons).

Building structures are even more complex than bridges. Several factors hinder robust vibration-based DID studies for building structures: (1) the impossibility to perform progressive damage tests on existing non-decommissioned structures; (2) the high risk and complexity to conduct such tests on decommissioned structures; (3) and the scarcity of recorded dynamic response of earthquake-damaged buildings. This lack of data has been somewhat addressed by shake table tests that have provided important, high-quality and unique data to evaluate the dynamic properties of buildings at different damage states.

Moaveni et al. (2011) estimated the modal properties of a 7-story reinforced concrete (RC) shear-wall building slice subjected to a sequence of earthquake base

motions of increasing intensity. Using output-only and input-output system identification (SID) methods with ambient vibration (AV) and white noise (WN) base excitation test data, they studied the variation of the identified natural frequencies and damping ratios as a function of structural damage. They concluded that the natural frequencies decreased as the damage progressed in the specimen. Similarly, but using only one input-output method, Moaveni et al. (2012) analyzed the effect of structural damage on the modal properties of a 2/3-scale 3-story infilled RC frame and obtained similar conclusions. Ji et al. (2011) used the frequency response function (FRF) curve-fitting and the autoregressive with exogenous input (ARX) methods to identify the modal properties of a full-scale specimen representing a high-rise steel building tested on the E-Defense shake table. They observed that the identified natural frequencies decreased as damage progressed, while the mode shapes remained essentially unchanged. In contrast, Hien and Mita (2011) used a subspace state-space system identification method (N4SID) to study the effect of damage on the modal properties of a full-scale 4-story steel building, also tested on the E-Defense shake table, but found variation in both natural frequencies and mode shapes as the damage progressed. Belleri et al. (2013) analyzed the effect of damage on the modal parameters of a 1/2-scale 3-story precast concrete building using the deterministic-stochastic subspace identification method, concluding that the natural frequencies decreased and the damping ratios increased as structural damage progressed.

None of the above-mentioned shake table tests involved RC frame specimens. It is reasonable to assume that distinct structural systems experience different type (including spatial distribution) of damage, which may affect the modal parameters dissimilarly. Furthermore, previous studies identified only a relatively small number of

modes (five or less); the effect of damage on higher modes of vibration was not analyzed. Although previous results on building structures were based on large or full-scale shake table tests, none of them strictly represented real-life conditions since typical non-structural components and systems (NCSs) were not installed on the specimens. Consequently, the effects of NCSs and their dynamic interaction with the structure have not been analyzed through full-scale shake table tests, and particularly for service-level earthquakes.

This chapter focuses on a full-scale 5-story RC frame building fully outfitted with a large variety of NCSs built and tested on the unidirectional NEES-UCSD shake table. Structural vibration data recorded on the specimen from AVs and low-amplitude WN base excitation tests were used to identify the modal properties of the building at different levels of structural and nonstructural damage, which were progressively induced by earthquake base motions of increasing intensity. Three output-only SID methods, namely, the Data-Driven Stochastic Subspace Identification (SSI-DATA) method, the Multiple-Reference Natural Excitation Technique combined with the Eigensystem Realization Algorithm (NExT-ERA), and the Enhanced Frequency Domain Decomposition (EFDD) method, were used in conjunction with the AV data. In addition to the three above-mentioned output-only methods, two input-output SID methods, namely, Deterministic-Stochastic Subspace Identification (DSI) and Observer/Kalman Filter Identification combined with the Eigensystem Realization Algorithm (OKID-ERA), were used in conjunction with the low-amplitude WN base excitation test data.

Detailed visual inspections of the damage between seismic tests permitted correlating the identified modal parameters and their changes with the actual damage on

the building structure and NCSs. The identified natural frequencies were used to determine the progressive loss of apparent stiffness of the building as a function of damage. The state-space models identified from WN base excitation test data were used to investigate the relative modal contributions to the measured building response at different damage states.

4.2. Description of the test specimen

The test building was a full-scale 5-story cast-in-place RC structure fully outfitted with a broad array of NCSs. The building had two bays in the longitudinal direction (direction of shaking) and one bay in the transverse direction, with plan dimensions of 11.0×6.6 m, respectively. The building had a floor-to-floor height of 4.27 m, a total height (measured from the top of the foundation to the top of the roof slab) of 21.34 m, and an estimated total weight of 3010 kN for the bare structure and 4420 kN for the structure with all the NCSs; these figures do not include the foundation, which weighed 1870 kN. The seismic resisting system was provided by two identical one-bay special RC moment resisting frames oriented in the East-West direction. One frame was placed on the North face of the building and the other on the South face. The beams, 0.30×0.71 m in cross-section, had different design details at different floors. A 0.20 m thick cast-in-place slab provided the floor support for each level. Six 0.66×0.46 m columns were reinforced with six #6 and four #9 longitudinal bars, and a prefabricated transverse reinforcement grid. There were two main openings in each slab to accommodate a steel stair assembly and a functioning elevator, each of which extended the full height of the

building. Two 0.15 m-thick transverse RC shear walls provided the support for the elevator guiderails. See Chen et al. (2013) for detailed information about the structural system, nonstructural components, and their design considerations and Hutchinson et al. (2014) and Pantoli et al. (2015a) for the dataset of the project. Figure 4.1 shows the test specimen and schematic elevation, and plan views.

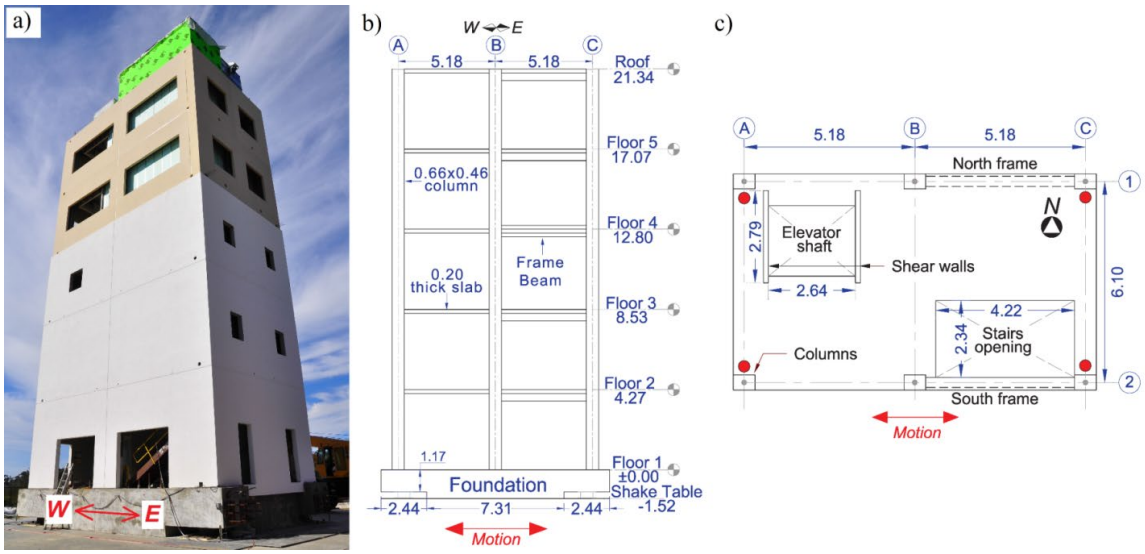

Figure 4.1: Test specimen: (a) completed building; (b) schematic elevation view; and (c) schematic plan view (dimensions are in meters).

4.3. Instrumentation plan and dynamic tests

4.3.1. Instrumentation plan

The building was densely instrumented with an array of accelerometers, load cells, strain gauges, LVDTs, string potentiometers, GPS antennas, and digital video cameras. The accelerometer array deployed prior to the seismic shake table tests consisted of four triaxial accelerometers per floor, one at each corner, as represented by red circles in Figure 4.1(c). Also, two triaxial accelerometers were placed on the North-East and South-West corners of the shake table platen. The accelerometers were force-

balance Episensor, with a full-scale of ±4g, a frequency bandwidth DC–200 Hz, and a wide dynamic range of 155dB. The data acquisition system consisted of Quanterra Q330 digitizers from Kinemetrics, Inc., which have a digital resolution of 24 bits, separate sigma-delta A/Ds on each channel, and digital linear-phase anti-alias filters at 80Hz. In this study, the acceleration response of the building, which was measured by 24 accelerometer channels (two for each translational direction of each floor including the foundation level) sampled at 200 Hz was used to identify the dynamic properties of the test specimen. Prior to performing SID, the time series were detrended and filtered using a band-pass IIR Butterworth filter of order 4 with cut-off frequencies at 0.15 and 25 Hz, which defined a frequency range containing all the vibration modes contributing noticeably to the building response.

4.3.2. Dynamic tests

The seismic shake table tests on the fixed-base (FB) building were conducted in May 2012. Ambient and forced vibration data, including pulse-like and low-amplitude WN base excitations, were recorded on the FB building between seismic tests. Six earthquake input motions (Table 4.1) were selected based on global and local performance criteria, and were applied to progressively damage the structure and NCSs. The building was designed for a location in Southern California, where site-specific ground motions were available. The available site-specific maximum considered earthquake (MCE) ground motion spectrum was developed for a Site Class D (stiff) soil conditions and had a short-period spectral acceleration S_{MS} = 2.10g and a 1-sec spectral acceleration S_{M1} = 1.43g. Performance-based design objectives of 2.5% peak interstory

drift ratio (PIDR) and maximum peak floor acceleration (PFA) between 0.7−0.8g were selected during the conceptual design phase. Figure 4.2 shows the acceleration time histories of the earthquake input motions (achieved on the shake table) together with their 5% damped displacement and pseudo-acceleration elastic response spectra. Ten minutes of AVs were recorded before and after each seismic test, and low-amplitude WN base excitation tests were conducted at key stages during the test protocol. Table 4.1 summarizes the seismic test protocol and the vibration data of the FB building used in this study.

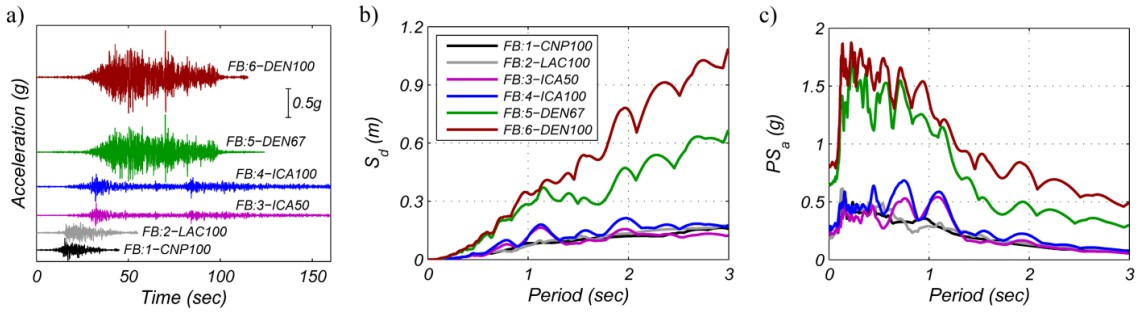

Figure 4.2: Achieved seismic input motions (a) acceleration time histories; (b) elastic displacement response spectra (ξ = 5%); and (c) pseudo-acceleration response spectra (ξ = 5%).

To show examples of the recorded structural vibration data, Figure 4.3(a) shows the time histories and Fourier amplitude spectra (FAS) of the acceleration responses recorded on the second floor and on the roof of the building for AV test AMB1. Figure 4.3(b) shows the time histories and FAS of the acceleration responses recorded on the first floor and on the roof for WN test WN1A.

Table 4.1: Dynamic tests performed.

Date	Description	Name	Type	Target [a]	Damage state
May 7, 2012	Ambient vibration 1	AMB1	-	-	DS0
	6 min WN (1.5%*g* RMS)	WN1A	-	-	DS0
	6 min WN (3.0%*g* RMS)	WN1B	-	-	DS0
	6 min WN (3.5%*g* RMS)	WN1C	-	-	DS0
	Canoga Park (1994 Northridge EQ.)	**FB:1-CNP100**	SM	SLE	-
	Ambient vibration 2	AMB2	-	-	DS1
May 9, 2012	**LA City Terrace (1994 Northridge EQ.)**	**FB:2-LAC100**	SM	SLE	-
	Ambient vibration 3	AMB3	-	-	DS2
	ICA 50% (2007 Pisco EQ.)	**FB:3-ICA50**	AM	-	-
May 11, 2012	Ambient vibration 4	AMB4	-	-	DS3
	ICA 100% (2007 Pisco EQ.)	**FB:4-ICA100**	AM	-	-
	6 min WN (1.5%*g* RMS)	WN2A	-	-	DS4
	Ambient vibration 5	AMB5	-	-	DS4
May 15, 2012	4 min WN (3.0%*g* RMS)	WN2B	-	-	DS4
	TAPS Pump Station 67% (2002 Denali EQ.)	**FB:5-DEN67**	SM	DE	-
	6 min WN (1.5%*g* RMS)	WN3A	-	-	DS5
	Ambient vibration 6	AMB6	-	-	DS5
	4 min WN (3.5%*g* RMS)	WN3B	-	-	DS5
	TAPS Pump Station 100% (2002 Denali EQ.)	**FB:6-DEN100**	SM	MCE	-
	Ambient vibration 7	AMB7	-	-	DS6

[a]: These test motions were spectrally matched to the reported performance targets (SLE = service-level earthquake, DE = design earthquake, and MCE = maximum considered earthquake), assuming properties of the test structure at the time of conceptual design. RMS = root-mean-square. SM = spectrum-matched motion, AM = actual motion.

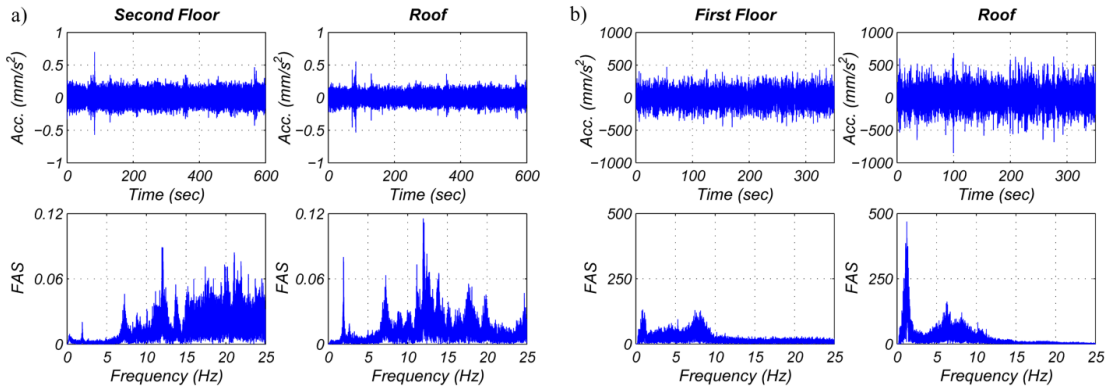

Figure 4.3: Time histories and Fourier amplitude spectra of the acceleration data recorded at different floors: (a) ambient vibration test AMB1; and (b) white-noise base excitation test WN1A.

Because the WN base excitations were applied only in the East-West (EW) direction, which corresponds to the longitudinal direction of the building, the level of structural responses in the North-South (NS) direction was low compared to the EW direction [Figure 4.4(a)]. As a result, contributions of the transverse modes to the total

response of the building were lower than those of the longitudinal and torsional modes; therefore, identification of transverse modes proved difficult when the WN base excitation test data was used. Conversely, the amplitudes of both translational components (NS and EW) of the response under AVs were comparable [Figure 4.4(b)]; therefore, the AV data was more appropriate for identifying the transverse modes of the building. Figure 4.4(a) shows the acceleration orbits of the roof during test AMB1, while Figure 4.4(b) shows the acceleration orbit of the roof during test WN1A.

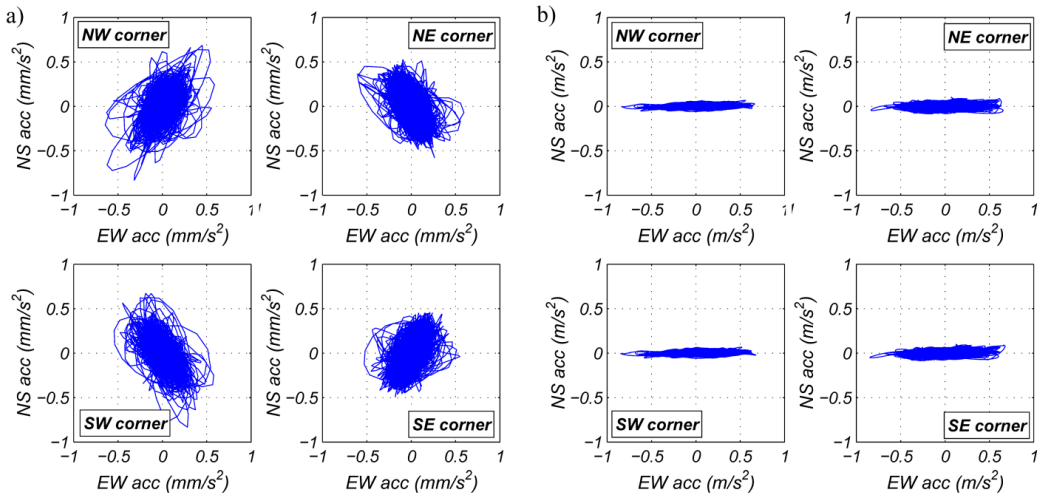

Figure 4.4: Acceleration orbits of the roof measured during (a) AMB1 (units: mm/sec^2) and (b) WN1A (units: m/sec^2).

4.4. Damage states

As mentioned earlier, structural and non-structural damage was progressively induced by six earthquake input motions of increasing intensity. Different damage states (DSs) were defined before and after each seismic test. DS0 corresponds to the baseline state of the building before the first seismic test in the FB configuration (FB-1:CNP100), while DS1, DS2, DS3, DS4, DS5, and DS6 correspond to the damage states after the seismic tests FB:1-CNP100, FB:2-LAC100, FB:3-ICA50, FB:4-ICA100, FB:5-DEN67,

and FB:6-DEN100, respectively (Table 4.1). Note that DS0 does not correspond to the undamaged state of the structure as this building specimen was previously tested in a base-isolated configuration; however, the observed structural damage was negligible. Further information about the structural and nonstructural damage can be found in Chen et al. (2015) and Pantoli et al. (2015b), respectively. Table 4.2 summarizes the damage observed in the structure and drywalls (interior partitions and façade-balloon framing) at the different DSs. Previous studies have shown that drywalls contribute substantially to the lateral stiffness of the building and, therefore, are expected to affect significantly the modal properties of the test specimen (Astroza et al. 2015).

Table 4.2: Summary of visual damage inspections performed at different damage states.

Damage state	Description
DS0	No damage
DS1	**Structure:** minor cracks on the slabs of floors 2 and 3 (< 0.2 mm). **Interior partition walls:** moderate damage (cracks at joints, crushing at corners) **Balloon framing:** moderate damage to interior gypsum (cracks at joints, crushing at corners), minor damage to exterior stucco (cracks around door openings), and no visible damage to clips.
DS2	
DS3	**Structure:** minor flexural cracks on the North beam on level 3 (< 0.15 mm), minor spalling at the bottom of NW column on level 2, minor cracking on levels 2, 3, and 4 slabs (< 0.25 mm), and moderate cracking on levels 2 and 3 slabs (< 0.25 mm). **Interior partition walls:** moderate damage (cracks at joints, crushing at corners) **Balloon framing:** moderate-severe damage to interior gypsumboard (severe crushing at corners, screw pull-out failure, joints with severe cracks), moderate damage to exterior stucco (diagonal and horizontal cracks), and minor clip failure (≤ 5%).
DS4	**Structure:** minor flexural cracks on the north beam on levels 2 and 3 (< 0.25 mm), minor flexural cracking on the columns on levels 1 and 2 (< 0.1 mm), and moderate cracking on levels 2, 3, and 4 slabs (< 0.30mm). **Interior partition walls:** severe damage (severe cracking to gypsumboard joints, gapping with adjacent elements, screw pull-out failure, severe crushing at corners). **Balloon framing:** moderate-severe damage to interior gypsumboard (severe crushing at corners, screw pull-out failure, joints with severe cracks), moderate-severe damage to exterior stucco (considerable diagonal and horizontal cracks) and minor clip damage (≈ 5%).
DS5	**Structure:** moderate flexural cracks on the North beam on levels 2 and 3 (< 0.5mm), moderate flexural cracks on the columns on levels 1 and 2 (<0.1mm) and moderate cracking on levels 2, 3 and 4 slabs (< 0.30mm). **Interior partition walls:** severe damage (gapping gypsumboard joints and screw pull-out failure, considerable amount of gypsum panel loosening, partial separation, and severe crushing at corners) **Balloon framing:** severe damage to interior gypsumboard (severe gapping at joints, panel partial separation), severe damage to exterior stucco (severe cracks and corner breaking), and severe failure to clips (40%)
DS6	**Structure:** severe damage to beams on levels 2 and 3 (buckling and fracture of the longitudinal reinforcing steel bars), severe spalling and cracking at the base of the columns on levels 1 and 2, and severe cracking on levels 2, 3, and 4 slabs. **Interior partition walls:** severe damage (complete gypsum separation, gypsum fracture, considerable amount of severe gapping of gypsumboard joints) **Balloon framing:** severe damage to interior gypsumboard (panel complete separation), severe damage to exterior stucco (top and bottom corners torn apart), and severe damage to clips (70% failed)

4.5. System identification methods

To estimate the modal properties of the building specimen at different damage states, three state-of-the-art output-only SID methods were used in conjunction with the AV data. These methods are: Data-Driven Stochastic Subspace Identification (SSI-DATA), Multiple-Reference Natural Excitation Technique combined with Eigensystem Realization Algorithm (NExT-ERA), and Enhanced Frequency Domain Decomposition (EFDD). It is noted that a single ten-minute long dataset of ambient vibration was used at each damage state to estimate the modal properties. In addition to the three above-mentioned output-only methods, two input-output methods were used in conjunction with the low-amplitude WN base excitation test data: Deterministic-Stochastic Subspace Identification (DSI) and Observer/Kalman Filter Identification combined with Eigensystem Realization Algorithm (OKID-ERA). Each SID method used herein is briefly described below. The complete dataset recorded for each WN base excitation test (see Table 4.1) was used for the system identification. Note that all the SID methods used in this study assumed a linear time-invariant (LTI) model of the structure, with all sources of energy dissipation represented by linear viscous damping. Consequently, the identified natural frequencies and damping ratios correspond to the modal parameters of an equivalent linear visco-elastic model.

To reduce the computational demand of the identification process, the acceleration time histories were decimated to 100 Hz. In the case of the SID methods based on state-space representation (SSI-DATA, NExT-ERA, DSI, and OKID-ERA), the stabilization diagram —which plots the identified modal parameters versus the model

order— was used to distinguish between physical and spurious (mathematical) modes. The following stability criteria were used:

$$\left|f_i - f_j\right| / f_j \le 1\% \quad ; \quad \left|\xi_i - \xi_j\right| / \xi_j \le 5\% \quad ; \quad \left(1\text{-}MAC_{\phi_i,\phi_j}\right)100 \le 2\% \quad ; \quad n_s \ge 6 \qquad (4.1)$$

where f_i, f_j, ξ_i, and ξ_j are the identified natural frequencies and damping ratios for models of consecutive orders, MAC_{ϕ_i,ϕ_j} is the modal assurance criterion (Allemang and Brown 1982) of a pair of corresponding modes shapes identified for models of consecutive orders, and n_s denotes the number of consecutive times (as the model order is increased progressively by increments of two) that an identified mode satisfies the triple stability (frequency, damping, and mode shape) criterion defined in Equation (4.1).

4.5.1. Data-Driven Stochastic Subspace Identification (SSI-DATA)

The data-driven stochastic subspace identification (SSI-DATA) method (Van Overschee and De Moor 1996) is a time-domain SID method that extracts a linear state-space model of the system using output-only measured vibration response data. Contrary to the two-stage time-domain methods (such as SSI-COV and NExT-ERA), it does not require computing the covariance matrices of the data and is numerically more robust because it does not require squaring up the output data (Peeters and De Roeck 2001). Moreover, robust numerical techniques such as QR factorization, singular value decomposition, and least squares are used in this method. For each test dataset, an output Hankel matrix was constructed considering 15 block rows with 20 (number of output channels) rows per block.

4.5.2. Multiple-Reference Natural Excitation Technique combined with Eigensystem Realization Algorithm (NExT-ERA)

The natural excitation technique (NExT) considers that the theoretical cross-correlation function of the measured vibration response (at two different outputs) to a broadband excitation has the same analytical form as the free vibration response of the structure (James et al. 1993). Once the cross-correlation vector for a given reference channel is estimated, the ERA method (Juang and Pappa 1985) can be used to estimate the modal parameters. To avoid selecting a reference channel that may coincide with a modal node, a vector of reference channels can be used (He et al. 2009). The cross-correlation functions were computed through the inverse Fourier transform of the corresponding cross-power spectral density (CPSD) functions, which were estimated using the Welch's method with a Hanning window of length 1/8 of the total length of the signal and 50% overlapping. The estimated cross-correlation functions were then used to construct the Hankel matrix with 150 block rows (20 rows per block) and 150 columns.

4.5.3. Enhanced Frequency Domain Decomposition (EFDD)

Introduced by Brincker et al. (Brincker et al. 2001a), the frequency-domain decomposition method corresponds to an extension of the peak-picking method. The enhanced frequency-domain decomposition method (Brincker et al. 2001b) estimates the modal properties of a system from the singular value decomposition (SVD) of the cross-power spectral density matrix of the outputs because the singular values can be interpreted as the auto-spectral densities of the modal coordinates and the singular vectors as the modes shapes (Brincker et al. 2001a). Returning the auto-spectral density back to

the time domain by inverse Fourier transform, the natural frequency and damping ratio can be determined from the corresponding modal single-degree-of-freedom auto-correlation function (ACF). Implementation of EFDD required estimating the CPSD functions using the Welch's method with a Hanning window of length 1/4 of the total length of the signal and 50% overlapping.

4.5.4. Deterministic-Stochastic Subspace Identification (DSI)

The combined deterministic-stochastic subspace identification method (DSI), a time-domain technique, was developed by Van Overschee and de Moor (1996). This method extracts a linear state-space model of the system from a Hankel block matrix constructed from the input-output measured vibration data. Then, assuming that: (i) the deterministic input is uncorrelated with both process and measurement noises, (ii) the deterministic input is persistently exciting, and (iii) the process and the measurement noises are not identically zero, DSI estimates the state-space matrices using the same numerical techniques as in SSI-DATA. For each test dataset, an input-output Hankel matrix was constructed considering 15 block rows with 21 (1 input and 20 output channels) rows per block.

4.5.5. Observer/Kalman Filter Identification Combined with Eigensystem Realization Algorithm (OKID-ERA)

This time-domain method was developed by Juang et al. (1991). The OKID method includes a feedback loop (observer) to make the system as stable as desired and computes both the system and observer Markov parameters from the input-output

recorded data by introducing prescribed eigenvalues for the observer. Then, the system Markov parameters are fed into the ERA to estimate the matrices of the state-space model of the structure. For each test dataset, an output matrix of dimensions $m \times l = 20 \times 2000$, where m = number of output channels, and an input-output matrix of dimensions $\left[r + (m+r)\, p \times l\right] = \left[1 + (20+1)\, 200 \times 2000\right] = 4201 \times 2000$, where r = number of input channels, p = integer such that $\mathbf{C}\bar{\mathbf{A}}^k\bar{\mathbf{B}} \approx \mathbf{0}$ for $k \geq p$ ($\bar{\mathbf{A}}, \bar{\mathbf{B}}$, and $\mathbf{C}$ are the state, input, and output matrices of the system with the observer, respectively), and l = number of data samples, are constructed from the recorded data.

4.6. System identification results

Using the five SID methods presented above together with the AV data and data recorded during low-amplitude WN base excitation tests (with three amplitude levels of base excitation, namely 1.5%, 3.0%, and 3.5%g root-mean-square or RMS), the modal properties of the building specimen were estimated at the different damage states; these results are presented and discussed below.

4.6.1. System identification based on ambient vibrations

Table 4.3 shows the natural frequencies and equivalent damping ratios (termed damping ratios from this point on) estimated using the three output-only methods from the AV data recorded at the different damage states. Eleven modes were identified using AV data. They correspond to the first five longitudinal (1-L, 2-L, 3-L, 4-L, and 5-L), first three torsional (1-To, 2-To, and 3-To), and first three coupled translational-torsional (1-

T+To, 2-T+To, and 2-L+To) modes of the building. Good agreement between natural frequencies identified using SSI-DATA, NExT-ERA, and EFDD was observed at each damage state. The identified damping ratios, which are mostly in the range 0–3%, show higher variability between different SID methods than the identified natural frequencies. Damping ratios of the lower modes identified using SSI-DATA, NExT-ERA, and EFDD are in good agreement and their variability is lower than that of the higher modes. The participation of the higher modes in the measured building response is lower than that of the lower modes; consequently, the signal-to-noise-ratio (SNR) is lower for the higher modes. These results suggest that damping ratio estimates are more sensitive to noise level than natural frequency estimates (e.g., Moaveni et al. 2014). Moreover, the damping ratios of higher modes (which do not contribute much to the response of the building) identified by EFDD are consistently lower than those identified using NExT-ERA and SSI-DATA. This observation is in agreement with previous studies (e.g., He et al. 2009, Antonacci et al. 2009, Moaveni et al. 2011, Astroza et al. 2015), and is attributable to the fact that a large threshold (e.g., 0.98) must be considered for the MAC in the correlation analysis performed when extracting the auto-spectrum of each modal SDOF. It is noted that the modal ACFs required in the EFDD method are obtained by inverse Fourier transformation of the corresponding auto-spectra.

Table 4.3: Natural frequencies and damping ratios identified using ambient vibration test data.

		Natural frequency (Hz)					Equivalent damping ratio (%)				
	Mode	**SSI-DATA**	**NExT-ERA**	**EFDD**	**Mean**	**c.o.v (%)**	**SSI-DATA**	**NExT-ERA**	**EFDD**	**Mean**	**c.o.v (%)**
AMB 1 / DS0	1-T+To	1.87	1.87	1.88	1.87	0.31	0.95	0.89	0.81	0.88	8.25
	1-L	1.93	1.93	1.94	1.93	0.33	1.02	1.01	1.11	1.05	5.09
	1-To	2.66	2.66	2.66	2.66	0.04	1.32	1.30	0.71	1.11	31.35
	2-T+To	6.86	6.87	6.86	6.86	0.08	1.90	1.41	0.87	1.39	37.10
	2-L	7.24	7.22	7.14	7.20	0.73	1.91	1.77	1.25	1.64	21.05
	2-L+To	7.84	7.75	7.76	7.78	0.63	2.61	1.63	0.65	1.63	60.20
	2-To	10.10	10.07	10.10	10.09	0.16	2.19	2.38	2.64	2.40	9.38
	3-L	11.79	11.40	11.83	11.67	2.04	4.68	2.14	0.02	2.28	102.20
	3-To	13.63	13.63	13.87	13.71	1.01	1.26	3.67	0.46	1.80	92.95
	4-L	19.92	19.78	19.69	19.80	0.59	1.34	0.69	0.19	0.74	77.68
	5-L	24.09	24.15	23.99	24.08	0.33	1.69	0.92	0.03	0.88	94.22
AMB 2 / DS1	1-T+To	1.84	1.84	1.84	1.84	0.10	1.17	1.17	0.77	1.04	22.27
	1-L	1.78	1.78	1.79	1.78	0.27	0.87	0.83	1.36	1.02	28.82
	1-To	2.56	2.57	2.59	2.57	0.55	1.50	1.91	1.88	1.76	12.94
	2-T+To	6.66	6.67	6.63	6.65	0.28	1.84	1.74	0.92	1.50	33.48
	2-L	6.91	6.92	6.95	6.93	0.27	1.35	1.30	0.75	1.13	29.64
	2-L+To	7.37	7.34	7.43	7.38	0.61	1.66	2.06	2.67	2.13	23.85
	2-To	10.01	10.08	9.99	10.03	0.49	1.63	1.52	1.88	1.68	11.13
	3-L	11.19	11.28	11.02	11.16	1.20	3.80	1.91	1.19	2.30	58.55
	3-To	13.52	13.65	13.55	13.57	0.50	1.15	0.91	0.38	0.81	48.34
	4-L	19.50	-	19.55	19.52	0.18	3.53	-	0.27	1.90	121.40
	5-L	24.00	-	23.86	23.93	0.42	2.42	-	1.68	2.05	25.59
AMB 3 / DS2	1-T+To	1.81	1.81	1.80	1.81	0.30	1.72	1.39	1.35	1.49	13.59
	1-L	1.69	1.70	1.69	1.69	0.33	3.05	3.13	2.02	2.73	22.66
	1-To	2.49	2.49	2.48	2.49	0.14	1.73	1.65	1.98	1.79	9.49
	2-T+To	6.48	6.46	6.45	6.46	0.23	1.63	1.85	2.53	2.00	23.49
	2-L	6.72	6.68	6.81	6.74	0.95	2.80	2.97	1.29	2.35	39.24
	2-L+To	6.92	6.89	6.81	6.87	0.86	0.76	1.34	1.59	1.23	34.71
	2-To	9.97	10.03	10.02	10.01	0.33	2.17	1.83	2.33	2.11	12.19
	3-L	11.03	11.14	11.11	11.09	0.51	2.93	2.97	0.67	2.19	60.26
	3-To	13.39	13.40	13.43	13.41	0.15	1.16	1.11	0.16	0.81	69.89
	4-L	19.41	19.44	19.42	19.42	0.08	0.90	0.64	0.24	0.59	56.23
	5-L	23.31	-	23.26	23.29	0.15	2.42	-	3.05	2.73	16.22
AMB 4 / DS3	1-T+To	1.80	1.80	1.81	1.80	0.41	1.04	0.95	0.88	0.96	8.26
	1-L	1.61	1.61	1.62	1.61	0.38	1.16	1.16	1.24	1.19	3.81
	1-To	2.45	2.45	2.44	2.45	0.13	1.11	1.26	1.07	1.15	8.68
	2-T+To	6.67	6.66	6.67	6.67	0.11	1.76	1.60	0.67	1.34	43.70
	2-L	6.57	6.53	6.54	6.55	0.33	1.83	1.46	0.67	1.32	44.69
	2-L+To	7.21	7.28	6.84	7.11	1.65	2.77	4.06	2.23	3.02	19.57
	2-To	9.74	9.80	9.61	9.72	1.02	2.58	1.40	0.09	1.36	92.02
	3-L	10.74	10.74	10.72	10.73	0.12	2.22	1.60	0.87	1.56	43.13
	3-To	13.52	13.59	13.46	13.52	0.48	2.09	3.25	0.47	1.94	72.28
	4-L	-	17.28	17.44	17.36	0.67	-	1.11	0.58	0.84	44.66
	5-L	22.34	21.47	21.66	21.82	2.09	1.34	1.01	0.14	0.83	74.87

Table 4.3: Natural frequencies and damping ratios identified using ambient vibration test data, continued.

		Natural frequency (Hz)					Equivalent damping ratio (%)				
AMB 5 / DS4	1-T+To	1.75	1.75	1.75	1.75	0.06	0.98	0.97	0.81	0.92	10.18
	1-L	1.44	1.44	1.43	1.44	0.23	1.84	1.71	1.71	1.75	4.36
	1-To	2.29	2.29	2.27	2.28	0.49	0.94	1.10	0.79	0.94	16.38
	2-T+To	6.41	6.42	6.37	6.40	0.45	1.39	1.41	1.74	1.51	12.94
	2-L	5.63	5.30	5.89	5.61	5.27	1.59	1.03	0.48	1.03	53.64
	2-L+To	5.96	5.98	5.95	5.96	0.25	1.26	1.44	0.77	1.16	29.71
	2-To	9.12	9.11	9.09	9.11	0.14	1.81	2.13	0.64	1.53	51.56
	3-L	9.82	9.44	9.65	9.64	1.98	2.64	3.13	0.31	2.03	74.23
	3-To	11.53	11.68	11.55	11.59	0.71	2.59	2.74	0.64	1.99	58.82
	4-L	15.82	15.59	15.67	15.69	0.74	1.97	1.90	0.49	1.45	57.20
	5-L	20.60	20.20	20.23	20.34	1.09	2.36	1.21	0.07	1.21	94.56
AMB 6 / DS5	1-T+To	1.59	1.58	1.59	1.59	0.43	1.33	1.52	1.87	1.57	17.28
	1-L	1.04	1.04	1.04	1.04	0.13	3.88	3.57	3.24	3.56	8.93
	1-To	2.00	2.00	2.02	2.01	0.58	2.06	1.75	2.06	1.96	9.18
	2-T+To	5.83	5.85	5.80	5.83	0.45	1.67	1.51	1.54	1.57	5.46
	2-L	4.65	4.66	4.65	4.65	0.12	2.61	2.62	2.42	2.55	4.31
	2-L+To	-	-	5.80	5.80	-	-	-	1.71	1.71	-
	2-To	8.83	8.89	8.84	8.85	0.35	0.41	1.02	0.11	0.51	90.35
	3-L	10.22	9.65	10.11	9.99	3.02	1.28	2.83	0.07	1.39	99.05
	3-To	11.57	11.42	11.90	11.63	2.09	2.18	4.31	0.72	2.40	75.25
	4-L	13.69	13.57	13.84	13.70	0.98	1.92	2.82	1.13	1.96	43.14
	5-L	17.61	17.51	17.66	17.59	0.44	5.22	2.93	0.12	2.76	92.53
AMB 7 / DS6	1-T+To	1.49	1.49	1.49	1.49	0.03	0.79	1.03	1.27	1.03	23.39
	1-L	0.86	0.86	0.86	0.86	0.04	3.57	3.97	4.00	3.85	6.24
	1-To	1.84	1.84	1.84	1.84	0.09	1.57	1.34	2.40	1.77	31.54
	2-T+To	5.69	5.70	5.69	5.69	0.11	1.77	1.54	1.60	1.64	7.28
	2-L	4.28	4.28	4.28	4.28	0.02	1.73	1.67	1.72	1.71	1.89
	2-L+To	5.98	5.83	5.69	5.83	2.50	0.16	0.18	1.52	0.62	125.66
	2-To	8.02	8.05	8.00	8.02	0.34	2.88	1.46	0.88	1.74	59.27
	3-L	7.64	7.66	7.73	7.68	0.59	2.09	1.96	0.69	1.58	49.18
	3-To	10.89	10.66	10.74	10.76	1.08	2.37	3.65	1.55	2.52	41.92
	4-L	13.09	13.00	13.23	13.11	0.89	3.35	2.82	0.16	2.11	80.90
	5-L	15.03	15.11	14.98	15.04	0.42	4.24	2.40	0.02	2.22	95.19

T: transverse / L: longitudinal / To: torsion

Figure 4.5, Figure 4.6, and Figure 4.7 show graphically the trends in the identified natural frequencies and damping ratios (reported in Table 4.3) as the damage progresses. Figure 4.5 clearly indicates that (1) all the identified natural frequencies consistently decrease as the damage in the building progresses; and (2) the natural frequencies of the modes with predominant component in the longitudinal direction decrease at a faster rate. Moreover, the largest reductions in the natural frequencies occur at damage states 4, 5,

and 6. This observation is consistent with the visual damage inspection results (Table 4.2) and the intensity of the earthquake base motions (Figure 4.2).

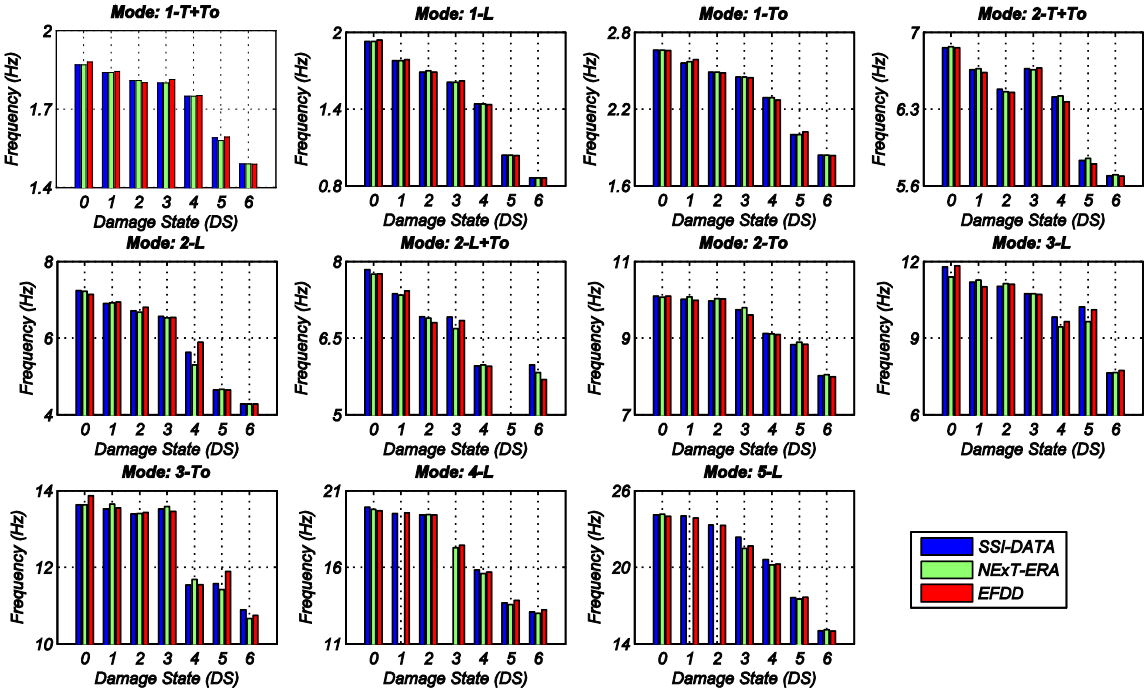

Figure 4.5: Natural frequencies identified at different damage states from ambient vibration test data.

Because the increasingly intense earthquake input motions were applied in the longitudinal direction of the building, a significant reduction of the lateral stiffness in this direction was expected. As a result, the identified natural frequencies of the longitudinal modes of the building experienced larger relative reductions than the other modes and the mode-crossing phenomenon occurred. At DS0, the mode 1-T+To had the lowest natural frequency (1.87 Hz) while the mode 1-L had a frequency of 1.93 Hz. At DS1 (after the structure was subjected to FB:1-CNP100), the mode 1-L had the lowest natural frequency (1.78 Hz), and the mode 1-T+To decreased its frequency to 1.84 Hz. Similar effects were also observed for higher modes. In particular, modes 2-T+To, 2-L, and 2-L+To also changed their order. Before DS2, they were sorted as 2-T+To, 2-L and 2-L+To, while at

DS3 the order changed to 2-L, 2-T+To, and 2-L+To, and from DS4 onwards to 2-L, 2-L+To, and 2-T+To. Similarly, modes 2-To and 3-L switched their order from DS5 to DS6.

Damage to the structure and to nonstructural components caused a reduction in the equivalent lateral stiffness of the building. Based on the information obtained by visual inspection, the damage observed before DS2 was mostly in the NCSs, especially the partition walls. Although the seismic base excitations were imposed in the longitudinal direction of the building, the torsional and transverse stiffness of the building also changed noticeably. This effect was quantified by analyzing the ratio between the natural frequencies at different damage states and the corresponding natural frequencies at DS0 (Figure 4.6). The longitudinal modes experienced higher relative reduction in their natural frequencies as damage progressed; in particular, the first longitudinal mode underwent the largest relative reduction. The identified natural frequency of mode 1-L decreased 8% and 56% (with respect to DS0) at DS1 and DS6, respectively. On the other hand, modes 1-T+To and 2-T+To experienced the least relative change. Their frequencies decreased 1.5% and 20% at DS1 and DS6, respectively. Higher longitudinal modes 3-L, 4-L, and 5-L were practically unaffected at low-intensity motions, but their frequencies reduced by almost 40% at DS6.

Figure 4.7 indicates that the damping ratios identified by the three different methods do not show any clear trend as damage progresses. However, it is well-known that the damping ratio estimates are sensitive to the amplitude of the structural response (e.g., Moaveni et al. 2011, Astroza et al. 2015); therefore, in order to directly compare the identified damping ratios, the level of motion should be similar at the different damage

states. That comparison is not strictly possible here because of the random nature of the ambient excitation. As mentioned previously, the identified damping ratios account for all sources of energy dissipation in the building, as assumed in the underlying mathematical model of the SID methods used.

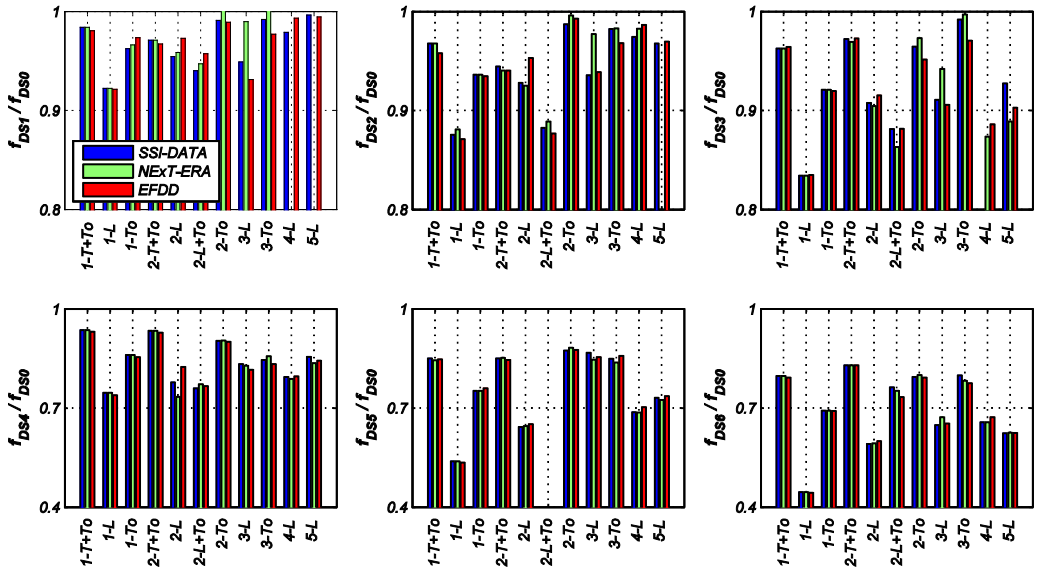

Figure 4.6: Ratio between natural frequencies identified at different damage states and their counterparts identified at DS0 from ambient vibration test data.

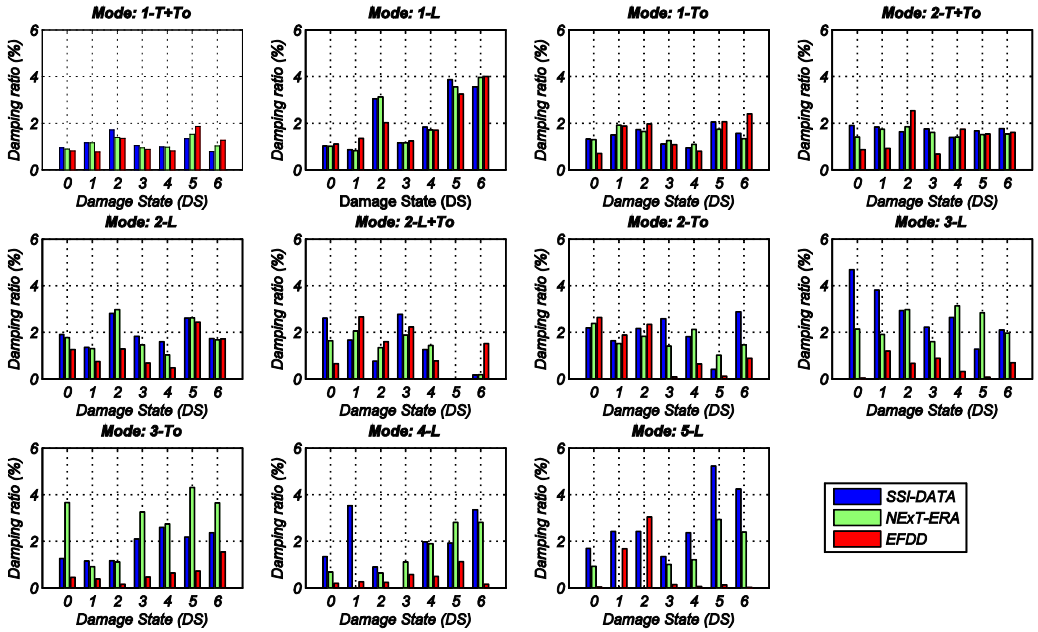

Figure 4.7: Equivalent damping ratios identified at different damage states from ambient vibration test data.

Since the mode shapes identified with the methods used herein are complex-valued, the corresponding real-valued approximations were computed using the approach proposed by Imregun and Ewins (1993). Figure 4.8 shows the real-valued approximations of the mode shapes of the building identified at DS0 using the SSI-DATA method and AV data.

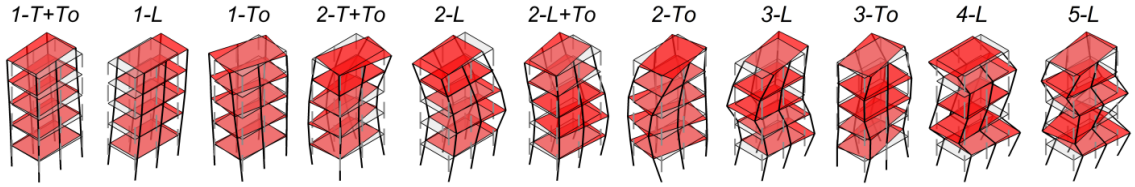

Figure 4.8: Real-valued approximations of mode shapes of the building identified at DS0 with the SSI-DATA method using the AMB1 test data.

The polar plot representation of the identified mode shapes in Figure 4.9 indicates the level of non-classical damping in the identified modes. Most of the identified mode shapes are almost purely classically damped since all the vectors (each of them representing a measured degree of freedom) in a polar plot are approximately collinear. However, modes 2-L+To, 3-L, 4-L, and 5-L appear to have a higher degree of non-classical damping than the other identified modes. Note that large estimation errors — which are likely due to noise— can cause a classically-damped mode to be identified as non-classically damped. There is higher uncertainty in the identification of higher modes compared to lower modes. As discussed earlier, lower participation of higher modes in the building response implies lower SNR for the higher modes than for the lower modes.

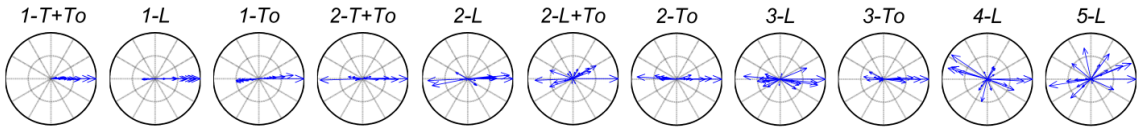

Figure 4.9: Polar plots of mode shapes identified at DS0 with the SSI-DATA method using the AMB1 test data.

The MAC was used to compare corresponding mode shapes estimated from the three output-only methods (Figure 4.10) using the AV test AMB1 conducted at DS0. Most of the MAC values along the diagonal (i.e., corresponding modes) of the matrix of MAC values were close to one, indicating that the mode shapes identified using different SID methods are consistent. The MAC value between modes 4 (2-T+To) and 6 (2-L+To) suggests some similarity in shape between them. A similar torsional component dominated the deformed shape of the building in these two modes, and the mode shapes differed primarily in their translational components. Because the higher modes are identified with higher estimation uncertainty, the MAC values between corresponding identified modes were consistently lower for higher modes than for lower modes. Similar results were obtained at all the states of damage but are not shown here due to space limitations. Note that the numbering of the modes in Figure 4.10 corresponds to that presented in Figure 4.8.

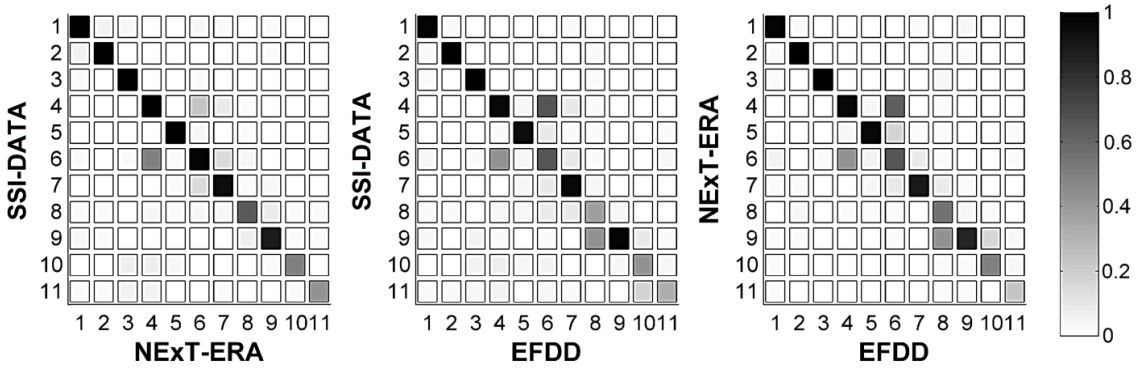

Figure 4.10: MAC values between mode shapes estimated at DS0 using the different SID methods from the AMB1 test data.

Figure 4.11 shows the MAC values between the mode shapes identified, using the SSI-DATA method with AV data, at different damage states and those identified at DS0. It is observed that lower modes (modes 1 to 5) remained almost unchanged as the damage

progressed, but higher modes (especially modes 8, 10, and 11 corresponding to 3-L, 4-L, and 5-L, respectively) changed at the states of highest damage (DS5 and DS6). Some off-diagonal entries of the MAC matrix show some significant correlation between non-corresponding modes. In particular, modes 1 (1-T+To) and 2 (1-L) show some correlation at DS0-DS1 and DS0-DS2, which is due to the crossing of these modes after the first seismic test FB:1-CNP100. Similarly, modes 4 (2-T+To), 5 (2-L), and 6 (2-L+To) show some correlation at DS0-DS2, DS0-DS3, and DS0-DS4. As pointed out before, these modes experienced mode crossing at damage states DS2, DS3, and DS4, which explains the large MAC values in the corresponding off-diagonal entries of the MAC matrix at those damage states.

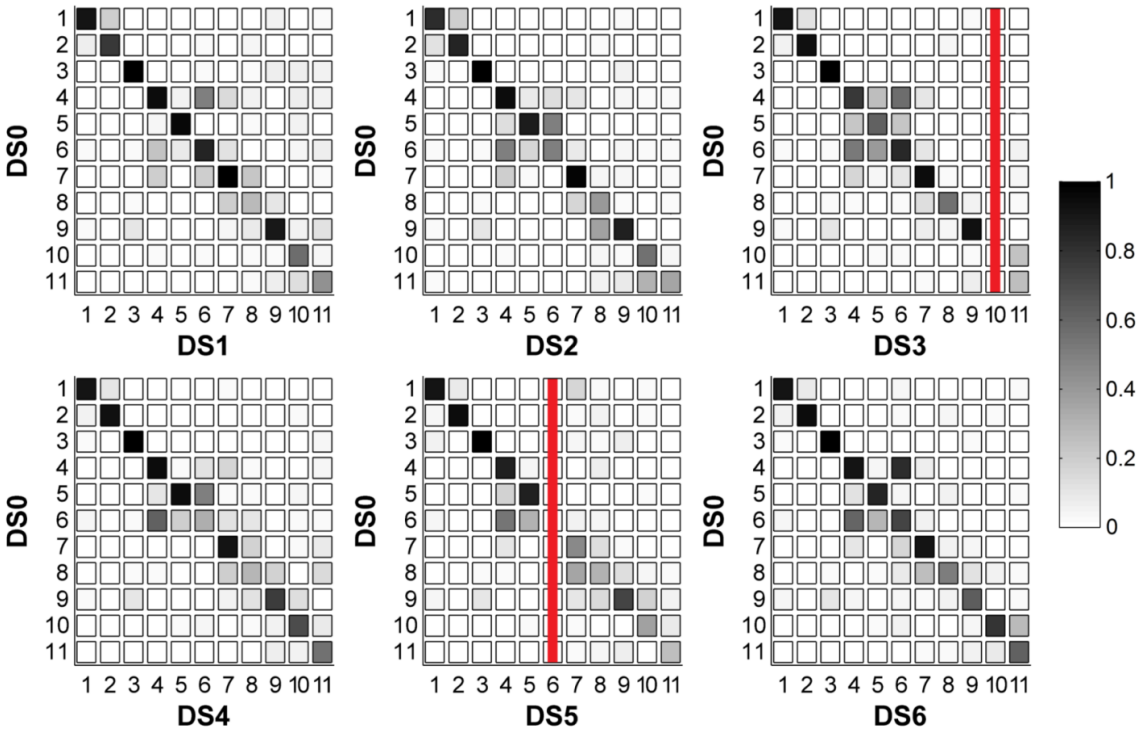

Figure 4.11: MAC values between mode shapes identified at different damage states and mode shapes identified at DS0 using the SSI-DATA method from the AMB1 test data.

The red lines in Figure 4.11 indicate modes that could not be identified using the SSI-DATA method with AV data. The corresponding normalized mode shapes (normalized with respect to the longitudinal component at the roof) identified at different damage states were also compared at each sensor location to analyze the potential of extracting damage location from comparison of corresponding mode shapes estimated before and after damage. These results are not presented herein due to space limitation. However, no clear trend was observed and it was not possible to identify the location of damage based on local differences of corresponding mode shapes estimated at different damage states.

4.6.2. System identification based on 1.5%g RMS white noise base excitation

Table 4.4 shows the natural frequencies and damping ratios identified using the three output-only and two input-output SID methods and the data recorded during the 1.5%*g* RMS WN base excitation tests performed at different damage states (see Table 4.1). Ten modes were identified using each of the three sets of WN test data (WN1A, WN2A, WN3A). They correspond to the first five longitudinal (1-L, 2-L, 3-L, 4-L, and 5-L), the first three torsional (1-To, 2-To, and 3-To), and two coupled translational-torsional (1-T+To and 2-L+To) modes. The natural frequencies identified using the various SID methods at each damage state (DS0, DS4 and DS5) are in good agreement. As in the case of AV data, the identified damping ratios, which are in the range 0–14%, show significantly higher variability across SID methods than the identified natural frequencies. The damping ratios identified using the 1.5%g RMS WN test data were significantly higher than those identified using the AV data. This observation confirms

the amplitude-dependent characteristic of identified damping ratios observed in other studies (e.g., Moaveni et al. 2011, Astroza et al. 2015).

Table 4.4: Natural frequencies and damping ratios identified using 1.5%*g* RMS white-noise base excitation test data.

		Natural frequency (Hz)							Equivalent damping ratio (%)						
	Mode	SSI-DATA	NExT-ERA	EFDD	DSI	OKID-ERA	Mean	c.o.v. (%)	SSI-DATA	NExT-ERA	EFDD	DSI	OKID-ERA	Mean	c.o.v. (%)
WN1A / DS0	1-L	1.24	1.41	1.34	1.40	1.37	1.35	5.04	10.69	10.13	9.40	6.75	8.30	9.05	17.32
	1-T+To	1.68	1.69	1.68	1.70	1.71	1.69	0.74	4.76	4.34	2.29	4.00	1.79	3.44	38.24
	1-To	2.28	2.28	-	2.29	-	2.28	0.25	3.64	4.16	-	2.34	-	3.38	27.74
	2-L	5.83	5.71	5.84	5.90	5.69	5.79	1.55	4.98	1.41	4.42	5.85	1.62	3.66	55.28
	2-L+To	6.18	6.51	6.35	6.32	6.20	6.31	2.11	2.39	2.46	2.54	3.19	1.16	2.35	31.38
	2-To	9.37	-	-	9.28	-	9.33	0.68	4.31	-	-	4.54	-	4.43	3.68
	3-L	11.02	10.31	10.29	10.19	10.19	10.40	3.37	3.69	1.51	5.35	4.54	5.56	4.13	39.70
	3-To	-	10.97	-	11.97	-	11.47	6.16	-	0.61	-	1.09	-	0.85	39.93
	4-L	18.07	18.51	18.46	18.21	19.63	18.58	3.32	3.07	4.25	5.37	6.65	4.86	4.84	27.40
	5-L	22.84	22.91	22.92	22.61	23.28	22.91	1.05	4.34	2.96	2.05	4.73	1.41	3.10	46.13
WN2A / DS4	1-L	0.81	0.82	0.84	0.86	0.88	0.84	3.42	6.89	6.41	6.39	8.89	9.09	7.53	17.86
	1-T+To	1.57	1.52	1.57	1.50	-	1.54	2.40	4.35	3.33	0.72	5.08	-	3.37	56.65
	1-To	1.71	1.77	-	1.74	-	1.74	1.72	4.23	4.16	-	1.24	-	3.21	53.16
	2-L	4.52	4.59	4.37	4.36	4.23	4.41	3.22	3.39	7.04	2.39	8.60	3.50	4.98	53.79
	2-L+To	4.87	4.71	-	4.84	4.91	4.83	1.79	3.54	3.81	-	1.59	0.20	2.29	74.66
	2-To	-	-	-	-	-	-	-	-	-	-	-	-	-	-
	3-L	8.71	8.63	8.72	8.37	8.59	8.60	1.65	4.89	3.93	3.39	5.00	5.84	4.61	20.83
	3-To	-	-	-	8.61	-	8.61	-	-	-	-	1.40	-	1.40	-
	4-L	12.75	12.46	12.81	12.97	13.24	12.85	2.24	4.87	4.98	0.12	3.03	3.95	3.39	58.76
	5-L	18.22	18.52	18.65	18.38	-	18.44	0.99	5.80	2.95	2.44	4.43	-	3.91	38.91
WN3A / DS5	1-L	0.63	0.63	0.63	0.65	0.67	0.64	2.82	7.13	6.69	4.97	8.66	10.06	7.50	25.92
	1-T+To	1.38	1.40	1.37	1.38	-	1.38	0.98	6.00	5.92	3.60	5.10	-	5.16	21.60
	1-To	1.72	1.80	-	1.73	-	1.75	2.49	6.83	7.60	-	5.08	-	6.50	19.86
	2-L	3.17	3.18	3.03	3.28	3.30	3.19	3.40	10.81	13.38	7.59	10.18	9.99	10.39	19.94
	2-L+To	3.70	3.55	3.58	3.53	3.84	3.64	3.56	1.60	0.90	1.52	1.68	4.99	2.14	75.99
	2-To	5.19	5.01	-	5.08	-	5.09	1.78	1.38	1.32	-	1.26	-	1.32	4.55
	3-L	6.26	6.37	6.41	6.48	6.43	6.39	1.30	8.68	9.01	5.09	6.75	4.08	6.72	32.16
	3-To	-	-	-	8.23	-	8.23	-	-	-	-	0.73	-	0.73	-
	4-L	11.16	11.18	11.49	12.08	12.09	11.60	3.98	1.82	2.00	2.64	3.68	5.52	3.13	48.54
	5-L	16.07	15.02	14.64	15.42	14.57	15.14	4.08	1.17	3.60	2.90	4.40	1.69	2.75	48.37

T: transverse / L: longitudinal / To: torsion

Figure 4.12, Figure 4.13, and Figure 4.14 show graphically the information reported in Table 4.4. Because the shake table excited the building specimen in its longitudinal direction only, the identification of the modes with torsional and transverse components was more difficult than when using the AV data, since the contributions of

those modes in the building response are substantially lower than those of the longitudinal modes (Figure 4.4). In particular, the mode 2-T+To cannot be identified using the 1.5%g RMS WN test data. Moreover, it is observed that the EFDD method was not able to identify the higher modes that are poorly excited by the longitudinal white noise base excitation, because peaks on the plots of the singular values of the PSD matrix of the measured response vector associated to these modes could not be accurately identified.

Figure 4.12 shows that all the identified natural frequencies consistently decreased as the damage induced by the different seismic tests progressed, with the longitudinal modes (1-L, 2-L, 3-L, 4-L, and 5-L) experienced a faster reduction. Because 1.5%*g* RMS WN base excitation tests were performed only at damage states DS0, DS4, and DS5 (Table 4.1), studying the effect of each seismic excitation on the identified modal parameters was not possible. However, it is observed that the amplitude of the reduction (in percent) of the natural frequencies from DS0 to DS4 was similar to that from DS4 to DS5. This confirms that the identified natural frequencies abruptly decreased at DS5, which is in agreement with the results obtained using AV data (Table 4.3 and Figure 4.5).

Due to the higher amplitude of the building response in the WN base excitation than in the AV tests (Figure 4.4), no mode crossing was observed for the WN test data. During the WN base excitation tests, the level of excitation was high enough to reduce the longitudinal stiffness of the building such that the first longitudinal mode corresponded to the lowest natural frequency at all states of damage, while the frequency of mode 2-L was always lower than the frequency of mode 2-L+To.

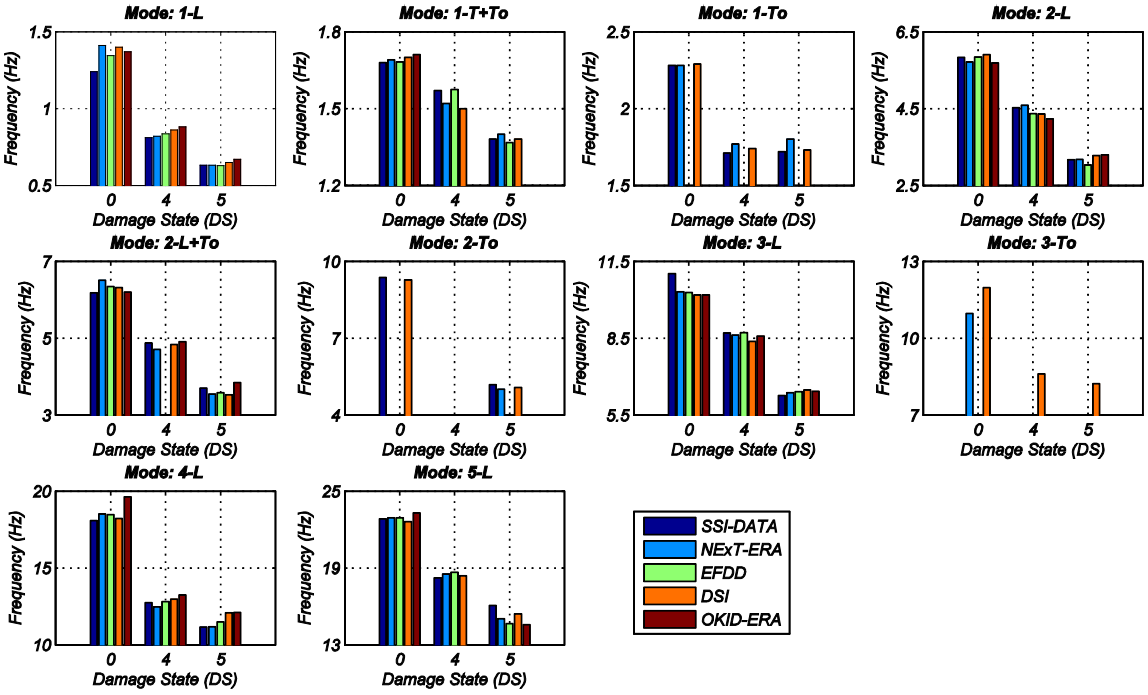

Figure 4.12: Natural frequencies identified at different damage states from 1.5%*g* RMS white noise base excitation test data.

The reduction of the building natural frequencies as the damage progressed is evident in all modes, as already observed when using the AV data. Figure 4.13 shows the ratio between the natural frequencies identified at different damage states and their counterparts identified at DS0. The identified natural frequency of the first longitudinal mode shows the highest relative reduction. The natural frequency of mode 1-L decreased by approximately 38% and 52% (with respect to DS0) at DS4 and DS5, respectively. In contrast, the natural frequency of mode 1-T+To (with the smallest relative reduction), decreased only by 8% and 18% at DS4 and DS5, respectively.

As expected and previously observed (e.g., Moaveni et al. 2011), the natural frequencies identified from WN base excitation test data were lower than those identified from AV data (compare Figure 4.6 and Figure 4.13). The difference is largest for mode 1-L and becomes, in general, progressively smaller for higher modes (2-L, 3-L, 4-L, 5-L).

At DS5, all modes except mode 1-T+To showed a much higher relative reduction in their identified natural frequency for the WN base excitation data than for the AV data. Since the building response is intrinsically nonlinear, the equivalent secant stiffness of the structure reduces as the amplitude of the response increases.

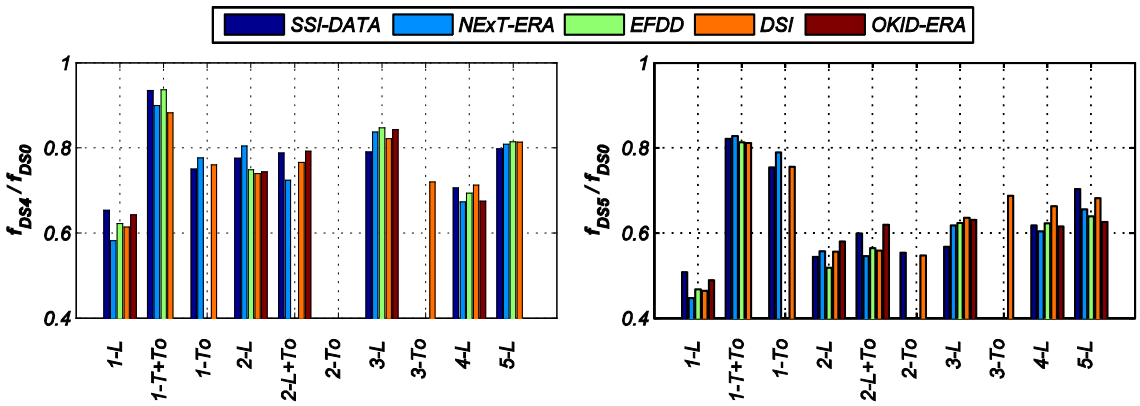

Figure 4.13: Ratio between natural frequencies identified at different damage states and their counterparts identified at DS0 from 1.5%*g* RMS white-noise base excitation test data.

Figure 4.14 shows that the damping ratios identified using the five different methods do not exhibit any clear trend as damage progresses; however, the highest estimated damping ratios are associated with the longitudinal modes. Since the seismic and WN base excitations were applied only in the longitudinal direction of the building, it is expected to obtain larger damping ratios for the longitudinal modes than for the other identified modes. Damping ratios identified from AV data (Figure 4.7) are considerable smaller than those identified from WN test data (Figure 4.14), especially for lower modes. This observation indicates the amplitude-dependency characteristic of the estimated damping ratios. Potential sources of energy dissipation are provided by the NCSs, their interaction with the structure, and hysteretic material behavior.

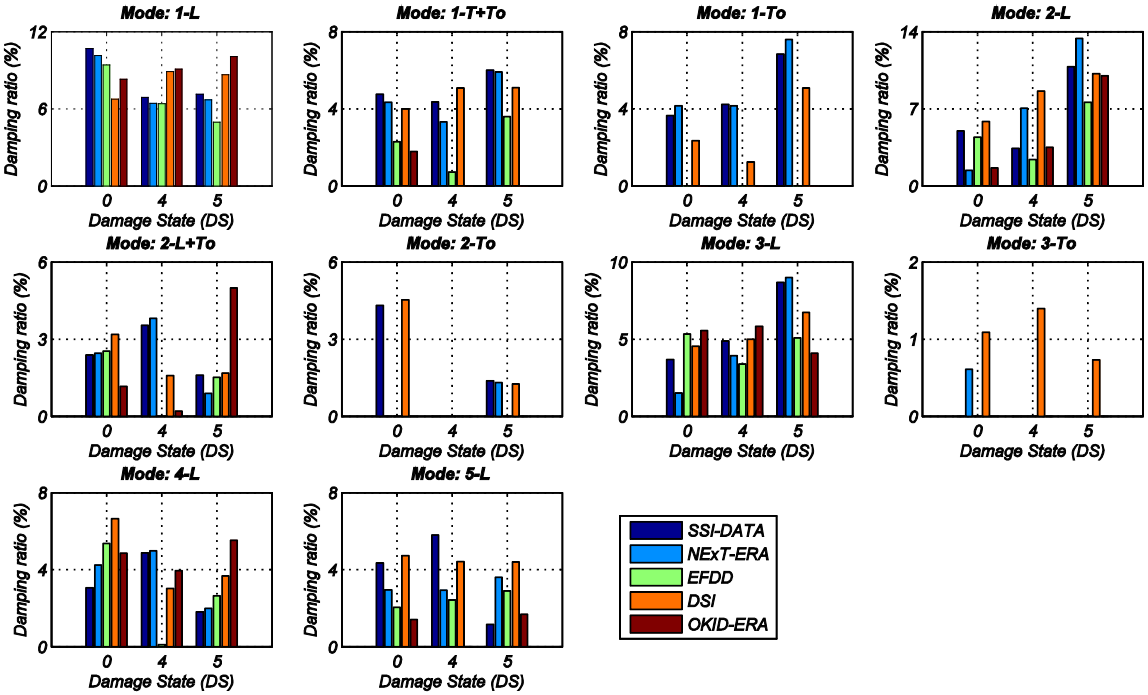

Figure 4.14: Equivalent damping ratios identified at different damage states from 1.5%*g* RMS white-noise base excitation test data.

The real-valued approximations of the mode shapes of the building identified at DS0 with the DSI method using the 1.5%*g* RMS WN test data are shown in Figure 4.15. These mode shapes correspond to the same mode shapes identified using the AV data (Figure 4.8), except for mode 2-T+To, which could not be identified from the WN test data, as discussed earlier.

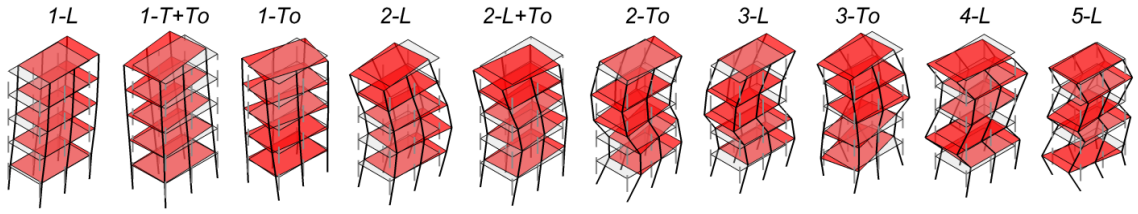

Figure 4.15: Real-valued approximations of mode shapes of the building identified at DS0 with the DSI method using the WN1A test data.

The polar plots in Figure 4.16 show that half of the identified mode shapes were estimated as almost purely classically damped (as indicated by the quasi-collinearity of

the vectors in the polar plot). Modes 2-L+To, 2-To, 3-To, 4-L, and 5-L were estimated with a higher degree of non-classical damping than the other modes, but a note of caution: the identified non-classical damping characteristics may be due to estimation errors. Higher modes contribute less to the response of the building than lower modes and, consequently, suffer from lower SNRs.

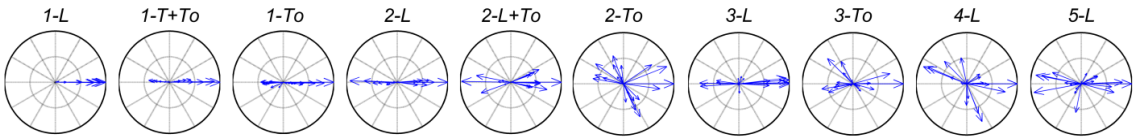

Figure 4.16: Polar plots of mode shapes identified at DS0 with the DSI method using the WN1A test data.

In order to compare the mode shapes identified using the five different SID methods, Figure 4.17 shows the MAC values between them at DS0. The MAC values along the diagonal of the MAC matrix are close to one, indicating that corresponding mode shapes identified using different methods are very similar. However, the mode shapes identified using the SSI-DATA, DSI, and NExT-ERA methods show better agreement; moreover, these three methods are able to identify more modes than the EFDD and OKID-ERA methods. The MAC value between modes 4 (2-L) and 5 (2-L+To) indicates some correlation between these two modes, which is not surprising since the longitudinal component dominates the deformed shape of the building in these two modes, and these two mode shapes differ primarily in their torsional components. Similar to the results obtained using AV data (Figure 4.10), the MAC values corresponding to the higher modes are lower than those corresponding to the lower modes. Similar MAC value results were obtained at damage states DS4 and DS5; they are not shown here due to

space limitation. Note that the numbering of the modes corresponds to that presented in Figure 4.15.

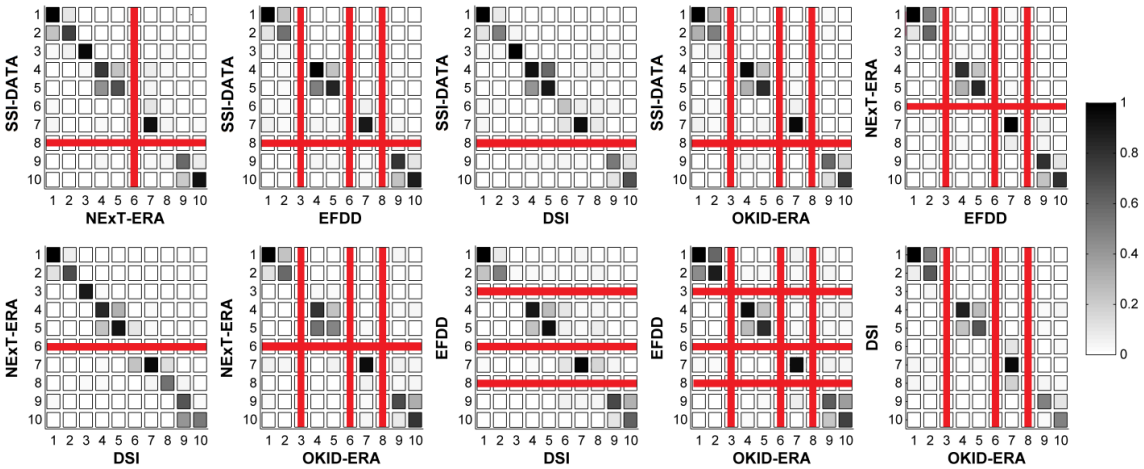

Figure 4.17: MAC values between mode shapes estimated at DS0 using different SID methods from the WN1A test data.

In order to detect the effects of damage on the identified mode shapes, Figure 4.18 shows the MAC values between the mode shapes identified at different damage states (DS4 and DS5) and the mode shapes identified at DS0 using the DSI method. The lower modes (modes 1 to 5) remain basically unchanged as the damage progresses, but the higher modes (modes 6 through 10 corresponding to 2-To, 3-L, 3-To, 4-L, and 5-L, respectively) changed at damage states DS4 and DS5. The same correlation between modes 4 (2-L) and 5 (2-L+To) as described above is observed.

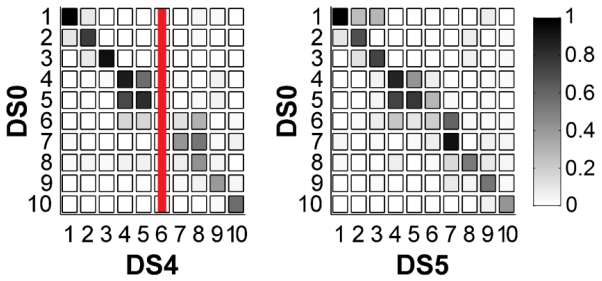

Figure 4.18: MAC values between mode shapes identified at different damage states and mode shapes identified at DS0 using the DSI method from the WN1A test data.

The SID study using the WN base excitation test data presented herein was also performed considering the rocking input excitation at the base of the building specimen, which was computed from the vertical accelerometers located at the first level. The SID results obtained from this multiple input (longitudinal and rocking base accelerations) - multiple output (translation accelerations at all floor levels) system model are similar to the results presented herein, which are based on a single input (longitudinal base acceleration) - multiple output (translation accelerations at all floor levels) system model. Relative differences of less than 7% for the natural frequencies (1.7% on average) and less than 30% for the damping ratios (15% on average) were obtained using both system models.

4.6.3. System identification based on 3.0% and 3.5%g RMS white-noise base excitation

In addition to the 1.5%g RMS WN base excitation, WN base excitations with a RMS of 3.0%g were applied to the building at DS0 and DS4; and WN base excitations with a RMS of 3.5%g were applied at DS0 and DS5. Figure 4.19 shows the natural frequencies and damping ratios identified with the DSI method using the input-output data recorded during WN base excitation tests of different amplitudes. The identified natural frequencies consistently decreased as the amplitude of the excitation increased, which is valid for all modes identified and the three damage states considered. These results clearly show the effect of cracking in the concrete and the consequent loss of the building equivalent stiffness during the WN base excitation tests, since cracks grow as the amplitude of the base excitation increases. On the other hand, the identified damping

ratios do not exhibit a clear trend as a function of the amplitude of the WN base excitation.

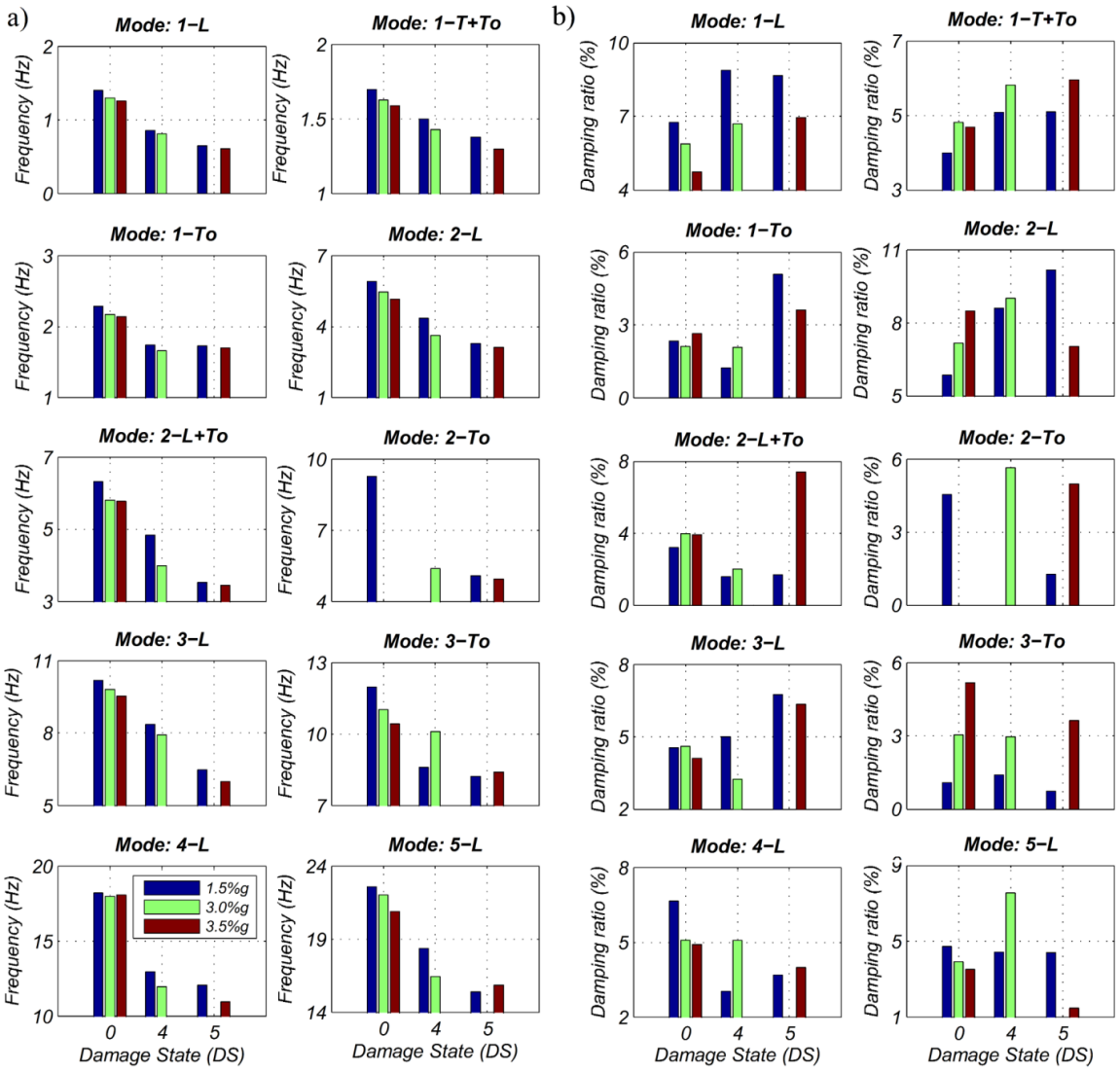

Figure 4.19: Effect of the amplitude of the WN base excitation on the modal properties identified using the DSI method: (a) natural frequencies, and (b) damping ratios.

Consistent results to those presented for 1.5%g RMS WN base excitation test data were obtained from 3.0% and 3.5%g RMS WN base excitation test data. For WN tests WN1B, WN1C, WN2B, and WN3B, the natural frequencies identified using the five different SID methods were in very good agreement, with coefficient of variations lower

than 7.5%. Method-to-method variability of the identified damping ratios was considerable larger, with coefficient of variations in the range 10−97%.

4.7. Estimated response and modal decomposition

Figure 4.20 compares the measured absolute acceleration time histories at the second and roof levels of the building with their counterparts predicted using the state-space model identified with the DSI method from WN base excitation test data at DS0 (test WN1C) and DS5 (test WN3B). This comparison was carried out for all WN base excitation tests. In each case, an excellent to very good match is obtained between the measured and predicted responses at all floors. However, the level of discrepancy between the recorded and predicted responses increases as the level of damage in the building specimen increases. This is because the level of nonlinearity in the structural response increases for the same level of input excitation as the damage progresses. Consequently, the LTI model assumed for SID purposes was not able to predict the building response accurately; therefore, discrepancies between the measured and predicted responses increased as the level of damage in the building and thus nonlinearity in its response increased. In other words, as the damage progresses in the building, detailed features of the measured building response time histories increasingly cannot be reproduced by a LTI model.

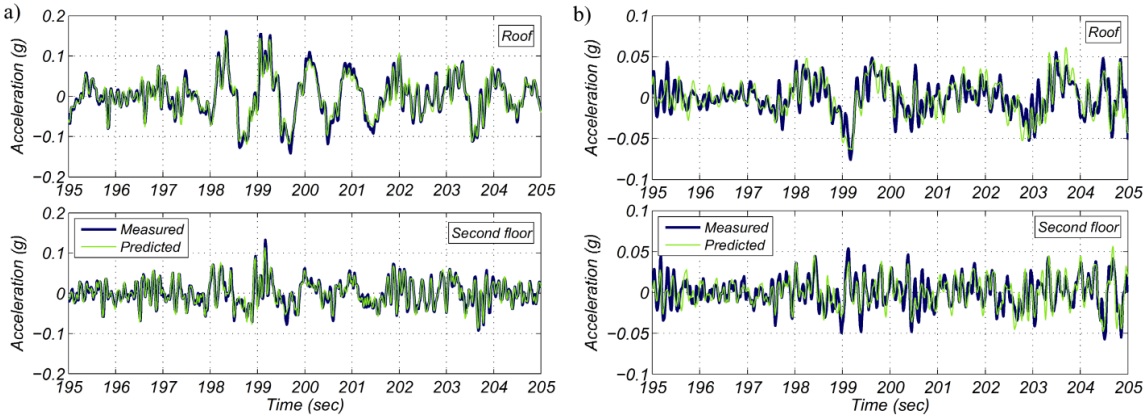

Figure 4.20: Comparison between measured and predicted (using identified state-space model) absolute translational acceleration responses at the second and roof levels: (a) DS0 (test WN1C), and (b) DS5 (test WN3B).

To study the relative contributions of the different modes to the building response, the modal decomposition of the building absolute acceleration response (see Appendix A for details and derivations) was estimated using the state-space model identified using the DSI method. Figure 4.21 shows the modal contributions to the building absolute acceleration response time histories at the second and roof levels at DS0 (test WN1C) and DS5 (test WN3B). The relative contribution of the higher modes to the total response was larger at the second floor than at the roof level. More importantly, as the damage in the structure increased (DS0 to DS5), the relative contributions of the higher modes (2-L, 3-L, and 4-L) increased drastically as compared to DS0; and thus the relative contribution of the fundamental mode (1-L) decreased considerably. This is due to the significant change (i.e., decrease) in the equivalent natural frequencies (especially of the longitudinal modes 1-L, 2-L, 3-L, and 4-L) of the building with the increase of damage. Similar results were obtained by analyzing the modal decomposition of the floor relative (to the base) acceleration responses predicted using the state-space model identified at different damage states.

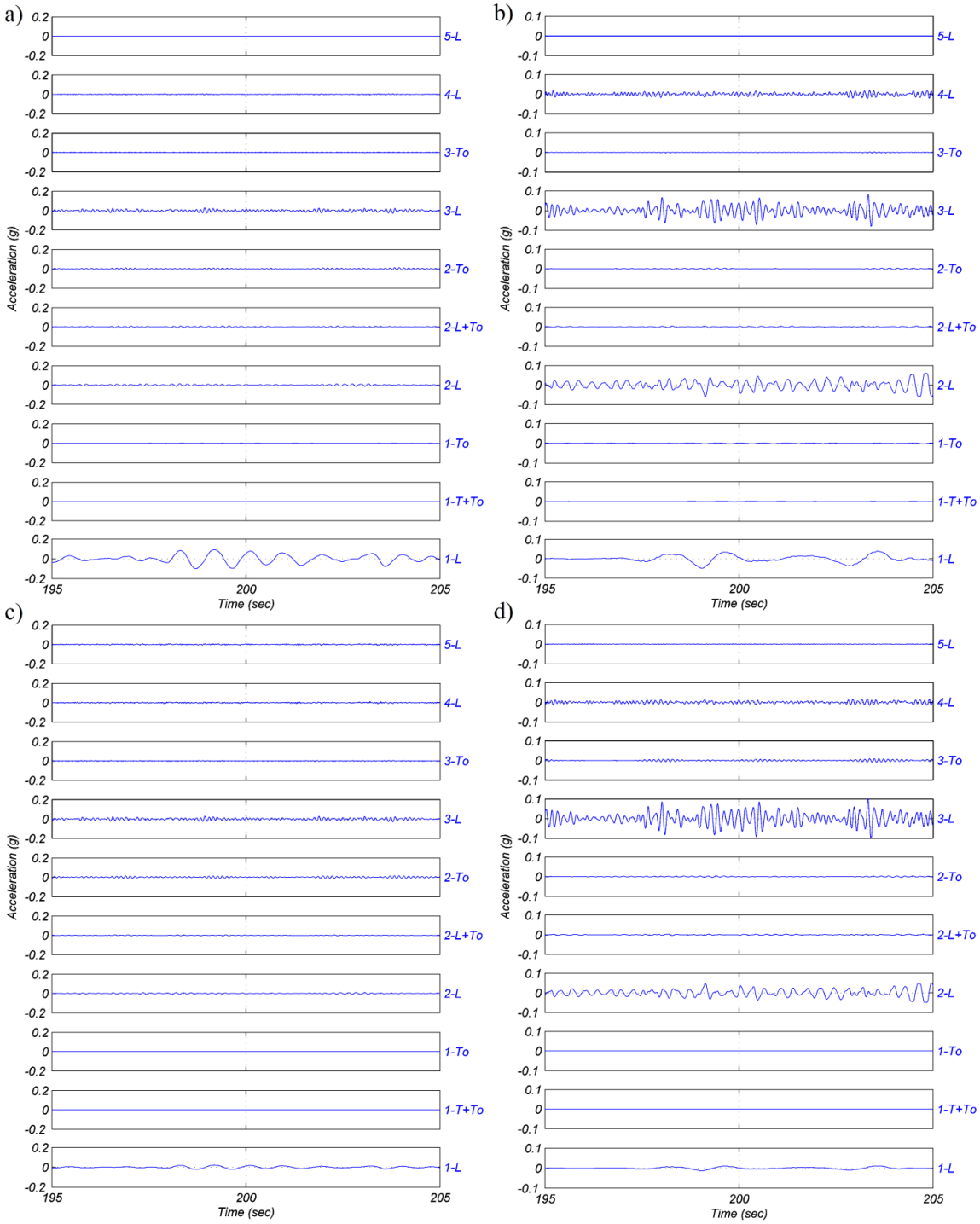

Figure 4.21: Modal decomposition of the identified absolute acceleration response time histories: (a) roof level at DS0 (test WN1C); (b) roof level at DS5 (test WN3B); (c) second floor level at DS0 (test WN1C); and (d) second floor level at DS5 (test WN3B).

4.8. Apparent story and global stiffness loss

The apparent story stiffness (defined as the ratio between the total story shear force and the interstory drift) and the apparent global structural stiffness (defined as the ratio between the total base shear and the roof drift) were estimated experimentally through linear least-squares fitting using the WN base excitation test data.

The total (inertial) story shear forces were computed as

$$V_{i/i+1}(t) = -\sum_{k=i+1}^{6} m_k \cdot a_k(t) \qquad i = 1,...,6 \tag{4.2}$$

where $V_{i/i+1}$ denotes the story shear at mid-height between levels i and $(i+1)$ of the building, a_k is the absolute acceleration at level k in the EW direction (computed as the average of the accelerations measured at the four corners), and m_k is the tributary mass of level k. The absolute displacements of all floors in the EW direction were computed through double integration of the recorded floor absolute acceleration time histories in the EW direction.

By using the story shear forces and interstory drifts obtained from test WN1A as reference, the apparent story and global stiffness losses $(1-k_{dam}/k_{ref})$, where k_{dam} is the stiffness of the damaged building and k_{ref} is the reference stiffness, were computed for tests WN1B, WN1C, WN2A, WN2B, WN3A, and WN3B [see Figure 4.22(a)]. Since the mass properties of the building remained unchanged, the ratio between the natural frequencies of the building in its damage states (tests WN1B, WN1C, WN2A, WN2B,

WN3A, and WN3B) and its reference state (test WN1A), f_{dam}/f_{ref}, can be approximated as

$$\frac{f_{dam}}{f_{ref}} = \sqrt{\frac{k_{dam}}{k_{ref}}} \tag{4.3}$$

Figure 4.22(a) shows clearly the degradation of the apparent story and global stiffnesses with increasing intensity of the seismic motion applied to the building. During the WN base excitation tests at DS0 (WN1A, WN1B, WN1C), the reduction of the apparent stiffness (relative to WN1A test) reached almost 20% (at WN1C) and was practically the same at the global and story levels. For damage states DS4 and DS5, the apparent story and global stiffnesses were reduced by approximately 60% (tests WN2A and WN2B) and 80% (tests WN3A and WN3B), respectively. Moreover, the apparent story stiffness losses were higher at the lower stories of the building, which is in agreement with the observed distribution of damage over the height of the building.

Degradation of the stiffness of the building can be also estimated from the identified natural frequencies reported in Figure 4.12 and Figure 4.19(a). This is done by calculating, for each mode, the ratio between the natural frequencies estimated from tests WN1B, WN1C, WN2A, WN2B, WN3A, and WN3B, and the natural frequency estimated from test WN1A. Figure 4.22(b) shows the ratio f_{dam}/f_{ref} for the longitudinal modes (1-L, 2-L, 3-L, 4-L, and 5-L) of the building computed from the SID results shown in Figure 4.12 and Figure 4.19(a). The ratio f_{dam}/f_{ref} obtained from Equation (4.3) for the global stiffness is also shown in Figure 4.22(b). It is observed that the ratio f_{dam}/f_{ref} estimated from the global response of the building correlates very well with

the ratio computed from the identified natural frequencies of mode 1-L. This suggests that the global hysteretic response of the building (described by the total base shear versus roof drift) is dominated by the first longitudinal mode. The ratio f_{dam}/f_{ref} of other longitudinal modes (2-L to 5-L) is larger than the ratio estimated from the global response of the building and, in general, the ratio f_{dam}/f_{ref} is larger (less reduction in stiffness) for higher modes.

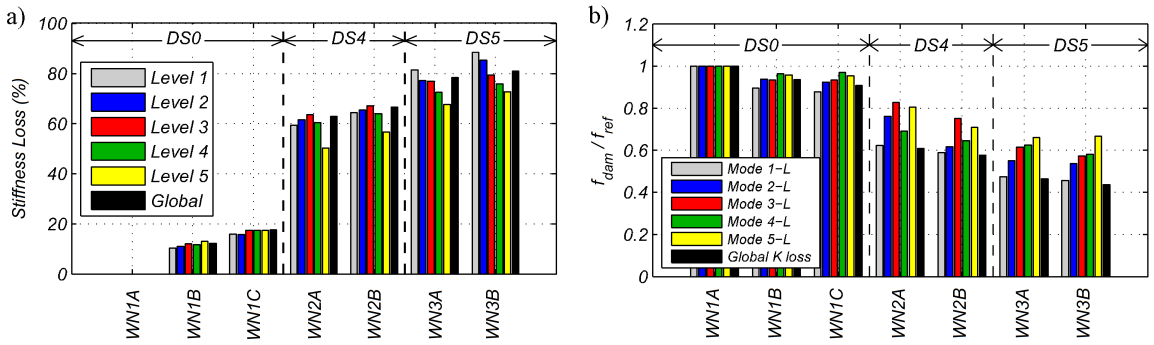

Figure 4.22: (a) Apparent story and global stiffness losses during the white-noise base excitation tests; and (b) ratios between natural frequencies of the building in its damaged states and its reference state obtained from the system identification and global stiffness loss results.

4.9. Conclusions

A full-scale 5-story reinforced concrete building fully outfitted with nonstructural components and systems (NCSs) was built and tested on the outdoor unidirectional NEES-UCSD shake table in April-May 2012. The purpose of this experimental program was to study the response of the structure and NCSs and their dynamic interaction during seismic excitations of increasing intensity. A suite of six earthquake motions were carefully designed and applied to the fixed-base (FB) building to progressively damage the structure and NCSs in a realistic manner. Vibration response data from different

sources of excitation, including ambient vibration (AV) and low-amplitude white-noise (WN) base excitation tests, were recorded at different damage states of the building to conduct system identification (SID) studies. In particular, AV data were recorded before and after each seismic test, and WN base excitation tests were conducted at key damage states. Using the structural vibration data recorded by an array of 24 uni-axial accelerometers, five state-of-the-art SID methods, including three output-only (SSI-DATA, NExT-ERA and EFDD) and two input-output (OKID-ERA and DSI), were employed to identify the modal properties of the structure (i.e., natural frequencies, damping ratios, and mode shapes) at different damage states. The low intensity of the excitation during AV and WN tests facilitated identifying the modal properties of an equivalent linear elastic viscously damped time-invariant model of the FB building. These identified modal properties changed at different stages of the test protocol because of the structural and nonstructural damage inflicted to the structure and NCSs by the earthquake base motions.

Eleven and ten modes were identified using the AV and WN base excitation test data, respectively. Natural frequencies and mode shapes identified using different SID methods were found in very good agreement, while the identified damping ratios showed higher method-to-method variability. The results showed that the identified natural frequencies decreased as damage in the structural and NCSs progressed. The magnitude of the reduction of the identified natural frequencies was greater for the longitudinal modes of the building because the equivalent stiffness of the building in that direction degraded more because it coincided with the direction of the WN and seismic excitations. This resulted in mode crossings at different damage states. Since the structural response

was intrinsically nonlinear —despite the low amplitude of the excitation— the equivalent secant stiffness of the building reduced as the amplitude of the response increased for a given damage state.

The damping ratios identified using AV data were considerably lower than those identified using low-amplitude WN base excitation data. The identified damping ratios did not show a clear trend as a function of damage, but longitudinal modes attained higher values than those of the coupled translational-torsional and torsional modes. This is most likely due to the higher hysteretic damping (or hysteretic energy dissipated) associated with longitudinal modes (direction of the excitation), which was identified as equivalent viscous damping because of the underlying mathematical model assumed in the SID methods used. The correlation between mode shapes at different damage states showed some variations but mostly at the higher modes; it is unclear if this was the effect of damage or due to estimation uncertainty because of the low SNR associated in the identification of those modes.

Detailed visual inspections of the damage performed between the seismic tests permitted correlating the identified modal parameters and their changes with the actual damage observed in the building. Apparent story and global stiffnesses of the building were computed from the experimental data recorded during the WN base excitation tests. The loss of global apparent stiffness was consistent with the reduction of the natural frequency of the first longitudinal mode (1-L) identified using the SID methods, suggesting that the global hysteretic response of the building was dominated by the first longitudinal mode. Higher modes showed less reduction in their associated stiffnesses. The modal contributions to the absolute acceleration response were also studied. As the

damage in the building progressed, the relative contribution of the higher modes increased significantly, and thus the relative contribution of the fundamental mode decreased notably.

This research provided a unique opportunity to investigate the performance of different state-of-the-art SID methods when applied to vibration data recorded with high spatial resolution in a real building subjected to progressive damage induced by a realistic source of dynamic excitation. The identified modal properties of the building at different levels of damage presented and discussed in this chapter provides the information required for vibration-based damage identification using linear finite element model updating. This case history contributes an important dataset for the structural and earthquake engineering community.

4.10. Acknowledgements

Chapter 4 is largely a reprint of the material that has been accepted for publication "System identification of a full-scale five-story reinforced concrete building tested on the NEES-UCSD shake table" in *Structural Control and Health Monitoring*, Astroza, Rodrigo; Ebrahimian, H.; and Conte, J.P.; Restrepo, J.I.; and Hutchinson, T.C. The dissertation author was the primary investigator and author of this paper.

References

Allemang, R.J. and Brown, D.L. (1982). "A correlation coefficient for modal vector analysis." *Proc. of 1st International Modal Analysis Conference (IMAC I)*, Orlando, FL, USA.

Antonacci, E., De Stefano, A., Gattulli, V., Lepidi, M., and Matta, E. (2009). "Comparative study of vibration-based parametric identification techniques for a three-dimensional frame structure." *Structural Control and Health Monitoring*, 19(5), 579–608.

Astroza, R., Ebrahimian, H., Conte, J.P., Restrepo, J.I., and Hutchinson, T.C. (2015). "Influence of the construction process and nonstructural components on the modal properties of a five-story building." Submitted to *Earthquake Engineering & Structural Dynamics*.

Belleri, A., Moaveni, B., and Restrepo, J.I. (2013). "Damage assessment through structural identification of a large-scale three-story precast concrete structure." *Earthquake Engineering & Structural Dynamics*, 43(1), 61–76.

Bernal, D., Dyke, S.J., Lam, H-F, and Beck, J.L. (2002). "Phase II of the ASCE Benchmark Study on SHM." *Proc. of the 15th ASCE Engineering Mechanics Conference*, Columbia University, NY.

Brincker, R., Ventura, C., and Andersen, P. (2001a). "Damping estimation by frequency domain decomposition." *Proc. of 29th International Modal Analysis Conference (IMAC XIX)*, Bethel, CT, USA.

Brincker, R., Zhang, L., and Andersen, P. (2001b). "Modal identification of output-only systems using frequency domain decomposition." *Smart Materials and Structures*, 10(3), 441–445.

Chen, M., Pantoli, E., Wang, X., Astroza, R., Ebrahimian, H., Hutchinson, T.C., Conte, J.P., Restrepo, J.I., Marin, C., Walsh, K.D., Bachman, R.E., Hoehler, M.S., Englekirk, R., Faghihi, M. (2015). Full-scale structural and nonstructural building system performance during earthquakes: Part I – Specimen description, test protocol and structural response. Submitted to *Earthquake Spectra*.

Chen, M., Pantoli, E., Wang, X., Astroza, R., Ebrahimian, H., Mintz, S., Hutchinson, T.C., Conte, J.P., Restrepo, J.I., Meacham, B., Kim, J., and Park, H. (2013). *BNCS Report #1: Full-scale structural and nonstructural building system performance during earthquakes and post-earthquake fire - Specimen design, construction and test protocol*. Structural Systems Research Project Report Series, SSRP 13/09, University of California San Diego, La Jolla, CA.

Dilena, M. and Morassi, A. (2012). "Dynamic testing of a damaged bridge." *Mechanical Systems and Signal Processing*, 25(5),1485–1507.

Doebling, S.W., Farrar, C.R., Prime, M.B., and Shevit, D.W. (1996). *Damage identification and health monitoring of structural and mechanical systems from changes in their vibration characteristics: A literature review*. Technical Report LA-13070-MS, Los Alamos National Laboratory, Los Alamos, NM.

Fan, W. and Qiao, P.Z. (2011). "Vibration-based damage identification methods: A review and comparative study." *Structural Health Monitoring*, 10(5), 83–111.

Farrar, C.R., Cornwell, P.J., Doebling, S.W., and Prime, M.B. (2000). *Structural health monitoring studies of the Alamosa Canyon and I-40 bridges*. Technical Report LA-13635-MS, Los Alamos National Laboratory, Los Alamos, NM.

Giraldo, D., Song, W., Dyke, S., and Caicedo, J. (2009). "Modal Identification through Ambient Vibration: Comparative Study." *ASCE Journal of Engineering Mechanics*, 135(8), 759–770.

He, X., Moaveni, B., Conte, J.P., Elgamal, A., and Masri, S.F. (2009). "System identification of Alfred Zampa Memorial Bridge using dynamic field test data." *ASCE Journal of Structural Engineering*, 135(1), 54–66.

Hien, H. and Mita, A. (2011). "Damage identification of full scale four-story steel building using multi-input multi-output models." *Proc. of SPIE 7981, Sensors and Smart Structures Technologies for Civil, Mechanical, and Aerospace Systems*, San Diego, CA.

Hutchinson, T.C., Restrepo, J.I., Conte, J.C., Pantoli, E., Chen, M.C., Wang, X., Astroza, R., and Ebrahimian, H. (2014). *Shake table testing of a five story building outfitted with NCSs (BNCS project)*. Network for Earthquake Engineering Simulation (distributor), Dataset, DOI: 10.4231/D38W38349

Huth, O., Feltrin, G., Maeck, J., Kilic, N., and Motavalli, M. (2005). "Damage identification using modal data: Experiences on a prestressed concrete bridge." *ASCE Journal of Structural Engineering*, 131(12), 1898–1910.

Imregun, M., and Ewins, D.J. (1993). "Realization of complex mode shapes." *Proc. of 11th International Modal Analysis Conference (IMAC XI)*, Kissimmee, FL, USA.

James, G.H., Carne, T.G., and Lauffer, J.P. (1993). *The natural excitation technique (NExT) for modal parameter extraction from operating wind turbines*. Technical Report SAND92-1666, UC-261, Sandia National Laboratories, Sandia, NM.

Ji, X., Fenves, G., Kajiwara, K., and Nakashima, M. (2011). "Seismic damage detection of a full-scale shaking table test structure." *ASCE Journal of Structural Engineering*, 137(1), 14–21.

Johnson, E., Lam, H., Katafygiotis, L., and Beck, J.L. (2004). "Phase I IASC-ASCE Structural Health Monitoring Benchmark Problem Using Simulated Data." *ASCE Journal of Engineering Mechanics*, 130(1), 3–15.

Juang, J.N. and Pappa, R.S. (1985). "An eigensystem realization algorithm for modal parameter identification and model reduction." *Journal of Guidance, Control, and Dynamics*, 8(5), 620–627.

Juang, J.N., Phan, M., Horta, L.G., and Longman, R.W. (1991*). Identification of observer Kalman filter Markov parameters - Theory and experiments*. NASA Technical Report TM-104069, Hampton, VA.

Lauzon, R. and DeWolf, J. (2006). "Ambient vibration monitoring of a highway bridge undergoing a destructive test." *ASCE Journal of Bridge Engineering*, 11(5), 602–610.

Moaveni, B., Barbosa, A.R., Conte, J.P., and Hemez, F.M. (2014). "Uncertainty analysis of system identification results obtained for a seven-story building slice tested on the UCSD-NEES shake table." *Structural Control and Health Monitoring*, 21(4), 466–483.

Moaveni, B., He, X., Conte, J.P., Restrepo, J.I., and Panagiotou, M. (2011). "System identification study of a seven-story full-scale building slice tested on the UCSD-NEES shake table." *ASCE Journal of Structural Engineering*, 137(6), 705–717.

Moaveni, B., Stavridis, A., Lombaert, G., Conte, J.P., and Shing, P.B. (2012). "Finite element model updating for assessment of progressive damage in a three-story infilled RC frame." *ASCE Journal of Structural Engineering*, 139, 1665–1674.

Pantoli, E., Chen, M.C., Hutchinson, T.C., Astroza, R., Conte, J.P., Ebrahimian, H., Restrepo, J.I., and Wang, X. (2015a). "Landmark dataset from the building nonstructural components and systems (BNCS) project." Submitted to *Earthquake Spectra*.

Pantoli, E., Chen, M., Wang, X., Astroza, R., Ebrahimian, H., Hutchinson, T.C., Conte, J.P., Restrepo, J.I., Marin, C., Walsh, K.D., Bachman, R.E., Hoehler, M.S., Englekirk, R., Faghihi, M. (2015b). "Full-scale structural and nonstructural building system performance during earthquakes: Part II – NCS damage states." Submitted to *Earthquake Spectra*.

Peeters, B. and De Roeck, G. (2001). "One-year monitoring of the Z24-Bridge: Environmental effects versus damage events." *Earthquake Engineering & Structural Dynamics*, 30(2), 149–171.

Peeters, B. and De Roeck, G. (2001). "Stochastic system identification for operational modal analysis: A review." *Journal of Dynamic Systems, Measurement, and Control*, 123(4), 659–667.

Siringoringo, D., Fujino, Y., and Nagayama, T. (2012). "Dynamic characteristics of an overpass bridge in a full-scale destructive test." *ASCE Journal of Engineering Mechanics*, 139, 691–701.

Van Overschee, P. and De Moor, B. (1996). *Subspace Identification for Linear Systems: Theory, Implementation, Applications*. Kluwer Academic Publishers: Dordrecht, The Netherlands.

CHAPTER 5

DYNAMIC PROPERTIES OF A FULL-SCALE FIVE-STORY BASE-ISOLATED BUILDING TESTED ON A SHAKE TABLE

5.1. Introduction

Seismic protection systems are becoming very important and popular technologies aiming to protect civil structures and their nonstructural components and systems (NCSs) during earthquakes (Housner et al. 1997, Naeim and Kelly 1999, Warn and Ryan 2012, de la Llera et al. 2015). Good performance of isolated structures during recent strong earthquakes (e.g., Celebi 1996, Moroni et al. 2012, Gavin and Nigbor 2012, Hijikata et al. 2012, Miwada et al. 2012, Kasai et al. 2013) has shown the effectiveness of this technology to mitigate and even avoid damage, allowing continuity of operation of structures following intense events. In the case of building structures, seismic isolation is usually provided at the base by introducing a flexible horizontal interface with high internal damping between the structure and its foundation. This results in an elongation of the fundamental period of the building, usually much longer than predominant periods of

typical ground motions, and an increase of the energy dissipation capabilities of the system. The structure experiences a reduction of floor accelerations and interstory drift demands due to the elongation of the fundamental period and because the lateral deformations are concentrated in the isolation layer.

In spite of the growing number of seismically isolated structures built in the last twenty years, especially in Japan after the 1995 Kobe earthquake, availability of vibration data recorded on densely instrumented buildings during large earthquakes is still limited. Nonetheless, important research efforts have focused on investigating the response and behavior of base-isolated (BI) buildings during earthquakes. Maison and Ventura (1992) studied the behavior of the San Bernardino County Foothill Communities Law and Justice Center building during the 1990 Upland earthquake. Several authors investigated the response of BI buildings during the 1994 Northridge earthquake (e.g., Celebi 1996, Stewart et al. 1999, Nagarajaiah and Sun 2000). Ventura et al. (2003) and Loh et al. (2011) identified the dynamic properties of buildings using ambient vibrations and low level earthquake excitations. Furukawa et al. (2005) conducted the identification of a building instrumented during the 1995 Kobe earthquake by using the prediction error method and a nonlinear single degree of freedom system. Gueguen (2012) investigated the predominant frequency of a building using the frequency domain decomposition (FDD) method with ambient vibration data and the Wigner-Ville distribution with low to moderate vibrations from earthquake events. Siringoringo and Fujino (2014,2015) analyzed the response and conducted the identification of the modal characteristics of a building instrumented during various earthquake events, including the 2011 Tohoku

earthquake. Sridhar et al. (2014) analyzed the vibration data recorded in the Christchurch Women's hospital during low to moderate earthquake events.

Although limited due to the high costs they involve, shake table tests of large or full-scale building specimens have provided invaluable data. In particular, test programs conducted on BI buildings at the E-Defense shake table in Japan represent the first efforts at investigating the response of steel and reinforced concrete (RC) buildings using different types of isolation technologies. A first test program consisted of a full-scale four-story RC frame building tested in two phases: in 2008 the specimen was subjected to various types of horizontal excitations and in 2010 to horizontal and vertical input excitations (Sato et al. 2011, Furukawa et al. 2013). Two isolation systems were investigated, the first consisting of natural rubber bearing combined with U-shaped steel dampers and the second of high-damping rubber bearings (HDRBs). A second test program consisted of a full-scale five-story steel moment frame building tested in 2011 and considered two different isolation solutions: triple friction pendulum bearings and a combination of lead rubber and cross-linear bearings (Ryan et al. 2012, Sasaki et al. 2012).

In 2012, a landmark project was conducted on the NEES@UCSD shake table. A fully furnished full-scale five-story RC frame building was tested in two configurations: BI and fixed at its base. The goal of the test program was to investigate the response of the structure and NCSs, their dynamic interaction when subjected to seismic base excitation of different intensities, and the mitigating effects of base isolation on the structure and NCSs (Chen et al. 2013,2015, Pantoli et al. 2015a). In the BI configuration, a sequence of seven earthquake motion tests were designed and applied to the building to

progressively increase the seismic demand on the structure and NCSs. Before and after each seismic test, low-amplitude white noise (WN) base excitation tests with three different amplitudes were conducted and ambient vibration (AV) data were continuously recorded for approximately sixteen days, from before the beginning until after the end of the seismic tests. Vibration data recorded in the test specimen provide a unique opportunity to identify the dynamic characteristics of the building during construction and placement of major NCSs (Astroza et al. 2015a) and on both configurations, fixed (Astroza et al. 2015b) and isolated at its base.

In this chapter, the effectiveness of the isolation system in reducing the floor acceleration and interstory drift demands by elongating the predominant period of the building, concentrating the lateral displacement in the isolation layer, and increasing the energy dissipation capability is first investigated. Then, the structural vibrations recorded during low-amplitude WN base excitation tests and AVs are used to identify the modal properties of the BI building as well as to investigate the amplitude-dependency of the dynamic characteristics of the specimen. Because of the low intensity of the WN base excitations and AVs, a quasi-linear response of the system is assumed and the modal parameters of an equivalent viscously-damped linear elastic time invariant model are identified. Using the structural vibration data recorded by twenty six accelerometers, five system identification (SID) methods, including three output-only (SSI-DATA, NExT-ERA and EFDD) and two input-output (OKID-ERA and DSI), are used to identify the modal properties of BI building.

5.2. Description of the building and isolation system

5.2.1. Building specimen

The test structure was a full-scale five-story cast-in place RC building fully outfitted with a broad array of NCSs. The building had two bays in the longitudinal direction (direction of shaking) and one bay in the transverse direction, with plan dimensions of 11.0×6.6 m, respectively. The building had a floor-to-floor height of 4.27 m, a total height (measured from the top of the foundation to the top of the roof slab) of 21.34 m and an estimated total weight of 3010 kN for the bare structure and 4420 kN for the structure with all the NCSs, both excluding the foundation, which weighted approximately 1870 kN. Two identical one-bay special RC moment resisting frames provided the seismic resisting system. The frames were oriented East-West (direction of shaking) with one placed on the north face of the building and the other on the south face. The beams had different details at different floors. Floors two and three were constructed with ASTM A1035 high strength steel frame beams with a nominal yield strength of 830 MPa, floor four had a special moment frame with upturned hybrid beams (post-tensioned by four tendons and connected to the columns by ductile rod connectors), the fifth floor had an off-the-shelf ductile connector frame beam, and the roof had a conventional concrete frame beam. A total of six 0.66×0.46 m columns were reinforced with 6 #6 and 4 #9 longitudinal bars and a prefabricated transverse reinforcement. The floor system consisted of a 0.2 m thick concrete slab for all floors. There were two main openings on each slab to accommodate the stairs and elevator. Two 0.15 m thick concrete shear walls in the transverse direction provided the support for the elevator guiderails and additional

torsional stiffness to the building. Metal stairs, interior partition walls, exterior façade, medical equipments, computer servers, a cooling tower, an air handling unit, etc, composed the NCSs installed on the specimen. Figure 5.1 shows the test specimen and schematic elevation and plan views. Detailed information about the structural system, nonstructural components and their design considerations can be found in Chen et al. (2013,2015) and Pantoli et al. (2015a), while the complete dataset of the project in Hutchinson et al. (2014) and Pantoli et al. (2015b).

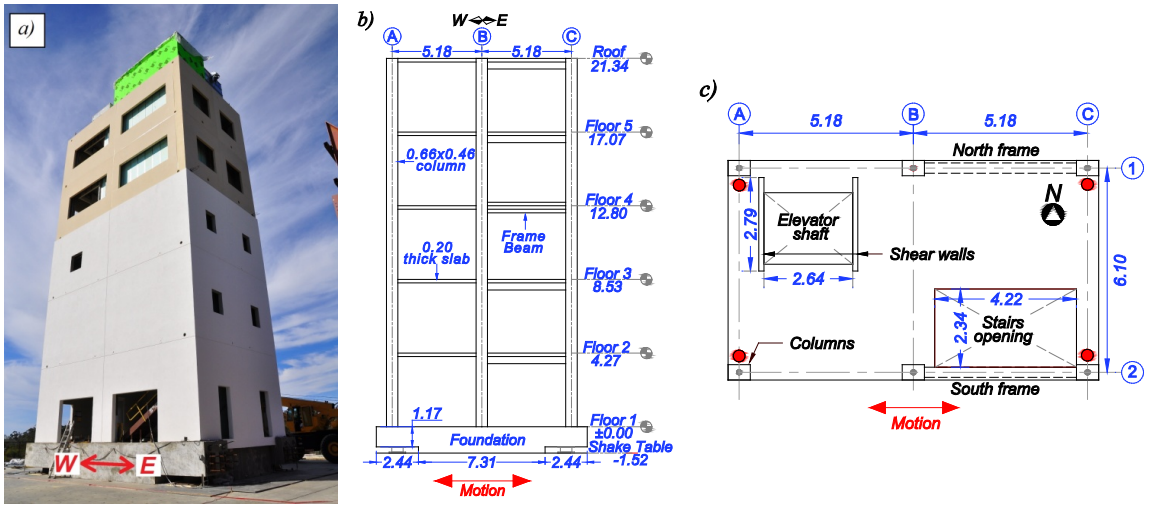

Figure 5.1: Test specimen: (a) completed building, (b) schematic elevation view, (c) schematic plan view. (Dimensions in m)

5.2.2. Isolators

The building was mounted on four HDRBs, which were placed between the shake table platen and the foundation near the four corners of the building. The isolators had a 0.65 m rubber diameter and a 0.10 m inside diameter. The total height of the bearings was 0.34 m, with 34 layers of 0.6 cm thick rubber corresponding to a total rubber height of 0.20 m and 33 steel shim plates with a nominal thickness of 0.3 cm each (Figure 5.2a and Figure 5.2b). Rubber layers and steel plates were protected with an exterior rubber

layer of 0.65m in diameter. Top and bottom cover plates of 2.0 cm thick were provided to connect the bearings with the shake table platen and foundation.

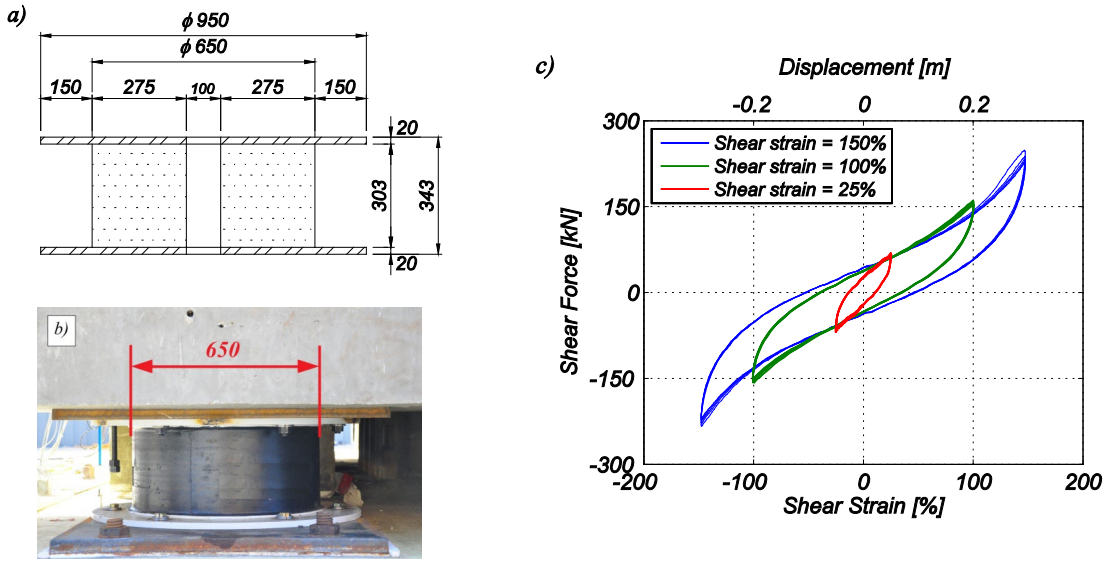

Figure 5.2: Isolator details: (a) schematic view, (b) actual isolator installed, (c) hysteretic curves of quality control tests. (Dimensions in mm)

Before the installation of the isolators, they were individually tested following standard quality control procedures. Such procedures consisted of seven sinusoidal, fully reversed sequences, to shear strains ranging from 25% to 150% at 25% increments. The data from the first cycle (scragging cycle) was discarded. Figure 5.2c shows the force-displacement curves obtained for 25, 100, and 150% shear strain. Effective or secant stiffness (k_{eff}) and effective damping ratio (ξ_{eff}) (equivalent viscous damping from hysteretic damping) are computed from the quality test data as (Priestley et al. 1996)

$$k_{eff} = \frac{F_{\max} - F_{\min}}{\Delta_{\max} - \Delta_{\min}} \tag{5.1}$$

$$\xi_{eff} = \frac{1}{2\pi} \frac{W_D}{k_{eff} \Delta_{\max}^2} \tag{5.2}$$

where $F_{\max}$, $F_{\min}$ = maximum and minimum applied forces, $\Delta_{\max}$, $\Delta_{\min}$ = maximum and minimum displacements of the isolator, and W_D = energy dissipated in one hysteresis

loop at displacement Δ_{max}. Figure 5.3 shows the values of k_{eff} and ξ_{eff} obtained from all the quality tests. It is noted that the shear strain is computed as the relative displacement between the top and bottom of the isolator divided by the total rubber height. Results obtained for different isolators are very similar and consistent with the behavior of HDRBs. The bearings exhibit a nonlinear behavior for shear strains equal to or larger than 25%. A high initial secant stiffness of about 1400 kN/m decreases as the shear strain increases, reaching a constant value of 750 kN/m at shear strains equal to or larger than 100%. The effective damping ratio decreases almost linearly as the shear strain increases, from a value of 19% at 25% shear strain down to a value of 11% at 150% shear strain.

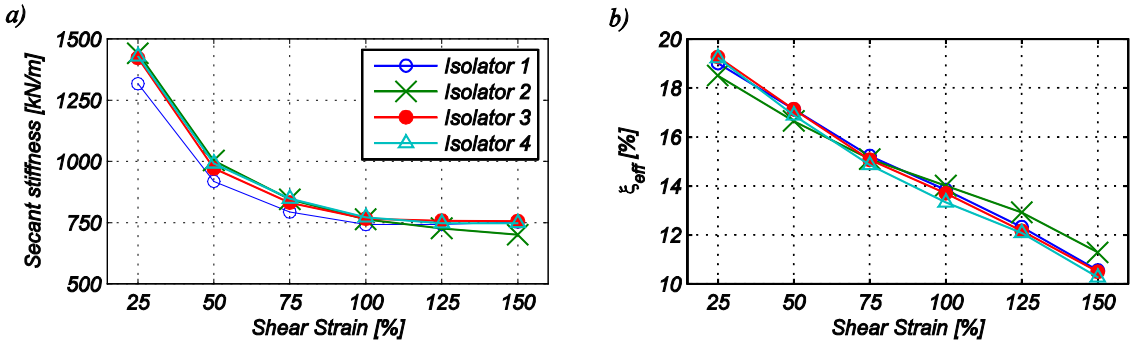

Figure 5.3: Effective properties of the isolators obtained from quality tests: (a) secant stiffness (k_{eff}), (b) effective damping ratio (ξ_{eff}).

5.3. Instrumentation plan test protocol

5.3.1. Instrumentation array

The building was instrumented with a dense accelerometer array consisting of four triaxial accelerometers per floor, one at each corner as represented by red circles in Figure 5.1c. In addition, two triaxial accelerometers were placed on the North-East (N-E) and South-West (S-W) corners of the shake table platen. The accelerometers were force-

balance Episensor, with a full-scale of ±4g, a frequency bandwidth DC–200 Hz, and a wide dynamic range of 155dB. The data acquisition system of these accelerometers (DAQ1) consisted of Quanterra Q330 data loggers from Kinemetrics, Inc., which includes signal conditioning, analog-to-digital (A/D) conversion, GPS time stamping for synchronization across multiple nodes, local memory buffer, and IP-network communication capabilities. This DAQ sampled data at 200 Hz. Another completely independent DAQ consisted of eight distributed National Instruments PXI chassis (DAQ2). Each chassis was capable of recording data from a maximum of 64 sensors channels. Sensors to monitor the acceleration and forces in specific NCSs and displacements and strains in the structural skeleton and various NCSs were included in this DAQ, which sampled data at 240 Hz.

In this study, the acceleration response of the building measured by twenty six accelerometers (two on each translational direction of each floor and two in the longitudinal direction at the shake table platen) sampled at 200 Hz is used to identify the dynamic properties of the test specimen. Before the SID process, the time series were detrended and filtered using a band-pass infinite impulse response (IIR) Butterworth filter of order 4 with cut-off frequencies at 0.1 and 25.0 Hz. This range covers all the modes having an important participation in the response of the system.

Displacement transducers (string potentiometers) in DAQ2 are used to define the cut-off frequencies of the filter applied to the acceleration data. As described later, this is done by minimizing the discrepancy between the displacement measured directly by string potentiometers and the corresponding displacement computed by double integration of the acceleration measurements.

5.3.2. Dynamic tests

The seismic tests on the building in the BI configuration were conducted in April 2012. In addition to the seismic tests, ambient vibration data were continuously recorded from April 13, 2012 to April 29, 2012. Low-amplitude WN base excitation tests using the NEES@UCSD shake table were carried out before and after each seismic test. The seismic input motions were designed and applied to the building with the intent to progressively increase the seismic demand on the structure and NCSs. Two serviceability-level spectrally-matched motions using Canoga Park and LA City Terrace (both corresponding to the 1994 Ms=6.7 Northridge earthquake) as seed motions and four actual motions, San Pedro from the 2010 Mw=8.8 Maule-Chile earthquake and Ica amplitude-scaled (50, 100, and 140%) from the 2007 Mw=8.0 Pisco-Peru earthquake, were applied to the building. To preserve the structure for the fixed-base testing phase, the input motions in the BI configuration were defined so that the peak interstory drift ratio remained less than 0.5%. In addition, it was desirable not to exceed the design limit of 150% shear strain in the isolators. It is noted that seismic and WN base excitations were applied in the East-West (E-W) direction, which coincides with the longitudinal direction of the building. Figure 5.4 shows the acceleration time histories of the seismic input motions (achieved on the shake table) and their displacement and pseudo-acceleration elastic response spectra (RS) for a damping ratio of 5%.

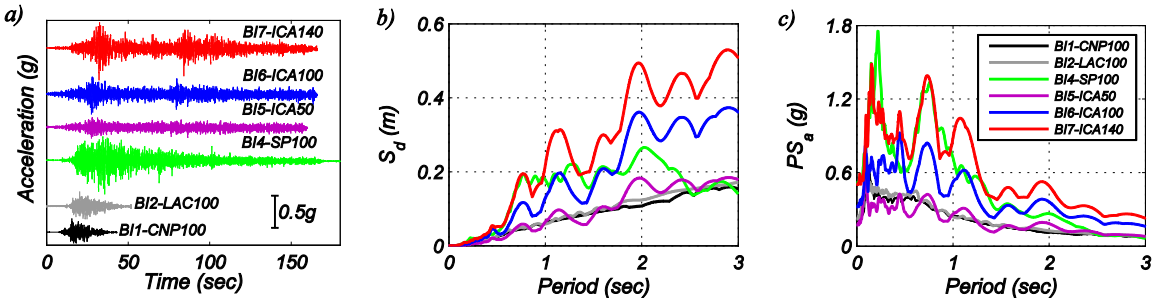

Figure 5.4: Achieved earthquake input motions in the BI building: (a) acceleration time histories, (b) elastic displacement RS (ξ=5%), (c) pseudo-acceleration RS (ξ=5%).

Table 5.1 summarizes the seismic test protocol and the recorded data of the BI building used in this study. This table includes the nominal and actual (achieved) root-mean-square (RMS) of the acceleration input excitations corresponding to the low-amplitude WN base excitation tests.

Table 5.1: Dynamic tests used in this study.

Date	Description	Name	RMS (%g)
April 16, 2012	Low-amplitude white noise base excitation	WN1A / WN1B / WN1C	Nominal: 1.5 / 3.0 / 3.5 Actual: 2.01 / 3.20 / 3.56
	Canoga Park - 1994 Northridge earthquake	**BI1-CNP100**	–
	Low-amplitude white noise base excitation	WN2A / WN2B / WN2C	Nominal: 1.5 / 3.0 / 3.5 Actual: 1.34 / 2.59 / 3.02
	LA City Terrace - 1994 Northridge earthquake	**BI2-LAC100**	–
	Low-amplitude white noise base excitation	WN3A / WN3B / WN3C	Nominal: 1.5 / 3.0 / 3.5 Actual: 1.27 / 2.57 / 3.03
April 17, 2012	**LA City Terrace - 1994 Northridge earthquake**	**BI3-LAC100**	–
	Low-amplitude white noise base excitation	WN4A / WN4B / WN4C	Nominal: 1.5 / 3.0 / 3.5 Actual: 2.01 / 3.22 / 3.76
	San Pedro - 2010 Maule (Chile) earthquake	**BI4-SP100**	–
April 25, 2012	Low-amplitude white noise base excitation	WN5A / WN5B / WN5C	Nominal: 1.5 / 3.0 / 3.5 Actual: 2.01 / 3.11 / 3.46
April 26, 2012	**ICA 50% - 2007 Pisco (Peru) earthquake**	**BI5-ICA50**	–
	Low-amplitude white noise base excitation	WN6A / WN6B / WN6C	Nominal: 1.5 / 3.0 / 3.5 Actual: 2.28 / 3.29 / 3.56
April 27, 2012	**ICA 100% - 2007 Pisco (Peru) earthquake**	**BI6-ICA100**	–
	Low-amplitude white noise base excitation	WN7A / WN7B / WN7C	Nominal: 1.5 / 3.0 / 3.5 Actual: 1.85 / 2.83 / 3.22
	ICA 140% - 2007 Pisco (Peru) earthquake	**BI7-ICA140**	–
	Low-amplitude white noise base excitation	WN8A / WN8B / WN8C	Nominal: 1.5 / 3.0 / 3.5 Actual: 1.99 / 3.28 / 3.88

RMS = root-mean-square

5.4. Recorded building response

The global response of the building, especially that of the isolators, during the seismic and WN tests is analyzed in this section. Most of the measurements in the structure and isolation system were collected using accelerometers; however, a correct evaluation of displacement response is of great importance in order to precisely estimate the shear strain, secant stiffness, and effective damping in the isolators.

In principle, there is no difficulty in obtaining a displacement from the double integration of the corresponding acceleration measurements, however, in practice this is not the case (e.g., Boore and Bommer 2005, Boore 2005). Here, a Tukey (tapered cosine) window is first applied to the raw measured acceleration and then the tapered acceleration time history is filtered using a band-pass IIR Butterworth filter of order 4. The low-pass cutoff frequency is 25 Hz and the high-pass cutoff frequency is calibrated such that the error between the total displacement directly measured at the foundation level by displacement transducers (string potentiometers) and that computed by integration of the acceleration measurements is minimized.

Displacement transducers were in DAQ2 and most of the accelerometers installed in the structure and isolation system were in DAQ1. As abovementioned, these systems recorded data independently, and therefore, must first be synchronized in time. Accelerometers from both DAQs located at the same position (S-E corner of the first floor) are used for this purpose. Data recorded in DAQ2 (originally sampled at 240 Hz) are resampled to 200 Hz; then the time lag between both DAQs is computed from the cross-correlation function between the acceleration time histories recorded at the S-E

corner of the first floor. With the systems synchronized, it is found that for the seismic and WN tests, high-pass cutoff frequencies of 0.04 and 0.1 Hz (for filtering the acceleration time histories), respectively, provide the better match between the total displacement of the foundation directly measured by string potentiometers and the corresponding displacement obtained by double integrating the acceleration time histories.

Figure 5.5 shows the comparison between total displacement in E-W direction of the S-E corner of the first floor measured by displacement transducers and computed by double integrating the acceleration time histories. In all the cases shown (BI1-CNP100, BI7-ICA140, WN4A, and WN8C) a very good agreement is observed, validating the processing of the measured acceleration data to compute displacement.

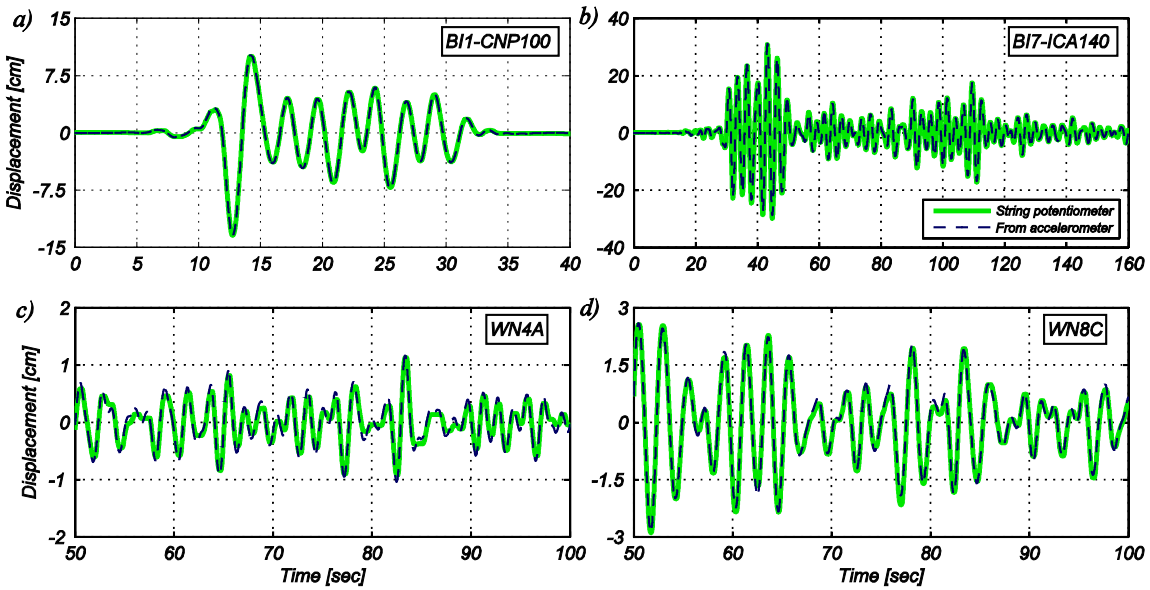

Figure 5.5: Total displacement in the direction of excitation of the S-E corner of the first floor (above isolation system) obtained from string potentiometer and by double integration of acceleration data: (a) BI1-CNP, (b) BI7-ICA140, (c) WN4A , (d) WN8C.

The relative RMS error (RRMSE) between the total foundation displacement in the E-W direction obtained from displacement transducers (d_{sp}) and that computed by double integrating the acceleration time histories (d_{ac}) are computed for all seismic and WN tests. To discard the low amplitude displacements at the beginning and end of the time histories, the RRMSEs are computed in the time interval between the 5% and 95% of the Arias Intensity (Arias 1970) of the input acceleration. Figure 5.6 and Table 5.2 summarize the RRMSE for all seismic and WN tests and the peak displacements obtained from both measurements are also listed in Table 5.2. A very good matching between d_{sp} and d_{ac} is observed for all the tests with RRMSEs lower than 30%. It is observed that the RRMSE decreases as the peak total displacement of the foundation increases (Figure 5.6) and that RRMSEs lower than 5% are attained for seismic tests.

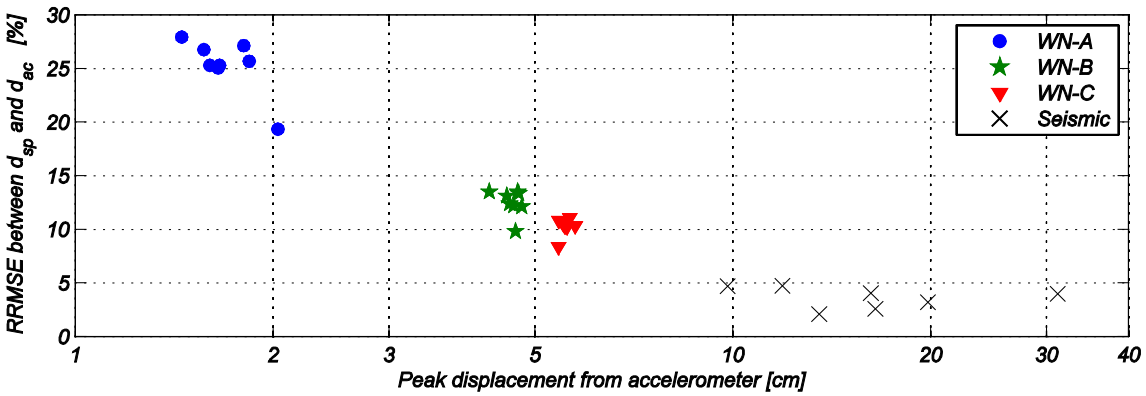

Figure 5.6: RRMSE between d_{sp} and d_{ac} as a function of peak displacement of the foundation level (d_{ac}^{peak}).

Table 5.2: RRMSE between total displacement in the E-W direction of the S-E corner of the foundation obtained from string potentiometer (d_{sp}) and by double integration of acceleration data (d_{ac}).

Test	RRMSE between d_{sp} and d_{ac} [%]	Peak displacement [cm]	
		String potentiometer (d_{sp}^{peak})	From accelerometer (d_{ac}^{peak})
WN1A / WN1B / WN1C	27.91 / 13.48 / 10.79	1.32 / 4.24 / 5.36	1.45 / 4.26 / 5.44
BI1-CNP100	2.06	13.41	13.53
WN2A / WN2B / WN2C	26.74 / 13.1 / 10.75	1.46 / 4.46 / 5.43	1.57 / 4.53 / 5.50
BI2-LAC100	4.02	15.92	16.21
WN3A / WN3B / WN3C	25.28 / 12.2 / 10.23	1.55 / 4.57 / 5.57	1.66 / 4.64 / 5.59
BI3-LAC100	2.55	16.17	16.47
WN4A / WN4B / WN4C	25.27 / 12.37 / 10.46	1.51 / 4.50 / 5.48	1.60 / 4.57 / 5.53
BI4-SP100	4.70	11.83	11.90
WN5A / WN5B / WN5C	25.02 / 12.11 / 10.32	1.55 / 4.70 / 5.70	1.65 / 4.78 / 5.76
BI5-ICA50	4.67	9.58	9.82
WN6A / WN6B / WN6C	27.11 / 13.49 / 11.07	1.76 / 4.58 / 5.60	1.80 / 4.71 / 5.65
BI6-ICA100	3.18	19.56	19.80
WN7A / WN7B / WN7C	25.65 / 13.34 / 10.28	1.75 / 4.68 / 5.52	1.84 / 4.72 / 5.55
BI7-ICA140	3.96	30.87	31.21
WN8A / WN8B / WN8C	19.31 / 9.79 / 8.36	2.03 / 4.75 / 5.56	2.03 / 4.67 / 5.43

The characteristics of the accelerations recorded on the shake table platen (below isolators), floor 1 (above isolators), and roof of the building are shown in Figure 5.7. Absolute acceleration time histories and normalized floor response spectra (FRS) (normalized by the peak floor acceleration or PFA) are presented for seismic tests BI1-CNP100, BI4-SP100, and BI7-ICA140 and WN tests WN1A, WN5A, and WN8A in Figure 5.7a and Figure 5.7b, respectively. In all cases, the effectiveness of the isolation system in reducing the peak accelerations in the building is clearly observed. In the case of the seismic tests presented here, the peak acceleration above the isolation layer is reduced by 2.6 (BI1-CNP100) to 5.2 (BI4-SP100) times the peak input acceleration achieved on the shake table platen. Peak roof accelerations are also significantly lower

than the peak input accelerations, with reductions varying between 2.3 (BI1-CNP100) and 4.3 (BI4-SP100). In the case of WN tests, the effect of the isolators in reducing the peak acceleration is even more significant. Reductions of 5.5 to 6.5 at the foundation level and of 4.0 to 6.5 at the roof level with respect to the input are observed.

The elongation of the fundamental period of the system as well as the shear stain dependency of the effective stiffness of the isolators is clearly evidenced from the normalized FRS. In the case of seismic tests, a predominant peak is observed at a period larger than 2.0 sec and its location varies depending on the intensity of the excitation. In tests BI1-CNP100 and BI4-SP100 the peak is about 2.3 and 2.4 sec, respectively, while in tests BI7-ICA140 the peak is about 3.2 sec. The increase in the predominant period is due to the reduction in the effective horizontal stiffness of the isolation system as the shear strain in the bearings increases, as shown from quality tests in Figure 5.3a. In the WN tests shown here, the predominant peak is about 2.0 sec, which suggests a significant elongation of the predominant period of the building as compared to its fixed-base configuration (which does not take in account the foundation), which was estimated in 0.75 sec by Astroza et al. (2015b) for the undamaged state (before to start the seismic tests on the fixed-based building). It is noted that in the WN tests, the peak in the normalized response spectra in the shake table platen (below isolators) at about 10.5 Hz corresponds to the oil column resonance of the shake table system.

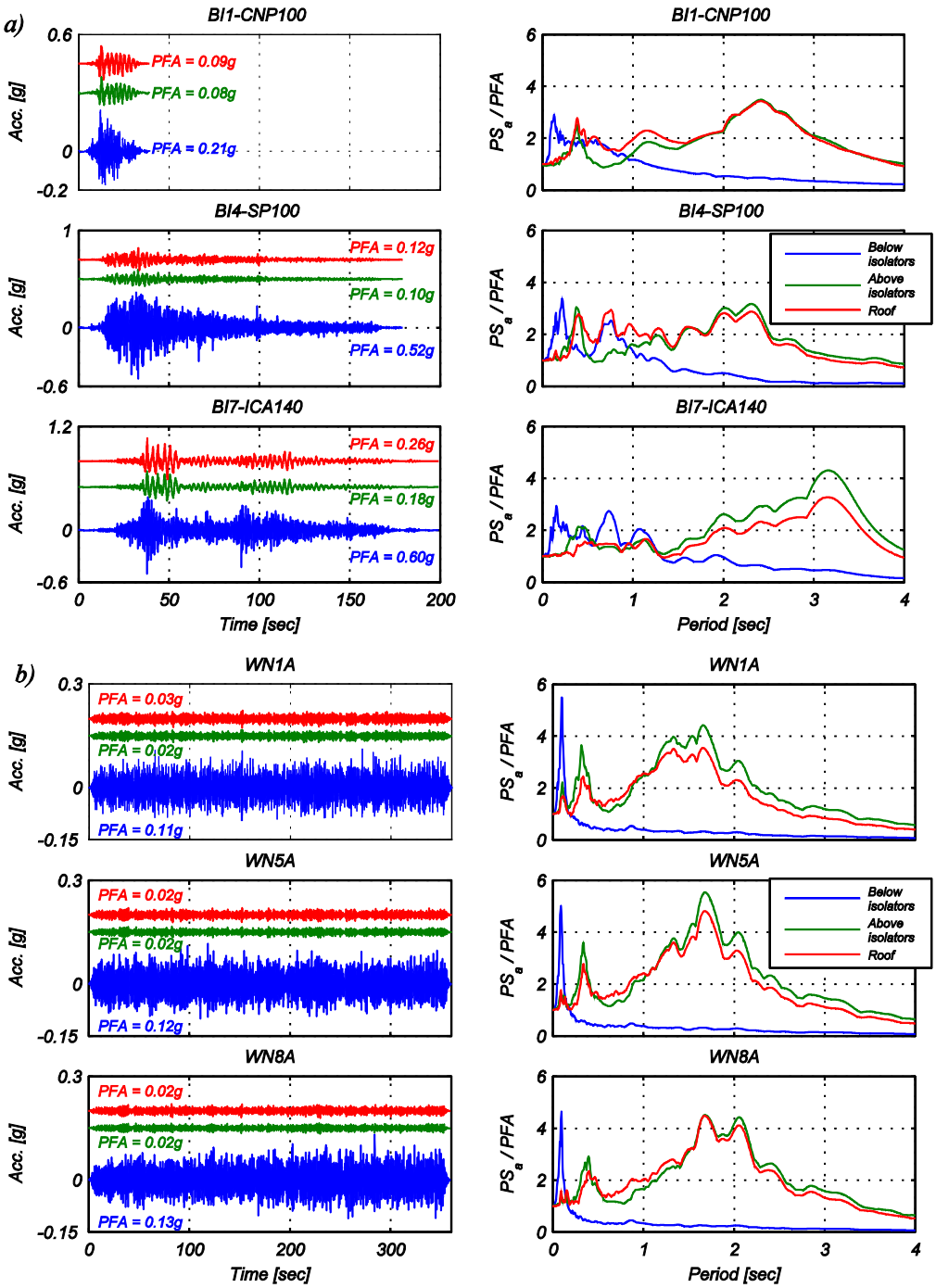

Figure 5.7: Absolute acceleration time histories and normalized pseudo-acceleration FRS of the data recorded below isolators (platen), above isolators (floor 1), and roof level: (a) BI1-CNP100, BI4-SP100, and BI7-ICA140; (b) WN1A, WN5A, and WN8A.

Figure 5.8 shows the PFA (positive and negative values) along the height of the building, taken as the average of the four corners on each floor of the building. PFA at

the foundation (Floor 1) are significantly reduced compared to the input peak accelerations (platen), confirming the effectiveness of the isolation system in reducing the acceleration demands. In the WN tests (Figure 5.8b) the reduction is more evident than in the seismic tests (Figure 5.8a). In all cases, the distribution of the PFA along the height of the building is practically constant, i.e., minor dynamic amplification due to the vibration of the superstructure (above isolation layer) is observed.

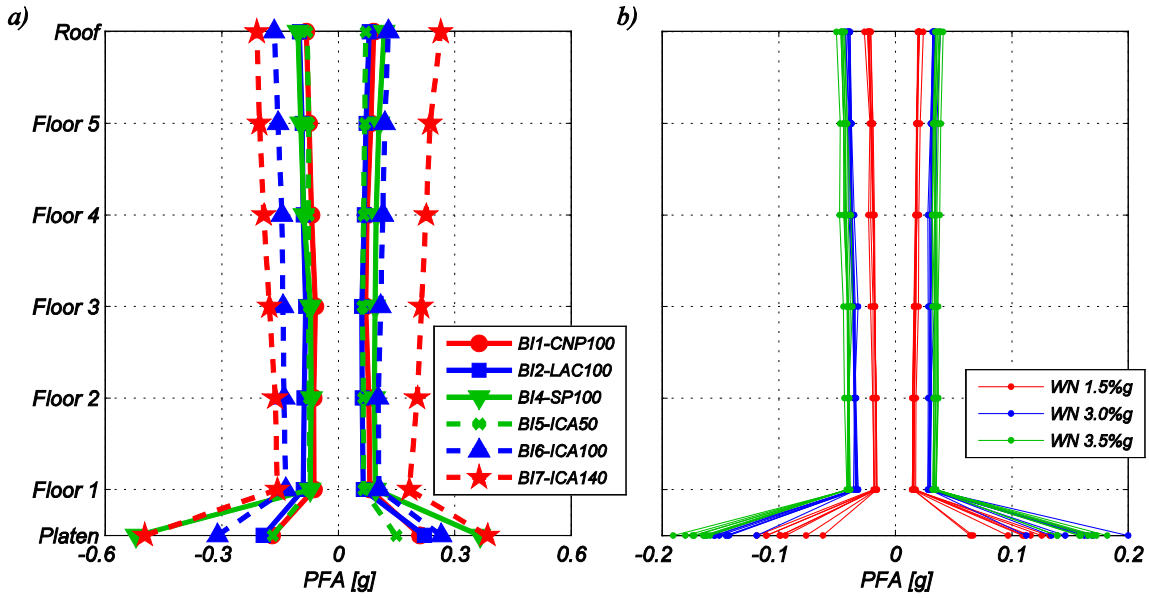

Figure 5.8: Peak floor acceleration (PFA): (a) Seismic tests, (b) WN tests.

Figure 5.9 presents the peak interstory drif ratio (PIDR), both positive and negative values, along the height of the building. The displacement time history at each floor of the building corresponds to the average of the four displacements time histories computed by double integrating the accelerations measured at the four corners of the building. The interstory drift ratio is then calculated as the difference of the averaged displacement time histories between sequential floors divided by the corresponding story height. In the seismic tests, the peak input displacement ranges between 82.7 mm (BI4-

SP100) and 129.2 mm (BI7-ICA140). However, as shown in Figure 5.9a, the PIDR is lower than 0.4% (or equivalently, the interstory drift is less than 17.1 mm). The low PIDRs and the large deformations of the isolation layer (see Figure 5.10 and Figure 5.11) confirm the effectiveness of the HDRBs in concentrating the lateral displacement induced by the seismic excitation and thus reducing the interstory drift demands. In the case of WN base excitation (Figure 5.9b), the PIDR is less than 0.06% (interstory drift less than 2.6 mm), while the deformation of the isolators ranges between 10.8 mm (test WN4A) and 46.2 mm (test WN8C), also confirming the concentration of the lateral displacement in the isolators.

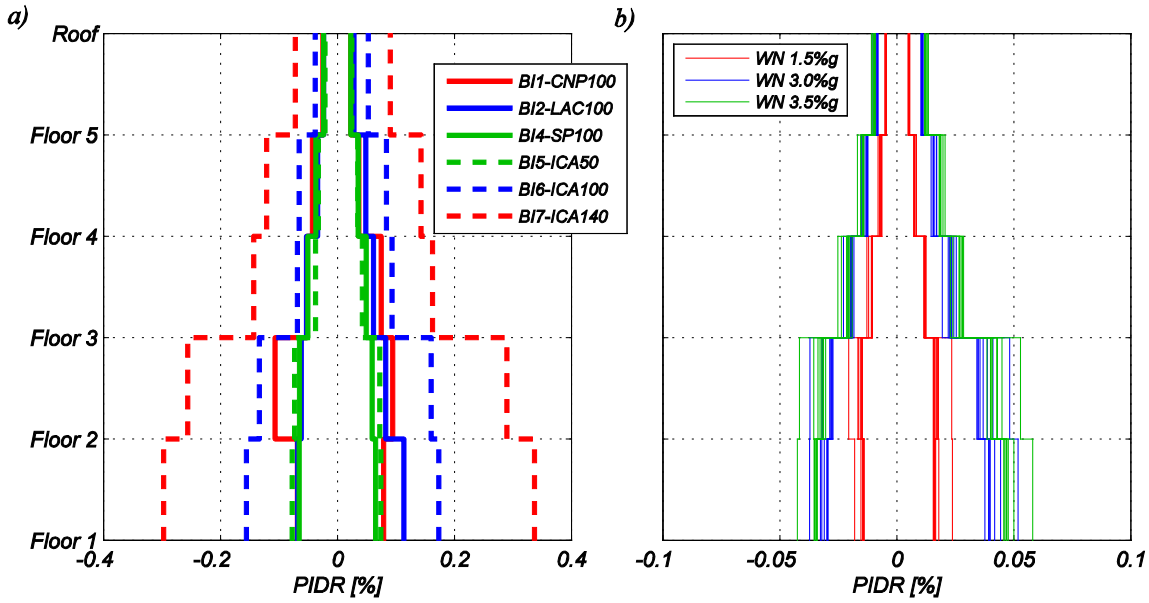

Figure 5.9: Peak interstory drift ratio (PIDR): (a) Seismic tests, (b) WN tests.

The hysteretic behavior of the isolators is investigated in Figure 5.10. The total base shear computed at the bottom of the foundation (V) normalized by the total weight of the building including the foundation (W) is plotted against the shear strain in the isolators. It is noted that the total base shear is computed as $V = \sum_{j=1}^{6} -m_j a_j$ with $a_j =$

average absolute floor acceleration in the E-W direction at floor j and m_j = tributary mass of floor j. Figure 5.10a shows the hysteretic curves for seismic tests BI1-CNP100, BI4-SP100 and BI-7ICA140. A nonlinear response in the isolation system is observed from small levels of shear deformation in the bearings. For shear strains larger than about 100% a hardening effect in the isolators is observed, which is consistent with the results obtained in the quality test (Figure 5.2c). The lowest maximum shear strain in the isolators during seismic tests is attained during test BI1-CNP100 and reaches about 45%. In the WN tests, shear strain in the isolators varies between about 5% and 25% and the reduction in the effective stiffness as the shear strain increases is clearly observed. Even at very low level of shear strain (e.g., test WN5A), the isolators exhibit a nonlinear hysteretic response.

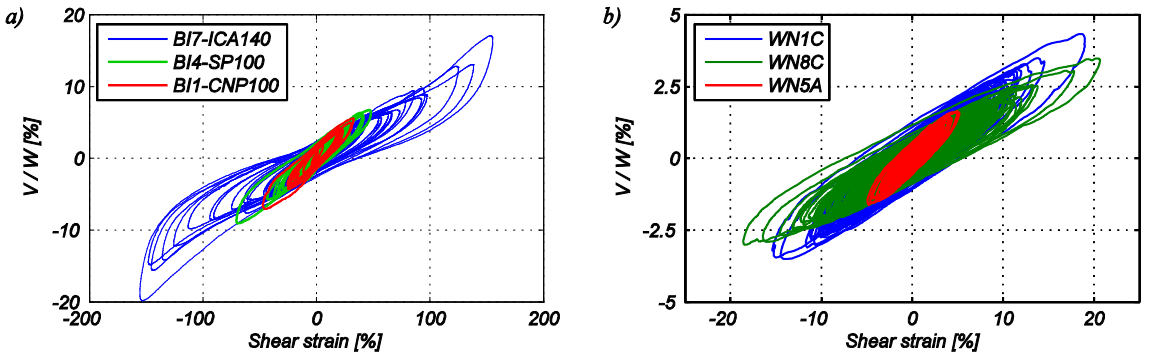

Figure 5.10: Total base shear versus shear strain in the isolation layer: (a) Seismic tests BI1-CNP100, BI4-SP100, and BI7-ICA140, (b) White noise tests WN1C, WN5A, and WN8C.

From the hysteretic response of one isolator (assuming that the total base shear is equally distributed in the four isolators), the secant stiffness of all seismic and WN test data is evaluated (Table 5.3) using the maximum and minimum shear strains as described by Equation (5.1). Figure 5.11 shows the secant stiffness versus the peak shear strain in the isolators for the seismic, WN, and quality tests data. From all the test data, which

include peak shear strain (γ_{shear}) ranging from 5% to 150%, it is noted that the secant stiffness follows a power function in γ_{shear} (see Figure 5.11).

Table 5.3: Secant stiffness of the isolators during seismic and WN shake table tests.

Test	Secant stiffness [kN/m]	Test	Secant stiffness [kN/m]	Test	Secant stiffness [kN/m]	Test	Secant stiffness [kN/m]
WN1A	2609	WN1B	1892	WN1C	1611	BI1-CNP100	1163
WN2A	2317	WN2B	1539	WN2C	1408	BI2-LAC100	1022
WN3A	2286	WN3B	1516	WN3C	1392	BI3-LAC100	1056
WN4A	2335	WN4B	1519	WN4C	1435	BI4-SP100	979
WN5A	2284	WN5B	1499	WN5C	1344	BI5-ICA50	1010
WN6A	2219	WN6B	1424	WN6C	1290	BI6-ICA100	863
WN7A	2167	WN7B	1384	WN7C	1287	BI7-ICA140	875
WN8A	1839	WN8B	1272	WN8C	1202		

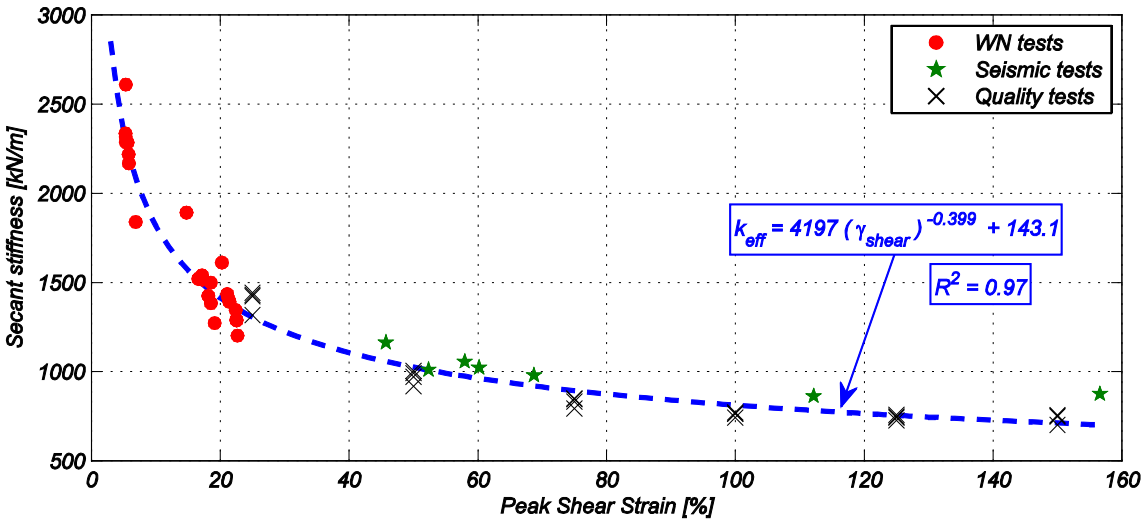

Figure 5.11: Secant stiffness (k_{eff}) against shear strain (γ_{shear}) for the isolators.

The effective damping for all the tests (seismic, WN, and quality) is also computed. The effective damping is a function of the energy dissipated in one cycle of oscillation (area enclosed by one cycle of the hysteretic behavior) and of the strain energy in the system at maximum displacement. For the case of seismic and WN test data, these

quantities are evaluated for each cycle; the effective damping ratio is then computed from the total energy dissipated and total strain energy. Figure 5.12 summarizes the computed effective damping ratio for all the tests, ranging from about 10% up to 19%. A decreasing trend of ξ_{eff} as γ_{shear} increases is observed for most cases, however, for the WN tests an almost constant value of about 16 – 17% is obtained in spite that the peak shear strains vary between 5% and 23%. It is further noted that the previously described effective damping represents an average value along the entire duration of the corresponding test.

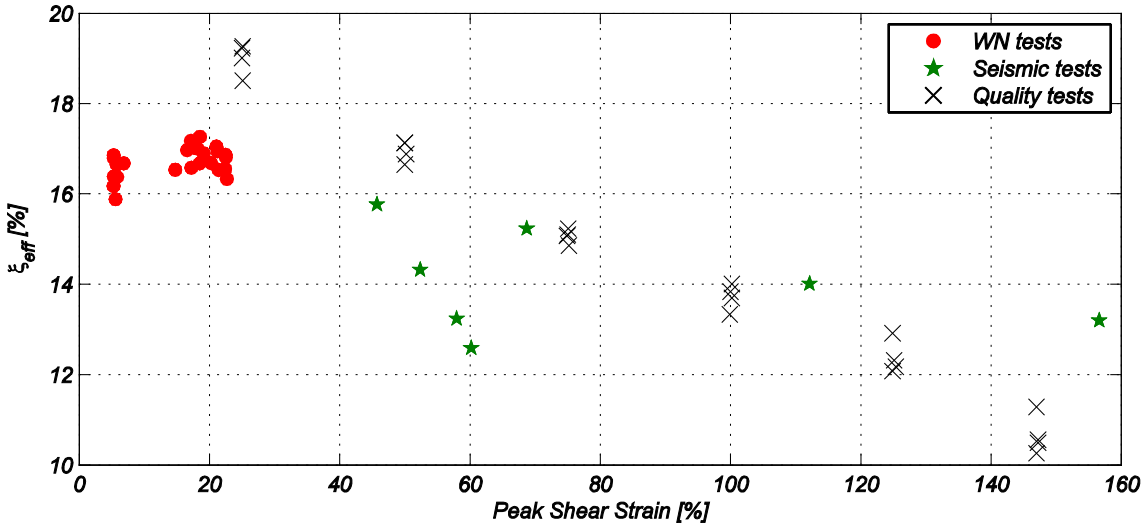

Figure 5.12: Effective damping ratio (ξ_{eff}) against shear strain (γ_{shear}) for one isolator.

Estimates of the acceleration transfer function in the E-W direction are computed at the foundation (above isolators) and roof levels with respect to the shake table platen level with the WN test data. The acceleration time history at each floor is taken as the average of the four corners on each floor of the building. The transfer function is estimated from the quotient between the cross-power spectral density (CSD) between input x (acceleration at shake table platen) and output y (acceleration at foundation and roof levels), P_{yx}, and power-spectral density (PSD) of the input, P_{xx}, i.e.,

$$H(\omega) = \frac{P_{yx}(\omega)}{P_{xx}(\omega)} \tag{5.3}$$

CSD and PSD are estimated using the Welch's method with a Hanning window of 10 sec and 50% overlapping. Figure 5.13a presents the transfer function estimates for WN tests WN1C, WN5A, and WN8C. At the roof level, a predominant frequency of 0.54, 0.62, and 0.44 Hz is identified for WN tests WN1C, WN5A, and WN8C, respectively. Very similar peaks are observed at the foundation level, indicating that this frequency is related to the isolation layer and it dominates the response of the entire system. A second peak is detected at about 2.3−2.9 Hz at both foundation and roof levels.

Figure 5.13b shows the normalized (to a unit value) PSD, also estimated using the Welch's method with a Hanning window of 10 sec and 50% overlapping, in the E-W direction at the roof and foundation levels of the building obtained with AV data recorded before seismic test BI1-CNP100 and after seismic test BI5-ICA50. Two predominant frequencies are clearly observed at the foundation and roof levels, the first at 1.15 Hz and the second at 3.58 Hz. As discussed previously for the WN test data, the presence of peaks in PSD of foundation and roof levels at the same frequency indicates that these predominant frequencies are related to the deformation of the isolation layer. While for the AV data recorded before BI1-CNP100 the main peak is the one at 3.58 Hz (al both roof and foundation levels), for the AV data recorded after BI5-ICA50 the main peak is the one at 1.15 Hz. As will be discussed in the next section, the frequencies at about 1.15 Hz and 3.58 Hz correspond to the first and second longitudinal modes of the BI building under AV excitation, with their relative contribution to the response of the building depending on the characteristics of the external (ambient) excitation.

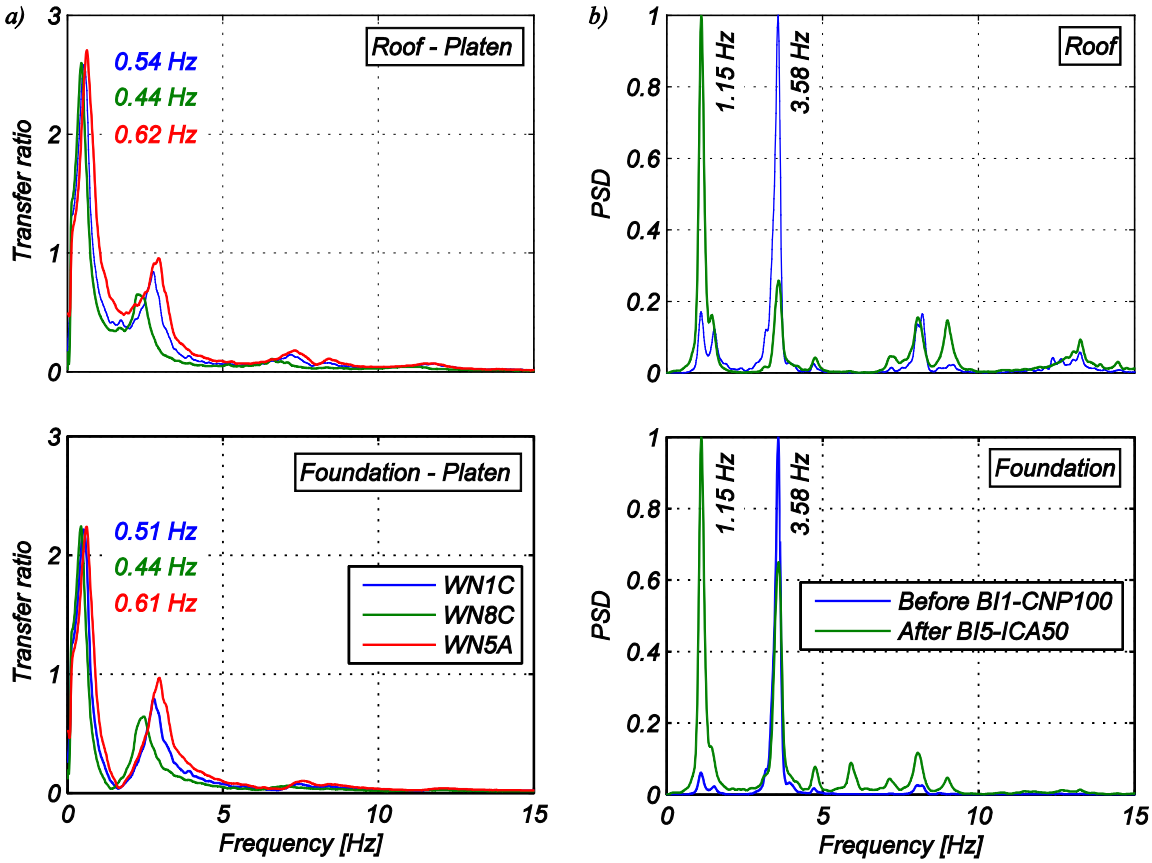

Figure 5.13: (a) Magnitude of the transfer function in the E-W direction at foundation and roof levels with respect to shake table platen for WN tests WN1C, WN5A, and WN8C, (b) PSD in the E-W direction at roof and foundation levels for AV data recorded before BI1-CNP100 and after BI5-ICA50.

5.5. Modal identification

5.5.1. Methods

To estimate the modal properties of the BI building, two state-of-the-art output-only SID methods assuming broad-band excitation are used with the continuously recorded AV data: the Data-Driven Stochastic Subspace Identification (SSI-DATA) method and the Natural Excitation Technique combined with Eigensystem Realization Algorithm (NExT-ERA). For the low-amplitude WN base excitation data, in addition to

the two above-referenced methods used with the AV data, the output-only Enhanced Frequency Domain Decomposition (EFDD) method and two input-output methods are employed. The latter include the Deterministic-Stochastic Subspace Identification (DSI) method and the Observer/Kalman Filter Identification combined with Eigensystem Realization Algorithm (OKID-ERA). A detailed explanation of these SID methods can be found elsewhere. In particular Van Overschee and De Moor (1996), Juang and Pappa (1985), Brincker et al. (2001a,b), and Juang (1994) provide detailed information about the SSI-DATA and DSI, NExT-ERA, EFDD, and OKID-ERA methods, respectively.

Acceleration time histories recorded by twenty six accelerometers (two on each translational direction of each floor and two in the longitudinal direction at the shake table platen) are used to conduct the identification of the modal properties of an equivalent linear time invariant model of the BI building. To reduce the computational requirements involved in the identification process, the acceleration time histories are decimated to 50 Hz. In the case of methods based on state-space representation (SSI-DATA, NExT-ERA, DSI, and OKID-ERA), stabilization diagrams are used to define the order of the model. For the EFDD method, the CSD functions are estimated using the Welch's method with a Hanning window of length 1/8 of the total length of the signal and 50% overlapping.

It is noteworthy that all the SID methods used in this chapter assume a linear time-invariant model with all the sources of energy dissipation (e.g., due to hysteretic behavior and friction) represented by a linear viscous damping. Therefore, the identified natural frequencies and damping ratios correspond to the modal parameters of an equivalent viscously-damped linear elastic model.

5.5.2. System identification results using ambient vibration data

Ambient vibration data recorded in the BI configuration for about sixteen days, from April 14, 2012 to April 30, 2012, are used to estimate the modal properties of the BI building. Output-only SSI-DATA and NExT-ERA methods are used to identify natural frequencies, damping ratios, and mode shapes of an equivalent linear time-invariant state-space model with all sources of energy dissipation represented by linear viscous damping. The identification process is performed using back-to-back, ten-minute long time windows of structural AV data, referred to as data sets hereafter. It is noted that 144 data sets correspond to one day. Because the sixteen days of continuous data produce 2400 data sets, which need to be processed to identify the dynamic characteristics of the BI building, an automated procedure is utilized. For this purpose, the stabilization diagram, which summarizes the identified modal parameters versus model order, is used to distinguish between physical and spurious (mathematical) modes. For the stability criteria, a mode is consider stable if the triple stability criterion defined in Equation (5.4) is satisfied eight times consecutively (as the model order is increased progressively by increments of two). Similar criteria have been previously used in the literature (e.g., Peeters and De Roeck 2001, Van der Auweraer and Peeters 2004, Hu et al. 2012).

$$\left|f_i - f_j\right| / f_j \le 1\% \quad ; \quad \left|\xi_i - \xi_j\right| / \xi_j \le 5\% \quad ; \quad \left(1\text{-}MAC_{\phi_i,\phi_j}\right)100 \le 2\% \tag{5.4}$$

where f_i, ξ_i and f_j, ξ_j are the identified natural frequencies and damping ratios for models of consecutive orders i and $j = i+2$, and MAC_{ϕ_i,ϕ_j} is the modal assurance criterion (Allemang and Brown 1982) of a pair of corresponding modes shapes identified for models of successive orders. Since the seismic tests were not equidistant in time (see

test protocol in Table 5.1), different numbers of data sets are available before and after each seismic test, as indicated in Table 5.4.

Table 5.4: Number of data sets used in the system identification with ambient vibration data.

Stage	Before BI1	After BI1	After BI2	After BI3	After BI4	After BI5	After BI6	After BI7	**Total**
# of data sets	420	114	6	1176	138	120	30	396	**2400**

The mode shapes identified with the methods used herein are complex-valued, and the corresponding real modes are computed using the method proposed by Imregun and Ewins (1993). Eight modes are identified using the AV data. The mode shapes identified using SSI-DATA with AV data recorded on April 13, 2012 between 18:00 and 18:10 PST (first data set before seismic test BI1-CNP100) are shown in Figure 5.14. These modes correspond to the first three coupled transverse and torsional modes (1-T+To, 2-T+To, and 3-T+To), first three longitudinal modes (1-L, 2-L, and 3-L), and the first two torsional modes (1-To and 2-To). These mode shapes are used as reference to compute the MAC of the corresponding mode shapes identified with each data set. Modes 1-T+To, 1-L, and 1-To correspond mainly to the deformation of the isolation system and are referred to as isolation modes, while modes 2-T+To to 3-L mostly involve deformation of the superstructure and are referred to as structural modes.

Polar plots, which are used to investigate the level of non-proportional or non-classical damping in the identified mode shapes, are presented below the corresponding mode shapes in Figure 5.14. Since all the vectors shown in the polar plots are almost collinear, it is concluded that the identified mode shapes are almost purely classically damped. The most likely reason is that the level of structural vibration is very low for

AVs and, consequently, the level of shear deformation in the isolators is small and the damping effect of the isolation system is minor.

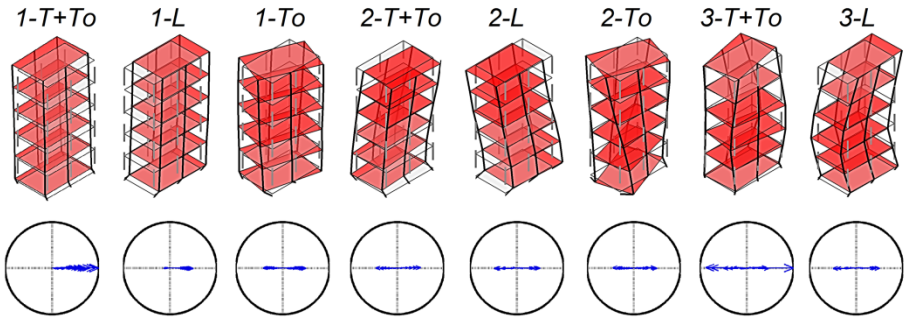

Figure 5.14: Mode shapes and corresponding polar plots of the BI building identified using SSI-DATA with AV data recorded on April 13, 2012 between 18:00 and 18:10 PST.

Table 5.5 summarizes the success rate of the automated modal identification process by showing, in percentage, the modes successfully identified according to the stability criteria defined in Equation (5.4) (Peeters and De Roeck 2001, Magalhães et al. 2009). The success rate of the isolation modes is equal to or larger than 60% for both SSI-DATA and NExT-ERA methods. For the structural modes, the success rate varies significantly for different modes, with 2-To and 3-T+To being the modes with the lowest (33% for SSI-DATA and NExT-ERA) and highest (88% for SSI-DATA and 85% for NExT-ERA) success rates, respectively. It is noted that the successful identification of a mode depends on its degree of participation in the response of the building and the signal-to-noise ratio (SNR) associated to the mode. This, however, can significantly change based on the characteristics of the excitation (e.g., traffic conditions near the building, wind features, etc.).

Table 5.5: Success rate (%) of the automated modal identification process.

Mode	Success rate [%]	
	SSI-DATA	NExT-ERA
1-T+To	72	70
1-L	70	69
1-To	62	60
2-T+To	57	55
2-L	52	49
2-To	33	33
3-T+To	88	85
3-L	58	57

The natural frequencies obtained from the automated identification process using SSI-DATA are plotted as a function of time in Figure 5.15. In this plot, vertical dashed lines indicate the times of the seven seismic tests conducted on the BI building. The natural frequencies of the isolation modes slightly decrease after each seismic test, but recover in time until the next seismic test (see also Figure 5.18a). Since the total mass of the building remained practically unchanged during the complete BI test phase, the decrease in the natural frequencies of the isolation modes is due to a reduction in the lateral (shear) stiffness of the isolators, which recovers in time while the building is not subjected to another seismic excitation. This temporary and recoverable stiffness reduction in HDRBs is known as Mullins' effect and has been previously observed in BI structures instrumented during earthquakes (e.g., Siringoringo and Fujino 2014). These modal identification results indicate that the BI building did not suffer any structural damage during the BI test phase, which is consistent with the visual inspections and the low interstory drift demands attained during the seismic tests in the BI configuration (peak interstory drift ratio < 0.4%).

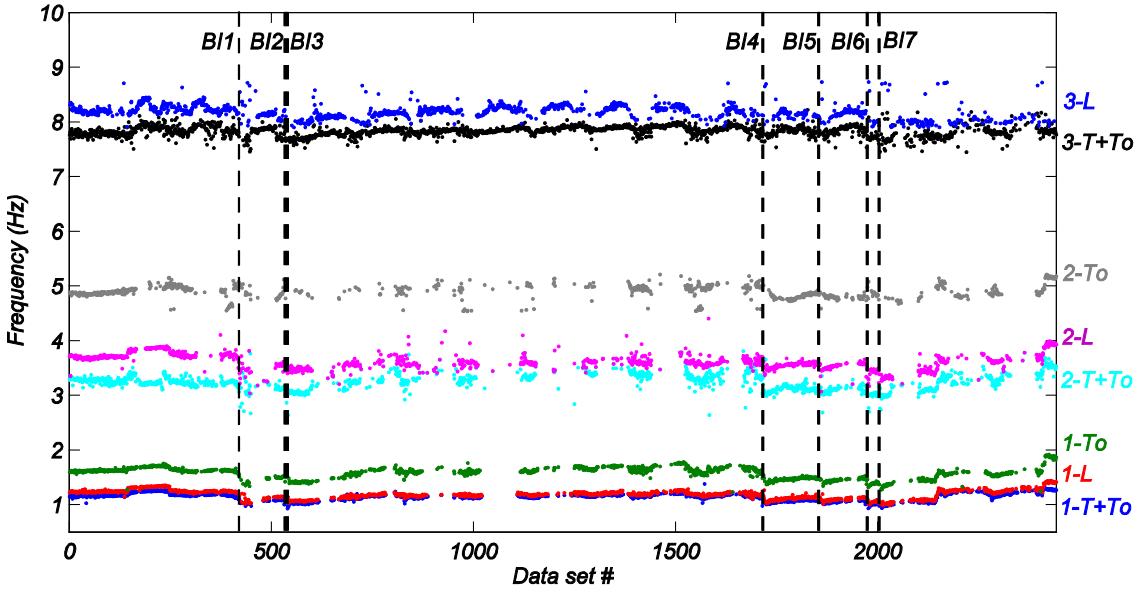

Figure 5.15: Temporal evolution of the natural frequencies of the BI building identified using SSI-DATA with ambient vibration data.

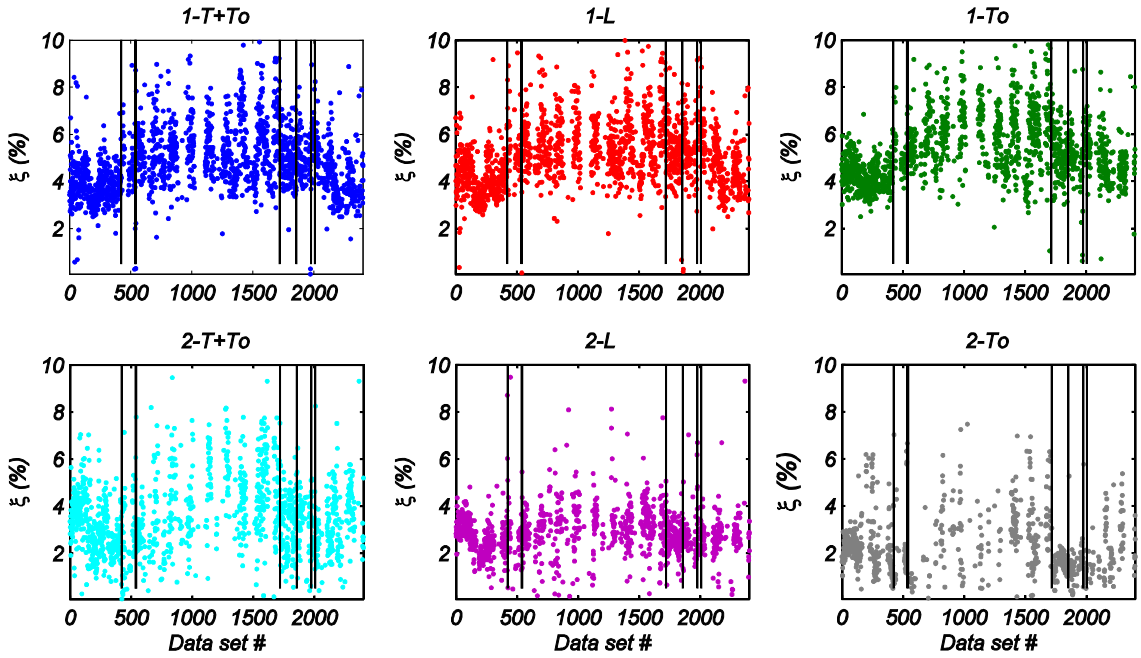

Figure 5.16: Temporal evolution of the equivalent viscous damping ratios of modes 1–T+To, 1–L, 1–To, 2–T+To, 2–L, and 2–To of the BI building identified using SSI-DATA with AV data (vertical black lines indicate seismic tests).

To analyze the overall trend of the identified modal damping ratios of the BI building, Figure 5.16 shows the evolution of the identified equivalent viscous damping

ratios for modes 1-T+To, 1-L, 1-To, 2-T+To, 2-L, and 2-To. The damping ratios of the isolation modes (1-T+To, 1-L, and 1-To) are on average about 5% – 6% and are higher than those of the structural modes 2-T+To, 2-L, and 2-To, whose averages are about 3%.

The identified natural frequencies and damping ratios vary almost periodically every 144 data sets, corresponding to a 1-day cycle. Although environmental conditions such as wind speed and temperature were not directly measured on the building specimen, hourly measurements compared at different stations located a few miles away from the site show very little variation. The temporal evolutions of the wind speed and temperature measured 4.5 km. away from the NEES@UCSD shake table are plotted in Figure 5.17 over the time interval for which the modal identification is conducted. Such plot shows that, similarly to the natural frequencies and damping ratios, both environmental parameters vary approximately every 144 data sets and peak around 2 pm.

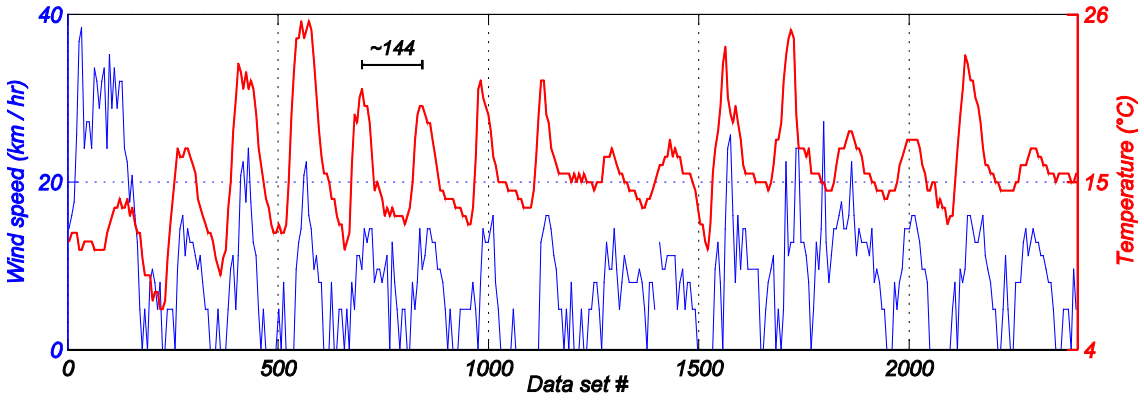

Figure 5.17: Wind speed and temperature profiles measured 3 miles away from the test site over 16-day monitoring period.

To analyze the correlation between the environmental conditions, the ambient vibration level of the building, and the identified modal properties, Figure 5.18 shows the time evolution of the RMS acceleration at the roof level (resultant in longitudinal and transverse directions) as well as the identified natural frequency and damping ratio of the

first mode (1-T+To). It is clearly observed that as the amplitude of the vibration at the roof level increases, the identified natural frequency decreases. In addition, although the variability of the identified damping ratio is large, it seems that as the amplitude of the vibration at the roof level increases, the identified damping ratio also increases. By comparing Figure 5.17 and the roof RMS acceleration profile in Figure 5.18, it is noted that the wind speed, temperature, and RMS acceleration at the roof level have a similar periodic variation and are in phase. Therefore, the effects of wind speed and temperature on the identified natural frequencies and damping ratios cannot be directly discriminated. It is also observed that the SID process does not identify the isolation modes when the RMS at the roof level is low.

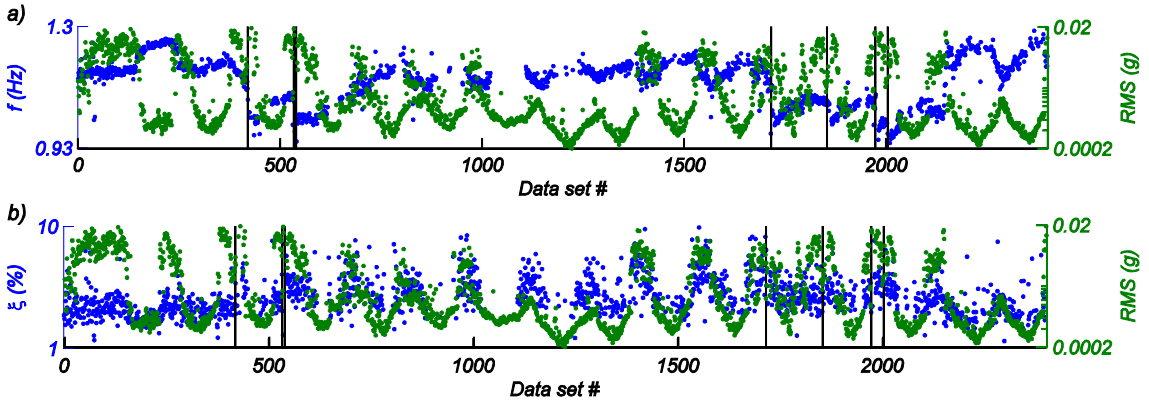

Figure 5.18: Time evolution of identified modal parameters of mode 1-T+To overlaid with roof RMS acceleration: (a) natural frequency, (b) damping ratio (vertical black lines indicate seismic tests).

Table 5.6 summarizes the mean value (μ) and coefficient of variation (CV) of the identified natural frequencies, damping ratios, and mode shapes considering all the data sets. It is noted that the mode shapes identified with the first data set (Figure 5.14) are used as a reference to compute the MAC values. Mean values and coefficients of variations obtained with SSI-DATA and NExT-ERA are very similar for all the modal

parameters. However, larger differences are observed for the damping ratios, which is consistent with previous studies that have found that damping ratio estimates may exhibit significantly higher method-to-method variability compared to natural frequencies (Ndambi et al. 2000, Astroza et al. 2015a,b). Since the seismic tests induce a reduction of the lateral stiffness of the isolators, CVs of natural frequencies of the isolation modes are higher than those of the structural modes. The mean values of damping ratios of isolation modes are higher than those of the structural modes. Finally, it is noted that the MAC values are higher than 0.9 for the first seven modes (1-T+To to 3-T+To) and they decrease for the highest identified mode 3-L. A larger variability in the identified modal parameters is expected for higher modes, because their participation in the measured responses is lower than that that of the lower modes; consequently, the SNR is lower for the higher modes. Furthermore, the variability in the identified damping ratios and mode shapes is expected to be more pronounced because they are more sensitive to the noise level.

Table 5.6: Mean (μ) and coefficient of variation (CV) of the identified natural frequencies (f), damping ratios (ξ), and MAC using ambient vibration data.

Mode	Natural frequency		Damping ratio		MAC	
	μ [Hz]	CV [%]	μ [%]	CV [%]	μ	CV [%]
	SSI-DATA / NExT-ERA	SSI-DATA / NExT-ERA	SSI-DATA / NExT-ERA	SSI-DATA / NExT-ERA	SSI-DATA / NExT-ERA	SSI-DATA / NExT-ERA
1-T+To	1.13 / 1.14	6.01 / 6.61	4.94 / 4.85	35.33 / 42.72	0.90 / 0.89	9.89 / 11.9
1-L	1.18 / 1.18	6.25 / 6.54	5.33 / 5.20	36.86 / 42.64	0.93 / 0.89	8.32 / 9.84
1-To	1.56 / 1.56	6.32 / 6.79	5.28 / 5.27	27.75 / 40.47	0.96 / 0.93	7.30 / 12.88
2-T+To	3.22 / 3.20	4.48 / 4.48	3.57 / 2.72	43.82 / 78.49	0.91 / 0.90	16.21 / 16.4
2-L	3.58 / 3.58	3.79 / 4.08	2.92 / 2.75	35.79 / 49.57	0.92 / 0.92	17.39 / 15.35
2-To	4.86 / 4.87	2.33 / 2.29	2.37 / 1.97	60.54 / 56.53	0.97 / 0.95	9.32 / 11.30
3-T+To	7.80 / 7.80	1.20 / 1.32	1.85 / 1.74	53.09 / 60.03	0.92 / 0.92	9.18 / 8.60
3-L	8.16 / 8.16	1.56 / 1.78	1.76 / 1.79	36.11 / 52.8	0.82 / 0.79	16.26 / 20.15

5.5.3. System identification results using white noise base excitation data

Using the vibration response data of the BI building recorded during the twenty-four WN tests (WN1A to WN8C), ten modes are identified. They correspond to the first four longitudinal (1-L, 2-L, 3-L, and 4-L), first three coupled longitudinal-transverse (1-L+T, 2-L+T, and 3-L+T), and first three coupled longitudinal-torsional (1-L+To, 2-L+To, and 3-L+To) modes. The mode shapes identified using DSI with WN1A test data and their corresponding polar plots are shown in Figure 5.19. The mode shapes of the structural modes (2-L to 4-L) are close to purely classically damped, while the isolation modes exhibit a higher degree of non-proportional damping. Since the isolation modes include large deformations of the isolators as well as a large damping ratio due to the energy dissipation characteristics of the rubber, the structure itself and the isolation layer have levels of damping significantly different then non-classical damping is anticipated. It is noted that the mode shapes identified using WN test data are similar to those identified using AV data. However, large excitation amplitudes during WN tests induce a reduction in the lateral effective stiffness of the isolation layer, especially in the longitudinal direction (direction of motion). Therefore, the modes identified using WN test data always contain a component in the longitudinal direction of the building.

It is also noted that the level of shear deformation induced by the WN base excitations in the isolation system is much larger than that induced by the AVs. Hence, the effective damping ratio in the isolators is expected to be much larger than the damping in the structure during the WN tests. This explains why a higher degree of non-proportional damping is observed with the WN test data compared to the AV data.

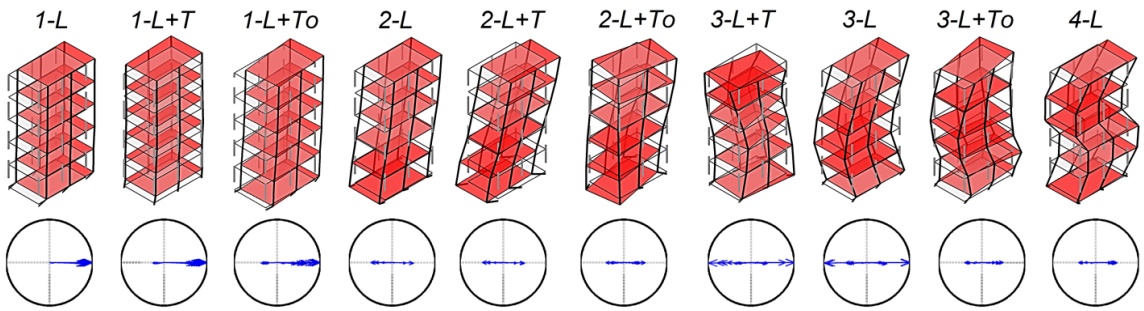

Figure 5.19: Mode shapes and corresponding polar plots of the base-isolated building identified using DSI with WN1A test data.

Natural frequencies, damping ratios, and mode shapes are identified using three output-only (SSI-DATA, NExT-ERA, and EFDD) plus two input-output (DSI and OKID-ERA) SID methods with vibration data recorded during the WN base excitation tests at different stages of the test protocol (see Table 5.1). Figure 5.20 shows the natural frequencies identified using data of tests WN1A, WN1C, WN5A, WN5C, WN8A, and WN8C, i.e., before test BI1-CNP100 and after tests BI4-SP100 and BI7-ICA140, with nominal amplitudes of 1.5%g and 3.5%g RMS. The natural frequencies identified for each data set using different SID methods are in good agreement with relative differences lower than 10%. Usually, differences between natural frequencies identified using different methods are larger for isolation modes than for structural modes. Since isolation modes have a non-negligible degree of nonlinearity due to the deformation of the isolation systems and the corresponding hysteretic behavior (see Figure 5.10b), modal properties of the equivalent linear system are expected to vary between different methods. Based on the results, the OKID-ERA method is less robust in the identification of poorly exited modes with transverse and torsional components, e.g., this method is not able to identify mode 3-L+To for any of the tests.

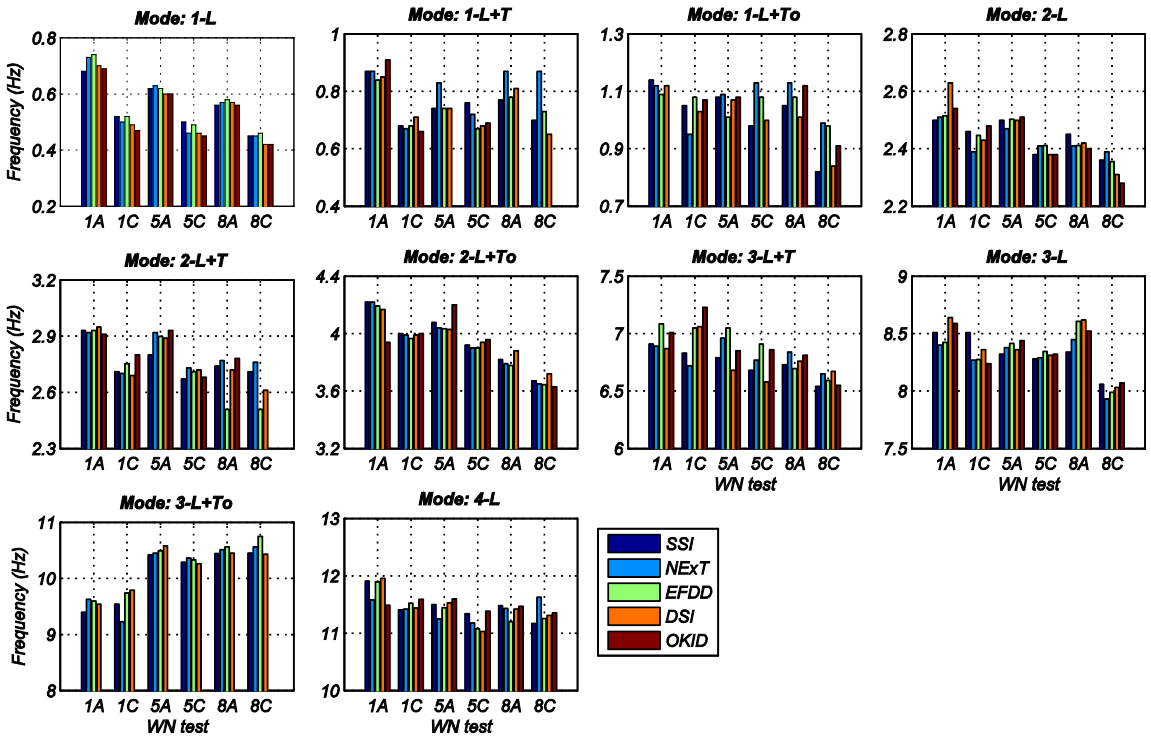

Figure 5.20: Natural frequencies identified using WN base excitation data with nominal RMS = 1.5% and 3.5%*g* recorded before BI1-CNP100 (WN1A and WN1C), after BI4-SP100 (WN5A and WN5C), and after BI7-ICA140 (WN8A and WN8C).

Identified natural frequencies of the isolation modes (1-L, 1-L+T, and 1-L+To) vary significantly for different WN tests. For example, the natural frequency of mode 1-L (averaged over all SID methods) varies between 0.44 Hz (test WN8C) and 0.71 Hz (test WN1A). Variations of about 60% for mode 1-L and 30% for modes 1-L+T and 1-L-To are also observed. Oppositely, natural frequencies identified for structural modes do not change much between different WN tests, with differences lower than 15%. This suggests that the natural frequencies of the isolation modes change due to variations in the stiffness of the isolation layer, while natural frequencies of structural modes remain practically unchanged since the structure itself exhibits essentially a linear elastic response during all the WN tests.

From the reduction of the natural frequencies as the amplitude of the excitation increases from AV to WN tests, a reduction of the effective stiffness of the isolation layer is clearly observed. For example, the identified natural frequency of mode 1-L with AV data is about 1.18 Hz, while it varies between 0.71 Hz and 0.44 Hz (depending on the amplitude of the WN base excitation) using WN test data. It is noteworthy that the reduction in the identified natural frequencies, from AV to WN tests, decreases for structural modes since the deformation of the isolation layer is smaller in those modes and the structure itself experienced a basically linear elastic response during the WN tests.

To analyze the effect of the excitation amplitude in the identified natural frequency of the fundamental mode 1-L, Figure 5.21 plots its variation as a function of the secant stiffness in the isolators (see Table 5.3). From such plot it is clearly observed that, as the amplitude of the WN base excitation increases, a higher deformation in the bearings is induced as the effective (secant) stiffness of the isolation layer decreases. Since the isolation modes mostly comprise deformation of the isolators, a reduction of the effective stiffness of the isolation layer implies a reduction in the frequency of those modes. This effect is clearly observed in Figure 5.21, where a linear correlation between the natural frequency of mode 1-L and that of the secant stiffness in an isolator is detected, with a coefficient of determination $R^2 = 0.94$.

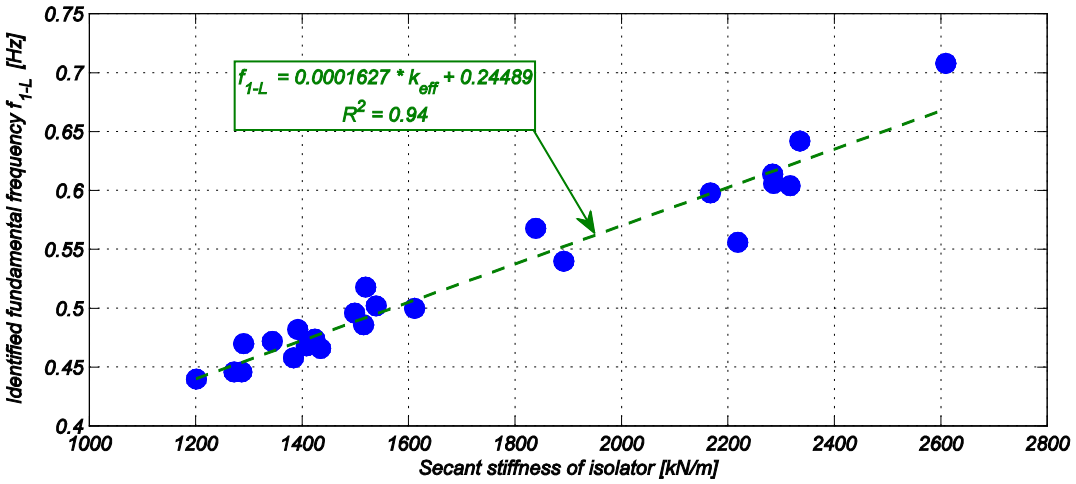

Figure 5.21: Identified frequency of mode 1-L versus secant stiffness of isolator for all WN tests.

The damping ratios of the ten identified modes are shown in Figure 5.22. While the damping ratios of the isolation modes are high, with values ranging between 7% and 15%, the damping ratios of the structural modes are significantly lower, with values between 1% and 5%. It is also noted that damping ratios identified for higher modes 3-L+To and 4-L are particularly low. As previously mentioned, a large deformation is concentrated in the isolation layer for the isolation modes, which in turn, causes hysteretic response of the bearings (see Figure 5.10b). This energy dissipated by hysteretic response of the isolators is identified as equivalent viscous damping because of the underlying mathematical model assumed in the SID methods used in this chapter.

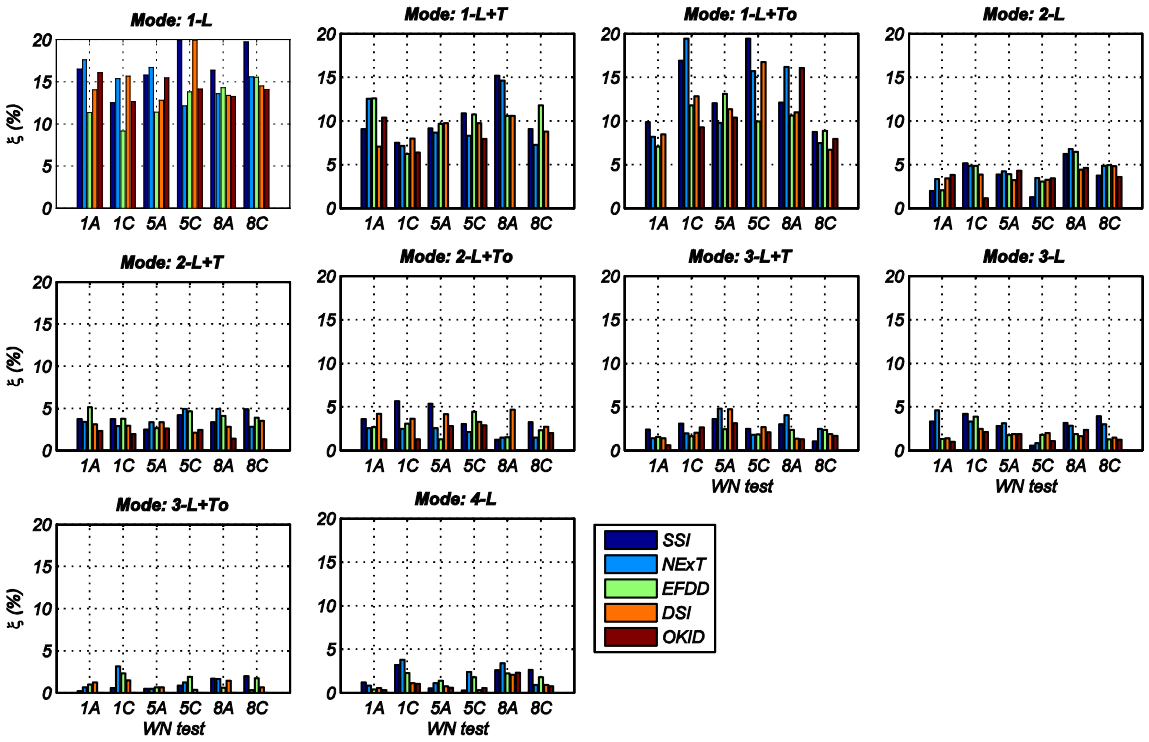

Figure 5.22: Damping ratios identified using WN base excitation data with nominal RMS = 1.5% and 3.5%g recorded before BI1-CNP100 (WN1A and WN1C), after BI4-SP100 (WN5A and WN5C), and after BI7-ICA140 (WN8A and WN8C).

For a given data set, the identified damping ratios show a method-to-method variability higher than those of the identified natural frequencies, which is consistent with previous studies (e.g., Ndambi et al. 2000, Astroza et al. 2015a,b). The damping ratios identified using WN test data are consistently higher than those estimated using AV data (see Table 5.6) for both isolation and structural modes. In contrast, identified damping ratios of the isolation modes do not change significantly for different WN tests and, for a given mode, their values are almost constant for different WN tests. As discussed in Section 5.4, the effective damping ratio (ξ_{eff}) computed from the hysteretic response of the isolators during the WN tests is about 16 – 17% for all the WN tests (Figure 5.12). This effective damping ratio is similar to the damping ratios identified for mode 1-L (

ξ_{1-L}) using the different SID methods with the WN test data (Figure 5.22). This suggests that most of the energy dissipated in the BI building is through hysteretic behavior of the isolators, which is identified as equivalent viscous damping because of the underlying mathematical model used for SID. Figure 5.23 shows the correlation between ξ_{eff} and the damping ratio of mode 1-L (ξ_{1-L}) identified using the five SID methods. It is observed that values for ξ_{1-L} can be larger or lower than ξ_{eff}, and no trend (e.g., as a function of amplitude of the excitation) is observed. On average, values identified of ξ_{1-L} are lower than ξ_{eff}.

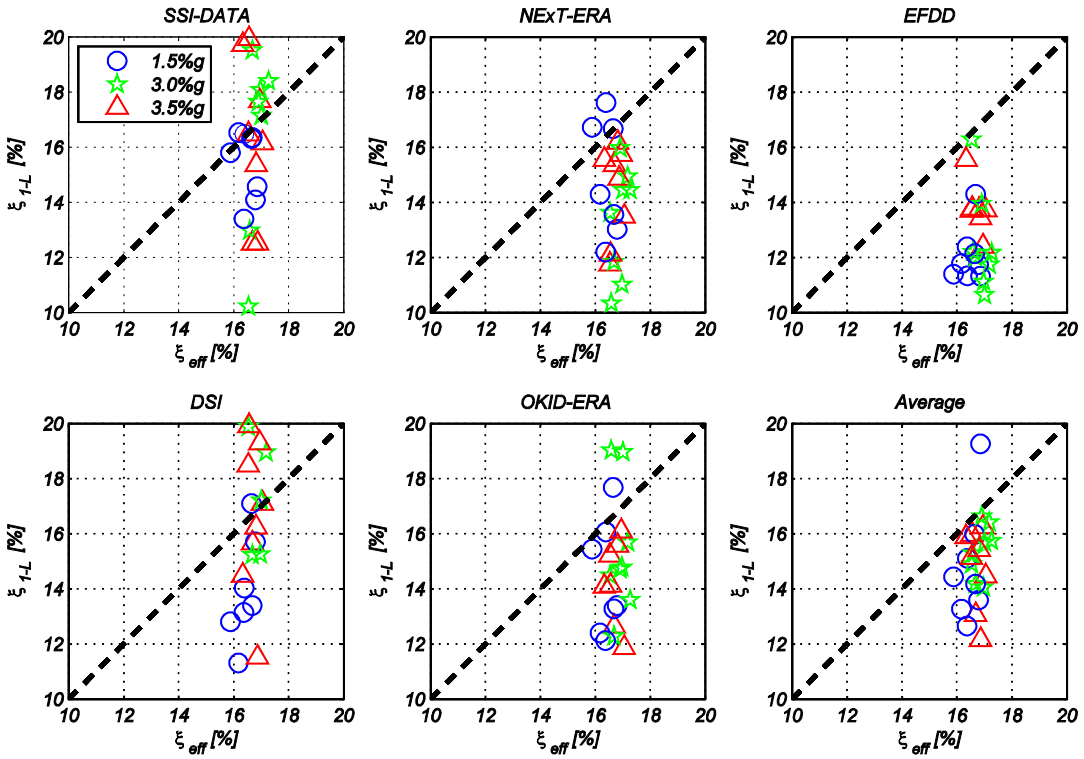

Figure 5.23: Correlation between ξ_{eff} and the damping ratio of mode 1-L (ξ_{1-L}) obtained using SID methods.

Table 5.7 presents the identified natural frequencies and damping ratios of the BI building using the recorded data of the twenty four WN base excitation tests. The results

obtained using the five different SID methods are summarized with the mean values and coefficients of variation also presented. Similar observations to those discussed above based on Figure 5.20 and Figure 5.22 can be drawn.

Table 5.7: Natural frequencies and damping ratios of the base-isolated building identified using low-amplitude WN base excitation data.

		Natural frequency (Hz)							Damping ratio (%)						
	Mode	SSI	NExT	EFDD	DSI	OKID	Mean	CV (%)	SSI	NExT	EFDD	DSI	OKID	Mean	CV (%)
WN1A	1-L	0.68	0.73	0.74	0.70	0.69	0.71	3.66	16.48	17.62	11.33	14.03	16.06	15.10	16.40
	1-L+T	0.87	0.87	0.84	0.85	0.91	0.87	3.09	9.09	12.56	12.61	7.07	10.38	10.34	22.85
	1-L+To	1.14	1.12	1.09	1.12	–	1.12	1.84	9.88	8.18	7.07	8.47	–	8.40	13.77
	2-L	2.50	2.51	2.51	2.63	2.54	2.54	2.09	2.01	3.34	2.07	3.43	3.83	2.94	28.60
	2-L+T	2.93	2.92	2.93	2.95	2.91	2.93	0.51	3.73	3.41	5.16	3.11	2.32	3.55	29.44
	2-L+To	4.22	4.22	4.19	4.17	3.94	4.15	2.86	3.62	2.58	2.68	4.20	1.28	2.87	38.86
	3-L+T	6.91	6.89	7.09	6.87	7.01	6.95	1.32	2.41	1.39	1.58	1.40	0.62	1.48	43.13
	3-L	8.51	8.40	8.42	8.64	8.59	8.51	1.22	3.34	4.63	1.31	1.42	0.99	2.34	67.49
	3-L+To	9.40	9.63	9.59	9.54	–	9.54	1.06	0.20	0.67	0.98	1.23	–	0.77	57.61
	4-L	11.91	11.58	11.90	11.96	11.49	11.77	1.83	1.21	0.86	0.40	0.56	0.32	0.67	54.60
WN1B	1-L	0.55	0.57	0.53	0.52	0.53	0.54	3.70	10.22	13.63	16.28	19.88	14.48	14.90	23.83
	1-L+T	0.79	0.74	0.73	0.74	0.73	0.75	3.36	14.00	14.21	10.76	12.66	14.42	13.21	11.60
	1-L+To	1.08	1.13	1.09	1.08	1.08	1.09	1.99	9.92	9.84	8.08	8.99	7.96	8.96	10.42
	2-L	2.39	2.39	2.39	2.26	2.38	2.36	2.43	1.90	2.02	2.13	2.44	2.47	2.19	11.56
	2-L+T	2.63	2.60	2.71	2.76	2.83	2.71	3.47	2.29	2.53	4.18	3.84	3.06	3.18	25.68
	2-L+To	4.03	4.11	4.07	4.03	3.95	4.04	1.47	5.97	4.42	1.71	3.05	1.60	3.35	55.51
	3-L+T	6.78	6.98	7.05	6.86	7.07	6.95	1.79	2.38	1.30	0.81	1.17	0.48	1.23	58.66
	3-L	8.58	8.68	8.45	8.60	8.66	8.59	1.04	3.10	1.38	0.59	1.44	1.80	1.66	55.10
	3-L+To	9.55	9.62	9.34	9.46	–	9.49	1.25	1.28	1.65	0.91	0.61	–	1.11	40.56
	4-L	11.68	11.38	11.37	11.40	11.74	11.51	1.57	2.03	0.67	0.62	0.78	0.90	1.00	58.66
WN1C	1-L	0.52	0.50	0.52	0.49	0.47	0.50	4.24	12.52	15.37	9.13	15.66	12.64	13.06	20.26
	1-L+T	0.68	0.67	0.68	0.71	0.66	0.68	2.75	7.53	7.16	6.22	7.99	6.39	7.06	10.63
	1-L+To	1.05	0.95	1.08	1.03	1.07	1.04	5.00	16.91	19.46	11.80	12.85	9.28	14.06	29.05
	2-L	2.46	2.39	2.45	2.43	2.48	2.44	1.40	5.14	4.89	4.87	3.87	1.16	3.99	41.47
	2-L+T	2.71	2.70	2.75	2.69	2.80	2.73	1.67	3.74	2.91	3.77	2.93	1.97	3.06	24.19
	2-L+To	4.00	3.99	3.97	3.99	4.00	3.99	0.33	5.65	2.47	3.08	3.66	1.31	3.23	49.70
	3-L+T	6.83	6.72	7.05	7.06	7.23	6.98	2.90	3.08	1.96	1.64	2.06	2.63	2.27	25.32
	3-L	8.51	8.27	8.28	8.36	8.24	8.33	1.31	4.22	3.31	3.90	2.51	2.14	3.22	27.55
	3-L+To	9.54	9.23	9.74	9.79	–	9.58	2.66	0.59	3.14	2.32	1.49	–	1.89	58.09
	4-L	11.41	11.42	11.52	11.44	11.59	11.48	0.68	3.22	3.80	2.29	1.13	1.06	2.30	53.25
WN2A	1-L	0.60	0.61	0.62	0.60	0.59	0.60	1.89	14.57	21.00	11.32	25.29	24.11	19.26	31.58
	1-L+T	0.86	0.87	0.84	0.87	0.87	0.86	1.51	6.69	8.53	9.46	7.16	6.24	7.62	17.62
	1-L+To	1.24	1.08	1.09	1.12	1.11	1.13	5.72	7.83	8.14	6.67	7.13	6.43	7.24	10.13
	2-L	2.59	2.49	2.51	2.57	2.54	2.54	1.63	3.85	2.09	2.24	4.08	2.90	3.03	29.93
	2-L+T	2.97	2.90	2.93	2.98	3.05	2.97	1.92	4.50	2.81	2.83	3.42	2.14	3.14	28.17
	2-L+To	4.17	3.97	4.06	4.17	4.10	4.09	2.05	3.73	1.49	1.19	3.23	1.23	2.17	55.74
	3-L+T	6.84	6.67	6.94	6.84	6.77	6.81	1.46	2.51	4.05	2.36	2.35	2.47	2.75	26.62
	3-L	8.36	8.33	8.42	8.40	–	8.38	0.47	2.13	3.74	3.02	2.63	–	2.88	23.59
	3-L+To	9.70	9.77	9.98	9.54	–	9.75	1.87	0.54	0.45	0.96	1.04	–	0.75	39.50
	4-L	11.69	11.65	11.58	11.52	11.67	11.62	0.60	0.50	1.87	2.99	1.03	0.33	1.34	81.76

Table 5.7: Natural frequencies and damping ratios of the base-isolated building identified using low-amplitude WN base excitation data, continued.

		Natural frequency (Hz)							Damping ratio (%)						
	Mode	SSI	NExT	EFDD	DSI	OKID	Mean	CV (%)	SSI	NExT	EFDD	DSI	OKID	Mean	CV (%)
WN2B	1-L	0.51	0.46	0.53	0.48	0.53	0.50	6.20	20.73	14.94	11.75	18.95	15.68	16.41	21.44
	1-L+T	0.77	0.72	0.67	0.74	0.72	0.72	5.04	14.39	14.11	11.72	9.07	10.36	11.93	19.43
	1-L+To	0.99	1.08	1.08	0.98	–	1.03	5.33	10.94	12.66	11.68	6.43	–	10.43	26.44
	2-L	2.44	2.38	2.41	2.34	2.34	2.38	1.85	4.87	3.79	5.07	3.39	2.35	3.89	28.68
	2-L+T	2.93	2.93	2.71	2.69	–	2.82	4.73	3.03	4.14	3.77	2.41	–	3.34	23.13
	2-L+To	3.95	4.11	4.03	4.02	4.09	4.04	1.56	6.07	5.23	3.04	2.94	1.42	3.74	50.33
	3-L+T	6.75	6.78	6.94	6.92	7.10	6.90	2.04	2.90	2.48	1.61	2.26	3.42	2.53	26.85
	3-L	8.46	8.43	8.42	8.6	8.39	8.46	0.98	0.78	3.75	2.26	1.78	2.38	2.19	49.15
	3-L+To	9.63	9.76	9.59	9.71	–	9.67	0.78	1.27	3.17	2.25	3.09	–	2.44	36.28
	4-L	11.48	11.39	11.67	11.86	11.62	11.60	1.56	3.82	2.65	2.73	3.35	1.30	2.77	34.32
WN2C	1-L	0.50	0.47	0.49	0.45	0.43	0.47	6.12	17.69	15.74	12.41	19.29	16.10	16.25	15.80
	1-L+T	0.74	0.69	0.67	0.71	–	0.70	4.25	7.49	8.47	9.39	8.70	–	8.51	9.26
	1-L+To	0.85	0.89	0.84	0.84	0.89	0.86	3.00	7.65	6.45	6.93	6.71	4.90	6.53	15.53
	2-L	2.38	2.42	2.40	2.33	2.41	2.39	1.49	1.41	2.37	2.54	2.27	2.43	2.20	20.61
	2-L+T	2.93	2.84	2.71	2.65	–	2.78	4.54	4.20	4.90	4.24	2.95	–	4.07	19.99
	2-L+To	3.92	3.84	3.90	3.91	–	3.89	0.92	5.89	6.96	3.29	4.23	–	5.09	32.27
	3-L+T	6.68	6.70	6.92	6.71	6.78	6.76	1.46	2.72	1.85	2.01	1.45	0.52	1.71	47.27
	3-L	8.31	8.22	8.17	8.28	8.40	8.28	1.08	1.55	3.86	2.02	2.61	3.29	2.67	35.02
	3-L+To	9.64	9.57	9.66	9.33	–	9.55	1.58	1.56	0.19	1.32	0.67	–	0.68	68.58
	4-L	11.23	11.21	11.26	11.39	11.57	11.33	1.33	1.16	0.95	1.18	0.52	0.52	0.87	37.86
WN3A	1-L	0.59	0.58	0.62	0.66	0.58	0.61	5.67	14.09	13.02	11.74	15.70	13.39	13.59	10.72
	1-L+T	0.87	0.86	0.81	0.87	0.83	0.85	3.16	9.37	8.64	6.06	11.44	15.72	10.25	35.28
	1-L+To	1.09	1.06	1.09	1.12	1.07	1.09	2.12	9.60	8.97	6.06	8.95	7.45	8.21	17.50
	2-L	2.52	2.47	2.51	2.45	2.48	2.49	1.15	3.10	1.98	2.04	3.26	2.78	2.63	22.53
	2-L+T	2.92	2.91	2.93	2.95	3.02	2.95	1.49	2.23	2.64	2.97	2.52	1.93	2.46	16.14
	2-L+To	4.13	3.91	4.03	3.99	–	4.01	2.28	4.64	1.58	3.29	3.36	–	3.22	39.03
	3-L+T	6.86	6.93	7.14	7.18	6.97	7.02	1.97	3.55	3.09	1.65	1.89	1.72	2.38	36.84
	3-L	8.37	8.35	8.42	8.37	8.48	8.40	0.62	2.87	3.34	2.83	1.65	2.18	2.57	25.69
	3-L+To	10.15	10.67	10.45	10.73	–	10.50	2.50	0.58	1.53	0.69	1.29	–	1.02	44.93
	4-L	11.89	11.90	11.81	12.01	11.76	11.87	0.80	1.39	0.78	1.76	1.07	1.00	1.20	31.75
WN3B	1-L	0.48	0.47	0.51	0.48	0.49	0.49	3.12	12.98	10.34	12.21	21.91	19.03	15.29	32.22
	1-L+T	0.79	0.80	0.78	0.81	–	0.80	1.62	9.99	13.70	12.81	10.78	–	11.82	14.60
	1-L+To	1.04	1.07	1.08	1.02	1.10	1.06	3.01	9.42	11.08	6.67	9.97	6.80	8.79	22.39
	2-L	2.47	2.34	2.40	2.41	2.40	2.40	1.92	4.72	2.98	4.21	3.35	3.88	3.83	17.96
	2-L+T	2.65	2.76	2.75	2.66	2.68	2.70	1.93	1.90	4.11	3.15	2.39	2.67	2.84	29.55
	2-L+To	3.98	3.95	3.95	3.94	3.78	3.92	2.03	2.47	1.78	3.57	4.18	3.93	3.19	32.08
	3-L+T	6.75	6.84	6.92	6.76	6.77	6.81	1.03	3.28	1.90	1.80	1.15	1.89	2.00	38.85
	3-L	8.24	8.35	8.42	8.53	8.46	8.40	1.32	2.42	4.03	2.05	1.51	1.72	2.35	42.75
	3-L+To	9.61	9.61	9.81	9.77	–	9.70	1.08	0.35	0.35	1.46	1.28	–	0.86	68.97
	4-L	11.47	11.19	11.35	11.41	11.43	11.37	0.97	3.32	2.30	2.90	2.47	1.53	2.50	26.89
WN3C	1-L	0.49	0.46	0.49	0.47	0.50	0.48	3.41	16.48	11.76	13.71	18.49	15.22	15.13	17.01
	1-L+T	0.72	0.82	0.74	0.78	–	0.77	5.80	17.16	16.74	13.73	15.56	–	15.80	9.72
	1-L+To	0.87	0.85	0.84	0.87	0.82	0.85	2.50	7.48	6.65	9.63	8.52	8.44	8.14	13.87
	2-L	2.46	2.47	2.45	2.42	2.40	2.44	1.19	8.67	7.21	5.65	3.92	3.40	5.77	38.30
	2-L+T	2.68	2.68	2.71	2.74	2.73	2.71	1.02	2.64	3.29	3.27	2.21	3.25	2.93	16.62
	2-L+To	4.03	3.97	4.00	3.94	–	3.99	0.99	5.90	1.88	2.45	4.08	–	3.58	50.50
	3-L+T	6.70	6.77	6.92	6.72	–	6.78	1.43	2.98	0.48	1.90	1.65	–	1.75	58.53
	3-L	8.28	8.25	8.42	8.26	–	8.30	0.94	2.75	0.18	1.62	1.14	–	1.42	75.08
	3-L+To	9.49	9.39	9.59	9.66	–	9.53	1.24	0.38	1.47	2.22	0.60	–	1.17	72.31
	4-L	11.60	11.67	11.88	11.74	11.55	11.69	1.10	3.38	3.68	2.35	3.12	2.86	3.08	16.51

Table 5.7: Natural frequencies and damping ratios of the base-isolated building identified using low-amplitude WN base excitation data, continued.

		Natural frequency (Hz)							Damping ratio (%)						
	Mode	SSI	NExT	EFDD	DSI	OKID	Mean	CV (%)	SSI	NExT	EFDD	DSI	OKID	Mean	CV (%)
WN4A	1-L	0.64	0.64	0.62	0.66	0.65	0.64	2.31	16.53	14.30	11.78	11.31	12.40	13.26	16.21
	1-L+T	0.76	0.85	0.78	0.78	0.82	0.80	4.55	9.61	7.74	9.76	8.90	9.47	9.10	9.07
	1-L+To	1.07	1.04	1.01	1.11	1.01	1.05	4.07	8.96	10.20	9.92	9.20	8.27	9.31	8.29
	2-L	2.45	2.36	2.42	2.34	2.35	2.38	2.00	1.12	2.80	1.95	2.55	2.65	2.21	31.22
	2-L+T	2.78	2.83	2.89	2.92	3.01	2.89	3.05	2.21	3.37	2.97	3.08	2.47	2.82	16.71
	2-L+To	4.11	4.09	4.11	4.09	–	4.10	0.27	1.83	3.67	1.69	4.65	–	2.96	48.79
	3-L+T	6.80	6.76	6.98	6.92	6.99	6.89	1.53	1.32	1.33	1.67	1.52	0.82	1.33	24.09
	3-L	8.45	8.49	8.42	8.41	8.39	8.43	0.46	2.80	3.48	2.06	2.67	2.39	2.68	19.82
	3-L+To	10.49	10.55	10.44	10.41	–	10.47	0.58	0.67	0.18	0.61	0.84	–	0.58	48.80
	4-L	11.98	11.59	11.58	11.62	11.86	11.73	1.56	1.48	3.29	2.13	1.32	1.40	1.92	43.05
WN4B	1-L	0.52	0.49	0.53	0.52	0.53	0.52	3.17	18.09	11.02	11.13	15.25	14.78	14.05	21.35
	1-L+T	0.78	0.81	0.73	0.73	0.72	0.75	5.19	7.05	12.52	11.16	8.69	8.87	9.66	22.44
	1-L+To	1.08	1.08	1.08	1.06	–	1.08	0.93	9.52	9.50	11.11	10.36	–	10.12	7.61
	2-L	2.36	2.46	2.40	2.23	2.27	2.34	4.00	3.20	4.54	3.37	2.71	1.19	3.00	40.49
	2-L+T	2.64	2.74	2.71	2.75	–	2.71	1.83	1.22	2.65	2.12	2.07	–	2.02	29.35
	2-L+To	3.89	3.89	3.91	3.81	–	3.87	1.12	5.05	0.82	3.13	2.50	–	2.87	60.78
	3-L+T	6.61	6.89	6.94	6.84	6.88	6.83	1.89	4.58	3.59	3.00	2.02	2.37	3.11	32.68
	3-L	8.58	8.46	8.42	8.38	8.54	8.48	0.99	3.06	3.50	2.63	1.73	1.44	2.47	35.28
	3-L+To	10.31	10.29	10.27	10.44	–	10.33	0.74	0.29	0.46	1.47	1.08	–	0.82	66.28
	4-L	11.39	11.67	11.40	11.27	11.40	11.43	1.29	2.11	1.59	2.04	1.64	0.73	1.62	33.89
WN4C	1-L	0.50	0.46	0.49	0.44	0.44	0.47	5.99	16.16	13.49	13.73	17.10	11.87	14.47	14.69
	1-L+T	0.80	0.81	0.78	0.77	–	0.79	2.31	7.35	9.40	9.62	10.09	–	9.12	13.29
	1-L+To	0.87	0.88	0.87	0.89	–	0.88	1.09	8.13	8.01	8.58	7.97	–	8.17	3.43
	2-L	2.43	2.40	2.41	2.45	2.41	2.42	0.82	5.43	6.15	4.70	4.06	5.13	5.09	15.37
	2-L+T	2.67	2.64	2.71	2.66	–	2.67	1.10	2.82	4.37	3.30	1.80	–	3.07	34.74
	2-L+To	3.87	3.89	3.90	3.87	3.79	3.86	1.12	5.70	4.78	3.60	3.33	3.84	4.25	22.99
	3-L+T	6.56	6.71	6.69	6.79	6.67	6.68	1.24	3.18	1.98	1.92	1.31	1.23	1.92	40.59
	3-L	8.33	8.36	8.42	8.35	8.33	8.36	0.43	3.31	3.16	1.96	3.98	3.69	3.22	24.06
	3-L+To	10.04	10.05	10.21	10.23	–	10.13	1.00	0.72	0.24	1.03	2.02	–	1.00	75.09
	4-L	11.55	11.31	11.35	11.44	11.44	11.42	0.82	0.64	2.04	1.98	0.90	0.69	1.25	56.08
WN5A	1-L	0.62	0.63	0.62	0.60	0.60	0.61	2.19	15.80	16.72	11.40	12.80	15.44	14.43	15.49
	1-L+T	0.74	0.83	0.74	0.74	–	0.76	5.90	9.15	8.66	9.68	9.74	–	9.31	5.44
	1-L+To	1.08	1.09	1.01	1.07	1.08	1.07	3.01	12.04	9.80	13.10	11.36	10.41	11.34	11.53
	2-L	2.50	2.47	2.50	2.50	2.51	2.50	0.62	3.86	4.22	3.91	3.25	4.32	3.91	10.71
	2-L+T	2.80	2.92	2.90	2.89	2.93	2.89	1.79	2.50	3.35	2.66	3.37	2.60	2.90	14.74
	2-L+To	4.08	4.04	4.03	4.03	4.20	4.08	1.76	5.38	2.59	1.29	4.19	2.82	3.25	48.35
	3-L+T	6.79	6.96	7.05	6.68	6.85	6.87	2.10	3.62	4.80	2.45	4.75	3.15	3.75	27.18
	3-L	8.32	8.38	8.42	8.36	8.44	8.38	0.56	2.81	3.14	1.77	1.88	1.90	2.30	27.37
	3-L+To	10.42	10.45	10.49	10.58	–	10.49	0.66	0.50	0.51	0.69	0.66	–	0.59	16.67
	4-L	11.50	11.25	11.44	11.53	11.60	11.46	1.16	0.50	1.12	1.42	0.76	0.59	0.88	43.69
WN5B	1-L	0.49	0.46	0.53	0.48	0.52	0.50	5.81	19.52	11.85	12.01	15.23	12.28	14.18	23.22
	1-L+T	0.82	0.82	0.73	0.82	0.76	0.79	5.37	10.45	13.60	12.60	11.82	14.70	12.63	12.91
	1-L+To	1.21	1.06	1.08	1.17	1.08	1.12	5.89	8.69	8.29	6.59	7.13	7.49	7.64	11.17
	2-L	2.40	2.45	2.41	2.55	2.41	2.44	2.54	6.40	5.20	5.16	4.21	4.57	5.11	16.31
	2-L+T	2.66	2.67	2.71	2.66	–	2.68	0.89	1.52	2.54	3.31	2.61	–	2.50	29.55
	2-L+To	4.03	4.14	4.06	3.95	4.07	4.05	1.71	4.53	4.09	3.88	1.77	1.27	3.11	47.59
	3-L+T	6.69	6.77	6.92	6.94	7.04	6.87	2.04	2.74	3.23	2.56	1.83	1.73	2.42	26.17
	3-L	8.40	8.60	8.42	8.39	8.52	8.47	1.08	1.87	3.03	2.02	2.16	2.49	2.31	19.97
	3-L+To	10.49	10.64	10.44	10.20	–	10.44	1.75	1.33	1.07	1.52	0.89	–	1.20	23.11
	4-L	11.32	11.61	11.31	11.60	11.50	11.47	1.28	1.49	2.66	2.85	3.80	2.54	2.67	30.90

Table 5.7: Natural frequencies and damping ratios of the base-isolated building identified using low-amplitude WN base excitation data, continued.

		Natural frequency (Hz)							Damping ratio (%)						
	Mode	SSI	NExT	EFDD	DSI	OKID	Mean	CV (%)	SSI	NExT	EFDD	DSI	OKID	Mean	CV (%)
WN5C	1-L	0.50	0.46	0.49	0.46	0.45	0.47	4.59	19.94	12.12	13.78	19.92	14.12	15.98	23.08
	1-L+T	0.76	0.72	0.67	0.68	0.69	0.70	5.18	10.86	8.30	10.76	9.74	7.94	9.52	14.27
	1-L+To	0.98	1.13	1.08	1.00	–	1.05	6.68	19.47	15.71	9.97	16.79	–	15.48	25.84
	2-L	2.38	2.41	2.41	2.38	2.38	2.39	0.70	1.25	3.47	3.07	3.28	3.43	2.90	32.26
	2-L+T	2.67	2.73	2.71	2.72	2.68	2.70	0.96	4.19	4.95	4.65	2.10	2.47	3.67	35.45
	2-L+To	3.92	3.90	3.90	3.94	3.96	3.92	0.66	3.03	2.15	4.46	3.29	2.88	3.16	26.56
	3-L+T	6.68	6.77	6.91	6.58	6.86	6.76	1.97	2.50	1.80	1.83	2.68	2.09	2.18	18.17
	3-L	8.28	8.29	8.34	8.31	8.32	8.31	0.30	0.58	0.87	1.80	1.99	1.08	1.26	48.01
	3-L+To	10.29	10.36	10.33	10.26	–	10.31	0.43	0.90	1.24	1.91	0.39	–	1.11	57.38
	4-L	11.34	11.18	11.08	11.03	11.38	11.20	1.38	0.28	2.41	1.80	0.31	0.55	1.07	91.10
WN6A	1-L	0.58	0.52	0.53	0.55	0.60	0.56	6.05	16.32	16.67	12.14	17.09	17.68	15.98	13.80
	1-L+T	0.89	0.81	0.81	0.85	–	0.84	4.56	10.73	10.40	1.08	7.71	–	7.48	59.84
	1-L+To	1.02	1.02	0.98	0.97	1.09	1.02	4.65	10.98	9.96	13.61	10.37	10.05	10.99	13.79
	2-L	2.44	2.43	2.41	2.42	2.43	2.43	0.46	3.46	1.46	2.89	2.51	3.40	2.74	29.76
	2-L+T	2.76	2.80	2.93	2.96	2.87	2.86	2.95	2.03	3.13	3.19	2.78	1.17	2.46	34.81
	2-L+To	3.97	3.96	3.95	4.01	4.03	3.98	0.87	2.40	2.02	2.58	2.43	1.51	2.19	19.73
	3-L+T	6.80	6.91	7.07	6.80	6.86	6.89	1.64	4.00	2.24	2.12	2.58	1.97	2.58	31.89
	3-L	8.33	8.31	8.35	8.31	8.38	8.34	0.36	3.34	4.40	2.50	1.45	2.88	2.91	37.24
	3-L+To	10.50	10.44	10.51	10.61	–	10.52	0.67	1.02	1.77	0.68	2.23	–	1.43	49.29
	4-L	11.30	11.29	11.46	11.63	11.92	11.52	2.28	1.54	1.55	2.36	0.56	0.63	1.33	56.38
WN6B	1-L	0.47	0.44	0.50	0.47	0.49	0.47	4.86	17.15	14.45	10.64	17.20	18.96	15.68	20.70
	1-L+T	0.77	0.83	0.83	0.82	0.84	0.82	3.39	11.65	13.20	10.71	9.59	8.53	10.74	16.84
	1-L+To	1.08	1.17	1.08	1.00	1.15	1.10	6.14	10.71	18.06	15.62	8.31	2.94	11.13	53.80
	2-L	2.41	2.43	2.41	2.43	2.42	2.42	0.40	3.32	2.51	2.76	1.56	1.86	2.40	29.34
	2-L+T	2.68	2.74	2.75	2.63	–	2.70	2.10	3.35	3.97	3.45	1.95		3.18	27.17
	2-L+To	3.81	4.09	4.02	3.83	3.79	3.91	3.52	2.35	2.61	3.05	3.72	2.49	2.84	19.52
	3-L+T	7.00	6.90	7.05	7.07	7.16	7.04	1.36	2.51	2.75	2.61	1.71	1.16	2.15	31.85
	3-L	8.37	8.64	8.29	8.33	8.41	8.41	1.62	3.34	1.05	2.42	0.58	2.82	2.04	57.71
	3-L+To	10.43	10.40	10.41	10.66	–	10.47	1.19	2.49	2.48	1.97	1.45	–	2.10	23.63
	4-L	11.33	11.40	11.44	11.56	11.69	11.48	1.24	2.74	1.40	1.85	0.60	1.17	1.55	51.70
WN6C	1-L	0.51	0.48	0.49	0.44	0.43	0.47	7.22	12.52	14.87	13.44	11.51	8.43	12.15	19.92
	1-L+T	0.78	0.78	0.77	0.72	–	0.76	3.77	6.79	6.15	7.82	6.11	–	6.72	11.90
	1-L+To	0.86	0.87	0.87	0.82	–	0.86	2.78	14.02	15.25	15.84	21.03	–	16.54	18.69
	2-L	2.39	2.36	2.39	2.43	2.48	2.41	1.91	1.22	0.81	2.54	3.16	3.72	2.29	54.36
	2-L+T	2.66	2.70	2.71	2.69	–	2.69	0.80	4.71	4.45	4.35	1.58	–	3.77	38.96
	2-L+To	3.84	3.88	3.86	3.93	–	3.88	0.98	2.63	5.30	5.64	1.98	–	3.89	47.62
	3-L+T	6.73	6.71	6.92	6.72	6.94	6.80	1.68	3.55	2.08	1.78	2.54	1.95	2.38	29.94
	3-L	8.24	8.23	8.42	8.31	8.43	8.33	1.14	3.17	1.10	1.39	1.74	1.76	1.83	43.40
	3-L+To	10.37	10.13	10.40	10.72	–	10.41	2.33	2.36	2.84	1.96	1.58	–	2.18	24.75
	4-L	11.54	11.42	11.57	11.50	11.53	11.51	0.49	0.95	4.05	2.40	0.55	0.35	1.66	93.86
WN7A	1-L	0.61	0.60	0.62	0.56	0.60	0.60	3.81	13.40	12.20	12.39	13.14	12.12	12.65	4.60
	1-L+T	0.86	0.84	0.81	0.86	0.91	0.86	4.26	11.59	10.30	10.78	5.67	4.89	8.65	36.08
	1-L+To	1.07	1.07	1.10	1.18	1.09	1.10	4.15	6.44	9.19	13.20	19.39	14.10	12.46	39.75
	2-L	2.47	2.43	2.42	2.44	2.44	2.44	0.80	3.44	2.53	2.05	2.19	1.34	2.31	33.19
	2-L+T	2.76	2.78	2.71	2.73	2.72	2.74	1.06	2.88	3.11	3.32	3.88	2.94	3.23	12.51
	2-L+To	4.06	3.93	3.86	4.00	4.03	3.98	2.00	3.50	0.80	1.78	3.28	2.94	2.46	46.33
	3-L+T	6.75	6.68	6.91	6.91	6.96	6.84	1.76	3.08	2.27	1.95	1.89	0.97	2.03	37.39
	3-L	8.68	8.84	8.61	8.71	8.64	8.70	1.04	4.21	2.30	2.23	1.03	0.90	2.13	62.37
	3-L+To	10.64	10.63	10.58	10.69	–	10.63	0.43	1.10	0.68	0.78	2.01	–	1.14	53.00
	4-L	11.28	11.63	11.60	11.62	11.28	11.48	1.61	1.89	1.91	2.63	0.55	1.89	1.77	42.53

Table 5.7: Natural frequencies and damping ratios of the base-isolated building identified using low-amplitude WN base excitation data, continued.

		Natural frequency (Hz)							Damping ratio (%)						
	Mode	SSI	NExT	EFDD	DSI	OKID	Mean	CV (%)	SSI	NExT	EFDD	DSI	OKID	Mean	CV (%)
WN7B	1-L	0.48	0.48	0.43	0.46	0.44	0.46	4.98	18.41	14.45	12.18	20.06	13.60	15.74	21.25
	1-L+T	0.75	0.76	0.73	0.74	–	0.75	1.73	7.84	7.47	8.68	8.92	–	8.23	8.34
	1-L+To	1.05	1.13	1.08	0.92	0.95	1.03	8.62	8.35	9.97	11.72	10.56	7.80	9.68	16.60
	2-L	2.36	2.37	2.35	2.47	2.41	2.39	2.06	3.13	3.57	2.70	3.53	3.23	3.23	10.86
	2-L+T	2.66	2.66	2.71	2.70	2.63	2.67	1.22	4.12	1.17	2.51	2.97	2.38	2.63	40.52
	2-L+To	3.92	3.89	3.92	3.88	–	3.90	0.56	3.57	1.37	2.10	2.97	–	2.50	38.58
	3-L+T	6.67	6.78	6.92	6.70	6.72	6.76	1.44	3.23	2.25	2.01	1.76	1.56	2.16	30.10
	3-L	8.79	8.30	8.42	8.43	8.51	8.49	2.17	3.49	3.23	2.22	2.01	1.53	2.50	33.33
	3-L+To	10.70	10.86	10.90	10.80	–	10.82	0.81	1.31	1.81	1.18	0.75	–	1.26	34.53
	4-L	11.61	11.25	11.31	11.54	11.59	11.46	1.46	3.44	3.34	2.21	1.27	1.93	2.44	38.35
WN7C	1-L	0.41	0.47	0.46	0.43	0.46	0.45	5.63	15.37	16.18	13.74	16.24	15.57	15.42	6.56
	1-L+T	0.79	0.79	0.73	0.71	–	0.76	5.46	9.55	15.49	11.74	9.11	–	11.47	25.40
	1-L+To	1.03	1.10	1.09	1.01	–	1.06	4.18	8.34	7.11	6.21	9.85	–	7.88	20.04
	2-L	2.42	2.39	2.41	2.45	2.41	2.42	0.90	1.87	0.93	4.05	1.70	0.98	1.91	66.60
	2-L+T	2.66	2.64	2.71	2.65	2.62	2.66	1.27	3.64	4.04	3.89	4.83	4.94	4.27	13.66
	2-L+To	3.86	3.95	3.92	3.88	–	3.90	1.05	4.64	2.52	5.60	3.91	–	4.17	31.15
	3-L+T	6.66	6.73	6.92	6.74	–	6.76	1.61	4.02	2.96	2.67	1.67	–	2.83	34.18
	3-L	8.39	8.47	8.42	8.32	8.28	8.38	0.91	3.38	3.14	3.29	3.60	2.82	3.25	8.95
	3-L+To	10.31	10.59	10.60	10.75	–	10.56	1.74	1.05	1.22	1.59	1.03	–	1.22	21.26
	4-L	11.40	11.33	11.41	11.54	11.58	11.45	0.91	0.80	3.99	2.21	3.45	2.73	2.64	46.65
WN8A	1-L	0.56	0.57	0.58	0.57	0.56	0.57	1.47	16.35	13.56	14.30	13.39	13.27	14.17	9.03
	1-L+T	0.77	0.87	0.78	0.81	–	0.81	5.57	15.21	14.63	10.61	10.58	–	12.76	19.66
	1-L+To	1.05	1.13	1.08	1.01	1.12	1.08	4.61	12.12	16.20	10.63	11.01	16.10	13.21	20.72
	2-L	2.45	2.41	2.41	2.42	2.40	2.42	0.79	6.24	6.78	6.47	4.44	4.63	5.71	19.14
	2-L+T	2.74	2.77	2.51	2.72	2.78	2.70	4.13	3.35	4.94	4.10	2.82	1.43	3.33	39.91
	2-L+To	3.82	3.79	3.78	3.88	–	3.82	1.19	1.25	1.48	1.54	4.69	–	2.24	73.07
	3-L+T	6.73	6.84	6.70	6.76	6.81	6.77	0.86	3.01	4.06	2.38	1.38	1.30	2.43	47.77
	3-L	8.34	8.45	8.61	8.62	8.52	8.51	1.36	3.17	2.85	1.87	1.65	2.36	2.38	26.88
	3-L+To	10.44	10.51	10.57	10.45	–	10.49	0.55	1.72	1.64	0.63	1.47	–	1.36	36.79
	4-L	11.48	11.43	11.20	11.42	11.47	11.40	1.01	2.60	3.39	2.24	2.10	2.33	2.53	20.27
WN8B	1-L	0.46	0.48	0.45	0.42	0.42	0.45	5.85	17.65	15.97	13.95	20.88	14.71	16.63	16.58
	1-L+T	0.73	0.82	0.73	0.68	–	0.74	7.88	7.23	7.78	7.85	6.89	–	7.44	6.15
	1-L+To	1.08	1.13	1.09	1.04	1.01	1.07	4.33	9.41	10.98	7.53	10.65	8.47	9.41	15.42
	2-L	2.37	2.37	2.35	2.33	2.37	2.36	0.76	6.82	7.20	7.23	5.85	4.92	6.40	15.60
	2-L+T	2.71	2.72	2.51	2.62	2.71	2.65	3.42	3.88	4.22	3.61	3.49	3.35	3.71	9.31
	2-L+To	3.66	3.66	3.65	3.68	3.80	3.69	1.69	3.51	1.93	2.56	2.86	1.91	2.55	26.35
	3-L+T	6.60	6.77	6.59	6.74	6.75	6.69	1.30	2.32	1.82	2.61	1.36	1.10	1.84	34.34
	3-L	8.40	8.39	8.48	8.49	8.38	8.43	0.64	2.70	2.81	2.80	1.05	1.30	2.13	41.22
	3-L+To	10.32	10.28	10.47	10.46	–	10.38	0.92	1.50	0.81	1.47	1.66	–	1.36	27.66
	4-L	11.52	11.28	11.24	11.35	11.37	11.35	0.94	3.73	3.33	1.83	4.20	4.10	3.44	27.93
WN8C	1-L	0.45	0.45	0.46	0.42	0.42	0.44	4.25	19.72	15.56	15.55	14.49	14.09	15.88	14.11
	1-L+T	0.70	0.87	0.73	0.65	–	0.74	12.79	9.09	7.27	11.80	8.81	–	9.24	20.38
	1-L+To	0.82	0.99	0.98	0.84	0.91	0.91	8.58	8.74	7.47	8.90	6.73	7.97	7.96	11.30
	2-L	2.36	2.39	2.36	2.31	2.28	2.34	1.87	3.73	4.89	4.95	4.81	3.58	4.39	15.42
	2-L+T	2.71	2.76	2.51	2.61	–	2.65	4.21	4.89	2.83	3.91	3.53	–	3.79	22.66
	2-L+To	3.67	3.65	3.64	3.72	3.63	3.66	0.96	3.26	1.48	2.34	2.75	1.99	2.36	28.96
	3-L+T	6.54	6.65	6.59	6.67	6.55	6.60	0.88	1.06	2.48	2.39	1.90	1.68	1.90	30.30
	3-L	8.06	7.93	7.99	8.03	8.07	8.02	0.72	3.92	3.00	1.31	1.48	1.25	2.19	55.02
	3-L+To	10.45	10.56	10.75	10.43	–	10.55	1.38	1.98	0.32	1.77	0.65	–	1.18	69.32
	4-L	11.17	11.63	11.25	11.31	11.35	11.34	1.53	2.65	0.93	1.81	0.94	0.78	1.42	56.09

T: transverse / L: longitudinal / To: torsion

The effect of the amplitude of the excitation in the dynamic properties of the BI building is clearly evidenced when the system identification results from the AV and WN, summarized in Table 5.6 and Table 5.7, are compared. Figure 5.24 shows the spectrogram, which plots the short-time Fourier transform obtained using a Hamming window applied to 180 second long data segments with 50% overlap; this corresponds to about 7 hours (see top of Figure 5.24) of the acceleration time history recorded in the EW direction at the North-East corner of the roof of the BI building. The temporal evolution of the frequencies of the first two longitudinal modes, which contribute the most to the response of the roof in the longitudinal direction, is observed. Initially, mode 1-L has a frequency of about 1.1 Hz, which then decreases to approximately 0.3 Hz, and 0.5 Hz during seismic test BI5-ICA100 and WN tests, respectively. After these base excitation tests, the frequency of mode 1-L under AV is recovered to a value around 1.1 Hz. The same behavior is repeated when the building is subjected to seismic test BI7-ICA140 and another set of WN base excitation tests. A similar pattern is also observed for mode 2-L, which has a frequency about 3.5 Hz under AV.

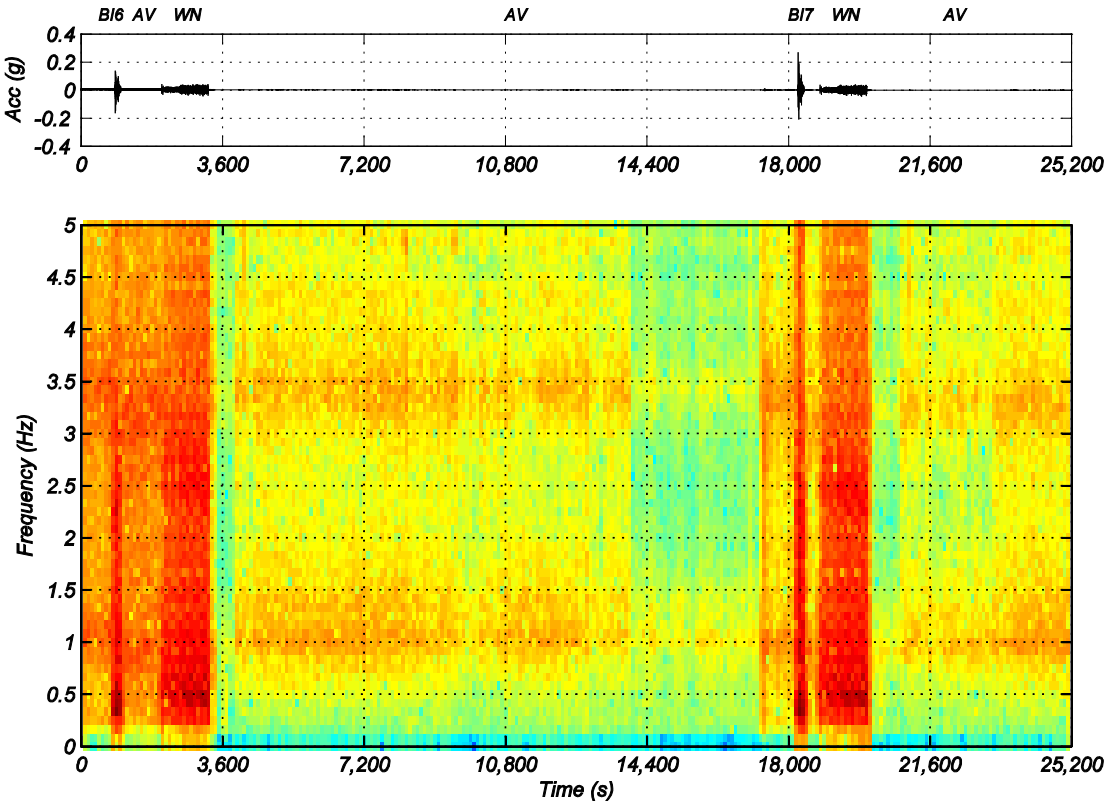

Figure 5.24: Spectrogram of the acceleration response measured in the North-East corner of the roof of the BI building.

Figure 5.25 compares the absolute acceleration time histories measured in the E-W direction (South-East corner) at the different floors of the building during WN test WN3C, with their counterparts simulated using the state-space model identified with DSI. A time interval between 120 and 190 seconds is shown. A very good match between the measured and identified responses is observed in all floors, confirming that the response reconstructed from the identified state-space model is in very good agreement with the measured acceleration response and, therefore, the accuracy of the identification process. Based on these results, it can be concluded that an equivalent linear elastic viscously damped model is able to accurately represent the response of the BI building at the level of excitation of the WN tests.

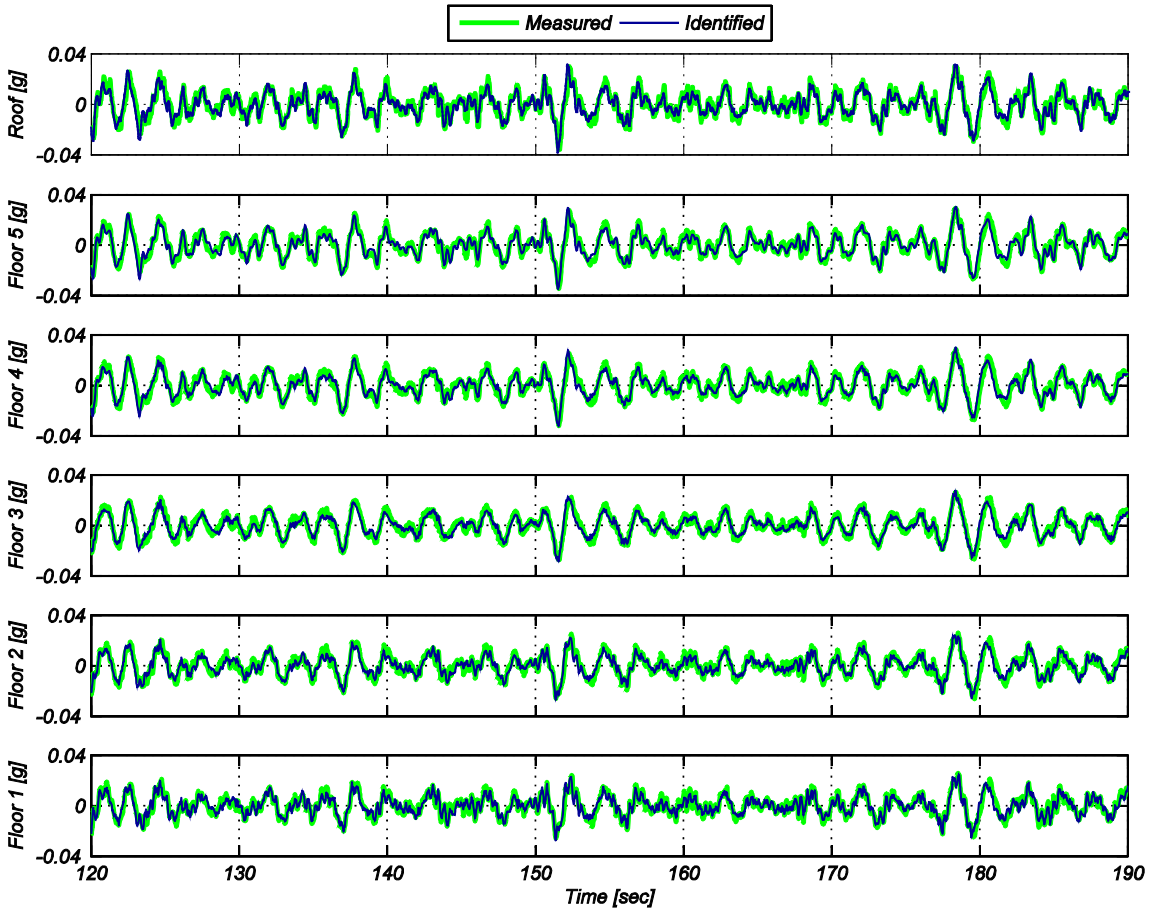

Figure 5.25: Comparison of measured and identified longitudinal absolute acceleration response in the E-W direction at the South-East corner for white noise test WN3C.

The RRMSE between the absolute measured and the identified acceleration time histories for the entire length of the WN data for all the accelerometers recording in the E-W direction, are shown in Table 5.8. By analyzing all the WN tests, it is concluded that the RRMSE is lower than 40% in all cases, once again confirming a very good agreement between the measured and the identified acceleration responses. It is further noticed that the RRMSE is practically constant for all the WN tests, and therefore independent of the peak shear strain (γ_{shear}) in the isolators.

Table 5.8: RRMSE between absolute measured and identified acceleration time histories of all the accelerometers recording in the E-W direction.

			Channel													
	RMS	**γ_{shear} [%]**	**66**	**72**	**54**	**60**	**42**	**48**	**30**	**36**	**18**	**24**	**6**	**12**	**μ [%]**	**CV [%]**
WN1A	**2.01**	**5.34**	37.9	37.7	37.9	37.5	37.1	36.2	36.7	35.8	36.3	35.3	38.4	37.8	37.1	2.7
WN1B	**3.2**	**14.76**	34.3	34.6	32.3	32.6	30.9	30.9	31.3	31.2	31.8	31.8	34.2	34.4	32.5	4.5
WN1C	**3.56**	**20.25**	36.7	37.2	35.0	35.5	33.6	34.0	33.9	34.1	34.4	34.8	36.6	37.1	35.2	3.7
WN2A	**1.34**	**5.32**	33.4	33.2	32.4	32.2	31.8	31.3	31.8	31.4	31.9	31.4	33.7	33.4	32.3	2.7
WN2B	**2.59**	**17.15**	36.8	37.3	34.7	35.3	33.1	33.5	33.4	33.7	34.2	34.6	36.0	36.5	34.9	4.1
WN2C	**3.02**	**21.27**	34.3	34.5	31.9	32.2	30.3	30.3	30.8	30.7	31.8	31.9	33.9	34.1	32.2	5.0
WN3A	**1.27**	**5.33**	35.7	35.4	34.7	34.4	33.7	33.2	33.6	33.0	33.7	33.1	35.3	34.8	34.2	2.8
WN3B	**2.57**	**17.21**	34.1	34.3	32.2	32.4	30.7	30.8	31.0	31.0	31.7	31.8	33.6	33.8	32.3	4.1
WN3C	**3.03**	**21.42**	33.8	33.9	31.4	31.6	29.9	29.8	30.4	30.2	31.3	31.3	33.5	33.7	31.7	5.0
WN4A	**2.01**	**5.28**	36.4	36.4	36.4	36.3	35.5	35.2	35.3	35.2	34.9	34.7	36.8	36.7	35.8	2.1
WN4B	**3.22**	**16.57**	33.9	34.3	33.1	33.5	32.0	32.1	31.8	32.0	31.9	32.2	34.2	34.6	33.0	3.2
WN4C	**3.76**	**21.06**	34.6	34.9	33.9	34.2	33.0	33.1	32.9	32.9	32.9	33.0	35.0	35.2	33.8	2.8
WN5A	**2.01**	**5.59**	35.1	35.1	34.6	34.6	33.7	33.5	33.5	33.4	33.3	33.1	35.6	35.5	34.2	2.7
WN5B	**3.11**	**18.52**	36.8	37.2	36.0	36.4	35.1	35.2	35.3	35.5	35.7	36.0	37.4	37.8	36.2	2.5
WN5C	**3.46**	**22.41**	42.0	42.1	41.8	41.8	41.4	41.2	42.0	41.9	42.5	42.4	43.5	43.6	42.2	1.8
WN6A	**2.28**	**5.78**	35.1	35.2	35.2	35.3	34.6	34.5	34.7	34.9	33.9	34.0	36.3	36.3	35.0	2.1
WN6B	**3.29**	**18.14**	35.7	36.0	35.1	35.5	34.1	34.2	34.0	34.2	34.1	34.4	36.1	36.5	35.0	2.6
WN6C	**3.56**	**22.5**	34.5	34.8	33.0	33.4	31.5	31.6	31.6	31.7	32.0	32.2	34.2	34.4	32.9	3.9
WN7A	**1.85**	**5.82**	33.6	33.7	33.8	33.8	32.8	32.5	32.4	32.3	32.0	31.9	34.4	34.2	33.1	2.7
WN7B	**2.83**	**18.55**	33.9	33.9	32.1	32.3	30.4	30.3	30.6	30.5	31.2	31.2	33.3	33.4	31.9	4.4
WN7C	**3.22**	**22.52**	34.1	34.1	32.8	32.8	31.8	31.6	32.0	31.8	32.4	32.3	34.3	34.1	32.8	3.2
WN8A	**1.99**	**6.85**	38.5	38.7	39.3	39.5	38.3	38.4	37.5	37.7	37.2	37.3	39.1	39.2	38.4	2.1
WN8B	**3.28**	**19.13**	34.4	34.6	33.2	33.6	31.7	31.8	31.9	32.0	32.0	32.2	34.2	34.3	33.0	3.5
WN8C	**3.88**	**22.66**	34.8	35.0	33.0	33.4	30.9	31.0	31.5	31.5	32.0	32.0	34.4	34.5	32.8	4.7

5.6. Conclusions

A full-scale five-story base-isolated (BI) reinforced concrete building was built and tested on the NEES@UCSD shake table in April 2012. The experimental program, which also included the testing of the building fixed at its base, aimed to investigate the behavior of the structure and the different types of nonstructural systems and components (NCSs) to obtain their dynamic interaction during seismic excitations of various intensities. In particular, the evaluation of base isolation as a seismic protection system for the structures and NCSs was of particular interest.

In the BI configuration of the building, a sequence of seven earthquake motion tests were designed and applied to the building to progressively increase the seismic

demand on the structure and NCSs. Before and after each seismic test, low-amplitude white noise (WN) base excitation tests with three different nominal amplitudes were carried out and ambient vibration (AV) data were recorded continuously for approximately sixteen days.

The effects of the isolation system in elongating the predominant periods of the building, augmenting the energy dissipation capability of the system, and concentrating the displacement in the isolation layer are clearly shown. The effectiveness of the isolation in reducing the peak floor acceleration and interstory drift demands is also demonstrated. The dependency of the secant stiffness and effective damping ratio on the shear deformation in the isolators is investigated using data from quality, WN, and seismic tests.

Because of the low intensity of the WN and ambient excitations, a quasi-linear response of the system is assumed and the modal parameters of an equivalent viscously-damped linear elastic time-invariant model are estimated using the vibration data recorded during these tests. Five system identification (SID) methods, including three output-only (SSI-DATA, NExT-ERA and EFDD) and two input-output (OKID-ERA and DSI) are used to estimate the modal properties (i.e., natural frequencies, damping ratios and mode shapes) of the BI building. An automated SID process using the SSI-DATA and NExT-ERA methods and based on the stabilization diagram is applied to the continuously-recorded AV data to identify the modal properties of the BI building under small amplitude excitations. Eight dominant modes were identified using the AV data. The first three correspond mainly to the deformation of the isolation layer, i.e., isolation modes, and higher modes correspond to structural modes mostly involving deformation

of the superstructure. With the WN test data, ten modes are identified, with the first three corresponding to the isolation modes.

By analyzing the polar plots, it is concluded that all modes identified with AV data are almost purely classically damped. The degree of non-classical damping is higher for the isolation modes identified from the WN test data. Results obtained further showed that the identified modal parameters obtained by different methods are in good agreement and that the natural frequencies and damping ratios have the lowest and highest variability, respectively. Natural frequencies of the isolation modes identified with WN data are larger than those identified using AV data because of the reduction of the effective stiffness of the isolation layer. However, the differences between natural frequencies of structural modes identified from WN and AV data are much lower, suggesting that the structure itself experienced a linear elastic response during the WN tests.

Damping ratios of the isolation modes are considerably higher than those of the structural modes, especially when the WN test data are used. This is because more intense excitations induce larger deformation of the isolators, implying that more energy is dissipated by hysteretic behavior of the bearings. This can be identified as equivalent viscous damping because of the assumed underlying mathematical model used for SID purposes. The identified damping ratios correlate well with the effective damping ratios computed from the hysteretic response of the bearings.

This research also provided a unique opportunity to study the performance of different state-of-the-art SID methods when applied to vibration data recorded in a full-scale BI building subjected to excitations of different amplitudes. It also helped to better

understand the behavior of high damping rubber bearings when subjected to dynamic loads from sinusoidal, ambient, WN, and seismic tests.

5.7. Acknowledgements

Part of Chapter 5 is a reprint of the material that is currently being prepared for submission for publication "Seismic response analyses and modal identification of a full-scale five-story base-isolated building tested on a shake table" in *ASCE Journal of Structural Engineering*, Astroza, Rodrigo; Ebrahimian, H.; Conte, J.P.; Restrepo, J.I.; and Hutchinson, T.C. The dissertation author was the primary investigator and author of this paper.

References

Allemang, R. J. and Brown, D. L. (1982). "A correlation coefficient for modal vector analysis." *Proc. of 1st International Modal Analysis Conference* (*IMAC I*), Orlando, FL.

Arias, A. (1970). "A measure of earthquake intensity." in *Seismic Design for Nuclear Power Plants* (Ed. R.J. Hansen), MIT Press, 438–483.

Astroza, R., Ebrahimian, H., Conte, J.P., Restrepo, J.I., and Hutchinson, T.C. (2015a). "Influence of the construction process and nonstructural components on the modal properties of a five-story building." Submitted to *Earthquake Engineering & Structural Dynamics*.

Astroza, R., Ebrahimian, H., Conte, J.P., Restrepo, J.I., and Hutchinson, T.C. (2015b). "System identification of a full-scale five-story reinforced concrete building tested on the NEES-UCSD shake table." Submitted to *Structural Control and Health Monitoring*.

Boore, D.M. (2005). "On pads and filters: Processing strong-motion data." *Bulletin of the Seismological Society of America*, 95(2), 745–750.

Boore, D.M. and Bommer, J.J. "Processing of strong-motion accelerograms: Needs, options and consequences.", 25(2), 93–115. *Soil Dynamics and Earthquake Engineering*

Brincker, R., Ventura, C., and Andersen, P. (2001a). "Damping estimation by frequency domain decomposition." *Proc. of 19th International. Modal Analysis Conference* (*IMAC XIX*), Bethel, CT.

Brincker, R., Zhang, L., and Andersen, P. (2001b). "Modal identification of output-only systems using frequency domain decomposition." *Smart Materials and Structures*, 10(3), 441–445.

Celebi, M. (1996). "Successful performance of a base-isolated hospital building during the 17 January 1994 Northridge earthquake." *The Structural Design of Tall Buildings*, 5(2), 95–109.

Chen, M., Pantoli, E., Wang, X., Astroza, R., Ebrahimian, H., Mintz, S., Hutchinson, T.C., Conte, J.P., Restrepo, J.I., Meacham, B., Kim, J., and Park, H. (2013). *BNCS Report #1: Full-scale structural and nonstructural building system performance during earthquakes and post-earthquake fire - Specimen design, construction and test protocol*. Structural Systems Research Project Report Series, SSRP 13/09, University of California San Diego, La Jolla, CA.

Chen, M.C., Pantoli, E., Wang, X., Astroza, R., Ebrahimian, H., Hutchinson, T.C., Conte, J.P., Restrepo, J.I., Marin, C., Walsh, K., Bachman, R., Hoehler, M., Englekirk, R., and Faghihi, M. (2015). "Full-scale structural and nonstructural building system performance during earthquakes: Part I - Specimen description, test protocol, and structural response." Submitted to *Earthquake Spectra*.

de la Llera, J.C., Vazquez, J., Poulus, A., and Favier, P. "Trends in research and design of structures with seismic protection systems." *Proc. of XI Chilean Conference on Seismology and Earthquake Engineering*, Santiago, Chile.

Furukawa S, Sato E, Shi Y, Becker TC, Nakashima M. (2013). "Full-scale shaking table test of a base-isolated medical facility subjected to vertical motions." *Earthquake Engineering & Structural Dynamics*, 42(13), 1931–1949.

Furukawa, T., Ito, M., Izawa, K., and Noori, M. (2005). "System identification of base-isolated building using seismic response data." *Journal of Engineering Mechanics*, 131(3), 268-275.

Gavin, H.and Nigbor, R. (2012). "Performance of the base-isolated Christchurch Women's Hospital in the Sep. 4 2010 Darfield Earthquake and the Feb.22 2011 Christchurch Earthquake." *Proc. of 20th Analysis & Computation Specialty Conference*, Chicago, IL.

Gueguen, P. (2012). "Experimental analysis of the seismic response of one base-isolation building according to different levels of shaking: Example of the Martinique earthquake (2007/11/29) Mw 7.3." *Bulletin of Earthquake Engineering*, 10(4), 1285–1298.

Han, J-P., Wang, H-T., Liu, Y-S., Du, Y-F., and Li, H. (2011). "Investigation on main dynamic characteristics of base-isolated structures under ambient excitation." *Journal of Vibration and Shock*, 30(11), 266–271.

Hijikata, K., Takahashi, M., Aoyagi, T., and Mashimo, M. (2012). "Behavior of a base-isolated building at Fukushima Dai-Ichi nuclear power plant during the Great East Japan earthquake." *International Symposium on Engineering Lessons Learned from the 2011 Great East Japan Earthquake*, Tokyo, Japan.

Housner, G., Bergman, L., Caughey, T., Chassiakos, A., Claus, R., Masri, S., Skelton, R., Soong, T., Spencer, B., and Yao, J. (1997) "Structural control: Past, present, and future." *Journal of Engineering Mechanics*, 123 (9), 897–971.

Hu, W-H., Moutinho, C., Caetano, E., Magalhães, F., and Cunha, A. (2012). "Continuous dynamic monitoring of a lively foot-bridge for serviceability assessment and damage detection." *Mechanical Systems and Signal Processing*, 33, 38–55.

Hutchinson, T.C., Restrepo, J.I., Conte, J.C., Pantoli, E., Chen, M.C., Wang, X., Astroza, R., and Ebrahimian, H. (2014). *Shake table testing of a five story building outfitted with NCSs (BNCS project)*. Network for Earthquake Engineering Simulation (distributor), dataset. DOI: 10.4231/D38W38349.

Imregun, M. and Ewins, D.J. (1993). "Realization of complex mode shapes." *Proc. of 11th International Modal Analysis Conference* (*IMAC XI*), Kissimmee, FL.

Juang, J.N. (1994). *Applied System Identification*. Prentice Hall, Upper Saddle River, N.J.

Juang, J.N. and Pappa, R.S. (1985). "An Eigensystem realization algorithm for modal parameter identification and model reduction." *Journal of Guidance, Control, and Dynamics*, 8(5), 620–627.

Kasai, K., Mita, A., Kitamura, H., Matsuda, K., Morgan, T.A., and Taylor, A.W. (2013). "Performance of seismic protection technologies during the 2011 Tohoku-Oki Earthquake." *Earthquake Spectra*, 29(1), S265-S293.

Loh, C-H., Weng, J-H., Chen, C-H., and Lu, K-C. (2013). "System identification of mid-story isolation building using both ambient and earthquake response data." *Structural Control and Health Monitoring*, 20(2), 139–155.

Magalhães, F., Cunha, A., and Caetano, E. (2009). "Online automatic identification of the modal parameters of a long span arch bridge." *Mechanical Systems and Signal Processing*, 23(2), 316–329.

Maison, B.F. and Ventura, C. (1992). "Seismic analysis of base- isolated San Bernardino County building." *Earthquake Spectra*, 8(4), 605–633.

Miwada, G., Yoshida, O., Ishikawa, R., and Nakamura, M. (2012). "Observation records of base-isolated buildings in strong motion area during the 2011 off-the-pacific-coast of Tohoku earthquake Great East Japan Earthquake." *International Symposium on Engineering Lessons Learned from the 2011 Great East Japan Earthquake*, Tokyo, Japan.

Moroni, M., Sarrazin, M., and Soto, P. (2012). "Behavior of instrumented base-isolated structures during the 27 February 2010 Chile Earthquake." *Earthquake Spectra*, 28(S1), S407−S427.

Naeim, F. and Kelly, J.M. (1999). *Design of seismic isolated structures: From theory to practice*. John Willey and Sons, Inc. New York, NY.

Nagarajaiah, S. and Sun, X. (2000) "Response of base isolated USC hospital building in Northridge earthquake," *Journal of Structural Engineering*, 126 (10), 1177-1186.

Ndambi, J.M., Peeters, B., Maeck, J., De Visscher, J., Wahab, M.A., Vantomme, J., De Roeck, G., and De Wilde, W.P. (2000). "Comparison of techniques for modal analysis of concrete structures." *Engineering Structures*, 22(9), 1159−1166.

Pantoli, E., Chen, M.C., Hutchinson, T.C., Astroza, R., Conte, J.P., Ebrahimian, H., Restrepo, J.I., and Wang, X. (2015b). "Landmark dataset from the building nonstructural components and systems (BNCS) project." Submitted to *Earthquake Spectra*.

Pantoli, E., Chen, M.C., Wang, X., Astroza, R., Ebrahimian, H., Hutchinson, T.C., Conte, J.P., Restrepo, J.I., Marin, C., Walsh, K., Bachman, R., Hoehler, M., Englekirk, R., and Faghihi, M. (2015a). "Full-scale structural and nonstructural building system performance during earthquakes: Part II - NCS damage states." Submitted to *Earthquake Spectra*.

Peeters, B., and De Roeck, G. (2001). "One-year monitoring of the Z24-bridge: Environmental effects versus damage events." *Earthquake Engineering & Structural Dynamics*, 30(2),149–171.

Priestley, M.J.N., Seible, F., and Calvi, G.M. (1996). *Seismic design and retrofit of bridges*. John Wiley and Sons, Inc., New York, NY.

Ryan, K., Dao, N., Sato, E., Sasaki, T., and Okazaki, T. (2012). "Aspects of isolation device behavior observed from full-scale testing of an isolated building at E-Defense." *Proc. of 20th Analysis and Computation Specialty Conference*, Chicago, IL.

Sasaki, T., Sato, E., Ryan, K.L., Okazaki, T., Mahin, S.A., and Kajiwara, K. (2012). "NEES/E-Defense base-isolation tests: Effectiveness of friction pendulum and lead-rubber bearings systems." *Proc. of 15th World Conference on Earthquake Engineering* (*WCEE*), Lisbon, Portugal.

Sato, E., Furukawa, S., Kakehi, A., and Nakashima, M. (2011). "Full shaking table test for examination of safety and functionality of base-isolated medical facilities." *Earthquake Engineering & Structural Dynamics*, 40 ,1435–1453.

Siringoringo, D. and Fujino, Y. (2014). "Long-term seismic monitoring of base-isolated building with emphasis on serviceability assessment." *Earthquake Engineering & Structural Dynamics*, Special Issue: Earthquake Engineering Applications of Structural Health Monitoring, 44(4), 637–655.

Siringoringo, D. and Fujino, F. (2015). "Seismic response analyses of an asymmetric base-isolated building during the 2011 Great East Japan (Tohoku) Earthquake." *Structural Control and Health Monitoring*, 22(1), 71–90.

Sridhar, A., Kuang, A., Garven, J., Gutschmidt, S., Chase, J.G., Gavin, H.P., Nigbor, R.L., Rodgers, G.W., and MacRae, G.A. (2014). "Christchurch Women's Hospital: Analysis of measured earthquake data during the 2011–2012 Christchurch Earthquakes." *Earthquake Spectra*, 30(1), 383–400.

Stewart, J., Conte, J.P, and Aiken, I. (1999). "Observed behavior of seismically isolated buildings." *Journal of Structural Engineering*, 125(9), 955–964.

Takewaki, I. and M. Nakamura (2010). "Temporal variation in modal properties of a base-isolated building during an earthquake." Jou*rnal of Zhejiang University - Science A*, 11(1): 1–8.

Van der Auweraer, H. and Peeters, B. (2004). "Discriminating physical poles from mathematical poles in high order systems: Use and automation of the stabilization diagram." *Proc. of 21th IEEE Instrumentation and Measurement Technology Conference*, Como, Italy.

Van Overschee, P., De Moor, B. (1996). *subspace identification for linear systems: Theory, implementation, applications*. Kluwer Academic Publishers, Dordrecht, The Netherlands.

Ventura, C. E., W. D. Liam Finn, et al. (2003). "Dynamic characteristics of a base isolated building from ambient vibration measurements and low level earthquake shaking." *Soil Dynamics and Earthquake Engineering*, 23(4), 313–322.

Warn, G.P. and Ryan, K.L. (2012). "A review of seismic isolation for buildings: Historical development and research needs." *Buildings*, 2012, 2(3), 300–325.

CHAPTER 6

STATISTICAL ANALYSIS OF THE MODAL PROPERTIES OF A FIVE-STORY REINFORCED CONCRETE SEISMICALLY-DAMAGED BUILDING IDENTIFIED USING AMBIENT VIBRATIONS

6.1. Introduction

The widespread availability of sensors networks for civil structures has attracted significant attention in the field of continuous-time health monitoring of bridge and building structures. Different methodologies to identify damage in monitored structures have been investigated and vibration-based methods have been one of the most popular approaches for this purpose. Vibration-based methodologies aim to identify the modal properties of an equivalent linear-elastic viscously-damped model of the structure from the recorded vibration response. Damage is then detected based on changes of the modal properties, or quantities derived therefrom, identified before and after the structure has suffered damage, because physical properties of the structure (mass, stiffness, and damping) directly affect the vibration characteristics (e.g., Doebling et al. 1996, Doebling

1998, Chang et al. 2003, Fan and Qiao 2011, Brownjohn et al. 2011). Usually, due to operational and cost constraints, recording of vibration data from forced-vibration tests (e.g., shaker and pull-back tests) is not feasible in civil structures. Consequently, the use of low-amplitude dynamic output-only vibration data (ambient vibration or AV) is of vital importance for damage detection (DD) purposes. In this approach, operational modal analysis (OMA) or output-only system identification (SID) techniques are used with AV data recorded before and after the structure has suffered damage. AV can be continuously recorded, allowing online processing of the data measured before and after a damaging event or while a structure is deteriorating along the time.

However, there are still important challenges in the application of autonomous SID and DD schemes. First, since the data need to be continuously processed, an automated SID procedure, allowing to distinguish between spurious and physical modes, needs to be implemented. Different methods to overcome this problem have been proposed in the literature (Pappa et al 1998, Peeters and De Roeck 2001, Verboven et al. 2002, Van der Auweraer and Peeters 2004, Brincker et al. 2007, Magalhães et al. 2009, Rainieri and Fabbrocino 2010, Hu et al. 2012, Reynders et al. 2012, Ubertini et al. 2013, Vanlanduit et al. 2003). Secondly, the statistical variability of the identified modal properties need to be adequately investigated and understood, because sources different to damage can also induce variation on the dynamic characteristics of civil structures, for example temperature, soil structure interaction, measurement noise level, change in the boundary conditions, wind speed, etc. (e.g., Nayeri et al. 2008, Siringoringo and Fujino 2008, Magalhães et al. 2009, Magalhães et al. 2012, Mikael et al. 2013, Peeters and De Roeck 2001, Hu et al. 2012). Third, availability of data recorded on real structures

undergoing real damage and degradation processes has been extremely limited. Most of the full-scale tests have been conducted on in-situ bridge structures condemned for demolition, in which artificial damage (e.g., partial saw cuts in steel I beams, partial cuts of post-tensioning tendons) was induced during the demolition process of the bridge (Farrar et al. 2000, Peeters and de Roeck 2001, Huth et al. 2005, Lauzon and DeWolf 2006, Siringoringo et al. 2013, Dilena and Morassi 2011). However, this kind of artificial damage is not representative of real damage caused by natural loads or aging. For building structures, shake table tests have provided unique data to assess the modal parameters of buildings at different states of damage (e.g., Moaveni et al. 2011, Ji et al. 2011, Hien and Mita 2011). Unfortunately, none of these test programs recorded AV data continuously, and therefore the implementation of an automated SID procedure using AV data recorded on a real structure subjected to damage induced by a realistic source of dynamic excitation has not been investigated.

This chapter presents an statistical analysis of the modal properties of a full-scale five-story reinforced concrete (RC) building identified using AV data continuously recorded by twenty accelerometers for about fifteen days. The building specimen was fully outfitted with a wide range of nonstructural components and systems (NCSs) and tested on the NEES@UCSD shake table in base-isolated (BI) and fixed-base (FB) configurations. A sequence of earthquake motions were designed and applied to the FB building in order to progressively damage the structure and NCSs. Two state-of-the-art methods of OMA, the Data-Driven Stochastic Subspace Identification (SSI-DATA) and the Natural Excitation Technique combined with Eigensystem Realization Algorithm (NExT-ERA), are used with the AV data to automatically identify the modal properties of

the FB building at different damage states. A statistical analysis of the identified modal parameters is performed to investigate the statistical variability and accuracy of the system identification results. The effects of the environmental conditions and response amplitude level on the variation of the modal parameters are discussed.

6.2. Description of the building

The tested structure was a full-scale five-story cast-in-place RC building. It had one bay in the transverse direction and two bays in the longitudinal direction (direction of shaking), with plan dimensions of 6.6×11.0 m, respectively. The building had a total height (from the top of the foundation to the top of the roof slab) of 21.34 m and a floor-to-floor height of 4.27 m. The estimated total weight was 3010 kN for the bare structure and 4420 kN for the structure with all the NCSs, both excluding the foundation which weighed about 1870 kN. Two identical one-bay special moment resisting frames, one placed on the north face and the other on the south face of the building, provided the lateral force resisting system in the direction of shaking (longitudinal direction of the building). Different design details were specified for the beams at different floors. Beams on floors two and three were reinforced with high-strength steel with a nominal yield strength of 830 MPa. Fourth floor had post-tensioned hybrid upturned beams connected to the columns with ductile rod connectors. Beams on the fifth floor had conventional moment resisting frame details but were connected to the columns with ductile rod connectors. The roof had special moment resisting frame beams. The six columns of the building had 0.66×0.46 m cross-section and were reinforced with 6 #6 and 4 #9 longitudinal bars and a prefabricated transverse reinforcement electro-welded grid. The

floor system consisted of 0.2 m thick concrete slab reinforced in both directions at top and bottom at all levels. Two main openings on each slab were provided to accommodate the stairs and elevator. Two 0.15 m thick transverse concrete shear walls provided the support for the elevator guiderails and additional stiffness in the transverse and torsional directions of the building. Figure 6.1 shows the building specimen and schematic plan and elevation views. Further details about the structure and NCSs are provided in Chen et al. (2013,2015) and Pantoli et al. (2015a). The complete dataset of the project is archived in NEES repository (Hutchinson et al. 2014) and description of the recorded data and detailed instrumentation can be found in Pantoli et al. (2015b).

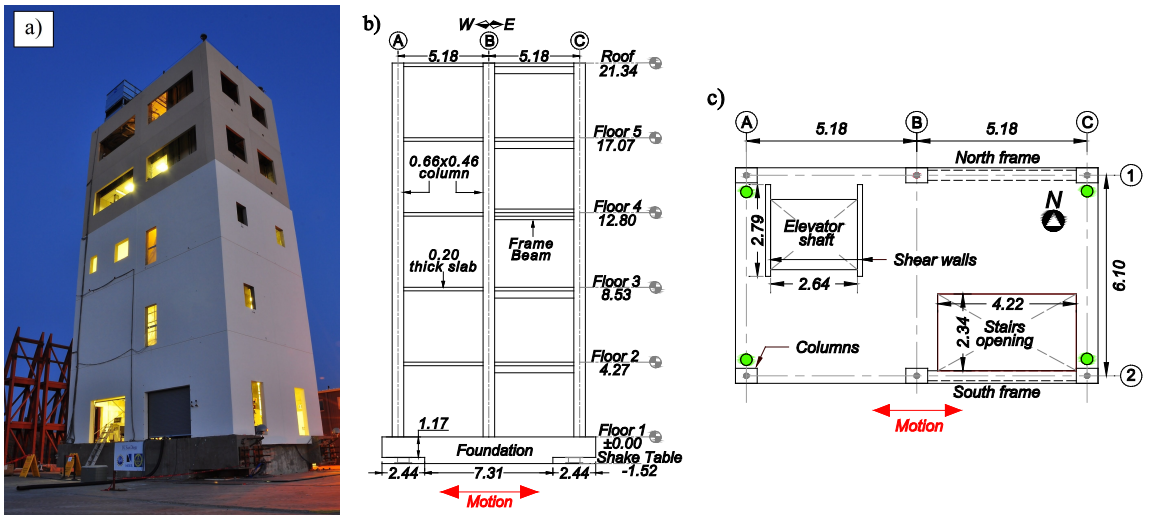

Figure 6.1: Building specimen: (a) completed building, (b) schematic elevation view, (c) schematic plan view. (all dimensions in m)

6.3. Instrumentation and test protocol

6.3.1. Instrumentation

A broad array of analog sensors with more than 500 acquisition channels was deployed in the structure and NCSs. These sensors included accelerometers, displacement

transducers (linear and string potentiometers), strain gauges, and load cells. In addition, a digital video camera array and a global positioning system (GPS) were installed. Two triaxial accelerometers were placed on the North-East and South-West corners of the shake table platen. The response of the structural skeleton was recorded using an accelerometer array consisting of four triaxial accelerometers per floor, one at each corner of each slab. These accelerometers, which are shown by green circles in Figure 6.1c, were force-balance Episensor, with a full-scale of ±4g, a frequency bandwidth DC–200 Hz, and wide dynamic range of 155dB. Their data acquisition system consisted of Quanterra Q330 data loggers from Kinemetrics, Inc., which includes signal conditioning, analog-to-digital (A/D) conversion, GPS time stamping for synchronization across multiple nodes, local memory buffer, and IP-network communication capabilities.

In this study, the acceleration response of the structure measured by twenty accelerometers, two on each translational direction of each floor, is used to identify the dynamic properties of the building. These data were sampled at 200 Hz and, before the system identification process, the acceleration time series were detrended and filtered using a band-pass infinite impulse response (IIR) Butterworth filter of order 4 with cut-off frequencies at 0.15 and 25.0 Hz, range covering all the modes having an important participation in the response of the system.

6.3.2. Test protocol

About two weeks prior to the beginning of the seismic tests in the BI configuration of the building, a system was deployed in the structure to record AV data

continuously. The system recorded data until May 18, 2012, three days after the completion of the seismic tests in the FB configuration.

In the FB configuration, six seismic input motions were defined based on global and local performance criteria and applied in order to progressively damage the structure and NCSs. Figure 6.2 shows the achieved input acceleration time histories and their displacement and pseudo-acceleration elastic response spectra for a damping ratio of ξ =5%. Because the seismic tests induced damage in the building, different damage states are defined before and after each seismic motion, ranging from DS0 (undamaged state before the first seismic test) to DS6 (damage state after the last seismic test). Table 6.1 summarizes the FB seismic test protocol, including the test dates.

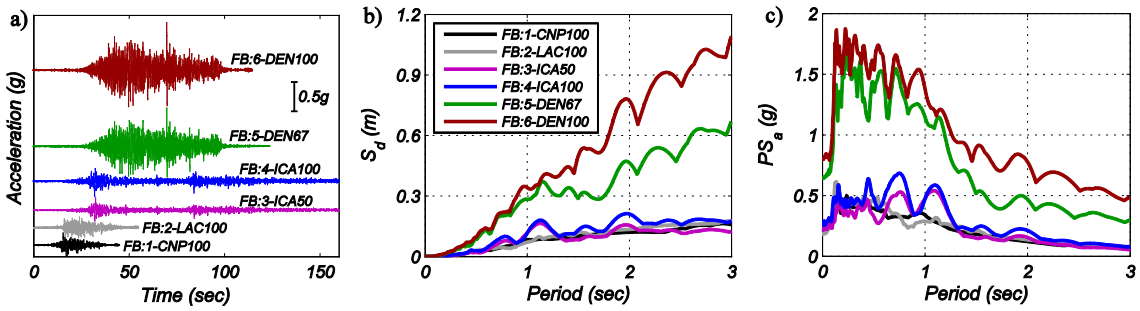

Figure 6.2: Achieved seismic input motions in the FB building: (a) acceleration time histories, (b) elastic displacement response spectra (ξ=5%), (c) pseudo-acceleration response spectra (ξ=5%).

Table 6.1: Seismic test protocol in the FB configuration.

Date	Description	Name
May 7, 2012	Canoga Park (1994 Northridge eq.)	FB1-CNP100
May 9, 2012	LA City Terrace (1994 Northridge eq.)	FB2-LAC100
	ICA 50% (2007 Pisco-Peru eq.)	FB3-ICA50
May 11, 2012	ICA 100% (2007 Pisco-Peru eq.)	FB4-ICA100
May 15, 2012	TAPS Pump Station 67% (2002 Denali eq.)	FB5-DEN67
	TAPS Pump Station 100% (2002 Denali eq.)	FB6-DEN100

6.3.3. Damage states

The seismic base excitations progressively induced damage on the structural members and NCSs. Because the FB building specimen was subjected to six earthquake motions, seven damage states (DS) are defined. DS0 corresponds to the baseline state of the building before the first seismic test (FB1-CNP100). DS1, DS2, DS3, DS4, DS5, and DS6 correspond to the damage states after the seismic test FB1-CNP100, FB2-LAC100, FB3-ICA50, FB4-ICA100, FB5-DEN6,7 and FB6-DEN100, respectively. It is noteworthy that DS0 does not correspond to the undamaged state of the structure because the building was previously tested in the BI configuration. However, the observed structural damage was negligible and the modal properties identified from AV data remained practically unchanged during the complete test phase of the BI building (Astroza et al. 2015a). The main damages observed by physical inspections in the structure and drywalls, which are the NCSs mostly affecting the dynamic characteristics of the building (Astroza et al. 2015b), are summarized in Table 6.2.

Table 6.2: Summary of damage observed by physical inspection conducted at different damage states.

Damage state	Description
DS0	No damage
DS1	**Structure:** minor cracks on the slabs of floors 2 and 3 (< 0.2 mm). **Interior partition walls:** moderate damage (cracks at joints, crushing at corners) **Balloon framing:** moderate damage to interior gypsum (cracks at joints, crushing at corners), minor damage to exterior stucco (cracks around door openings), and no visible damage to clips.
DS2	
DS3	**Structure:** minor flexural cracks on the North beam of floor 3 (< 0.15 mm), minor spalling at the bottom of NW column at level 2, minor cracking on the slabs of floors 2, 3, and 4 (< 0.25 mm), and moderate cracking on the slabs of floors 2 and 3 (< 0.25 mm). **Interior partition walls:** moderate damage (cracks at joints, crushing at corners) **Balloon framing:** moderate-severe damage to interior gypsumboard (severe crushing at corners, screw pull-out failure, joints with severe cracks), moderate damage to exterior stucco (diagonal and horizontal cracks), and minor clip failure (≤ 5%).

Table 6.2: Summary of damage observed by physical inspection conducted at different damage states, continued.

Damage state	Description
DS4	**Structure:** minor flexural cracks on the North beam of levels 2 and 3 (< 0.25 mm), minor flexural cracking on the columns at levels 1 and 2 (< 0.1 mm), and moderate cracking on the slabs of floors 2, 3, and 4 (< 0.30mm). **Interior partition walls:** severe damage (severe cracking to gypsumboard joints, gapping with adjacent elements, screw pull-out failure, severe crushing at corners). **Balloon framing:** moderate-severe damage to interior gypsumboard (severe crushing at corners, screw pull-out failure, joints with severe cracks), moderate-severe damage to exterior stucco (considerable diagonal and horizontal cracks) and minor clip damage (≈ 5%).
DS5	**Structure:** moderate flexural cracks on the North beam on floors 2 and 3 (< 0.5mm), moderate flexural cracks on the columns at levels 1 and 2 (<0.1mm) and moderate cracking on the slabs of floors 2, 3 and 4 (< 0.30mm). **Interior partition walls:** severe damage (gapping gypsumboard joints and screw pull-out failure, considerable amount of gypsum panel loosening, partial separation, and severe crushing at corners) **Balloon framing:** severe damage to interior gypsumboard (severe gapping at joints, panel partial separation), severe damage to exterior stucco (severe cracks and corner breaking), and severe failure to clips (40%)
DS6	**Structure:** severe damage to beams of floors 2 and 3 (buckling and fracture of the longitudinal reinforcing steel bars), severe spalling and cracking at the base of the columns at levels 1 and 2, and severe cracking on the slabs of 2, 3, and 4. **Interior partition walls:** severe damage (complete gypsum separation, gypsum fracture, considerable amount of severe gapping of gypsumboard joints) **Balloon framing:** severe damage to interior gypsumboard (panel complete separation), severe damage to exterior stucco (top and bottom corners torn apart), and severe damage to clips (70% failed)

6.4. Automated operational modal analysis

Two state-of-the-art output-only system identification methods are used to estimate the modal properties of the building specimen with the recorded AV data. These methods are the Data-Driven Stochastic Subspace Identification (SSI-DATA) and the Natural Excitation Technique combined with Eigensystem Realization Algorithm (NExT-ERA). Both methods estimate the modal parameters of the building from an equivalent linear time-invariant (LTI) state-space (SS) model with all the sources of energy dissipation represented by linear viscous damping.

In general, a discrete-time LTI-SS model can be written as:

$$\mathbf{x}_{k+1} = \mathbf{A_d}\mathbf{x}_k + \mathbf{B_d}\mathbf{u}_k + \mathbf{w}_k \tag{6.1a}$$

$$\mathbf{y}_k = \mathbf{C_d}\mathbf{x}_k + \mathbf{D_d}\mathbf{u}_k + \mathbf{v}_k \tag{6.1b}$$

where $\mathbf{x}_k \in \mathbb{R}^n$ = state vector, $\mathbf{y}_k \in \mathbb{R}^l$ = measured output vector (i.e., l = number of outputs), $\mathbf{u}_k \in \mathbb{R}^m$ = input vector (i.e., m = number of inputs), $\mathbf{A_d} \in \mathbb{R}^{n \times n}$ = state matrix, $\mathbf{B_d} \in \mathbb{R}^{n \times m}$ = input matrix, $\mathbf{C_d} \in \mathbb{R}^{l \times n}$ = output matrix, $\mathbf{D_d} \in \mathbb{R}^{l \times m}$ = direct feed-through matrix, $\mathbf{w}_k \in \mathbb{R}^n$ and $\mathbf{v}_k \in \mathbb{R}^l$ = process and measurement noise, respectively, and k denotes the discrete time instant.

Using the SID methods, the discrete-time state matrix ($\mathbf{A_d}$) and the output matrix ($\mathbf{C_d}$) can be estimated. From the relationship between the discrete and continuous state matrices ($\mathbf{A_d} = e^{\mathbf{A_c}\,\Delta t}$, where $\mathbf{A_c}$ = continuous-time state matrix and Δt = sampling time) it can be shown that their eigenvectors ($\boldsymbol{\Psi}$) are identical, while the eigenvalues of $\mathbf{A_c}$ and $\mathbf{A_d}$ (λ_i and μ_i, respectively), satisfy the condition

$$\lambda_i = \frac{\ln(\mu_i)}{\Delta t} \tag{6.2}$$

From the eigenvalues and eigenvectors of the discrete-time state matrix ($\mathbf{A_d}$) and the discrete-time output matrix ($\mathbf{C_d}$), the modal frequencies (f_i), modal damping ratios (ξ_i), and mode shapes ($\boldsymbol{\phi}_i$) of the system can be obtained using

$$f_i = \frac{\sqrt{\lambda_i\,\lambda_i^*}}{2\pi} = \frac{|\lambda_i|}{2\pi} \tag{6.3}$$

$$\xi_i = \frac{-\left(\lambda_i + \lambda_i^*\right)}{2\sqrt{\lambda_i\,\lambda_i^*}} = \frac{-real(\lambda_i)}{|\lambda_i|} \tag{6.4}$$

$$\boldsymbol{\Phi} = \mathbf{C_d}\,\boldsymbol{\Psi} = \left[\boldsymbol{\phi}_1, \ldots, \boldsymbol{\phi}_n\right] \tag{6.5}$$

where the superscript * and $|\cdot|$ denote complex conjugate and absolute value, respectively.

6.4.1. Natural Excitation Technique combined with Eigensystem Realization Algorithm (NExT-ERA)

The first step of the method is based on the fact that the theoretical cross-correlation function between the responses of two degrees of freedom of a structure excited by a broadband process (ambient vibration) and its free vibration response have the same analytical expression (James et al. 1993). Then, the ERA method (Juang and Pappa 1985) is used to estimate the matrices ($\mathbf{A_d}$ and $\mathbf{C_d}$) of the state space model (with $\mathbf{u}_k = 0$) using the cross-correlation functions of the output responses measured on the structure to construct the Hankel matrix with the Markov parameters $\mathbf{Y}_k$ (impulse responses)

$$\mathbf{H}(k-1) = \begin{bmatrix} \mathbf{Y}_k & \mathbf{Y}_{k+1} & \cdots & \mathbf{Y}_{k+\beta-1} \\ \mathbf{Y}_{k+1} & \mathbf{Y}_{k+2} & \cdots & \mathbf{Y}_{k+\beta} \\ \cdots & \cdots & \cdots & \cdots \\ \mathbf{Y}_{k+\alpha-1} & \mathbf{Y}_{k+\alpha} & \cdots & \mathbf{Y}_{k+\alpha+\beta-2} \end{bmatrix} \in \mathbb{R}^{\alpha m \times \beta l} \quad ; \quad \mathbf{Y}_k = \mathbf{C_d} \mathbf{A_d}^{k-1} \mathbf{B_d} \in \mathbb{R}^{l \times m} \tag{6.6}$$

in which α, β are user-defined parameters, such that if $\alpha \geq n$ and $\beta \geq n$ the matrix $\mathbf{H}(k-1)$ is of rank n. For $k=1$ and $k=2$, the matrices $\mathbf{H}(0)$ and $\mathbf{H}(1)$ can be decomposed using singular value decomposition (SVD) as

$$\mathbf{H}(0) = \mathbf{U}\boldsymbol{\Sigma}\mathbf{V}^T = \mathbf{U_n}\,\boldsymbol{\Sigma_n}\,\mathbf{V_n}^T \qquad \mathbf{H}(1) = \mathbf{U_n}\,\boldsymbol{\Sigma_n}^{1/2}\,\mathbf{A}\,\boldsymbol{\Sigma_n}^{1/2}\,\mathbf{V_n}^T \tag{6.7}$$

where the matrices $\mathbf{U_n}, \mathbf{\Sigma_n}, \mathbf{V_n}^T$ are obtained eliminating the rows and columns corresponding to small singular values (spurious modes). Then, the state and output matrices ($\mathbf{A_d}$ and $\mathbf{C_d}$) corresponding to the minimum realization can be computed by

$$\mathbf{A} = \mathbf{\Sigma_n}^{-1/2}\ \mathbf{U_n}^T\ \mathbf{H}(1)\ \mathbf{V_n}\ \mathbf{\Sigma_n}^{-1/2} \qquad \mathbf{C} = \begin{bmatrix}\mathbf{I} & \mathbf{0}\end{bmatrix} \mathbf{U_n}\ \mathbf{\Sigma_n}^{1/2} \tag{6.8}$$

In this study, the cross-correlation functions are computed through the inverse Fourier transform of the cross-power spectral density function, which are estimated using the Welch's method with a Hanning window of length 1/8 of the total length of the signal and 50% overlapping.

6.4.2. Data-Driven Stochastic Subspace Identification (SSI-DATA)

The data-driven stochastic subspace identification (SSI-DATA) method assumes purely stochastic systems with no external input (i.e., $\mathbf{u}_k = 0$ in Equation 6.1) and that the process and measurement noises are zero mean white vectors. From the measured accelerations, the output extended block Hankel matrix ($\mathbf{Y}_{0|2i\text{-}1}$), which is composed by $2i$ block rows and j columns, is constructed:

$$\mathbf{Y}_{0|2i-1} = \left(\begin{array}{cccc} \mathbf{y}_0 & \mathbf{y}_1 & \cdots & \mathbf{y}_{j-1} \\ \cdots & \cdots & \cdots & \cdots \\ \mathbf{y}_{i-2} & \mathbf{y}_{i-1} & \cdots & \mathbf{y}_{i+j-3} \\ \mathbf{y}_{i-1} & \mathbf{y}_i & \cdots & \mathbf{y}_{i+j-2} \\ \hline \mathbf{y}_i & \mathbf{y}_{i+1} & \cdots & \mathbf{y}_{i+j-1} \\ \mathbf{y}_{i+1} & \mathbf{y}_{i+2} & \cdots & \mathbf{y}_{i+j} \\ \cdots & \cdots & \cdots & \cdots \\ \mathbf{y}_{2i-1} & \mathbf{y}_{2i} & \cdots & \mathbf{y}_{2i+j-2} \end{array}\right) = \left(\frac{\mathbf{Y}_{0|i-1}}{\mathbf{Y}_{i|2i-1}}\right) = \left(\frac{\mathbf{Y}_p}{\mathbf{Y}_f}\right) \tag{6.9a}$$

$$\mathbf{Y}_{0|2i-1} = \left(\begin{array}{cccc} \mathbf{y}_0 & \mathbf{y}_1 & \cdots & \mathbf{y}_{j-1} \\ \cdots & \cdots & \cdots & \cdots \\ \mathbf{y}_{i-1} & \mathbf{y}_i & \cdots & \mathbf{y}_{i+j-2} \\ \hline \mathbf{y}_i & \mathbf{y}_{i+1} & \cdots & \mathbf{y}_{i+j-1} \\ \mathbf{y}_{i+1} & \mathbf{y}_{i+2} & \cdots & \mathbf{y}_{i+j} \\ \mathbf{y}_{i+2} & \mathbf{y}_{i+3} & \cdots & \mathbf{y}_{i+j+1} \\ \cdots & \cdots & \cdots & \cdots \\ \mathbf{y}_{2i-1} & \mathbf{y}_{2i} & \cdots & \mathbf{y}_{2i+j-2} \end{array}\right) = \left(\begin{array}{c} \mathbf{Y}_{0|i} \\ \hline \mathbf{Y}_{i+1|2i-1} \end{array}\right) = \left(\begin{array}{c} \mathbf{Y}_p^+ \\ \hline \mathbf{Y}_f^- \end{array}\right) \tag{6.9b}$$

where $\mathbf{y}_k$ is the response of the system at discrete time $t_k = k\,\Delta t$, where Δt is the sampling time. The extended observability matrix ($\mathbf{\Gamma}_i$) is obtained from the singular value decomposition of the weighted projection $\mathbf{W}_1\,\vartheta_i\,\mathbf{W}_2 = \mathbf{W}_1\left(\mathbf{Y}_f / \mathbf{Y}_p\right)\mathbf{W}_2 = \mathbf{USV}^T$. Finally, the matrices of the state-space model ($\mathbf{A_d}$ and $\mathbf{C_d}$) are estimated from $\mathbf{\Gamma}_i$ as

$$\mathbf{A_d} = \underline{\mathbf{\Gamma}_i}^{\dagger}\,\overline{\mathbf{\Gamma}_i} \tag{6.10}$$

$$\mathbf{C_d} = \text{first } l \text{ rows of } \mathbf{\Gamma}_i \tag{6.11}$$

where $\underline{\mathbf{\Gamma}_i}$ = $\mathbf{\Gamma}_i$ without the last l rows, $\overline{\mathbf{\Gamma}_i}$ = $\mathbf{\Gamma}_i$ without the first l rows, and the superscript † denotes the Moore-Penrose pseudo-inverse. In this study, the principal component (PC) algorithm is used and consequently the weighting matrices are $\mathbf{W}_1 = \mathbf{I}_{ni}$ and $\mathbf{W}_2 = \mathbf{Y}_p^T\,\mathbf{\Phi}_{\mathbf{Y}_p,\mathbf{Y}_p}^{-1/2}\,\mathbf{Y}_p$. Detailed description about the SSI-DATA can be found in Van Overschee and De Moor (1996).

6.4.3. Automated identification process

The identification process is performed using back-to-back ten-minute long time windows of structural vibration data, referred to as data sets hereafter. Since

approximately 15 days of continuous data, producing 1983 data sets need to be processed to identify the dynamic properties of the building, an automated procedure is used. For this, the stabilization diagram, which summarizes the identified modal parameters versus, is utilized to distinguish between physical and spurious (mathematical) modes. Values suggested in the literature are used for the stability criteria (e.g., Peeters and De Roeck 2001, Van der Auweraer and Peeters 2004, Hu et al. 2012):

$$\frac{\left|f_i - f_j\right|}{f_j} \le 1\% \quad ; \quad \frac{\left|\xi_i - \xi_j\right|}{\xi_j} \le 5\% \quad ; \quad \left(1 - MAC_{\phi_i,\phi_j}\right)100 \le 2\% \quad ; \quad n_s \ge 10 \qquad (6.12)$$

where f_i, ξ_i and f_j, ξ_j are the identified natural frequencies and damping ratios for models of consecutive orders i and $j = i + 2$, MAC_{ϕ_i,ϕ_j} is the modal assurance criterion (Allemang and Brown 1982) of a pair of corresponding mode shapes identified for models of successive orders, and n_s denotes the number of times (as the model order is increased progressively by increments of 2) that an identified mode has triple stability defined in Equation 6.12. Modes with natural frequencies lower than 10 Hz are considered in the identification because they are expected to have a sufficiently high signal-to-noise ratio (SNR) (Astroza et al. 2015c). In addition, identified damping ratios higher than 7% are discarded as non-physical.

It is well known that the degree of contamination of the stabilization diagrams depends on some specific parameters used on each SID method. In the case of SSI-DATA and ERA the stabilization diagram are sensitive to the number of block rows and columns in the Hankel matrix used to compute the state ($\mathbf{A_d}$) and output ($\mathbf{C_d}$) matrices of the state-space model. To keep a reasonable computational cost and based on prior

analyses, a maximum model order of 60, $i = 25$, and $j = n_{tot} - 2i + 1$ (n_{tot} = total number of data points, i.e., all data of each data set are used) in SSI-DATA and $\alpha = \beta = 150$ in ERA are chosen. Figure 6.3 shows the stabilization diagram obtained using SSI-DATA with the ambient vibration data set recorded on the building on May 04, 2012 between 15:00 and 15:10 PST.

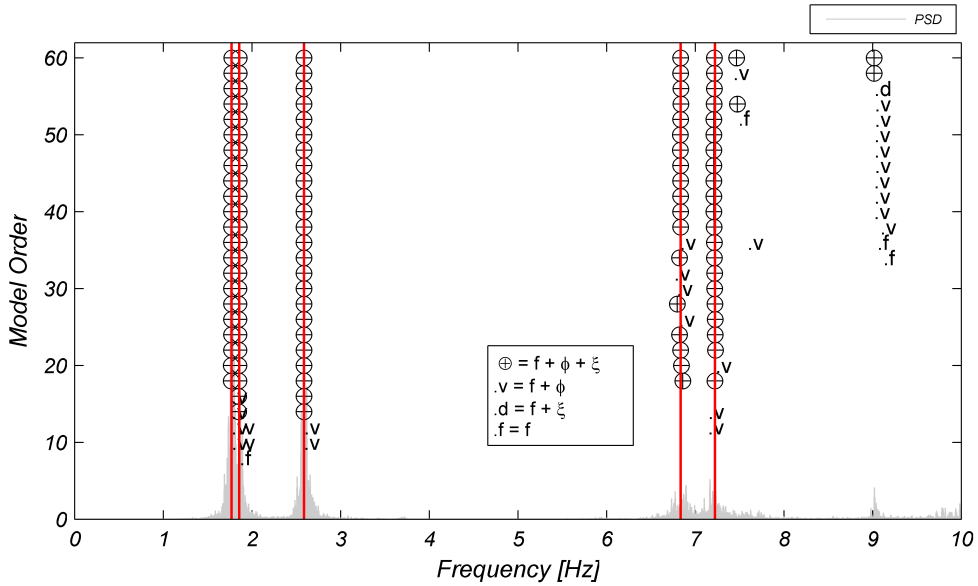

Figure 6.3: Stabilization diagram generated by the automated SSI-DATA for the ambient vibration data recorded on May 4, 2012 between 15:00 and 15:10 PST (DS0).

Because of the test protocol, different numbers of data sets are available for the different damage states (Table 6.3). It is observed that at DS2 and DS5 there are only 18 and 42 data sets available, respectively, because two seismic tests per day were conducted on May 9 and May 15, 2012. It is noted that because a low number of data samples for DS2 and DS5 are available, a careful interpretation of the statistical analysis conducted at those damage states is needed. The results for DS2 and DS5 are required to provide a complete analysis of the continuously recorded ambient vibration data.

Table 6.3: Number of data sets for different damage states.

Damage State	Number of data sets
DS0	444
DS1	270
DS2	18
DS3	258
DS4	573
DS5	42
DS6	378
Total	**1983**

6.5. System identification results

Five modes are identified using the automated SID procedure. They correspond to the first two longitudinal (1-L and 2-L), first two coupled transverse-torsional (1-T+To and 2-T+To), and first torsional (1-To) modes of the building. The mode shapes indentified from the first data set at the undamaged state (DS0) using SSI-DATA are shown in Figure 6.4. These mode shapes are used later as reference to compute the modal assurance criterion (MAC) (Allemang and Brown 1982) for each of the identified mode shape as the damage in building progresses.

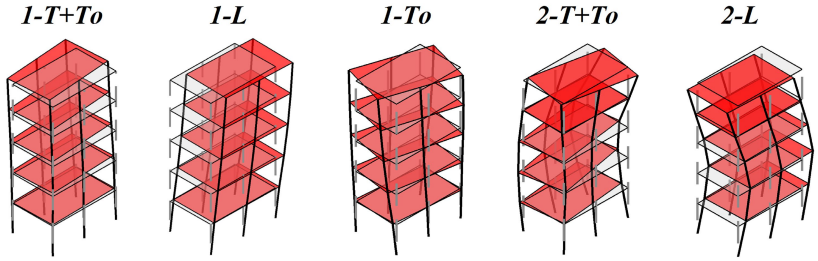

Figure 6.4: Mode shapes identified using SSI-DATA with the ambient vibration data recorded on May 4, 2012 between 17:00 and 17:10 PST (DS0).

Table 6.4 summarizes the success rate of the automated modal identification process, which represents, in percentage, the modes identified successfully (e.g., Peeters and De Roeck 2001, Magalhães et al. 2009) accordingly to the stability criteria defined in

Equation 6.12. The success rate of both SID methods are similar for all the identified modes at the different DSs. The damage does not show any clear effect on the success rate of the identification process. For most DSs, the success rate is usually higher than 85%, except for mode 1-To (which exhibits a success rate lower than other modes in DS0 and DS1) and mode 2-T+To at DS2, DS3, and DS5 (recall that DS2 and DS5 have only 18 and 42 data sets, respectively). It is noted that the degree of participation of the different modes in the response of the building depends on the characteristics of the excitation. For ambient vibrations, it is expected that higher modes have a lower SNR than lower modes because of their lower participation in the response of the building. Success rates presented in Table 6.4 indicate a satisfactory performance of the automated identification process.

Table 6.4: Success rate of the automated modal identification results.

Mode	DS0		DS1		DS2		DS3		DS4		DS5		DS6	
	N-E	SSI	N-E	SSI	N-E	SSI	N-E	SSI	N-E	SSI	N-E	SSI	N-E	SSI
1-T+To	100	99	87	81	94	89	99	97	100	98	90	93	99	92
1-L	97	95	82	73	89	78	97	96	94	90	86	88	84	81
1-To	68	69	51	53	78	83	85	88	82	82	88	90	80	76
2-T+To	98	98	90	91	56	61	56	55	79	75	38	33	99	98
2-L	97	96	97	97	78	78	59	54	48	52	86	83	94	97

N-E: NExT-ERA SSI: SSI-DATA

The natural frequencies obtained with the automated identification process using NExT-ERA and SSI-DATA are plotted as a function of time in Figure 6.5. In this figure, vertical black dashed lines mark the times of the six seismic tests conducted on the building. Results of both SID methods are in very good agreement. It can be clearly observed that the natural frequencies undergo significant reductions after each seismic test, and mode crossing appears between modes 1-L and 1-T+To following test FB1-CNP100 and between mode 2-T+To and 2-L following test FB3-ICA50. Since the

building was primarily excited in its longitudinal direction, stiffness reduction is expected mainly in that direction. Consequently, the longitudinal modes are affected more significantly by the damage and experience a relatively larger decrease in their natural frequencies than the modes with transverse and torsional components. It is observed that for a given DS, the identified natural frequencies vary periodically. A discussed in Section 6.7, this fluctuation is due to the variation of the magnitude of the vibration response of the building caused by changes in the environmental conditions.

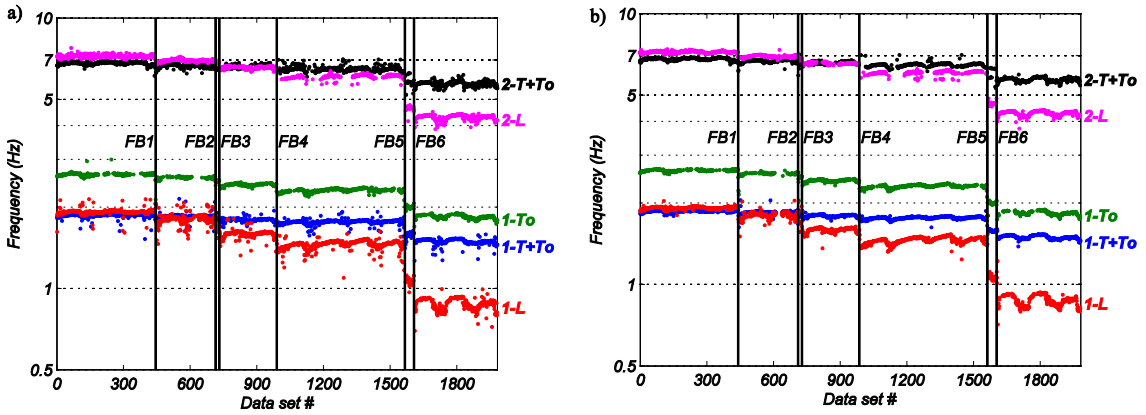

Figure 6.5: Evolution in time of the identified natural frequencies: (a) NExT-ERA, (b) SSI-DATA.

To analyze the overall trend of the identified damping ratios with increasing level of damage, Figure 6.6 shows the evolution of the identified equivalent viscous damping ratios. Similarly to the case if natural frequencies, cyclic variations due changes in environmental conditions are observed and will be discussed in Section 6.7. A systematic increase of the damping ratio with increasing level of damage is noticed only for mode 1-L, which is purely longitudinal (direction of the imposed seismic excitation). The estimated damping ratios obtained by NExT-ERA and SSI are in good agreement but larger method-to-method variability than that of the identified natural frequencies is

observed. In addition, from Figure 6.5 and Figure 6.6 a slightly larger variability of the identified natural frequencies and damping ratios is observed for NExT-ERA than for to SSI-DATA. The identified natural frequencies and damping ratios obtained using SSI-DATA are better group together, following the cyclic variation with less estimates far from this trend (outliers).

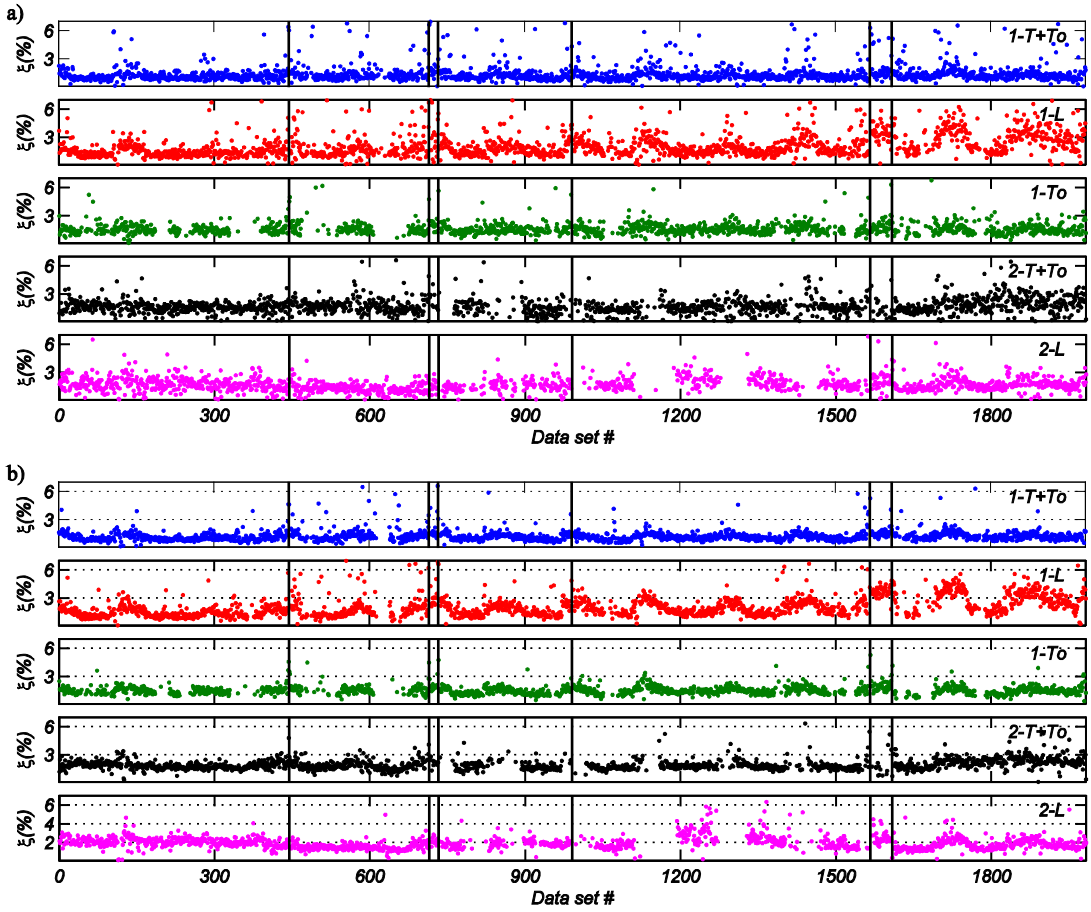

Figure 6.6: Evolution in time of the identified damping ratios: (a) NExT-ERA, (b) SSI-DATA.

The evolution of the MAC values over time is presented in Figure 6.7. The MAC values are computed using the mode shapes shown in Figure 6.4 as reference. Since the same reference modes are used to compute the MAC values of the mode shapes identified over time using NExT-ERA and SSI-DATA methods, a good agreement between the

mode shapes identified by both methods is observed from Figure 6.7. It is observed that the MAC values for modes 1-T+To and 1-L decrease at DS1 (after seismic test FB1-CNP100), reaching values as low as 0.5. At DS2 (after seismic tests FB2-LAC100), the MAC of these two modes stabilize at values about 0.90. A similar phenomena is observed for modes 2-T+To and 2-L, which MAC values at DS3 (after test FB3-ICA50) show large variability and they stabilize at DS4. As previously discussed, mode crossing between modes 1-T+To and 1-L is observed after seismic test FB1-CNP100 and between modes 2-T+To and 2-L after seismic test FB3-ICA50. Oppositely to identified natural frequencies and damping ratios, no cyclic variation is detected for the MAC values.

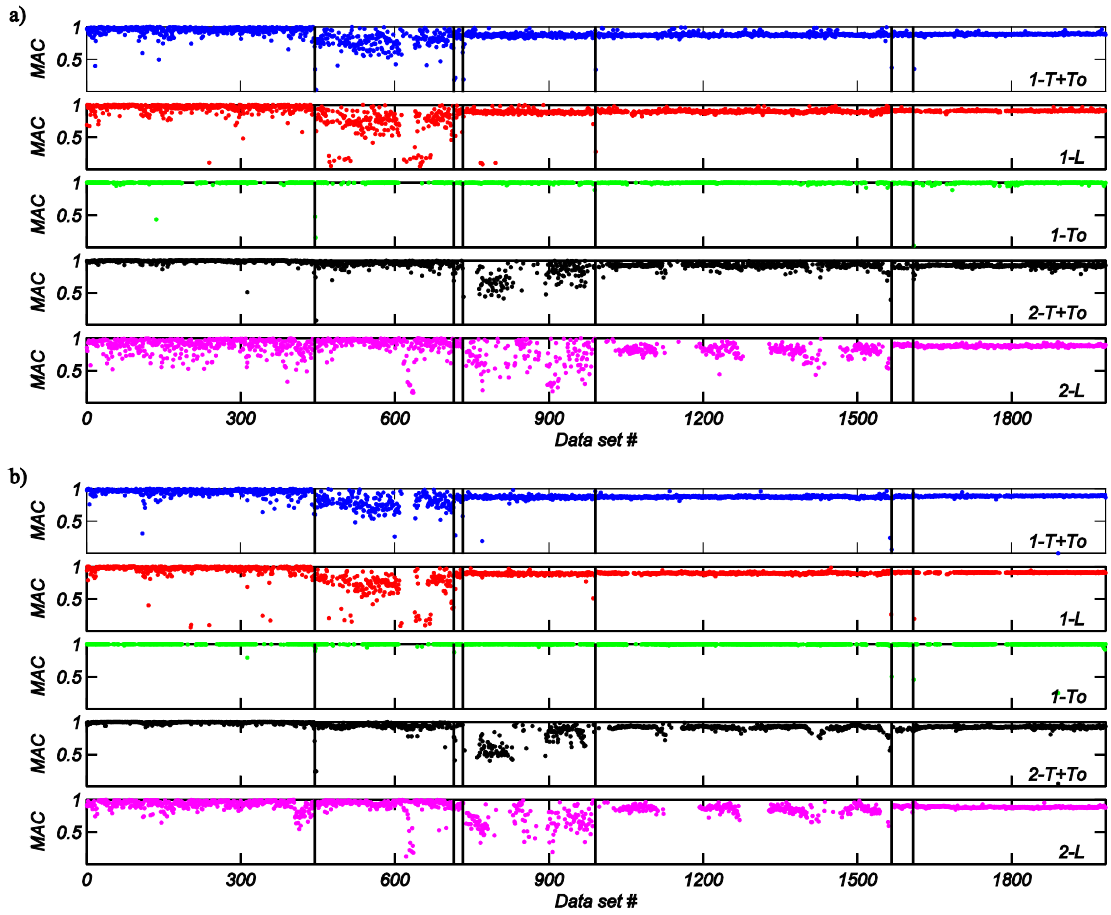

Figure 6.7: Evolution in time of the MAC values: (a) NExT-ERA, (b) SSI-DATA.

6.6. Statistical analysis of the identified modal parameters

6.6.1. Preliminary analysis

To analyze the variability of the modal parameters identified using the two different SID methods, the mean (μ) and coefficient of variation (CV) of the estimated modal parameters are computed for each DS. Mean and CV of the identified natural frequencies are summarized in Table 6.5 and Table 6.6 for NExT-ERA and SSI-DATA, respectively. Mean values of natural frequencies identified using NExT-ERA and SSI-DATA are very similar for all the modes and at different DSs. Except for DS2 and DS5, which have a low number of data sets (Table 6.3) an therefore the statistics for those DSs need to be carefully analyzed, CVs of the natural frequencies identified using NExT-ERA are noticeably higher than those of SSI-DATA.

Table 6.5: Mean and coefficient of variation of the natural frequencies identified using NExT-ERA.

Mode	DS0		DS1		DS2		DS3		DS4		DS5		DS6	
	μ (Hz)	CV (%)	μ (Hz)	CV (%)	μ (Hz)	CV (%)	μ (Hz)	CV (%)	μ (Hz)	CV (%)	μ (Hz)	CV (%)	μ (Hz)	CV (%)
1-T+To	1.858	1.676	1.849	2.398	1.798	3.140	1.790	1.905	1.759	1.987	1.569	2.639	1.492	2.477
1-L	1.917	2.421	1.798	4.592	1.664	3.147	1.589	3.276	1.451	3.737	1.059	2.654	0.874	5.489
1-To	2.636	1.351	2.557	2.380	2.490	1.086	2.414	1.026	2.300	1.342	2.000	0.969	1.838	1.937
2-T+To	6.796	1.208	6.663	1.547	6.481	1.101	6.637	1.475	6.484	1.975	5.823	5.322	5.710	1.949
2-L	7.214	1.155	6.955	0.898	6.848	0.684	6.553	1.043	6.076	1.576	4.641	2.023	4.286	2.267

Table 6.6: Mean and coefficient of variation of the natural frequencies identified using SSI-DATA.

Mode	DS0		DS1		DS2		DS3		DS4		DS5		DS6	
	μ (Hz)	CV (%)	μ (Hz)	CV (%)	μ (Hz)	CV (%)	μ (Hz)	CV (%)	μ (Hz)	CV (%)	μ (Hz)	CV (%)	μ (Hz)	CV (%)
1-T+To	1.861	0.888	1.845	1.720	1.792	3.634	1.788	1.192	1.759	1.091	1.580	2.891	1.495	1.869
1-L	1.914	1.167	1.794	2.824	1.702	5.697	1.586	1.990	1.452	2.689	1.071	7.528	0.870	5.606
1-To	2.630	1.216	2.558	1.994	2.460	4.883	2.413	1.069	2.300	1.304	1.993	1.832	1.834	1.811
2-T+To	6.794	1.159	6.677	1.414	6.523	2.989	6.605	1.137	6.473	1.474	5.958	5.730	5.709	1.598
2-L	7.211	0.821	6.951	0.859	6.817	0.684	6.549	0.769	6.054	1.564	4.650	1.150	4.284	2.193

Figure 6.8 shows the normalized mean (normalized with respect to the mean at DS0) and CV of the identified natural frequencies (μ_f and CV_f, respectively) using NExT-ERA and SSI. From the μ_f at different DSs, the effect of damage in reducing the identified natural frequencies is clearly observed. The seismic excitation progressively damaged the structure and NCSs and consequently reduced the lateral stiffness of the building. It is noted that the natural frequencies of the longitudinal modes undergo larger relative reduction than torsional and coupled transverse-torsional modes as damage progressed. Mode 1-L experiences the largest relative reduction (with respect to DS0), ranging between 6% and 55% for DS1 and DS6, respectively. The normalized mean of the natural frequency of mode 2-L decreases between 4% and 41% for DS1 and DS6, respectively. Coupled transverse-torsional and torsional modes experience less relative reductions, e.g., mean values of the identified natural frequencies of modes 1-T+To and 1-To reduce 1% and 3% at DS1 and 20% and 30% at DS6. In spite the seismic excitations were applied only in the longitudinal direction of the building, transverse and torsional stiffness of the building also changed noticeably.

The CV of the identified natural frequencies (Figure 6.8) seems not sensitive to the level of damage. CV_f is lower than 10% for all the modes and at different DSs. Furthermore, the CV_f of each mode at a given damage state identified using NExT-ERA and SSI are similar, suggesting that the variability is most likely coming from a physical phenomenon more than from the uncertainty associated to the SID methods themselves.

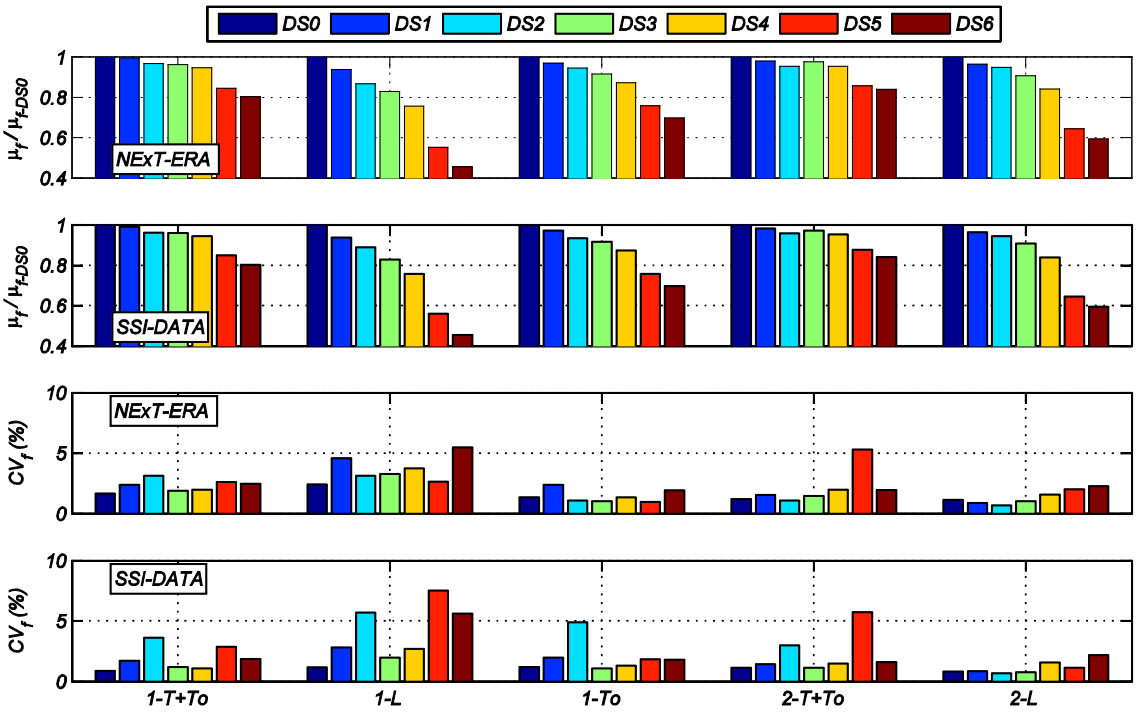

Figure 6.8: Mean and coefficient of variation of the identified natural frequencies.

Figure 6.9 shows the mean and CV of the damping ratios (μ_ξ and CV_ξ, respectively) at different DSs identified using NExT-ERA and SSI-DATA. The mean values across all the identified modes range from 1.0% to 3.0%. For mode 1-L, μ_ξ is higher at DS5 and DS6, which can also be observed in Figure 6.6. The structural and nonstructural damage observed at DS5 and DS6 is moderate to severe (see Table 6.2), specifically, significant cracks were developed in beams and columns of the structure. The mathematical model assumed in the SID methods used in this work assumed that all the sources of energy dissipation are represented by linear viscous damping. Therefore, the higher μ_ξ of mode 1-L identified at DS5 and DS6 is most likely due to the higher hysteretic energy dissipated associated with this mode (recall that mode 1-L undergoes the highest reduction of natural frequency as damage progressed), which is identified as

equivalent viscous damping by the SID methods. Damping ratio estimates are sensitive to the amplitude of the structural response; however, as discussed in Section 6.7, the magnitude of structural vibration at different DSs is comparable. No clear trend in the identified damping ratios of other modes as damage progresses is observed.

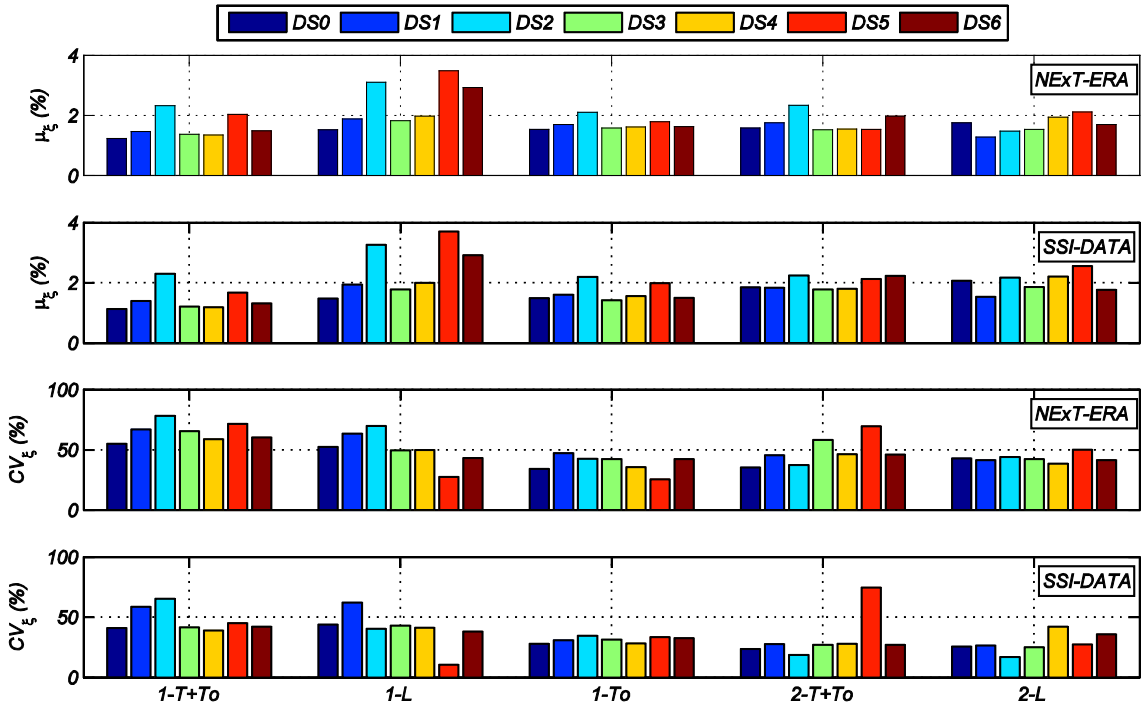

Figure 6.9: Mean and coefficient of variation of the identified damping ratios.

Consistent with the results obtained for the identified natural frequencies, the CVs of the identified damping ratios do not appear sensitive to the level of damage; however they are much larger than the CVs of the corresponding natural frequencies, with values ranging mostly between 30% and 70%. Analytical and experimental studies on system identification have shown that the CVs of natural frequencies are considerably smaller than those of damping ratios (e.g., Gersch 1974, Pakzad and Fenves 2009).

Figure 6.10 shows the mean and CV corresponding to the MAC values of the modes (μ_{MAC} and CV_{MAC}, respectively) identified using NExT-ERA and SSI-DATA. MAC values are computed utilizing the modes shapes shown in Figure 6.4 (identified from the first data set at DS0) as reference. μ_{MAC} and CV_{MAC} associated to NExT-ERA and SSI-DATA are very similar. For each mode, the values of μ_{MAC} at DS0 are larger than 0.9, confirming a good agreement between the mode shapes identified for different data sets at DS0.

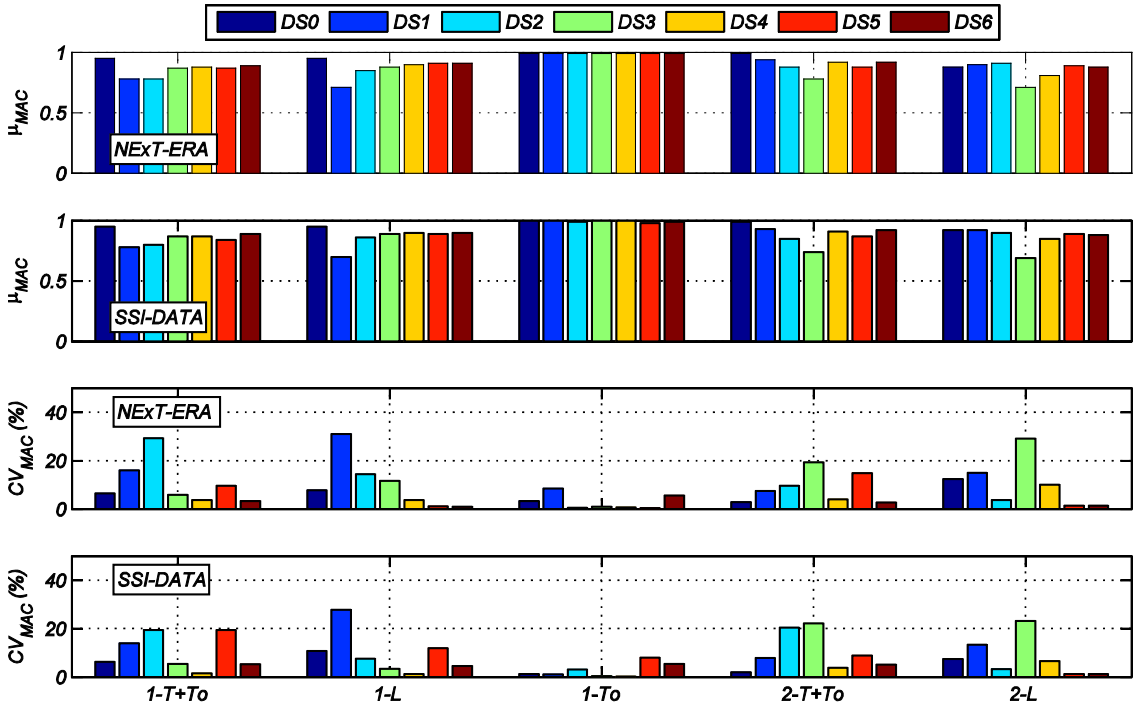

Figure 6.10: Mean and coefficient of variation for the MAC values of the identified mode shapes with respect to the reference modes.

Values of μ_{MAC} for modes 1-T+To and 1-L change noticeably after the test FB1-CNP100. As previously discussed, mode crossing between 1-T+To and 1-L is detected after FB1-CNP100. The μ_{MAC} values for these two modes converge to about 0.90 at DS5

and DS6. It is noted that higher CV_{MAC} are estimated for these two modes at DS1 and DS2, therefore their μ_{MAC} have a larger uncertainty associated. The value μ_{MAC} of mode 1-To remains practically equal to one for the different DSs. μ_{MAC} of higher modes tend to decrease from DS0 to DS3, but then it increases from DS4 to DS6. Particularly, low values of μ_{MAC} are observed for modes 2-T+To and 2-L at DS3. Mode crossing between these modes is noticed after FB2-LAC100, then the same phenomena observed when modes 1-T+To and 1-L cross is observed here.

6.6.2. Probability distributions

Histograms are used as nonparametric estimation of the probability density functions (*pdf*) of the identified modal parameters. To construct the histograms, the number of bins is chosen equal to the square root of the number of observations (or data sets), as suggested by Montgomery and Runger (2010). Figure 6.11a,b present the histograms of the natural frequencies and damping ratios, respectively, of the five modes identified at DS0 using SSI-DATA. Figure 6.11c,d present the histograms of the natural frequencies and damping ratios, respectively, of the five modes identified at DS6 using NExT-ERA. The identified natural frequencies have an approximate symmetric and bell-shaped distribution, suggesting they approximately follow a normal distribution. On the other hand, the positive skew of the histograms corresponding to the damping ratios indicates that a lognormal distribution might be a good choice to characterize the *pdf* of the identified damping ratios. It is worth noting that similar results were obtained for all

the identified modes at the different damage states, but are not presented herein because of space limitations.

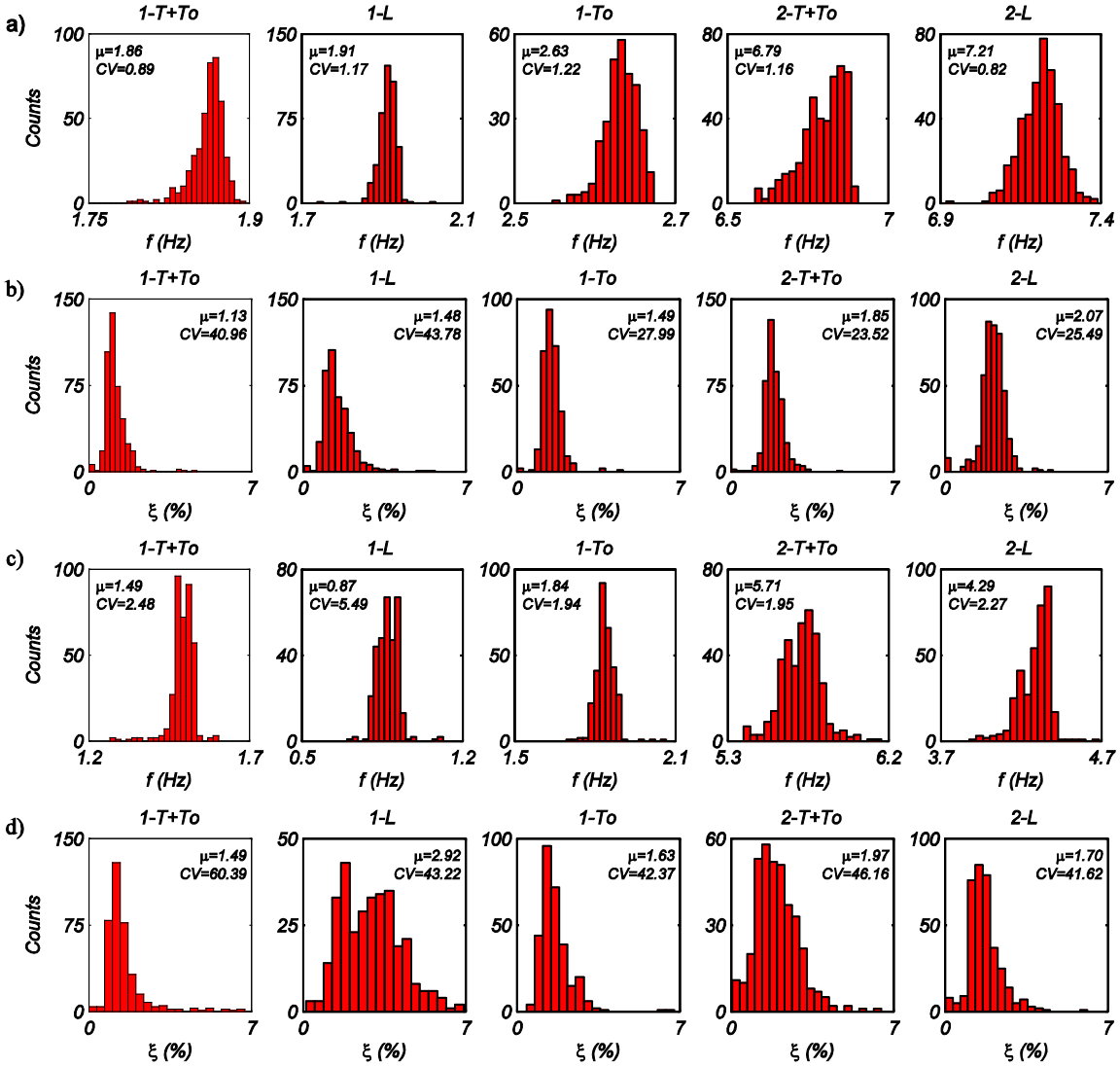

Figure 6.11: Histograms for natural frequencies and damping ratios: (a) Natural frequencies at DS0 using SSI, (b) Damping ratios at DS0 using SSI, (c) Natural frequencies at DS6 using NExT-ERA, (d) Damping ratios at DS6 using NExT-ERA.

Probability plots are used to determine more quantitatively which underlying probability distributions are followed by the identified modal parameters. This technique is especially useful to investigate small and moderate size data samples, such as the datasets of each damage state in this work (18 to 573 data sets are available for different

damage states). If the data points plotted on a probability paper corresponding to a given *pdf* show a linear trend, this indicates that the hypothesized *pdf* appropriately characterizes the data (Montgomery and Runger 2010). Figure 6.12a,b present the normal and lognormal probability plots for the natural frequencies and damping ratios, respectively, identified at DS0 using SSI-DATA. Figure 6.12c,d present the normal and lognormal probability plots for the natural frequencies and damping ratios, respectively, identified at DS6 using NExT-ERA. Each "×" symbol represents a data point against its respective probability assuming the given *pdf* ; a reference straight line between the 25th and 75th percentile points is drawn to assess the closeness of the points to a straight line. For the natural frequencies, the S shaped-curve indicates that the data has shorter tails than a normal distribution with the same mean and standard deviation. For the damping ratios, the data also have shorter tails than a lognormal distribution with the same log mean and log standard deviation. Based on the results presented above, the identified natural frequencies and damping ratios are assumed to be reasonably modeled by normal and lognormal random variables, respectively. The determination of confidence intervals in the next section makes use of these assumptions. It is noteworthy that in addition to normal and lognormal distributions, the extreme value, Rayleigh, and Weibull distributions were also investigated. The fit of normal distribution for the identified natural frequencies and lognormal distribution for the identified damping ratios are the best among all the analyzed *pdf* . It is noted that Pakzad and Fenves (2000) found that the mean of identified natural frequencies and damping ratios of the Golden Gate Bridge also approximately follow normal and lognormal distributions, respectively.

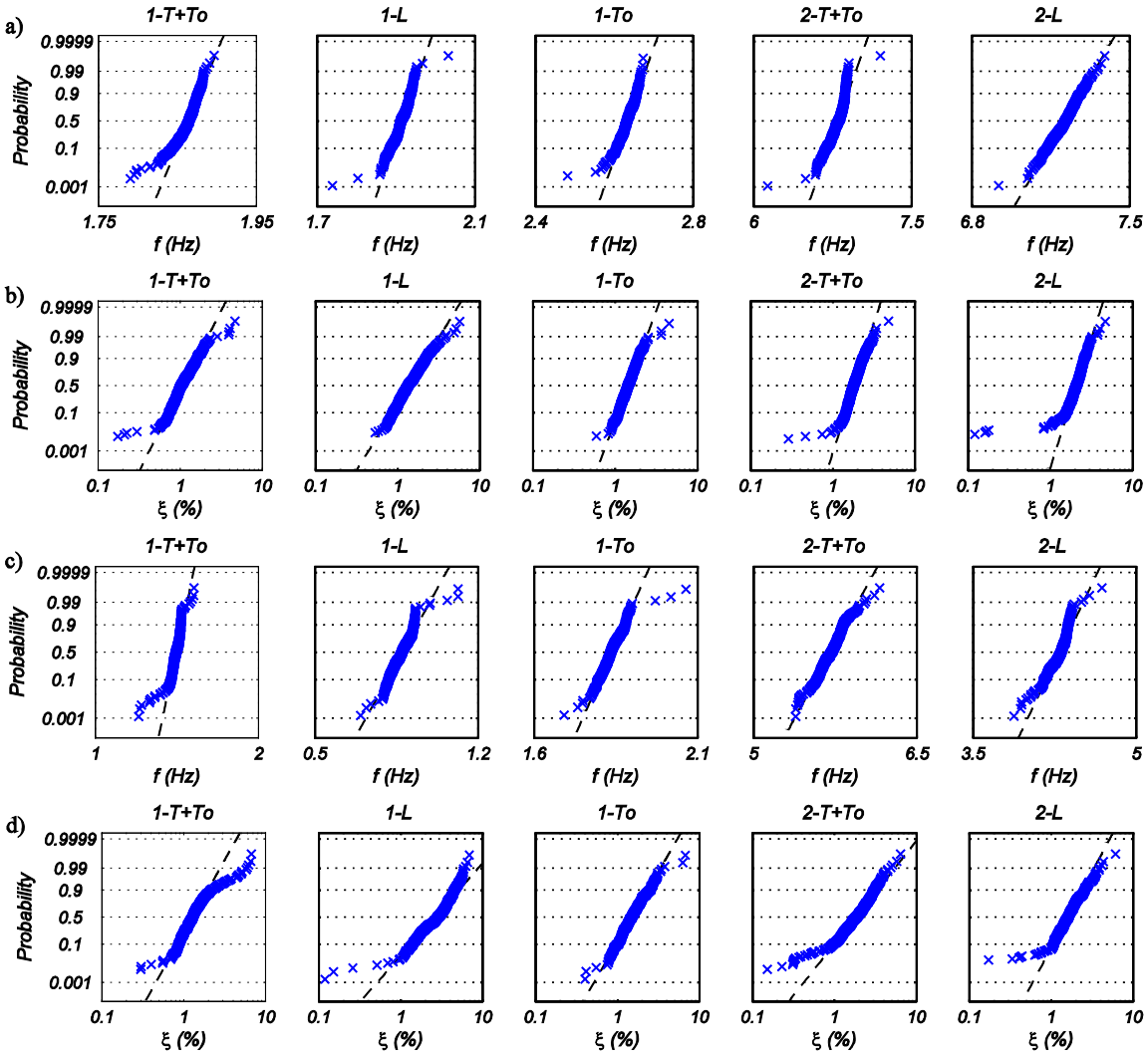

Figure 6.12: Probability plots for natural frequencies and damping ratios (a) Frequency at DS0 using SSI; (b) Damping at DS0 using SSI; (c) Frequency at DS6 using NExT-ERA; (d) Damping at DS6 using NExT-ERA.

6.6.3. Confidence intervals

The confidence interval (CI) on the mean of the identified natural frequencies and damping ratios are computed. Recall that a confidence interval estimate for a parameter θ is an interval $l \le \theta \le u$, where l and u are called lower and upper confidence bounds and are obtained from the data, such that the true value of θ resides in that interval with confidence $100(1-\alpha)\%$. A short CI implies more precision or equivalently less

uncertainty in the estimated values of the parameter. Since the identified natural frequency of each mode for a given DS approximately follows a normal distribution, the CI on its means (over a monitoring period for a fixed DS) is obtained using the $t-$ distribution (Montgomery and Runger 2010) as

$$\hat{\mu}_f - t_{\alpha/2,n-1}\frac{\hat{\sigma}_f}{\sqrt{n}} \le \mu_f \le \hat{\mu}_f + t_{\alpha/2,n-1}\frac{\hat{\sigma}_f}{\sqrt{n}} \tag{6.13}$$

where $\hat{\mu}_f$ and $\hat{\sigma}_f$ are the sample mean and sample standard deviation of the natural frequency, n is the number of samples, and $t_{\alpha/2,n-1}$ is the upper $100\alpha/2$ percentage point of the $t-$ distribution with $(n-1)$ degrees of freedom. For the identified damping ratios, which approximately follow a lognormal distribution, the Cox's method (Land 1972) is used to obtain the confidence intervals on the mean as recommended by Zhou and Gao (1997). Table 6.7 and Table 6.8 present the 95% CIs for the mean of the identified natural frequencies estimated using NExT-ERA and SSI-DATA, respectively. It is observed that the CIs are narrow implying low variability in the identification results for the natural frequencies. Although CIs of the mean of the identified natural frequencies obtained using both SID methods are very similar, CIs corresponding to NExT-ERA are wider than those obtained for SSI-DATA, which is consistent with the results presented in Figure 6.5, Table 6.5, and Table 6.6.

Table 6.7: Confidence intervals for the natural frequencies identified using NExT-ERA.

Mode	DS0		DS1		DS2		DS3		DS4		DS5		DS6	
	l	***u***	***l***	***u***	***l***	***u***	***l***	***u***	***l***	***u***	***l***	***u***	***l***	***u***
1-T+To	1.855	1.861	1.843	1.855	1.769	1.827	1.785	1.794	1.756	1.762	1.555	1.583	1.488	1.496
1-L	1.913	1.922	1.787	1.809	1.636	1.692	1.582	1.595	1.446	1.455	1.050	1.069	0.869	0.879
1-To	2.632	2.640	2.547	2.568	2.475	2.506	2.411	2.417	2.297	2.303	1.994	2.007	1.834	1.842
2-T+To	6.789	6.804	6.650	6.676	6.430	6.532	6.620	6.653	6.472	6.496	5.658	5.988	5.699	5.721
2-L	7.206	7.222	6.947	6.962	6.821	6.875	6.542	6.564	6.064	6.087	4.610	4.673	4.276	4.296

Table 6.8: Confidence intervals for the natural frequencies identified using SSI-DATA.

Mode	DS0		DS1		DS2		DS3		DS4		DS5		DS6	
	l	*u*	*l*	*u*	*l*	*u*	*l*	*u*	*l*	*u*	*l*	*u*	*l*	*u*
1-T+To	1.860	1.863	1.841	1.850	1.757	1.827	1.786	1.791	1.758	1.761	1.565	1.595	1.492	1.498
1-L	1.911	1.916	1.787	1.801	1.646	1.758	1.582	1.590	1.448	1.455	1.044	1.098	0.865	0.876
1-To	2.627	2.634	2.550	2.567	2.393	2.526	2.410	2.417	2.297	2.303	1.981	2.005	1.830	1.838
2-T+To	6.787	6.802	6.665	6.689	6.392	6.654	6.593	6.618	6.464	6.482	5.761	6.156	5.699	5.718
2-L	7.206	7.217	6.943	6.958	6.790	6.844	6.540	6.557	6.043	6.065	4.632	4.668	4.275	4.294

The 95% CIs for the damping ratios estimated using NExT-ERA and SSI-DATA are shown in Table 6.9 and Table 6.10, respectively. The CIs are narrow and always contain the corresponding sample mean, but they are relatively broader than those of the identified natural frequencies. Differences between the CIs of the mean of the damping ratios obtained using NExT-ERA and SSI-DATA are noticeably larger than those of the natural frequencies.

Table 6.9: Confidence intervals for the damping ratios identified using NExT-ERA .

Mode	DS0		DS1		DS2		DS3		DS4		DS5		DS6	
	l	*u*	*l*	*u*	*l*	*u*	*l*	*u*	*l*	*u*	*l*	*u*	*l*	*u*
1-T+To	1.19	1.33	1.35	1.52	1.56	4.56	1.26	1.41	1.29	1.40	1.65	2.40	1.48	1.69
1-L	1.49	1.67	1.74	2.07	2.05	5.57	1.73	1.97	1.94	2.15	3.08	4.43	2.82	3.19
1-To	1.49	1.61	1.58	1.78	1.72	2.56	1.50	1.64	1.57	1.67	1.65	1.95	1.56	1.69
2-T+To	1.57	1.75	1.67	1.89	1.85	2.98	1.42	1.84	1.56	1.78	1.03	2.65	1.92	2.18
2-L	1.80	2.07	1.24	1.42	1.14	2.00	1.48	1.86	1.89	2.13	1.77	2.90	1.76	2.07

Table 6.10: Confidence intervals for the damping ratios identified using SSI-DATA .

Mode	DS0		DS1		DS2		DS3		DS4		DS5		DS6	
	l	*u*	*l*	*u*	*l*	*u*	*l*	*u*	*l*	*u*	*l*	*u*	*l*	*u*
1-T+To	1.11	1.21	1.30	1.46	1.74	2.97	1.15	1.26	1.17	1.25	1.50	1.83	1.31	1.46
1-L	1.45	1.61	1.79	2.08	2.71	3.91	1.69	1.87	1.96	2.14	3.58	3.84	2.81	3.13
1-To	1.48	1.64	1.53	1.68	1.90	2.55	1.37	1.47	1.54	1.65	1.82	2.15	1.46	1.60
2-T+To	1.90	2.11	1.77	1.90	1.98	2.55	1.71	1.85	1.78	1.90	1.45	3.09	2.18	2.33
2-L	2.31	2.72	1.49	1.58	1.99	2.38	1.78	1.94	2.15	2.44	2.35	2.78	1.84	2.12

It is noted that some studies have proposed methods to estimate the uncertainty bounds on the modal parameters of linear systems identified in a single experiment (e.g., Reynders et al. 2008, Dohler et al. 2013). The uncertainty bounds presented in this chapter also include other effects different to the inherent uncertainty of the SID methods,

such as environmental effects as discussed later. Analysis of the uncertainty related to the SID methods is out of the scope of this chapter.

6.6.4. Effect of damage

From the histograms presented previously, the best-fit *pdf* for the identified natural frequencies and damping ratios are calculated assuming they follow normal and lognormal distributions respectively, as confirmed by the probably plots presented in Section 6.6.2. Figure 6.13 shows the best-fit normal *pdf* of the natural frequencies identified using SSI and NExT-ERA at the different DSs as contour plots. Although the number of data sets available for damage states DS2 and DS5 is much lower than for other DSs, their results are included to provide a complete description and analysis of the recorded data. It is observed that the mean of the natural frequency of each mode decrease as the damage increases. The relative reduction of the natural frequencies is higher for the longitudinal modes (1-L and 2-L) than for modes with transverse and torsional components because the input base excitation was applied only in the longitudinal direction of the building. From DS0 to DS4 the reduction in the natural frequencies is gradual, however, from DS4 to DS5 abrupt reduction of the natural frequencies of all identified modes is observed. It is noted that seismic motion FB5-DEN67 correspond to the design earthquake and it produced moderate to severe structural damage and severe nonstructural damage (see Table 6.2).

Most vibration-based damage identification methods rely on the changes of the identified modal parameters. However, as observed in Figure 6.13, changes in the identified modal parameters due to environmental effects can be even larger than those

due to structural or nonstructural damage, especially for minor levels of damage (e.g., those induced by motions between serviceability and design level earthquakes). Different approaches to account for the effects environmental effects on identified modal parameters have been proposed in the literature, such as principal component analysis (e.g., Hsu and Loh 2010) and black-box models, e.g. the Autoregressive with eXogenous inputs (ARX) (e.g., Peeters and De Roeck 2001, He 2008).

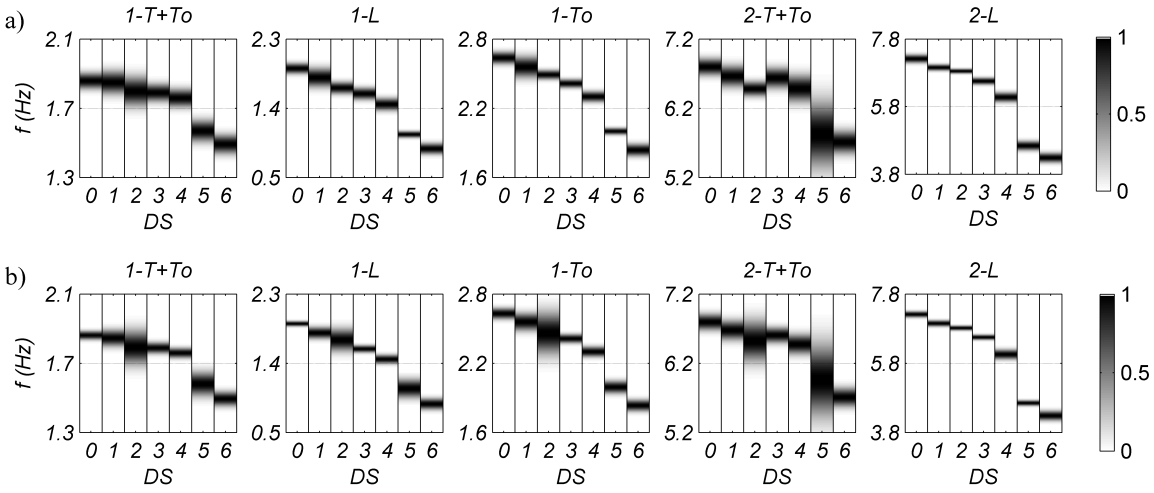

Figure 6.13: Contour plot of the best-fit *pdf* of the identified natural frequencies (a) NExT-ERA, (b) SSI.

6.7. Effects of environmental conditions on the identified modal properties

In spite the environmental conditions were not measured on the site where the building specimen was tested, hourly measurements recorded at different climate stations located a few miles from the site were compared and not significant variations were detected. The wind speed and temperature measured about 4.5 kilometers away from the shake table site are plotted in Figure 6.14 over the time window for which the modal identification is conducted. It is observed that environmental parameters vary approximately periodically every 144 data sets, i.e., 1 day cycles with peaks at around 2

p.m. Unfortunately, the accuracy of the climate station was not very high, especially for wind speed measurements, and data were collected only at one hour intervals.

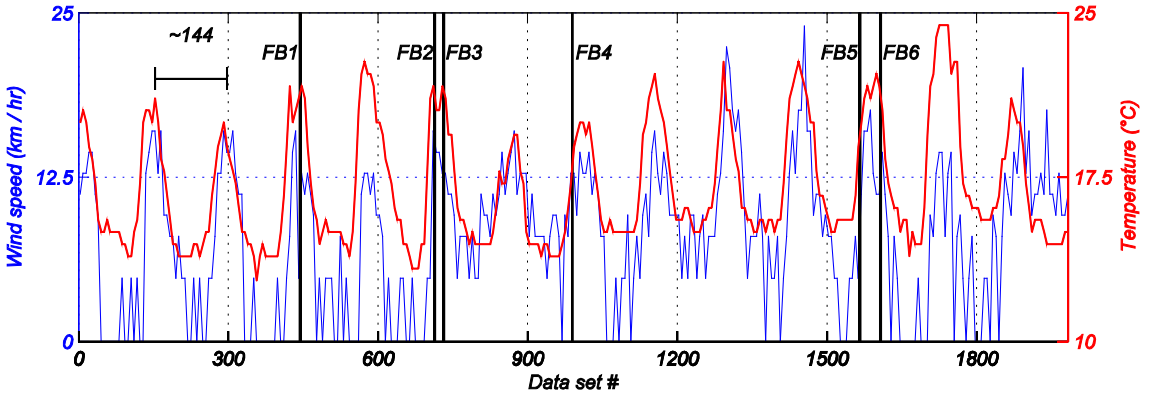

Figure 6.14: Wind speed and air temperature profiles measured 3 miles away from the building over the 15-day monitoring period.

To analyze the correlation between the environmental conditions, ambient vibration level of the building response, and the identified modal properties, Figure 6.15 shows the root-mean-square (RMS) acceleration at the roof level (magnitude of horizontal components) and the identified natural frequencies and damping ratios of the first four modes for the different data sets corresponding to DS0 and DS6. Figure 6.15a and c shows the RMS acceleration at the roof and the identified natural frequencies of the first four modes for the data sets of DS0 and DS6, respectively. Similarly, Figure 6.15b and d shows the RMS acceleration at the roof level and the identified damping ratios of the first four modes for the different data sets corresponding to DS0 and DS6, respectively.

By comparing Figure 6.14 and the RMS acceleration at the roof plotted in Figure 6.15, it is observed that the wind speed, temperature, and RMS acceleration at the roof level have a similar periodic variation and are in phase, all of them having the maximum approximately at the same time (2 p.m). The effects of wind speed and temperature on

the identified natural frequencies and damping ratios cannot be discriminated because both environmental parameters exhibited a similar periodic variation over time. Other studies have also pointed out the difficulty or impossibility of separating the effects of wind speed and temperature on the identified modal parameters (Sohn 2007, Kuok and Yuen 2012). From Figure 6.15 it is clearly observed that as the amplitude of the vibration response at the roof increases, the identified natural frequencies decrease and the damping ratios increase.

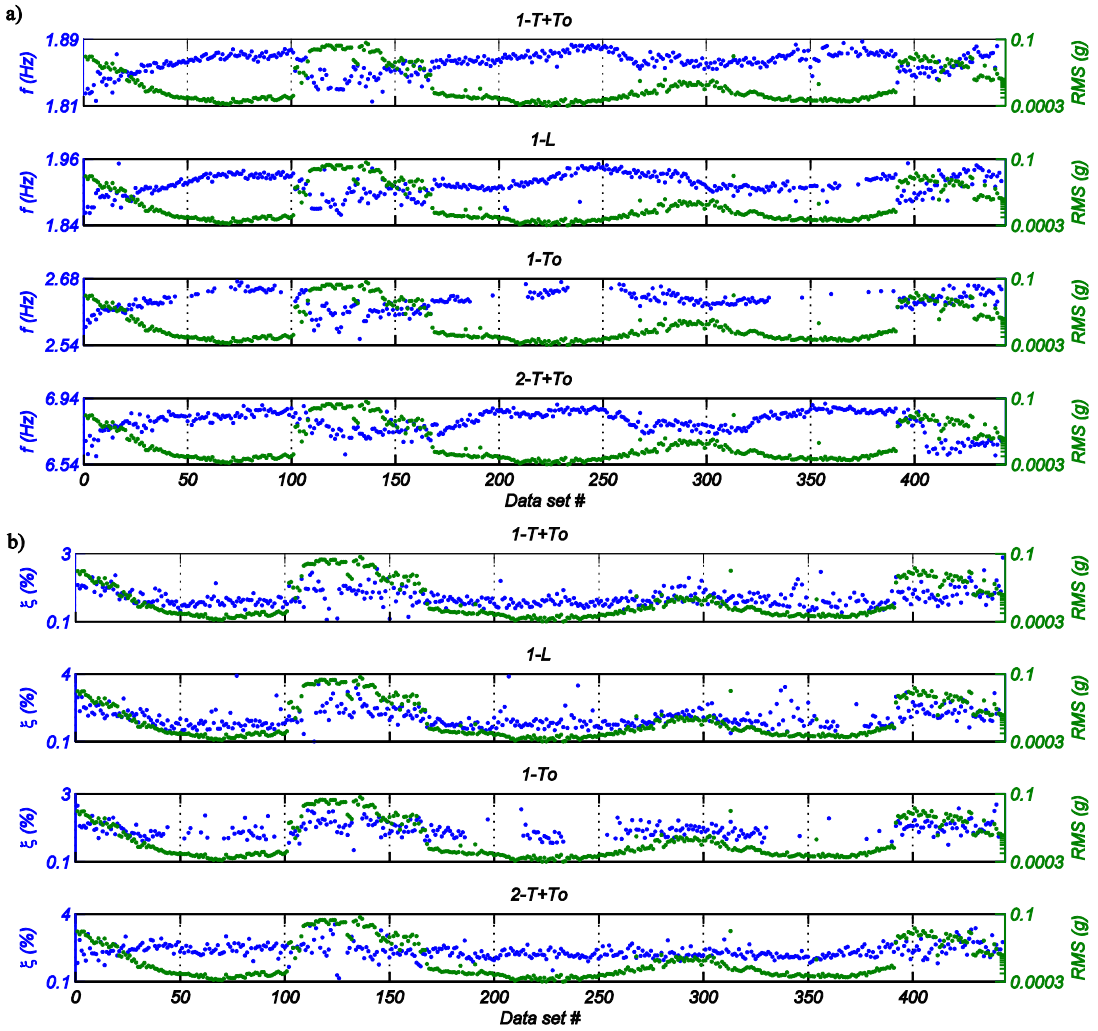

Figure 6.15: Evolution of natural frequency and damping ratios overlaid with RMS values (a) Frequency at DS0 using SSI; (b) Damping at DS0 using SSI; (c) Frequency at DS6 using NExT-ERA; (d) Damping at DS6 using NExT-ERA.

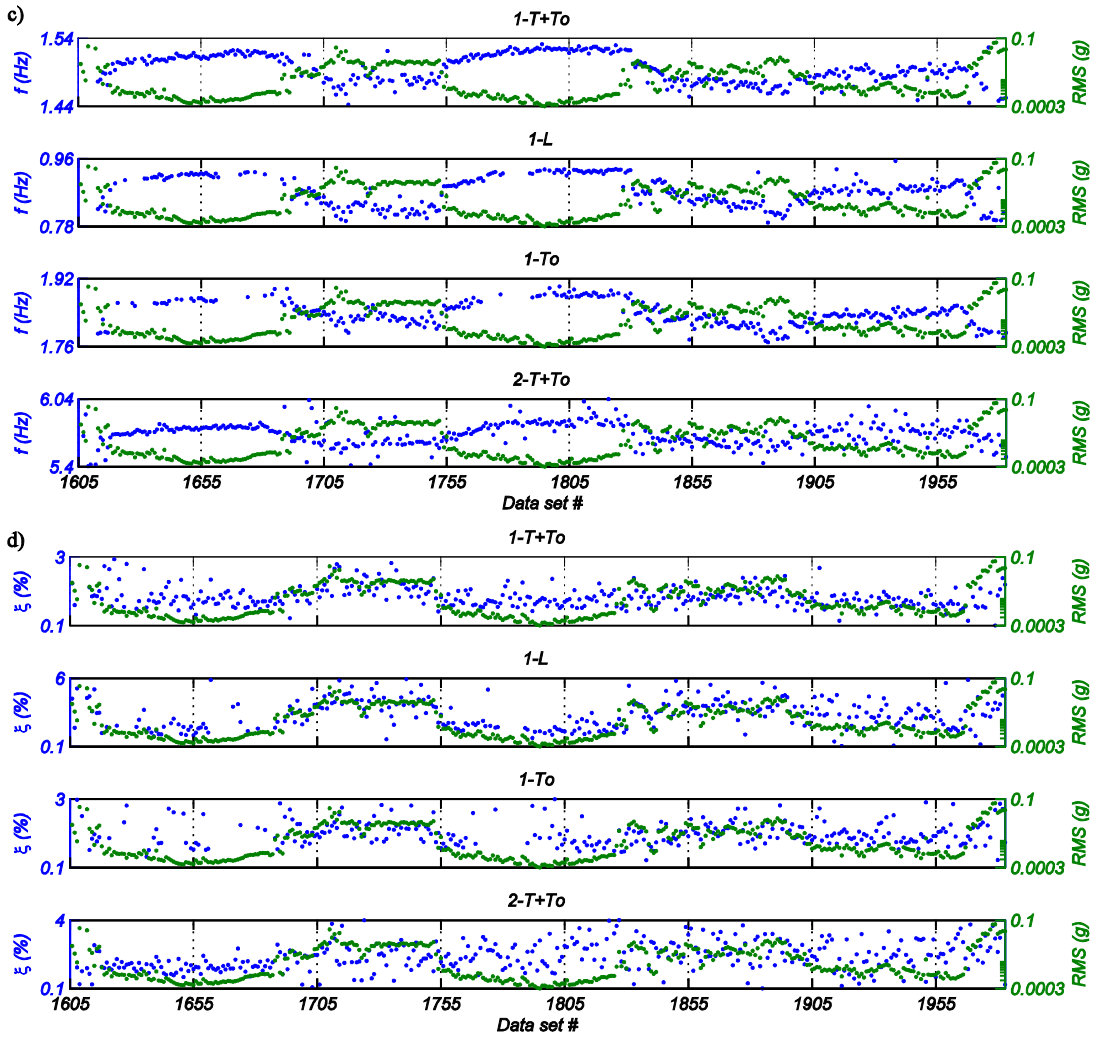

Figure 6.15: Evolution of natural frequency and damping ratios overlaid with RMS values (a) Frequency at DS0 using SSI; (b) Damping at DS0 using SSI; (c) Frequency at DS6 using NExT-ERA; (d) Damping at DS6 using NExT-ERA, continued.

To summarize the data in Figure 6.15, the natural frequencies and damping ratios of the modes identified at DS0 and DS6 using SSI and NExT-ERA versus the RMS at the roof are plotted in Figure 6.16. As the amplitude of the building response (RMS at the roof) increases, the identified natural frequencies decrease (see Figure 6.16a and c) and the identified damping ratios increase (see Figure 6.16b and d). The trends are very clear form the five identified modes, however, the scatter increases for higher modes. It is

noted that the participation of the higher modes in the measured building response is lower than that of the lower modes; consequently, the SNR is lower for the higher modes higher modes and therefore a higher estimation uncertainty is expected for higher modes.

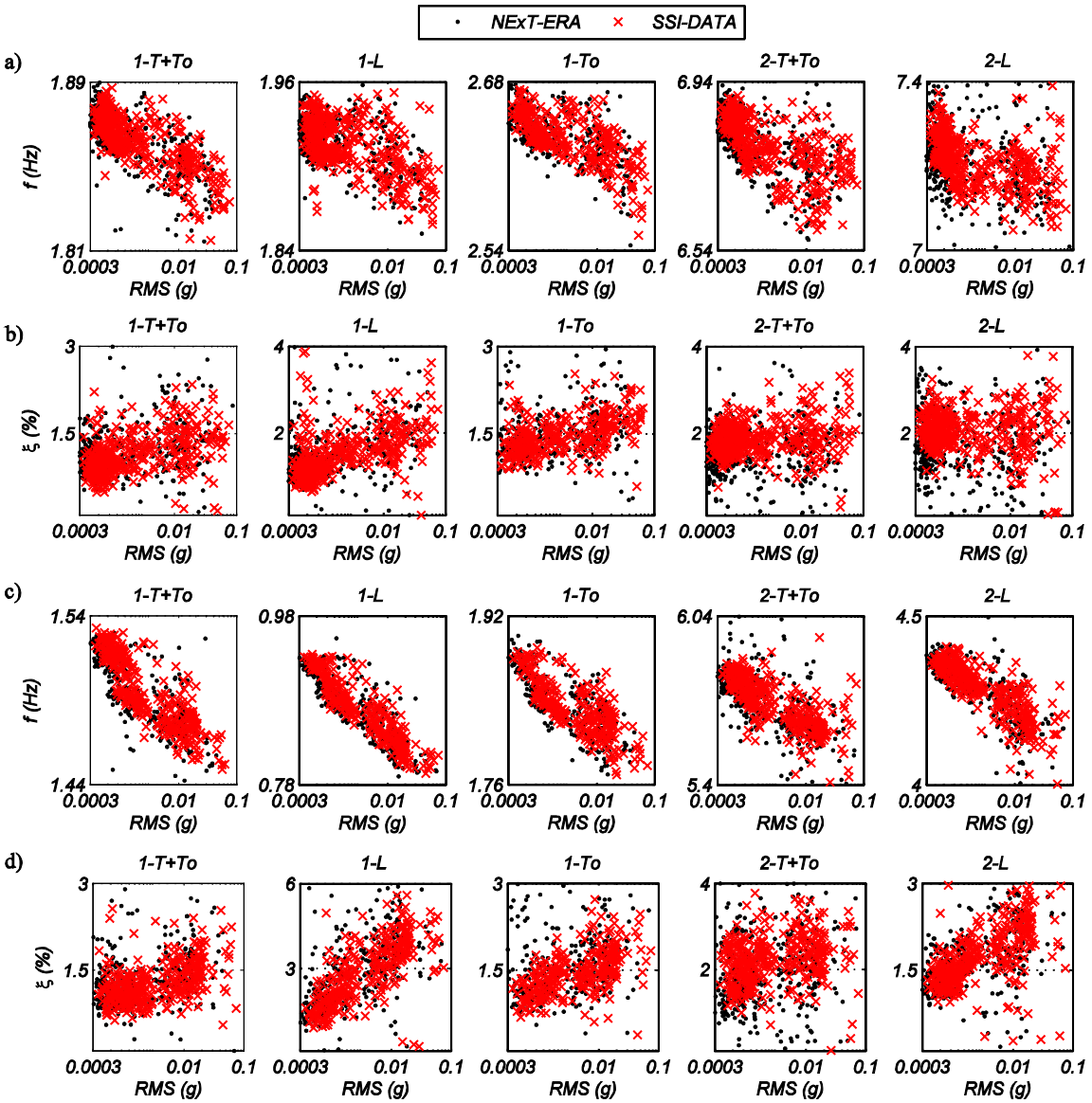

Figure 6.16: Identified natural frequencies and damping ratios versus RMS at the roof (a,b) DS0; (c,d) DS6.

6.8. Conclusions

This chapter presented the results of an automated system identification process performed on a full-scale five-story reinforced concrete (RC) seismically-damaged building specimen fully equipped with a variety of non-structural components and systems (NCSs). The building was built and tested at the NEES-UCSD shake table and, when fixed at its base, was subjected to a sequence of earthquake motions selected to progressively damage the structure and NCSs. Using ambient vibration data recorded continuously at different damage states of the building during approximately 15 days, the stochastic subspace identification method (SSI-DATA) and the Natural Excitation Technique combined with the Eigensystem Realization Algorithm were used to estimate the modal parameters (natural frequencies, damping ratios, and mode shapes) of the building.

An automated identification procedure, based on the concept of the stabilization diagram, was implemented and used with back-to-back ten-minute long time windows (data sets) of structural ambient vibration to identify the modal properties of five modes of the building. Modal parameters of a total of 1983 data sets were identified. The identified modal properties for a fixed damage state of the building were statistically analyzed using histograms, their fitted probability distributions, probability plots, and confidence intervals. Furthermore, the temporal variations in the identified modal parameters were investigated versus changes in environmental conditions (temperature and wind speed) and versus the amplitude of the structural ambient vibrations as measured by the root mean square (RMS) acceleration at the roof level.

The results obtained showed that the modal properties identified using SSI-DATA and NExT-ERA are in very good agreement. In addition, among the identified modal parameters for a fixed damage state, the natural frequencies and damping ratios showed the lowest and highest variability, respectively. The effects of damage were investigated through the probability distributions and confidence bounds of the identified modal parameters, which may be used as a statistical damage detection tool. The mean value of the identified natural frequencies decreased as the damage in the building progressed. However, changes in the identified natural frequencies due to environmental conditions and amplitude of the building response can be larger than those due to structural or nonstructural damage, especially for minor levels of damage (e.g., those induced by motions between serviceability and design level earthquakes). Based on the analysis of probability plots, it was concluded that the fit of normal distribution for the identified natural frequencies and lognormal distribution for the identified damping ratios are the best among all the analyzed probability density functions.

6.9. Acknowledgements

Chapter 6 is a reprint of the material that is currently being prepared for submission for publication "Statistical analysis of the modal properties of a five-story reinforced concrete seismically-damaged building identified using ambient vibrations" in *Engineering Structures*, Astroza, Rodrigo; Ebrahimian, H.; Conte, J.P.; Restrepo, J.I., and Hutchinson, T.C. The dissertation author was the primary investigator and author of this paper.

References

Allemang, R.J. and Brown, D.L. (1982). "A correlation coefficient for modal vector analysis." *1st International Modal Analysis Conference* (*IMAC I*), Orlando, FL.

Astroza, R., Conte, J.P., Restrepo, J.I., and Hutchinson T.C. (2015a). "Seismic response analyses and modal identification of a full-scale five-story base-isolated building tested on a shake table." To be submitted to *ASCE Journal of Structural Engineering.*

Astroza, R., Ebrahimian, H., Conte, J.P., Restrepo, J.I., and Hutchinson T.C. (2015b). "Influence of the construction process and nonstructural components on the modal properties of a five-story building." Submitted to *Earthquake Engineering & Structural Dynamics.*

Astroza, R., Ebrahimian, H., Conte, J.P., Restrepo, J.I., and Hutchinson T.C. (2015c). "System identification of a full-scale five-story reinforced concrete building tested on the NEES-UCSD shake table." Submitted to *Structural Control and Health Monitoring.*

Brincker, R., Andersen, P., and Jacobsen, N.J. (2007). "Automated frequency domain decomposition for operational modal analysis." *25th International Modal Analysis Conference* (*IMAC XXV*), Orlando, FL.

Brownjohn. J.M.W., De Stefano, A., Xu, Y-L., Wenzel, H., and Aktan, A.E. (2011). "Vibration-based monitoring of civil infrastructure: challenges and successes." *Journal of Civil Structural Health Monitoring*, 1(3-4), 79–95.

Chang, P.C., Flatau, A., and Liu, S.C. (2003). "Review paper: Health monitoring of civil infrastructure." *Structural Health Monitoring*, 2(3), 257–267.

Chen, M., Pantoli, E., Wang, X., Astroza, R., Ebrahimian, H., Mintz, S., Hutchinson, T.C., Conte, J.P., Restrepo, J.I., Meacham, B., Kim, J., and Park, H. (2013). BNCS Report #1: Full-scale structural and nonstructural building system performance during earthquakes and post-earthquake fire - Specimen design, construction and test protocol. Structural Systems Research Project Report Series, SSRP 13/09, University of California San Diego, La Jolla, CA.

Chen, M.C., Pantoli, E., Wang, X., Astroza, R., Ebrahimian, H., Hutchinson, T.C., Conte, J.P., Restrepo, J.I., Marin, C., Walsh, K., Bachman, R., Hoehler, M., Englekirk, R., and Faghihi, M. (2015). "Full-scale structural and nonstructural building system performance during earthquakes: Part I - Specimen description, test protocol, and structural response." Submitted to *Earthquake Spectra*.

Dilena, M. and Morassi, A. (2011). "Dynamic testing of a damaged bridge." *Mechanical Systems and Signal Processing*, 25(5), 1485–1507.

Doebling, S.W., Farrar, C.R., and Prime, M.B. (1998). "A summary review of vibration-based damage identification methods." *Shock and Vibration Digest*, 30(2), 91–105.

Doebling, S.W., Farrar, C.R., Prime, M.B., and Shevitz, D.W. (1996). "Damage identification and health monitoring of structural and mechanical systems from changes in their vibration characteristics: A literature review." *Report No. LA-13070-MS, Los Alamos National Laboratory*, Los Alamos, NM.

Döhler, M., X-B. Lam and L. Mevel. (2013). "Uncertainty quantification for modal parameters from stochastic subspace identification on multi-setup measurements." *Mechanical Systems and Signal Processing*, 36(2), 562–581.

Fan, W. and Qiao, P.Z. (2011). "Vibration-based damage identification methods: A review and comparative study." *Structural Health Monitoring*, 10, 83–111.

Farrar, C.R.; Cornwell, P.J.; Doebling, S.W. and Prime, M.B. (2000). "Structural health monitoring studies of the Alamosa Canyon and I-40 bridges." *Los Alamos National Laboratory Report LA-13635-MS*, Los Alamos, NM

Gersch, W. (1974). "On the achievable accuracy of structural system parameter estimates." *Journal of Sound and Vibration*, 34(1), 63–79.

He, X. (2008). *Vibration-based damage identification and health monitoring of civil structure*s. Ph.D. dissertation, Department of Structural Engineering, University of California, San Diego.

Hien, H. and Mita, A. (2011) . "Damage identification of full scale four-story steel building using multi-input multi-output models." *Proc. of SPIE Sensors and Smart Structures Technologies for Civil, Mechanical, and Aerospace Systems*, vol. 7981, San Diego, CA.

Hsu, T-Y. and Loh, C-H. (2010). "Damage detection accommodating nonlinear environmental effects by nonlinear principal component analysis." *Structural Control and Health Monitoring*, 17(3), 338–354.

Hu, W-H, Moutinho C, Caetano E, Magalhães F, Cunha A. (2012). "Continuous dynamic monitoring of a lively footbridge for serviceability assessment and damage detection." *Mechanical Systems and Signal Processing*, 33, 38–55.

Hutchinson, T.C., Restrepo, J.I., Conte, J.C., Pantoli, E., Chen, M.C., Wang, X., Astroza, R., and Ebrahimian, H. (2014). *Shake table testing of a five story building outfitted with NCSs (BNCS project)*. Network for Earthquake Engineering Simulation (distributor), dataset. DOI: 10.4231/D38W38349.

Huth, O., Feltrin, G., Maeck, J., Kilic, N., and Motavalli, M. (2005). "Damage identification using modal data: Experiences on a prestressed concrete bridge." *ASCE Journal of Structural Engineering*, 131(12), 1898–1910.

James, G. H., Carne, T.G., and Lauffer, J.P. (1993). *The natural excitation technique (NExT) for modal parameter extraction from operating wind turbines*. Report SAND92-1666, Sandia National Laboratories, Sandia, NM.

Ji, X., Fenves, G., Kajiwara, K., and Nakashima, M. (2011). "Seismic damage detection of a full-scale shaking table test structure." *ASCE Journal of Structural Engineering*, 137(1), 14–21.

Juang, J.N. and Pappa, R.S. (1985). "An Eigensystem realization algorithm for modal parameter identification and model reduction." *Journal of Guidance, Control, and Dynamics*, 8(5), 620–627.

Kuok, S-C. and Yuen, K-V. (2012). "Structural health monitoring of Canton Tower using Bayesian framework." *Smart Structures and Systems*, 10(4-5), 375–391.

Land, C.E. (1972). "An evaluation of approximate confidence interval estimation methods for lognormal means." *Technometrics*, 14(1), 145–158.

Lauzon, R. and DeWolf, J. (2006). "Ambient vibration monitoring of a highway bridge undergoing a destructive test." *ASCE Journal of Bridge Engineering*, 11(5), 602–610.

Magalhães, F., Cunha, A., Caetano, E. (2009). "Online automatic identification of the modal parameters of a long span arch bridge." *Mechanical Systems and Signal Processing*, 23(2), 316–329.

Magalhães, F., Cunha, A., and Catano, E. (2012). "Vibration based structural health monitoring of an arch bridge: From automated OMA to damage detection." *Mechanical Systems and Signal Processing*, 28, 212–228.

Mikael, A., P. Gueguen, P.Y. Bard, P. Roux and M. Langlais (2013). "The analysis of long-term frequency and damping wandering in buildings using the random decrement technique." *Bulletin of the Seismological Society of America*, 103(1), 236–246.

Moaveni, B., He, X., Conte, J.P., Restrepo, J.I., and Panagiotou, M. (2011). "System identification study of a 7-story full-scale building slice tested on the UCSD-NEES shake table." *ASCE Journal of Structural Engineering*, 137(6), 705–717.

Montgomery, D.C. and Runger, G.C. (2010). *Applied Statistics and Probability for Engineers*. John Wiley & Sons, New York, NY.

Nayeri, R., S. F. Masri, Ghanem, R.G. and Nigbor, R.L. (2008). "A novel approach for the structural identification and monitoring of a full-scale 17-story building based on ambient vibration measurements." *Smart Materials and Structures*, 17(2), 025006.

Pakzad, S.N. and Fenves, G.L. (2009). "Statistical analysis of vibration modes of a suspension bridge using spatially dense wireless sensor network." *ASCE Journal of Structural Engineering*, 135(7), 863–872.

Pantoli, E., Chen, M.C., Wang, X., Astroza, R., Ebrahimian, H., Hutchinson, T.C., Conte, J.P., Restrepo, J.I., Marin, C., Walsh, K., Bachman, R., Hoehler, M., Englekirk, R., and Faghihi, M. (2015a). "Full-scale structural and nonstructural building system performance during earthquakes: Part II - NCS damage states." Submitted to *Earthquake Spectra*.

Pantoli, E., Chen, M.C., Hutchinson, T.C., Astroza, R., Conte, J.P., Ebrahimian, H., Restrepo, J.I., and Wang, X. (2015b). "Landmark dataset from the building nonstructural components and systems (BNCS) project." Submitted to *Earthquake Spectra*.

Pappa, R., James, G., and Zimmerman, D. (1998). "Autonomous modal identification of the space shuttle tail rudder." *Journal of Spacecraft and Rockets*, 35, 163–169.

Peeters, B. and De Roeck, G. (2001). "One-year monitoring of the Z24-bridge: Environmental effects versus damage events." *Earthquake Engineering & Structural Dynamics*, 30(2), 149–171.

Rainieri, C. and G. Fabbrocino (2010). "Automated output-only dynamic identification of civil engineering structures." *Mechanical Systems and Signal Processing*, 24(3), 678–695.

Reynders, E., Pintelon, R., and De Roeck, G. (2008). "Uncertainty bounds on modal parameters obtained from stochastic subspace identification." *Mechanical Systems and Signal Processing*, 22(4), 948–969.

Reynders, E., Houbrechts, J., and De Roeck, G. (2012). "Fully automated (operational) modal analysis." *Mechanical Systems and Signal Processing*, 29(0), 228–250.

Siringoringo, D. M. and Y. Fujino (2008). "System identification of suspension bridge from ambient vibration response." *Engineering Structures*, 30(2), 462–477.

Siringoringo, D., Fujino, Y., and Nagayama, T. (2013). "Dynamic characteristics of an overpass bridge in a full-scale destructive test." *ASCE Journal of Engineering Mechanics*, 139, SPECIAL ISSUE: Dynamics and Analysis of Large-Scale Structures, 691–701.

Sohn, H. (2007). "Effects of environmental and operational variability on structural health monitoring." Philosophical Transactions of the Royal Society of London A, 365(1851), 539-560.

Ubertini, F., Gentile, C., and Materazzi, A.L. (2013). "Automated modal identification in operational conditions and its application to bridges." *Engineering Structures*, 46, 264–278.

Van der Auweraer, H. and Peeters, B. (2004). "Discriminating physical poles from mathematical poles in high order systems: Use and automation of the stabilization diagram." *Proc. of IMTC2004, the 21th IEEE Instrumentation and Measurement Technology Conf.*, Como, Italy, 2193–219.

Van Overschee P., De Moor B. (1996). *Subspace identification for linear systems: Theory, implementation, applications*. Kluwer Academic Publishers, Dordrecht, The Netherlands.

Vanlanduit, S., Verboven, P., Guillaume, P. and Schoukens, J. (2003). "An automatic frequency-domain modal parameter estimation algorithm." *Journal of Sound and Vibration*, 265(3), 647–661.

Verboven, P., Parloo, E., Guillaume, P., and Van Overmeire, M. (2002). "Autonomous structural health monitoring - Part I: Modal parameter estimation and tracking." *Mechanical Systems and Signal Processing*, 16(4), 637–657.

Zhou, X-H. and Gao, S. (1997). "Confidence intervals for the log-normal mean." *Statistics in Medicine*, 16, 783–790.

CHAPTER 7

MATERIAL PARAMETER IDENTIFICATION IN DISTRIBUTED PLASTICITY FE MODELS OF FRAME-TYPE STRUCTURES USING NONLINEAR STOCHASTIC FILTERING

7.1. Introduction

The fields of system and damage identification have attracted significant attention in the structural engineering community over the last forty years. Important life-safety and economic benefits can be attained by providing information about the condition of a structure after it has been exposed to natural or man-made hazards or aging. Because of the significance that structural health monitoring (SHM) has gained with the aim of implementing damage identification and control strategies, the research in structural system identification has increased significantly during the last twenty years. Numerous studies have focused on vibration-based damage identification methods, which relate changes in the identified modal parameters of structures to damage (e.g., Doebling et al. 1996, Housner et al. 1997); but only in recent years, these methods have been applied to

real structures or full-scale structural specimens (e.g., Ji et al. 2011, Moaveni et al. 2010, Moaveni et al. 2011, Astroza et al. 2013). However, some researchers have objected the use of modal parameters for damage identification purposes, because modal properties are related to global properties of the structure, while damage occurs locally. In addition, linearity is an idealization of the response behavior of real structures, since nonlinearities are intrinsically present in structural dynamics (Kerschen et al. 2006). Considering the importance of nonlinearities (mainly material and geometric nonlinearities) in the dynamic response of civil structures, system and damage identification for nonlinear structures have been the subject of intense research. When nonlinearities are properly considered in the system identification process, damage can be directly determined from the identified nonlinear model. Early studies in nonlinear structural system identification were conducted based on simplified structural models and different techniques, such as the extended Kalman filter (EKF) and least-squares (LS), were utilized in the identification process (e.g., Masri and Caughey 1979, Yun and Shinozuka 1980, Imai et al. 1989). More recently, new estimation techniques have been proposed (e.g., unscented Kalman Filter, Particle Filters, recursive LS) for parametric identification of nonlinear structures (e.g., Chassiakos et al. 1998, Yang and Lin 2004, Corigliano and Mariani 2004, Wu and Smyth 2007, Chatzi and Smyth 2009). However, all of these studies have used highly idealized structural models (e.g., chain-like MDOF system, shear building models), localizing the modeling of nonlinear (hysteretic) behavior in a few prescribed elements defined by nonlinear hysteretic force-deformation laws, such as the Bouc-Wen model (Ismail et al. 2009). The nonlinear hysteretic laws used in these studies are not traditionally used in state-of-the-art modeling and simulation of civil structures, because

they are not sufficiently accurate to simulate the actual behavior of structural materials. Also, an important drawback is that the parameters of the localized nonlinear behavioral models of the prescribed nonlinear elements are purely empirical. The values of these parameters vary from one element to another; consequently, the identification process must deal with the estimation of tens or hundreds of parameters even for small size structural models.

To use more realistic structural models in the system and damage identification processes, finite element (FE) model updating has emerged as a powerful methodology (Friswell and Mottershead 1995, Housner et al. 1997, Marwala 2010, Moaveni et al. 2010). Finite element model updating can be defined as the process of calibrating a FE model to minimize the discrepancy between the FE predicted and measured responses of real structures. This process can be conducted in the frequency, time, or modal domains and it can be formulated for deterministic or stochastic models of structures. Defined as dynamic models subjected to stochastic loading, stochastic models can be used to assess the uncertainty of the estimated parameters as a part of the FE model updating procedure (Beck and Katafygiotis 1998).

In recent years, Bayesian techniques have been used for FE model updating of linear and nonlinear structures, for both static and dynamic loading (e.g., Ching et al. 2006, Muto and Beck 2008, Huang et al. 2010, Nasrellah and Manohar 2011, Yang et al. 2012, Yuen and Kuok 2011, Giagopoulos et al. 2013, Simoen et al. 2013). However, for numerical simulation of the nonlinear structural response, these studies have used highly simplified nonlinear structural or FE models (such as lumped plasticity models, shear building models, empirical-based nonlinear material models) which are not capable to

represent well the actual structural behavior. None of these studies have used state-of-the-art, advanced, mechanics-based structural FE models that are currently used for analysis and design of nonlinear structures (Filippou and Fenves 2004).

The FE method, or more specifically computational structural mechanics, is still an active area of research aiming at high-fidelity nonlinear response simulation of structures up to incipient collapse. Different types of finite elements (e.g., 1D beam-column elements, 2D plate/shell elements, 3D continuum/brick elements) with different formulations (e.g., displacement-based, force/stress-based, mixed) and various nonlinear material constitutive models (e.g., pseudo-elasticity, plasticity, coupled damage-plasticity, smeared crack, etc.) have been and are still being developed for this purpose. For frame-type steel or reinforced-concrete structures, force-based and displacement-based nonlinear beam-column finite element models provide a good compromise between computational cost, numerical robustness, and accuracy (Taucer et al. 1991). In this FE modeling approach the element is discretized into longitudinal steel and/or concrete fibers; the section force-deformation relation is derived by numerical integration (over the element cross-section) of the nonlinear uniaxial material constitutive behavior of the fibers; the element force-displacement behavior is obtained through numerical integration of the section force-deformation behavior along the element length.

This chapter proposes a novel framework to combine an advanced nonlinear Bayesian filtering technique, referred to as the unscented Kalman filter (UKF) (Julier and Uhlmann 1997, Wan and van der Merwe 2000), and state-of-the-art mechanics-based FE models for frame-type structures, for the identification of nonlinear (hysteretic) structures. The proposed framework aims to fill the gap between advances in the

subfields of SHM and nonlinear mechanics-based FE modeling of civil structures. This scheme allows updating the nonlinear FE models using the UKF by recursively processing measured input-output records from the structure of interest. To implement this framework, the open-source object-oriented software framework OpenSees (Mazzoni et al. 2005) is used to model the structure and simulate its response to dynamic loads. OpenSees is interfaced with Matlab (2012) to interact recursively with the Bayesian filtering technique programmed in the Matlab environment. Although in this chapter the proposed framework is applied to frame-type structures with distributed plasticity, it is applicable to any nonlinear finite element model defined by time-invariant material parameters, and it can be used with measured input-output data under static, quasi-static, or dynamic loads.

7.2. Bayesian approach for state and parameter estimation of dynamic systems

A nonlinear discrete-time state-space model of a dynamical system can be defined by a state transition (also called system or process) equation

$$\mathbf{x}_k = \mathbf{f}_{k-1}\left(\mathbf{x}_{k-1}, \mathbf{u}_{k-1}, \mathbf{w}_{k-1}\right) \tag{7.1}$$

and a measurement (or observation) equation

$$\mathbf{y}_k = \mathbf{h}_k\left(\mathbf{x}_k, \mathbf{u}_k, \mathbf{v}_k\right) \tag{7.2}$$

where $\mathbf{x}_k \in \mathbb{R}^{n_x}$, $\mathbf{u}_k \in \mathbb{R}^{n_u}$, and $\mathbf{y}_k \in \mathbb{R}^{n_y}$ are the state vector (defined as the smallest subset of variables needed to completely characterize the system at time $t_k = k\Delta t$, where Δt = time step), input vector (deterministic and known), and measurement vector at time

t_k, respectively. The process noise $\mathbf{w}_k \in \mathbb{R}^{n_w}$ accounts for modeling uncertainties and unmeasured random disturbances exciting the system; $\mathbf{v}_k \in \mathbb{R}^{n_v}$ is the measurement noise; the components of $\mathbf{w}_k$ and $\mathbf{v}_k$ are assumed to be statistically independent processes. The terms $\mathbf{f}_{k-1}$ and $\mathbf{h}_k$ are deterministic and known nonlinear vector-valued functions, linking the prior state ($\mathbf{x}_{k-1}$) to the current state ($\mathbf{x}_k$), and the current state to the current measurement ($\mathbf{y}_k$), respectively. The goal of a nonlinear filtering technique is to recursively estimate at least the first two statistical moments of the state vector, $\mathbf{x}_k$, using the measured input and noisy measurement vectors up to the current time, $\mathbf{u}_{1:k}$ and $\mathbf{y}_{1:k}$, respectively (Haug 2005). For the case of joint (state and parameter) estimation, $\mathbf{x}_k$ is augmented to contain both state variables and unknown parameters ($\boldsymbol{\theta}_k$). If the measurement equation contains the system dynamics, the estimation problem becomes a parameter estimation problem (Haykin 2001), and only $\boldsymbol{\theta}_k$ is present in the state equation. For the sake of simplicity, the Bayesian approach presented below considers the system state $\mathbf{x}_k$ as the variable to be identified, but it is also valid for joint (state and parameter) as well as parameter-only estimation problems. This issue will be discussed in more detail later in the chapter.

From a Bayesian viewpoint, the recursive nonlinear filtering problem consists of computing the posterior probability density function (PDF) of $\mathbf{x}_k$ given the input and measurements up to time t_k ($\mathbf{u}_{1:k} \triangleq \{\mathbf{u}_1 \quad \mathbf{u}_2 \quad \cdots \quad \mathbf{u}_k\}$ and $\mathbf{y}_{1:k} \triangleq \{\mathbf{y}_1 \quad \mathbf{y}_2 \quad \cdots \quad \mathbf{y}_k\}$, respectively), i.e., to compute $p\left(\mathbf{x}_k \middle| \mathbf{y}_{1:k}, \mathbf{u}_{1:k}\right)$. Besides, the PDFs of the initial state

vector, $p(\mathbf{x}_0|\mathbf{y}_0,\mathbf{u}_0) \equiv p(\mathbf{x}_0)$, process noise, $p(\mathbf{w}_k)$, and measurement noise, $p(\mathbf{v}_k)$, are assumed to be known. Because of the deterministic nature of the input vector $\mathbf{u}_k$ and for the sake of notation simplicity, dependence on $\mathbf{u}_k$ will be dropped in this section.

Assuming that the posterior PDF at time t_{k-1}, $p(\mathbf{x}_{k-1}|\mathbf{y}_{1:k-1})$, is known, the posterior PDF at time t_k, $p(\mathbf{x}_k|\mathbf{y}_{1:k})$, can be obtained through a Bayesian prediction-correction scheme. The prediction step propagates the PDF of the state from time t_{k-1} to time t_k via the Chapman-Kolmogorov equation (Arulampalam et al. 2002) as

$$p(\mathbf{x}_k|\mathbf{y}_{1:k-1}) = \int p(\mathbf{x}_k|\mathbf{x}_{k-1})\, p(\mathbf{x}_{k-1}|\mathbf{y}_{1:k-1})\, d\mathbf{x}_{k-1} \tag{7.3}$$

From Equation (7.1) which describes $\mathbf{x}_k$ as a first-order Markov process, it follows that $p(\mathbf{x}_k|\mathbf{x}_{k-1},\mathbf{y}_{1:k-1}) = p(\mathbf{x}_k|\mathbf{x}_{k-1})$. The PDF $p(\mathbf{x}_k|\mathbf{x}_{k-1})$ is determined based on Equation (7.1) and the PDF of the process noise, $p(\mathbf{w}_k)$. The correction step computes the posterior PDF $p(\mathbf{x}_k|\mathbf{y}_{1:k})$ updating the prior PDF obtained in Equation (7.3), by assimilating the measurement $\mathbf{y}_k$ through the Bayes' theorem (Arulampalam et al. 2002) as

$$p(\mathbf{x}_k|\mathbf{y}_{1:k}) = \frac{p(\mathbf{y}_k|\mathbf{x}_k,\mathbf{y}_{1:k-1})\, p(\mathbf{x}_k|\mathbf{y}_{1:k-1})}{p(\mathbf{y}_k|\mathbf{y}_{1:k-1})} = \frac{p(\mathbf{y}_k|\mathbf{x}_k)\, p(\mathbf{x}_k|\mathbf{y}_{1:k-1})}{\int p(\mathbf{y}_k|\mathbf{x}_k)\, p(\mathbf{x}_k|\mathbf{y}_{1:k-1})\, d\mathbf{x}_k} \tag{7.4}$$

where the conditional PDF $p(\mathbf{y}_k|\mathbf{x}_k)$ is the likelihood function and is obtained using Equation (7.2) and the PDF of the measurement noise, $p(\mathbf{v}_k)$; $p(\mathbf{y}_k|\mathbf{y}_{1:k-1})$ is a

normalization constant which depends on $p\left(\mathbf{y}_k|\mathbf{x}_k\right)$; and $p\left(\mathbf{x}_k|\mathbf{y}_{1:k-1}\right)$ is the prior PDF computed in Equation (7.3). Knowledge of $p\left(\mathbf{x}_k|\mathbf{y}_{1:k}\right)$ allows obtaining a point estimate of the state $\mathbf{x}_k$ and a measure of the uncertainty in this state estimate.

Equations (7.3) and (7.4) define a conceptual scheme to recursively compute the exact Bayesian solution for the state, $\mathbf{x}_k$, of the state-space model defined in Equations (7.1) and (7.2). However, the multidimensional integrals in Equations (7.3) and (7.4) in general cannot be solved in closed-form, and approximate or suboptimal solutions need to be adopted. One of these suboptimal solutions is the UKF, which was first introduced by Julier and Uhlmann (1997) and is presented in the following section.

7.3. The unscented Kalman filter (UKF)

Consider the state transition equation, Equation (7.1), and the measurement equation, Equation (7.2), in the case of additive Gaussian white noises:

$$\mathbf{x}_k = \mathbf{f}_{k-1}\left(\mathbf{x}_{k-1}, \mathbf{u}_{k-1}\right) + \mathbf{w}_{k-1} \tag{7.5}$$

$$\mathbf{y}_k = \mathbf{h}_k\left(\mathbf{x}_k, \mathbf{u}_k\right) + \mathbf{v}_k \tag{7.6}$$

where $\mathbf{w}_k$ and $\mathbf{v}_k$ are zero-mean, Gaussian, white, random vectors with covariance matrices $\mathbf{Q}_k$ and $\mathbf{R}_k$, respectively. The initial state $\mathbf{x}_0$ (before any measurements are available) is also modeled as a Gaussian random vector, independent of the noises, with estimated mean $\hat{\mathbf{x}}_0$ and estimated covariance matrix $\hat{\mathbf{P}}_0^{\mathbf{xx}}$.

It is now assumed that the posterior PDF of the state at time t_{k-1} can be approximated by a Gaussian distribution:

$$p\left(\mathbf{x}_{k-1}\middle|\mathbf{y}_{1:k-1}\right)=\mathcal{N}^{\circ}\left(\mathbf{x}_{k-1};\hat{\mathbf{x}}_{k-1|k-1},\hat{\mathbf{P}}^{\mathbf{xx}}_{k-1|k-1}\right) \tag{7.7}$$

where $\mathcal{N}^{\circ}\left(\mathbf{x}_{k-1};\hat{\mathbf{x}}_{k-1|k-1},\hat{\mathbf{P}}^{\mathbf{xx}}_{k-1|k-1}\right)$ represents a multivariate Gaussian distribution with the components of $\mathbf{x}_{k-1}$ as random variables; and $\hat{\mathbf{x}}_{k-1|k-1}$ and $\hat{\mathbf{P}}^{\mathbf{xx}}_{k-1|k-1}$ denote the posterior mean and posterior covariance matrix of $\mathbf{x}_{k-1}$ given $\mathbf{y}_{1:k-1}$. Using Equations (7.3), (7.5), and (7.7), the following relations are obtained:

$$\hat{\mathbf{x}}_{k|k-1}=\int \mathbf{f}_k\left(\mathbf{x}_{k-1},\mathbf{u}_{k-1}\right)\mathcal{N}^{\circ}\left(\mathbf{x}_{k-1};\hat{\mathbf{x}}_{k-1|k-1},\hat{\mathbf{P}}^{\mathbf{xx}}_{k-1|k-1}\right)d\mathbf{x}_{k-1} \tag{7.8}$$

$$\begin{aligned}\mathbf{P}^{\mathbf{xx}}_{k|k-1}=&\int \mathbf{f}_k\left(\mathbf{x}_{k-1},\mathbf{u}_{k-1}\right)\mathbf{f}_k^T\left(\mathbf{x}_{k-1},\mathbf{u}_{k-1}\right)\mathcal{N}^{\circ}\left(\mathbf{x}_{k-1};\hat{\mathbf{x}}_{k-1|k-1},\hat{\mathbf{P}}^{\mathbf{xx}}_{k-1|k-1}\right)d\mathbf{x}_{k-1}\\&-\hat{\mathbf{x}}_{k|k-1}\,\hat{\mathbf{x}}^T_{k|k-1}+\mathbf{Q}_{k-1}\end{aligned} \tag{7.9}$$

Now, considering a Gaussian approximation for $p\left(\mathbf{x}_k\middle|\mathbf{y}_{1:k-1}\right)$, it follows that

$$p\left(\mathbf{x}_k\middle|\mathbf{y}_{1:k-1}\right)=\mathcal{N}^{\circ}\left(\mathbf{x}_k;\hat{\mathbf{x}}_{k|k-1},\hat{\mathbf{P}}^{\mathbf{xx}}_{k|k-1}\right) \tag{7.10}$$

The mean and covariance matrix of $\mathbf{y}_k$ given $\mathbf{y}_{1:k-1}$ can be derived using Equations (7.6) and (7.10) as

$$\hat{\mathbf{y}}_{k|k-1}=\int \mathbf{h}_k\left(\mathbf{x}_k,\mathbf{u}_k\right)\mathcal{N}^{\circ}\left(\mathbf{x}_k;\hat{\mathbf{x}}_{k|k-1},\hat{\mathbf{P}}^{\mathbf{xx}}_{k|k-1}\right)d\mathbf{x}_k \tag{7.11}$$

$$\mathbf{P}^{\mathbf{yy}}_{k|k-1}=\int \mathbf{h}_k\left(\mathbf{x}_k,\mathbf{u}_k\right)\mathbf{h}_k^T\left(\mathbf{x}_k,\mathbf{u}_k\right)\mathcal{N}^{\circ}\left(\mathbf{x}_k;\hat{\mathbf{x}}_{k|k-1},\hat{\mathbf{P}}^{\mathbf{xx}}_{k|k-1}\right)d\mathbf{x}_k-\hat{\mathbf{y}}_{k|k-1}\,\hat{\mathbf{y}}^T_{k|k-1}+\mathbf{R}_k \tag{7.12}$$

Similarly, the cross-covariance matrix of $\mathbf{x}_k$ and $\mathbf{y}_k$ given $\mathbf{y}_{1:k-1}$, $\mathbf{P}^{\mathbf{xy}}_{k|k-1}$, can be obtained as

$$\mathbf{P}^{\mathbf{xy}}_{k|k-1}=\int \mathbf{x}_k\,\mathbf{h}_k^T\left(\mathbf{x}_k,\mathbf{u}_k\right)\mathcal{N}^{\circ}\left(\mathbf{x}_k;\hat{\mathbf{x}}_{k|k-1},\hat{\mathbf{P}}^{\mathbf{xx}}_{k|k-1}\right)d\mathbf{x}_k-\hat{\mathbf{x}}_{k|k-1}\,\hat{\mathbf{y}}^T_{k|k-1} \tag{7.13}$$

Since the Kalman filter (Kalman 1960, Kalman and Bucy 1961) is applicable to nonlinear state-space models for which $p\left(\mathbf{x}_{k-1}\middle|\mathbf{y}_{1:k-1}\right)$ is approximated as Gaussian, as

stated in Equation (7.7), and the process and measurement equations have additive Gaussian white noises, the Kalman filter can be used to construct a Gaussian approximation of the posterior PDF of $\mathbf{x}_k$ given $\mathbf{y}_{1:k-1}$ with mean and covariance matrix obtained as (Haug 2005)

$$\hat{\mathbf{x}}_{k|k} = \hat{\mathbf{x}}_{k|k-1} + \mathbf{K}_k \left(\mathbf{y}_k - \hat{\mathbf{y}}_{k|k-1} \right) \tag{7.14}$$

$$\hat{\mathbf{P}}^{\mathbf{xx}}_{k|k} = \hat{\mathbf{P}}^{\mathbf{xx}}_{k|k-1} - \mathbf{K}_k \hat{\mathbf{P}}^{\mathbf{yy}}_{k|k-1} \mathbf{K}_k^T \tag{7.15}$$

where the Kalman gain matrix $\mathbf{K}_k$ is defined as

$$\mathbf{K}_k = \hat{\mathbf{P}}^{\mathbf{xy}}_{k|k-1} \left(\hat{\mathbf{P}}^{\mathbf{yy}}_{k|k-1} \right)^{-1} \tag{7.16}$$

To solve for the posterior mean and covariance matrix given in Equations (7.14) and (7.15), integrals of the form $E\left[\mathbf{g}(\mathbf{x})\right] = \int \mathbf{g}(\mathbf{x}) \mathcal{N}\left(\mathbf{x}; \hat{\mathbf{x}}, \hat{\mathbf{P}}^{\mathbf{xx}}\right) d\mathbf{x}$ must be solved in Equations (7.8), (7.9), and (7.11)–(7.13). To this end, the unscented transformation (UT) is used. The UT represents a random vector $\mathbf{z}$ by a set of deterministically chosen sample points (referred to as sigma points or SPs) such that the sample mean and sample covariance matrix obtained from the SPs match exactly the true mean and covariance matrix of the random vector $\mathbf{z}$. When the SPs are propagated through a nonlinear (vector) function, they capture the true mean and covariance matrix up to the second order of the Taylor series expansion of the nonlinear function (third order of the Taylor series expansion for a Gaussian random vector $\mathbf{z}$) (Wan and van der Merwe 2000). Different UTs have been proposed in the literature (see Simon 2006, for further details). The scaled UT (Wan and der Merwe 2000) is adopted herein.

7.3.1. The scaled unscented transformation

Consider a random vector $\mathbf{z} \in \mathbb{R}^{n_z}$ (Gaussian or non-Gaussian) with mean $\boldsymbol{\mu}_\mathbf{z}$ and covariance matrix $\mathbf{P}$ that undergoes a nonlinear transformation $\mathbf{s} = \mathbf{g}(\mathbf{z})$. To estimate the mean vector and covariance matrix of $\mathbf{s}$, the scaled UT defines the following $(2n_z + 1)$ SPs, denoted by $\mathcal{Z}^{(i)}$, such that their sample mean and sample covariance matrix equal the true mean and true covariance matrix of $\mathbf{z}$, respectively:

$$\begin{aligned} \mathcal{Z}^{(0)} &= \boldsymbol{\mu}_\mathbf{z} && \text{(mean value)} \\ \mathcal{Z}^{(i)} &= \boldsymbol{\mu}_\mathbf{z} + \left[\left(\gamma\sqrt{\mathbf{P}}\right)_i\right]^T && i = 1, \ldots, n_z \\ \mathcal{Z}^{(i)} &= \boldsymbol{\mu}_\mathbf{z} - \left[\left(\gamma\sqrt{\mathbf{P}}\right)_{i-n_z}\right]^T && i = n_z + 1, \ldots, 2n_z \end{aligned} \tag{7.17}$$

where $\sqrt{\mathbf{P}}$ = square-root of the covariance matrix $\mathbf{P}$, $(\cdots)_i$ represents the i^{th} row of the matrix inside the parentheses, $\gamma = \sqrt{n_z + \lambda}$, $\lambda = \tilde{\alpha}^2(n_z + \kappa) - n_z$, $\tilde{\alpha} \in [10^{-4}, 1]$ is a constant related to the spread of the SPs around the mean $\boldsymbol{\mu}_\mathbf{z}$, and κ is a secondary scaling parameter. The SPs are then propagated through the nonlinear transformation to estimate the mean and covariance matrix of $\mathbf{s} = \mathbf{g}(\mathbf{z})$ as

$$\boldsymbol{\mu}_\mathbf{s} \approx \hat{\mathbf{s}} = \sum_{i=0}^{2n_z} W_m^{(i)}\, \mathbf{g}\left(\mathcal{Z}^{(i)}\right) \tag{7.18}$$

$$\mathbf{P}^{\mathbf{ss}} \approx \hat{\mathbf{P}}^{\mathbf{ss}} = \sum_{i=0}^{2n_z} W_\mathrm{c}^{(i)} \left[\mathbf{g}\left(\mathcal{Z}^{(i)}\right) - \hat{\mathbf{s}}\right]\left[\mathbf{g}\left(\mathcal{Z}^{(i)}\right) - \hat{\mathbf{s}}\right]^T \tag{7.19}$$

where the weight coefficients of the SPs to estimate the mean and covariance matrix of $\mathbf{s}$, $W_m^{(i)}$ and $W_c^{(i)}$ respectively, are

$$W_m^{(0)} = \frac{\lambda}{n_z + \lambda} \; ; \; W_c^{(0)} = \frac{\lambda}{n_z + \lambda} + \left(1 - \tilde{\alpha}^2 + \tilde{\beta}\right) \; ; \; W_m^{(i)} = W_c^{(i)} = \frac{1}{2\left(n_z + \lambda\right)} \; , i = 1, \ldots, 2n_z \quad (7.20)$$

in which $\tilde{\beta}$ = scaling factor used to emphasize the relative weight of SP $\mathbf{\mathcal{Z}}^{(0)}$ in the calculation of $\hat{\mathbf{P}}^{\mathbf{ss}}$, which can be utilized to minimize certain higher-order error terms based on known higher-order moments of $\mathbf{z}$ (van der Merwe et al. 2004). The UKF algorithm uses the scaled UT to solve the recursive estimation problem defined by Equations (7.14) and (7.15), as shown in Figure 7.1. In this study, the parameters of the scaled UT are chosen as $\tilde{\alpha} = 0.01$, $\kappa = 0$, and $\tilde{\beta} = 2$ as recommended by Wan and der Merwe (2000).

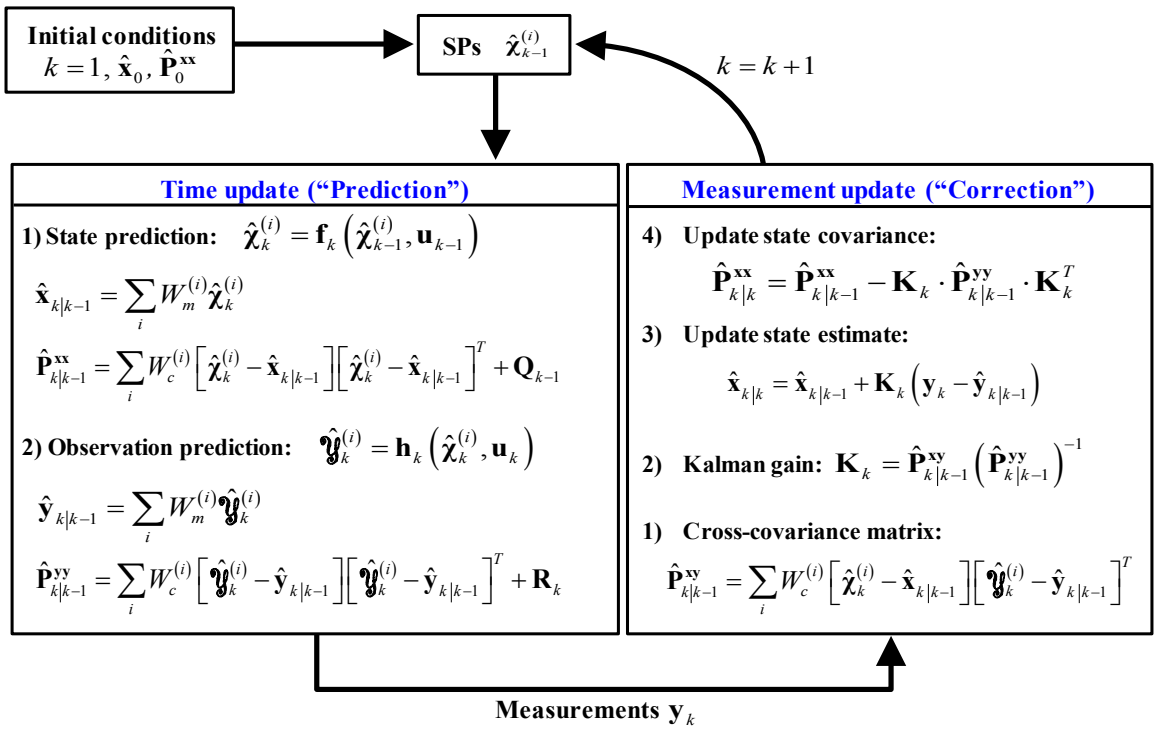

Figure 7.1: Flow chart of the Unscented Kalman Filter for the state-space model defined by Equations (7.5) and (7.6). (adapted from Lee 2005).

7.4. Distributed plasticity finite element models of frame-type structures

Over the years, several approaches have been developed to model frame-type structures and simulate their nonlinear response behavior under earthquake excitation. These methods can be classified in three main categories (Taucer et al. 1991): (i) global models, (ii) structural FE models, and (iii) continuum FE models (Figure 7.2). Global models, the simplest among the three, concentrate material nonlinearities at global DOFs (e.g., each story of a building is represented by a hysteretic rule for the story shear force - interstory drift relation), but lack accuracy and resolution in predicting the nonlinear response of real structures. Also, they require significant work from the user to calibrate the force-deformation rule at each nonlinear DOF. Structural FE models characterize the structure by an assembly of interconnected frame elements. Structural FE models can be further categorized into: (a) lumped or concentrated plasticity (usually located at the end of the beam-column elements), and (b) distributed plasticity (along the element and over the element cross-section). Continuum FE models are the most sophisticated and computationally expensive, since they discretize the beams and columns of frame-type structures into 3D solid finite elements with 3D nonlinear material constitutive models.

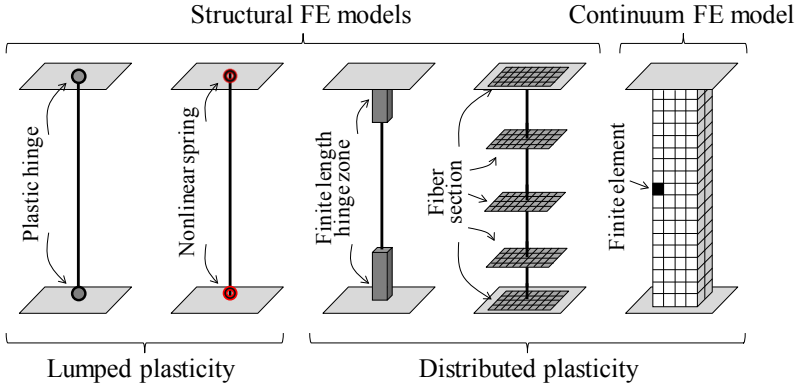

Figure 7.2: Types of models of frame elements (adapted from Deierlein et al. 2010)

Because of their accuracy in matching experimental results, formulation simplicity, and computational feasibility and efficiency, frame-type FE models with distributed plasticity (Figure 7.2 and Figure 7.3) are widely used in research and engineering practice. In this type of FE models, material nonlinearity can occur at any numerically monitored cross-section (also called element integration point or IP) along the element, and the element behavior is obtained by numerically integrating the section response behavior along the element. Discretization of the element cross-section into longitudinal fibers allows to simulate the section nonlinear response behavior using uniaxial material constitutive laws for the fibers. This formulation accounts for the interaction between bending and axial force at the section level, while the interaction with the shear force occurs at the element level through equilibrium. It is noted that a uniaxial material model depends on physical properties (or parameters) of the corresponding material.

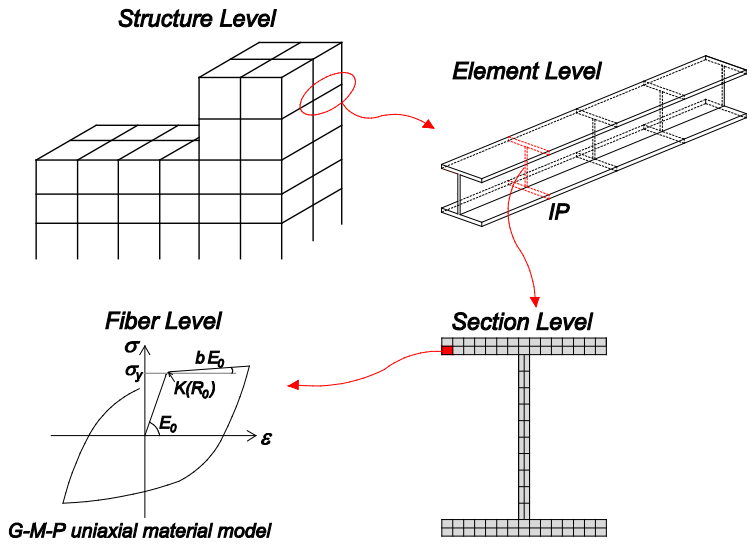

Figure 7.3: Hierarchical levels in distributed plasticity FE models of frame-type structures.

There are two main formulations at the element level (Figure 7.3) for distributed plasticity using fiber section discretization: (i) displacement-based (DB) and (ii) force-based (FB). In the former, interpolation functions (cubic Hermitian polynomials) approximate the displacement field along the element as a function of the nodal displacements. To achieve an accurate approximation of the exact response, many (usually 4 to 8) elements per member (beam, column) need to be used. On the other hand, force-based elements use equilibrium to interpolate exactly the internal force fields along the element as a function of the nodal forces. Because force-based elements are exact within the framework of classical beam theories, only one element per frame (beam or column) member is required (Taucer et al. 1991).

After direct stiffness assembly of the distributed plasticity beam-column elements with section fiber discretization (Figure 7.3), the equations of dynamic equilibrium at the structure level can be expressed as

$$\mathbf{M}(\boldsymbol{\theta})\ddot{\mathbf{q}}(t,\boldsymbol{\theta})+\mathbf{C}(\boldsymbol{\theta})\dot{\mathbf{q}}(t,\boldsymbol{\theta})+\mathbf{r}\left[\mathbf{q}(t,\boldsymbol{\theta}),\boldsymbol{\theta},t\right]=\mathbf{p}(t) \tag{7.21}$$

where t = time, $\mathbf{M}$ = mass matrix, $\mathbf{C}$ = damping matrix, $\mathbf{r}$ = internal (inelastic) resisting force vector, $\mathbf{p}$ = applied external force vector, $\mathbf{q}$, $\dot{\mathbf{q}}$, $\ddot{\mathbf{q}}$ = nodal displacement, velocity, and acceleration response vectors, and $\boldsymbol{\theta}$ = vector of time-invariant material parameters and/or other parameters defining the mass and damping matrices. In the case of rigid base excitation (e.g., earthquakes), the load vector takes the form $\mathbf{p}(t)=-\mathbf{M}\boldsymbol{\ell}\ddot{u}_g(t)$ where $\boldsymbol{\ell}$ and $\ddot{u}_g(t)$ are the influence vector and input ground acceleration, respectively. Equation (7.21) is integrated numerically in time using a time-stepping method, such as the Newmark-β method (Chopra 2011), yielding a set of coupled nonlinear algebraic

equations to be solved for $\mathbf{q}_{k+1} = \mathbf{q}(t_{k+1}, \boldsymbol{\theta})$ at time $t_{k+1} = (k+1)\Delta t$. Considering that $\boldsymbol{\theta}$ is a time-invariant parameter vector, the set of coupled nonlinear algebraic equations can be written as

$$\boldsymbol{\Psi}(\mathbf{q}_{k+1}) = \tilde{\mathbf{p}}_{k+1} - \left[\frac{1}{\beta(\Delta t)^2}\mathbf{M}\mathbf{q}_{k+1} + \frac{\alpha}{\beta(\Delta t)}\mathbf{C}\mathbf{q}_{k+1} + \mathbf{r}(\mathbf{q}_{k+1}) \right] = \mathbf{0} \tag{7.22}$$

in which

$$\begin{aligned} \tilde{\mathbf{p}}_{k+1} = \mathbf{p}_{k+1} &+ \mathbf{M}\left[\frac{1}{\beta(\Delta t)^2}\mathbf{q}_k + \frac{1}{\beta(\Delta t)}\dot{\mathbf{q}}_k - \left(1 - \frac{1}{2\beta}\right)\ddot{\mathbf{q}}_k \right] \\ &+ \mathbf{C}\left[\frac{\alpha}{\beta(\Delta t)}\mathbf{q}_k - \left(1 - \frac{\alpha}{\beta}\right)\dot{\mathbf{q}}_k - (\Delta t)\left(1 - \frac{\alpha}{2\beta}\right)\ddot{\mathbf{q}}_k \right] \end{aligned} \tag{7.23}$$

where α and β = parameters controlling the accuracy and stability of the Newmark-β time stepping scheme, Δt = time integration step, and the subscript k or $k+1$ indicates that the corresponding quantity is evaluated at discrete time $k\Delta t$ or $(k+1)\Delta t$, respectively.

Equation (7.22) can be solved using a numerical scheme such as the Newton-Raphson incremental-iterative algorithm, which requires the derivative of the dynamic unbalance force vector $\boldsymbol{\Psi}_{k+1}$ with respect to $\mathbf{q}_{k+1}$:

$$\left.\frac{\partial \boldsymbol{\Psi}(\mathbf{q}_{k+1})}{\partial \mathbf{q}_{k+1}}\right|_i = -\left[\frac{\mathbf{M}}{\beta(\Delta t)^2} + \frac{\alpha\mathbf{C}}{\beta(\Delta t)} + \left(\mathbf{K}_{\mathrm{T}}^{stat}(\mathbf{q}_{k+1})\right)\Big|_i \right] = -\left(\mathbf{K}_{\mathrm{T}}^{dyn}(\mathbf{q}_{k+1})\right)\Big|_i \tag{7.24}$$

where $\mathbf{K}_{\mathrm{T}}^{stat}(\mathbf{q}_{k+1}) = \dfrac{\partial \mathbf{r}(\mathbf{q}_{k+1})}{\partial \mathbf{q}_{k+1}}$ is the static consistent tangent stiffness matrix of the structure at the $(k+1)$-*th* time step and $(\cdots)\big|_i$ represents the iteration number in the

Newton-Rhapson algorithm until convergence is satisfied according to a specified displacement, force, or energy criterion.

Considering distributed plasticity DB elements with section fiber discretization to model the members of the frame-type structure, the resisting force vector, $\mathbf{r}$, and the static consistent tangent stiffness matrix of the structure, $\mathbf{K}_{\mathrm{T}}^{stat}$, can be computed, respectively, as

$$\mathbf{r}\left(\mathbf{q}_{k+1}\right) = \mathop{\mathrm{A}}_{e=1}^{N_{el}} \left\{ \mathbf{p}_e\left(\mathbf{q}_{k+1}\right) \right\} = \mathop{\mathrm{A}}_{e=1}^{N_{el}} \left\{ \sum_{h=1}^{N_{IP}} \mathbf{B}_h^T \left[\sum_{i=1}^{N_{fib}} \left(\mathbf{a}_i^h\right)^T \sigma_i\left(\mathbf{q}_{k+1}\right) A_i \right] w_h \right\} \tag{7.25}$$

$$\mathbf{K}_{\mathrm{T}}^{stat}\left(\mathbf{q}_{k+1}\right) = \mathop{\mathrm{A}}_{e=1}^{N_{el}} \left\{ \mathbf{K}_{\mathrm{T}}^{e}\left(\mathbf{q}_{k+1}\right) \right\} = \mathop{\mathrm{A}}_{e=1}^{N_{el}} \left\{ \sum_{h=1}^{N_{IP}} \mathbf{B}_h^T \left[\sum_{i=1}^{N_{fib}} \left(\mathbf{a}_i^h\right)^T \left(E_{\mathrm{T},i}\left(\mathbf{q}_{k+1}\right) A_i \right) \mathbf{a}_i^h \right] \mathbf{B}_h \, w_h \right\} \tag{7.26}$$

where A = finite element assembly operator, $\mathbf{p}_e$ = element end forces, N_{el} = number of frame finite elements in the FE model of the structure, N_{IP} = number of integration points along the element, $\mathbf{B}_h = \mathscr{D}\,\mathbf{N}(x)$ where $\mathscr{D}$ is a differential operator matrix and $\mathbf{N}(x)$ = displacement shape function matrix evaluated at the section located at local coordinate x along the element length, N_{fib} = number of fibers in the cross-section h, $\mathbf{a}_i^h$ = kinematic vector defining the location of fiber i in cross-section h, σ_i = axial stress in fiber i, A_i = area of fiber i, w_h = weight of IP number h, and $E_{\mathrm{T},i} = \dfrac{\partial \sigma_i}{\partial \varepsilon_i}$ = tangent modulus of fiber i, where ε_i = axial strain in fiber i. Therefore, $\mathbf{r}$ and $\mathbf{K}_T^{stat}$ depend on the axial stress and tangent modulus of each fiber, respectively, which are defined by the nonlinear uniaxial material constitutive law assigned to the fiber. It is important to note that a

structural system is typically composed of a relatively small number of structural materials with different nominal parameter values, each of which is represented by a single nonlinear uniaxial material model. Consequently, if all components of a structure are made of the same material, only one uniaxial material model is needed to describe the nonlinear behavior of all fibers in the FE model of the structure.

In the case of FB beam-column elements, an iterative algorithm at the element level is needed to compute, using numerical integration, the element end forces $\mathbf{p}_e$ and element tangent flexibility matrix $\mathbf{F}_{\mathrm{T}}^{e}$, from which the element tangent stiffness matrix $\mathbf{K}_{\mathrm{T}}^{e}$ can be obtained. In the FB element formulation, equilibrium is satisfied in strong form, while compatibility is satisfied in weak form through the principle of virtual forces (Taucer et al. 1991). In both formulations (DB and FB), the static tangent stiffness matrix of the structure, $\mathbf{K}_{\mathrm{T}}^{stat}$, and resisting force vector, $\mathbf{r}$, both depend on the time-invariant material parameters governing the uniaxial material constitutive laws assigned to the fibers.

7.5. Proposed framework

To formulate the equation of dynamic equilibrium of a nonlinear hysteretic (history dependent) structural FE model as a state equation (first-order matrix differential equation), all the unobserved (unmeasured) history dependent variables (at the material level) of the FE model must be included in the state vector ($\mathbf{x}$). For frame-type FE models using fiber discretization of the element cross-section, in addition to the unobserved nodal displacements and velocities of the structure ($\mathbf{q}$ and $\dot{\mathbf{q}}$, respectively),

all the history dependent variables of each fiber of each monitored cross-section (stress and material history variables of the fiber material model used) need to be included in the state vector. If the unknown time-invariant parameters of the material models used ($\boldsymbol{\theta}$) also need to be estimated, the state vector $\mathbf{x}$ must be augmented with these parameters into the augmented state vector, $\tilde{\mathbf{x}}_a = \begin{bmatrix} \mathbf{x}^T & \boldsymbol{\theta}^T \end{bmatrix}^T$. Then, unobserved state variables and unknown material parameters can be estimated simultaneously (joint estimation problem) using the UKF.

When using frame FE models with section fiber discretization, the total number of fibers in the FE model is usually large; consequently, it is not feasible to tackle the joint estimation problem. In addition, if the estimation problem is formulated to obtain $\tilde{\mathbf{x}}_a$ at time t_{k+1} using $\tilde{\mathbf{x}}_a$ at time t_k, equilibrium is violated because of the dependence of the FE response on the primary material parameters to be identified (i.e., when primary material parameters are changed at a specific time step as part of the recursive estimation process, the response of the structure has to be re-run from time zero at the next time step). However, extensive research in the field of nonlinear modeling and analysis of structures has shown that adequate mechanics-based FE models can predict with reasonable accuracy the actual response of structures if realistic and well calibrated material constitutive models are used (e.g., Uriz et al. 2008, Martinelli and Filippou 2009, Koutromanos et al. 2011, Ebrahimian et al. 2014). Therefore, relying on the FE model developed for a given frame-type structure, the estimation of the states variables can be omitted, since they can be obtained as output of the FE model with identified unknown parameters. As a result, a parameter estimation problem, in which only the

unknown time-invariant material model parameters are considered in the state equation, can be formulated instead of a joint (state-parameter) estimation problem.

Estimation of time-invariant material parameters is possible because the time-invariant parameters describing the uniaxial material model uniquely define the nonlinear response of the structure, including stiffness degradation and strength deterioration, for a given input motion. Indeed, the nonlinear stress response σ at the fiber level is governed by the corresponding nonlinear uniaxial material constitutive law, and depends on the strain history ε in the fiber and on the material parameters $\boldsymbol{\theta}$, i.e., $\sigma = \sigma\left(\varepsilon\left(\boldsymbol{\theta}\right), \boldsymbol{\theta}\right)$. Furthermore, the equation of motion of the structure is embedded in the measurement equation through the FE model, i.e., the measurement equation contains all the system dynamics. On the other hand, any desired structural response variable can be obtained from the FE model. Hence, only the response quantities corresponding to the measured responses are extracted from the FE model to construct the measurement equation.

Based on the previous remarks, the state-space model defined by Equations (7.5) and (7.6) in the present case reduces to

$$\begin{cases} \boldsymbol{\theta}_{k+1} = \boldsymbol{\theta}_k + \mathbf{w}_k \\ \mathbf{y}_k = \mathbf{h}_k\left(\boldsymbol{\theta}_k, \mathbf{u}_{1:k}\right) + \mathbf{v}_k \end{cases} \tag{7.27}$$

where $\boldsymbol{\theta}_k \in \mathbb{R}^{n\theta} =$ vector of unknown material parameters to be identified, $\mathbf{w}_k \in \mathbb{R}^{n\theta} \sim \mathcal{N}\left(\mathbf{0}, \mathbf{Q}_k\right) =$ process noise vector at time t_k assumed to be white and Gaussian with zero mean and covariance matrix $\mathbf{Q}_k$, $\mathbf{y}_k \in \mathbb{R}^{ny} =$ measurement vector at time t_k, $\mathbf{h}_k\left(\boldsymbol{\theta}_k, \mathbf{u}_{1:k}\right) =$ vector of observed outputs (or measured response quantities)

obtained from the nonlinear FE model characterized by material parameters $\boldsymbol{\theta}_k$ and subjected to the deterministic input vector from time t_1 to t_k, $\mathbf{u}_{1:k}$, and $\mathbf{v}_k \in \mathbb{R}^{n_y} \sim \mathcal{N}\left(\mathbf{0}, \mathbf{R}_k\right)$= measurement noise vector at time t_k assumed to be white and Gaussian with zero mean and covariance matrix $\mathbf{R}_k$. The process and measurement noise vectors, $\mathbf{w}_k$ and $\mathbf{v}_k$, and the initial material parameter estimate, $\hat{\boldsymbol{\theta}}_0$, also modeled as a Gaussian random vector with mean $\hat{\boldsymbol{\theta}}_0$ and covariance matrix $\hat{\mathbf{P}}_0^{\boldsymbol{\theta}\boldsymbol{\theta}}$, are assumed to be statistically independent. In Equation (7.27), $\boldsymbol{\theta}_k$ corresponds to a stationary process driven by the noise process $\mathbf{w}_k$. It is noted that the presented formulation does not take into account the effects of hidden or unmeasured input random excitations, and the measurement noise is modeled as a Gaussian white noise vector process uncorrelated at different times and across different output channels.

The proposed approach to formulate the identification problem of nonlinear frame-type structures is convenient and practical, because only one set of material parameters for each material present in the structure needs to be considered in $\boldsymbol{\theta}$, and any measured response can be easily considered in the measurement equation (e.g., acceleration, velocity, displacement, local deformation, strain, etc.).

The UKF with scaled UT is proposed for the identification process, because it is a good compromise between accuracy, since it does not involve linearization of the nonlinear FE model as the EKF (Simon 2006), and computational feasibility, because it only requires generating $\left(2n_\theta + 1\right)$ SPs, which is also equal to the number of runs of the FE model, at each time step. This last comment on computational cost represents a

significant advantage of the UKF compared to the computationally more demanding Particle Filter, also called Monte Carlo filter (Ristic et al. 2004). In the Particle Filter, a large number of samples (or particles) need to be considered to yield accurate results for highly nonlinear problems (Ristic et al. 2004). Furthermore, the UKF lends itself to parallel or distributed computations at each time step when running the nonlinear FE models corresponding to the different SPs. Figure 7.4 summarizes the proposed framework, including the interaction between the UKF, coded in *Matlab*, and the nonlinear FE model, which is developed in the object-oriented *OpenSees* platform.

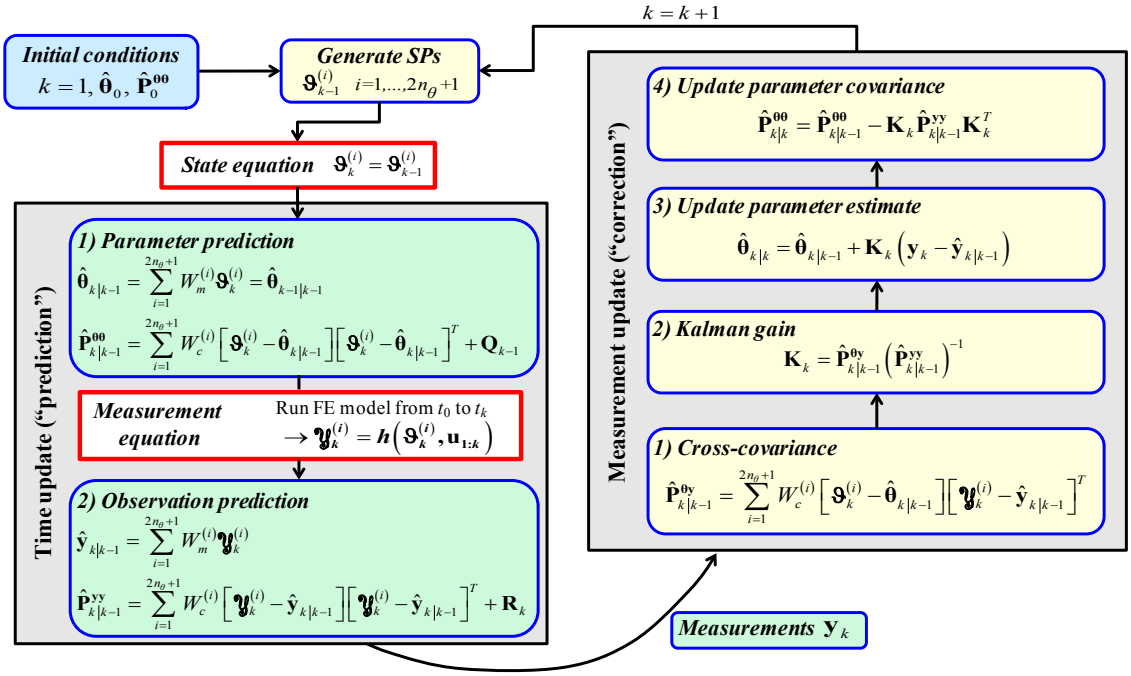

Figure 7.4: Flow chart of the UKF algorithm combined with FE model simulations for material parameter estimation.

7.6. Applications using simulated seismic response data

In this section, two examples based on realistic steel structures are presented. They correspond to (i) a steel cantilever bridge column, and (ii) a 2D steel building

frame. In both structures, the steel fibers are modeled using the modified Giuffre-Menegotto-Pinto (G-M-P) material constitutive model (Filippou et al. 1983). A suite of nine actual earthquake motions are used as input motions to obtain simulated recorded data, which are then contaminated by measurement noise. In both application examples, the gravity loads are applied quasi-statically before running a time-history dynamic analysis for each input earthquake ground motion considered. The Newmark-β average acceleration method is employed to integrate the equations of motion in time using a time step $\Delta t = 1/f_s$, where f_s is the sampling rate of the input earthquake motion (see Table 7.1). The Newton algorithm is used to iteratively solve the set of coupled nonlinear algebraic equations resulting from the equations of motion. The framework presented above is used to identify the material parameters and update the nonlinear finite element model in each example. It is important to note that for both application examples, the same FE model is employed to simulate the response and to estimate the material parameters; therefore, the effects of modeling uncertainty is not considered here. All analyses were performed using a desktop workstation with an Intel Xeon 2.66 GHz processor and 48GB RAM.

7.6.1. Input earthquake motions

Nine actual earthquake ground motions recorded during the Loma Prieta 1989 (Mw=6.9) and Northridge 1994 (Mw=6.7) earthquakes are selected as input motions for both frame-type structures considered in this study. The seismic input motions are chosen such that the structural response ranges from linear to highly nonlinear. This enables studying the level of structural response required to reliably identify the different

parameters (stiffness, strength, and post-yield related) associated with the uniaxial material model(s) used for the steel fibers. Table 7.1 summarizes the main characteristics of the earthquake input motions and their acceleration time histories are shown in Figure 7.5.

Table 7.1: Earthquake motions.

ID	Station	Comp.	Earthquake	PGA (g)	Epicentral distance (km)	PDR (%) Column	PDR (%) Frame
EQ1	Los Gatos	0	1989 Loma Prieta	0.45	20.6	5.02	4.31
EQ2	14145 Mulholland Dr.	N09E	1994 Northridge	0.44	12.7	3.14	2.38
EQ3	Tarzana	90	1994 Northridge	1.78	5.5	2.83	1.94
EQ4	Corralitos	90	1989 Loma Prieta	0.48	7.1	2.49	1.33
EQ5	6334 Katherine Rd.	N90E	1994 Northridge	0.51	13.0	1.97	1.16
EQ6	Capitola - Fire Station	90	1989 Loma Prieta	0.40	9.4	1.43	0.91
EQ7	3036 Fletcher Dr.	S54W	1994 Northridge	0.25	29.3	1.41	0.44
EQ8	600 E. Grand Ave.	S90W	1994 Northridge	0.24	43.3	0.64	0.59
EQ9	Wrightwood – Nielson	90	1994 Northridge	0.04	92.4	0.14	0.13

Note: PDR = Peak Drift Ratio (peak horizontal relative displacement of the top of the structure normalized by the height of the structure). $f_s = 50$ Hz for motions EQ1 to EQ8 and $f_s = 100$ Hz for motion EQ9.

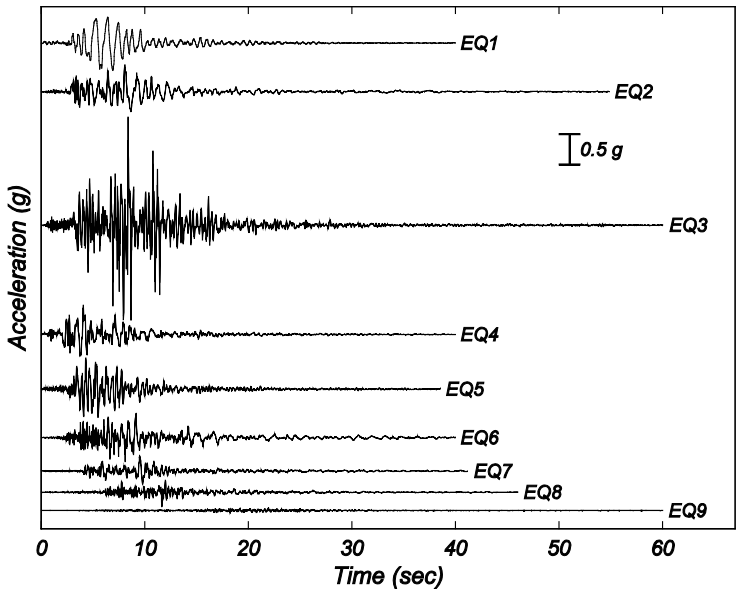

Figure 7.5: Acceleration time histories of the seismic input motions.

7.6.2. Modified Giuffre-Menegotto-Pinto (G-M-P) constitutive model

The modified G-M-P material constitutive model, originally proposed by Menegotto and Pinto (1973) and modified by Filippou et al. (1983) to account for isotropic hardening, has been used extensively and successfully to describe the nonlinear response of both structural steel (e.g., Ayoub and Filippou 2000, Uriz et al. 2008) and reinforcing steel (e.g., Filippou et al. 1983, Taucer et al. 1991). The G-M-P model is governed by physical parameters of the material as well as empirical parameters fitted to experimental data, and is commonly used in state-of-the-art modeling and simulation of civil structures.

The G-M-P model is a smooth material constitutive law (see Figure 7.3) governed by ten constant (i.e., time-invariant) material parameters and material history variables that are updated at each strain reversal and depend on the material parameters and certain features/metrics of the history of deformation (e.g., maximum plastic strain). The ten material parameters can be classified into four primary parameters controlling the monotonic stress-strain curve (or back-bone curve) and six secondary parameters controlling the evolution of the cyclic stress-strain behavior, specifically the curvature of the elastic-to-plastic transition curve and the isotropic hardening for each branch of the hysteresis loops produced by the stress-strain cycles. In the proof-of-concept examples presented here, without loss of generality, only the four primary material parameters are considered as unknown and estimated using unscented Kalman filtering. These four parameters are (see Figure 7.3): elastic Young's modulus (E_0), initial yield stress (σ_y), strain hardening ratio (b), and a parameter (R_0) describing the curvature of the transition

curve between the asymptotes of the elastic and plastic branches during the first loading. Further details about the G-M-P model can be found in Filippou et al. (1983).

7.6.3. Steel cantilever bridge column

A cantilever steel column of height 6.0 m representing a bridge pier is modeled using 17 DB beam-column elements. The bottom 2.5 m is discretized into 10 DB elements, each with a length of 0.25 m and 5 Gauss-Lobatto IPs along its length, while the top 3.5 m is discretized into 7 DB elements, each with a length of 0.5 m and 3 Gauss-Lobatto IPs along its length (Figure 7.6a). The cross section of the column consists of a built-up box-shaped section of steel ASTM A36. The dimensions of the cross section are $550\,\text{mm} \times 550\,\text{mm} \times 20\,\text{mm}$, meeting the highly ductile member requirements of the AISC code (AISC 2010). This design avoids local and lateral-torsional buckling and allows to attain the fully plastic capacity of the cross section. Each of the two webs of the section is discretized into 36 fibers along its length and one fiber along its width, while each flange of the section is represented by a single fiber (Figure 7.6b). The uniaxial G-M-P material model with parameters $\boldsymbol{\theta}^{true} = \left\{E_0^{true}, \sigma_y^{true}, b^{true}, R_0^{true}\right\}^T = \{200\,\text{GPa}, 250\,\text{MPa}, 0.1, 18\}^T$ is used to model the steel fibers and simulate the column response. A lumped mass M = 80 kN·s^2/m, representing dead and live loads on the bridge over the tributary area of the column, is considered at the top of the column (Figure 7.6a). The effects of nonlinear geometry are accounted for by using the P-Delta approximation (Filippou and Fenves 2004). The damping properties representing sources of energy dissipation beyond the hysteretic

energy dissipated through inelastic material behavior are modeled using tangent stiffness-proportional Rayleigh damping (based on the tangent stiffness matrix at the last converged step of analysis) for a critical damping ratio of 2% at the first (fundamental) mode. An "elastic" fundamental period of the column of $T_1 = 0.77$ sec was obtained from eigenanalysis based on the tangent stiffness of the structure after static application of the gravity loads. This cantilever bridge column model is used to simulate the transverse bridge response due to seismic base excitation.

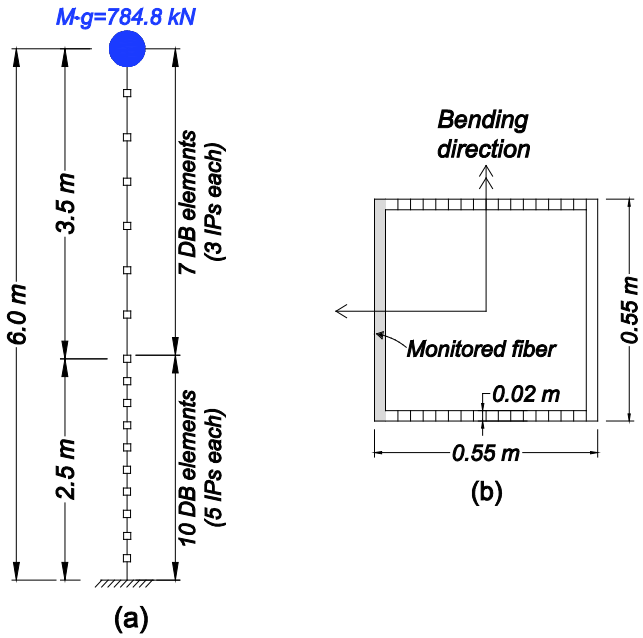

Figure 7.6: Steel cantilever bridge column: (a) general geometry and FE discretization, (b) cross section fiber discretization.

In the identification phase, the UKF algorithm requires 9 SPs $(=2\times 4+1)$, and it is assumed that only the horizontal acceleration response of the top mass M is measured. The initial estimates of the parameters are taken as 70% of their true values, $\hat{\boldsymbol{\theta}}_0 = 0.7\,\boldsymbol{\theta}^{true} = \{140\,\text{GPa}, 175\,\text{MPa}, 0.07, 12.6\}^T$, and the initial covariance matrix

estimate $\hat{\mathbf{P}}_0^{\boldsymbol{\theta\theta}}$ is assumed to be diagonal with terms computed assuming a coefficient of variation (of the initial values $\boldsymbol{\theta}_0$) of 15% for σ_y and E_0, and 25% for b and R_0. To study the robustness of the identification process to the measurement noise, the case of a zero-mean Gaussian white noise process with 5% root mean square (RMS) noise-to-signal-ratio (NSR) superimposed on the simulated acceleration response is considered in addition to the base case of noise-free simulated measurement. It is noted that the measurement noise is added after completion of the structural response simulation and because the noise level depends on the total length (including initial and final tails) and time-dependent amplitude modulation function of the corresponding response time history, the value of the RMS NSR cannot be interpreted in a general sense as in the case of stationary signals. It is assumed that the process noises $\mathbf{r}_k$ and measurement noise v_k, see Equation (7.27), are statistically independent zero-mean Gaussian white noise processes with time-invariant diagonal covariance matrices $\mathbf{Q}$ and R, respectively. A coefficient of variation of 1×10^{-3} is assumed for the initial estimates of the material parameters ($\boldsymbol{\theta}_0$) to construct the process noise covariance matrix $\mathbf{Q}$ for both measurement noise levels (0 and 5% RMS NSR). A standard deviation (or RMS) of the measurement noise v_k of 1×10^{-2} and 7×10^{-2} of the RMS of the corresponding measurement (horizontal acceleration at top of column) is assumed in the measurement noise covariance matrix R for the actual measurement noise levels 0 and 5% RMS NSR, respectively. It is important to note that, in this problem, the statistics of the simulated measurement noise are known from the assumed RMS NSR. However, when data is recorded in real structures, the variances of the measurement noises are unknown, and

need to be estimated based on the noise sources, experience and engineering judgment. Thus, to mimic real-world applications, in this problem $\mathbf{R}$ is not considered equal to the actual statistics of the simulated measurement noise processes.

The quantities $\hat{\boldsymbol{\theta}}_0$, $\hat{\mathbf{P}}_0^{\boldsymbol{\theta}\boldsymbol{\theta}}$, $\mathbf{Q}$, and $\mathbf{R}$ affect the performance and convergence rate of the parameter estimation process (Haykin 2001, Simon 2006). Studying the effect of $\hat{\boldsymbol{\theta}}_0$, $\hat{\mathbf{P}}_0^{\boldsymbol{\theta}\boldsymbol{\theta}}$, $\mathbf{Q}$, $\mathbf{R}$, and scaled UT variables on the convergence and performance of the parameter estimation is not in the scope of this chapter, but will be the topic of future investigations.

For all nine seismic inputs considered and for the two levels (0% and 5% RMS NSR) of measurement noise, Table 7.2 reports the final estimated values of the four primary parameters of the G-M-P material constitutive law used to model all steel fibers of the column. From Table 7.2 and Figure 7.7 (for EQ3), it is observed that the final parameters estimates are stable and converged to the true parameter values. The UKF is able to estimate successfully the G-M-P material parameters from the input-output data for seismic inputs EQ1 to EQ7, which induce a peak drift ratio (PDR) larger than or equal to 1.4% (see Table 7.1). It is noteworthy that the cantilever column experiences a moderately nonlinear global response for EQ5 to EQ7 (1.41% ≤ PDR ≤ 1.97%); and the extreme fibers at the base of the column respond in the nonlinear range during the strong motion part of these earthquakes. This level of nonlinearity in the response allows to estimate correctly the parameters associated to the nonlinear parts (or strength related parameters) of the G-M-P model (σ_y, b, R_0). For EQ8, parameters E_0, σ_y, and R_0 are properly estimated, while the initial value of b (0.07) is not modified by the filtering

process, because the response in the nonlinear range is limited; consequently, the structural response measurements do not contain enough information to update the initial estimate of the strain hardening ratio. Since EQ9 produces a very low excitation (PDR = 0.14%), the response of the column is quasi-linear and no yielding occurs. This implies that only the stiffness related material parameter E_0 is identified, while the time-histories of the strength and post-yield related parameters σ_y, b, and R_0 remain essentially unchanged from their initial estimates.

Table 7.2: Final estimates of the G-M-P material constitutive model parameters for the bridge column.

Parameter	Noise level (%)	Estimation results								
		EQ1	EQ2	EQ3	EQ4	EQ5	EQ6	EQ7	EQ8	EQ9
E_0/E_0^{true}	0	1.00	1.00	1.00	1.00	1.00	1.00	1.00	1.00	1.00
	5	1.00	1.00	0.99	1.00	1.00	1.00	1.00	1.00	1.00
σ_y/σ_y^{true}	0	1.00	1.02	1.00	1.01	1.01	1.00	1.02	1.01	0.70
	5	1.01	1.01	1.01	1.02	0.96	0.99	1.02	0.96	0.70
b/b^{true}	0	1.00	1.00	0.99	1.02	1.00	1.00	0.95	0.71	0.70
	5	1.00	0.98	1.00	0.96	1.05	1.07	0.94	0.71	0.70
R_0/R_0^{true}	0	1.00	0.99	1.00	0.98	1.00	1.00	0.99	1.03	0.70
	5	1.00	1.00	1.01	1.00	1.08	1.00	1.03	1.03	0.70

Figure 7.7 shows the time histories of the mean ($\hat{\mu}$) and standard deviation ($\hat{\sigma}$) estimates of the identified G-M-P material parameters for EQ3. For the noise-free measurement case, parameter E_0 converges quickly to the true value after a few time steps, because it is related to the initial linear elastic stiffness, and from the first time step the measured response contains information about this parameter. Then, σ_y converges to the true value at around t = 5 sec, and parameters b and R_0 converge to their true values at around t = 8 sec. After some steel fibers yield at the base of the column, the initial

yield stress σ_y is accurately estimated. Finally, more and larger excursions of an increasing number of fibers into the nonlinear range are needed to produce enough information in the measured response data to identify parameters b and R_0. Figure 7.7 also shows that the parameter estimation results for 5% RMS NSR are also accurate, showing the robustness of the identification process to the measurement noise. The standard deviations as uncertainty measures of the identified material parameters decrease rapidly to zero as measured response data are progressively processed by the UKF.

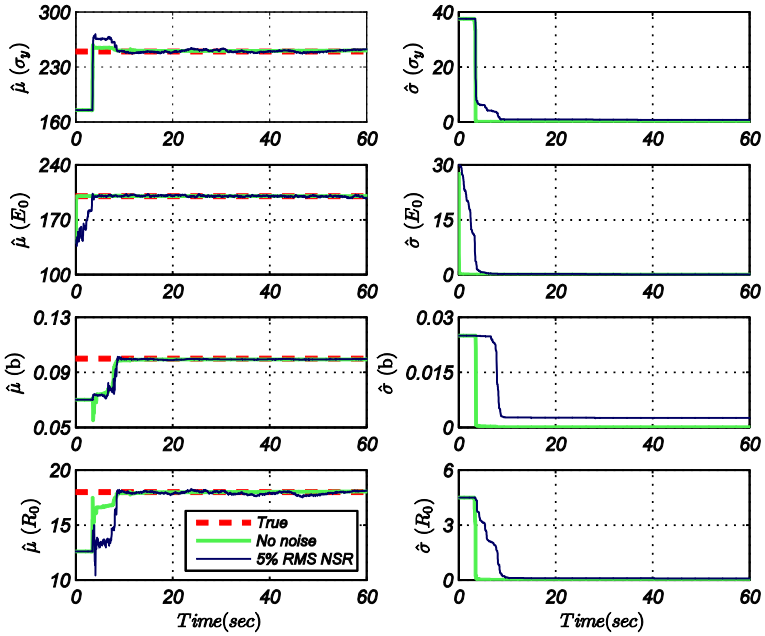

Figure 7.7: Estimation results for the primary G-M-P parameters for the steel cantilever bridge column subjected to EQ3. Left column: mean values / Right column: standard deviations.

Figure 7.8 compares global and local responses of the column to EQ3 (with 5% RMS NSR) obtained based on the true material parameter values ($\boldsymbol{\theta}^{true}$), the initial parameter estimates ($\hat{\boldsymbol{\theta}}_0$), and final identified parameter estimates ($\hat{\boldsymbol{\theta}}_N$). These column

responses consist of: the absolute horizontal acceleration time history at the top of the column (A), the base shear (V) versus drift ratio (D), the moment (M) versus curvature (κ) at the column base section, and the stress (σ) versus strain (ε) at the extreme fiber of the column base section (see Figure 7.6b). It is observed that all the responses computed from the final estimated parameters are in excellent agreement with the corresponding true simulated responses. The successful updating of the nonlinear FE model is clear when comparing the responses obtained from the initial and final estimates of the material parameters with the corresponding true response.

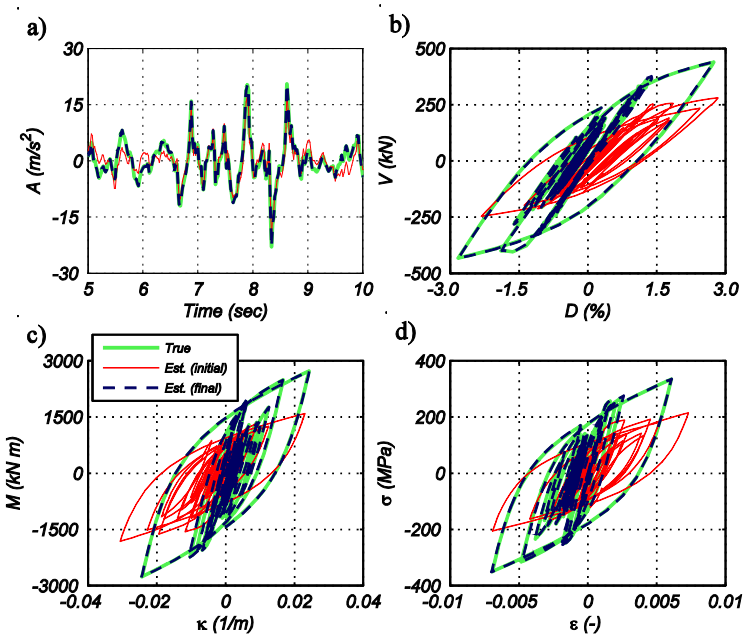

Figure 7.8: Comparison of true and estimated responses of the steel bridge column subjected to EQ3 with 5% RMS NSR: (a) absolute horizontal acceleration at the top, (b) base shear versus drift ratio, (c) moment versus curvature of the column base section, (d) stress versus strain in a extreme fiber at the base of the column.

To quantify the error in the time histories of the considered global and local responses for all seismic inputs, the relative RMS error measure defined as

$$\text{Relative RMS error} = \frac{\sqrt{\left(\frac{1}{N}\sum_{k=1}^{N}\left(resp_k^{true} - resp_k^{est}\right)^2\right)}}{\sqrt{\left(\frac{1}{N}\sum_{k=1}^{N}\left(resp_k^{true}\right)^2\right)}} \times 100 \quad (\%) \qquad (7.28)$$

is used, where $resp_k^{true}$ and $resp_k^{est}$ are the noiseless simulated true and the estimated response at time t_k, respectively, and N denotes the total number of data points in the time histories. The estimated time histories can be obtained using: (i) the initial parameter values $\hat{\boldsymbol{\theta}}_0$, (ii) the estimated parameter values at each time step $\hat{\boldsymbol{\theta}}_k$ to obtain the responses at time t_k by re-running the time history analysis from time zero to t_k (i.e., pseudo-online), or (iii) the final estimated parameter values $\hat{\boldsymbol{\theta}}_N$. The relative RMS errors for A, D, V, M, κ, σ, and ε simulated based on $\hat{\boldsymbol{\theta}}_0$ and $\hat{\boldsymbol{\theta}}_N$ are reported in Table 7.3. The relative RMS error between the simulated true responses and corresponding responses obtained using the initial parameter values $\hat{\boldsymbol{\theta}}_0$ varies in the range [48.5 – 271.3]%. This indicates that the response time histories of the initial FE model (with material constitutive model parameters $\hat{\boldsymbol{\theta}}_0$) are very different from the simulated true responses for all the global and local responses considered. When the final estimates of the material model parameters, $\hat{\boldsymbol{\theta}}_N$, are used to compute the responses, the relative RMS error varies in the range [0.1 – 2.9]% and [0.5 – 7.9]% for the cases of noise-free and 5% RMS NSR measurements, respectively. This illustrates the effectiveness, robustness, and accuracy of the material parameter estimation process in updating the nonlinear FE model. When the bridge column response time histories are computed using the material

model parameters identified at each time step (pseudo-online), similar results are obtained, with a relative RMS error varying in the range [0.1 – 5.8]% and [0.9 – 9.2]% for the cases of noise-free and 5% RMS NSR measurements, respectively.

Table 7.3: Relative RMS error (in %) of the responses of the bridge column between the simulated true responses (true), responses obtained using the initial parameter estimates (initial), and responses obtained using the final parameter estimates (final).

Motion	Pair	A	D	V	M	κ	σ	ε
EQ1	true / initial	67.8	147.3	77.7	78.5	129.4	78.4	141.6
	true / final	0.5 (0.8)	0.6 (0.9)	0.6 (0.9)	0.6 (0.9)	0.5 (0.8)	0.6 (0.9)	0.5 (0.7)
EQ2	true / initial	92.1	103.4	97.3	97.4	115.3	96.9	110.6
	true / final	2.4 (0.6)	2.5 (0.5)	2.5 (0.6)	2.5 (0.6)	2.5 (0.8)	2.5 (0.7)	2.6 (0.8)
EQ3	true / initial	48.5	137.4	93.2	93.4	167.2	91.9	108.7
	true / final	0.3 (4.0)	0.8 (5.7)	0.5 (7.6)	0.5 (7.6)	1.1 (5.2)	0.5 (7.7)	0.9 (4.2)
EQ4	true / initial	79.0	106.7	91.1	91.2	118.3	90.8	139.1
	true / final	1.0 (1.5)	2.0 (1.7)	1.1 (1.8)	1.1 (1.8)	2.3 (3.0)	1.1 (1.8)	2.9 (2.5)
EQ5	true /initial	89.3	216.7	121.0	121.7	271.3	119.6	176.6
	true / final	0.8 (2.7)	1.8 (7.9)	1.1 (3.5)	1.1 (3.6)	1.8 (5.6)	1.1 (3.8)	1.5 (4.1)
EQ6	true / initial	92.8	112.8	104.6	104.6	113.3	104.6	102.2
	true / final	0.4 (0.7)	0.5 (1.3)	0.5 (1.0)	0.5 (0.8)	0.5 (4.2)	0.5 (1.3)	0.5 (4.5)
EQ7	true / initial	82.7	93.5	92.4	92.5	87.0	92.7	71.6
	true / final	1.1 (2.0)	1.2 (2.3)	1.3 (2.2)	1.2 (2.2)	1.6 (4.4)	1.3 (2.3)	1.4 (4.2)
EQ8	true / initial	92.7	118.2	104.6	104.9	118.1	95.1	108.3
	true / final	0.1 (1.3)	0.1 (1.5)	0.1 (1.5)	0.1 (1.5)	0.2 (1.5)	0.4 (1.4)	0.2 (1.3)
EQ9	true / initial	131.9	178.2	142.7	143.5	178.0	65.1	89.3
	true / final	0.1 (3.1)	0.1 (3.4)	0.1 (3.4)	0.1 (3.4)	0.1 (3.4)	0.1 (1.5)	0.1 (1.6)

Note: for the relative RMS error between true responses and responses obtained using the final parameter estimates, the values in parentheses are those corresponding to the 5% relative RMS measurement noise level.

Time histories of response quantities different from those considered in Table 7.3 (e.g., section and fiber responses along the height of the column) were also analyzed. All the results obtained are similar and consistent with those presented in this chapter.

7.6.4. Steel building frame (SAC-LA-3)

A 3-story steel moment resisting frame (MRF) structure studied under the SAC venture, known as the SAC-LA-3 story building (FEMA-355C 2000), is selected as second application example. The building is designed according to the UBC 1994 code. The exterior North-South frame is selected for this study (Figure 7.9a), since it has been extensively studied previously (e.g., Gupta and Krawinkler 2000). The modeled 2D frame has 3 stories and 3 bays, with a story height of 3.96 m and a bay width of 9.14 m. Exterior and interior columns are made of A572 steel with W14×257 and W14×311 cross-sections, respectively. Second, third, and roof level beams are made of A36 steel with W33×118, W30×116, and W24×68 cross-sections, respectively.

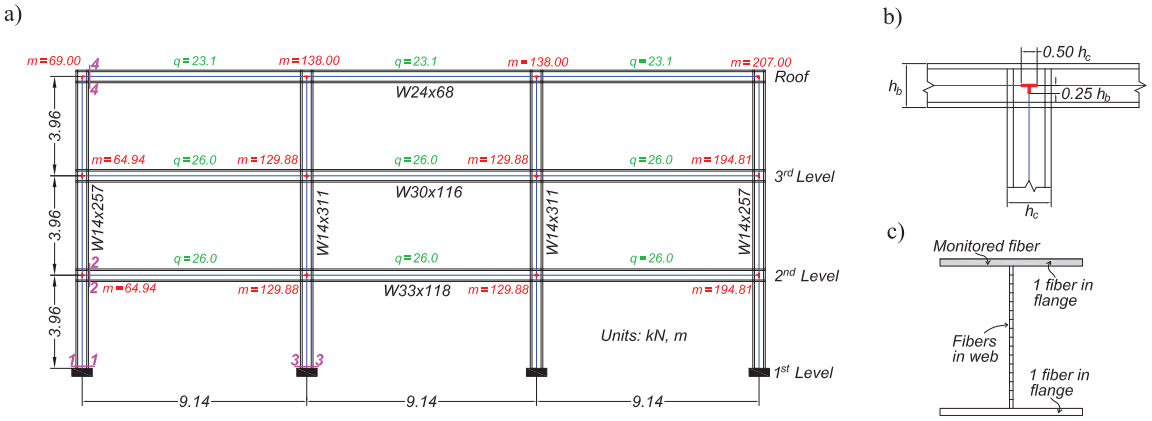

Figure 7.9: SAC-LA-3 steel building frame: (a) overall geometry, (b) rigid end zones, (c) cross-section fiber discretization.

The beam-to-column joints are assumed to be fully restrained, and rigid end zones are modeled at the ends of beams and columns (Figure 7.9b). In contrast to the bridge column example, beams and columns are modeled using FB beam-column elements; therefore, only one element is used to model each beam and column. Numerical integration over the length of the elements is performed by using Gauss-Lobatto

quadrature with 6 and 7 IPs for columns and beams, respectively. Column webs are discretized into 6 fibers along their length and one fiber across their width, while a single fiber is used to represent each flange of the cross-section (Figure 7.9c). The webs of the second, third, and roof level beams are discretized into 16, 14, and 11 fibers along their length, respectively, and one fiber across their width. A single fiber is used to represent each flange of the cross-section (Figure 7.9c). A linear elastic section shear force-deformation model is aggregated with the inelastic coupled flexure-axial behavior at the section level and along the element. The flexure-axial behavior is uncoupled from the shear behavior at the section level. The uniaxial G-M-P material model with primary parameters $\boldsymbol{\theta}^{true} = \begin{Bmatrix} \left[E_0^{col}, \sigma_y^{col}, b^{col}, R_0^{col}\right]^T \\ \left[E_0^{beam}, \sigma_y^{beam}, b^{beam}, R_0^{beam}\right]^T \end{Bmatrix} = \begin{Bmatrix} [200\,\text{GPa}, 345\ \text{MPa}, 0.08, 20]^T \\ [200\,\text{GPa}, 250\ \text{MPa}, 0.05, 18]^T \end{Bmatrix}$ is used to model the axial behavior of the fibers of the beam and column cross-sections and to simulate the true dynamic response of the frame structure to seismic base excitation. The nodal masses and distributed gravity loads on the beams are obtained from the design dead and live loads as reported in FEMA-355C and are shown in Figure 7.9a. The sources of energy dissipation beyond hysteretic energy dissipated through material inelastic action are modeled using mass and tangent stiffness-proportional Rayleigh damping assuming a critical damping ratio of 2% for the first two initial natural periods (after application of the gravity loads), T_1 = 1.06 sec and T_2 = 0.35 sec. These two initial natural periods coincide with the first two elastic natural periods of the building since all the steel fibers remain elastic after application of the gravity loads.

In the material parameter identification process, the UKF algorithm requires 17 SPs $(=2\times 8+1)$ and it is assumed that only one horizontal acceleration response is measured at each level (at the left column). The initial estimates of the material parameters to be identified are taken as 140% of their true values, $\hat{\boldsymbol{\theta}}_0 = 1.4\boldsymbol{\theta}^{true}$, and the initial covariance matrix $\hat{\mathbf{P}}_0^{\boldsymbol{\theta}\boldsymbol{\theta}}$ is assumed diagonal with terms computed assuming a coefficient of variation of the initial parameter estimates (with $\hat{\boldsymbol{\theta}}_0$ as initial mean) of 15% for E_0^{col} and E_0^{beam}, and 25% for $\sigma_y^{col}, \sigma_y^{beam}, b^{col}, R_0^{col}, b^{beam}$, and R_0^{beam}. As in the first application example, two cases are considered for the measurement noise, namely noise-free and 5% RMS NSR. It is assumed that the process noise $\mathbf{r}_k$ and measurement noise $\mathbf{v}_k$ are zero-mean Gaussian white noise processes with time-invariant diagonal covariance matrices $\mathbf{Q}$ and $\mathbf{R}$, respectively. A coefficient of variation of 1×10^{-4} is assumed for the initial estimates of the material parameters ($\boldsymbol{\theta}_0$) to construct the process noise covariance matrix $\mathbf{Q}$ for both measurement noise levels (0 and 5% RMS NSR). A standard deviation (or RMS) of the measurement noise $\mathbf{v}_k$ of 1×10^{-2} and 7×10^{-2} of the RMS of the corresponding simulated measurements (horizontal acceleration at the 2nd, 3rd, and roof levels) is assumed in the measurement noise covariance matrix $\mathbf{R}$ for the measurement noise levels 0 and 5% RMS NSR, respectively.

For all nine seismic inputs and the two measurement noise levels, Table 7.4 reports the final estimated values of the eight G-M-P primary material constitutive model parameters for the beam and column elements. The material stiffness parameters E_0^{col}

and E_0^{beam} are accurately estimated for all the seismic inputs. For EQ1 to EQ3 (PDR ≥ 1.94%), the remaining six material parameters are accurately estimated with relative errors lower than 6%. Since the design satisfies the weak beam-strong column requirement of the UBC 1994 code, the nonlinear response is more pronounced in the beams than in the columns. Therefore, all the material parameters associated with the beams are successfully identified for EQ1 to EQ5, while all the material parameters of the columns are successfully identified for EQ1 to EQ3 (three most intense seismic inputs considered). For EQ4 to EQ6 (0.91% ≤ PDR ≤ 1.33%), only some of the column material parameters are successfully identified (in addition to E_0^{col}, σ_y^{col} and R_0^{col} are properly identified for EQ5 and for EQ4 with noise-free measurements). For EQ6, the beam material parameters E_0^{beam}, σ_y^{beam} and R_0^{beam} are properly identified, while b^{beam} is not accurately estimated because of the limited excursions of the response into the nonlinear range. For EQ7 and EQ8 (PDR = 0.44% and 0.59%, respectively), the extent of material nonlinearity in the response of the beams is limited, but still σ_y^{beam} is well identified for EQ8 (at both measurement noise levels) and for EQ7 (only for the noise free measurement case), and R_0^{beam} is well identified for EQ8 only for the noise-free measurement case. For EQ7 and EQ8, the columns respond quasi linearly with therefore only E_0^{col} is well identified. For EQ9 (PDR = 0.13%), the response of all beam and column members of the frame remain linear elastic and therefore the strength and post-yield related beam and column material parameters cannot be identified.

Table 7.4: Final estimates of the G-M-P material constitutive model parameters for the SAC-LA-3 frame.

El.	Parameter	Noise level (%)	Estimation results								
			EQ1	EQ2	EQ3	EQ4	EQ5	EQ6	EQ7	EQ8	EQ9
Columns	E_0/E_0^{true}	0	1.00	1.00	1.00	1.00	1.00	1.00	1.00	1.00	1.00
		5	1.00	1.00	1.00	1.00	1.00	1.00	1.00	1.00	1.00
	σ_y/σ_y^{true}	0	1.00	1.00	1.00	1.00	0.99	1.40	1.40	1.40	1.40
		5	1.00	1.00	0.99	1.40	1.00	1.40	1.40	1.40	1.40
	b/b^{true}	0	0.98	1.01	1.00	1.38	1.20	1.40	1.40	1.40	1.40
		5	1.00	1.06	1.06	1.40	1.02	1.40	1.40	1.40	1.40
	R_0/R_0^{true}	0	0.98	0.98	1.00	1.03	1.06	1.40	1.40	1.40	1.40
		5	1.01	0.97	1.02	1.40	1.03	1.40	1.40	1.40	1.40
Beams	E_0/E_0^{true}	0	1.00	1.00	1.00	1.00	1.00	1.00	1.00	1.00	1.00
		5	1.00	1.00	1.00	1.00	1.00	1.00	1.00	1.00	1.00
	σ_y/σ_y^{true}	0	1.00	1.00	1.00	1.00	1.00	0.99	1.01	1.00	1.40
		5	1.00	1.01	1.00	1.00	1.00	0.99	1.40	1.03	1.40
	b/b^{true}	0	0.98	1.01	1.00	0.98	0.96	1.18	1.40	1.35	1.40
		5	0.99	0.97	0.99	0.99	1.00	1.09	1.40	1.40	1.40
	R_0/R_0^{true}	0	0.99	1.00	1.00	1.00	1.00	1.01	1.07	1.00	1.40
		5	1.00	0.99	0.98	1.00	1.00	1.02	1.40	0.91	1.40

Time histories of the mean ($\hat{\mu}$) and standard deviation ($\hat{\sigma}$) estimates of the material parameters for SAC-LA-3 building frame subjected to EQ1 are shown in Figure 7.10. The eight parameters are accurately identified and the standard deviation estimates of all these parameters decrease asymptotically to zero. The stiffness related parameters E_0^{beam} and E_0^{col} quickly converge to their true values after a few time steps, the strength or yield related parameters σ_y^{beam} and σ_y^{col} converge to their true values soon after the strong motion phase of the earthquake begins (at around t = 4 sec, see Figure 7.5) and some steel fibers have yielded, and the post-yield related parameters b^{beam}, b^{col}, R_0^{beam}, and R_0^{col} converge to their true values after the strain ductility demand of enough steel fibers has increased sufficiently.

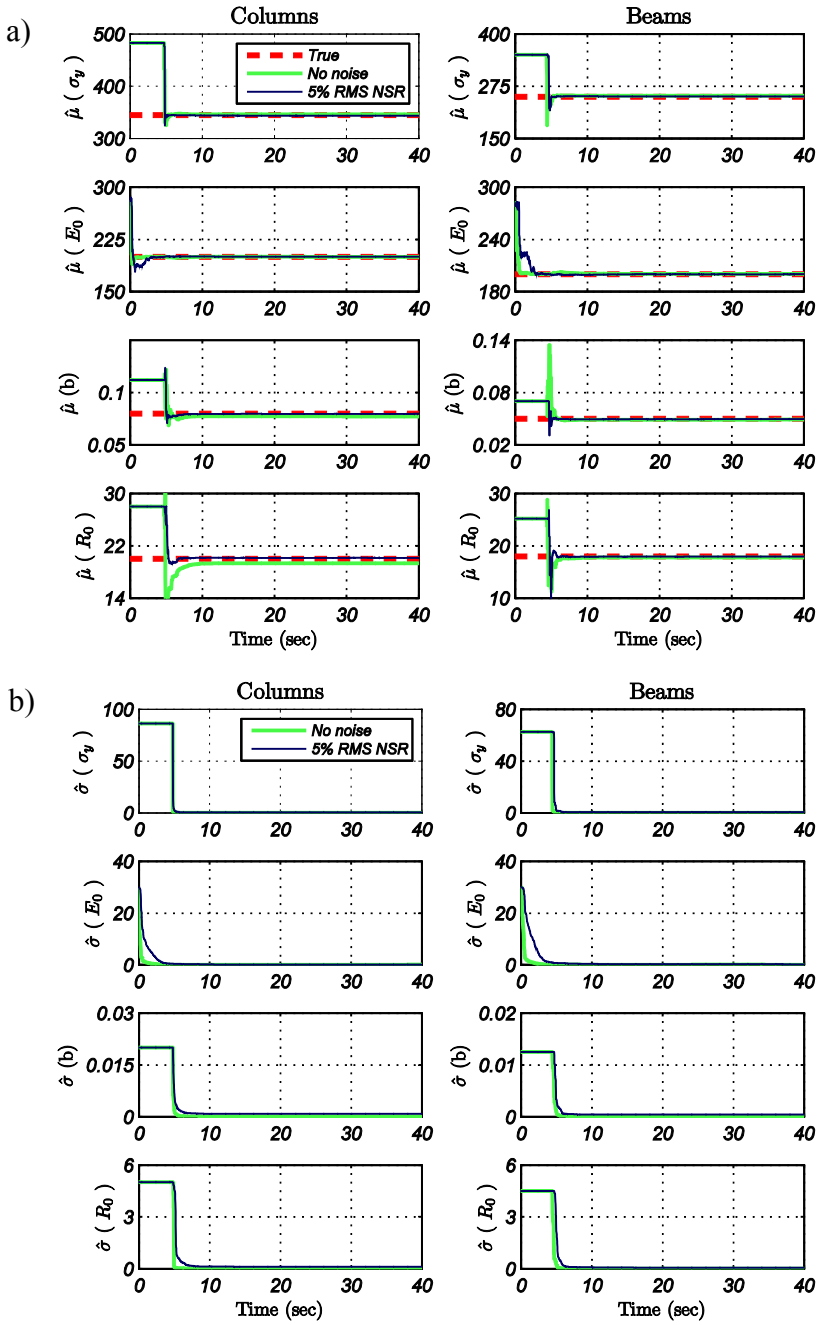

Figure 7.10: Estimation results for the G-M-P primary material parameters of the beams and columns for the SAC-LA-3 building frame subjected to EQ1: (a) mean values, (b) standard deviations.

Figure 7.11 compares different global and local responses of the frame to EQ1 (with 5% RMS NSR) obtained using the true material parameter values ($\boldsymbol{\theta}^{true}$), the initial

parameter estimates ($\hat{\boldsymbol{\theta}}_0$), and the final identified parameter estimates ($\hat{\boldsymbol{\theta}}_N$). The following frame response quantities are plotted in Figure 7.11: the absolute horizontal acceleration response history at the roof level (A_{roof}), the base shear (V) versus roof drift ratio (Δ), the moment (M_{1-1}) versus curvature (κ_{1-1}) hysteretic response at the base of the left column (section 1-1 in Figure 7.9a), the moment (M_{2-2}) versus curvature (κ_{2-2}) hysteretic response at the left section of the 2nd level beam (section 2-2 in Figure 7.9a), the stress (σ_{3-3}) versus strain (ε_{3-3}) hysteretic response at one of the extreme fibers at the base of the central-left column (section 3-3 in Figure 7.9a), and the stress (σ_{4-4}) versus strain (ε_{4-4}) hysteretic response at one of the extreme fibers at the left section of the roof beam (section 4-4 in Figure 7.9a). All the responses computed using the final estimates of the material parameters are in excellent agreement with the simulated true responses and the successful updating of the nonlinear FE model is evident by comparing the responses obtained using the initial and final material parameter estimates with the corresponding true response.

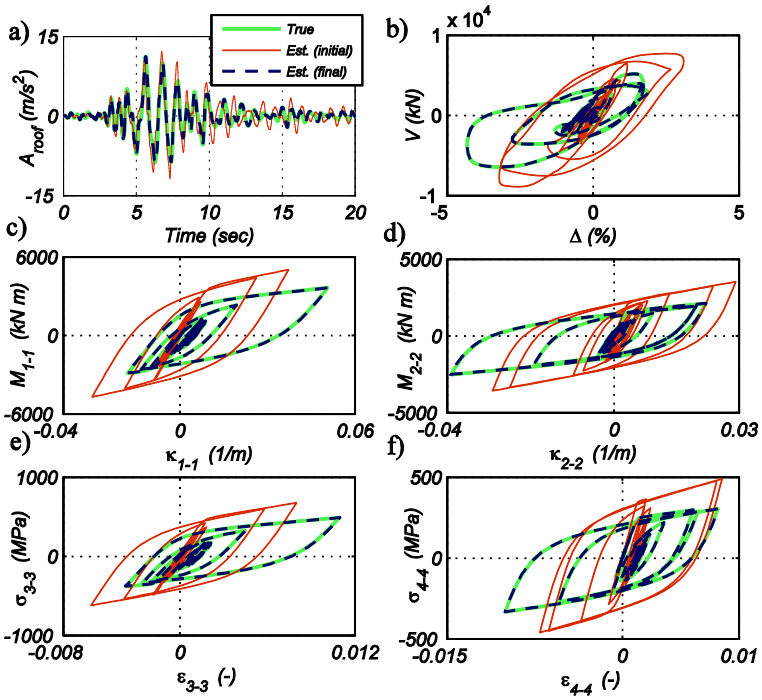

Figure 7.11: Comparison of true and estimated responses of the SAC-LA-3 building frame subjected to EQ1 with 5% RMS NSR. (a) absolute horizontal acceleration at the roof, (b) base shear versus roof drift ratio, (c) moment versus curvature at the base of left column section (section 1-1 in Figure 7.9a), (d) moment versus curvature at the left section of the 2nd level beam (section 2-2 in Figure 7.9a), (e) stress versus strain in extreme fiber at the base of the left-central column (section 3-3 in Figure 7.9a), (f) stress versus strain in extreme fiber at the left section of the roof beam (section 4-4 in Figure 7.9a).

The same global and local responses but for EQ6 (with 5% RMS NSR) are compared in Figure 7.12. In this case, both local responses associated with the columns (M_{1-1} vs. κ_{1-1} and σ_{3-3} vs. ε_{3-3}) remain linear elastic, while the sections (M_{2-2} vs. κ_{2-2}) and fibers (σ_{4-4} vs. ε_{4-4}) of the beams experience nonlinear behavior. Consequently, the strength and post-yield related material parameters associated with the columns ($\sigma_y^{col}, b^{col}, R_0^{col}$) cannot be identified for this seismic input motion (see Table 7.4). The match between the simulated true responses and the corresponding responses of the FE

model updated using the final estimates of the material parameters is very good, for both global and local response quantities.

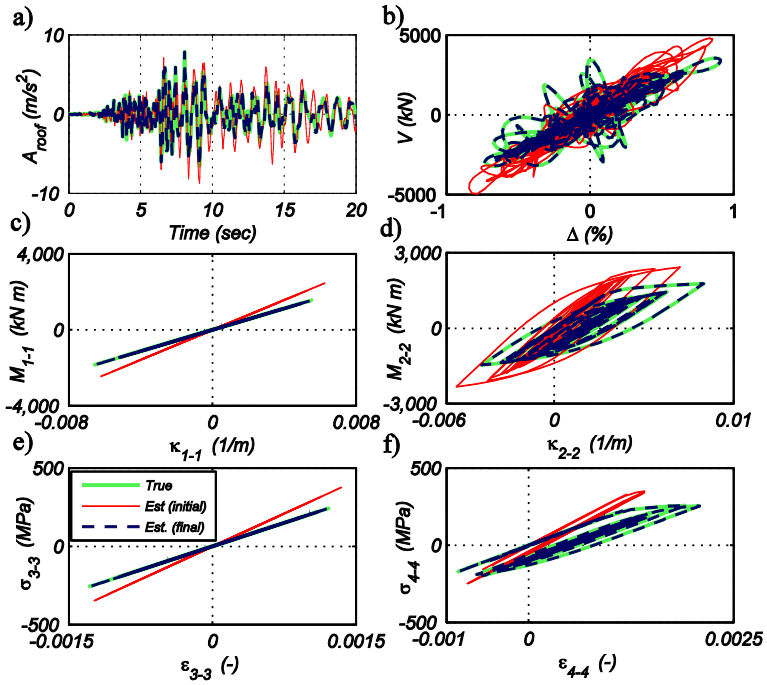

Figure 7.12: Comparison of true and estimated responses of the SAC-LA-3 building frame subjected to EQ6 with 5% RMS NSR. (a) absolute horizontal acceleration at the roof, (b) base shear versus roof drift ratio, (c) moment versus curvature at the base of the left column (section 1-1 in Figure 7.9a), (d) moment versus curvature at the left section of the 2nd level beam (section 2-2 in Figure 7.9a), (e) stress versus strain in a extreme fiber at the base of the left-central column (section 3-3 in Figure 7.9a), (f) stress versus strain in extreme fiber at the left section of the roof beam (section 4-4 in Figure 7.9a).

Table 7.5 reports the relative RMS errors of the time histories of eleven different response quantities simulated based on $\hat{\boldsymbol{\theta}}_0$ and $\hat{\boldsymbol{\theta}}_N$. The response quantities consist of the absolute horizontal acceleration and relative horizontal displacement responses at the roof level (A_{roof} and D_{roof}, respectively), base shear (V), moment and curvature at sections 1-1 and 2-2 (see Figure 7.9a), and stress and strain in an extreme fiber of sections 1-1 and 2-2. The relative RMS errors between the simulated true responses and responses obtained using the initial values of the material parameters vary in the range [66.94 –

213.76]%, indicating that the response of the initial FE model (with $\boldsymbol{\theta} = \hat{\boldsymbol{\theta}}_0$) differs significantly from the corresponding true response for all the global and local response quantities considered. When the final estimates of the material parameters are used to compute the responses, the relative RMS errors vary in the range [0.14 – 10.98]% for the case of 5% RMS NSR.

Table 7.5: Relative RMS error of the responses of the SAC-LA-3 frame between the simulated true responses (true), responses obtained using the initial parameter estimates (initial), and responses obtained using the final parameter estimates (final). Noise level 5% RMS NSR.

Motion	Pair	A_{roof}	D_{roof}	V	$M_{1\text{-}1}$	$\kappa_{1\text{-}1}$	$M_{2\text{-}2}$	$\kappa_{2\text{-}2}$	$\sigma_{1\text{-}1}$	$\varepsilon_{1\text{-}1}$	$\sigma_{2\text{-}2}$	$\varepsilon_{2\text{-}2}$
EQ1	true/initial	75.82	82.61	132.37	124.38	90.67	131.49	76	123.85	85.06	123.86	75.7
	true/final	0.14	0.4	0.17	0.36	0.87	0.16	0.55	0.44	0.56	0.15	0.56
EQ2	true/initial	101.92	94.77	149.28	142.94	74.59	147.1	66.94	141.86	95.67	144.1	67.58
	true/final	0.3	1.13	0.37	0.43	4.58	0.46	0.97	0.49	4.52	0.68	0.98
EQ3	true/initial	96.95	100.28	142.68	140.8	131.23	142.17	74.3	141.67	179.44	130.84	77.86
	true/final	0.47	0.99	0.58	0.62	4.81	0.8	0.77	0.65	4.66	0.77	0.81
EQ4	true/initial	101.16	107.42	148.24	145.31	147.5	145.05	88.61	146.34	147.75	140.62	91.49
	true/final	0.19	1.32	0.23	1.06	10.98	0.74	1.89	2.57	3.38	0.8	2.48
EQ5	true/initial	111.94	151.72	197.2	203.16	116.87	213.76	126	200.85	105.44	210.87	126.91
	true/final	0.26	0.59	0.45	0.55	2.04	0.54	0.74	0.55	1.18	0.67	0.86
EQ6	true/initial	105.65	106.25	127.93	127.42	109.28	126.22	91.64	127.63	109.56	127.24	92.36
	true/final	0.32	0.39	0.38	0.39	0.5	0.44	0.78	0.39	0.39	0.57	0.88
EQ7	true/initial	121.33	126.69	164.33	164.72	129.37	154.46	125.44	164.32	129.4	167.3	127.65
	true/final	0.3	0.39	0.26	0.25	0.26	0.31	1.05	0.26	0.27	1.35	1.34
EQ8	true/initial	112.61	111.14	120.53	119.74	111.96	115.81	106.18	120	112.1	113.29	107.1
	true/final	0.37	0.39	0.39	0.39	0.39	0.42	0.92	0.39	0.39	1.1	1.11
EQ9	true/initial	142.03	136.99	159.22	154.34	129.32	102.64	88.15	153.72	129.04	109.12	93.19
	true/final	0.76	0.77	0.8	0.75	0.78	0.51	0.58	0.76	0.79	0.54	0.6

When the responses are computed using the material parameters identified at each time step (pseudo-online), a good agreement between estimated and true responses is also obtained, with relative RMS errors lower than 12%. Over 40 response quantities, global and local, associated to different beam and column elements, cross-sections, and fibers

were investigated (but not presented herein due to space limitation) with results similar to and consistent with those presented above.

7.7. Conclusions

This chapter proposes and investigates the performance of a novel framework that combines state-of-the-art advanced nonlinear finite element (FE) models and the unscented Kalman filter, to estimate unknown time-invariant parameters of nonlinear inelastic material models in frame-type structures under earthquake ground excitation. The proposed framework formulates the state-space model by including the time-invariant material parameters in the state transition equation and the responses (outputs) of the nonlinear FE model corresponding to the measured response quantities are used to define the measurement equation. In other words, the equation of motion of the nonlinear FE model is inserted in the measurement equation. It is noteworthy that the proposed framework is not limited to certain types of FE models, loading conditions, or FE model parameterization. Different types of finite element analysis (e.g., quasi-static, dynamic), various finite elements (e.g., beam-column, plate, shell, solid elements), and different types of material constitutive models (e.g., pseudo-elasticity, plasticity, damage-plasticity, smeared-crack) can be used with the proposed framework. In addition, other time-invariant FE model parameters such as those characterizing the inertia, damping, geometric, and constraint properties of the structure can also be incorporated in the estimation procedure.

Two numerical examples, a cantilever steel column representing a bridge pier and a two-dimensional 3-story, 3-bay steel frame, are presented to demonstrate the proposed

approach for material parameter identification in nonlinear FE models. Nine actual earthquake ground motions are used as known seismic input to compute (simulate) the responses of the test structures, which are then contaminated by numerical white noise to study the robustness of the identification scheme to measurement noise. Because of the varying intensity of the selected seismic input motions, the response of each test structure ranges from quasi-linear to highly nonlinear. Using the simulated response data, noise-free and noisy, and the corresponding seismic input motion (noiseless), the proposed framework accurately estimates the unknown time-invariant material parameters of the nonlinear FE model, provided that: (i) the loading intensity is sufficient to exercise the parts (branches) of the nonlinear material models which are governed by the material parameters to be identified, and (ii) the measured dynamic response quantities are sufficiently sensitive to the material parameters to be identified. The relative root-mean-square error measure is used to compare true and estimated time histories of various global and local response quantities and to confirm the effectiveness of the proposed nonlinear FE model updating approach. The proposed framework provides a powerful tool for model updating of advanced mechanics-based nonlinear FE models, even when a limited number of measurement data are available.

Additional research is needed to analyze and further validate the proposed methodology for nonlinear FE model updating, especially when applied to large-scale real-world structures subjected to real earthquake excitations. In the latter case, it is expected that modeling uncertainty, unmeasured excitations, and unknown measurement noise level will significantly affect the estimation results, and will therefore require an extension of the framework presented here. Finally, it is important to mention that this

approach can be used directly, through the updated nonlinear FE model, for the purpose of damage identification (structural health monitoring) and damage prognosis.

7.8. Acknowledgements

Chapter 7, in full, is a reprint of the material as it appears in Material parameter identification in distributed plasticity FE models of frame-type structures using nonlinear stochastic filtering in *Journal of Engineering Mechanics ASCE* (2014), Astroza, Rodrigo; Ebrahimian, H.,, and Conte, J.P. The dissertation author was the primary investigator and author of this paper.

References

AISC (2010). *Seismic provisions for structural steel buildings*. Chicago, IL.

Arulampalam, S., Maskell, S., Gordon, N., and Clapp, T. (2002). "A tutorial on particle filters for on-line non-linear/non-Gaussian Bayesian tracking". *IEEE Transactions on Signal Processing*, 50(2), 174–189.

Astroza, R., Ebrahimian, H., Conte, J.P., Restrepo, J., and Hutchinson, T.C. (2013). "Modal identification of 5-story RC building tested on NEES-UCSD shake table." *31st International Modal Analysis Conference* (*IMAC XXXI*), Garden Grove, CA.

Ayoub, A. and Filippou, F. (2000). "Mixed formulation of nonlinear steel-concrete composite beam element." *ASCE Journal of Structural Engineering*, 126(3), 371–381.

Beck, J.L. and Katafygiotis, L. (1998). "Updating models and their uncertainties. I: Bayesian statistical framework." *ASCE Journal of Engineering Mechanics*, 124(4), 455–461.

Chassiakos, A.G., Masri, S.F., Smyth, A.W., and Caughey, T.K. (1998). "On-line identification of hysteretic systems." *Journal of Applied Mechanics*, 65(1), 194–203.

Chatzi, E.N. and Smyth, A.W. (2009). "The unscented Kalman filter and particle filter methods for nonlinear structural system identification with non-collocated heterogeneous sensing." *Structural Control and Health Monitoring*, 16(1), 99–123.

Ching, J., Beck, J.L., Porter, K.A., and Shaikhutdinov, R. (2006). "Bayesian state estimation method for nonlinear systems and its application to recorded seismic response." *ASCE Journal of Engineering Mechanics*, 132(4), 396–410.

Chopra, A.K. (2011). Dynamics of structures. 4th edition, Prentice Hall, New Jersey.

Corigliano, A. and Mariani, S. (2004). "Parameter identification in explicit structural dynamics: performance of the extended Kalman filter." *Computer Methods in Applied Mechanics and Engineering*, 193(36–38), 3807–3835.

Deierlein, G.G., Reinhorn, A.M., and Willford, M.R. (2010). *Nonlinear structural analysis for seismic design, a guide for practicing engineers*. NEHRP Seismic Design Technical Brief No. 4, NIST GCR 10-917-5.

Doebling, S.W., Farrar, C.R., Prime, M.B., and Shevit, D.W. (1996). *Damage identification and health monitoring of structural and mechanical systems from changes in their vibration characteristics: A literature review*. Los Alamos National Laboratory Report LA-13070-MS.

Ebrahimian, H., Astroza, R., Conte, J.P., Restrepo, J.I, and Hutchinson, T.C. (2014). "Experimental validation of dynamic nonlinear FE model of full-scale five-story reinforced concrete building." *9th International Conference on Structural Dynamics* (*EURODYN 2014*), Porto, Portugal.

FEMA-355C (2000). *State-of-the-art report on systems performance of steel moment frames subjected to earthquake ground shaking*. Prepared by the SAC Joint Venture for the Federal Emergency Management Agency, Washington, DC.

Filippou, F.C., Popov, E.P., and Bertero, V.V. (1983). *Effects of bond deterioration on hysteretic behavior of reinforced concrete joints*. Report EERC 83–19, Earthquake Engineering Research Center, University of California, Berkeley.

Filippou, F.C. and Fenves, G.L. (2004). *Methods of analysis for earthquake-resistant structures", Chapter 6 in Earthquake Engineering: From Engineering Seismology to Performance-Based Engineering*. CRC Press, Boca Raton, FL, USA.

Friswell, M.I., and Mottershead, J.E. (1995). *Finite element model updating in structural dynamics*. Kluwer Academic Publishers, Boston, USA.

Giagopoulos, D., Papadioti, D-C., Papadimitriou, C., and Natsiavas, S. (2013). "Bayesian uncertainty quantification and propagation in nonlinear structural dynamics." *31st International Modal Analysis Conference* (*IMAC XXXI*), Garden Grove, CA.

Gupta, A. and Krawinkler, H. (2000). "Behavior of ductile SMRFS at various seismic hazard levels." *ASCE Journal of Structural Engineering*, 126(1), 98–107.

Haug, A.J. (2005). *A tutorial on Bayesian estimation and tracking techniques applicable to nonlinear and non-Gaussian processes*. MITRE technical report 05W0000004.

Haykin, S. (editor) (2001). *Kalman filtering and neural networks*. John Wiley & Sons, New York.

Housner, G., Bergman, L., Caughey, T., Chassiakos, A., Claus, R., Masri, S., Skelton, R., Soong, T., Spencer, B., and Yao, J. (1997). "Structural control: Past, present, and future." *ASCE Journal of Engineering Mechanics*, 123(9), 897–971.

Huang, H., Yang, J.N., and Zhou, L. (2010). "Adaptive quadratic sum-squares error with unknown inputs for damage identification of structures." *Structural Control and Health Monitoring*, 17(4), 404–426.

Imai, H., Yun, C.B., Maruyama, O., and Shinozuka, M. (1989). "Fundamentals of system identification in structural dynamics." *Probabilistic Engineering Mechanics*, 4(4), 162–173.

Ismail, M., Ikhouane, F., and Rodellar, J. (2009). "The Hysteresis Bouc-Wen model, A Survey." *Archives of Computational Methods in Engineering*, 16(2), 161–188.

Ji, X., Fenves, G., Kajiwara, K., and Nakashima, M. (2011). "Seismic damage detection of a full-scale shaking table test structure." *ASCE Journal of Structural Engineering*, 137(1), 14–21.

Julier, S.J. and Uhlmann, J.K. (1997). "A new extension of the Kalman filter to nonlinear systems." *11th International Symposium on Aerospace/Defense Sensing, Simulation and Controls*, Orlando, FL.

Kalman, R.E. (1960). "A new approach to linear filtering and prediction problems." *ASME Journal of Fluids Engineering*, 82(1), 35–45.

Kalman, R.E. and Bucy, R. (1961). "New results in linear filtering and prediction theory." *ASME Journal of Fluids Engineering*, 83(1), 95–107.

Kerschen, G., Worden, K., Vakakis, A.F., and Golinval, J.C. (2006). "Past, present and future of nonlinear system identification in structural dynamics." *Mechanical Systems and Signal Processing*, 20(3), 505–592.

Koutromanos, I., Stavridis, A., Shing, P.B., and Willam, K. (2011). "Numerical modeling of masonry-infilled RC frames subjected to seismic loads. " *Computers and Structures*, 89(11–12), 1026–1037.

Lee, D-J. (2005). *Nonlinear Bayesian filtering with applications to estimation and navigation*. PhD thesis, Department of Aerospace Engineering, Texas A&M University.

Martinelli, P. and Filippou, F.C. (2009). "Simulation of the shaking table test of a seven-story shear wall building." *Earthquake Engineering & Structural Dynamics*, 38(5), 587-607.

Marwala, T. (2010). *Finite element model updating using computational intelligence techniques: Applications to structural dynamics*. Springer-Verlag, London.

Masri, S.F. and Caughey, T.K. (1979). "A nonparametric identification technique for nonlinear dynamic problems." *Journal of Applied Mechanics*, 46(2), 433–447.

MATLAB (2012). The MathWorks Inc., Natick, Massachusetts, United States.

Mazzoni, S., McKenna, F., and Fenves, G.L. (2005). *Opensees command language manual*. http://opensees.berkeley.edu/. Pacific Earthquake Engineering Research.

Menegotto, M. and Pinto, E. (1973). "Method of analysis for cyclically loaded reinforced concrete plane frames including changes in geometry and non-elastic behavior of elements under combined normal force and bending." *IABSE Symposium on resistance and ultimate deformability of structures acted on by well-defined repeated loads*. Lisbon, Portugal.

Moaveni, B., He, X., Conte, J.P., and Restrepo, J.I. (2010). "Damage identification study of a seven-story full-scale building slice tested on the UCSD-NEES shake table." *Structural Safety*, 32(5), 347–356.

Moaveni, B., He, X., Conte, J.P., Restrepo, J.I., and Panagiotou (2011). "System Identification Study of a 7-Story Full-Scale Building Slice Tested on the UCSD-NEES Shake Table." *ASCE Journal of Structural Engineering*, 137(6), 705–717.

Muto M. and Beck, J.L. (2008). "Bayesian updating and model class selection using stochastic simulation." *Journal of Vibration and Control*, 14(1–2), 7–34.

Nasrellah, H.A. and Manohar, C.S. (2011). "Finite element method based Monte Carlo filters for structural system identification." *Probabilistic Engineering Mechanics*, 26(2), 294–307.

Ristic, B., Arulampalam S., and Gordon, N. (2004*). Beyond the Kalman filter, Particle filters for tracking applications*. Artech House, Publishers, Boston, London.

Simoen, E., Moaveni, B., Conte, J.P., and Lombaert, G. (2013). "Uncertainty quantification in the assessment of progressive damage in a seven-story full-scale building slice." *ASCE Journal of Engineering Mechanics*, 139(12), 1818–1830.

Simon, D. (2006). *Optimal State Estimation*. Wiley, New York.

Taucer, F.F., Spacone, E., and Filippou, F.C. (1991). *A fiber beam-column element for seismic response analysis of reinforced concrete structures*. Report 91/17, EERC, Earthquake Engineering Research Center (EERC), University of California, Berkeley.

Uriz, P., Filippou, F., and Mahin, S. (2008). "Model for cyclic inelastic buckling of steel braces." *ASCE Journal of Structural Engineering*, 134(4), 619–628.

Wan, E.A. and van der Merwe, R. (2000). "The unscented Kalman filter for nonlinear estimation." *IEEE 2000 Adaptive Systems for Signal Processing, Communications, and Control Symposium*, Lake Louise, AB, Canada.

van der Merwe, R., Wan, E.A., and Julier, S. (2004). "Sigma-Point Kalman filters nonlinear estimation and sensor fusion – Applications in integrated navigation." *Proc. AIAA Guidance Navigation and Controls Conference*, Providence, RI.

Wu, M. and Smyth, A.W. (2007). "Application of the unscented Kalman filter for real-time nonlinear structural system identification." *Structural Control and Health Monitoring*, 14(7), 971–990.

Yang, J.N., Xia, Y., and Loh, C. (2012). "Damage detection of hysteretic structures with pinching effect." *ASCE Journal of Engineering Mechanics*, 140(3), 462–472.

Yang, J.N, and Lin, S. (2004). "On-line identification of non-linear hysteretic structures using an adaptive tracking technique." *International Journal of Non-Linear Mechanics*, 39(9), 1481–1491.

Yuen, K.V. and Kuok, S.C. (2011). "Bayesian methods for updating dynamic models." *Applied Mechanics Review*, 64(1):010802.

Yun, C.B. and Shinozuka, M. (1980). "Identification of nonlinear structural dynamic systems." *Journal of Structural Mechanics*, 8(2), 187–203.

CHAPTER 8

NONLINEAR SYSTEM IDENTIFICATION FOR HEALTH MONITORING OF CIVIL STRUCTURES

8.1. Introduction

Information obtained from adequate damage identification (DID) methods can be used to support decision-making related to emergency response, post-disaster rehabilitation, maintenance, and inspection of civil structures. In this regard, implementation of accurate and robust DID strategies for civil structures using recorded vibration data plays an important role in two of the recently introduced Grand Challenges in Civil Engineering, namely poor infrastructure resilience to disasters and poor and degrading infrastructures (Becerik-Gerber et al. 2014).

Five hierarchical levels have been adopted by the structural health monitoring (SHM) community to define the DID problem and to classify the proposed methods (Rytter 1993 and Worden and Dulieu-Barton 2004). These levels are: Level 1 − Detection, Level 2 − Localization, Level 3 − Classification, Level 4 − Assessment, and Level 5 – Prediction/Prognosis. Methods based on linear system identification (SID),

modal parameter identification being the most popular in this group, and nonlinear SID have been proposed for DID purposes. DID based on changes in the modal properties of an equivalent linear-elastic viscously damped model of the structure has been undoubtedly one of the most popular approaches. This approach requires low-amplitude input-output or output-only vibration data recorded before (reference) and after the structure has suffered damage. Damage is then identified based on the changes in the estimated modal properties, quantities derived thereof (e.g., curvature mode shapes), or based on linear FE models calibrated using the vibration data measured in the structure before and after the damage-inducing event. Because these methods assume a linear-elastic response of the structure, damage is identified as a loss of effective stiffness (e.g., Teughels and De Roeck 2004, Moaveni et al. 2010, Simoen et al. 2013), and therefore they are unable to reveal information about loss of strength, history of response nonlinearities, and related damage in the structure. As a result, Levels 3 and 4 of DID are difficult to attain using methods based on linear models. In addition, the use of linear models disallows Level 5 of DID.

Methods of DID based on nonlinear SID have mostly been applied to numerically simulated response data from highly idealized models of nonlinear civil structures (e.g., shear building model, single degree-of-freedom, and chain-like multi degree-of-freedom systems) –topic initiated by the pioneering work of Distefano and coworkers (1975a,b;1976)–, which are not suitable for nonlinear response prediction of civil structures with real-world complexities. In recent years, nonlinear FE model updating of civil structures subjected to static and dynamic loadings has attracted significant attention (e.g., Ching et al. 2006, Nasrellah and Manohar 2011, Liu and Au 2013, Song and Dyke

2013, Omrani et al. 2013, Yang et al. 2014). However, in the case of nonlinear hysteretic FE model updating of structures subjected to dynamic excitation, previous studies have used simplified structural models with lumped nonlinearities (e.g., plastic hinges) described using empirically-derived nonlinear models, such as the Bouc-Wen model (Ismail et al. 2009). These simplified and empirical models are not capable to properly represent the actual nonlinear behavior of structures and, consequently, are not typically used in state-of-the-art mechanics-based structural FE models that are being increasingly employed for modeling and simulation of nonlinear civil structures (Filippou and Fenves 2004). Incorporating the use of high-fidelity mechanics-based nonlinear FE models in advanced SHM techniques will help to make progress towards wide application of state-of-the-art SHM methods on large and complex civil structures. Nonlinear FE models able to capture the damage mechanism to be identified enables reconstruction of the nonlinear response process experienced by the structure during the damage-inducing loading, which in turn provides invaluable information about the location, type, and extent of damage in the structure.

Recently, methodologies for model updating of state-of-the-art nonlinear FE models using input/output data recorded during damage-inducing events, i.e., loading events strong enough to force the structure into its nonlinear range of behavior, have been proposed in the literature. This approach represents an important progress in the field of SHM of civil structures, because it will potentially provide a rapid post-earthquake performance assessment of structural safety from the updated nonlinear mechanics-based FE model. In addition, damage prognosis can be also conducted using the updated FE model and possible future loading scenarios. Using numerically simulated response data

from a 2D 1-story 1-bay steel frame with distributed-plasticity subjected to an harmonic lateral force excitation, Shahidi and Pakzad (2014) used the response surface method to update two parameters of a bilinear material constitutive law (modulus of elasticity and post yielding stiffness ratio), which was utilized to model the fibers of the members of the frame. Astroza et al. (2015) and Ebrahimian et al. (2015) used the unscented Kalman filter (UKF) and the extended Kalman filter (EKF), respectively, to estimate time-invariant parameters describing the nonlinear material constitutive models of simple but realistic steel structures. Their application examples used numerically simulated response data of a cantilever steel pier and a 2D 3-story 3-bay steel frame and involved the estimation of three to eight parameters.

This chapter aims to extend the formulation proposed by Astroza et al. (2015). The performance and robustness of the proposed framework are analyzed when limited response data are available and, in addition to parameters characterizing the nonlinear material constitutive laws, damping parameters (which are known to have a key influence on nonlinear response of structures) of the FE model are considered in the estimation process. To alleviate the computational burden of the methodology proposed by the authors, in this chapter three non-sequential updating approaches are presented and analyzed. The effects of using heterogeneous sensor arrays on the identifiability of the modeling parameters and updating of the nonlinear FE model are also investigated. In addition, an adaptive filtering approach is proposed to estimate the measurement noise covariance in addition to the time-invariant modeling parameters. Finally, effects of input noise in the estimation results are studied. Although the proposed framework is general in principle, the verification example presented in this chapter considers the problem of

updating a mechanics-based nonlinear FE model of a three-dimensional (3D) 5-story 2-by-1 bay reinforced concrete (RC) frame building subjected to bi-directional earthquake excitation.

8.2. Problem statement

The discrete-time equation of motion of a nonlinear FE model of a structure can be formulated as

$$\mathbf{M}(\boldsymbol{\theta})\,\ddot{\mathbf{q}}_{k+1}(\boldsymbol{\theta})+\mathbf{C}(\boldsymbol{\theta})\,\dot{\mathbf{q}}_{k+1}(\boldsymbol{\theta})+\mathbf{r}_{k+1}\left(\mathbf{q}_{k+1}(\boldsymbol{\theta}),\boldsymbol{\theta}\right)=\mathbf{f}_{k+1} \tag{8.1}$$

where $\boldsymbol{\theta}\in\mathbb{R}^{n_\theta}=$ vector of unknown time-invariant modeling parameters, $\mathbf{q}, \dot{\mathbf{q}}, \ddot{\mathbf{q}}\in\mathbb{R}^{n}=$ nodal displacement, velocity, and acceleration vectors, respectively, $\mathbf{M}\in\mathbb{R}^{n\times n}=$ mass matrix, $\mathbf{C}\in\mathbb{R}^{n\times n}=$ damping matrix, $\mathbf{r}\left(\mathbf{q}(\boldsymbol{\theta}),\boldsymbol{\theta}\right)\in\mathbb{R}^{n}=$ history-dependent internal resisting force vector, $\mathbf{f}\in\mathbb{R}^{n}=$ dynamic load vector, and the subscript indicates the time step. For the case of rigid base earthquake excitation, the dynamic load vector takes the form $\mathbf{f}_{k+1}=-\mathbf{M}\boldsymbol{\mathcal{L}}\ddot{\mathbf{u}}^{g}_{k+1}$, where $\boldsymbol{\mathcal{L}}\in\mathbb{R}^{n\times r}=$ influence matrix and $\ddot{\mathbf{u}}^{g}\in\mathbb{R}^{r\times 1}=$ input ground acceleration vector with $r=$ number of base excitation components (in the general case of rigid base excitation $r=$ 6, i.e., 3 rotations and 3 translations base excitation components).

The response of the structure can be recorded using a heterogeneous sensor array (e.g., accelerometers, GPS, long-gauge fiber optic sensors, strain gauges) and at time $t_{k+1}=(k+1)\Delta t$, in which $k=0,1,\ldots$ and $\Delta t=$ time step, can be expressed as

$$\mathbf{y}_{k+1}=\mathbf{L}_{y}\left[\ddot{\mathbf{q}}^{T}_{k+1},\dot{\mathbf{q}}^{T}_{k+1},\mathbf{q}^{T}_{k+1},\left(\ddot{\mathbf{u}}^{g}_{k+1}\right)^{T}\right]^{T}+\mathbf{v}_{k+1}=\hat{\mathbf{y}}_{k+1}+\mathbf{v}_{k+1} \tag{8.2}$$

where $\mathbf{y} \in \mathbb{R}^{n_y}$ = vector of recorded structural response quantities, $\hat{\mathbf{y}} \in \mathbb{R}^{n_y}$ = vector of predicted structural response quantities from the FE model, $\mathbf{L}_y \in \mathbb{R}^{n_y \times 3n+r}$ = output matrix (known), and $\mathbf{v} \in \mathbb{R}^{n_y}$ = output measurement noise vector assumed to be additive white Gaussian noise (AWGN) with zero-mean and covariance matrix $\mathbf{R}_{k+1}$, i.e., $\mathbf{v}_{k+1} \sim \mathcal{N}\left(\mathbf{0}, \mathbf{R}_{k+1}\right)$. Equation (8.2) assumes that the nonlinear FE model can predict with reasonable accuracy the actual response of the structure of interest. Research conducted in the field of nonlinear modeling and response simulation of civil structures has shown that this goal can be achieved using mechanics-based nonlinear FE models with well calibrated material constitutive models (e.g., Uriz et al. 2008, Martinelli and Filippou 2009, Ebrahimian et al. 2014).

From Equations (8.1) and (8.2), the vector of recorded response quantities at time t_{k+1}, $\mathbf{y}_{k+1}$, can be expressed as a nonlinear function of the modeling parameters ($\boldsymbol{\theta}$), input ground acceleration time histories ($\ddot{\mathbf{U}}_{k+1}^{g}$), and initial conditions ($\mathbf{q}_0, \dot{\mathbf{q}}_0$) of the FE model, i.e.,

$$\mathbf{y}_{k+1} = \mathbf{h}_{k+1}\left(\boldsymbol{\theta}, \ddot{\mathbf{U}}_{k+1}^{g}, \mathbf{q}_0, \dot{\mathbf{q}}_0\right) + \mathbf{v}_{k+1} \tag{8.3}$$

where $\mathbf{h}_{k+1}(\cdot)$ is a nonlinear response function of the nonlinear FE model at time t_{k+1} and $\ddot{\mathbf{U}}_{k+1}^{g} = \left[\left(\ddot{\mathbf{u}}_1^{g}\right)^T, \left(\ddot{\mathbf{u}}_2^{g}\right)^T, ..., \left(\ddot{\mathbf{u}}_{k+1}^{g}\right)^T\right]^T$ is the input ground acceleration time history from time t_1 to t_{k+1}. Without loss of generality, it is assumes that the initial nodal displacement and velocity vectors, $\mathbf{q}_0$ and $\dot{\mathbf{q}}_0$, are equal to zero henceforth.

If the unknown time-invariant modeling parameter vector, $\boldsymbol{\theta}$, is modeled as a stationary process according to the Bayesian approach, the evolution of which is characterized by a random walk process, the nonlinear parameter estimation problem at time t_{k+1} ($k = 0,1,\ldots,N-1$ with $N =$ number of data samples of the input excitation) can be formulated as

$$\begin{cases} \boldsymbol{\theta}_{k+1} = \boldsymbol{\theta}_k + \boldsymbol{\gamma}_k \\ \mathbf{y}_{k+1} = \mathbf{h}_{k+1}\left(\boldsymbol{\theta}_{k+1}, \ddot{\mathbf{U}}^g_{k+1}\right) + \mathbf{v}_{k+1} \end{cases} \tag{8.4}$$

where $\boldsymbol{\gamma}_k$ and $\mathbf{v}_k$ are called process noise and measurement noise, respectively, and are assumed to be independent AWGN processes with zero mean vectors and diagonal covariance matrices $\mathbf{Q}_k$ and $\mathbf{R}_k$, respectively, i.e., $\boldsymbol{\gamma}_k \sim \mathcal{N}(\mathbf{0}, \mathbf{Q}_k)$ and $\mathbf{v}_{k+1} \sim \mathcal{N}(\mathbf{0}, \mathbf{R}_{k+1})$. Equation (8.4) represent a nonlinear state-space model, which can be used to estimate the unknown modeling parameter vector, $\boldsymbol{\theta}$, by using Bayesian filtering techniques (Haykin 2001, Simon 2006). In this chapter, the UKF (Julier and Uhlmann 1997, Wan and van der Merwe 2000) is used as parameter estimation tool. The parameter estimation problem for the identification of hysteretic structures formulated in Equation (8.4) is convenient and practical, because it requires estimating a low number of parameters by taking advantage of the mechanics-based nonlinear FE model. Only one set of material parameters needs to be considered in $\boldsymbol{\theta}$ for each material present in the structure. The formulation described by Equation (8.4) does not account for unmeasured input excitations and model uncertainty. Potential detrimental effects of input measurement noise will be studied later in the chapter, whereas study of model uncertainty is beyond the scope of this chapter.

For frame-type structures, distributed-plasticity FE models (force-based and displacement-based nonlinear beam-column FE models) provide a good compromise between computational cost, numerical robustness, and accuracy (Taucer et al. 1991). In these types of FE models, material nonlinearity can occur at any monitored cross-section (integration point or IP) along the element. The element behavior is obtained by numerical integration of the section response along the element. Element cross-sections are discretized in longitudinal fibers, which permit to simulate the section nonlinear response using uniaxial material constitutive laws for the fibers, which are defined by time-invariant parameters. Figure 8.1 shows a schematic representation of the hierarchical discretization levels in distributed plasticity FE models of RC frame-type structures.

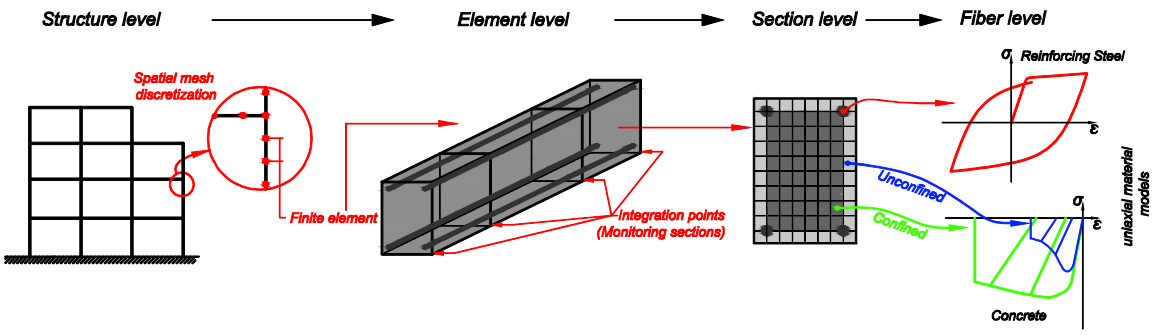

Figure 8.1: Hierarchical discretization levels in distributed plasticity FE models of frame-type RC structures.

8.3. Unscented Kalman filter for nonlinear FE model updating

The UKF is proposed to solve the parameter estimation problem defined by the nonlinear state-space model in Equation (8.4). The goal is to estimate the probability density function (*pdf*) of the modeling parameters at time t_{k+1} given the known noisy

input and output measurement data until time t_{k+1}, i.e., $p\left(\boldsymbol{\theta}_{k+1}\middle|\ddot{\mathbf{U}}_{k+1}^{g},\mathbf{Y}_{k+1}\right)$ where $\mathbf{Y}_{k+1}=\left[\mathbf{y}_1^T,\mathbf{y}_2^T,\ldots,\mathbf{y}_{k+1}^T\right]^T$. To this end, a recursive prediction-correction process is employed. In the prediction step the *a priori pdf* at time t_{k+1} is computed as

$$p\left(\boldsymbol{\theta}_{k+1|k}\right)=p\left(\boldsymbol{\theta}_{k+1}\middle|\ddot{\mathbf{U}}_{k}^{g},\mathbf{Y}_{k}\right)=\int_{\mathbb{R}^{n_\theta}}p\left(\boldsymbol{\theta}_{k}\middle|\ddot{\mathbf{U}}_{k}^{g},\mathbf{Y}_{k}\right)p\left(\boldsymbol{\theta}_{k+1}\middle|\boldsymbol{\theta}_{k},\ddot{\mathbf{U}}_{k}^{g}\right)d\boldsymbol{\theta}_{k} \tag{8.5}$$

where $p\left(\boldsymbol{\theta}_{k}\middle|\ddot{\mathbf{U}}_{k}^{g},\mathbf{Y}_{k}\right)$ is the *a posteriori pdf* at time t_k and $p\left(\boldsymbol{\theta}_{k+1}\middle|\boldsymbol{\theta}_{k},\ddot{\mathbf{U}}_{k}^{g}\right)$ is obtained from the first expression in Equation (8.4). In the correction step, the *a posteriori pdf* at time t_{k+1} is computed as

$$p\left(\boldsymbol{\theta}_{k+1|k+1}\right)=p\left(\boldsymbol{\theta}_{k+1}\middle|\ddot{\mathbf{U}}_{k+1}^{g},\mathbf{Y}_{k+1}\right)=\frac{p\left(\boldsymbol{\theta}_{k+1}\middle|\ddot{\mathbf{U}}_{k}^{g},\mathbf{Y}_{k}\right)p\left(\mathbf{y}_{k+1}\middle|\boldsymbol{\theta}_{k+1},\ddot{\mathbf{U}}_{k+1}^{g}\right)}{\int_{\mathbb{R}^{n_\theta}}p\left(\boldsymbol{\theta}_{k+1}\middle|\ddot{\mathbf{U}}_{k}^{g},\mathbf{Y}_{k}\right)p\left(\mathbf{y}_{k+1}\middle|\boldsymbol{\theta}_{k+1},\ddot{\mathbf{U}}_{k+1}^{g}\right)d\boldsymbol{\theta}_{k+1}} \tag{8.6}$$

Multi-dimensional integrals involved in Equations (8.5) and (8.6) are usually intractable and consequently approximate solutions to find $p\left(\boldsymbol{\theta}_{k+1|k+1}\right)$ need to be adopted. Local and global approaches (Arasaratnam and Haykin 2009) are proposed in the literature to find approximate solutions. Methods in the local approach assume a given distribution for the posterior *pdf*, $p\left(\boldsymbol{\theta}_{k+1|k+1}\right)$, being Gaussian the most popular choice. The EKF and UKF are in this category. Methods in the global approach do not make any assumption about the posterior *pdf*, but they are computationally very demanding. Particle filters fall in this group.

The UKF assumes that the posterior *pdf* is Gaussian, consequently it is completely determined by its mean vector and covariance matrix, i.e., $p\left(\boldsymbol{\theta}_{k+1|k+1}\right)=\mathcal{N}^{\circ}\left(\boldsymbol{\theta}_{k+1};\overline{\boldsymbol{\theta}}_{k+1|k+1},\mathbf{P}_{k+1|k+1}^{\boldsymbol{\theta}\boldsymbol{\theta}}\right)$, where $\mathcal{N}^{\circ}\left(\boldsymbol{\theta}_{k+1};\overline{\boldsymbol{\theta}}_{k+1|k+1},\mathbf{P}_{k+1|k+1}^{\boldsymbol{\theta}\boldsymbol{\theta}}\right)$ represents a

multivariate Gaussian distribution with the components of $\boldsymbol{\theta}_{k+1}$ as random variables and $\bar{\boldsymbol{\theta}}_{k+1|k+1}$ and $\mathbf{P}^{\boldsymbol{\theta\theta}}_{k+1|k+1}$ denote the posterior mean and posterior covariance matrix of $\boldsymbol{\theta}_{k+1}$ given $\mathbf{Y}_{k+1}$ and $\ddot{\mathbf{U}}^{g}_{k+1}$.

The UKF uses the unscented transform (UT) to obtain estimates of the mean vector and covariance matrix of the modeling parameter vector ($\boldsymbol{\theta}$), denoted by $\hat{\boldsymbol{\theta}}$ and $\hat{\mathbf{P}}^{\boldsymbol{\theta\theta}}$, respectively, by defining a set of deterministically chosen sample points (referred to as sigma points or *SP*s) denoted as $\mathfrak{S}$. When the *SP*s are propagated through a nonlinear vector function, they capture the true mean and covariance matrix up to the second order of the Taylor series expansion of the nonlinear function (third order of the Taylor series expansion for a Gaussian random vector) (Wan and van der Merwe 2000). The UKF avoids linearization of the nonlinear response function of the nonlinear FE model and consequently does not require computation of the Jacobian matrix of $\mathbf{h}_{k+1}(\cdot)$ with respect to the modeling parameters ($\boldsymbol{\theta}$). However, at every time step that the FE model needs to be updated, $(2n_{\theta}+1)$ FE models need to be run , which corresponds to the number of *SP*s for the case of the scaled UT. Figure 8.2 summarizes the UKF algorithm for the parameter estimation problem of the nonlinear FE model. $\mathcal{Y}^{(i)}_{k+1}$ is the output vector at time t_{k+1} corresponding to the *SP* $\mathfrak{S}^{(i)}_{k+1}$, and W_m and W_c are the weight coefficients of the SPs to estimate the mean vector and covariance matrix, respectively. $\hat{\boldsymbol{\theta}}_{k+1|k+1}$ and $\hat{\mathbf{P}}^{\boldsymbol{\theta\theta}}_{k+1|k+1}$ denote, respectively, the estimates of the mean vector and covariance matrix of the modeling parameter vector at time t_{k+1} given $\mathbf{Y}_{k+1}$ and $\ddot{\mathbf{U}}^{g}_{k+1}$. $\hat{\boldsymbol{\theta}}_0$

and $\hat{\mathbf{P}}_0^{\boldsymbol{\theta\theta}}$ are the initial estimates of the mean vector and covariance matrix of the modeling parameters. In this chapter the scaled UT with parameters $\alpha = 0.01$, $\kappa = 0$, and $\beta = 2$ is used. More details about the formulation of the parameter estimation problem for frame-type distributed-plasticity FE models using the UKF and the UT is discussed elsewhere (Astroza et al. 2015).

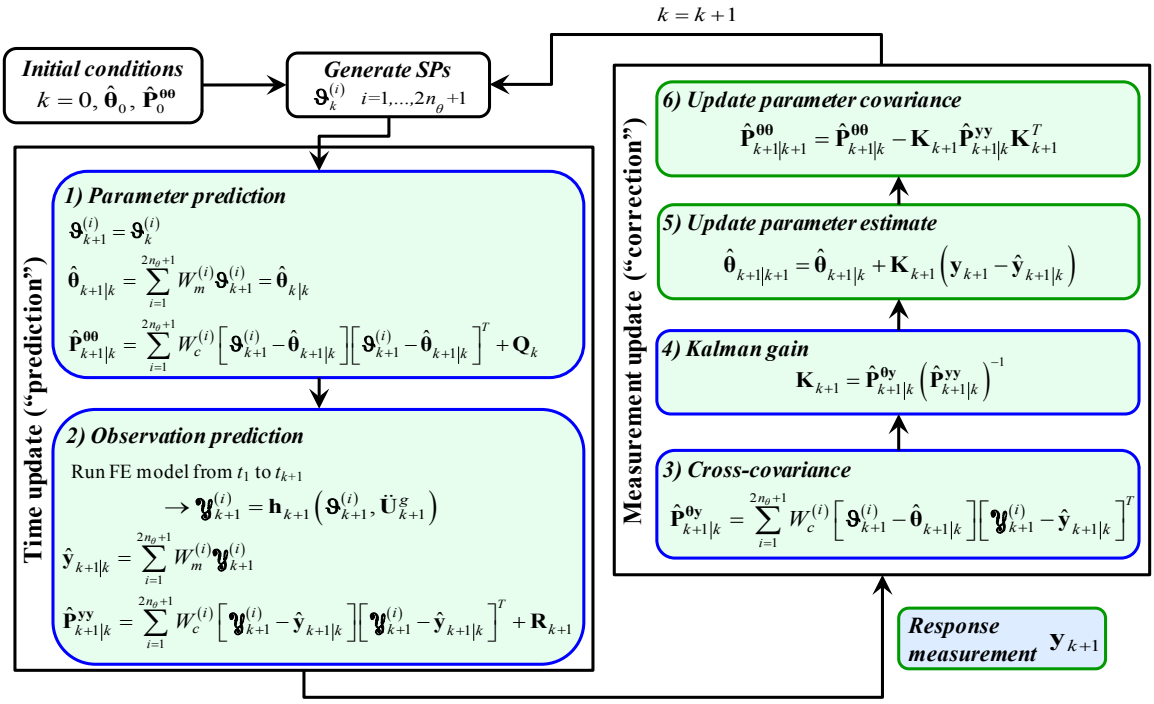

Figure 8.2: Framework for nonlinear FE model updating using the UKF.

8.4. Verification study

Nonlinear response of a mechanics-based nonlinear 3D 5-story 2-by-1 bay RC frame building subjected to bidirectional seismic excitation is simulated using the open-source object-oriented software framework *OpenSees* (2014). Translation components of ground acceleration recorded at the Sylmar County Hospital (EQ1) during the 1994 Northridge earthquake and at Los Gatos station (EQ2) during the 1989 Loma Prieta

earthquake are independently considered as input base excitations. Components 360° and 90° of EQ1 and EW and NS of EQ2 are applied in the longitudinal and transverse direction of the building, respectively (Figure 8.3). The acceleration ground motions were recorded at a sampling rate of 50 Hz, filtered with a band-pass filter with cutoff frequencies of 0.1 and 23.0 Hz, and have $N = 750$ and $N = 600$ data samples for EQ1 and EQ2, respectively. The peak ground acceleration (PGA) of components 360° and 90° of EQ1 were 0.84*g* and 0.60*g* , respectively, while PGA of components EW and NS of EQ2 were 0.33*g* and 0.45*g*, respectively.

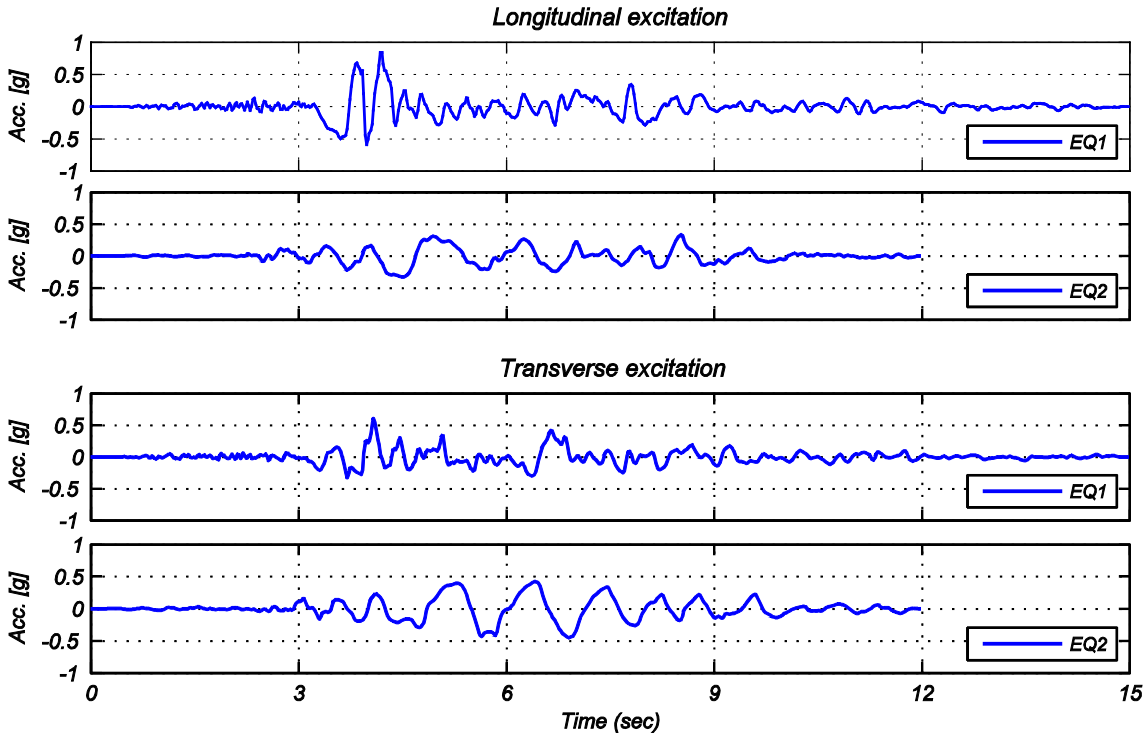

Figure 8.3: Acceleration time history of the input seismic motion.

The building is designed as an intermediate moment-resisting frame according to the 2006 International Building Code (ICC 2006) for a location in downtown Seattle, WA, with Site Class D soil conditions and a short-period spectral acceleration

$S_{MS} = 1.37g$ and a one-second spectral acceleration $S_{M1} = 0.53g$. The frame has a story height of 4.0 m and bay width of 5.0 m and 6.0 m in the longitudinal (X) and transverse (Z) directions, respectively (Figure 8.4a). The frame has six identical 0.45×0.45 m RC columns reinforced with 8 #8 longitudinal reinforcement bars and #3 @ 150 mm transverse reinforcement. RC beams in longitudinal direction are 0.40×0.40 m and are reinforced with 6 #8 longitudinal reinforcement bars and #3 @ 100 mm transverse reinforcement. RC beams in transverse direction are 0.40×0.45 m and are reinforced with 8 #8 longitudinal reinforcement bars and #3 @ 100 mm transverse reinforcement. All reinforcements in beams and columns are of Grade 60 steel.

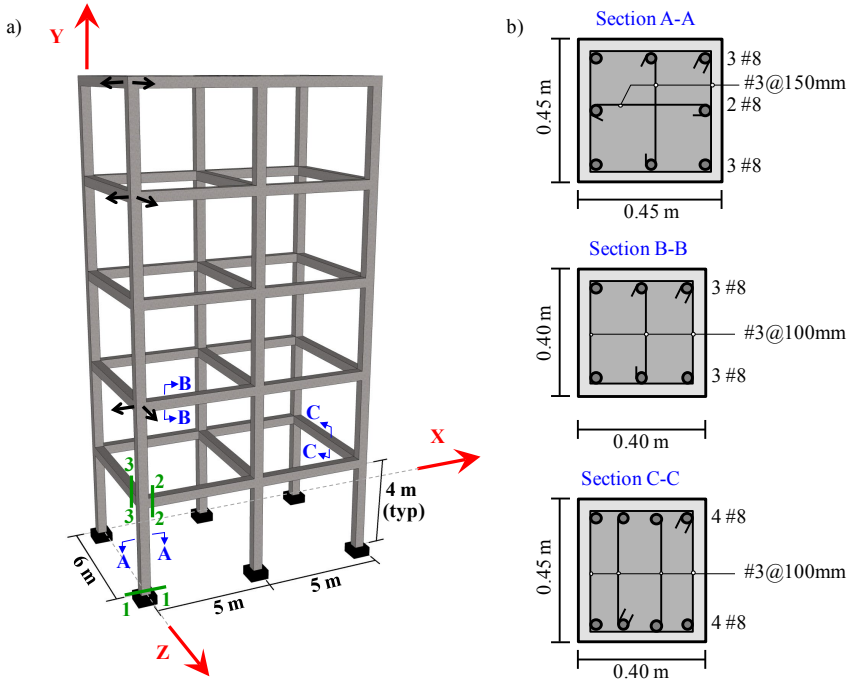

Figure 8.4: 3D RC frame building structure: (a) Isometric view, (b) Cross-section of columns and beams elements.

The Popovics concrete constitutive law (Popovics 1973), *Concrete04* in *OpenSees*, without tension is used to model the concrete fibers. Four material parameters define the uniaxial stress-strain relationship in the Popovics material model. These

parameters are the modulus of elasticity (E_c), peak compressive strength (f'_{cc}), strain at peak compressive strength (ε_{cc}), and strain at crushing strength (ε_{cu}). The values of f'_{cc}, ε_{cc}, and ε_{cu} correspond to the confined state of concrete and are computed based on the undamaged properties of the concrete material. f'_{cc} and ε_{cc} account for confinement effects of the transverse reinforcement according to Mander et al. 1988, whereas ε_{cu} is computed as suggested by Scott et al. (1982). The modified Giuffré-Menegotto-Pinto model (Filippou et al. 1983), *Steel02* in *OpenSees*, is used to model the nonlinear uniaxial stress-strain behavior of the reinforcing steel fibers. Four primary parameters of this constitutive model consists of modulus of elasticity (E_s), yield strength (f_y), strain-hardening ratio (b), and a parameter describing the curvature of the transition curve between the asymptotes of the elastic and plastic branches during the first loading (R_0). Figure 8.5 shows the uniaxial material constitutive laws used to model concrete and reinforcing steel fibers and the parameters describing them.

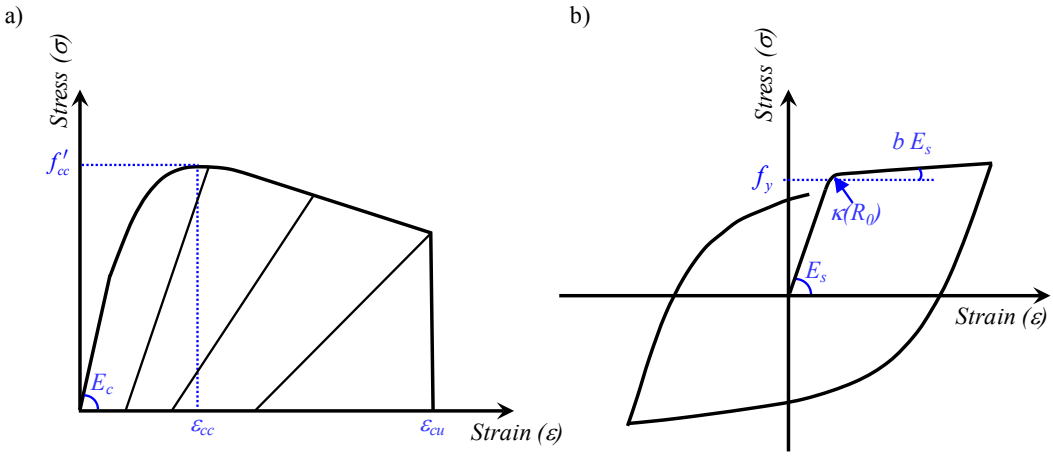

Figure 8.5: Uniaxial material constitutive laws used in the FE model: (a) Concrete, (b) Reinforcing steel.

Each beam and column member is modeled using one force-based (FB) beam-column element. Numerical integration along the length of the elements is performed using Gauss-Lobatto quadrature with five IPs for columns, five IPs for longitudinal beams, and six IPs for transverse beams. In force-based beam-column elements deformations localize at a single IP, therefore the number of IPs on each member is selected such that the weight of the IP associated with the section accumulating the deformation approximately equals the expected physical length where deformation concentrates (plastic hinge). In this chapter, the plastic hinge length is taken equal to one half of the cross-section height for beams and equal to the cross-section height for columns. Column and beams cross-sections are discretized into longitudinal fibers as shown in Figure 8.6b. Linear section shear and torsion force-deformation models are aggregated, uncoupled with the inelastic coupled flexural-axial behavior, at the section level and along the element. Nodal masses and distributed gravity loads acting on longitudinal and transverse beams considered in the FE model are computed from the design dead and live loads (ICC 2006) and are shown in Figure 8.6a.

A set of modeling parameter values, referred to as true values, are assumed for concrete and reinforcing steel materials. These values of the material parameters are: $E_s^{true} = 200\ GPa$, $f_y^{true} = 414\ MPa$, $R_0^{true} = 18$, $b^{true} = 0.05$, $E_c^{true} = 27600\ MPa$, $f_{cc}'^{\,true} = 40\ MPa$, and $\varepsilon_{cc}^{true} = 0.0035$. It is noteworthy that ε_{cu} is not considered as a parameter to be estimated because its effect on the response of the structure is negligible. In addition to the parameters characterizing the nonlinear material constitutive laws, damping parameters will also be considered later in the estimation phase. The sources of

energy dissipation beyond energy dissipated through hysteretic material behavior are modeled using mass and tangent stiffness-proportional Rayleigh damping (based on the tangent stiffness matrix at the last converged step of analysis). A critical damping ratio of 2% for the first and second natural periods (after application of the gravity loads) in the longitudinal direction of the building, T_1 = 1.67 sec and T_2 = 0.54 sec, is considered. Therefore, the mass and stiffness proportional parameters used to describe the Rayleigh damping are $\alpha_M^{true} = 0.1137$ and $\beta_K^{true} = 0.0026$, respectively. The FE model described above and the true values of the parameters are used to simulate the response of the structure, which is referred as true response hereafter.

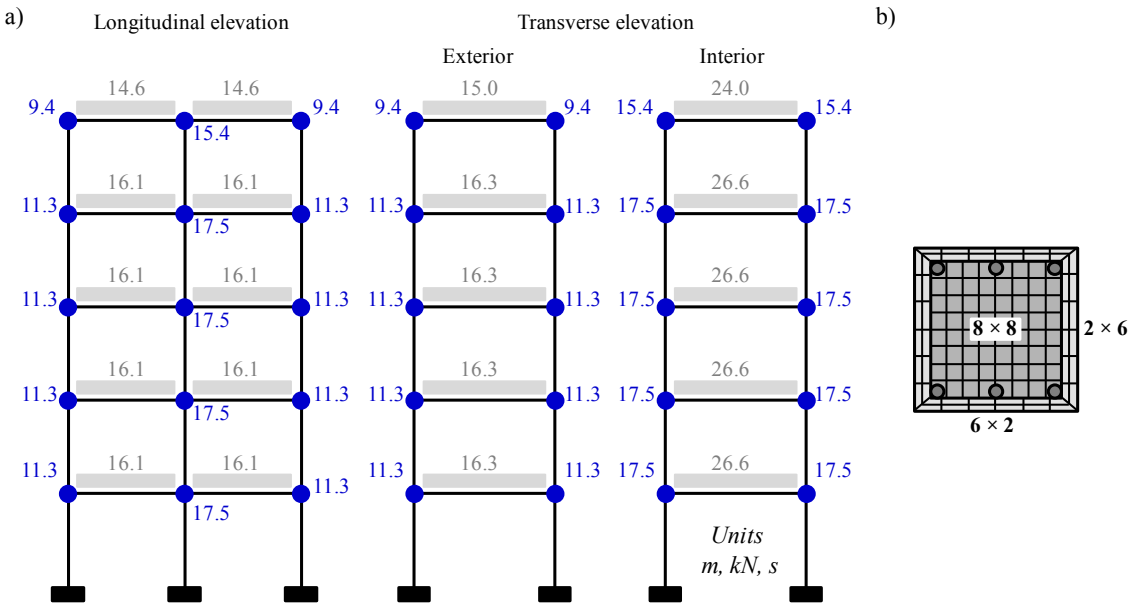

Figure 8.6: Finite element model: (a) nodal masses and distributed loads on beams, (b) cross-section fiber discretization.

Ten modeling parameters describing the concrete and reinforcing steel constitutive laws and the Rayleigh damping are considered as unknown and define the modeling parameter vector ($\boldsymbol{\theta}$), i.e., $\boldsymbol{\theta} = [E_s, f_y, R_0, b, E_c, f'_{cc}, \varepsilon_{cc}, \alpha_M, \beta_K]^T \in \mathbb{R}^{9\times 1}$. The

true responses of the structure are polluted by output measurement noise to define the measured output data ($\mathbf{y}$), which in conjunction with the translational components of input ground acceleration ($\ddot{\mathbf{u}}^g$) recorded at Sylmar and Los Gatos stations (Figure 8.3) are used to estimate the modeling parameter vector and update the nonlinear FE model of the 3D RC structure. The output measurement noise is modeled as a zero-mean AWGN vector, and it represents all the sources of noise existing when recording data in real world, e.g., sensor and data acquisition (DAQ) system noises and ambient vibrations. In what follows, the same FE model of the structure as used to obtain the true responses is considered for parameter estimation, i.e., it is assumed that there is no modeling uncertainty. In addition, no input measurement noise is considered initially. Potential detrimental effects of presence of input measurement noise are studied in Section 8.4.5.

8.4.1. Structural response recorded by a sparse accelerometer array

To analyze the robustness of the parameter estimation framework for the case of limited output measurements, a sparse accelerometer array consisting of two accelerometers, one for each translational direction, at 3rd, 5th, and roof floors is considered (black arrows in Figure 8.4 indicate the location of accelerometers used to measure the relative acceleration responses). A 1.0%*g* root-mean-square (RMS) zero-mean white Gaussian output measurement noise is added to each true relative acceleration response after completion of the structural response simulation to pollute the true responses, i.e., the actual covariance matrix of the output measurement noise is $0.96\times10^{-2}\mathbf{I}_6\left(m/s^2\right)^2$ where $\mathbf{I}_i = i\times i$ identity matrix. Statistically uncorrelated

realizations of output measurement noise are considered for different acceleration responses. In the estimation, it is assumed that the output measurement noise is a zero-mean Gaussian process with a covariance matrix $\mathbf{R}_{k+1} = \mathbf{R} = 0.24 \times 10^{-2} \mathbf{I}_6 \left(m/s^2 \right)^2$, i.e., a standard deviation (or RMS) of 0.5%*g* RMS is estimated for the output measurement noise. A covariance matrix of the output measurement noise different to the true one is considered in the estimation, because in practice only an estimate of the actual variances of the output measurement noises can be inferred based on the characteristics of the sensors and DAQ system, experience, and engineering judgment. Time-invariant second order statistics are assumed for the process noise $\boldsymbol{\gamma}_k$, with zero-mean and covariance matrix $\mathbf{Q}_k = \mathbf{Q}$. The diagonal entries of $\mathbf{Q}$ are assumed equal to $(q \times \hat{\theta}_0^i)^2$ where $i = 1, \ldots, 9$ and $q = 1 \times 10^{-4}$, i.e., the process noise covariance matrix is constructed assuming a coefficient of variation of 1×10^{-4} for the initial estimate of the mean of the material parameters ($\hat{\boldsymbol{\theta}}_0$).

Two cases are considered to study the effect of the initial estimate of the mean of the modeling parameters ($\hat{\boldsymbol{\theta}}_0$), namely, $\hat{\boldsymbol{\theta}}_0 = 1.4\boldsymbol{\theta}^{true}$ and $\hat{\boldsymbol{\theta}}_0 = 2.0\boldsymbol{\theta}^{true}$. For all cases the initial estimate of the covariance matrix of the modeling parameters, $\hat{\mathbf{P}}_0^{\boldsymbol{\theta}\boldsymbol{\theta}}$, is assumed to be diagonal (initial estimates of the modeling parameters are statistically uncorrelated) with terms computed assuming a coefficient of variation of 25% of the initial estimate of the mean $\hat{\boldsymbol{\theta}}_0$, i.e., the diagonal entries of $\hat{\mathbf{P}}_0^{\boldsymbol{\theta}\boldsymbol{\theta}}$ are computed as $(p \times \hat{\theta}_0^i)^2$ where $i = 1, \ldots, 9$ and $p = 0.25$.

The UKF is used to estimate the *a posteriori* mean vector and covariance matrix of the modeling parameters at each time step (see Figure 8.2). Because nine modeling parameters need to be estimated, 19 SPs $(=2\times 9+1)$ are used. This means that 19 nonlinear FE models (one for each *SP*) need to be run from the t_1 to t_k, with $k=1,\ldots,N$ and $N=750$ for EQ1 and $N=600$ for EQ2, when updating the modeling parameters at time t_k. Table 8.1 reports the final *a posteriori* mean estimates of the modeling parameters (which correspond to stable and converged values) normalized by their corresponding true parameter values for both input motions and the two cases of $\hat{\boldsymbol{\theta}}_0$ considered. For the case $\hat{\boldsymbol{\theta}}_0 = 1.4\boldsymbol{\theta}^{true}$ the eight modeling parameters associated to the nonlinear constitutive material models are accurately estimated with relative errors less than 6%. The stiffness-proportional of Rayleigh damping coefficient (β_K) is also accurately estimated, however for the mass-proportional Rayleigh damping coefficient (α_M) is estimated with the largest relative error, 8% and 16% for EQ1 and EQ2, respectively, among all the modeling parameters considered in the estimation.

Table 8.1: Final estimates of the mean of the modeling parameters obtained using a sparse accelerometer array**.**

Case	$\hat{\boldsymbol{\theta}}_0$	EQ	Modeling parameter								
			$\frac{E_s}{E_s^{true}}$	$\frac{f_y}{f_y^{true}}$	$\frac{R_0}{R_0^{true}}$	$\frac{b}{b^{true}}$	$\frac{E_c}{E_c^{true}}$	$\frac{f'_{cc}}{f'^{\,true}_{cc}}$	$\frac{\varepsilon_{cc}}{\varepsilon_{cc}^{true}}$	$\frac{\alpha_M}{\alpha_M^{true}}$	$\frac{\beta_K}{\beta_K^{true}}$
1	$1.4\boldsymbol{\theta}^{true}$	EQ1	1.00	1.00	1.00	1.00	0.98	0.98	1.03	1.08	0.99
2		EQ2	1.00	1.00	0.98	1.02	1.01	1.00	1.06	1.16	1.00
3	$2.0\boldsymbol{\theta}^{true}$	EQ1	1.00	0.98	1.07	1.09	1.01	1.03	0.99	0.87	1.00
4		EQ2	1.00	1.01	0.97	1.07	1.02	0.90	1.00	1.35	1.00

For the case $\hat{\boldsymbol{\theta}}_0 = 2.0\boldsymbol{\theta}^{true}$ consistent results are obtained. Nevertheless, in this case the relative errors of some modeling parameters increase. Relative error of α_M increases to 13% and 35% for EQ1 and EQ2, respectively. Post-yield parameters associated to the modified Giuffre-Menegotto-Pinto constitutive law, R_0 and b, are estimated with relative errors of 7% and 9% for EQ1 and 3% and 7% for EQ2, while f'_{cc} is estimated with an error of 10% for EQ2. Convergence to inaccurate values of some of the modeling parameters can be due to: (i) inadequate performance of the parameter estimation framework, (ii) low sensitivity of the output measurements with respect to these parameters (i.e., some parameters might not be identifiable), or (iii) these modeling parameters are not activated during the response of the structure. In the latter case, not activated modeling parameters do not change their initial values (Astroza et al. 2015, Ebrahimian et al. 2015), which is not the case here. To check that the estimation process performs correctly given the input and output measurements, the relative RMS error (*RRMSE*) between the true responses and their counterparts obtained using the final estimates of the modeling parameters ($\hat{\boldsymbol{\theta}}_N$) are computed (Table 8.2). It is noted that the RRMS error between two signals $\mathbf{s}^1$ and $\mathbf{s}^2$ is compute as $RRMSE[\%] = \sqrt{\left[1/Ns\sum_{k=1}^{Ns}\left(s_k^1 - s_k^2\right)^2\right]} \Big/ \sqrt{\left[1/Ns\sum_{k=1}^{Ns}\left(s_k^1\right)^2\right]} \times 100$, where Ns is the total number of data samples. In Table 8.2 the output measurement $\ddot{\mathbf{q}}_{ij}^t$ represent the relative acceleration time history at story i in direction j, where L and T are longitudinal and transverse directions, respectively. The *RRMSE*s between the true responses and their

counterparts obtained using the initial estimate of the modeling parameters ($\hat{\boldsymbol{\theta}}_0$) are also included. From the *RRMSE*s between the true output measurements and their counterparts based on the initial and final estimates of the modeling parameters is evident that the FE model updating framework (i.e., parameter estimation procedure) works properly and therefore the considered output measurement responses are not very sensitive to parameters α_M, b, and f'_{cc}. It is noteworthy that the noisy measured responses for EQ2 have a lower signal-to-noise ratio than those for EQ1, because the amplitude of the responses are lower for EQ1 and the same noise is considered for both cases. A detailed study about identifiability, which investigates if the modeling parameter vector $\boldsymbol{\theta}$ can be determined from the measured data and in the general case can be evaluated by examining the rank of the Fisher Information matrix of the model, is out of the scope of this chapter and is the subject of ongoing research by the authors.

Table 8.2: Relative RMS errors (in %) of the output measurements.

	Case	$\hat{\boldsymbol{\theta}}$	EQ	Output measurement					
				$\mathbf{y}_1=\ddot{\mathbf{q}}^t_{3L}$	$\mathbf{y}_2=\ddot{\mathbf{q}}^t_{3T}$	$\mathbf{y}_3=\ddot{\mathbf{q}}^t_{5L}$	$\mathbf{y}_4=\ddot{\mathbf{q}}^t_{5T}$	$\mathbf{y}_5=\ddot{\mathbf{q}}^t_{6L}$	$\mathbf{y}_6=\ddot{\mathbf{q}}^t_{6T}$
Initial estimates	1	$\hat{\boldsymbol{\theta}}_0=1.4\boldsymbol{\theta}^{true}$	EQ1	70.5	79.87	97.71	101.97	89.88	106.68
	2		EQ2	126.02	57.41	78.45	113.52	38.59	62.69
	3	$\hat{\boldsymbol{\theta}}_0=2.0\boldsymbol{\theta}^{true}$	EQ1	96.64	118.23	142.97	105.52	104.72	121.27
	4		EQ2	129.78	87.72	96.01	116.82	66.22	76.36
Final estimates	1	$\hat{\boldsymbol{\theta}}_N\left(\hat{\boldsymbol{\theta}}_0=1.4\boldsymbol{\theta}^{true}\right)$	EQ1	1.21	1.17	1.32	1.85	1.69	1.75
	2		EQ2	3.67	2.29	1.74	2.35	1.43	1.51
	3	$\hat{\boldsymbol{\theta}}_N\left(\hat{\boldsymbol{\theta}}_0=2.0\boldsymbol{\theta}^{true}\right)$	EQ1	4.65	2.44	2.49	3.09	2.84	2.49
	4		EQ2	5.96	4.01	3.29	5.30	3.29	3.04

Figure 8.7 and Figure 8.8 show the time histories of the *a posteriori* estimates of the mean and coefficient of variation (CV) of the modeling parameters, respectively, for EQ1 and the two initial mean estimates ($\hat{\boldsymbol{\theta}}_0$) aforementioned. The mean estimates of all the modeling parameters, which are normalized by their corresponding true values, converge to stable values soon after the strongest part of the input excitations at around 5 sec (Figure 8.7). Stiffness-related (E_s and E_c) and damping-related (α_M and β_K) modeling parameters start to update from the beginning of the excitation, because data contained in the measured structural responses (outputs) during low amplitude excitation carry information about these parameters. Parameter E_s reaches its converged value at around 2 sec, while E_c and β_K converge to their stable values at around 4 sec. Later, as the amplitude of the excitation increases and the structure experiences nonlinear behavior, the measured response data carry information about the parameters associated to the nonlinear behavior of concrete and reinforcing steel material models. Parameters $\varepsilon_{cc}, f'_{cc}, f_y, R_0$, and b start to update at around 3.5 sec when some concrete fibers reach their maximum strength and some reinforcing steel fibers yield and experience excursions into its nonlinear range of behavior. Accurate estimation of parameters related to the post-yield behavior of the reinforcing steel material model (R_0 and b) require that the strain ductility demand of enough steel fibers increase sufficiently. On the other hand, at the same time that the measured response data contain enough information about a modeling parameter and it starts to update and converge to its true value, the estimate of the coefficient of variation of the parameter decrease asymptotically to zero, i.e., the uncertainty in the estimation of the parameter decreases towards zero (Figure 8.8).

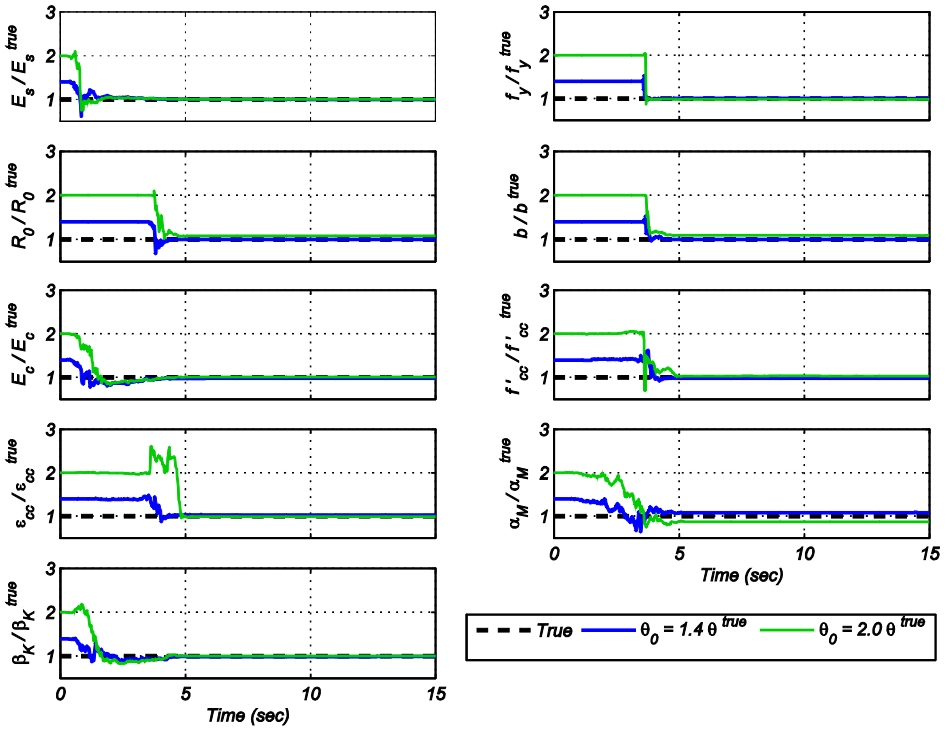

Figure 8.7: Time histories of the estimates of the mean of the modeling parameters for EQ1.

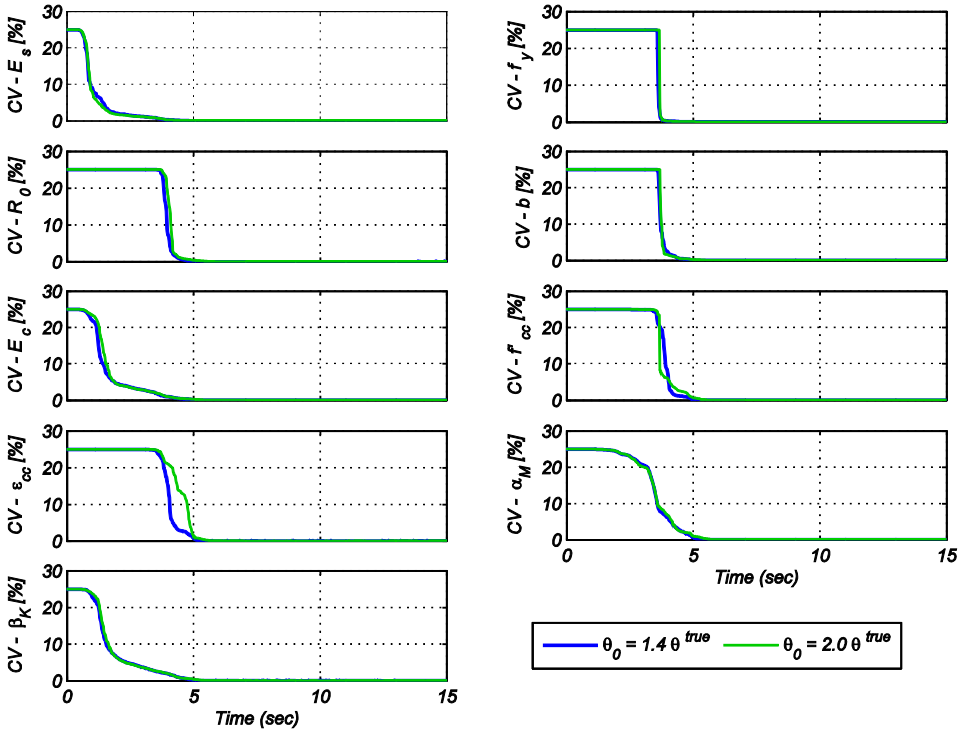

Figure 8.8: Time histories of the estimates of the standard deviations of the modeling parameters for EQ1.

Figure 8.9 compares different global and local structural response quantities of the building obtained using the true parameters $\boldsymbol{\theta}^{true}$ (i.e., true responses), the initial mean estimate of the modeling parameters ($\hat{\boldsymbol{\theta}}_0$), and the final mean estimate of the modeling parameters ($\hat{\boldsymbol{\theta}}_N$) for EQ1 and $\hat{\boldsymbol{\theta}}_0 = 1.4\boldsymbol{\theta}^{true}$. Relative acceleration response time histories of the roof of the building in its longitudinal (a^x_{roof}) and transverse (a^z_{roof}) directions are compared in Figure 8.9a-b, respectively. Figure 8.9c-d compare the base shear in longitudinal and transverse directions (V_b^x and V_b^z, respectively) normalized by the total weight of the building (W), versus the roof drift ratio in the corresponding direction (RDR^x and RDR^z). Section level responses are compared in Figure 8.9e-h, which show the moment-curvature ($M-\kappa$) responses at the base of a column (section 1-1 in Figure 8.4a), at the end of a 2nd floor longitudinal beam (section 2-2 in Figure 8.4a), and at the end of a 2nd floor transverse beam (section 3-3 in Figure 8.4a). Finally, Figure 8.9i-j compare the stress-strain responses of monitored concrete and reinforcing steel fibers at the bottom of a column (section 1-1 in Figure 8.4a). Comparison of global and local responses indicates that the updated FE model match almost perfectly the true responses. These results confirm that the proposed methodology successfully updates the nonlinear FE model by properly driving the initial mean estimate of the modeling parameters ($\hat{\boldsymbol{\theta}}_0$) to their true values ($\boldsymbol{\theta}^{true}$).

The results show the capabilities of the proposed methodology for accurate and complete DID, including detection, localization, classification, and quantification of damage provided that the mechanics-based nonlinear FE structural model is able to capture the damage mechanisms to be identified. The udpated nonlinear FE model can be

examined to asses the state of health of the structure after a potential damage-inducing event and it provides information about loss of stiffness, strength degradation, and history of the response nonlinearities experienced by the structure.

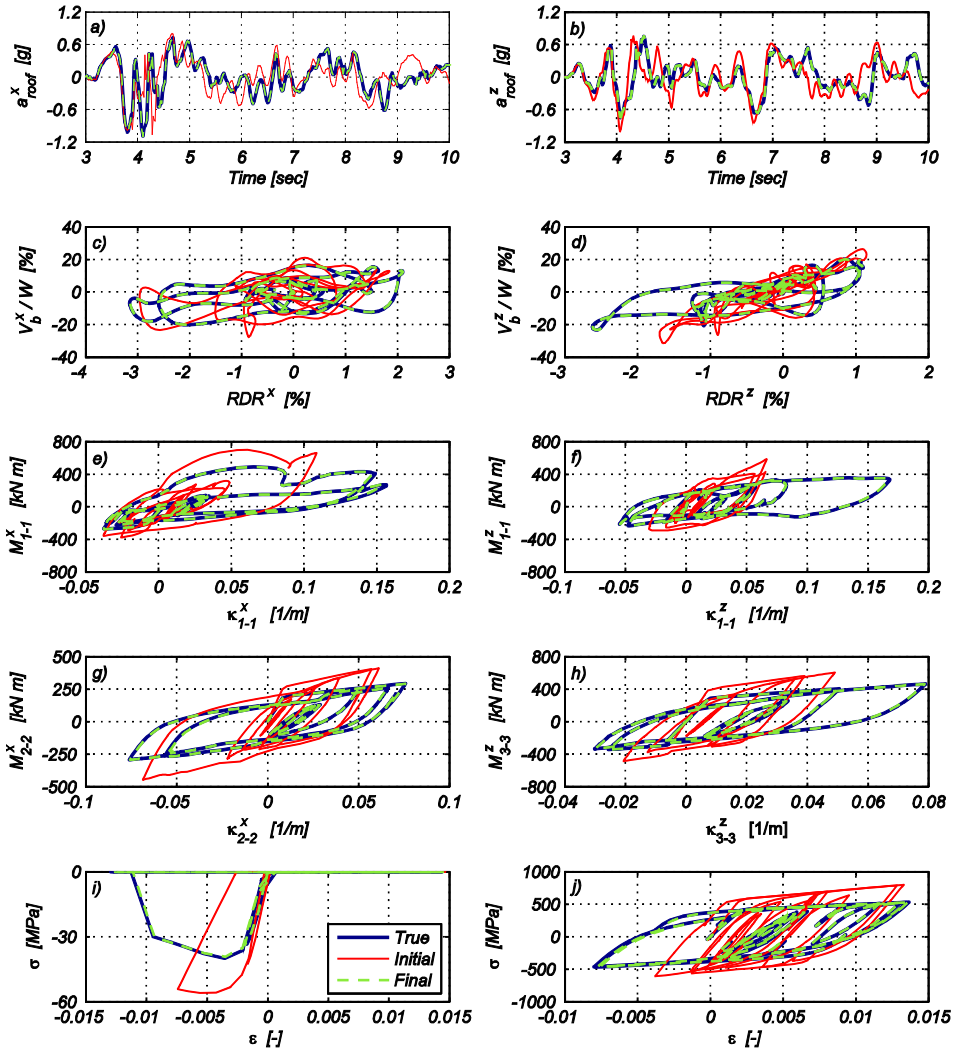

Figure 8.9: Comparison of true global and local responses of the building with their initial and final estimated counterparts for EQ1 and $\hat{\boldsymbol{\theta}}_0 = 1.4\boldsymbol{\theta}^{true}$: (a) rel. acc. response time history of the roof in longitudinal direction; (b) rel. acc. response time history of the roof in transverse direction; (c) normalized base shear vs. roof drift ratio in longitudinal direction; (d) normalized base shear vs. roof drift ratio in transverse direction; (e-f) moment vs. curvature at the base of a column (section 1-1 in Figure 8.4a); (g) moment vs. curvature at the end of a longitudinal beam (section 2-2 in Figure 8.4a); (h) moment vs. curvature at the end of a transverse beam (section 3-3 in Figure 8.4a); (i) stress vs. strain in a concrete fiber at the base of a column (section 1-1 in Figure 8.4a); (j) stress vs. strain in a reinforcing steel fiber at the base of a column (section 1-1 in Figure 8.4a).

8.4.2. Non-sequential model updating

The computational demand of the estimation framework presented in Section 8.3 is considerable because $(2n_\theta + 1)$ FE models (the number of *SP*s) need to be run from the t_1 to t_k ($k = 1,\ldots,N$ with $N =$ number of data samples of the earthquake input excitation) when updating the modeling parameters at time t_k. Recall that the response of the nonlinear FE model is history-dependent, therefore when updating the model at time t_k the FE model needs to be run from time t_1 to t_k. Three approaches to reduce the computational burden are proposed and discussed in this section. These methodologies are referred to as non-sequential because they do not need to perform the estimation process at every time step of the input earthquake excitation. All the analyses in this section consider the case of $\hat{\boldsymbol{\theta}}_0 = 1.4\boldsymbol{\theta}^{true}$ for EQ1. Results for other initial mean estimates and for EQ2 were also analyzed and found similar to and consistent with those presented in this chapter, but are not shown herein because of space limitation. The purpose of this section is to investigate the robustness, efficiency, and computational cost of the proposed non-sequential model updating schemes and compare them with the results obtained when the FE model is updated at every time step.

8.4.2.1. Non-cumulative innovation approach

One approach to reduce the computational cost of the proposed nonlinear FE model updating framework is to update the FE model every $D > 1$ time steps (D: updating step parameter) and only consider the output measurements at those time steps to construct the innovation ($\mathbf{y}_k - \hat{\mathbf{y}}_{k|k-1}$), i.e., modeling parameters are updated at time

steps $k = k + D$ instead of at time steps $k = k + 1$ (Figure 8.10a). This approach might considerably reduce the computational burden of the nonlinear FE model updating framework because most of the computational resources are consumed when running the FE models. The main disadvantage of this approach is that the measurements between updating samples are not taken into account, and consequently, a large part of the information contained in the vibration data is missed and not considered when minimizing the discrepancy between the recorded and estimated output measurements. However, the accelerometers used in earthquake engineering applications have sampling frequencies $f_s \geq 50\ Hz$, therefore the amount of data considered to estimate the modeling parameters using this non-cumulative approach might still be enough to accurately update the nonlinear FE model if the variable D is not set very large. Values $D = 5$ and $D = 3$ are considered to study this non-cumulative innovation approach.

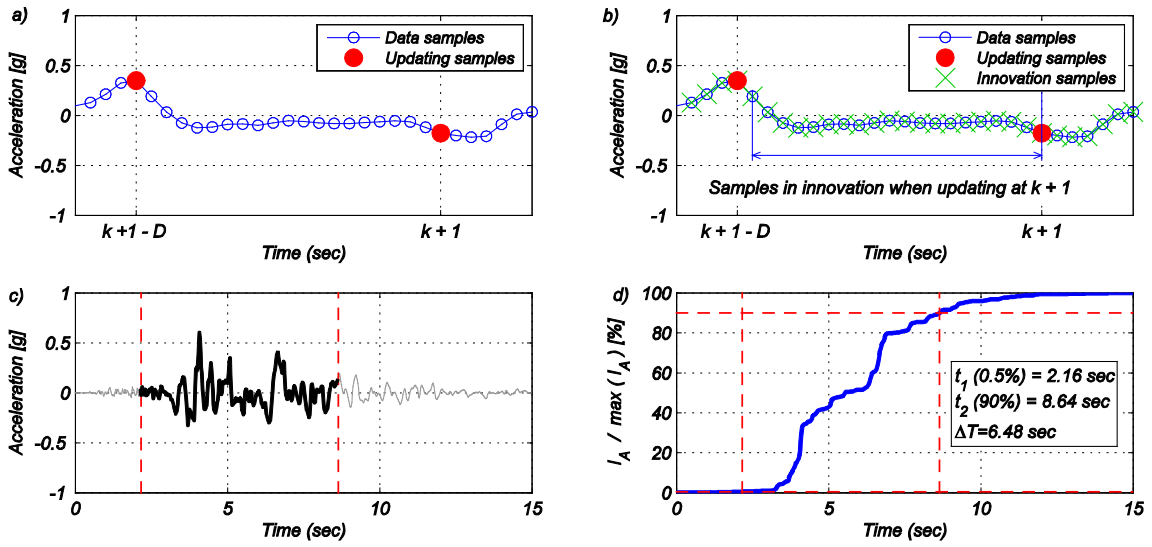

Figure 8.10: Approaches for non-sequential model updating (a) non-cumulative innovation approach, (b) cumulative innovation approach, (c) earthquake input motion and time-window for updating, (c) Husid plot and time-window for updating.

8.4.2.2. Cumulative innovation approach

A second approach of non-sequential updating also consider updating the FE model every $D>1$ time steps, but it takes into account all the output measurements from $k-D+2$ to $k+1$ when constructing the innovation vector and updating the model at time step $k+1$ (Figure 8.10b). This scheme allows to minimize the discrepancies between the estimated and actual output measurements at time steps $k-D+2$ to $k+1$, although only considers updating the FE model at time step $k+1$. Defining the augmented output measurement vector $\tilde{\mathbf{Y}}=\left[\mathbf{y}_{k-D+2}^T,\ldots,\mathbf{y}_{k-1}^T,\mathbf{y}_k^T,\mathbf{y}_{k+1}^T\right]^T\in\mathbb{R}^{Dn_y\times 1}$, the measurement covariance matrix, the cross-covariance matrix, and the Kalman gain can be computed, respectively, by

$$\hat{\mathbf{P}}_{k+1|k-D+2}^{\tilde{\mathbf{Y}}\tilde{\mathbf{Y}}}=\sum_{i=1}^{2n_\theta+1}W_c^{(i)}\left[\hat{\tilde{\mathbf{y}}}_{k+1}^{(i)}-\tilde{\mathbf{Y}}_{k+1|k-D+2}\right]\left[\hat{\tilde{\mathbf{y}}}_{k+1}^{(i)}-\tilde{\mathbf{Y}}_{k+1|k-D+2}\right]^T+\tilde{\mathbf{R}}_{k+1} \tag{8.7a}$$

$$\hat{\mathbf{P}}_{k+1|k-D+2}^{\boldsymbol{\theta}\tilde{\mathbf{Y}}}=\sum_{i=1}^{2n_\theta+1}W_c^{(i)}\left[\hat{\boldsymbol{\vartheta}}_{k+1}^{(i)}-\hat{\boldsymbol{\theta}}_{k+1|k-N+1}\right]\left[\hat{\tilde{\mathbf{y}}}_{k+1}^{(i)}-\tilde{\mathbf{Y}}_{k+1|k-D+2}\right]^T \tag{8.7b}$$

$$\tilde{\mathbf{K}}_{k+1}=\mathbf{P}_{k+1|k-D+2}^{\boldsymbol{\theta}\tilde{\mathbf{Y}}}\left(\mathbf{P}_{k+1|k-D+2}^{\tilde{\mathbf{Y}}\tilde{\mathbf{Y}}}\right)^{-1} \tag{8.7c}$$

where $\hat{\tilde{\mathbf{y}}}_{k+1}^{(i)}=\left[\hat{\mathbf{y}}_{k-D+2}^T,\ldots,\hat{\mathbf{y}}_{k-1}^T,\hat{\mathbf{y}}_k^T,\hat{\mathbf{y}}_{k+1}^T\right]^T\in\mathbb{R}^{Dn_y\times 1}=$ augmented output measurement vector corresponding to the *SP* $\hat{\boldsymbol{\vartheta}}_{k+1}^{(i)}$, which includes the responses from time steps $k-D+2$ to $k+1$ and $\tilde{\mathbf{R}}_{k+1}=diag\left[\mathbf{R}_{k-D+2},\ldots,\mathbf{R}_k,\mathbf{R}_{k+1}\right]\in\mathbb{R}^{Dn_y\times Dn_y}$. $\hat{\mathbf{P}}_{k+1|k-D+2}^{\tilde{\mathbf{Y}}\tilde{\mathbf{Y}}}$, $\hat{\mathbf{P}}_{k+1|k-D+2}^{\boldsymbol{\theta}\tilde{\mathbf{Y}}}$, and $\tilde{\mathbf{K}}_{k+1}$ replace $\hat{\mathbf{P}}_{k+1|k}^{\mathbf{yy}}$, $\hat{\mathbf{P}}_{k+1|k}^{\boldsymbol{\theta}\mathbf{y}}$, and $\mathbf{K}_{k+1}$, respectively, in Figure 8.2, while other expressions remain identical. As in previous approach, values $D=5$ and $D=3$ are considered to study the cumulative innovation approach.

8.4.2.3. Time-window update

The information required to update the modeling parameters is mostly contained in the data of the strong motion part of the earthquake excitation, therefore only input/output data corresponding to that time-window can be considered to estimate the modeling parameters and update the nonlinear FE model. The time-window considered to update the nonlinear FE model is defined here as the time interval between 0.5% and 90% of the Arias Intensity (I_A) (Arias 1970) as shown in Figure 8.10c and Figure 8.10d. The lower bound 0.5% is considered because data contained in the small amplitude part of the excitation contains information about the initial stiffness (linear-elastic) related parameters, and consequently these parameters converge still with input/output data from low-amplitude excitation (Astroza et al. 2015, Ebrahimian et al. 2015). The upper bound 90% is chosen to include the higher seismic demands and therefore the most likely time interval to include nonlinear response behavior of the structure. Since there are two components of earthquake base excitation, the time window is defined by the lowest lower bound and the highest upper bound. For the ground acceleration records of EQ1 and EQ2 the times corresponding to $0.5\% I_A$ and $90\% I_A$ and the time-window used to update the nonlinear FE model are summarized in Table 8.3. Using the time-window approach only $N = 325$ and $N = 292$ instead of $N = 750$ and $N = 600$ are used to update the FE model for EQ1 and EQ2, respectively. All analyses of this section were conducted using a desktop workstation with an Intel Xeon CPU X5660 2.66-GHz processor and 48-GB random-access memory.

Table 8.3: Times corresponding to 0.5% and 90% of the Arias intensity and time-window used to update the FE model.

EQ	Component	t (0.5% I_A) [sec]	t (90% I_A) [sec]	Time-window [sec]
EQ1	360°	2.36	7.94	[2.16,8.64]
	90°	2.16	8.64	
EQ2	EW	2.72	8.54	[2.72, 8.54]
	NS	3.04	8.20	

8.4.2.4. Results of non-sequential updating

Table 8.4 summarizes the final estimates of the mean of the modeling parameters obtained by the different non-sequential estimation approaches proposed above for EQ1 and $\hat{\boldsymbol{\theta}}_0 = 1.4\boldsymbol{\theta}^{true}$. In addition, the CPU time required by each estimation procedure, including the sequential approach presented in Section 8.4.1, is also included to compare the computational cost of the different approaches.

Table 8.4: Final estimates of the mean of the modeling parameters obtained with non-sequential updating procedures for EQ1 and $\hat{\boldsymbol{\theta}}_0 = 1.4\boldsymbol{\theta}^{true}$.

Case	Updating method	CPU time (s)	Final estimates of the mean of the modeling parameters								
			$\frac{E_s}{E_s^{true}}$	$\frac{f_y}{f_y^{true}}$	$\frac{b}{b^{true}}$	$\frac{R_0}{R_0^{true}}$	$\frac{E_c}{E_c^{true}}$	$\frac{f'_{cc}}{f'^{\,true}_{cc}}$	$\frac{\varepsilon_{cc}}{\varepsilon_{cc}^{true}}$	$\frac{\alpha_M}{\alpha_M^{true}}$	$\frac{\beta_K}{\beta_K^{true}}$
1	Sequential	755.1	1.00	1.00	1.00	1.00	0.98	0.98	1.03	1.08	0.99
5	Non-cumulative innovation (D=5)	136.4	1.00	0.97	1.24	1.20	0.94	0.93	0.97	1.16	1.09
6	Cumulative innovation (D=5)	135.8	1.00	1.00	1.00	1.01	0.99	1.00	1.08	1.02	1.00
7	Non-cumulative innovation (D=3)	186.4	1.00	1.00	1.02	0.98	1.00	1.00	1.10	1.06	0.99
8	Cumulative innovation (D=3)	190.3	1.00	1.00	0.98	0.99	0.99	0.98	1.02	1.13	0.99
9	Time-window	231.8	1.00	1.01	1.00	1.01	1.00	0.97	1.00	0.93	1.04

The computational cost of all the non-sequential updating procedures is considerably lower than that of the sequential procedure presented in Section 8.4.1. Non-

cumulative and cumulative innovations approaches have very similar computational cost for a fixed value of D, and obviously their CPU time increases as D decreases. The CPU time of non-cumulative approaches is about 18% and 25% for $D=5$ and $D=3$, respectively, of the CPU time of the sequential procedure. Time-window approach reaches about 30% of the CPU time of the sequential updating method. Non-cumulative innovation approach with $D=5$ does not provide accurate estimates of parameters b, R_0, and α_M, with relative errors higher or equal than 16%, while estimation of parameters E_c, f'_{cc}, and β_K also increases their relative errors noticeably compared to the sequential approach, reaching values higher than 7%. These results clearly show that skipping output data in the updating of the nonlinear FE model have detrimental effects in the accuracy of the estimation of modeling parameters which are less sensitive to the measured response quantities and/or those parameters that are activated only in limited time frames, such as post-yield parameters of the reinforcing steel, which are activated when the steel fibers undergo large strains when the nonlinear response of the structure is accentuated. However, when the non-cumulative approach with $D=3$ is considered, the estimation results are as good as in the case of sequential updating.

When measured response quantities corresponding to the time steps at which the nonlinear FE model is not updated are included in the innovation vector, i.e. cumulative innovation approach, the performance of the estimation framework improves considerably and the final estimates of mean and covariance of the modeling parameters are as accurate as when the model is updated at every time step. Very good estimation results are obtained using the cumulative innovation approach for $D=5$ and $D=3$.

Finally, the time-window approach also provides accurate final estimates of the modeling parameters, comparable to the results obtained using sequential updating. The time-window defined between $0.5\% I_A$ and $90\% I_A$ contains enough information about modeling parameters governing the initial linear-elastic response and nonlinear response of the structure, therefore the values of these parameters are successfully estimated provided that they are sensitive enough to the measured response quantities. Time histories of the estimates of the *a posteriori* mean of the modeling parameters for the three non-sequential procedures are presented in Figure 8.11. The estimates of the modeling parameters, which are normalized by their corresponding true parameter values, converge to stable values and accurate estimation of the modeling parameters is achieved for cumulative innovation, non-cumulative innovation with $D = 3$, and time-window approaches as aforementioned. The time of convergence of the different modeling parameters is practically the same as in the case of sequential updating (Figure 8.7). Since the information of some modeling parameters is contained in a short time frame, do not taking into account the measured response quantities in many time steps implies degrading effects in the performance of the estimation. This is the reason why non-cumulative approach with $D = 5$ is not able to accurately estimate some modeling parameters, such as b and R_0 which are exercised only in the time window [3.5 – 4.5] sec of EQ1.

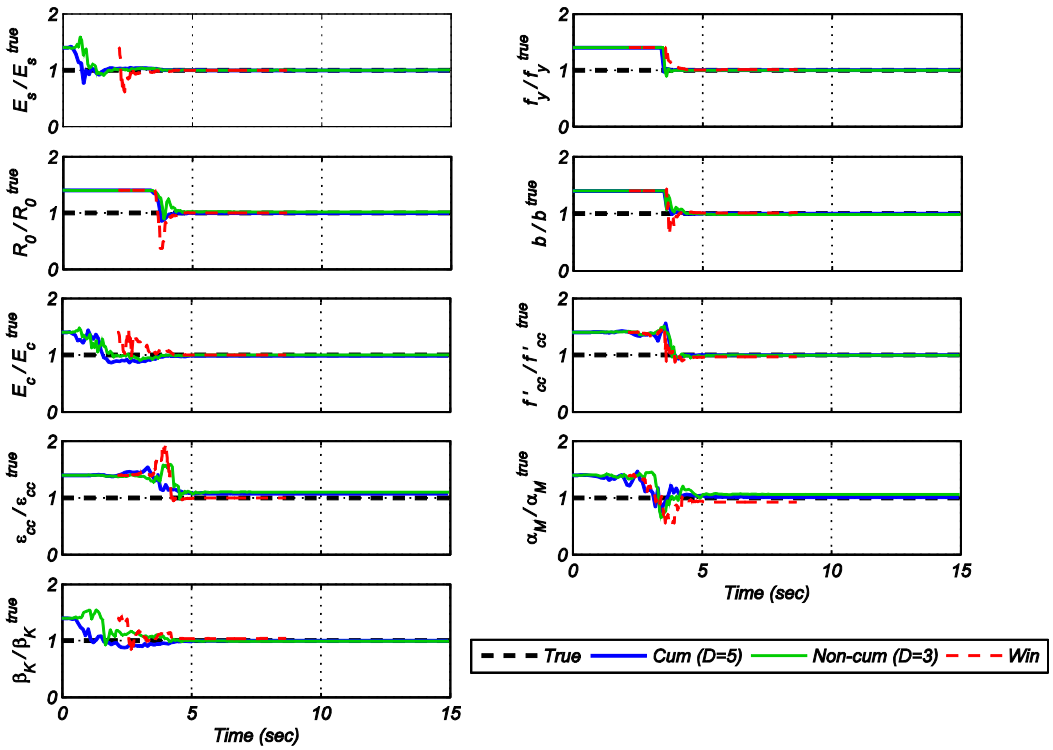

Figure 8.11: Time histories of the mean estimates of the modeling parameters using different non-sequential procedures for EQ1 and $\hat{\boldsymbol{\theta}}_0 = 1.4\boldsymbol{\theta}^{true}$.

The *RRMSE*s between the true measured responses and their counterparts obtained using the final estimates of the modeling parameters ($\hat{\boldsymbol{\theta}}_N$) for EQ1 and $\hat{\boldsymbol{\theta}}_0 = 1.4\boldsymbol{\theta}^{true}$ are shown in Table 8.5. Non-cumulative innovation approach with $D = 5$ has the poorest performance with *RRMSE*s ranging between 6.18% and 7.99%. All the other non-sequential approaches perform very similar to the sequential approach, with *RRMSE*s between 1% and 3%. The use of cumulative innovation and time-window approaches are computationally very efficient and provides accurate estimates of the modeling parameters, which in turn implies low *RRMSE*s between the true responses and responses based on $\hat{\boldsymbol{\theta}}_N$.

Table 8.5: Relative RMS errors (in %) of the output measurements obtained with non-sequential updating procedures for EQ1 and $\hat{\boldsymbol{\theta}}_0 = 1.4\boldsymbol{\theta}^{true}$.

Case	Updating method	Output measurement					
		$\mathbf{y}_1 = \ddot{\mathbf{q}}^t_{3L}$	$\mathbf{y}_2 = \ddot{\mathbf{q}}^t_{3T}$	$\mathbf{y}_3 = \ddot{\mathbf{q}}^t_{5L}$	$\mathbf{y}_4 = \ddot{\mathbf{q}}^t_{5T}$	$\mathbf{y}_5 = \ddot{\mathbf{q}}^t_{6L}$	$\mathbf{y}_6 = \ddot{\mathbf{q}}^t_{6T}$
1	Sequential	1.21	1.17	1.32	1.85	1.69	1.75
5	Non-cumulative innovation (D=5)	6.99	6.18	6.36	7.23	7.99	7.34
6	Cumulative innovation (D=5)	1.26	0.94	0.95	1.35	1.25	1.20
7	Non-cumulative innovation (D=3)	2.11	1.86	1.83	3.27	2.30	2.15
8	Cumulative innovation (D=3)	1.43	1.00	1.07	1.52	1.47	1.32
9	Time-window	1.87	1.87	1.98	2.47	2.18	2.36

8.4.3. Structural response recorded by heterogeneous sensor arrays

Nowadays, the most common instrumentation of civil structures consists of accelerometer arrays, however considering the emergence and advances in low-cost and high-quality sensor technology, measurement of other response quantities, such as displacements and strains, are becoming more feasible and affordable. The analysis of potential advantages of using heterogeneous sensor arrays for DID purposes is important. In this section the use of heterogeneous sensor arrays and its effects on estimation results are explored. Two cases of heterogeneous sensor arrays are considered. First (Case 10), the relative displacements at the roof level of the building, which in practice can be measured using GPS antennas, are considered in addition to the six accelerations responses considered before. It is assumed that the displacements are recorded in both directions and at the same location where the acceleration responses are measured (see Figure 8.4a). A 5 mm RMS zero-mean AWGN is used to pollute the simulated displacement responses. In the estimation, the diagonal entries of $\mathbf{R}$ corresponding to the

displacement measurements assume a standard deviation of 3 mm. The second case (Case 11) considers the measurement of the strain, which in practice can be measured using strain gauges or fiber optic sensors, in concrete and reinforcing steel at the bottom of a corner column (section 1-1 in Figure 8.4a) in addition to the accelerations responses considered in Section 8.4.1. A 0.5 mm/m RMS zero-mean AWGN is used to pollute the simulated strain responses. In this case, for the estimation a standard deviation of 0.3 mm/m is taken for the diagonal entries of $\mathbf{R}$ corresponding to the strain measurements. A third case (Case 12) with only acceleration measurements is considered for comparison purposes. Here the acceleration responses in both directions at the 3rd, 4th, 5th, and roof levels are considered. For the three cases the same magnitude of output measurement noise for the accelerations responses as in Section 8.4.1 is considered, i.e., 1.0%*g* RMS zero-mean AWGNs are used to pollute the simulated acceleration responses and in the estimation phase 0.5%*g* RMS is assumed for the diagonal entries of $\mathbf{R}$ corresponding to the acceleration measurements. It is noted that the three cases considered in this section use 8 sensor output channels and that the levels of output measurement noise are within values expected for the different types of sensors used currently for earthquake engineering applications.

Table 8.6 shows the final mean estimates of the modeling parameters normalized by their corresponding true values for EQ1 and $\hat{\boldsymbol{\theta}}_0 = 1.4\boldsymbol{\theta}^{true}$. When displacement or strain output measurements are considered, in addition to the six accelerations, to update the nonlinear FE model (Cases 10 and 11, respectively) more accurate estimation results of the modeling parameters are obtained. A maximum relative error of 3% (for α_M)

among all the modeling parameters is achieved when the relative roof displacements and strains at the bottom of a column are included as recorded measurements. When only accelerations are recorded (Case 12), the relative errors of the modeling parameters are similar to those reported in Section 8.4.1 when six acceleration time histories are considered as output measurements. For Case 12, the relative error of the final estimates of the modeling parameters are consistently higher than those obtained in Cases 10 and 11 when heterogeneous sensor arrays are used to record output responses.

Table 8.6: Final estimates of the mean of the modeling parameters obtained using heterogeneous arrays for EQ1 and $\hat{\boldsymbol{\theta}}_0 = 1.4\boldsymbol{\theta}^{true}$.

Case	Sensor array	Final estimates of the mean of the modeling parameters								
		$\frac{E_s}{E_s^{true}}$	$\frac{f_y}{f_y^{true}}$	$\frac{b}{b^{true}}$	$\frac{R_0}{R_0^{true}}$	$\frac{E_c}{E_c^{true}}$	$\frac{f'_{cc}}{f'^{\,true}_{cc}}$	$\frac{\varepsilon_{cc}}{\varepsilon_{cc}^{true}}$	$\frac{\alpha_M}{\alpha_M^{true}}$	$\frac{\beta_K}{\beta_K^{true}}$
10	6 relative accelerations + 2 relative displacements	1.00	1.00	1.00	1.00	0.98	0.98	1.02	1.03	0.99
11	6 relative accelerations + 2 strains	1.00	1.00	1.00	1.00	0.98	0.99	1.02	1.03	1.01
12	8 relative accelerations	1.01	1.00	1.02	1.02	0.99	0.91	1.02	1.03	1.00

8.4.4. Adaptive filtering

The performance and convergence of the UKF might be significantly affected by the noise covariance matrices $\mathbf{Q}_k$ and $\mathbf{R}_{k+1}$, therefore they need to be selected appropriately (Simon 2006, Patwardhan et al. 2012). The proposed formulation for parameter estimation of mechanics-based nonlinear FE models uses a process noise $\boldsymbol{\gamma}_k$ to drive the time-invariant modeling parameter $\boldsymbol{\theta}$, i.e., $\boldsymbol{\gamma}_k$ is an artificial noise without physical meaning. The noises driving different modeling parameters to be estimated are

uncorrelated, i.e., $\mathbf{Q}_k$ is a diagonal matrix whose diagonal entries are the process noise variances associated with the corresponding parameters to be estimated. Based on previous studies (Astroza et al. 2015), good estimation results are obtained if $\mathbf{Q}_k$ is assumed time-invariant ($\mathbf{Q}_k = \mathbf{Q} = E\left[\boldsymbol{\gamma}\boldsymbol{\gamma}^T\right]$) with the diagonal entries computed as $\left(c\,\hat{\boldsymbol{\theta}}_0^i\right)^2, i = 1,...,n_\theta$ with $c \in \left[1\times10^{-3}, 1\times10^{-5}\right]$. On the other hand, $\mathbf{R}_{k+1}$ represents the level of noise contained in the output measurements, which can be initially estimated according to the type of sensor, DAQ system, and engineering judgment. An accurate estimation of the measurement noise is desirable; otherwise, if the assumed measurement noise variances deviate significantly from the actual level of noise, the parameter estimates might be biased.

In Sections 8.4.1 and 8.4.3 different cases of accelerometer and heterogeneous sensor arrays were investigated. The measurement noise covariance matrix, $\mathbf{R}_{k+1}$, was assumed diagonal and time-invariant and, to mimic real world applications, the values of the measurement noise variances (diagonal entries of $\mathbf{R}$) were taken different to the actual variances of the noises used to pollute the simulated responses. In the estimation phase, standard deviations in the range [50 – 60]% of the actual values were assumed for acceleration, displacement, and strain response measurements, and accurate estimation of the modeling parameter and successful updating of the nonlinear FE model were obtained. This scenario is expected to be valid in many practical applications when it is possible to have a fairly good estimation of the standard deviation of the output noise. However, in some real world applications a good estimation of standard deviation of

output measurement noise might not be possible, for example, because of sensor malfunctioning or unwanted surrounded noise. In this section, the detrimental effects of poor assessment of the standard deviation of output measurement noise are shown and an adaptive filtering approach (filter tuning) to solve this problem is presented and verified.

8.4.4.1. Dual estimation approach

Assuming that the measurement noises in different sensors are uncorrelated, $\mathbf{R}_{k+1}$ can be expressed as a diagonal matrix with diagonal entries corresponding to the associated measurement noise variances, i.e., $\mathbf{R}_{k+1} = diag\left(\boldsymbol{\sigma}_{k+1}^2\right) = diag\left(\mathbf{r}_{k+1}\right)$. A dual estimation approach can be used to estimate the measurement noise covariance in addition to the modeling parameters (Song et al. 2007). At every time step, a master filter (MF) is used to estimate the modeling parameter vector $\boldsymbol{\theta}$ using the output noise covariance estimated by a parallel slave filter (SF). The MF solves the nonlinear state-space model described in Equation (8.4) and the SF uses the innovation (or residual), $\mathbf{e}_{k+1|k} = \mathbf{y}_{k+1} - \hat{\mathbf{y}}_{k+1|k}$, generated by the MF to estimate the output noise variances (diagonal entries of $\mathbf{R}_{k+1}$). This approach of adaptive filtering corresponds to a covariance matching technique, in which the goal of the SF is to make the innovations compatible with their expected covariance (Mehra, 1972). Figure 8.12 and Figure 8.13 show the pseudo-code and block diagram of the proposed dual filtering approach. The additional computational cost added by the SF filter is minimal because it is a linear Kalman filter.

Initialization:	
$\hat{\boldsymbol{\theta}}_0$, $\hat{\mathbf{P}}_0^{\boldsymbol{\theta\theta}}$: Initial estimates of mean vector and covariance matrix of modeling parameters	
$\mathbf{Q}$: Process noise covariance of master filter (MF)	
$\hat{\mathbf{r}}_0$, $\hat{\mathbf{P}}_0^{\mathbf{rr}}$: Initial estimate of mean vector and covariance matrix of output noise variances	
$\mathbf{T}$, $\mathbf{U}$: Process and measurement noise covariance of slave filter (SF)	
for $k = 0,1,\ldots,N-1$	Loop over time step
MF Prediction:	
(i) $\mathfrak{S}_k^{(i)}$ i=1,...,$2n_\theta+1$	Generate SPs
(ii) $\mathfrak{S}_{k+1}^{(i)} = \mathfrak{S}_k^{(i)}$	State eq. (MF)
(iii) $\hat{\boldsymbol{\theta}}_{k+1\|k} = \hat{\boldsymbol{\theta}}_{k\|k}$; $\hat{\mathbf{P}}_{k+1\|k}^{\boldsymbol{\theta\theta}} = \hat{\mathbf{P}}_{k\|k}^{\boldsymbol{\theta\theta}} + \mathbf{Q}$	A priori mean and covariance (MF)
(iv) $\mathcal{Y}_{k+1}^{(i)} = \mathbf{h}_{k+1}\left(\mathfrak{S}_{k+1}^{(i)}, \ddot{\mathbf{U}}_{k+1}^{g}\right)$	Measurement eq. (MF)
(v) $\hat{\mathbf{y}}_{k+1\|k} = \sum_{i=1}^{2n_\theta+1} W_m^{(i)} \mathcal{Y}_{k+1}^{(i)}$	Predicted output (MF)
(vi) $\mathbf{e}_{k+1} = \mathbf{y}_{k+1} - \hat{\mathbf{y}}_{k+1\|k}$	Innovation
(vii) $\mathbf{z}_{k+1} = diag\left(\mathbf{e}_{k+1}\mathbf{e}_{k+1}^T\right)$	Diagonal of innovation covariance
SF Prediction:	
(viii) $\hat{\mathbf{r}}_{k+1\|k} = \hat{\mathbf{r}}_{k\|k}$; $\hat{\mathbf{P}}_{k+1\|k}^{\mathbf{rr}} = \hat{\mathbf{P}}_{k\|k}^{\mathbf{rr}} + \mathbf{T}$	A priori mean and covariance (SF)
(ix) $\hat{\mathbf{z}}_{k+1\|k} = \hat{\mathbf{r}}_{k+1\|k} + diag\left(\sum_{i=1}^{2n_\theta+1} W_c^{(i)}\left[\mathcal{Y}_{k+1}^{(i)} - \hat{\mathbf{y}}_{k+1\|k}\right]\left[\mathcal{Y}_{k+1}^{(i)} - \hat{\mathbf{y}}_{k+1\|k}\right]^T\right)$	Predicted diagonal of innovation covariance (SF)
SF Correction:	
(x) $\hat{\mathbf{P}}_{k+1\|k}^{\mathbf{zz}} = \hat{\mathbf{P}}_{k+1\|k}^{\mathbf{rr}} + \mathbf{U}$; $\hat{\mathbf{P}}_{k+1\|k}^{\mathbf{rz}} = \hat{\mathbf{P}}_{k+1\|k}^{\mathbf{rr}}$	Estimated auto- and cross-covariance (SF)
(xi) $\mathbf{K}_{k+1}^{\mathbf{r}} = \hat{\mathbf{P}}_{k+1\|k}^{\mathbf{rz}}\left(\hat{\mathbf{P}}_{k+1\|k}^{\mathbf{zz}}\right)^{-1}$	Kalma gain (SF)
(xii) $\hat{\mathbf{r}}_{k+1\|k+1} = \hat{\mathbf{r}}_{k+1\|k} + \mathbf{K}_{k+1}^{\mathbf{r}}\left(\mathbf{z}_{k+1} - \hat{\mathbf{z}}_{k+1\|k}\right)$	A posteriori mean (SF)
(xiii) $\hat{\mathbf{P}}_{k+1\|k+1}^{\mathbf{rr}} = \hat{\mathbf{P}}_{k+1\|k}^{\mathbf{rr}} - \mathbf{K}_{k+1}^{\mathbf{r}}\hat{\mathbf{P}}_{k+1\|k}^{\mathbf{zz}}\left(\mathbf{K}_{k+1}^{\mathbf{r}}\right)^T$	A posteriori covariance (SF)
(xiv) $\hat{\mathbf{R}}_{k+1} = diag\left(\hat{\mathbf{r}}_{k+1\|k+1}\right)$	Estimated measurement noise covariance
MF Correction:	
(xv) $\hat{\mathbf{P}}_{k+1\|k}^{\mathbf{yy}} = \sum_{i=1}^{2n_\theta+1} W_c^{(i)}\left[\mathcal{Y}_{k+1}^{(i)} - \hat{\mathbf{y}}_{k+1\|k}\right]\left[\mathcal{Y}_{k+1}^{(i)} - \hat{\mathbf{y}}_{k+1\|k}\right]^T + \hat{\mathbf{R}}_{k+1}$	Estimated output covariance (MF)
(xvi) $\hat{\mathbf{P}}_{k+1\|k}^{\boldsymbol{\theta}\mathbf{y}} = \sum_{i=1}^{2n_\theta+1} W_c^{(i)}\left[\mathfrak{S}_{k+1}^{(i)} - \hat{\boldsymbol{\theta}}_{k+1\|k}\right]\left[\mathfrak{S}_{k+1}^{(i)} - \hat{\boldsymbol{\theta}}_{k+1\|k}\right]^T$	Estimated state/output cross-covariance (MF)
(xvii) $\mathbf{K}_{k+1} = \hat{\mathbf{P}}_{k+1\|k}^{\boldsymbol{\theta}\mathbf{y}}\left(\hat{\mathbf{P}}_{k+1\|k}^{\mathbf{yy}}\right)^{-1}$	Kalman gain (MF)
(xviii) $\hat{\boldsymbol{\theta}}_{k+1\|k+1} = \hat{\boldsymbol{\theta}}_{k+1\|k} + \mathbf{K}_{k+1}\left(\mathbf{y}_{k+1} - \hat{\mathbf{y}}_{k+1\|k}\right)$	A posteriori mean (MF)
(xix) $\hat{\mathbf{P}}_{k+1\|k+1}^{\boldsymbol{\theta\theta}} = \hat{\mathbf{P}}_{k+1\|k}^{\boldsymbol{\theta\theta}} - \mathbf{K}_{k+1}\hat{\mathbf{P}}_{k+1\|k}^{\mathbf{yy}}\mathbf{K}_{k+1}^T$	A posteriori covariance (MF)
end for	

Figure 8.12: Pseudo-code of the proposed approach for adaptive filtering.

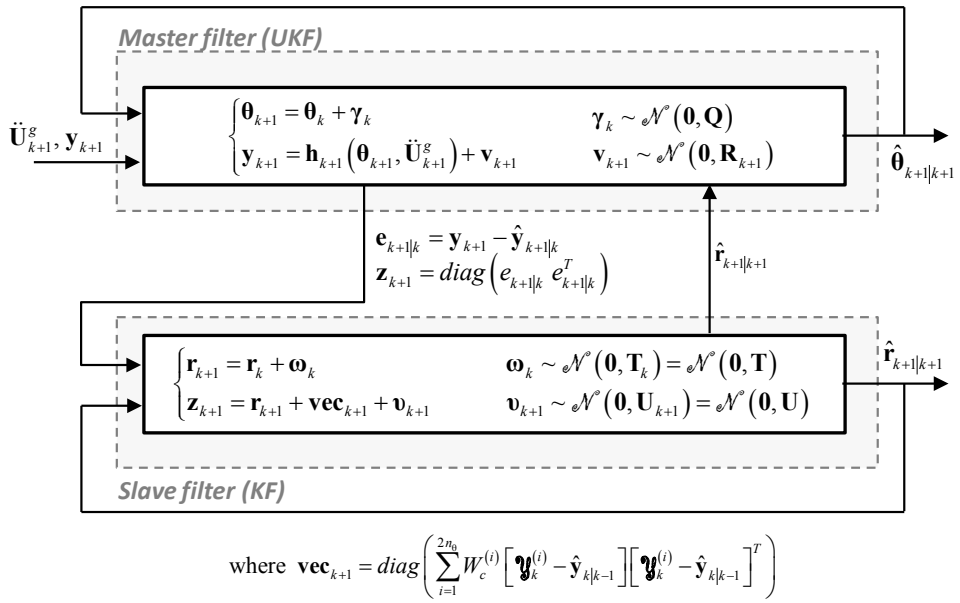

Figure 8.13: Diagram of the adaptive filtering structure.

8.4.4.2. Results of adaptive filtering

To verify the proposed adaptive filtering approach, two cases are considered. The first one considers the RC frame subjected to EQ1 with $\hat{\boldsymbol{\theta}}_0 = 1.4\boldsymbol{\theta}^{true}$ and six acceleration measurements. Unlike to Case 1 presented in Section 8.4.1, here the output measurements are polluted with zero-mean AWGN with 0.7, 0.2, 1.5, 0.3, 0.8, and 1.5%*g* RMS for $\ddot{\mathbf{q}}^t_{3L}, \ddot{\mathbf{q}}^t_{3T}, \ddot{\mathbf{q}}^t_{5L}, \ddot{\mathbf{q}}^t_{5T}, \ddot{\mathbf{q}}^t_{6L}$, and $\ddot{\mathbf{q}}^t_{6T}$, respectively. In the estimation, all the diagonal entries of $\mathbf{R}_{k+1}$ assume an initial standard deviation of 0.5%*g*, i.e., RMS values in the range [33 – 250]% of the actual values. The second case corresponds to Case 10 presented in Section 8.4.3 (i.e., EQ1, $\hat{\boldsymbol{\theta}}_0 = 1.4\boldsymbol{\theta}^{true}$, and output measurements consist of six acceleration and two displacement time histories), but zero-mean AWGN with 0.7, 0.2, 1.5, 0.3, 0.8, and 1.5%*g* RMS are used to pollute the simulated responses $\ddot{\mathbf{q}}^t_{3L}, \ddot{\mathbf{q}}^t_{3T}, \ddot{\mathbf{q}}^t_{5L}, \ddot{\mathbf{q}}^t_{5T}, \ddot{\mathbf{q}}^t_{6L}$, and $\ddot{\mathbf{q}}^t_{6T}$,

respectively, while zero-mean AWGN with 7 and 1 mm RMS are used to contaminate the simulated displacement responses in longitudinal and transverse directions, respectively. In the estimation, diagonal entries of $\mathbf{R}_{k+1}$ corresponding to acceleration and displacement responses assume an initial standard deviation of 0.5%g and 3 mm, respectively, i.e., RMS values in the range [33 – 300]% of the actual values are assumed.

The estimation is conducted with and without using the adaptive filtering approach proposed. When the adaptive filtering approach is employed, the covariance matrices $\mathbf{T}$ and $\mathbf{U}$ of the SF are assumed time-invariant with diagonal entries equal to 1×10^{-20}. The initial covariance matrix of the measurement noise variances of the SF, $\hat{\mathbf{P}}_0^{\mathbf{rr}}$, is assumed to be diagonal with terms computed assuming a coefficient of variation of 20% of the initial estimate of the mean $\hat{\mathbf{r}}_0$, i.e., the diagonal entries of $\hat{\mathbf{P}}_0^{\boldsymbol{\theta\theta}}$ are computed as $(p\times\hat{r}_0^i)^2$ where $i=1,\ldots,n_y$ and $p=0.20$.

Table 8.7 summarizes the final mean estimates of the modeling parameters normalized by their corresponding true parameter values with (Cases 14 and 16) and without (Cases 13 and 15) the adaptive filtering approach. For both cases (acceleration-only and heterogeneous sensor arrays) the estimation of modeling parameters improves considerably when the adaptive filtering approach is employed. For the case of acceleration-only measurements, estimation of modeling parameters $b, R_0, f'_{cc}, \varepsilon_{cc}$, and α_M enhance significantly when the adaptive filter approach is used. For the case of heterogeneous sensor array (accelerations and displacements), estimation errors of the modeling parameters are low even when the filter is not tuned, confirming results presented in Section 8.4.3 and verifying the robustness of the estimation approach to poor

estimation of measurement noise covariance when displacement measurements are considered to update the nonlinear FE model. Estimation of modeling parameters are even more accurate when the adaptive filtering approach is used, especially for parameters E_c and α_M.

From the *RRMSE*s between the true measured responses and their counterparts obtained using the final estimates of the modeling parameters for EQ1 and $\hat{\boldsymbol{\theta}}_0 = 1.4\boldsymbol{\theta}^{true}$ with and without the adaptive filtering approach (Table 8.8) is also concluded that the proposed filter tuning method improves the update of the nonlinear FE model. Lower *RRMSE*s are obtained for all response measurements when the filter is tuned using the proposed approach.

Table 8.7: Final estimates of the mean of the modeling parameters for EQ1 and $\hat{\boldsymbol{\theta}}_0 = 1.4\boldsymbol{\theta}^{true}$ obtained with and without the proposed adaptive filtering approach.

Case	Sensor array	Adaptive filtering	Final estimates of the mean of the modeling parameters								
			$\frac{E_s}{E_s^{true}}$	$\frac{f_y}{f_y^{true}}$	$\frac{b}{b^{true}}$	$\frac{R_0}{R_0^{true}}$	$\frac{E_c}{E_c^{true}}$	$\frac{f'_{cc}}{f'^{\,true}_{cc}}$	$\frac{\varepsilon_{cc}}{\varepsilon_{cc}^{\,true}}$	$\frac{\alpha_M}{\alpha_M^{true}}$	$\frac{\beta_K}{\beta_K^{true}}$
13	6 abs. acc.	No	1.01	0.98	1.10	1.14	0.95	0.85	0.90	1.19	1.02
14		Yes	1.01	1.01	1.00	1.01	0.98	0.95	1.04	1.06	0.99
15	6 abs. acc. + 2 rel. disp.	No	1.00	1.00	1.00	1.00	0.98	0.99	0.93	1.10	0.99
16		Yes	1.00	1.00	1.00	1.00	1.00	1.01	1.07	1.02	0.99

Table 8.8: Relative RMS errors (in %) of the output measurements for EQ1 and $\hat{\boldsymbol{\theta}}_0 = 1.4\boldsymbol{\theta}^{true}$ obtained with and without the proposed adaptive filtering approach.

Case	Sensor array	Adaptive filtering	Output measurement							
			$\ddot{\mathbf{q}}^t_{3L}$	$\ddot{\mathbf{q}}^t_{3T}$	$\ddot{\mathbf{q}}^t_{5L}$	$\ddot{\mathbf{q}}^t_{5T}$	$\ddot{\mathbf{q}}^t_{6L}$	$\ddot{\mathbf{q}}^t_{6T}$	$\mathbf{q}_{6L}$	$\mathbf{q}_{6T}$
13	6 abs. acc.	No	5.24	3.60	3.73	4.70	5.56	4.80	-	-
14		Yes	1.89	1.68	1.66	2.40	2.65	2.20	-	-
15	6 abs. acc. + 2 rel. disp.	No	1.78	1.59	1.71	2.40	2.25	2.28	1.23	1.03
16		Yes	1.36	0.84	0.74	1.38	1.26	1.18	0.43	0.27

8.4.5. Effect of input measurement noise

The proposed FE model updating approach can be adversely affected by unmeasured random excitation because the formulation does not explicitly account for this. The effects of input measurement noise in the performance of the nonlinear FE model updating framework are investigated in this section. To this end, the response of the frame is simulated using a noise-free input excitation, but in the estimation phase different levels of input measurement noise, which is modeled as zero-mean AWGN, are employed to pollute the noise-free input excitation. Levels of input measurement noise ranging from 0.3 to 1.5%*g* RMS are used to contaminate the earthquake input motion. This input noise is included to represent unmeasured random excitation and/or noise in the recorded input excitation due to sensor and DAQ errors. For all the analyses in this section, the outputs measurements used in the estimation correspond to the simulated responses contaminated by 1.0%*g* RMS AWGN and the measurement noise covariance matrix, $\mathbf{R}_{k+1}$, is assumed time-invariant with diagonal entries defined by a standard deviation of 0.5%*g*. Table 8.9 lists the final mean estimates of the modeling parameters

normalized by their corresponding true values for EQ1, $\hat{\boldsymbol{\theta}}_0 = 1.4\boldsymbol{\theta}^{true}$, and the four levels of input noise considered. The input noise, which is considered AWGN, is filtered by the nonlinear structure and therefore becomes a colored noise in the output measurements. Since the proposed approach considers white Gaussian output measurement noise in its formulation, it might be expected that colored output noises bias the parameter estimation results. However, for all levels of input noise the parameter estimation results are very good and comparable with those obtained when no input measurement noise is considered (see Section 8.4.1). The final estimates of the mean of the modeling parameters converge to their true values in most of the cases, except ε_{cc} for 0.5% and 1.5%*g* RMS input noise (with relative errors of 11% and 21%, respectively) and α_M for 1.0%*g* RMS input noise (with a relative error of 13%). As the input noise increases, the estimation of those parameters for which the measured responses contain less information (ε_{cc}, α_M, f'_{cc}, and R_0) loses accuracy. To further analyze the effects of input measurement noise, the *RRMSE* between the noise-free simulated responses ($\mathbf{y}$) and their counterparts computed with the final estimates of the modeling parameters ($\hat{\boldsymbol{\theta}}_N$) and the noise-free input are shown in Figure 8.14. The *RRMSE* between the noise-free simulated responses and their counterparts computed with the initial estimates of the modeling parameters ($\hat{\boldsymbol{\theta}}_0$) are also included. The successful and accurate updating of the nonlinear FE model is clearly evidenced. *RRMSE*s for $\hat{\boldsymbol{\theta}}_0$ range between 70 and 107% and after the model is updated the *RRMSE*s for $\hat{\boldsymbol{\theta}}_N$ decrease to values lower than 8%, which confirms the effective updating of the model even for high levels of input noise. As the level of

input noise increases, the accuracy in estimating the modeling parameters decay and consequently the *RRMSE* of the different measured responses increase.

Table 8.9: Final estimates of the mean of the modeling parameters for EQ1, $\hat{\boldsymbol{\theta}}_0 = 1.4\,\boldsymbol{\theta}^{true}$, and different levels of input noise.

Case	Input noise level (%g RMS)	Final estimates of the mean of the modeling parameters								
		$\frac{E_s}{E_s^{true}}$	$\frac{f_y}{f_y^{true}}$	$\frac{b}{b^{true}}$	$\frac{R_0}{R_0^{true}}$	$\frac{E_c}{E_c^{true}}$	$\frac{f'_{cc}}{f'^{\,true}_{cc}}$	$\frac{\varepsilon_{cc}}{\varepsilon_{cc}^{true}}$	$\frac{\alpha_M}{\alpha_M^{true}}$	$\frac{\beta_K}{\beta_K^{true}}$
1	0.0	1.00	1.00	1.00	1.00	0.98	0.98	1.03	1.08	0.99
17	0.3	1.00	1.00	1.00	1.00	0.98	1.00	0.97	1.04	1.00
18	0.5	1.01	1.00	1.00	0.99	0.97	0.98	0.89	1.01	1.01
19	1.0	1.00	1.00	0.99	0.97	1.00	0.96	1.02	0.87	1.04
20	1.5	1.00	0.98	0.98	0.93	1.00	0.94	0.79	1.00	1.01

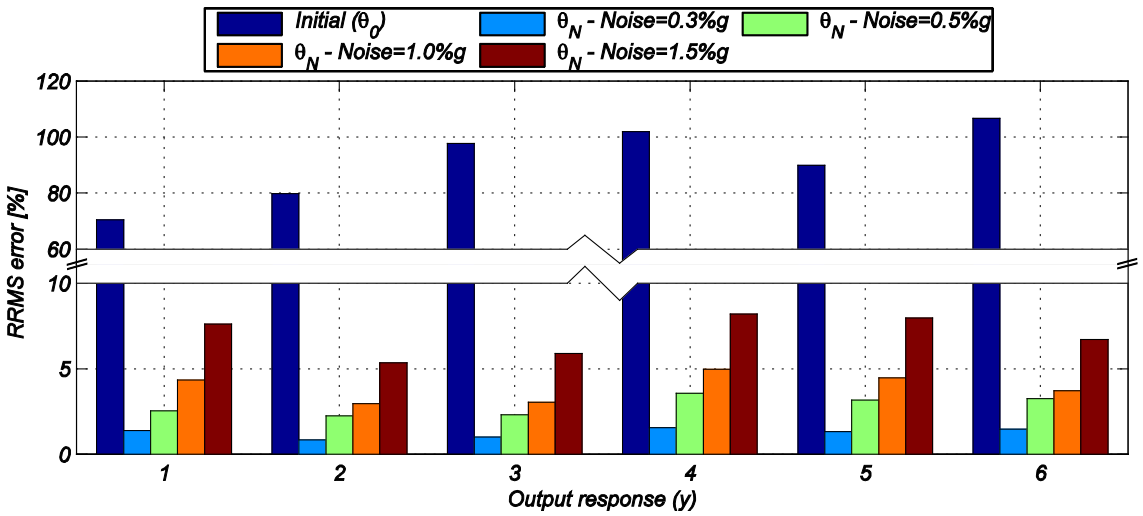

Figure 8.14: Relative RMS error between true responses and estimated responses using final parameter estimates and noise-free input for different levels of input measurement noise, EQ1, and $\hat{\boldsymbol{\theta}}_0 = 1.4\,\boldsymbol{\theta}^{true}$.

8.5. Conclusions

This chapter studied and evaluated the performance of a novel framework for nonlinear structural FE model updating. The framework uses recorded input/output data to estimate unknown modeling parameters of advanced mechanics-based nonlinear FE modeling techniques using the UKF. The updated FE model provides accurate and complete information about potential damage in the structure, including loss of stiffness, strength degradation, and history of response nonlinearities.

Accuracy, convergence, and robustness of the framework were investigated using numerically simulated response data of a realistic 3D 5-story 2-by-1 bay RC frame building subjected to bi-directional earthquake excitation. Parameters characterizing the nonlinear material constitutive laws and Rayleigh damping characteristics of the FE model are successfully estimated when limited response data (6 acceleration time histories) are available. Excellent results are obtained for two different earthquake excitations and two initial estimate of the mean the modeling parameters.

Three non-sequential updating procedures –so called non-cumulative innovation, cumulative innovation, and time-window approaches– to reduce the computational burden of the estimation framework were presented and examined. The proposed non-sequential approaches reduce the computational cost by about 70–80% as compared to the sequential updating approach. Accurate estimation results are achieved with cumulative innovation and time-window approaches, while non-cumulative approach requires a small updating step parameter (D) to properly estimate the modeling parameters.

The use of heterogeneous sensor arrays was explored and its effects on the identifiability of the modeling parameters were discussed. It is found that the fusion of acceleration and displacement and strain response data improves considerable the accuracy of the parameter estimation results because sensitivity of modeling parameters to different types of recorded responses may vary significantly, and consequently, heterogeneous sensor data are more informative than acceleration-only data.

An adaptive filtering (filter tuning) approach based on a covariance matching technique is proposed to estimate the measurement noise covariance in addition to the time-invariant modeling parameters. Favorable effects of the proposed adaptive filtering approach are observed, especially when the guess of the standard deviations of the output measurement noise is far from the actual level of measurement noise and only acceleration outputs are recorded.

Because the model updating framework does not explicitly account for unmeasured random excitations, the potential detrimental effects of input noise in the estimation results were studied. It is concluded that the framework is very robust to input noise, achieving good estimation results even for unrealistically high levels of input noise.

8.6. Acknowledgements

Chapter 8 is a reprint of the material that is currently being prepared for submission for publication “Nonlinear system identification for health monitoring of civil structures” in *Computers & Structures*, Astroza, Rodrigo; Ebrahimian, H.; and Conte, J.P. The dissertation author was the primary investigator and author of this paper.

References

Arasaratnam, I. and Haykin, S. (2009). "Cubature Kalman filters." *IEEE Trans. Automatic Control*, 54(6), 1254–1269.

Arias, A. (1970). "A measure of earthquake intensity." In *Seismic design for nuclear power plants*, by Hansen, R. (Ed.), 438–483. Cambridge, MA: MIT Press.

Astroza, R., Ebrahimian, H., and Conte, J. P. (2015). "Material parameter identification in distributed plasticity FE models of frame-type structures using nonlinear stochastic filtering." *ASCE Journal of Engineering Mechanics*, 141(5), 04014149.

Becerik-Gerber, B., Siddiqui, M., Brilakis, I., El-Anwar, O., El-Gohary, N., Mahfouz, T., Jog, G., Li, S., and Kandil, A. (2014). "Civil engineering grand challenges: Opportunities for data sensing, information analysis, and knowledge discovery." *ASCE Journal of Computing in Civil Engineering*, 28(4), 04014013.

Ching, J., Beck, J. L., Porter, K. A., and Shaikhutdinov, R. (2006). "Bayesian state estimation method for nonlinear systems and its application to recorded seismic response." *ASCE Journal of Engineering Mechanics*, 132(4), 396–410.

Distefano, N. and Rath, A. (1975a). "System identification in nonlinear structural seismic dynamics." *Computer Methods in Applied Mechanics and Engineering*, 5, 353–372.

Distefano, N. and Rath, A. (1975b). "Sequential identification of hysteretic and viscous models in structural seismic dynamics." *Computer Methods in Applied Mechanics and Engineering*, 6, 219–232.

Distefano, N. and Pena-Pardo, B. (1976). "System identification of frames under seismic loads." *Journal of the Engineering Mechanics Division,* 102(EM2), 313–330.

Ebrahimian, H., Astroza, R., and Conte, J. P. (2015). "Extended Kalman filter for material parameter estimation in nonlinear structural finite element models using direct differentiation method." Accepted for publication in *Earthquake Engineering & Structural Dynamics*.

Ebrahimian, H., Astroza, R., Conte, J.P., Restrepo, J.I, and Hutchinson, T.C. (2014). "Experimental validation of dynamic nonlinear FE model of full-scale five-story reinforced concrete building*." 9th International Conference on Structural Dynamics* (*EURODYN 2014*), Porto, Portugal.

Filippou, F. C., E. P. Popov, and V. V. Bertero. (1983). "Effects of bond deterioration on hysteretic behavior of reinforced concrete joints. " UCB/EERC-83/19, Berkeley, CA: EERC Report 83-19, Earthquake Engineering Research Center.

Filippou, F. C. and Fenves, G. L. (2004). "Methods of analysis for earthquake-resistant structures." In *Earthquake Engineering: From Engineering Seismology to Performance-Based Engineering*, Boca Raton, FL, CRC Press.

Haykin, S. (editor) (2001). *Kalman Filtering and Neural Networks*, New York: John Wiley & Sons, Inc.

ICC (2006). *International building code*, International Code Council, Washington, DC.

Ismail, M., Ikhouane, F., Rodellar, J. (2009). "The hysteresis Bouc-Wen model, A Survey." *Archives of Computational Methods in Engineering*, 16(2), 161–188.

Julier, S.J. and Uhlmann, J.K. (1997). "A new extension of the Kalman filter to nonlinear systems." *11th International Symposium on Aerospace/Defense Sensing, Simulation and Controls*, Orlando, FL.

Liu, P. and Au, S-K. (2013). "Bayesian parameter identification of hysteretic behavior of composite walls." *Probabilistic Engineering Mechanics*, 34, 101–109.

Mander, J. B., M. J. N. Priestley, and R. Park. (1988). "Theoretical stress-strain model for confined concrete." *ASCE Journal of Structural Engineering*, 114(8), 1804–1826.

Martinelli, P. and Filippou, F.C. (2009). "Simulation of the shaking table test of a seven-story shear wall building." *Earthquake Engineering & Structural Dynamics*, 38(5), 587–607.

Mehra, R.K. (1972). "Approaches for adaptive filtering." *IEEE Transactions on Automatic Control*, 17(5), 693-698.

Moaveni, B., He, X., Conte, J.P., and Restrepo, J.I. (2010). "Damage identification study of a seven-story full-scale building slice tested on the UCSD-NEES shake table." *Structural Safety*, 32(5), 347–356.

Nasrellah, H. A. and Manohar, C. S. (2011). "Finite element method based monte carlo filters for structural system identification." *Probabilistic Engineering Mechanics*,26(2), 294–307.

Omrani, R., Hudson, R., and Taciroglu, E. (2013). "Parametric identification of non-degrading hysteresis in a laterally-torsionally coupled building using an unscented Kalman filter," *ASCE Journal of Engineering Mechanics*, 139(4), 452–468.

OpenSees 2.4.2 [Computer software]. Berkeley, CA, Pacific Earthquake Engineering Research Center, Univ. of California at Berkeley.

Patwardhan, S.C., Narasimhan, S., Prakash, J., Gopaluni, R.B., and Shah, S.L. (2012) "Nonlinear Bayesian state estimation: a review of recent developments." *Control Engineering Practice*, 20(10), 933–953.

Popovics, S. (1973). "A numerical approach to the complete stress strain curve for concrete." *Cement and concrete research*, 3(5), 583–599.

Rytter, A. (1993). "Vibration based inspection of civil engineering structures." PhD Thesis, Department of Building Technology and Structural Engineering, University of Aalborg, Denmark.

Scott, B. D., R. Park, and M. J. N. Priestley. (1982). "Stress-strain behavior of concrete confined by overlapping hoops at low and high strain rates. " *American Concrete Institute (ACI) Journal*, 79(1), 13–27.

Shahidi, S. and Pakzad, S. (2014). "Generalized response surface model updating using time domain data." *ASCE Journal of Structural Engineering*, 140, SPECIAL ISSUE: Computational Simulation in Structural Engineering, A4014001.

Simoen, E., Moaveni, B., Conte, J.P., and Lombaert, G. (2013). "Uncertainty quantification in the assessment of progressive damage in a seven-story full-scale building slice." *ASCE Journal of Engineering Mechanics*, 139(12), 1818–1830.

Simon, D. (2006). *Optimal State Estimation: Kalman, H∞, and Nonlinear Approaches*, Hoboken, New Jersey: John Wiley & Sons, Inc.

Song, W. and Dyke, S. J. (2013). "Real-time dynamic model updating of a hysteretic structural system." *ASCE Journal of Structural Engineering*, 140(3), 04013082.

Song, Q., Jiang, Z.H., and Han, J.D. (2007). "Noise covariance identification based adaptive UKF with application to mobile robot systems." *2007 IEEE International Conference on Robotics and Automation*, Roma, Italy, 4164–4169.

Taucer, F.F., Spacone, E., and Filippou, F.C. (1991). "A fiber beam-column element for seismic response analysis of reinforced concrete structures." Report 91/17, EERC, Earthquake Engineering Research Center (EERC), University of California, Berkeley.

Teughels, A. and De Roeck, G. (2004). "Structural damage identification of the highway bridge Z24 by FE model updating." *Journal of Sound and Vibration*, 278(3), 589–610.

Uriz, P., Filippou, F., and Mahin, S. (2008). "Model for cyclic inelastic buckling of steel braces." *ASCE Journal of Structural Engineering*, 134(4), 619–628.

Wan, E.A. and van der Merwe, R. (2000). "The unscented Kalman filter for nonlinear estimation." *IEEE 2000 Adaptive Systems for Signal Processing, Communications, and Control Symposium*, Lake Louise, AB, Canada.

Worden, K., and J. M. Dulieu-Barton. (2004). "An overview of intelligent fault detection in systems and structures." *Structural Health Monitoring*, 3(1), 85–98.

Yang, J., Xia, Y., and Loh, C. (2014). "Damage detection of hysteretic structures with pinching effect." *ASCE Journal of Engineering Mechanics*, 140(3), 462–472.

CHAPTER 9

PERFORMANCE COMPARISON OF KALMAN−BASED FILTERS FOR NONLINEAR STRUCTURAL FINITE ELEMENT MODEL UPDATING

9.1. Introduction

Finite element (FE) model updating is the most popular model-based method for condition assessment and damage identification (DID) of civil structures using input-output or output-only vibration data. In this methodology an initial FE model of the structure is updated by tuning a set of unknown parameters of the model such that the discrepancies between the model predictions and the experimental data or properties derived therefrom are minimized. FE model updating techniques and their use for structural health monitoring (SHM) purposes have attracted significant attention from the structural engineering community. Several books (Friswell and Mottershead 1996, Marwala 2010) and review papers (e.g., Fritzen et al. 1998, Mottershead and Friswell 1993, Teughels and De Roeck 2005, Simoen et al. 2014) have summarized the research efforts and advances in the field of FE model updating.

In general, data recorded from force or ambient vibration tests are used to update the FE model, process that can be conducted in the frequency (e.g., Imregun et al. 1995, Sipple and Sanayei 2014), time (e.g., Chen and Feng 2009, Asgarieh et al. 2014, Astroza et al. 2015a, Ebrahimian et al. 2015), or modal (e.g., Teughels and De Roeck 2005, Simoen et al. 2014) domains. Furthermore, the FE model updating problem can be tackled in a deterministic (e.g., Zarate and Caicedo 2008, Li et al. 2014) or probabilistic manner (e.g., Simoen et al. 2013, Erdogan et al. 2014). In the former, point estimates for the unknown parameters of the FE model are determined, while in the latter the uncertainty in the estimation of the parameters is also quantified. A probabilistic approach is desirable because it quantifies the uncertainty on the prediction of different response quantities.

Most research on damage identification of civil structures has focused on employing linear FE models and using modal properties (natural frequencies and mode shapes) to define the objective functions in the optimization problem. In this approach, linear FE models are calibrated using low-amplitude vibration data recorded before (baseline or reference model) and after a damaging event, and the damage is defined as the reduction of effective stiffness over one or more regions of the structure. Parameterization of the FE model is crucial to avoid ill-conditioning problems in the optimization process, and the standard and most widely accepted solution is to limit the number of updating parameters by grouping them for different sets of adjacent elements (Simoen et al. 2014). In spite of its popularity in the structural engineering field, linear FE models cannot provide any information about loss of strength, loss of ductility

capacity, and/or nonlinearities experienced by the structure, which are required for a comprehensive condition assessment of the structure and collapse risk evaluation.

To overcome this limitation, in the last years important efforts and progresses have been made in the field of nonlinear FE model updating of civil structures (e.g., Ching et al. 2006, Nasrellah and Manohar 2011, Liu and Au 2013, Song and Dyke 2013, Omrani et al. 2013, Yang et al. 2014), topic that was first explored in the pioneering work by Distefano and coworkers in the 1970's (Distefano and Rath 1975a, Distefano and Rath 1975b, Distefano and Pena-Pardo 1976). These studies used simplified models with lumped nonlinearities, defined by empirical nonlinear models, such as the Bouc-Wen model, to describe the hysteretic behavior. However, such models are not typically used in state-of-the-art mechanics-based structural FE modeling and response simulation because they are not adequate to capture the actual nonlinear behavior of large and complex civil structures. In addition, these models are not parameterized by physical properties, and therefore require calibration on a case-by-case basis. Some methodologies to update mechanics-based nonlinear FE models of structures using input/output data recorded during damage-inducing events have been recently proposed (Shahidi and Pakzad 2014, Astroza et al. 2015a, Ebrahimian et al. 2015). The main benefit of using advanced nonlinear FE models is that adequately calibrated nonlinear models can capture the complex damage mechanisms in a structural system, providing accurate information about presence, location, type, and extent of damage in the structure. The updated mechanics-based nonlinear FE model can be used for rapid post-event condition assessment and provides a powerful tool to support the decision-making for emergency response, post-disaster rehabilitation, maintenance, and inspection of civil structures.

The use of recursive filtering techniques to update mechanics-based nonlinear FE models has shown promising results. Astroza et al. (2015a) and Ebrahimian et al. (2015) proposed a framework to update mechanics-based nonlinear FE models using the unscented Kalman filter (UKF) and the extended Kalman filter (EKF), respectively. Their application examples addressed the estimation of parameters describing the nonlinear material constitutive models of simple but realistic two-dimensional steel structures.

Feasible and efficient formulations to update mechanics-based nonlinear FE models are required, such that they can be employed for large and complex civil structures. Furthermore, probabilistic approaches are desirable because they also provide a measure of the uncertainty in the estimates. The so-called Gaussian filters provide a good alternative to achieve this goal. Examples of these filters are the EKF, which is based on analytical-linearized approximation of the nonlinear state-space model, the UKF, a Jacobian-free filter based on statistical linearization, and the iterated EKF (IEKF), a modified version of the EKF with an approximate Gauss-Newton iterative scheme (Bell and Cathey 1993). Previous studies have compared the performance of the EKF and UKF in different types of applications, such as aerodynamic parameter estimation (Chowdhary and Jategaonkar 2010), chemical reactors (Geetha et al. 2014), spacecraft localization (Giannitrapani et al. 2011), structural dynamics of a single degree of freedom (Mariani and Ghisi 2007, Askari and Li 2016), and navigation systems (St-Pierre and Gingras 2004).

This chapter introduces the IEKF to update mechanics-based nonlinear FE models and then compares the performance of the EKF, IEKF, and UKF in terms of convergence, accuracy, robustness, and computational requirements. For the derivative-

based filters (EKF and IEKF), the FE response sensitivities with respect to the modeling parameters to be estimated are required. To this end, the use of the direct differentiation method (DDM), which is an accurate and computationally efficient approach based on the exact (consistent) differentiation of the FE numerical scheme with respect to the unknown modeling parameters is investigated. A comprehensive comparison of the performance of the different filters is required to analyze their applicability to nonlinear structural FE model updating of large and complex civil structures. An application example using numerically simulated data of a realistic three-dimensional 5-story 2-by-1 bay reinforced concrete (RC) frame building subjected to bi-directional earthquake excitation is presented to illustrate the performance of the different filters.

9.2. The Kalman filter (KF)

The KF is a well-known optimal recursive state estimator (linear minimum variance unbiased estimator) for state-space models described by linear process and measurement equations with additive white Gaussian noises (AWGN)

$$\mathbf{x}_{k+1} = \mathbf{A}_k \mathbf{x}_k + \mathbf{B}_k \mathbf{u}_k + \mathbf{w}_k = \mathbf{A}_k \mathbf{x}_k + \mathbf{b}_k + \mathbf{w}_k \tag{9.1}$$

$$\mathbf{y}_{k+1} = \mathbf{C}_{k+1} \mathbf{x}_{k+1} + \mathbf{D}_{k+1} \mathbf{u}_{k+1} + \mathbf{v}_{k+1} = \mathbf{C}_{k+1} \mathbf{x}_{k+1} + \tilde{\mathbf{d}}_{k+1} + \mathbf{v}_{k+1} \tag{9.2}$$

where $\mathbf{x}_k \in \mathbb{R}^{n_x}$ = state vector, $\mathbf{A}_k \in \mathbb{R}^{n_x \times n_x}$, $\mathbf{B}_k \in \mathbb{R}^{n_x \times n_u}$, $\mathbf{C}_k \in \mathbb{R}^{n_y \times n_x}$, and $\mathbf{D}_k \in \mathbb{R}^{n_y \times n_u}$ = state, input, output, and feed-through matrices, respectively, $\mathbf{u}_k \in \mathbb{R}^{n_u}$ = deterministic input vector, $\mathbf{y}_{k+1} \in \mathbb{R}^{n_y}$ = output measurement vector, $\mathbf{w}_k \in \mathbb{R}^{n_x}$ = process noise vector, $\mathbf{v}_{k+1} \in \mathbb{R}^{n_y}$ = measurement noise vector, and the subscript indicates the time step.

Definitions of $\mathbf{b}_k \in \mathbb{R}^{n_x}$ and $\tilde{\mathbf{d}}_{k+1} \in \mathbb{R}^{n_y}$ follows directly from Equations (9.1) and (9.2), respectively. Noise processes $\mathbf{w}_k$ and $\mathbf{v}_{k+1}$ are assumed to be white Gaussian with zero-mean and covariance matrix $\mathbf{Q}_k$ and $\mathbf{R}_{k+1}$, respectively, i.e., $\mathbf{w}_k \sim \mathcal{N}\left(\mathbf{0}, \mathbf{Q}_k\right)$ and $\mathbf{v}_{k+1} \sim \mathcal{N}\left(\mathbf{0}, \mathbf{R}_{k+1}\right)$. If Gaussian distribution is also assumed for the initial state, i.e. $p\left(\mathbf{x}_0\right) = \mathcal{N}\left(\hat{\mathbf{x}}_{0|0}, \hat{\mathbf{P}}^{\mathbf{xx}}_{0|0}\right)$, the estimates of the expected value and covariance matrix of $\mathbf{x}$ can be recursively estimated by the following prediction-correction scheme (see Simon 2006 for details),

$$\hat{\mathbf{x}}_{k+1|k} = \mathbf{A}_k \hat{\mathbf{x}}_{k|k} + \mathbf{B}_k \mathbf{u}_k = \mathbf{A}_k \hat{\mathbf{x}}_{k|k} + \mathbf{b}_k \tag{9.3}$$

$$\hat{\mathbf{P}}^{\mathbf{xx}}_{k+1|k} = \mathbf{A}_k \hat{\mathbf{P}}^{\mathbf{xx}}_{k|k} \mathbf{A}_k^T + \mathbf{Q}_k \tag{9.4}$$

$$\hat{\mathbf{x}}_{k+1|k+1} = \hat{\mathbf{x}}_{k+1|k} + \mathbf{K}_{k+1}\left(\mathbf{y}_{k+1} - \hat{\mathbf{y}}_{k+1|k}\right) \tag{9.5}$$

$$\hat{\mathbf{P}}^{\mathbf{xx}}_{k+1|k+1} = \hat{\mathbf{P}}^{\mathbf{xx}}_{k+1|k} - \mathbf{K}_{k+1} \hat{\mathbf{P}}^{\mathbf{yy}}_{k+1|k} \mathbf{K}_{k+1}^T \tag{9.6}$$

where

$$\hat{\mathbf{y}}_{k+1|k} = \mathbf{C}_{k+1} \hat{\mathbf{x}}_{k+1|k} + \mathbf{D}_{k+1} \mathbf{u}_{k+1} = \mathbf{C}_{k+1} \hat{\mathbf{x}}_{k+1|k} + \tilde{\mathbf{d}}_{k+1} \tag{9.7}$$

$$\mathbf{e}_{k+1} = \mathbf{y}_{k+1} - \hat{\mathbf{y}}_{k+1|k} \tag{9.8}$$

$$\hat{\mathbf{P}}^{\mathbf{yy}}_{k+1|k} = \mathbf{C}_{k+1} \hat{\mathbf{P}}^{\mathbf{xx}}_{k+1|k} \mathbf{C}_{k+1}^T + \mathbf{R}_{k+1} \tag{9.9}$$

$$\hat{\mathbf{P}}^{\mathbf{xy}}_{k+1|k} = \hat{\mathbf{P}}^{\mathbf{xx}}_{k+1|k} \mathbf{C}_{k+1}^T \tag{9.10}$$

$$\mathbf{K}_{k+1} = \hat{\mathbf{P}}^{\mathbf{xy}}_{k+1|k} \left(\hat{\mathbf{P}}^{\mathbf{yy}}_{k+1|k}\right)^{-1} \tag{9.11}$$

$\hat{\mathbf{x}}_{k+1|k}$ and $\hat{\mathbf{P}}^{\mathbf{xx}}_{k+1|k}$ denote the estimates of state vector and state covariance matrix at time step $(k+1)$ given $\mathbf{u}_{1:k} = \left[\mathbf{u}_1^T, \mathbf{u}_2^T, \ldots, \mathbf{u}_k^T\right]^T$ and $\mathbf{y}_{1:k} = \left[\mathbf{y}_1^T, \mathbf{y}_2^T, \ldots, \mathbf{y}_k^T\right]^T$, $\hat{\mathbf{y}}_{k+1|k}$ = predicted output, $\mathbf{e}_{k+1}$ = innovation, $\hat{\mathbf{P}}^{\mathbf{yy}}_{k+1|k}$ = innovation covariance, $\hat{\mathbf{P}}^{\mathbf{xy}}_{k+1|k}$ = cross-

covariance matrix, and $\mathbf{K}_{k+1}$ = Kalman gain. Equations (9.3) and (9.4) are referred as the process update (prediction) and Equations (9.5−9.11) as the measurement update (correction). $\hat{\mathbf{x}}_{k+1|k}$ and $\hat{\mathbf{x}}_{k+1|k+1}$ ($\hat{\mathbf{P}}^{\mathbf{xx}}_{k+1|k}$ and $\hat{\mathbf{P}}^{\mathbf{xx}}_{k+1|k+1}$) are called predicted and corrected state estimates (state covariance matrices), respectively. More details on the KF can be found in Simon (2006).

9.3. Problem formulation

The discrete-time equation of motion of an n-DOF viscously-damped nonlinear FE model of a structure at time step (k+1) can be expressed as

$$\mathbf{M}(\boldsymbol{\theta})\,\ddot{\mathbf{q}}_{k+1}(\boldsymbol{\theta})+\mathbf{C}(\boldsymbol{\theta})\,\dot{\mathbf{q}}_{k+1}(\boldsymbol{\theta})+\mathbf{r}_{k+1}\left(\mathbf{q}_{k+1}(\boldsymbol{\theta}),\boldsymbol{\theta}\right)=\mathbf{p}_{k+1} \tag{9.12}$$

in which $\mathbf{q}_{k+1}, \dot{\mathbf{q}}_{k+1}, \ddot{\mathbf{q}}_{k+1} \in \mathbb{R}^n$ = relative displacement, velocity, and acceleration vectors, respectively, $\mathbf{M} \in \mathbb{R}^{n\times n}$ = mass matrix, $\mathbf{C} \in \mathbb{R}^{n\times n}$ = damping matrix, $\mathbf{r}_{k+1}\left(\mathbf{q}_{k+1}(\boldsymbol{\theta}),\boldsymbol{\theta}\right) \in \mathbb{R}^n$ = history-dependent internal resisting force vector, n = number of degrees of freedom, $\boldsymbol{\theta} \in \mathbb{R}^{n_\theta}$ = vector of unknown time-invariant modeling parameters, $\mathbf{p}_{k+1} \in \mathbb{R}^n$ = dynamic load vector, which in the case of rigid base earthquake excitation takes the form $\mathbf{p}_{k+1} = -\mathbf{M}\,\mathbf{L}\,\ddot{\mathbf{u}}^g_{k+1}$ with $\mathbf{L} \in \mathbb{R}^{n\times r}$ = influence matrix and $\ddot{\mathbf{u}}^g_{k+1} \in \mathbb{R}^{r\times 1}$ = input ground accelerations with r = number of base excitation components, and the subscript indicates the time step.

From Equation (9.12) and the fact that the desired predicted response of the nonlinear FE model at time step $(k+1)$ ($\hat{\mathbf{y}}_{k+1} \in \mathbb{R}^{n_y}$) can be written as a function of the

input excitation and the nodal displacement, velocity, and acceleration vectors ($\mathbf{q}_{k+1}, \dot{\mathbf{q}}_{k+1}, \ddot{\mathbf{q}}_{k+1}$), the predicted response of the nonlinear FE model to earthquake excitation at time step $(k+1)$ can be expressed as (Astroza et al. 2015a, Ebrahimian et al. 2015)

$$\hat{\mathbf{y}}_{k+1} = \mathbf{h}_{k+1}\left(\boldsymbol{\theta}, \ddot{\mathbf{u}}^{g}_{1:k+1}, \mathbf{q}_0, \dot{\mathbf{q}}_0\right) \tag{9.13}$$

where $\mathbf{h}_{k+1}(\cdot)$ is the nonlinear response function of the nonlinear FE model at time t_{k+1}, $\ddot{\mathbf{u}}^{g}_{1:k+1} = \left[\left(\ddot{\mathbf{u}}^{g}_{1}\right)^T, \left(\ddot{\mathbf{u}}^{g}_{2}\right)^T, ..., \left(\ddot{\mathbf{u}}^{g}_{k+1}\right)^T\right]^T$ is the input ground acceleration time history from time t_1 to t_{k+1}, and $\mathbf{q}_0, \dot{\mathbf{q}}_0 \in \mathbb{R}^n$ are the initial displacement and velocity conditions which are omitted hereafter to simplify the notation.

The measured response of the structure ($\mathbf{y} \in \mathbb{R}^{n_y}$) can include different response quantities recorded by a heterogeneous sensor array and is related to the FE model predicted response ($\hat{\mathbf{y}}$) by (Astroza et al. 2015a, Ebrahimian et al. 2015)

$$\mathbf{y}_{k+1} = \hat{\mathbf{y}}_{k+1} + \mathbf{v}_{k+1} \tag{9.14}$$

where $\mathbf{v}_k \in \mathbb{R}^{n_y}$ = prediction error assumed to be white Gaussian with zero-mean and covariance matrix $\mathbf{R}_k$, i.e., $\mathbf{v}_k \sim \mathcal{N}\left(\mathbf{0}, \mathbf{R}_k\right)$. Equation (9.14) accounts for model parameter uncertainty and uncertainty related to measurement; however, it does not account for model structure uncertainty (Simoen et al. 2014). Therefore, Equation (9.14) implicitly assumes that the nonlinear FE model can predict with reasonable precision the actual response of the structure of interest, which can be accomplished by using adequate mechanics-based nonlinear FE models with well calibrated material constitutive models

(e.g., Uriz et al. 2008, Martinelli and Filippou 2009, Ebrahimian et al. 2014). On the other hand, $\boldsymbol{\theta}$ contains unknown time-invariant modeling parameters, i.e.,

$$\boldsymbol{\theta}_{k+1} = \boldsymbol{\theta}_k + \mathbf{w}_k \tag{9.15}$$

In other words, $\boldsymbol{\theta}$ is modeled as a random process according to the Bayesian approach and the evolution of $\boldsymbol{\theta}$ is described by a random walk process. Equation (9.14), which represents a linear process equation, and Equation (9.15), which represents a nonlinear measurement equation, define the following nonlinear state-space model

$$\boldsymbol{\theta}_{k+1} = \boldsymbol{\theta}_k + \mathbf{w}_k \tag{9.16}$$

$$\mathbf{y}_{k+1} = \mathbf{h}_{k+1}\left(\boldsymbol{\theta}_{k+1}, \ddot{\mathbf{u}}^g_{1:k+1}\right) + \mathbf{v}_{k+1} \tag{9.17}$$

where $\mathbf{w}_k$ and $\mathbf{v}_{k+1}$ are mutually uncorrelated and uncorrelated between sampling times Gaussian processes with zero-mean and known covariance matrices $\mathbf{Q}_k$ and $\mathbf{R}_{k+1}$, respectively, i.e., $\mathbf{w}_k \sim \mathcal{N}\left(\mathbf{0}, \mathbf{Q}_k\right)$ and $\mathbf{v}_{k+1} \sim \mathcal{N}\left(\mathbf{0}, \mathbf{R}_{k+1}\right)$. A filtering technique can be used to recursively estimate at least the first two statistical moments of the unknown modeling parameter vector in the nonlinear state-space model [Equations (9.16) and (9.17)] using the input and measured output response of the system. In particular, the so-called Gaussian-based filters for nonlinear systems can be employed for this purpose. In this chapter, the EKF, IEKF, and UKF, which are presented in Section 9.4, are used to recursively estimate the states (modeling parameters) of the nonlinear state-space model in Equations (9.16) and (9.17) knowing the input ($\ddot{\mathbf{u}}^g$) and measured output response of the system ($\mathbf{y}$). Since the formulation described by Equations (9.16) and (9.17) does not take into account the effects of input noise, its potential detrimental effects on the parameter estimation results will be analyzed later on.

The application example in this chapter will deal with RC frame-type structures, which nonlinear behavior can be modeled using nonlinear mechanics-based distributed-plasticity FE models (Taucer et al. 1991). In this modeling technique, uniaxial material constitutive laws, defined by time-invariant parameters, model the nonlinear stress-strain response of uniaxial material fibers, which are then used to obtain the response at the section, element, and structure levels. Figure 9.1 shows a schematic representation of the hierarchical discretization levels in distributed-plasticity FE models of RC frame-type structures.

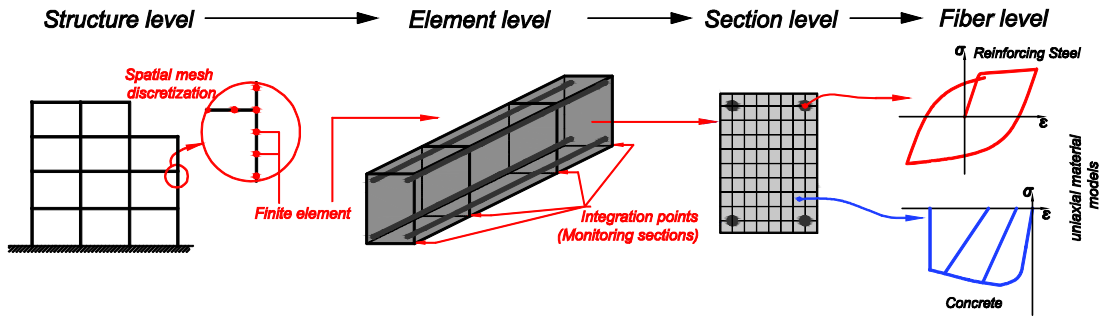

Figure 9.1: Hierarchical discretization levels in distributed-plasticity FE models of RC frame-type structures.

9.4. Kalman filters for nonlinear FE model updating

In the case of the nonlinear state-space model described by Equations (9.16) and (9.17), the KF algorithm can be applied to a linearized version of the model. Three different approaches to linearize the nonlinear measurement equation are studied in this chapter, leading to the well-known KF-based schemes EKF, IEKF, and UKF. The performance of the three filters is compared in terms of convergence, accuracy, robustness, and computational requirements.

A linearized version of Equations (9.16) and (9.17) can be expressed as (Lefebvre et al. 2005):

$$\boldsymbol{\theta}_{k+1} = \boldsymbol{\theta}_k + \mathbf{w}_k \tag{9.18}$$

$$\mathbf{y}_{k+1} = \mathbf{H}_{k+1}\boldsymbol{\theta}_{k+1} + \mathbf{d}_{k+1} + \boldsymbol{\rho}_{k+1} + \mathbf{v}_{k+1} \tag{9.19}$$

in which $\mathbf{H}_{k+1}, \mathbf{d}_{k+1},$ and $\boldsymbol{\rho}_{k+1}$ differ between different linearization strategies and will be derived for each filter independently. The vector $\boldsymbol{\rho}_{k+1} \in \mathbb{R}^{n_y}$ represents errors related to the linearization of the measurement equation, modeled by a zero-mean Gaussian distribution with covariance matrix $\mathbf{R}^*_{k+1} \in \mathbb{R}^{n_y \times n_y}$. The linearized state-space model described by Equations (9.18) and (9.19) is analogous to the linear state-space model described by Equations (9.1) and (9.2), and consequently can be solved using the KF algorithm presented in Section 9.2.

9.4.1. Extended Kalman filter (EKF)

In the EKF the nonlinear measurement equation [Equation (9.17)] is linearized around the latest predicted parameter estimate ($\hat{\boldsymbol{\theta}}_{k+1|k}$) using a first-order approximation of the Taylor series expansion of $\mathbf{h}_{k+1}\left(\boldsymbol{\theta}_{k+1}, \ddot{\mathbf{u}}^g_{1:k+1}\right)$, therefore,

$$\mathbf{H}_{k+1} = \left.\frac{\partial \mathbf{h}_{k+1}\left(\boldsymbol{\theta}, \ddot{\mathbf{u}}^g_{1:k+1}\right)}{\partial \boldsymbol{\theta}^T}\right|_{\hat{\boldsymbol{\theta}}_{k+1|k}} \tag{9.20}$$

$$\mathbf{d}_{k+1} = \hat{\mathbf{y}}_{k+1|k} - \mathbf{H}_{k+1}\hat{\boldsymbol{\theta}}_{k+1|k} = \mathbf{h}_{k+1}\left(\hat{\boldsymbol{\theta}}_{k+1|k}, \ddot{\mathbf{u}}^g_{1:k+1}\right) - \mathbf{H}_{k+1}\hat{\boldsymbol{\theta}}_{k+1|k} \tag{9.21}$$

The EKF does not take into account the linearization errors, i.e. $\mathbf{R}^*_{k+1} = 0$. Table 9.1 summarizes the EKF algorithm for the parameter estimation problem. In the

implementation of the EKF, the matrix $\partial \mathbf{h}_{k+1}\left(\boldsymbol{\theta}, \ddot{\mathbf{u}}^{g}_{1:k+1}\right) \big/ \partial \boldsymbol{\theta}^{T}$, which is known as FE response sensitivities, can be computed accurately and efficiently using the DDM or the more computationally demanding finite difference method (FDM) (Tsay and Arora 1990, Zhang and Der Kiureghian 1993, Conte 2001). Details about the formulation of the parameter estimation problem for frame-type distributed-plasticity FE models using the EKF can be found in Ebrahimian et al. (2015). It is noted that in this chapter only the DDM is employed to compute the FE response sensitivities, because its efficiency compared to FDM was already shown by the authors (Ebrahimian et al. 2015).

Table 9.1: Algorithm for nonlinear FE model updating using the EKF.

Initialization: $\hat{\boldsymbol{\theta}}_{0\|0}$ and $\hat{\mathbf{P}}^{\boldsymbol{\theta}\boldsymbol{\theta}}_{0\|0}$	Initial estimates of parameter vector and parameter covariance matrix
for $k = 0,1,2,\ldots,N-1$	Loop over time steps
Prediction:	
(i) $\hat{\boldsymbol{\theta}}_{k+1\|k} = \hat{\boldsymbol{\theta}}_{k\|k}$	A priori estimate of parameter vector
(ii) $\hat{\mathbf{P}}^{\boldsymbol{\theta}\boldsymbol{\theta}}_{k+1\|k} = \hat{\mathbf{P}}^{\boldsymbol{\theta}\boldsymbol{\theta}}_{k\|k} + \mathbf{Q}_{k}$	A priori estimate of parameter covariance matrix
(iii) $\hat{\mathbf{y}}_{k+1} = \mathbf{h}_{k+1}\left(\hat{\boldsymbol{\theta}}_{k+1\|k}, \ddot{\mathbf{u}}^{g}_{1:k+1}\right)$	Predicted output vector
(iv) $\mathbf{H}_{k+1} = \left.\dfrac{\partial \mathbf{h}_{k+1}\left(\boldsymbol{\theta}, \ddot{\mathbf{u}}^{g}_{1:k+1}\right)}{\partial \boldsymbol{\theta}^{T}}\right\|_{\hat{\boldsymbol{\theta}}_{k+1\|k}}$	FE response sensitivities matrix
(v) $\hat{\mathbf{P}}^{\mathbf{yy}}_{k+1\|k} = \mathbf{H}_{k+1}\hat{\mathbf{P}}^{\boldsymbol{\theta}\boldsymbol{\theta}}_{k+1\|k}\mathbf{H}^{T}_{k+1} + \mathbf{R}_{k+1}$	Estimated response covariance matrix
(vi) $\hat{\mathbf{P}}^{\boldsymbol{\theta}\mathbf{y}}_{k+1\|k} = \hat{\mathbf{P}}^{\boldsymbol{\theta}\boldsymbol{\theta}}_{k+1\|k}\mathbf{H}^{T}_{k+1}$	Estimated cross-covariance matrix
Correction: output measurement $\mathbf{y}_{k+1}$ is recorded	
(vii) $\mathbf{K}_{k+1} = \hat{\mathbf{P}}^{\boldsymbol{\theta}\mathbf{y}}_{k+1\|k}\left(\hat{\mathbf{P}}^{\mathbf{yy}}_{k+1\|k}\right)^{-1}$	Kalman gain
(viii) $\hat{\boldsymbol{\theta}}_{k+1\|k+1} = \hat{\boldsymbol{\theta}}_{k+1\|k} + \mathbf{K}_{k+1}\left(\mathbf{y}_{k+1} - \hat{\mathbf{y}}_{k+1\|k}\right)$	A posteriori estimate of parameter vector
(ix) $\hat{\mathbf{P}}^{\boldsymbol{\theta}\boldsymbol{\theta}}_{k+1\|k+1} = \hat{\mathbf{P}}^{\boldsymbol{\theta}\boldsymbol{\theta}}_{k+1\|k} - \mathbf{K}_{k+1}\hat{\mathbf{P}}^{\mathbf{yy}}_{k+1\|k}\mathbf{K}^{T}_{k+1}$	A posteriori estimate of parameter covariance matrix
end for	

9.4.2. Iterated Extended Kalman filter (IEKF)

In the EKF $\mathbf{h}_{k+1}\left(\boldsymbol{\theta}_{k+1}, \ddot{\mathbf{u}}^{g}_{1:k+1}\right)$ is linearized around $\hat{\boldsymbol{\theta}}_{k+1|k}$, the best available estimate of $\boldsymbol{\theta}_{k+1}$ before $\mathbf{y}_{k+1}$ is taken into account. The IEKF linearizes $\mathbf{h}_{k+1}(\cdot,\cdot)$ around

$\hat{\boldsymbol{\theta}}_{k+1|k+1}$, which is the corrected parameter estimate of $\boldsymbol{\theta}_{k+1}$ after $\mathbf{y}_{k+1}$ is assimilated. This is achieved by an iterative procedure. First, the filter linearizes $\mathbf{h}_{k+1}(\cdot,\cdot)$ around $\hat{\boldsymbol{\theta}}^0_{k+1|k+1}$ (where the superscript indicates the iteration number), usually assumed equals to $\hat{\boldsymbol{\theta}}_{k+1|k}$, and computes the updated parameter and parameter covariance estimates, $\hat{\boldsymbol{\theta}}^1_{k+1|k+1}$ and $\hat{\mathbf{P}}^{\boldsymbol{\theta}\boldsymbol{\theta},1}_{k+1|k+1}$, respectively. Then, the filter linearizes $\mathbf{h}_{k+1}(\cdot,\cdot)$ around $\hat{\boldsymbol{\theta}}^1_{k+1|k+1}$ and computes a new updated parameter and parameter covariance estimates $\hat{\boldsymbol{\theta}}^2_{k+1|k+1}$ and $\hat{\mathbf{P}}^{\boldsymbol{\theta}\boldsymbol{\theta},2}_{k+1|k+1}$, respectively. The iterative process finishes when the difference between two consecutive updated parameter estimates is less than a defined threshold ($\left\|\hat{\boldsymbol{\theta}}^i_{k+1|k+1}-\hat{\boldsymbol{\theta}}^{i-1}_{k+1|k+1}\right\| \le \varepsilon \left\|\hat{\boldsymbol{\theta}}^0_{k+1|k+1}\right\|$) or after a maximum number of iterations (N_{iter} Niter) is reached. It is found that the majority of the improvement is achieved in the initial iterations (Simon 2006). Based on the described iterative procedure, quantities $\mathbf{H}_{k+1}$ and $\mathbf{d}_{k+1}$ in Equation (9.19) can be expressed at iteration i as

$$\mathbf{H}^i_{k+1} = \left.\frac{\partial \mathbf{h}_{k+1}\left(\boldsymbol{\theta}, \ddot{\mathbf{u}}^g_{1:k+1}\right)}{\partial \boldsymbol{\theta}^T}\right|_{\hat{\boldsymbol{\theta}}^i_{k+1|k+1}} \tag{9.22}$$

$$\mathbf{d}^i_{k+1} = \hat{\mathbf{y}}^i_{k+1|k+1} - \mathbf{H}^i_{k+1}\hat{\boldsymbol{\theta}}^i_{k+1|k+1} = \mathbf{h}_{k+1}\left(\hat{\boldsymbol{\theta}}^i_{k+1|k+1}, \ddot{\mathbf{u}}^g_{1:k+1}\right) - \mathbf{H}_{k+1}\hat{\boldsymbol{\theta}}^i_{k+1|k+1} \tag{9.23}$$

Like the EKF, the IEKF does not take into account the linearization errors, i.e., $\mathbf{R}^*_{k+1} = 0$.

Table 9.2 summarizes the IEKF algorithm for the parameter estimation problem. To compute the matrix of FE response sensitivities, $\partial \mathbf{h}_{k+1}\left(\boldsymbol{\theta}, \ddot{\mathbf{u}}^g_{1:k+1}\right)\big/\partial \boldsymbol{\theta}^T$, the DDM is

employed. In this chapter, the procedure proposed in Simon (2006) is used, with a maximum number of iterations $N_{iter} = 5$, and the convergence threshold for the parameter estimate at $\varepsilon = 0.1\%$.

Table 9.2: Algorithm for nonlinear FE model updating using the IEKF.

Initialization: $\hat{\boldsymbol{\theta}}_{0\|0}$ and $\hat{\mathbf{P}}^{\boldsymbol{\theta}\boldsymbol{\theta}}_{0\|0}$	Initial estimates of parameter vector and parameter covariance matrix
for $k = 0,1,2,\ldots,N-1$	Loop over time steps
Prediction:	
(i) $\hat{\boldsymbol{\theta}}_{k+1\|k} = \hat{\boldsymbol{\theta}}_{k\|k}$	A priori estimate of parameter vector
(ii) $\hat{\mathbf{P}}^{\boldsymbol{\theta}\boldsymbol{\theta}}_{k+1\|k} = \hat{\mathbf{P}}^{\boldsymbol{\theta}\boldsymbol{\theta}}_{k\|k} + \mathbf{Q}_k$	A priori estimate of parameter covariance matrix
Measurement update is performed iteratively	
(iii) $\hat{\boldsymbol{\theta}}^{0}_{k+1\|k+1} = \hat{\boldsymbol{\theta}}_{k+1\|k}$; $\hat{\mathbf{P}}^{\boldsymbol{\theta}\boldsymbol{\theta},0}_{k+1\|k+1} = \hat{\mathbf{P}}^{\boldsymbol{\theta}\boldsymbol{\theta}}_{k+1\|k}$; $i = 0$	Initialize the iterated EKF estimate
while $i \le N_{iter}$ *or* $\left\|\hat{\boldsymbol{\theta}}^{i}_{k+1\|k+1} - \hat{\boldsymbol{\theta}}^{i-1}_{k+1\|k+1}\right\| > \varepsilon\left\|\hat{\boldsymbol{\theta}}_{k+1\|k}\right\|$	Loop over measurement update
(iv) $\hat{\mathbf{y}}^{i}_{k+1\|k+1} = \mathbf{h}_{k+1}\left(\hat{\boldsymbol{\theta}}^{i}_{k+1\|k+1}, \ddot{\mathbf{u}}^{g}_{1:k+1}\right)$	Predicted output vector
(v) $\mathbf{H}^{i}_{k+1} = \left.\dfrac{\partial \mathbf{h}_{k+1}\left(\boldsymbol{\theta}, \ddot{\mathbf{u}}^{g}_{1:k+1}\right)}{\partial \boldsymbol{\theta}^{T}}\right\|_{\hat{\boldsymbol{\theta}}^{i}_{k+1\|k+1}}$	FE response sensitivities matrix
(vi) $\hat{\mathbf{P}}^{\mathbf{yy},i}_{k+1\|k+1} = \mathbf{H}^{i}_{k+1}\hat{\mathbf{P}}^{\boldsymbol{\theta}\boldsymbol{\theta},i}_{k+1\|k+1}\left(\mathbf{H}^{i}_{k+1}\right)^{T} + \mathbf{R}_{k+1}$	Estimated response covariance matrix
(vii) $\hat{\mathbf{P}}^{\boldsymbol{\theta}\mathbf{y},i}_{k+1\|k+1} = \hat{\mathbf{P}}^{\boldsymbol{\theta}\boldsymbol{\theta},i}_{k+1\|k+1}\left(\mathbf{H}^{i}_{k+1}\right)^{T}$	Estimated cross-covariance matrix
Correction: output measurement $\mathbf{y}_{k+1}$ is recorded	
(viii) $\mathbf{K}^{i}_{k+1} = \hat{\mathbf{P}}^{\boldsymbol{\theta}\mathbf{y},i}_{k+1\|k+1}\left(\hat{\mathbf{P}}^{\mathbf{yy},i}_{k+1\|k+1}\right)^{-1}$	Kalman gain
(ix) $\hat{\boldsymbol{\theta}}^{i+1}_{k+1\|k+1} = \hat{\boldsymbol{\theta}}_{k+1\|k} + \mathbf{K}^{i}_{k+1}\left[\mathbf{y}_{k+1} - \hat{\mathbf{y}}^{i}_{k+1\|k+1} - \mathbf{H}^{i}_{k+1}\left(\hat{\boldsymbol{\theta}}_{k+1\|k} - \hat{\boldsymbol{\theta}}^{i}_{k+1\|k+1}\right)\right]$	A posteriori estimate of parameter vector
(x) $\hat{\mathbf{P}}^{\boldsymbol{\theta}\boldsymbol{\theta},i+1}_{k+1\|k+1} = \hat{\mathbf{P}}^{\boldsymbol{\theta}\boldsymbol{\theta}}_{k+1\|k} - \mathbf{K}^{i}_{k+1}\hat{\mathbf{P}}^{\mathbf{yy},i}_{k+1\|k+1}\left(\mathbf{K}^{i}_{k+1}\right)^{T}$	A posteriori estimate of parameter covariance matrix
end while	
(xi) $\hat{\boldsymbol{\theta}}_{k+1\|k+1} = \hat{\boldsymbol{\theta}}_{k+1\|k+1,N_{iter}+1}$	Final a posteriori estimate of parameter vector
(xii) $\hat{\mathbf{P}}^{\boldsymbol{\theta}\boldsymbol{\theta}}_{k+1\|k+1} = \hat{\mathbf{P}}^{\boldsymbol{\theta}\boldsymbol{\theta}}_{k+1\|k+1,N_{iter}+1}$	Final a posteriori estimate of parameter vector
end for	

9.4.3. Unscented Kalman filter (UKF)

The UKF evaluates the nonlinear measurement equation around the predicted parameter estimate $\hat{\boldsymbol{\theta}}_{k+1|k}$ in a set of $(2n_\theta + 1)$ regression points $\vartheta^{(i)}_{k+1|k}$ $(i = 1,\ldots,2n_\theta + 1)$,

referred to as sigma points (SPs). The SPs are deterministically chosen such that their sample mean and covariance matrix are equal to the predicted parameter estimate ($\hat{\boldsymbol{\theta}}_{k+1|k}$) and the predicted parameter covariance matrix estimate ($\hat{\mathbf{P}}^{\boldsymbol{\theta\theta}}_{k+1|k}$), respectively. The SPs are propagated through the nonlinear measurement function yielding

$$\boldsymbol{\gamma}^{(i)}_{k+1} = \mathbf{h}_{k+1}\left(\boldsymbol{\vartheta}^{(i)}_{k+1|k}, \ddot{\mathbf{u}}^{g}_{1:k+1}\right) \tag{9.24}$$

The UKF uses a linearized measurement equation with $\mathbf{H}_{k+1}, \mathbf{d}_{k+1}$, and $\boldsymbol{\rho}^{m}_{k+1}$ obtained by statistical linear regression (Lefebvre et al. 2005) though the pairs $\left(\boldsymbol{\vartheta}^{(i)}_{k+1|k}, \boldsymbol{\gamma}^{(i)}_{k+1}\right)$, $i = 1, \ldots, 2n_{\theta}+1$. This statistical linear regression is defined to minimize the difference ($\mathbf{e}_i$) between the nonlinear and linearized functions evaluated in the SPs in a least-squares sense:

$$\mathbf{e}_i = \boldsymbol{\gamma}^{(i)}_{k+1} - \left(\mathbf{H}\boldsymbol{\vartheta}^{(i)}_{k+1|k} + \mathbf{d}\right) \tag{9.25}$$

$$\left(\mathbf{H}_{k+1}, \mathbf{d}_{k+1}\right) = \arg\min_{(\mathbf{H},\mathbf{d})} \sum_{i=1}^{2n_{\theta}+1} \mathbf{e}_i \mathbf{e}_i^T \tag{9.26}$$

The solution of Equation (9.26) is given by (Lefebvre et al. 2005):

$$\mathbf{H}_{k+1} = \left(\hat{\mathbf{P}}^{\boldsymbol{\theta y}}_{k+1|k}\right)^T \left(\hat{\mathbf{P}}^{\boldsymbol{\theta\theta}}_{k+1|k}\right)^{-1} \quad ; \quad \mathbf{d}_{k+1} = \hat{\mathbf{y}}_{k+1|k} - \mathbf{H}_{k+1}\hat{\boldsymbol{\theta}}_{k+1|k} \tag{9.27}$$

where $\hat{\mathbf{P}}^{\boldsymbol{\theta\theta}}_{k+1|k}$ = predicted parameter covariance estimate computed as a weighted sample covariance of $\boldsymbol{\vartheta}^{(i)}_{k+1|k}$, $\hat{\mathbf{P}}^{\boldsymbol{\theta y}}_{k+1|k}$ = predicted cross-covariance estimate computed as the weighted sample covariance of $\boldsymbol{\vartheta}^{(i)}_{k+1|k}$ and $\boldsymbol{\gamma}^{(i)}_{k+1}$, and $\hat{\boldsymbol{\theta}}_{k+1|k}$ = predicted parameter

estimate computed as a weighted sample mean of $\boldsymbol{\vartheta}_{k+1|k}^{(i)}$. The sample covariance of $\mathbf{e}_i$ provides a measure of the magnitude of the linearization errors:

$$\mathbf{R}_{k+1}^{*} = \hat{\mathbf{P}}_{k+1|k}^{\mathbf{yy}} - \mathbf{H}_{k+1}\hat{\mathbf{P}}_{k+1|k}^{\boldsymbol{\theta\theta}}\mathbf{H}_{k+1}^{T} \tag{9.28}$$

in which $\hat{\mathbf{P}}_{k+1|k}^{\mathbf{yy}}$ = predicted output covariance estimate computed as a weighted sample covariance of $\boldsymbol{\psi}_{k+1}^{(i)}$, $i = 1,\ldots,2n_{\theta}+1$. Further details on the mathematical derivation of the UKF as the solution of a statistical linearization problem can be found in Lefebvre et al. 2005. Table 9.3 summarizes the UKF algorithm for the parameter estimation problem. In this chapter, the scaled unscented transformation (Wan and van der Merwe 2000) is used. Details about the formulation of the parameter estimation problem for frame-type distributed-plasticity FE models using the UKF can be found in Astroza et al. (2015a).

Table 9.3: Algorithm for nonlinear FE model updating using the UKF.

Initialization: $\hat{\boldsymbol{\theta}}_{0\|0}$ and $\hat{\mathbf{P}}_{0\|0}^{\boldsymbol{\theta\theta}}$	Initial estimates of parameter vector and parameter covariance matrix
for $k = 0,1,2,\ldots$	Loop over time steps
Prediction:	
(i) $\boldsymbol{\vartheta}_{k+1\|k}^{(i)} = \boldsymbol{\vartheta}_{k\|k}^{(i)}$ i=1,...,$2n_0+1$	Generate SPs
(ii) $\hat{\boldsymbol{\theta}}_{k+1\|k} = \hat{\boldsymbol{\theta}}_{k\|k}$	A priori estimate of parameter vector
(iii) $\hat{\mathbf{P}}_{k+1\|k}^{\boldsymbol{\theta\theta}} = \hat{\mathbf{P}}_{k\|k}^{\boldsymbol{\theta\theta}} + \mathbf{Q}_k$	A priori estimate of parameter covariance matrix
(iv) $\boldsymbol{\psi}_{k+1}^{(i)} = \mathbf{h}_{k+1}\left(\boldsymbol{\vartheta}_{k+1\|k}^{(i)}, \ddot{\mathbf{u}}_{1:k+1}^{g}\right)$	Output vector for each SP
(v) $\hat{\mathbf{y}}_{k+1\|k} = \sum_{i=1}^{2n_0+1} W_m^{(i)} \boldsymbol{\psi}_{k+1}^{(i)}$	Predicted output vector
(vi) $\hat{\mathbf{P}}_{k+1\|k}^{\mathbf{yy}} = \sum_{i=1}^{2n_0+1} W_c^{(i)}\left[\boldsymbol{\psi}_{k+1}^{(i)} - \hat{\mathbf{y}}_{k+1\|k}\right]\left[\boldsymbol{\psi}_{k+1}^{(i)} - \hat{\mathbf{y}}_{k+1\|k}\right]^{T} + \mathbf{R}_{k+1}$	Estimated response covariance matrix
(vii) $\hat{\mathbf{P}}_{k+1\|k}^{\boldsymbol{\theta}\mathbf{y}} = \sum_{i=1}^{2n_0+1} W_c^{(i)}\left[\boldsymbol{\vartheta}_{k+1\|k}^{(i)} - \hat{\boldsymbol{\theta}}_{k+1\|k}\right]\left[\boldsymbol{\psi}_{k+1}^{(i)} - \hat{\mathbf{y}}_{k+1\|k}\right]^{T}$	Estimated cross-covariance matrix
Correction: output measurement $\mathbf{y}_{k+1}$ is recorded	
(viii) $\mathbf{K}_{k+1} = \hat{\mathbf{P}}_{k+1\|k}^{\boldsymbol{\theta}\mathbf{y}}\left(\hat{\mathbf{P}}_{k+1\|k}^{\mathbf{yy}}\right)^{-1}$	Kalman gain
(ix) $\hat{\boldsymbol{\theta}}_{k+1\|k+1} = \hat{\boldsymbol{\theta}}_{k+1\|k} + \mathbf{K}_{k+1}\left(\mathbf{y}_{k+1} - \hat{\mathbf{y}}_{k+1\|k}\right)$	A posteriori estimate of parameter vector
(x) $\hat{\mathbf{P}}_{k+1\|k+1}^{\boldsymbol{\theta\theta}} = \hat{\mathbf{P}}_{k+1\|k}^{\boldsymbol{\theta\theta}} - \mathbf{K}_{k+1}\hat{\mathbf{P}}_{k+1\|k}^{\mathbf{yy}}\mathbf{K}_{k+1}^{T}$	A posteriori estimate of parameter covariance matrix
end for	

9.4.4. Non-sequential updating procedure

The computational burden of the FE model updating methodologies presented in Sections 9.4.1 to 9.4.3 is significant because the nonlinear FE model needs to be run from t_1 to t_k ($k = 1,\ldots,N$ where $N =$ number of data samples of the earthquake input excitation) when estimating the modeling parameters at time t_k. Astroza et al. (2015b) proposed three different non-sequential approaches to reduce the computational requirements of the model updating method for the case of the UKF. Here, one of these approaches, referred to as cumulative innovation, is also implemented for the EKF and IEKF. In this non-sequential updating approach the nonlinear FE model is updated at every $D > 1$ (D is called step update) time steps to reduce the computational demand. Nevertheless, all the output measurement from time step $(k - D + 2)$ to time step $(k + 1)$ are included in the innovation when updating the model at time step $(k + 1)$ (Figure 9.2); therefore, no information contained in the measured data are discarded. More details about the non-sequential updating procedure can be found in Astroza et al. (2015b).

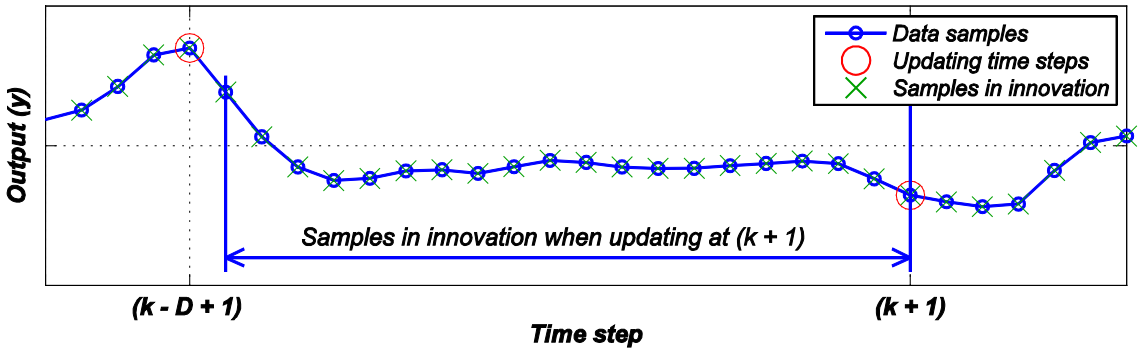

Figure 9.2: Cumulative innovation approach for non-sequential model updating.

9.5. Application example: 3D RC frame building under seismic excitation

A 3D 5-story 2-by-1 bay RC frame building subjected to bi-directional seismic excitation is considered to verify the performance of the proposed FE model updating methodology using the EKF, IEKF, and UKF and compare their performances. A mechanics-based nonlinear FE model of the building, developed in the open-source object-oriented software framework *OpenSees*, is used to simulate the response of the building. In the estimation phase, the simulated response data are contaminated by Gaussian noise and used as measured output ($\mathbf{y}$). Then, the input excitation and the measured output are used to estimate the parameters characterizing the nonlinear material constitutive laws of concrete and reinforcing steel. In addition, the performance of the FE model updating procedure is also analyzed when the input ($\ddot{\mathbf{u}}^g$) is also polluted by noise.

9.5.1. Nonlinear finite element model and input earthquake motions

The structure is designed as an intermediate moment-resisting RC frame for a moderate/intermediate seismic risk zone (downtown Seattle, WA) with Site Class D soil conditions, a short-period spectral acceleration S_{MS} = 1.37g, and a one-second spectral acceleration S_{M1} = 0.53g. The building has two bays in the longitudinal direction (X) and one bay in the transverse (Z) direction, with plan dimensions of 10.0×6.0 m, respectively. The frame has 5 stories with a floor-to-floor height of 4.0 m. Dead and live loads and the corresponding seismic masses are computed according to the 2006 International Building Code (ICC 2006). The building has six identical 0.45×0.45 m RC columns reinforced with 8 #8 longitudinal reinforcement bars and #3 bars spaced at 150 mm as transverse reinforcement. Grade 75 reinforcing steel is considered for the columns. Longitudinal

beams have a square cross-section of 0.40×0.40 m and are reinforced with 6 #8 longitudinal reinforcement bars and #3 bars spaced at 100 mm as transverse reinforcement. Transverse beams have a rectangular cross-section of 0.40×0.45 m and are reinforced with 8 #8 longitudinal reinforcement bars and #3 bars spaced at 100 mm as transverse reinforcement. Grade 60 reinforcing steel is considered for the beams in both directions. Figure 9.3 shows the overall geometry of the building and the cross-sections of beams and columns.

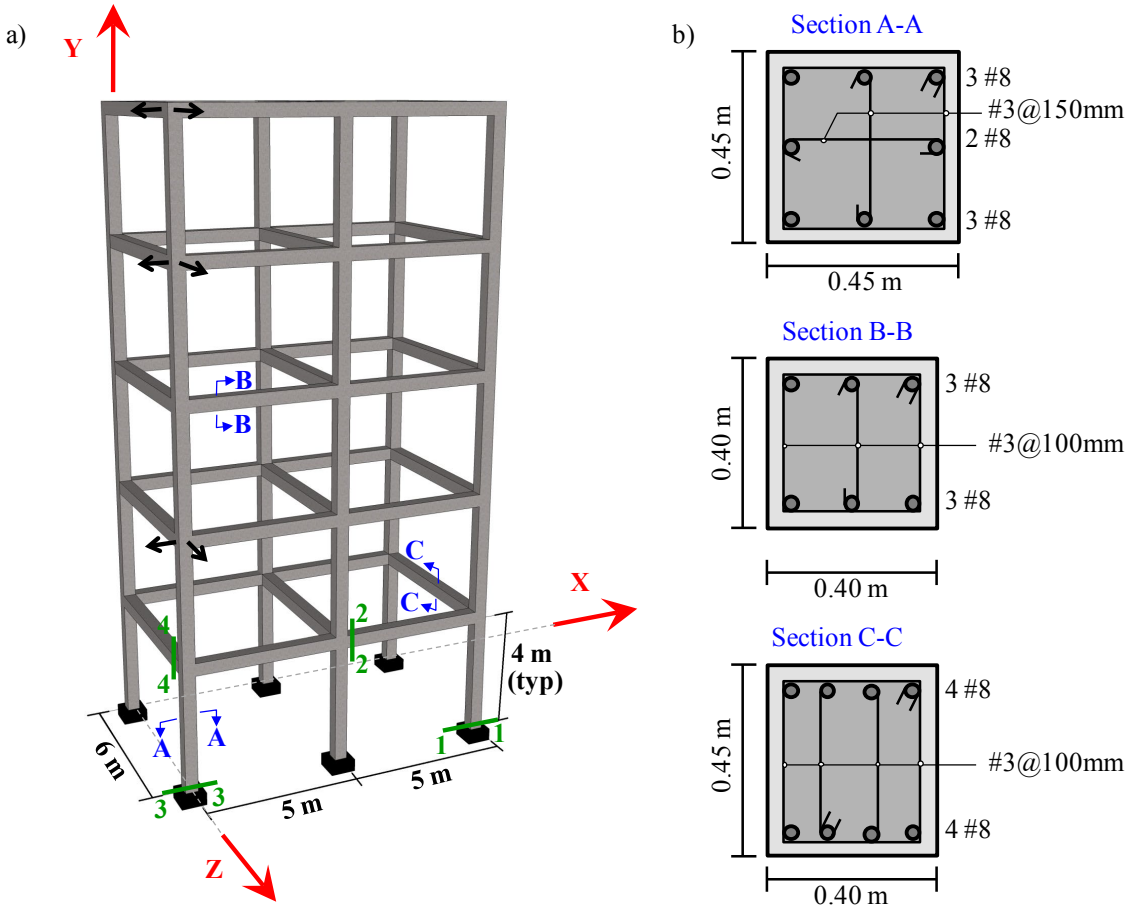

Figure 9.3: RC frame building: (a) Isometric view (black arrows represent the location of measured acceleration responses), (b) Cross-section of beams and columns.

The computation of the FE response sensitivities, required by the EKF and IEKF, is accomplished using DDM. To have a direct and fair comparison of the filters'

performance, the same FE model is used to simulate the response of the building and to conduct the parameter estimation. The modified Giuffré-Menegotto-Pinto model (Filippou et al. 1983) is used to model the nonlinear uniaxial stress-strain behavior of the reinforcing steel. This material model is governed by eight parameters, five of which control the curvature of the hysteretic loops and three corresponding to primary physical parameters. The latter consist of the elastic modulus (E_s), initial yield strength (f_y), and strain hardening ratio (b) and will be considered as unknown parameters to be estimated in this study. The Popovics-Saenz model (Popovics 1973, Saenz 1964, Balan et al. 2001) is used to model the concrete. Five material parameters define the nonlinear uniaxial stress-strain relationship in this material model. These parameters are the modulus of elasticity (E_c), peak compressive strength (f_c), strain at peak compressive strength (ε_c), crushing strength (f_u), and strain at crushing strength (ε_u). The values of f_c, ε_c, f_u, and ε_u correspond to the confined state of concrete and are computed based on the initial (undamaged) properties of the concrete material. f_c and ε_c account for confinement effects of the transverse reinforcement according to Mander et al. 1988, whereas ε_u is computed as suggested by Scott et al. (1982). Figure 9.4 shows the uniaxial material models used for concrete and reinforcing steel fibers and their corresponding parameters. The set of modeling parameter values, referred to as true values hereafter, for concrete and reinforcing steel materials are: $E_{s-col}^{true} = 200\ GPa$, $f_{y-col}^{true} = 517\ MPa$, $b_{col}^{true} = 0.01$, $E_{s-beam}^{true} = 200\ GPa$, $f_{y-beam}^{true} = 414\ MPa$, $b_{beam}^{true} = 0.05$, $E_c^{true} = 27600\ MPa$, $f_c^{true} = 40\ MPa$, $\varepsilon_c^{true} = 0.0035$, $f_u^{true} = 10\ MPa$, $\varepsilon_u^{true} = 0.01$. In Section 9.5.2 the sensitivities of these modeling parameters to a set of response quantities measured in the

building will be investigated and used to select the modeling parameters that will be included in the estimation process.

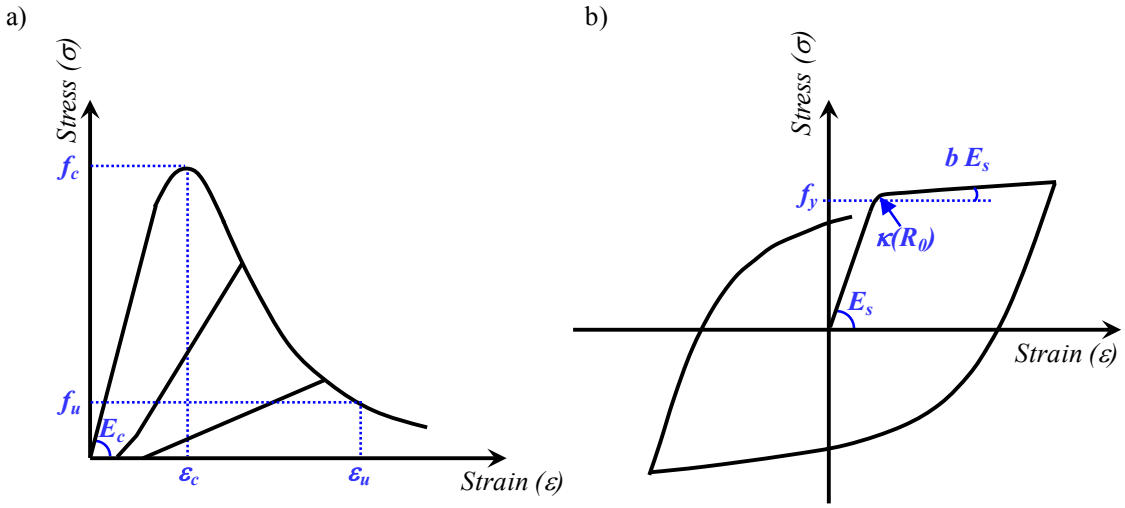

Figure 9.4: Uniaxial material models used in the FE model: (a) Concrete, (b) Reinforcing steel.

Figure 9.5 shows details of the FE model including mesh discretization, nodal masses, and gravity loads acting on beams. Displacement-based elements are used to model the beams and columns and Gauss-Lobatto quadrature is used for numerical integration along the elements. As displacement-based elements tend to localize deformations over a single element, referred to as plastic hinge (PH) element, the length of PH elements are selected to represent the physical plastic hinge zone of beams and columns, taken equal to 0.25 m for beams (≈ half of the height of the cross-section) and equal to 0.5 m for columns (≈ full height of the cross-section). Cross-sections of beams and column are discretized in longitudinal fibers as shown in Figure 9.5b. Linear shear and torsion force-deformation models are aggregated at the section level and along the element, uncoupled from the inelastic flexural-axial behavior.

The sources of energy dissipation beyond energy dissipated through hysteretic material behavior are modeled using mass and tangent stiffness-proportional Rayleigh damping (based on the tangent stiffness matrix at the last converged step of analysis). A critical damping ratio of 2% for the first and second natural periods (after application of the gravity loads) in the longitudinal direction of the building, T_1 = 2.01 sec and T_2 = 0.64 sec, is considered. The resulting mass and stiffness proportional parameters used to describe the Rayleigh damping are $\alpha_M = 0.0948$ and $\beta_K = 0.0031$, respectively. The FE model described above and the true values of the parameters are used to simulate the response of the structure, referred as true response hereafter.

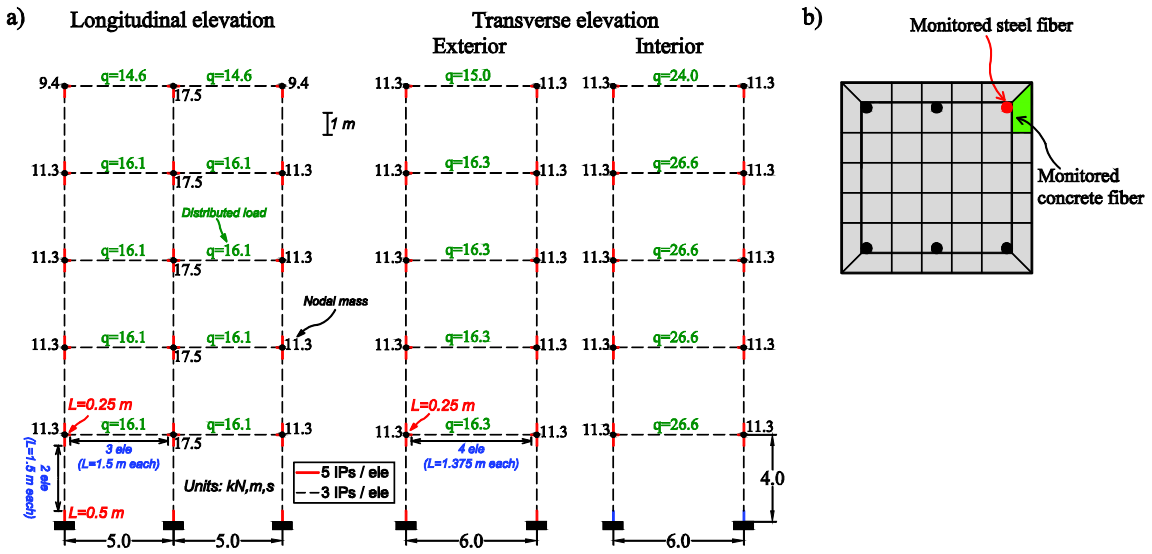

Figure 9.5: Finite element model: (a) mesh discretization, nodal masses, and distributed loads on beams, (b) cross-section fiber discretization.

Translation components of ground acceleration recorded at the Sylmar County Hospital during the 1994 Northridge earthquake are considered as input base excitation (Figure 9.6). Components 360° and 90° are applied in the longitudinal and transverse direction of the building, respectively. The acceleration ground motions were recorded at

a sampling rate of 50 Hz, filtered with a band-pass filter with cutoff frequencies of 0.1 and 23.0 Hz, and have $N = 550$ data samples. The peak ground acceleration (PGA) was 0.84g and 0.60g for components 360° and 90°, respectively.

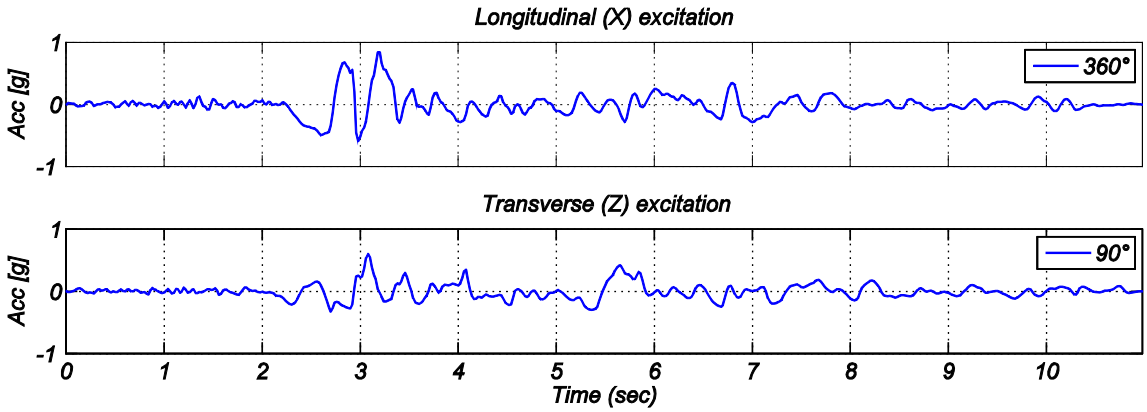

Figure 9.6: Base acceleration time history recorded at Sylmar County Hospital during the 1994 Northridge earthquake.

9.5.2. Sensitivity analysis for parameter selection

Before conducting the updating of the nonlinear FE model, the modeling parameters to be included in the estimation process ($\boldsymbol{\theta}$) need to be chosen. Parameters with negligible uncertainty (i.e., modeling parameters which deterministic values are known in advance) and parameters which variation has negligible effects on the measured outputs (i.e., the measured outputs are practically insensitive with respect to these parameters) should be removed from the model updating scheme. An appropriate parameter selection step should ensure the identifiability of the modeling parameters (Cheung and Beck 2009, Wan and Ren 2014).

In this section a simple first-order sensitivity analysis using the DDM is used to analyze the sensitivity of the measured responses with respect to the parameters of the constitutive laws used for steel and concrete (see Figure 9.4). It is noteworthy that the

analysis presented here corresponds to a local sensitivity approach. Unlike global sensitivity analysis, local sensitivity methods provide a local measure about the effect of a given parameter on a given measured response and are related to a fixed value in the space of modeling parameters. More details about local and global sensitivity analysis can be found in the literature (e.g., Saltelli et al. 2004, Kucherenko et al. 2009, Wan and Ren 2014).

A sparse instrumentation is assumed for the measured responses. Only two accelerometers, one for each translational direction, at the 3rd, 5th, and roof levels are considered (see Figure 9.3). In terms of modeling parameters, 3 primary material parameters define the constitutive law of each reinforcing steel (E_s, f_y, and b) and 5 material parameters define the constitutive law of the concrete (E_c, f_c, ε_c, f_u, and ε_u). Since the grade of the reinforcing steel in beams and columns is different, the total number of modeling parameters is 2×3+5=11. The sensitivity of each of the six outputs with respect to each of the eleven material parameters is computed using DDM. Figure 9.7 shows the time histories of the normalized roof transverse acceleration FE response sensitivities with respect to the eleven material parameters. It can be observed that the transverse roof acceleration ($\mathbf{a}_{6t}$) is less sensitive to f_u and ε_u than to other material parameters. For example, the roof transverse acceleration response is less sensitive to f_u than to b_{beam} by a factor of 5. Similar sensitivity results are obtained for all output response measurements, then all the measured responses are almost insensitive to f_u and ε_u. Therefore, these material parameters, for which all the response sensitivities are lower than 1.0, are eliminated from the modeling parameter vector to be estimated. As a

result, only nine modeling parameters are included in the estimation phase to update the nonlinear FE model: the three primary parameters of the reinforcing steel of columns (E_{s-col} , f_{y-col} , b_{col}), the three primary parameters of the reinforcing steel of beams (E_{s-beam} , f_{y-beam} , b_{beam}), and the three parameters of the concrete (E_c , f_c , ε_c).

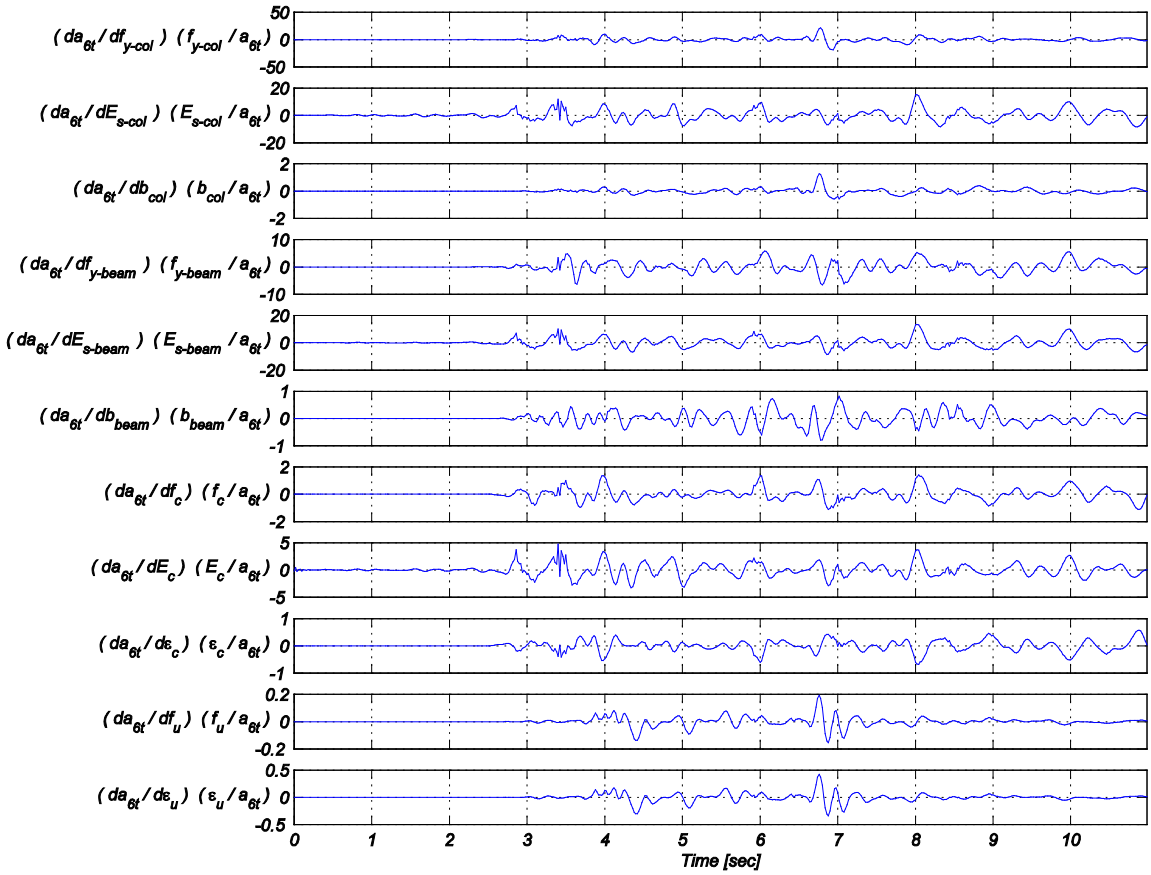

Figure 9.7: Time histories of the normalized sensitivity of the transverse acceleration at the roof with respect to the eleven modeling parameters.

9.5.3. FE Model updating results

Based on the analysis presented in Section 9.5.2, nine modeling parameters describing the concrete and reinforcing steel constitutive laws are considered as unknown and define the modeling parameter vector to be estimated, i.e.,

$\boldsymbol{\theta} = \left[E_{s-col}, f_{y-col}, b_{col}, E_{s-beam}, f_{y-beam}, b_{beam}, E_c, f_c, \varepsilon_c \right]^T \in \mathbb{R}^{9\times 1}$. The response of the structure is simulated using the true values of the parameters (see Section 9.5.1) and is referred to as the true response hereafter. After completion of the response simulation, the true relative accelerations at the 3rd, 5th, and roof levels in both translational directions are polluted by AWGN (representing output measurement noise, e.g., sensor and data acquisition system noises) defining the measured response data ($\mathbf{y}$). The contaminated measured response data and the translational components of the input ground acceleration ($\ddot{\mathbf{u}}^g$) recorded at Sylmar station during the 1994 Northridge earthquake (Figure 9.6) are used to estimate the modeling parameter vector and to update the nonlinear FE model of the structure. It is noted that the same FE model of the structure used to simulate the response is considered in the parameter estimation phase, i.e., the effects of modeling uncertainty are neglected. In what follows, the effects of output measurement noise level (Section 9.5.3.1), input measurement noise level (Section 9.5.3.2), and the non-sequential updating approach previously proposed for the UKF by Astroza et al. (2015b) to alleviate the computational burden (Section 9.5.3.3) are studied.

9.5.3.1. Effect of output measurement noise

The robustness of the nonlinear FE model updating methodologies with respect to output measurement noise is investigated by considering two levels of AWGN polluting the output response measurements, namely 1.0%*g* RMS and 2.0%*g* RMS. The indicated RMS values result in covariance matrices $0.96\times10^{-2}\mathbf{I}_6\left(m/s^2\right)^2$ and $3.85\times10^{-2}\mathbf{I}_6\left(m/s^2\right)^2$, respectively, where $\mathbf{I}_j = j\times j$ identity matrix. Output noises of different measurements

are assumed statistically uncorrelated. Both levels of measurement noise are high compared to the level of noise expected in acceleration responses recorded in building structures during real earthquakes, however, they are used here to verify the performance of the estimation procedure under extreme output noise conditions.

Because in practice only an estimate of the actual covariance matrix of the output measurement noise can be obtained, a zero-mean Gaussian process with a covariance matrix $\mathbf{R}_{k+1} = \mathbf{R} = 0.47 \times 10^{-2} \mathbf{I}_6 \left(m/s^2 \right)^2$ is assumed for the output measurement noise in the estimation phase, i.e., a standard deviation of 0.7%*g* RMS. Zero-mean and covariance matrix $\mathbf{Q}_k = \mathbf{Q}$ (i.e., time invariant) are assumed for the process noise $\boldsymbol{\gamma}_k$. The diagonal entries of $\mathbf{Q}$ are assumed equal to $(q \times \hat{\theta}^i_{0|0})^2$, with $i = 1, \ldots, 9$ and $q = 1 \times 10^{-5}$, i.e., it is constructed assuming a coefficient of variation (c.o.v.) of 1×10^{-5} of the initial estimate ($\hat{\boldsymbol{\theta}}_{0|0}$). In all the analyses conducted the initial unknown modeling parameter vector is assumed equal to $\hat{\boldsymbol{\theta}}_{0|0} = \left[0.7E^{true}_{s-col}, 1.3f^{true}_{y-col}, 1.25b^{true}_{col}, 1.3E^{true}_{s-beam}, 0.8f^{true}_{y-beam}, 0.75b^{true}_{beam}, 1.2E^{true}_{c}, 0.85f^{true}_{c}, 0.9\varepsilon^{true}_{c} \right]^T$. The initial estimate of the covariance matrix of the modeling parameters, $\hat{\mathbf{P}}^{\boldsymbol{\theta}\boldsymbol{\theta}}_{0|0}$, is assumed to be diagonal (i.e., statistically uncorrelated initial estimates of the modeling parameters) with terms computed as $(p \times \hat{\theta}^i_{0|0})^2$, with $i = 1, \ldots, 9$ and $p =$ c.o.v. of the initial estimate $\hat{\boldsymbol{\theta}}_{0|0}$. Values of $p = 15\%$ and $p = 5\%$ are studied.

Table 9.4 summarizes the final estimate (i.e., estimated at the last time step, $\hat{\boldsymbol{\theta}}_{N|N}$) and the corresponding c.o.v. of the modeling parameters obtained using the UKF, EKF,

and IEKF for both levels of output measurement noise. It is noted that these estimates correspond to stable and converged values. Excellent estimation results are obtained with all filters for modeling parameters E_{s-col}, f_{y-col}, E_{s-beam}, f_{y-beam}, b_{beam}, E_c, and f_c, with relative errors less or equal to 2%. The relative error between the final estimate of a parameter and its corresponding true value is computed as $\left(\hat{\boldsymbol{\theta}}_{N|N} - \boldsymbol{\theta}^{true}\right) \Big/ \boldsymbol{\theta}^{true} \times 100\,[\%]$. Modeling parameters b_{col} and ε_c are estimated with larger relative errors (≤ 7%), at the same time these parameters have associated larger estimates of the c.o.v. (about 1.5 – 2.0%). Larger relative errors and c.o.v. in the final estimates of b_{col} and ε_c stem from the small sensitivity of the measured responses to these parameters (see Section 9.5.2) and, therefore, less information about them is contained in $\mathbf{y}$. As the output measurement noise level increases from 1% to 2% RMS, the accuracy of the modeling parameter estimates slightly deteriorate, mainly for the modeling parameters with less information in the measured output responses (b_{col} and ε_c). The final estimate of the c.o.v. (or covariance matrix $\hat{\mathbf{P}}^{\boldsymbol{\theta\theta}}_{N|N}$) remains practically unchanged as the output measurement noise increases. In Table 9.4, the dash symbol (–) indicates the runs for which the nonlinear FE model experienced convergence problems due to the values of the modeling parameters estimates at some specific time step, and therefore no final estimate of the modeling parameters are reported for those cases since the estimation process did not finish. It is observed that in Case 1 (1% noise) the three filters provide very similar final estimates and c.o.v.s with both p = 5% and p = 15%, showing that for this application example and

initial modeling parameter vector ($\hat{\boldsymbol{\theta}}_{0|0}$), even small values in the diagonal of $\hat{\mathbf{P}}^{\boldsymbol{\theta}\boldsymbol{\theta}}_{0|0}$ allow the filters to drive the estimates to their true values.

Table 9.4: Final estimate and coefficient of variation (in parenthesis) of the modeling parameters for different levels of output measurement noise.

Case	Output Noise (%)	Input noise (%)	Step update (D)	Filter	Initial c.o.v. (p) (%)	Modeling parameter								
						$\frac{E_{s-col}}{E^{true}_{s-col}}$	$\frac{f_{y-col}}{f^{true}_{y-col}}$	$\frac{b_{col}}{b^{true}_{col}}$	$\frac{E_{s-beam}}{E^{true}_{s-beam}}$	$\frac{f_{y-beam}}{f^{true}_{y-beam}}$	$\frac{b_{beam}}{b^{true}_{beam}}$	$\frac{E_c}{E^{true}_c}$	$\frac{f_c}{f^{true}_c}$	$\frac{\varepsilon_c}{\varepsilon^{true}_c}$
1	1.0	0.0	1	UKF	15	1.00 (0.09)	1.00 (0.06)	1.01 (1.47)	1.00 (0.13)	1.00 (0.08)	0.99 (0.32)	1.00 (0.21)	1.01 (0.87)	0.98 (1.88)
					5	1.00 (0.08)	1.00 (0.06)	1.06 (1.26)	1.00 (0.13)	1.00 (0.07)	1.00 (0.29)	1.01 (0.19)	1.00 (0.63)	0.94 (1.34)
				EKF	15	1.00 (0.11)	1.00 (0.07)	1.04 (1.58)	1.00 (0.15)	1.00 (0.09)	0.99 (0.31)	1.00 (0.33)	1.00 (0.95)	0.99 (2.11)
					5	1.00 (0.11)	1.00 (0.07)	1.04 (1.51)	1.00 (0.15)	1.00 (0.10)	1.00 (0.31)	1.01 (0.35)	1.00 (0.83)	0.95 (1.73)
				IEKF	15	1.00 (0.11)	1.00 (0.07)	1.04 (1.51)	1.00 (0.15)	1.00 (0.10)	1.00 (0.31)	1.01 (0.35)	1.00 (0.82)	0.95 (1.71)
					5	1.00 (0.11)	1.00 (0.07)	1.06 (1.49)	1.01 (0.15)	1.00 (0.09)	0.99 (0.31)	0.99 (0.32)	0.98 (0.84)	0.98 (1.76)
2	2.0	0.0	1	UKF	15	1.00 (0.09)	0.99 (0.06)	1.08 (1.40)	0.99 (0.13)	1.00 (0.08)	0.99 (0.31)	1.02 (0.21)	1.02 (0.80)	0.93 (1.71)
					5	1.00 (0.08)	1.00 (0.06)	1.07 (1.32)	0.99 (0.13)	1.00 (0.08)	1.00 (0.29)	1.01 (0.20)	1.01 (0.73)	0.92 (1.47)
				EKF	15	–	–	–	–	–	–	–	–	–
					5	1.00 (0.11)	1.00 (0.07)	1.07 (1.50)	1.00 (0.15)	1.00 (0.09)	0.99 (0.31)	1.01 (0.33)	1.01 (0.88)	0.96 (1.76)
				IEKF	15	–	–	–	–	–	–	–	–	–
					5	1.00 (0.11)	1.00 (0.07)	1.07 (1.48)	1.00 (0.15)	1.00 (0.09)	0.99 (0.31)	1.01 (0.33)	1.00 (0.84)	0.94 (1.67)

It is observed that in Case 2 with $p = 15\%$, and in many other cases with $p = 15\%$ discussed later, the EKF and IEKF do not provide estimates of the modeling parameters due to convergence problems of the nonlinear FE model during the updating procedure. It is noted that larger p implies that the filter relies more on the measured response data and less in the initial estimate of the modeling parameters and therefore a faster convergence rate in the estimation can be obtained if $\hat{\mathbf{P}}^{\boldsymbol{\theta}\boldsymbol{\theta}}_{0|0}$ is larger, however, this may negatively affect the stability (e.g., Hoshiya and Saito 1984). Since the EKF and IEKF are based on the analytical linearization of the nonlinear state-space model (see

Sections 9.4.1 and 9.4.2), it is expected that large initial values in $\hat{\mathbf{P}}_{0|0}^{\boldsymbol{\theta\theta}}$ will induce large and abrupt changes in the modeling parameters when the measured data become sensitive to them, which in turn can produce convergence issues in the mechanics-based nonlinear FE model. In the case of the UKF, large and abrupt changes in the estimates of the modeling parameters are prevented by avoiding the analytical linearization of the nonlinear state-space model. Moreover, in the particular case of the scaled unscented transformation (UT), the convergence rate can also be controlled by a parameter defining the spread of the SPs around the mean value, which in this study is set equal to 0.01 as recommended by Wan and der Merwe (2000). These remarks can be observed in Figure 9.8, where the time histories of the *a posteriori* normalized estimates (normalized by their corresponding true values) of three modeling parameters, (b_{col}, b_{beam}, and E_c) obtained with the UKF and EKF for Case 1 and both values of p (5 and 15%) are shown. In this figure, the area between the envelopes mean ± standard deviation ($\mu \pm \sigma$) for $p = 15\%$ is shaded in grey. From Figure 9.8a, it is noted that the UKF converges smoothly to the true values of the modeling parameters and that the convergence is faster and with more oscillations in the case of $p = 15\%$. In addition, the uncertainty (measured by σ or c.o.v.) in the estimates decreases asymptotically to zero as more output data sensitive to the corresponding parameters are assimilated. From Figure 9.8b, it is noted that the EKF produces abrupt changes in the estimate of a modeling parameter as soon as output data contain information about that parameter, especially when $p = 15\%$. This effect is clearly observed for E_c and b_{beam}, in which large and abrupt jumps in the estimates are observed at the beginning of the excitation ($t < 1.0\,\text{sec}$) and at around $t = 2.5\,\text{sec}$, respectively. As

pointed out before, these abrupt and large jumps in the estimates of the modeling parameters can lead to problems of convergence of the nonlinear FE model. It is noted that a large initial covariance matrix $\hat{\mathbf{P}}_{0|0}^{\theta\theta}$ (large p) is required when the initial estimate $\hat{\boldsymbol{\theta}}_{0|0}$ is far from the true value of the modeling parameter vector. In the case of mechanics-based nonlinear FE models, many parameters to be estimated are physical quantities and therefore a fairly good initial estimate might be guessed based on engineering experience and material testing. However, larger errors in the initial estimates are expected for empirical parameters or in the case that actual construction in the field does not follow the values specified in the as-built drawings/specifications of the structure.

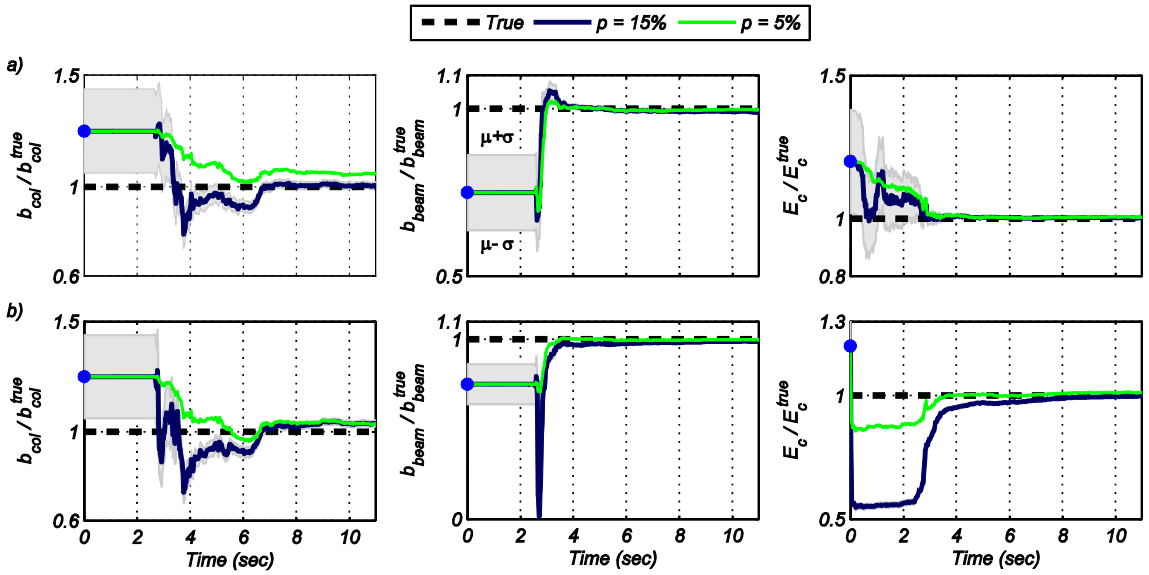

Figure 9.8: Time histories of the *a posteriori* estimates of the modeling parameter for Case 1 (noiseless input, 1.0%*g* RMS output measurement noise, and step update=1) and both initial coefficients of variation (5 and 15%). (a) UKF, (b) EKF.

Figure 9.9 shows the time histories of the *a posteriori* normalized estimates of the nine modeling parameters for Case 1 (noiseless input, 1.0%*g* RMS output measurement

noise, and step update = 1) and $p = 5\%$. The estimates of the three filters converge to the true values for those parameters that the output measured response are very sensitive to (E_{s-col}, f_{y-col}, E_{s-beam}, f_{y-beam}, b_{beam}, E_c, and f_c). In the case of b_{col} and ε_c, the time histories of the estimates approach to the true values but the estimates do not stabilize and fluctuate until the end of the time history, because there is no enough information about them in the output measured response. Astroza et al. (2015b) demonstrate that the use of heterogeneous sensor arrays, in addition to displacement and/or strain output measurements, improve the identifiability of those parameters that acceleration responses might be not very sensitive to, such as post-yield parameters of reinforcing steel (b) and compressive strength parameters of concrete (f_c and ε_c).

Stiffness related parameters (E_{s-col}, E_{s-beam} and E_c) start updating from the first time steps, because output measured response during low amplitude excitation contain information about them. In particular, FE response sensitivities of $\mathbf{y}$ with respect to E_c during the first time steps are much higher than those of other modeling parameters. Consequently, as discussed above, the EKF and IEFK induce large and abrupt jumps in the estimate of E_c at the beginning of the excitation. Stiffness related parameters converge to their true values at around 4 sec. When the input excitation increases and the structure undergo nonlinear behavior, the yield (f_y) and post-yield (b) parameters of steel and compressive strength parameters of concrete (f_c and ε_c) start to update at about $t = 2.5\,\text{sec}$. Because the design of the frame satisfies the strong column–weak beam requirement, the nonlinear response in beams is larger than in columns, and therefore

b_{beam} is estimated more accurately than b_{col}, since post-yield parameters of the reinforcing steel material model require that the strain ductility demand of enough steel fibers increase sufficiently. In general, the UKF and EKF have a similar convergence rate, faster and more stable than that of the IEKF.

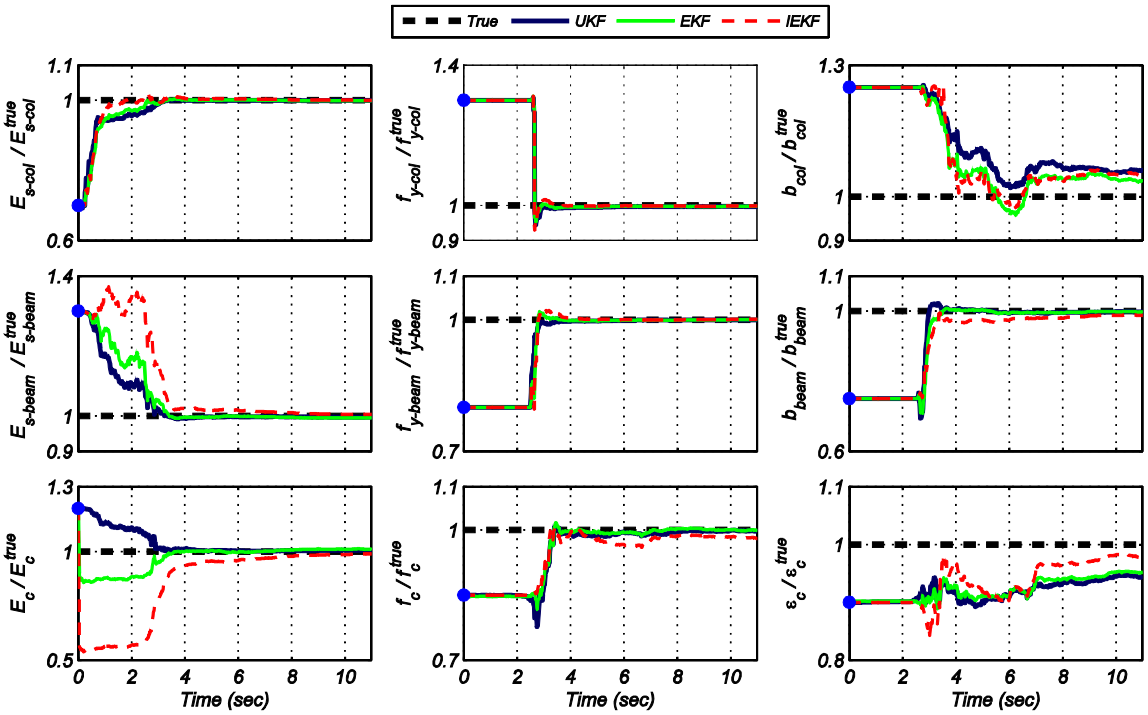

Figure 9.9: Time histories of the *a posteriori* estimates of the modeling parameter for Case 1 (noiseless input, 1.0%*g* RMS output measurement noise, and step update=1) and initial c.o.v.=5%.

Table 9.5 summarizes the relative RMS error (*RRMSE*) between the true responses and their counterparts obtained using the final estimate of the modeling parameters ($\hat{\boldsymbol{\theta}}_{N|N}$). Recall that the *RRMSE* between two signals $\mathbf{s}^1$ (reference) and $\mathbf{s}^2$ is computed as $RRMSE[\%] = \sqrt{\left[1/Nt\sum_{i=1}^{Nt}\left(s_i^1 - s_i^2\right)^2\right]} \Big/ \sqrt{\left[1/Nt\sum_{i=1}^{Nt}\left(s_i^1\right)^2\right]} \times 100$, where Nt is the total number of data samples in the signals. Here, output response $\mathbf{a}_{ij}$ corresponds

to the relative acceleration time history at story i in direction j, where l and t stand for longitudinal and transverse directions, respectively. The *RRMSE*s between the true and corresponding simulated responses using the initial estimate of the modeling parameter ($\hat{\boldsymbol{\theta}}_{0|0}$) are equal to 58.89, 38.33, 37.86, 39.62, 45.48, and 40.64 for $\mathbf{a}_{3l}$, $\mathbf{a}_{5l}$, $\mathbf{a}_{6l}$, $\mathbf{a}_{3t}$, $\mathbf{a}_{5t}$, and $\mathbf{a}_{6t}$, respectively. Based on the results exhibited in Table 9.5, the successful updating of the nonlinear FE model is clearly observed. The discrepancies between the true measured and simulated responses of the updated FE model are almost negligible, with most of the *RRMSE*s lower than 1.0%. The lowest *RRMSE*s for a given value of p are obtained with the UKF, however the differences between the three different filters are insignificant. The low *RRMSE*s also confirm that the measured acceleration responses do not contain enough information about modeling parameters b_{col} and ε_c, and therefore they cannot be accurately estimated (see Table 9.4).

Table 9.5: *RRMSE* between true and estimated output response measurements for different levels of output measurement noise.

Case	Output Noise (%)	Input noise (%)	Step updat e(D)	Filter	Initial c.o.v. (p) (%)	Output response measurement ($\mathbf{y}$)					
						$\mathbf{a}_{3l}$	$\mathbf{a}_{5l}$	$\mathbf{a}_{6l}$	$\mathbf{a}_{3t}$	$\mathbf{a}_{5t}$	$\mathbf{a}_{6t}$
1	1.0	0.0	1	UKF	15	0.41	0.28	0.23	0.24	0.24	0.25
					5	0.34	0.27	0.28	0.40	0.35	0.37
				EKF	15	0.56	0.28	0.22	0.33	0.25	0.30
					5	0.47	0.29	0.27	0.45	0.40	0.47
				IEKF	15	0.47	0.30	0.29	0.49	0.45	0.51
					5	0.58	0.32	0.30	0.53	0.42	0.50
2	2.0	0.0	1	UKF	15	1.05	0.67	0.58	0.73	0.71	0.83
					5	0.65	0.56	0.50	0.70	0.69	0.67
				EKF	15	–	–	–	–	–	–
					5	0.72	0.52	0.37	0.48	0.45	0.48
				IEKF	15	–	–	–	–	–	–
					5	0.63	0.46	0.36	0.52	0.49	0.51

Several unobserved global and local response quantities of the building obtained using the true modeling parameters (i.e., true responses) and the final estimate of the modeling parameters ($\hat{\boldsymbol{\theta}}_{N|N}$) are compared in Figure 9.10. Base shear in longitudinal and transverse directions (V_b^x and V_b^z, respectively) normalized by the total weight of the building (W) versus the roof drift ratio in the corresponding direction (RDR^x and RDR^z) are plotted in Figure 9.10a−b, respectively. Moment (M) versus curvature (κ) for sections at the base of a column (section 1−1 in Figure 9.3a) and at the end of a 2nd floor longitudinal beam (section 2−2 in Figure 9.3a) are shown in Figure 9.10c−d, respectively. Fiber level response are presented in Figure 9.10e−f, where the stress (σ) versus strain (ε) of a monitored reinforcing steel fiber at the bottom of a column (section 1−1 in Figure 9.3a) and a monitored concrete fiber at the end of a 2nd floor transverse beam (section 4−4 in Figure 9.3a) are plotted. The excellent agreement between the true and estimated response based on $\hat{\boldsymbol{\theta}}_{N|N}$ corroborates that the updated FE models obtained using UKF, EKF, and IEKF can be reliably used for damage identification purposes.

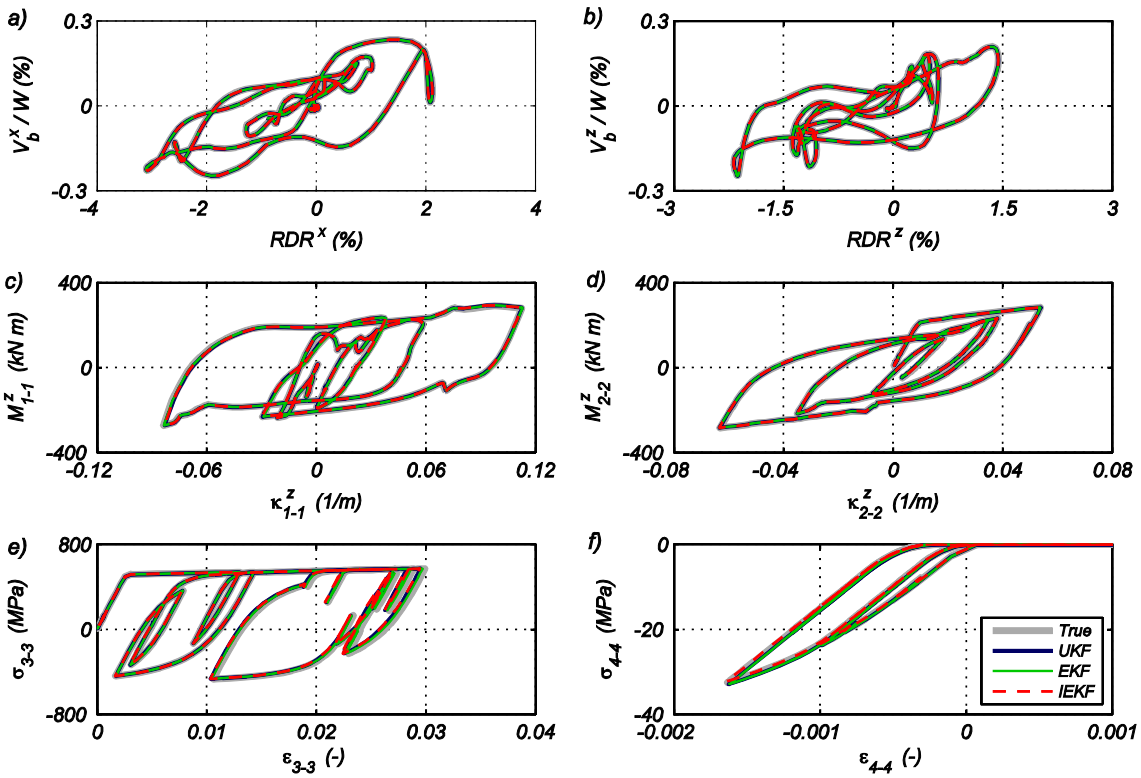

Figure 9.10: Comparison of true unobserved responses and estimated unobserved responses based on the final estimate of modeling parameters for Case 1 (noiseless input, 1.0%*g* RMS output measurement noise, and D = 1) and p = 5%. (a) normalized base shear versus roof drift ratio in the longitudinal direction, (b) normalized base shear versus roof drift ratio in the transverse direction, (c) moment versus curvature at the base of a column (section 1−1 in Figure 9.3a), (d) moment versus curvature at the end of longitudinal beam (section 2−2 in Figure 9.3a), (e) stress versus strain of a reinforcing steel fiber at the bottom of a column (section 1−1 in Figure 9.3a), (f) stress versus strain of a concrete fiber at the end of a transverse beam (section 4−4 in Figure 9.3a).

9.5.3.2. Effect of input measurement noise

The parameter estimation framework presented in Section 9.4 does not explicitly account for input measurement noise; therefore the potential detrimental effects of this assumption are studied in this section. Two cases of AWG input measurement noise level are considered: 0.5% and 1.0%*g* RMS. An output measurement noise of 1.0%*g* RMS is assumed, therefore Case 1 presented in Section 9.5.3.1 corresponds to the noiseless input measurement situation. Table 9.6 summarizes the final estimate (i.e., estimated at the last

time step, $\hat{\boldsymbol{\theta}}_{N|N}$) and the corresponding c.o.v. of the modeling parameters obtained using the UKF, EKF, and IEKF for both levels of input measurement noise. Figure 9.11 shows the relative error between the true values of the modeling parameters and the final estimates obtained using the UKF, EKF, and IEKF for both values of *p*. Figure 9.12 shows the time histories of the *a posteriori* estimates of the modeling parameters for Case 3 (see Table 9.6) and initial c.o.v.=5%. Similarly to the results discussed in Section 9.5.3.1, convergence problems of the nonlinear FE model are faced during the updating process when using the EKF and IEKF and $p = 15\%$, and therefore these cases do not provide estimates of the modeling parameters. For the three filters, as the level of input measurement noise increases the relative error for those parameters for which the output measured responses are less sensitive to, i.e., ε_c, b_{col}, and f_c, increases considerably, especially for ε_c with 1.0%*g* RMS input noise. For the remaining parameters (E_{s-col}, f_{y-col}, E_{s-beam}, f_{y-beam}, b_{beam}, and E_c), the output measured response contain considerable information and consequently the relative error is lower than 4% regardless the level of input measurement noise. This observation confirms the robustness of the parameter estimation framework (with all filters) to input measurement noise, in spite that it is not considered in the formulation.

Table 9.6: Final estimate and coefficient of variation (in parenthesis) of the modeling parameters for different levels of input measurement noise.

Case	Output Noise (%)	Input noise (%)	Step update (D)	Filter	Initial c.o.v. (p)(%)	Modeling parameter								
						$\frac{E_{s-col}}{E_{s-col}^{true}}$	$\frac{f_{y-col}}{f_{y-col}^{true}}$	$\frac{b_{col}}{b_{col}^{true}}$	$\frac{E_{s-beam}}{E_{s-beam}^{true}}$	$\frac{f_{y-beam}}{f_{y-beam}^{true}}$	$\frac{b_{beam}}{b_{beam}^{true}}$	$\frac{E_c}{E_c^{true}}$	$\frac{f_c}{f_c^{true}}$	$\frac{\varepsilon_c}{\varepsilon_c^{true}}$
3	1.0	0.5	1	UKF	15	1.00 (0.09)	1.00 (0.08)	1.04 (1.49)	0.99 (0.12)	1.00 (0.09)	1.01 (0.34)	1.01 (0.22)	0.98 (0.71)	0.93 (1.57)
					5	1.00 (0.08)	1.00 (0.06)	1.07 (1.41)	0.99 (0.13)	0.99 (0.09)	1.02 (0.33)	1.01 (0.21)	0.99 (0.76)	0.92 (1.47)
				EKF	15	–	–	–	–	–	–	–	–	–
					5	1.00 (0.11)	1.00 (0.07)	1.05 (1.52)	0.99 (0.15)	1.00 (0.10)	1.01 (0.31)	1.02 (0.35)	0.99 (0.78)	0.92 (1.63)
				IEKF	15	–	–	–	–	–	–	–	–	–
					5	1.00 (0.11)	1.00 (0.07)	1.08 (1.60)	1.01 (0.15)	1.00 (0.10)	0.99 (0.31)	0.97 (0.29)	0.95 (0.83)	0.97 (1.78)
4	1.0	1.0	1	UKF	15	1.00 (0.09)	1.00 (0.06)	1.12 (1.55)	0.99 (0.13)	1.00 (0.09)	1.05 (0.32)	1.01 (0.22)	0.91 (0.68)	0.78 (1.30)
					5	1.00 (0.08)	1.00 (0.06)	1.13 (1.46)	0.99 (0.13)	0.99 (0.08)	1.04 (0.33)	1.01 (0.21)	0.94 (0.69)	0.82 (1.33)
				EKF	15	–	–	–	–	–	–	–	–	–
					5	1.00 (0.11)	1.00 (0.07)	1.07 (1.61)	0.99 (0.15)	1.00 (0.10)	1.02 (0.31)	1.03 (0.35)	0.96 (0.78)	0.84 (1.59)
				IEKF	15	–	–	–	–	–	–	–	–	–
					5	1.00 (0.11)	1.00 (0.07)	1.09 (1.63)	0.99 (0.15)	1.00 (0.10)	1.02 (0.31)	1.03 (0.35)	0.95 (0.77)	0.83 (1.55)

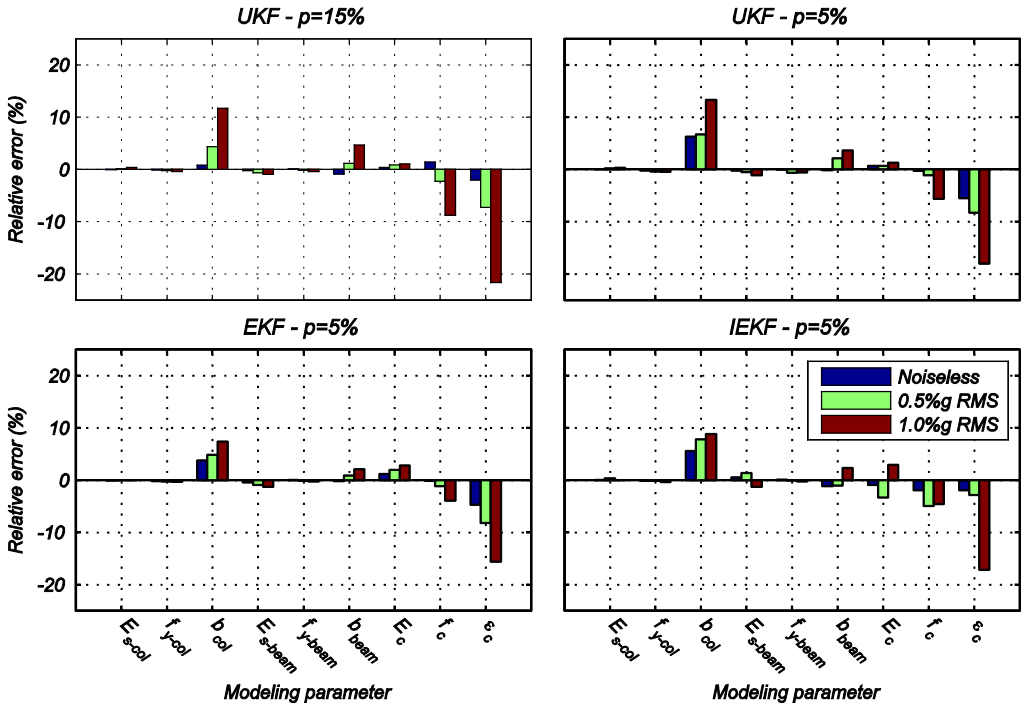

Figure 9.11: Relative errors between true modeling parameter values (reference) and the corresponding final estimates for different levels of input measurement noise.

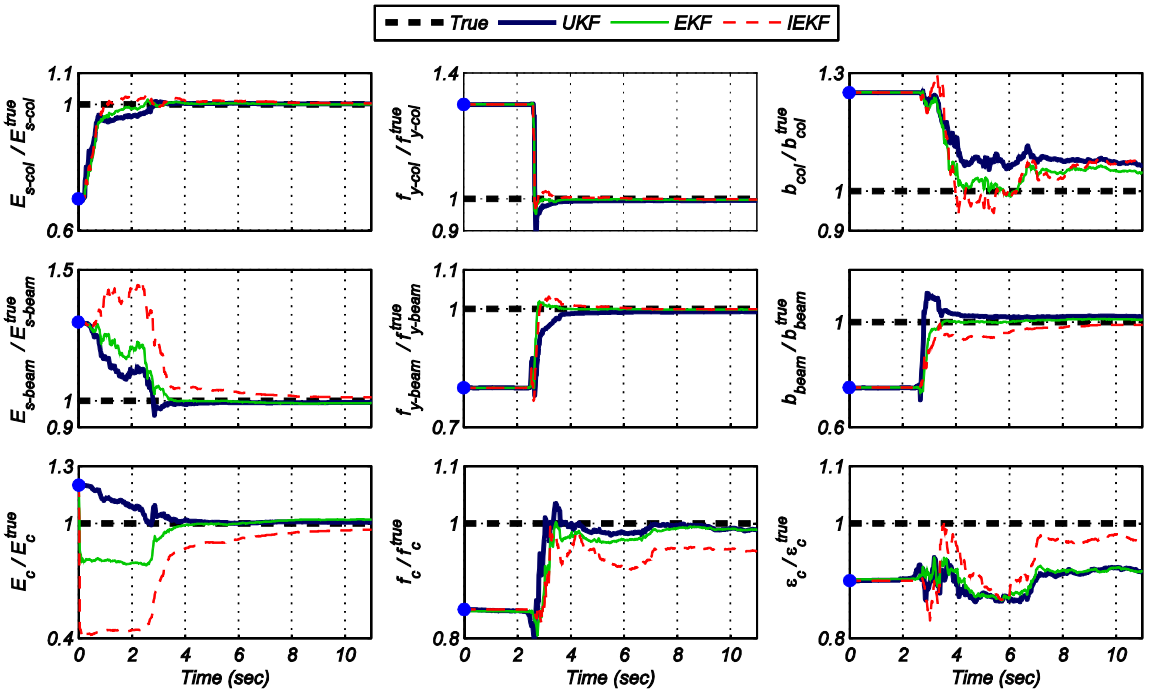

Figure 9.12: Time histories of the a posteriori estimates of the modeling parameter for Case 3 (0.5%g RMS input measurement noise, 1.0%g RMS output measurement noise, and step update=1) and initial c.o.v.=5%.

Figure 9.13 summarizes the *RRMSE*s between the true measured responses and their counterparts obtained using the final estimate of the modeling parameters and the noiseless input excitation for different levels of input measurement noise. The *RRMSE* slightly increases as the level of AWGN in the input excitation increases. Similar errors are obtained with all three filters. In all cases the *RRMSE* is lower than 1.5%, which demonstrates the excellent robustness to input measurement noise of the FE model updating methodology when the UKF, EKF, or IEKF are used as parameter estimation tool. Recall that the levels of input and output measurement noises used in this chapter are significantly higher than those expected in real-world earthquake engineering applications; nonetheless, they are considered to investigate the performance and robustness of the estimation framework under adverse conditions.

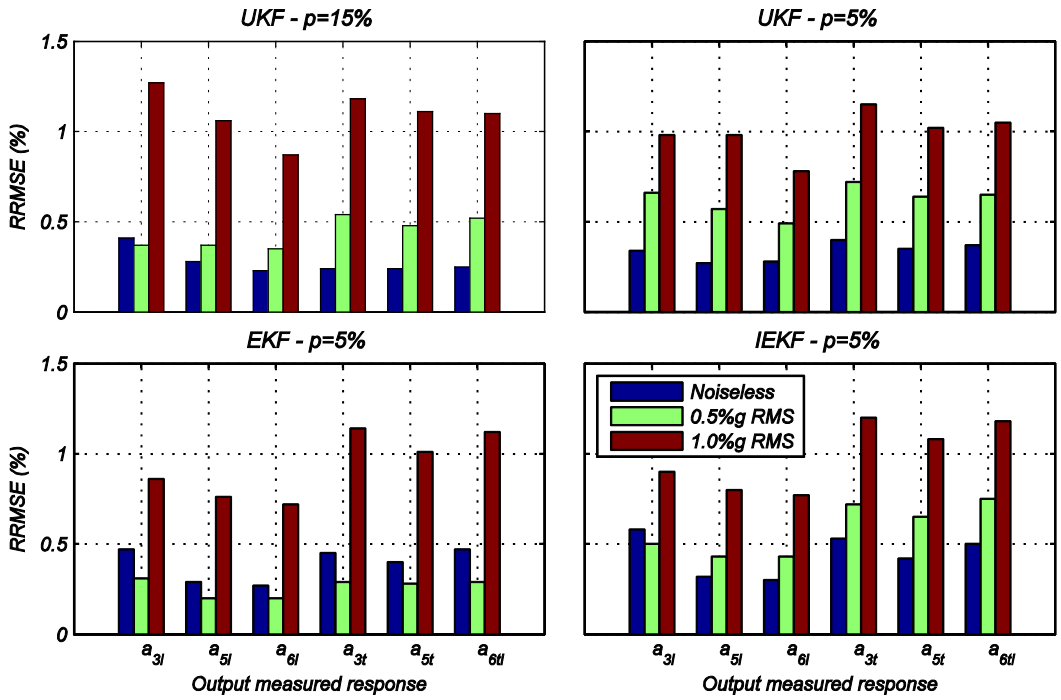

Figure 9.13: Relative RMS errors between true responses and their counterparts obtained using the final estimate of the modeling parameters and the noiseless input for different levels of input measurement noise.

To analyze if the deterioration in the estimates of the modeling parameters for which the output measured responses are less sensitive to (see Figure 9.11), the same unobserved global and local response quantities analyzed in Section 9.5.3.1, are plotted in Figure 9.14. The agreement between true responses and those estimated from the final estimate of the modeling parameters is excellent. This confirms that the updated FE model can be reliable used to identify and quantify the damage in the structure at different resolution levels, from global system to local member and sub-component levels (e.g., yielding in reinforcing steel and crushing of concrete), even in the presence of high levels of input measurement noise.

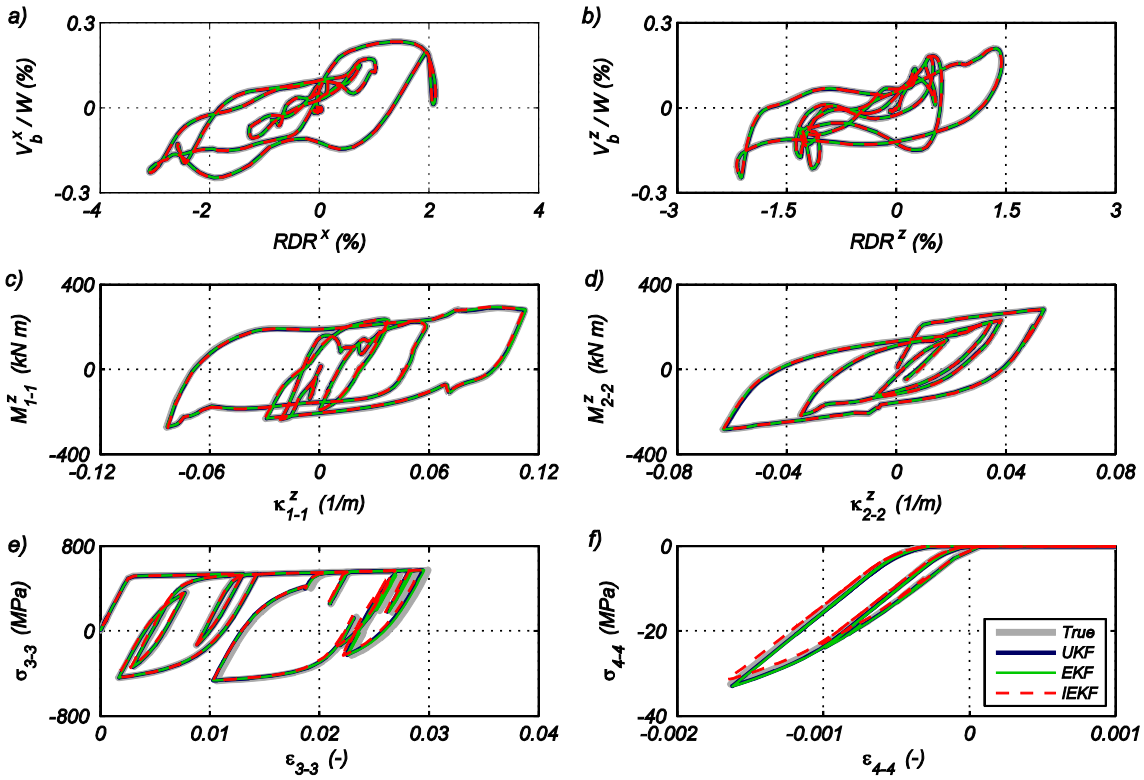

Figure 9.14: Comparison of true unobserved responses and estimated unobserved responses from the final estimate of modeling parameters for the case with 0.5%g RMS input measurement noise, 1.0%*g* RMS output measurement noise, $D = 1$, and $p = 5\%$. (a) normalized base shear versus roof drift ratio in the longitudinal direction, (b) normalized base shear versus roof drift ratio in the transverse direction, (c) moment versus curvature at the base of a column (section 1−1 in Figure 9.3a), (d) moment versus curvature at the end of longitudinal beam (section 2−2 in Figure 9.3a), (e) stress versus strain of a reinforcing steel fiber at the bottom of a column (section 1−1 in Figure 9.3a), (f) stress versus strain of a concrete fiber at the end of a transverse beam (section 4−4 in Figure 9.3a).

9.5.3.3. Effect of non-sequential updating

In this section the non-sequential updating procedure (see Section 9.4.4) previously proposed by Astroza et al. (2015b), which was originally developed for the UKF, is also implemented for the EKF and IEKF. The performance of the parameter estimation framework using non-sequential updating and the three filters is investigated in terms of convergence, accuracy, and robustness for the three filters. Three updating

steps, in addition to the reference case in which the FE model is updated at every time step, are studied: D = 5, 10, 20. Here, the results for noiseless input excitation are summarized; however, consistent results are also obtained when 0.5%g RMS input measurement noise is considered.

Figure 9.15 shows the relative error between the true values and the final estimate of the unknown modeling parameters obtained using the different filters and for both values of p. Similarly to the results shown in Section 9.5.3.1 and 9.5.3.2, the EKF and IEKF experienced problems associated to convergence of the nonlinear FE model when D = 5 and p = 15%, however this is not the case with $D=10$ and $D=20$. This is because in the non-sequential procedure when the FE model is updated at time step $(k+1)$, the innovation vector includes the output measured responses from time steps $(k-D+1)$ to $(k+1)$ (last D time steps). Therefore, the new estimate of the modeling parameters minimize the discrepancies between the measured and estimated response for those D time steps, which avoids large and abrupt changes in the estimates of the modeling parameters when D is large. However, it is noted that D cannot be increased indefinitely as to avoid the loss of information extracted from the response data.

The relative error in the estimates of the modeling parameters obtained by the UKF, EKF, and IEKF slightly increases as D increases. The UKF and EKF have similar performance in terms of accuracy in the estimation of the parameters, except for b_{col}, f_c, and ε_c when p=15%. The IEKF outperforms the UKF and EKF because of its iterative scheme, which allows to further minimize the estimation error at every updating step and therefore to extract more information from the data. The relative errors obtained by all

filters for parameters E_{s-col}, f_{y-col}, E_{s-beam}, f_{y-beam}, b_{beam}, and E_c are lower than 3% for the different values of D analyzed (i.e., 1, 5, 10, and 20), while relative errors for ε_c, b_{col}, and f_c reach a peak of about 10% when using the UKF and EKF with $D = 20$. This confirms that the proposed non-sequential model updating method has a very good performance, even for large values of D, and that the estimation accuracy only downgrades for those parameters for which the output measured responses are not very sensitive to.

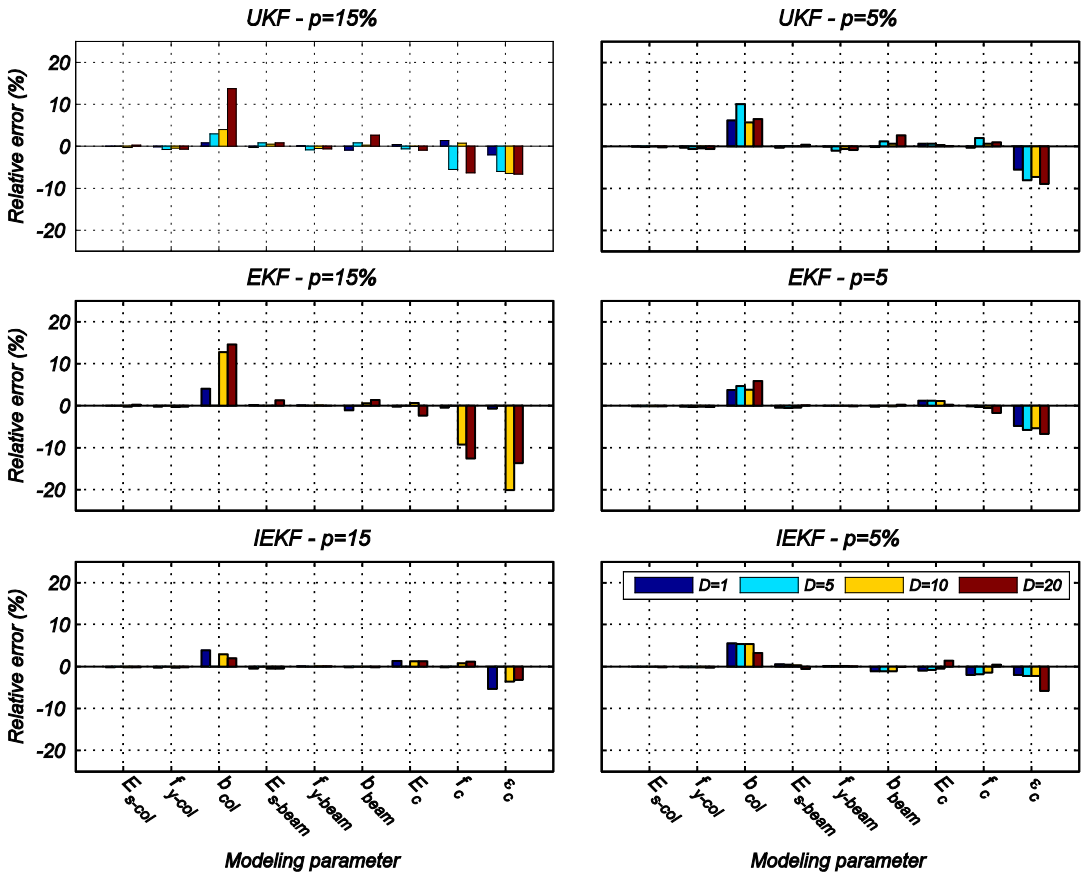

Figure 9.15: Relative errors between true modeling parameter values (reference) and the corresponding final estimates for noiseless input and different update step (D) values.

Figure 9.16 shows the *RRMSE*s between the true measured responses and their counterparts obtained using the final estimate of the modeling parameters for different

values of parameter *D*. The lowest *RRMSE* values are obtained when using the IEKF, which is in agreement with the results obtained for the estimation of the modeling parameters (Figure 9.15), due to the iterative procedure in the IEKF. In the case of the IEKF, the *RRMSE*s do not vary as *D* increases, confirming that the iterative procedure extracts most of the information contained in the response data even for large values of *D*. Finally, the *RRMSE*s for all the filters are lower than 1.5%, which demonstrates the excellent agreement between the true and estimated output measured responses.

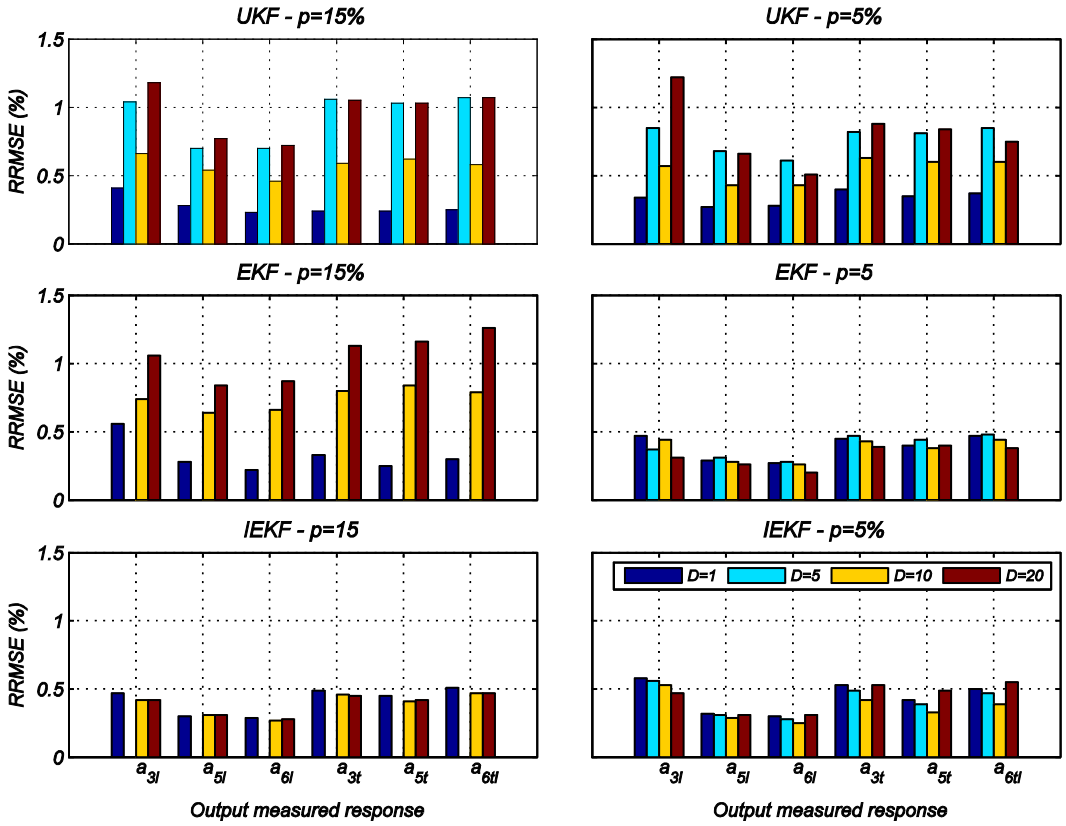

Figure 9.16: Relative RMS errors between true responses and their counterparts obtained using the final estimate of the modeling parameters for noiseless input and different update step (*D*) values.

9.5.3.4. Computational requirements

The proposed framework aims to be implemented in advanced mechanics-based nonlinear FE models of large and complex civil structures. The application example used in this chapter represents a first step in this direction by considering a 3D RC frame building modeled with displacement-based nonlinear fiber-section beam-column elements and using state-of-the-art uniaxial material constitutive models. In spite the increasing low-cost computational power available nowadays, integration of high-fidelity mechanics-based nonlinear FE structural modeling and stochastic filtering techniques (e.g., UKF, EKF, and IEKF) still demands a significant amount of computational resources. Consequently, it is of great importance to investigate the computational cost of the FE model updating framework, compare the resources required by the different filters, and examine the savings introduced by the non-sequential updating procedure. All the results presented in this section are obtained from analyses performed using a desktop workstation with an Intel Xeon 2.66 GHz processor and 48 GB random-access memory. It is noteworthy that the UKF can make use of parallel computing, because at each updating time step the nonlinear FE models corresponding to different SPs can be run at the same time.

Figure 9.17 compares the computation time (total process time) required by the different filters in the estimation of the modeling parameters in the case of 1.0%g RMS output measurement noise, 0.5%g RMS input measurement noise, and $p = 5\%$. In the case of the UKF, ten processing units (cores) are used to conduct the estimation process. When the nonlinear FE model is updated at every time step, the computational cost

associated to the EKF and IEKF are the lowest and highest, with process time of 92 and 138 hours, respectively, while the process time of the UKF is 106 hours. When the non-sequential estimation procedure is implemented, the computational cost is significantly reduced. The process time decreases by approximately 75, 90, and 95% for cases D = 5, 10, 20 relative to the case D = 1. In the case of non-sequential updating cases (D = 5, 10, 20), for a fixed D, the IEKF is the most expensive estimation tool because of his iterative procedure, and the EKF and UKF have very similar computational costs, with a relative difference lower than 10%. It is noted that in the case of the UKF, the use of ten cores alleviate considerable the computational burden of this estimation technique.

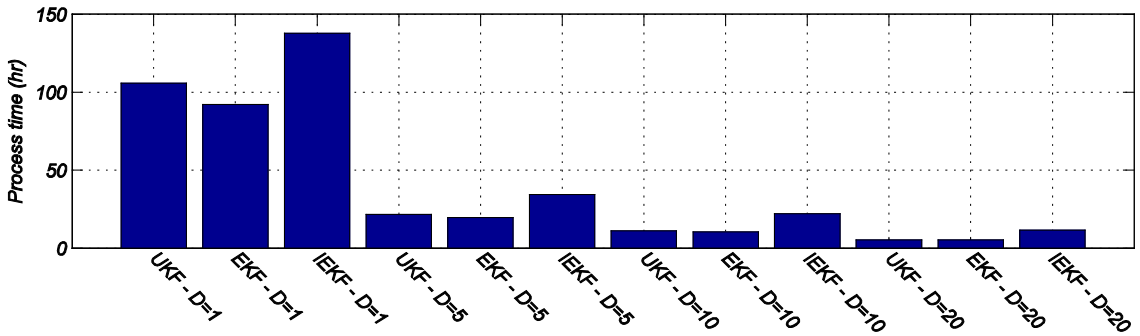

Figure 9.17: Computational cost of the FE model updating procedure when using different filters. Results for Case of 1.0%g RMS output measurement noise, 0.5%g RMS input measurement noise, and p = 5%.

9.6. Conclusions

This chapter investigated and compared the performance of a methodology to update mechanics-based nonlinear structural finite element (FE) models when different variants of the Kalman filter for nonlinear state-space models are used as estimation tools. The Unscented Kalman filter (UKF), Extended Kalman filter (EKF), and iterated Extended Kalman filter (IEKF) were applied to estimate unknown modeling parameters

of the nonlinear FE model and their performance in terms of convergence, accuracy, robustness, and computational requirements is examined. It is noted that the updated FE model provides a comprehensive description of damage in the structure, and therefore can be use for damage identification and structural health monitoring purposes.

Numerically simulated data of a three-dimensional 5-story 2-by-1 bay reinforced concrete frame building subjected to bi-directional earthquake excitation was used as a verification example. The FE response sensitivities with respect to eleven modeling parameter describing the nonlinear constitutive law of the materials (reinforcing steel and concrete) were first analyzed. Based on the obtained results, only nine parameters were found to significantly influence the output measured response, and therefore they were chosen as unknown parameters to be estimated. Excellent estimation results of these modeling parameters were obtained using the UKF, EKF, and IEKF. Because of the analytical linearization used in the EKF and IEKF, abrupt and large jumps in the estimate of the modeling parameters were observed when using these filters, which may lead to problems of convergence of the nonlinear FE model. The UKF slightly outperforms the EKF and IEKF and prevents large and abrupt changes in the estimates of the modeling parameters because it does not use analytical linearization of the nonlinear FE model, but it has a higher computational cost.

A non-sequential estimation procedure, which makes use of all the recorded data, previously proposed by the authors for the UKF is also implemented for the EKF and IEKF. The capabilities of the non-sequential scheme to reduce the computational cost, keeping accurate and robust estimation results, are proven. The non-sequential procedure alleviates the problems related to abrupt and large jumps in the estimate of the modeling

parameters when using the EKF and IEKF. Because of its iterative nature, the IEKF outperforms the UKF and EKF when the non-sequential updating procedure is used, but at a higher computational cost.

9.7. Acknowledgements

Part of Chapter 9 is a reprint of the material that is currently being prepared for submission for publication "Performance comparison of Kalman−based filters for nonlinear structural finite element model updating" in *Structural Health Monitoring*, Astroza, Rodrigo; Ebrahimian, H.; and Conte, J.P. The dissertation author was the primary investigator and author of this paper.

References

Asgarieh, E., Moaveni, B., and Stavridis, A. (2014). "Nonlinear finite element model updating of an infilled frame based on identified time-varying modal parameters during an earthquake." *Journal of Sound and Vibration*, 333(23), 6057–6073.

Askari, M. and Li, J. (2016). "Application of Kalman filtering methods to online real-time structural identification: A comparison study." *International Journal of Structural Stability and Dynamics*, 16, 1550016.

Astroza, R., Ebrahimian, H., and Conte, J.P. (2015a). "Material parameter identification in distributed plasticity FE models of frame-type structures using nonlinear stochastic filtering." *ASCE Journal of Engineering Mechanics*, 141(5), 04014149.

Astroza, R., Ebrahimian, H., and Conte, J.P. (2015b). "Nonlinear system identification for health monitoring of civil structures." To be submitted to *Computers and Structures*.

Balan, T.A., Spacone, E., and Kwon, M. (2001). "A 3D hypoplastic model for cyclic analysis of concrete structures." *Engineering Structures*, 23(4), 333–342.

Bell, B.M. and Cathey, F.W. (1993). "The iterated Kalman filter update as a Gauss-Newton method." *IEEE Transactions on Automatic Control*, 38(2):294–297.

Bellman, R.E. (1961). Adaptive Control Processes. Princeton, NJ, Princeton Univ. Press.

Chen, Y. and Feng, M. (2009). "Structural health monitoring by recursive Bayesian filtering." *ASCE Journal of Engineering Mechanics*, 135(4), 231–242.

Cheung, S.H. and Beck, J.L. (2009). "Bayesian model updating using hybrid Monte Carlo simulation with application to structural dynamic models with many uncertain parameters." *ASCE Journal of Engineering Mechanics*, 135(4), 243–255.

Ching, J., Beck, J.L., Porter, K.A., and Shaikhutdinov, R. (2006). "Bayesian state estimation method for nonlinear systems and its application to recorded seismic response." *ASCE Journal of Engineering Mechanics*, 132(4), 396–410.

Chodhary, G. and Jategaonkar, R. (2010). "Aerodynamic parameter estimation from flight data applying extended and unscented Kalman filter." *Aerospace Science and Technology*, 14, 106–117.

Conte, J.P. (2001). "Finite element response sensitivity analysis in earthquake engineering." In *Earthquake Engineering Frontiers in the New Millennium*. Lisse, The Netherlands.

Distefano, N. and Rath, A. (1975a). "System identification in nonlinear structural seismic dynamics." *Computer methods in applied mechanics and engineering,* 5, 353–372.

Distefano, N. and Rath, A. (1975b). "Sequential identification of hysteretic and viscous models in structural seismic dynamics." *Computer methods in applied mechanics and engineering,* 6, 219–232.

Distefano, N. and Pena-Pardo, B. (1976). "System identification of frames under seismic loads." *Journal of the Engineering Mechanics, Division,* 102(EM2), 313–330.

Ebrahimian, H., Astroza, R., and Conte, J.P. (2015) "Extended Kalman filter for material parameter estimation in nonlinear structural finite element models using direct differentiation method." *Earthquake Engineering & Structural Dynamics*, In Press.

Ebrahimian, H., Astroza, R., Conte, J.P., Restrepo, J.I, and Hutchinson, T.C. (2014). "Experimental validation of dynamic nonlinear FE model of full-scale five-story reinforced concrete building." *9th International Conference on Structural Dynamics* (*EURODYN 2014*), Porto, Portugal.

Erdogan, Y., Gul, M., Catbas, F., and Bakir, P. (2014). "Investigation of uncertainty changes in model outputs for finite-element model updating using structural health monitoring data." *ASCE Journal of Structural Engineering*, 140(11), 04014078.

Filippou, F.C., Popov, E.P., and Bertero, V.V. (1983). *Effects of bond deterioration on hysteretic behavior of reinforced concrete joints.* UCB/EERC-83/19, Berkeley, CA: EERC Report 83-19, Earthquake Engineering Research Center.

Friswell, M.I. and Mottershead, J.E. (1995). *Finite element model updating in structural dynamics*. Kluwer Academic Publishers, Dordrecht, The Netherlands.

Fritzen, C-P., Jennewein, D., and Kiefer, T. (1998). "Damage detection based on model updating methods." *Mechanical Systems and Signal Processing*, 12(1), 163–186.

Geetha, M., Kumar, A., and Jerome, J. (2014). "Comparative assessment of a chemical reactor using Extended Kalman filter and Unscented Kalman filter." *Procedia Technology*, 14, 75–84.

Giannitrapani, A., Ceccarelli, N., Scortecci, F., and Garulli, A. (2011). "Comparison of EKF and UKF for spacecraft localization via angle measurements." *IEEE Transactions on Aerospace and Electronic Systems*, 47(1), 75–84.

Hoshiya, M. and Sato, E. (1984). "Structural identification by extended Kalman filter." *ASCE Journal of Engineering Mechanics*, 110(12), 1757–1770.

International Code Council (ICC) (2006), *International building code*, 2006 Ed., Falls Church, VA.

Imregun, M., Visser, W.J., and Ewins, D.J. (1995). "Finite element model updating using frequency response function data: I. Theory and initial investigation." *Mechanical Systems and Signal Processing*, 9(2), 187–202.

Kucherenko, S., Rodriguez-Fernandez, M., Pantelides, C., and Shah, N. (2009). "Monte Carlo evaluation of derivative-based global sensitivity measures." *Reliability Engineering & System Safety*, Special issue on Sensitivity Analysis, 94(7), 1135–1148.

Lefebvre, T., Bruyninckx, H., and de Schutter, J. (2005). *Nonlinear Kalman Filtering for Force-Controlled Robot Tasks*. Springer-Verlag Berlin, Germany.

Li, X., Zhang, D-Y., Yan, W-M., Xie, W-C, and Pandey, M.D. (2014). "Effects of model updating on the estimation of stochastic seismic response of a concrete-filled steel tubular arch bridge." *Structure and Infrastructure Engineering*, 10(12), 1620–1637.

Liu, P. and Au, S-K. (2013). "Bayesian parameter identification of hysteretic behavior of composite walls." *Probabilistic Engineering Mechanics*, 34, 101–109.

Mander, J.B., Priestley, M.J.N., and Park, R. (1988). "Theoretical stress-strain model for confined concrete." *ASCE Journal of Structural Engineering*, 114(8), 1804–1826.

Mariani, S. and Ghisi, A. (2007). "Unscented Kalman filtering for nonlinear structural dynamics." *Nonlinear Dynamics*, 49 (1-2), 131-150

Martinelli, P. and Filippou, F.C. (2009). "Simulation of the shaking table test of a seven-story shear wall building." *Earthquake Engineering and Structural Dynamics*, 38(5), 587–607.

Marwala, T. (2010). *Finite element model updating using computational intelligence techniques: Applications to structural dynamics.* Springer-Verlag, London.

Mottershead, J.E. and Friswell, M.I. (1993). "Model updating in structural dynamics: A survey." *Journal of Sound and Vibration*, 167(2), 347−375.

Nasrellah, H.A. and Manohar, C.S. "Finite element method based Monte Carlo filters for structural system identification." *Probabilistic Engineering Mechanics*, 26(2), 294–307.

Omrani, R., Hudson, R., and Taciroglu, E. (2013). "Parametric identification of non-degrading hysteresis in a laterally-torsionally coupled building using an unscented Kalman filter," *ASCE Journal of Engineering Mechanics*, 139(4), 452–468.

Popovics, S. (1973). "A numerical approach to the complete stress–strain curve of concrete." *Cement Concrete Research*, 3(5), 583–599.

Saenz, I.P. (1964). "Discussion of 'Equation for the stress–strain curve of concrete, by P. Desay and S. Krishan'". *American Concrete Institute (ACI) Journal*, 61(9), 1229–35.

Saltelli, A., Tarantola, S., Campolongo, F., and Ratto, M. (2004). *Sensitivity Analysis in Practice: A Guide to Assessing Scientific Models*. John Wiley & Sons, England.

Scott, B.D., Park, R., and Priestley, M.J.N. (1982). "Stress-strain behavior of concrete confined by overlapping hoops at low and high strain rates." *American Concrete Institute (ACI) Journal*, 79(1), 13–27.

Shahidi, S. and Pakzad, S. (2014). "Generalized response surface model updating using time domain data." *ASCE Journal of Structural Engineering*, 140, SPECIAL ISSUE: Computational Simulation in Structural Engineering, A4014001.

Simoen, E., De Roeck, G., and Lombaert, G. (2014) "Dealing with uncertainty in model updating for damage assessment: A review." *Mechanical Systems and Signal Processing*, In Press.

Simoen, E., Moaveni, B., Conte, J.P., and Lombaert, G. (2013). "Uncertainty quantification in the assessment of progressive damage in a seven-story full-scale building slice." *ASCE Journal of Engineering Mechanics*, 139(12), 1818–1830.

Simon, D. (2006). *Optimal State Estimation: Kalman, H Infinity, and Nonlinear Approaches*. Hoboken, New Jersey, John Wiley & Sons, Inc.

Sipple, J.D. and Sanayei, M. (2014). "Finite element model updating using frequency response functions and numerical sensitivities." *Structural Control and Health Monitoring*, 21(5), 784–802.

Song, W. and Dyke, S.J. (2014). "Real-time dynamic model updating of a hysteretic structural system." *ASCE Journal of Structural Engineering*, 140(3), 04013082.

St-Pierre, M. and Gingras, D. (2004). "Comparison between the unscented Kalman filter and the extended Kalman filter for the position estimation module of an integrated navigation information system." *IEEE Intelligent Vehicles Symposium*, June 14-17, Parma, Italy.

Taucer, F.F., Spacone, E., and Filippou, F.C. (1991). *A fiber beam-column element for seismic response analysis of reinforced concrete structures*. Report 91/17, EERC, Earthquake Engineering Research Center (EERC), University of California, Berkeley.

Teughels, A. and De Roeck, G. (2005). "Damage detection and parameter identification by FE model updating." *Archives of Computational Methods in Engineering*, 12(2), 123–164.

Tsay, J.J. and Arora, J.S. (1990). "Nonlinear structural design sensitivity analysis for path dependent problems. Part 1: General theory." *Computer Methods in Applied Mechanics and Engineering*, 81(2), 183–208.

Uriz, P., Filippou, F., and Mahin, S. (2008). "Model for cyclic inelastic buckling of steel braces." *ASCE Journal of Structural Engineering*, 134(4), 619–628.

Wan, H-P. and Ren, W-X. (2014). "Parameter selection in finite-element-model updating by global sensitivity analysis using Gaussian process metamodel." *ASCE Journal of Structural Engineering*, 10.1061/(ASCE)ST.1943-541X.0001108 , 04014164.

Wan, E.A. and van der Merwe, R. (2000). "The unscented Kalman filter for nonlinear estimation." *IEEE 2000 Adaptive Systems for Signal Processing, Communications, and Control Symposium*, Lake Louise, AB, Canada.

Yang, J., Xia, Y., and Loh, C. (2014). "Damage Detection of Hysteretic Structures with Pinching Effect." *ASCE Journal of Engineering Mechanics*, 140(3), 462–472.

Zarate, B. and Caicedo, J.M. (2008). "Finite element model updating: Multiple alternatives." *Engineering Structures*, 30(12) 3724–3730.

Zhang, Y. and Der Kiureghian, A. (1993). "Dynamic response sensitivity of inelastic structures." *Computer Methods in Applied Mechanics and Engineering*, 108(1−2), 23–36.

CHAPTER 10

BAYESIAN NONLINEAR STRUCTURAL FE MODEL UPDATING FOR DAMAGE IDENTIFICATION OF CIVIL STRUCTURES SUBJECTED TO UNKNOWN INPUTS: INPUT AND NONLINEAR SYSTEM IDENTIFICATION

10.1. Introduction

Rapid condition assessment of structures plays a key role in supporting the decision-making process following extreme events. These major events, such as earthquakes, can potentially induce critical damage to civil structures, and consequently decisions related to emergency response, inspection, evacuation, and retrofit of structures are of vital importance. Damage initiation and progression cannot always be detected through visual screening and thus sometimes time-consuming, costly, and invasive post-event inspection and evaluation methods are required to detect certain damage. Potential impacts of earthquakes as well as other natural and man-made hazards on communities can be reduced through accurate and timely risk mitigation decisions after catastrophic events, which can be supported and facilitated by the use of structural health monitoring

(SHM), diagnosis, and prognosis to help assess the damage in and residual strength of civil structures.

Several approaches for SHM, and in particular for system identification (SID) and damage identification (DID) of civil structures, have been proposed and studied in the literature for rapid post-earthquake assessment of structural safety. Most existing methods in DID use measured low-amplitude input-output or output-only dynamic data recorded from the structure of interest before and after a potentially damaging event to update a linear-elastic viscously-damped structural model (e.g., Mottershead and Friswell 1993, Ren and De Roeck 2002, Teughels and De Roeck 2004, Simoen et al. 2013). These methods then identify damage as a loss of effective stiffness in one or more regions of the structure. Methods using the vibration data recorded solely during the damage inducing event have also been investigated (e.g., Distefano and Pena-Pardo 1976, Ching et al. 2006, Huang et al. 2010, Liu and Au 2013, Omrani et al. 2013). However, these studies have been based on highly idealized structural models with simplified hysteretic rules, which are not suitable to predict the response of large and complex civil structures and, consequently, are not employed in state-of-the-art mechanics-based structural models, which are increasingly used for analysis and design of structures.

The structural response during damage-inducing events is far from being linear elastic. Therefore, it is crucial to develop reliable, robust, and accurate DID methods able to capture the complex nonlinear behavior exhibited by structural systems when they are subjected to strong excitations. Incorporating high-fidelity mechanics-based nonlinear finite element (FE) models in advanced SHM techniques enables reconstruction of the nonlinear response process experienced by the structure during the damage-inducing

loading, which in turn provides invaluable information about the location, type, and extent of damage in the structural system. For this purpose, Astroza et al. (2014) and Ebrahimian et al. (2015) used the unscented Kalman filter (UKF) and the extended Kalman filter (EKF), respectively, to estimate time-invariant parameters describing the nonlinear material constitutive models of mechanics-based nonlinear FE models of frame-type structures given input-output dynamic data recorded during damage-inducing earthquake events.

In many practical applications, the actual input excitations acting on the structure of interest are difficult to be accurately and precisely measured (e.g., due to soil-structure-interaction effects) or the input excitations may be only partially measured (e.g., extended civil structures such as long-span bridges with sensors at some supports only). Such erroneous and/or incomplete input components, if not treated correctly, will introduce some errors in the estimation of the modeling parameters involved in the model updating procedure. This chapter proposes a Bayesian nonlinear FE model updating methodology for damage identification of civil structures when the inputs are unknown, i.e. only limited output measurements are available. The proposed methodology allows estimating unknown time-invariant modeling parameters of the mechanics-based nonlinear FE model of the structure and the unknown input excitation simultaneously using spatially sparse structural output response measurements recorded during a damage-inducing earthquake event. Although previous studies have proposed methods for SID of structures with unknown inputs, for both linear (e.g., Kitanidis 1987, Wang and Haldar 1997, Chen and Li 2004, Hsieh 2011, Zhang et al. 2011, Lourens et al. 2012, Sun and Betti 2013, Eftekhar Azam et al. 2015, Al-Hussein and Haldar 2015a,b) and

nonlinear (e.g., Yang et al. 2006, Yang and Huang 2007, Huang et al. 2010, Radhika and Manohar 2013) models, this chapter represents the first effort to identify the structural system and the unknown inputs when high-fidelity mechanics-based nonlinear FE models are used for DID purposes. The use of state-of-the-art nonlinear FE models for DID represents an important progress in the field of SHM, because a comprehensive damage diagnosis at different resolution levels, from global to local levels, can be achieved from the updated FE model.

10.2. Nonlinear FE model updating with unknown input

The discrete-time equation of motion of a nonlinear FE model of a structure at time $t_{k+1} = (k+1)\Delta t$, in which $k = 0, 1, ...$ and $\Delta t =$ time step, can be formulated as

$$\mathbf{M}(\boldsymbol{\theta})\,\ddot{\mathbf{q}}_{k+1}(\boldsymbol{\theta}) + \mathbf{C}(\boldsymbol{\theta})\,\dot{\mathbf{q}}_{k+1}(\boldsymbol{\theta}) + \mathbf{r}_{k+1}\left(\mathbf{q}_{k+1}(\boldsymbol{\theta}), \boldsymbol{\theta}\right) = \mathbf{f}_{k+1} + \mathbf{g}_{k+1} \tag{10.1}$$

where $\boldsymbol{\theta} \in \mathbb{R}^{n_\theta \times 1}$ = vector of unknown time-invariant modeling parameters, $\mathbf{q}, \dot{\mathbf{q}}, \ddot{\mathbf{q}} \in \mathbb{R}^{n \times 1}$ = nodal displacement, velocity, and acceleration vectors, $\mathbf{M} \in \mathbb{R}^{n \times n}$ = mass matrix, $\mathbf{C} \in \mathbb{R}^{n \times n}$ = damping matrix, $\mathbf{r}\left(\mathbf{q}(\boldsymbol{\theta}), \boldsymbol{\theta}\right) \in \mathbb{R}^{n \times 1}$ = history-dependent internal resisting force vector, $\mathbf{f} \in \mathbb{R}^{n \times 1}$ = known dynamic excitation vector, $\mathbf{g} \in \mathbb{R}^{n \times 1}$ = unknown dynamic excitation vector, and the subscript indicates the time step. In the case of rigid base earthquake excitation the dynamic load vectors take the form $\mathbf{f}_{k+1} = -\mathbf{M}\,\mathbf{L}\,\ddot{\mathbf{u}}_{k+1}$ and $\mathbf{g}_{k+1} = -\mathbf{M}\,\mathbf{L}^*\,\ddot{\mathbf{s}}_{k+1}$, where $\mathbf{L} \in \mathbb{R}^{n \times n_u}$ = influence matrix of the known excitation, $\ddot{\mathbf{u}}_{k+1} \in \mathbb{R}^{n_u \times 1}$ = known input ground accelerations with n_u = number of known base excitation components, $\mathbf{L}^* \in \mathbb{R}^{n \times n_s}$ = influence matrix of the unknown

excitation, and $\ddot{\mathbf{s}}_{k+1} \in \mathbb{R}^{n_s \times 1} =$ unknown input ground accelerations with $n_s =$ number of unknown base excitation components.

In general, different structural responses (output) can be recorded using a heterogeneous sensor array (e.g., accelerometers, strain gauges, GPS) and can be expressed analytically as

$$\mathbf{y}_{k+1} = \mathbf{l}_{k+1}\left(\ddot{\mathbf{q}}_{k+1}, \dot{\mathbf{q}}_{k+1}, \mathbf{q}_{k+1}, \ddot{\mathbf{u}}_{k+1}, \ddot{\mathbf{s}}_{k+1}\right) + \mathbf{v}_{k+1} \tag{10.2}$$

where $\mathbf{y}_{k+1} \in \mathbb{R}^{n_y \times 1} =$ vector of recorded structural output response quantities (output response measurements), $\mathbf{l}_{k+1} =$ nonlinear response function, and $\mathbf{v}_{k+1} \in \mathbb{R}^{n_y \times 1} =$ output measurement noise vector assumed to be white Gaussian with zero-mean and covariance matrix $\mathbf{R}_{k+1} \in \mathbb{R}^{n_y \times n_y}$, i.e., $\mathbf{v}_{k+1} \sim \mathcal{N}\left(\mathbf{0}, \mathbf{R}_{k+1}\right)$. Moreover, the measured output responses can be estimated by the FE model of the structure, and their relationship can be written as

$$\mathbf{y}_{k+1} = \hat{\mathbf{y}}_{k+1} + \mathbf{v}_{k+1} \tag{10.3}$$

where $\hat{\mathbf{y}}_{k+1} \in \mathbb{R}^{n_y \times 1} =$ predicted structural output response quantities from the FE model (predicted output response measurements). Equation (10.3) presumes that a nonlinear FE model can predict with reasonable accuracy the response of the structure of interest. Based on extensive investigations carried out in the field of nonlinear modeling and response simulation of structures, adequate mechanics-based nonlinear FE models with well calibrated modeling parameters are able to properly predict the actual response of civil structures (e.g., Uriz et al. 2008, Martinelli and Filippou 2009, Ebrahimian et al. 2014).

From Equations (10.1–10.3), the vector of recorded output response quantities from time t_1 to t_{k+1}, $\mathbf{y}_{1:k+1} = \left[\mathbf{y}_1^T, \mathbf{y}_2^T, \ldots, \mathbf{y}_{k+1}^T\right]^T \in \mathbb{R}^{\left[n_y(k+1)\right]\times 1}$, can be expressed as a nonlinear function of the modeling parameters ($\boldsymbol{\theta}$), known multi-dimensional input ground acceleration time histories from time t_1 to t_{k+1} ($\ddot{\mathbf{u}}_{1:k+1} = \left[\ddot{\mathbf{u}}_1^T, \ddot{\mathbf{u}}_2^T, \ldots, \ddot{\mathbf{u}}_{k+1}^T\right]^T \in \mathbb{R}^{\left[n_u(k+1)\right]\times 1}$), unknown multi-dimensional input ground acceleration time histories from time t_1 to t_{k+1} ($\ddot{\mathbf{s}}_{1:k+1} = \left[\ddot{\mathbf{s}}_1^T, \ddot{\mathbf{s}}_2^T, \ldots, \ddot{\mathbf{s}}_{k+1}^T\right]^T \in \mathbb{R}^{\left[n_s(k+1)\right]\times 1}$), initial conditions ($\mathbf{q}_0, \dot{\mathbf{q}}_0$) of the FE model, and the output measurement noise vector from time t_1 to t_{k+1} ($\mathbf{v}_{1:k+1} = \left[\mathbf{v}_1^T, \mathbf{v}_2^T, \ldots, \mathbf{v}_{k+1}^T\right]^T \in \mathbb{R}^{\left[n_y(k+1)\right]\times 1}$), i.e.,

$$\mathbf{y}_{1:k+1} = \mathbf{h}_{k+1}\left(\boldsymbol{\theta}, \ddot{\mathbf{u}}_{1:k+1}, \ddot{\mathbf{s}}_{1:k+1}, \mathbf{q}_0, \dot{\mathbf{q}}_0\right) + \mathbf{v}_{1:k+1} \tag{10.4}$$

Here $\mathbf{h}_{k+1}(\cdot)$ is a nonlinear response function of the nonlinear FE model at time t_{k+1}. For notational convenience and without loss of generality, it is assumed that the initial nodal displacement and velocity vectors are equal to zero hereafter.

The unknown time-invariant parameter vector ($\boldsymbol{\theta}$) contains the unknown modeling parameters, which are time-invariant and therefore its evolution can be modeled as a random walk according to the Bayesian approach. On the other hand, initially assuming that: (i) the different n_s components of the unknown input ground acceleration are uncorrelated at each time step (spatially uncorrelated at each time step) and (ii) unknown input ground acceleration at different time steps ($\ddot{\mathbf{s}}_i$ and $\ddot{\mathbf{s}}_j$ for $i \neq j$) are uncorrelated, then each component $\ddot{\mathbf{s}}_i$ ($i = 1, 2, \ldots, N$, where N is the total number of data samples of the input ground accelerations) can be modeled evolving as a random

walk. Therefore, the nonlinear joint, i.e. input and model parameter, estimation problem at time step $(k+1)$ ($k=0,1,\ldots,N-1$) can be mathematically formulated as

$$\begin{cases} \tilde{\mathbf{x}}_{k+1} = \tilde{\mathbf{x}}_k + \tilde{\boldsymbol{\gamma}}_k \\ \mathbf{y}_{1:k+1} = \mathbf{h}_{k+1}\left(\tilde{\mathbf{x}}_{k+1}, \ddot{\mathbf{u}}_{1:k+1}\right) + \mathbf{v}_{1:k+1} \end{cases} \tag{10.5}$$

where $\tilde{\mathbf{x}}_{k+1} = \left[\boldsymbol{\theta}_{k+1}^T, \left(\ddot{\mathbf{s}}_{k+1}^1\right)^T, \left(\ddot{\mathbf{s}}_{k+1}^2\right)^T, \ldots, \left(\ddot{\mathbf{s}}_{k+1}^k\right)^T, \left(\ddot{\mathbf{s}}_{k+1}^{k+1}\right)^T\right]^T \in \mathbb{R}^{\left[n_\theta + n_s(k+1)\right]\times 1}$ is the augmented unknown vector at time t_{k+1}, $\tilde{\mathbf{x}}_k = \left[\boldsymbol{\theta}_k^T, \left(\ddot{\mathbf{s}}_k^1\right)^T, \left(\ddot{\mathbf{s}}_k^2\right)^T, \ldots, \left(\ddot{\mathbf{s}}_k^k\right)^T, \left(\ddot{\mathbf{s}}_k^k\right)^T\right]^T \in \mathbb{R}^{\left[n_\theta + n_s(k+1)\right]\times 1}$ is the augmented unknown vector at time t_k, $\ddot{\mathbf{s}}_{k+1}^i$ denotes the unknown ground accelerations at time t_i to be estimated at time t_{k+1}, i.e. given the recorded output response quantities and known input from time t_1 to t_{k+1} ($\mathbf{y}_{1:k+1}$ and $\ddot{\mathbf{u}}_{1:k+1}$, respectively), and $\tilde{\boldsymbol{\gamma}}_k$ = process noise which is assumed to be a Gaussian noise sequence with zero mean vector and covariance matrix $\tilde{\mathbf{Q}}_k \in \mathbb{R}^{\left[n_\theta + n_s(k+1)\right]\times\left[n_\theta + n_s(k+1)\right]}$, i.e. $\tilde{\boldsymbol{\gamma}}_k \sim \mathcal{N}\left(\mathbf{0}, \tilde{\mathbf{Q}}_k\right)$, and independent of $\mathbf{v}_i$ $(i=1,2,\ldots)$. In the first expression of Equation (10.5) it is assumed that $\ddot{\mathbf{s}}_{k+1}^{k+1} = \ddot{\mathbf{s}}_k^k + \tilde{\boldsymbol{\gamma}}_k^k$. This is a reasonable assumption based on the fact that earthquake ground motions are usually recorded at more than 50 samples per second. Equation (10.5) represents a nonlinear state-space model, which enables the use of Bayesian filtering techniques to estimate the modeling parameter vector ($\boldsymbol{\theta}$) and the unknown input ground acceleration time histories ($\ddot{\mathbf{s}}$). The dimension of the unknown vector $\tilde{\mathbf{x}}_{k+1}$ increases as k increases, thus the computational burden required to solve the estimation problem increases considerably,

making the estimation of $\tilde{\mathbf{x}}_{k+1}$ $(k=0,2,\ldots,N-1)$ in the case of real-world structures under unknown earthquake excitation extremely computationally intensive. Therefore, an affordable and simplified approach to reduce the computational cost is proposed. Here, the components of $\ddot{\mathbf{s}}$ corresponding only to the last L time steps are considered in the estimation. This approximation is based on the fact that in a recursive approach the measured data are progressively assimilated in time, therefore input data samples belonging far in the past are already properly estimated when the FE model is updated at the present time step. Then, Equation (10.5) can be recast into

$$\begin{cases} \mathbf{x}_{k+1} = \mathbf{x}_k + \boldsymbol{\gamma}_k \\ \mathbf{y}_{1:k+1} = \mathbf{h}_{k+1}\left(\mathbf{x}_{k+1}, \ddot{\mathbf{u}}_{1:k+1}\right) + \mathbf{v}_{1:k+1} \end{cases} \tag{10.6}$$

where $\mathbf{x}_{k+1} = \left[\boldsymbol{\theta}_{k+1}^T, \left(\ddot{\mathbf{s}}_{k+1}^{k-L+2}\right)^T, \left(\ddot{\mathbf{s}}_{k+1}^{k-L+3}\right)^T, \ldots, \left(\ddot{\mathbf{s}}_{k+1}^{k}\right)^T, \left(\ddot{\mathbf{s}}_{k+1}^{k+1}\right)^T\right]^T \in \mathbb{R}^{n_x \times 1}$ is the reduced-length augmented unknown vector at time t_{k+1}, $\mathbf{x}_k = \left[\boldsymbol{\theta}_k^T, \left(\ddot{\mathbf{s}}_k^{k-L+2}\right)^T, \left(\ddot{\mathbf{s}}_k^{k-L+3}\right)^T, \ldots, \left(\ddot{\mathbf{s}}_k^{k}\right)^T, \left(\ddot{\mathbf{s}}_k^{k}\right)^T\right]^T \in \mathbb{R}^{n_x \times 1}$ is the reduced-length augmented unknown vector at time t_k, $n_x = n_\theta + n_s \min\left(k+1, L\right)$, $L =$ memory factor such that $1 \le L \le N$, and $\boldsymbol{\gamma}_k =$ process noise which is assumed to be a Gaussian noise sequence with zero mean vector and covariance matrix $\mathbf{Q}_k \in \mathbb{R}^{n_x \times n_x}$, i.e. $\boldsymbol{\gamma}_k \sim \mathcal{N}\left(\mathbf{0}, \mathbf{Q}_k\right)$, and independent of $\mathbf{v}_i \, (i=1,2,\ldots)$. It is noteworthy that the proposed formulation does not account for modeling errors, and their presence might contaminate the estimation of modeling parameters and input excitations.

In this dissertation, the UKF (Julier and Uhlmann 1997) is used to solve the estimation problem defined by the nonlinear state-space model in Equation (10.6). The UKF assumes that the posterior *pdf* $p\left(\mathbf{x}_{k+1|k+1}\right)=p\left(\mathbf{x}_{k+1}\middle|\mathbf{y}_{1:k+1},\ddot{\mathbf{u}}_{1:k+1}\right)$ is Gaussian and provides estimates of the mean vector and covariance matrix of $\mathbf{x}_{k+1}$ given only the known input and output response measurements from time t_1 to t_{k+1}, $\ddot{\mathbf{u}}_{1:k+1}$ and $\mathbf{y}_{1:k+1}$, respectively. Therefore, the posterior *pdf* is defined as $p\left(\mathbf{x}_{k+1|k+1}\right)=\mathcal{N}^{\circ}\left(\mathbf{x}_{k+1};\overline{\mathbf{x}}_{k+1|k+1},\mathbf{P}^{\mathbf{xx}}_{k+1|k+1}\right)$, where $\mathcal{N}^{\circ}\left(\mathbf{x}_{k+1};\overline{\mathbf{x}}_{k+1|k+1},\mathbf{P}^{\mathbf{xx}}_{k+1|k+1}\right)$ represents a multivariate Gaussian distribution with the components of $\mathbf{x}_{k+1}$ as random variables and $\overline{\mathbf{x}}_{k+1|k+1}$ and $\mathbf{P}^{\mathbf{xx}}_{k+1|k+1}$ denote the posterior mean and posterior covariance matrix of $\mathbf{x}_{k+1}$ given $\ddot{\mathbf{u}}_{1:k+1}$ and $\mathbf{y}_{1:k+1}$, respectively.

The UKF uses the unscented transform (UT) to obtain estimates of the mean vector and covariance matrix of random vector $\mathbf{x}$ (which includes the unknown input and modeling parameters) denoted by $\hat{\mathbf{x}}$ and $\hat{\mathbf{P}}^{\mathbf{xx}}$, respectively, by defining a set of deterministically chosen sample points (referred to as sigma points or SPs) denoted by $\boldsymbol{\chi}$. Because the UKF avoids analytical linearization of the nonlinear state-space model in Equation (10.5), FE response sensitivities with respect to modeling parameters and input excitation are not required. Because the scaled UT (Wan and van der Merwe 2000) is used here, in the implementation of the UKF, $\left(2n_x+1\right)$ FE models −each corresponding to a SP− need to be run at each time step. Figure 10.1 summarizes the approach proposed to estimate the unknown modeling parameters of the nonlinear FE model and the unknown input excitation using the UKF. Here $\boldsymbol{\gamma}^{(i)}_{k+1}\in\mathbb{R}^{\left[n_y(k+1)\right]\times 1}$ is the vector of

estimated response quantities corresponding to the SP $\boldsymbol{\chi}_{k+1}^{(i)}$ and includes the responses from time t_1 to t_{k+1}, and W_m and W_c are the weighting coefficients of the SPs to estimate the mean and covariance matrices, respectively. $\tilde{\mathbf{R}}_{k+1} = diag\left(\mathbf{R}_1,...,\mathbf{R}_{k+1}\right)$ is a block diagonal matrix including the covariance matrices of the output measurement noises from t_1 to t_{k+1}. $\hat{\mathbf{x}}_{k+1|k+1}$ and $\hat{\mathbf{P}}^{\mathbf{xx}}_{k+1|k+1}$ denote, respectively, the *a posteriori* estimates of the mean vector and covariance matrix of the unknown augmented vector $\mathbf{x}$ at time t_{k+1} given $\mathbf{y}_{1:k+1}$ and $\ddot{\mathbf{u}}_{1:k+1}$. $\hat{\mathbf{x}}_{0|0}$ and $\hat{\mathbf{P}}^{\mathbf{xx}}_{0|0}$ are the initial estimates of the mean and covariance matrix of the unknown augmented vector $\mathbf{x}$. It is noted that the SPs $\boldsymbol{\chi}_{k+1}^{(i)}$, $i = 1,...,2n_x + 1$, are defined based on the scaled UT, i.e., they depend on $\hat{\mathbf{x}}_{k|k}$, $\hat{\mathbf{P}}^{\mathbf{xx}}_{k|k}$ and the constant parameters α, β, and κ, which values are taken as $\alpha = 0.1$, $\beta = 2$, and $\kappa = 0$ (Wan and van der Merwe 2000). More details about the UKF and its use in the context of calibration of nonlinear FE models can be found in Wan and van der Merwe (2000) and Astroza et al. (2014), respectively.

Initialization: $\hat{\mathbf{x}}_{0\|0}$ and $\hat{\mathbf{P}}^{\mathbf{xx}}_{0\|0}$	Initial estimates of mean vector and covariance matrix
for $k = 0,1,\ldots,N-1$	Loop over time step
Prediction:	
(i) $\boldsymbol{\chi}^{(i)}_{k+1}$ i=1,...,$2n_x+1$ based on $\hat{\mathbf{x}}_{k\|k}$ and $\hat{\mathbf{P}}^{\mathbf{xx}}_{k\|k}$	Generate SPs
(ii) $\hat{\mathbf{x}}_{k+1\|k} = \hat{\mathbf{x}}_{k\|k}$; $\hat{\mathbf{P}}^{\mathbf{xx}}_{k+1\|k} = \hat{\mathbf{P}}^{\mathbf{xx}}_{k\|k} + \mathbf{Q}_k$	A priori estimates of mean vector and covariance matrix
(iii) $\boldsymbol{\gamma}^{(i)}_{1:k+1} = \mathbf{h}_{k+1}\left(\boldsymbol{\chi}^{(i)}_{k+1}, \ddot{\mathbf{u}}_{1:k+1}\right)$	Output vector for each SP
(iv) $\hat{\mathbf{y}}_{1:k+1\|k} = \sum_{i=1}^{2n_x+1} W^{(i)}_m \boldsymbol{\gamma}^{(i)}_{1:k+1}$	Predicted output vector
(v) $\hat{\mathbf{P}}^{\mathbf{yy}}_{k+1\|k} = \sum_{i=1}^{2n_x+1} W^{(i)}_c \left[\boldsymbol{\gamma}^{(i)}_{1:k+1} - \hat{\mathbf{y}}_{1:k+1\|k}\right]\left[\boldsymbol{\gamma}^{(i)}_{1:k+1} - \hat{\mathbf{y}}_{1:k+1\|k}\right]^T + \tilde{\mathbf{R}}_{k+1}$	Estimated output covariance matrix
(vi) $\hat{\mathbf{P}}^{\mathbf{xy}}_{k+1\|k} = \sum_{i=1}^{2n_x+1} W^{(i)}_c \left[\boldsymbol{\chi}^{(i)}_{k+1} - \hat{\mathbf{x}}_{k+1\|k}\right]\left[\boldsymbol{\gamma}^{(i)}_{1:k+1} - \hat{\mathbf{y}}_{k+1\|k}\right]^T$	Estimated state/output cross-covariance matrix
Correction: output measurement $\mathbf{y}_{k+1}$ is recorded	
(vii) $\mathbf{K}_{k+1} = \hat{\mathbf{P}}^{\mathbf{xy}}_{k+1\|k}\left(\hat{\mathbf{P}}^{\mathbf{yy}}_{k+1\|k}\right)^{-1}$	Kalman gain
(viii) $\hat{\mathbf{x}}_{k+1\|k+1} = \hat{\mathbf{x}}_{k+1\|k} + \mathbf{K}_{k+1}\left(\mathbf{y}_{1:k+1} - \hat{\mathbf{y}}_{1:k+1\|k}\right)$	A posteriori mean vector estimate
(ix) $\hat{\mathbf{P}}^{\mathbf{xx}}_{k+1\|k+1} = \hat{\mathbf{P}}^{\mathbf{xx}}_{k+1\|k} - \mathbf{K}_{k+1}\hat{\mathbf{P}}^{\mathbf{yy}}_{k+1\|k}\mathbf{K}^T_{k+1}$	A posteriori covariance matrix estimate
end for	

Figure 10.1: Pseudo-code of the proposed augmented approach for nonlinear FE model updating with unknown input.

10.3. Numerical application 1: 3D steel frame

10.3.1. Finite element model and earthquake input excitation

The first application example consists of a three-dimensional (3D) 4-story 2-by-1 bay steel frame building subjected to bidirectional seismic base excitations. Nonlinear seismic response of the structure is simulated using a nonlinear FE model with force-based fiber beam-column elements (distributed plasticity) developed in the open-source object-oriented software framework *OpenSees* (Mazzoni et al. 2005). As discussed in Taucer et al. (1991), distributed-plasticity FE models are a good alternative for nonlinear analysis and response simulation of frame-type structures whose behavior is dominated

by flexural-axial interaction. In these mechanics-based nonlinear models, FEs with fiber-discretized monitored cross sections (integration points or IPs) are used to characterize the spread of plastic regions along the element length. The nonlinear material behavior of each fiber is defined by uniaxial material constitutive laws modeling the stress-strain behavior of the corresponding material. These uniaxial material constitutive laws are defined with time-invariant parameters. More details about distributed-plasticity FE models using displacement-based and force-based elements can be found in Taucer et al. (1991). Translation components 360° and 90° of ground acceleration recorded at the Sylmar County Hospital during the 1994 Northridge earthquake are considered as base excitation in the longitudinal and transverse direction of the building, respectively (Figure 10.2). Ground acceleration time histories were recorded at a sampling rate of 50 Hz and the peak ground acceleration (PGA) were 0.84*g* and 0.60*g* for components 360° and 90°, respectively.

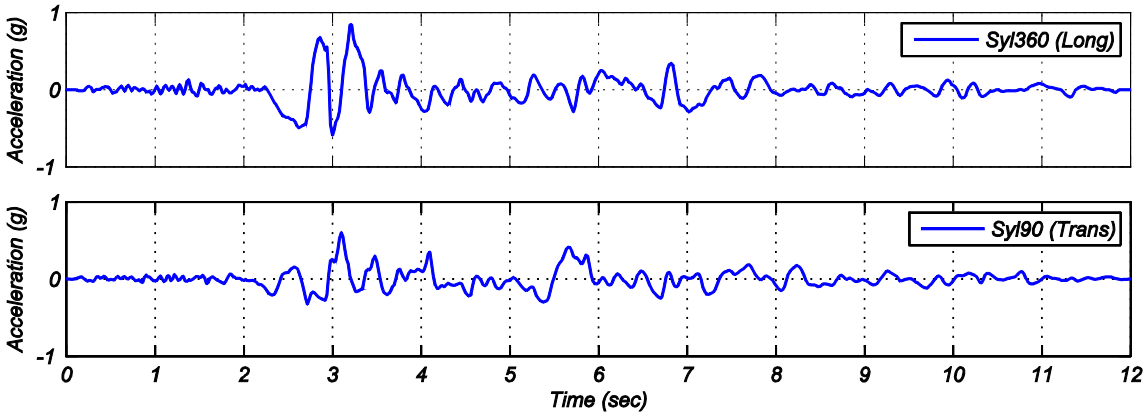

Figure 10.2: Acceleration time history of the input seismic motion for the 3D steel frame.

The building is designed as an intermediate moment-resisting frame according to the 2006 International Building Code (ICC 2006) for a location in downtown Seattle,

WA, with Site Class D soil conditions and a short-period spectral acceleration S_{MS} = 1.37g and a one-second spectral acceleration S_{M1} = 0.53g. The frame has a story height of 3.5 m and bay width of 7.0 m and 8.0 m in the longitudinal (X) and transverse (Z) directions, respectively (Figure 10.3a). The frame has four corner and two interior columns made of A992 steel with W14×61 and W14×90 cross sections, respectively. Longitudinal beams on second and third levels have W21×62 cross section, while on fourth and roof levels have W21×55 cross section. Transverse beams on second and third levels have W18×40 cross section, while on fourth and roof levels have W18×35 cross section. All beams are made of A36 steel.

The modified Giuffré-Menegotto-Pinto (GMP) model (Filippou et al. 1983) is used to model the nonlinear uniaxial stress-strain behavior of the steel fibers. The GMP material model depends on ten time-invariant parameters. Five of these parameters, which are assumed known in this application example, control the curvature of the hysteretic loops and the isotropic hardening. Three primary physical parameters of the model consists of modulus of elasticity (E), yield strength (f), and strain-hardening ratio (b), and will be considered as unknown in the estimation phase. Figure 10.3b shows the GMP uniaxial material constitutive law used to model the steel fibers and the three primary parameters describing it.

A single force-based element is used to model each beam-column member. Gauss-Lobatto quadrature with seven IPs for columns and beams is used to numerically integrate along the length of the elements. The number of IPs on each element is selected such that the weight of the IP associated with the section accumulating the deformation

(in force-based beam-column elements deformations localize at a single IP) approximately equals the expected physical length where deformation concentrates (plastic hinge). The plastic hinge length (L_{PH}) is taken as $L_{PH} = L/18$, where L is the element length, as suggested by Ribeiro et al. (2014).

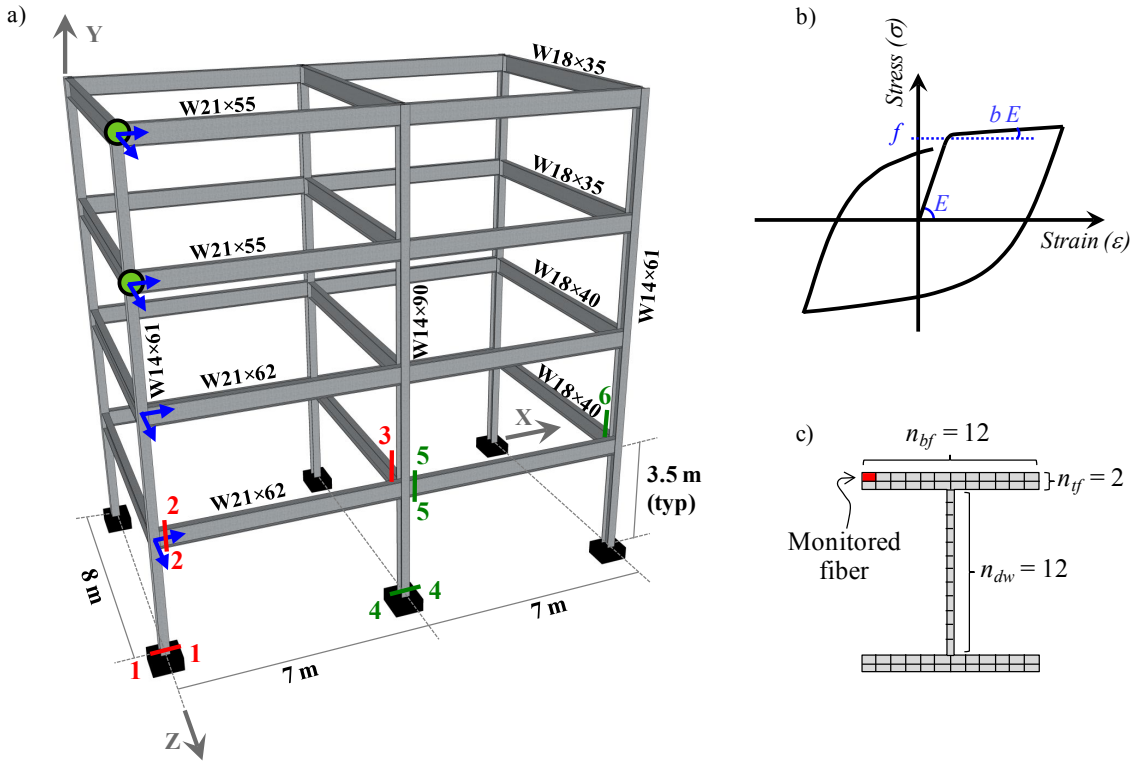

Figure 10.3: (a) 3D steel frame building structure. Blue arrows indicate acceleration measurements, Green circles indicate displacement measurements, and Red lines indicate location of strain measurements; (b) GMP uniaxial material constitutive law used to model the steel fibers; (c) cross section fiber discretization.

Cross sections of columns and beams are discretized into longitudinal fibers as shown in Figure 10.3c. Twelve fibers along web depth (n_{dw}), twelve fibers along flange width (n_{bf}), one fiber along web thickness, and two fibers along flange thickness (n_{tf}) are considered for all elements' cross sections. Linear section shear and torsion force-deformation models are aggregated, uncoupled with the inelastic coupled flexural-axial

behavior, at the section level and along the element. Nodal masses and distributed gravity loads acting on beams are computed from the design loads (ICC 2006) and are shown in Figure 10.4. Effects of nonlinear geometry are taken into account by using the P-Δ approximation (Filippou and Fenves 2004). Mechanisms of energy dissipation distinct to hysteresis due to nonlinear material behavior are modeled using mass and tangent stiffness-proportional Rayleigh damping based on the tangent stiffness matrix at the last converged step of analysis. A critical damping ratio of 2% for the first and second natural periods in the longitudinal direction of the building, T_1 = 1.47 sec and T_2 = 0.76 sec, is considered.

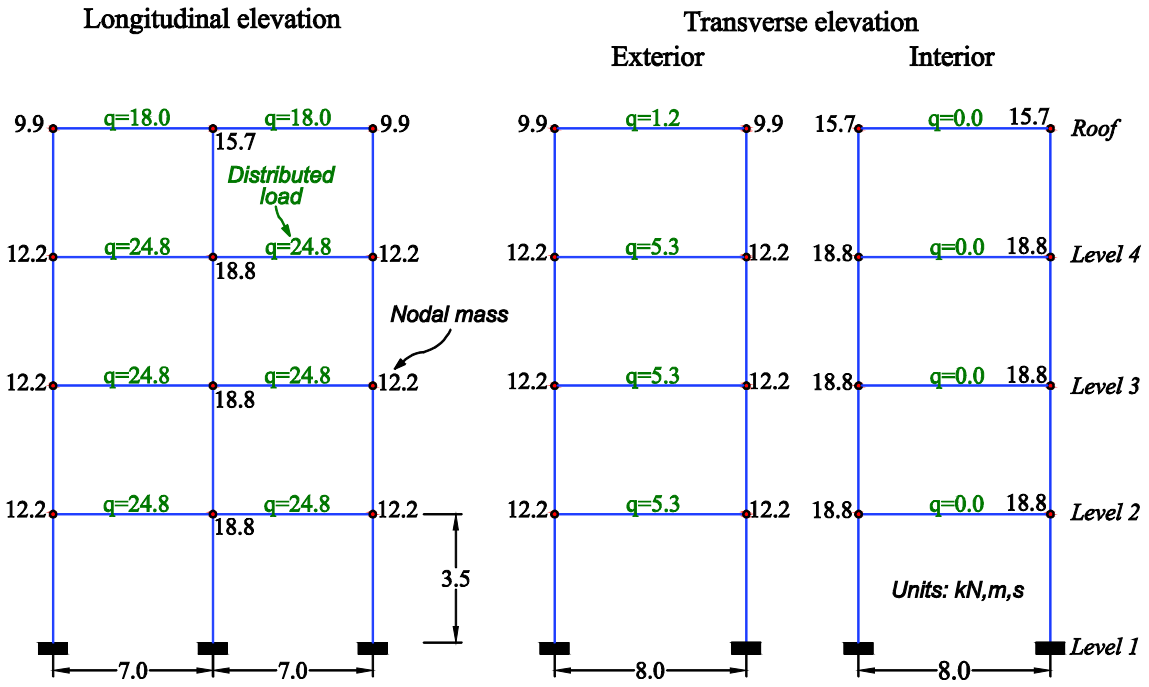

Figure 10.4: Nodal masses and distributed loads on beams in the FE model of the steel frame.

10.3.2. Response simulation

A set of material parameter values are assumed for the steel fibers of beams and columns. The values, which are referred to as true modeling parameter values hereafter, are: $\boldsymbol{\theta}^{true} = \left[E_{col}^{true}, f_{col}^{true}, b_{col}^{true}, E_{beam}^{true}, f_{beam}^{true}, b_{beam}^{true}\right]^T \in \mathbb{R}^{6\times 1}$ with $E_{col}^{true} = 200\,GPa$, $f_{col}^{true} = 345\,MPa$, $b_{col}^{true} = 0.04$, $E_{beam}^{true} = 200\,GPa$, $f_{beam}^{true} = 250\,MPa$, and $b_{beam}^{true} = 0.03$. The FE model described in Section 10.3.1 with the true modeling parameters' values is used to simulate the response of the structure to the ground acceleration time histories recorded at Sylmar station during the 1994 Northridge earthquake (Figure 10.2). This simulated response of the FE model is referred as true response hereafter.

10.3.3. Estimation of modeling parameters and unknown input

In the estimation phase different response quantities of the true (simulated) response of the structure are polluted by additive white Gaussian noise (AWGN) and used as output response measurements. Absolute acceleration response time histories (measured by accelerometers) in both translational directions at the four levels of the building, relative displacement response time histories (measured by GPS antennas) in both translational directions at the fourth and roof levels, and strain response time histories (measured by strain gauges) at the bottom of a column and ends of longitudinal and transverse beams are assumed to be recorded and used to define different combinations of the output response measurements ($\mathbf{y}$). The location of the accelerometers, GPS, and strain gauges used to measured different output response

quantities are represented by blue arrows, green circles, and red lines, respectively, in Figure 10.3a.

Both translational components of ground acceleration time histories used as input excitation and the six primary modeling parameters describing the constitutive law of the steel fibers in beams and columns are considered as unknown in the estimation phase. Six material parameters define the unknown modeling parameter vector $\boldsymbol{\theta} = \left[E_{col}, f_{col}, b_{col}, E_{beam}, f_{beam}, b_{beam}\right]^T \in \mathbb{R}^{6\times 1}$ and the unknown input ground acceleration time histories define the unknown input $\ddot{\mathbf{s}}_{1:600} \in \mathbb{R}^{2\times 600}$. Note that in this application example $n_s = 2$ and $N = 600$. It is noteworthy that the same FE model is used to simulate the response of the structure and to conduct the estimation of unknown modeling parameters and unknown input excitation, i.e., model uncertainty, which is out of the scope of this chapter, is not accounted for.

10.3.3.1. Structural response recorded by an accelerometer array

First, it is assumed that only the response time histories measured by the accelerometers are available, i.e. $\mathbf{y}_{k+1} \in \mathbb{R}^{8\times 1}$ with $k = 0, 1, \ldots, 599$. Two levels of output measurement noise ($\mathbf{v}$) are used to pollute the true acceleration responses. The first case considers noiseless true acceleration responses to define the measured output response data. In the second case a 0.5%g root-mean-square (RMS) zero-mean white Gaussian noise is added, after completion of the structural response simulation, to each true absolute acceleration response to pollute the true responses, i.e., the actual covariance matrix of the output measurement noise is $0.24\times 10^{-2}\mathbf{I}_8\left(m/s^2\right)^2$ where $\mathbf{I}_i = i\times i$ identity

matrix. Statistically uncorrelated realizations of noise are considered to pollute the different true acceleration responses. The polluted measured output response ($\mathbf{y}$) is employed to estimate the unknown augmented vector ($\mathbf{x}$), which includes the modeling parameter vector ($\boldsymbol{\theta}$) and the time histories of both components of the earthquake base excitation ($\ddot{\mathbf{s}}$). Because in practice the level of measurement noise is not known exactly and can only be estimated based on engineering experience and judgment, in the estimation it is assumed that the output measurement noise is a zero-mean Gaussian process with a covariance matrix $\mathbf{R}_{k+1} = \mathbf{R} = 0.87 \times 10^{-3} \mathbf{I}_8 \left(m/s^2 \right)^2$, i.e., a standard deviation (or RMS) of 0.3%*g* is considered for the output measurement noise. Time-invariant second order statistics with zero-mean and covariance matrix $\mathbf{Q}_k = \mathbf{Q} \in \mathbb{R}^{n_x \times n_x}$, where $n_x = n_\theta + n_s \min\left(k+1, L\right) = 6 + 2\min\left(k+1, L\right)$, are assumed for the process noise $\boldsymbol{\gamma}_k$. The diagonal entries of $\mathbf{Q}$ are assumed equal to $(q \times \hat{x}_{0|0}^i)^2$ where $i = 1, \ldots, n_x$ and $q = 1 \times 10^{-5}$, i.e., the process noise covariance matrix is constructed assuming a coefficient of variation of 1×10^{-5} of the initial estimate of the modeling parameters and unknown input excitations.

The initial unknown augmented vector is equal to $\hat{\mathbf{x}}_{0|0} = \left[\hat{\boldsymbol{\theta}}_{0|0}^T, \hat{\ddot{\mathbf{s}}}_{0|0}^T \right]^T \in \mathbb{R}^{8 \times 1}$. For the modeling parameters ($\hat{\boldsymbol{\theta}}$), the initial estimate is assumed as $\hat{\boldsymbol{\theta}}_{0|0} = \left[1.4\, E_{col}^{true}, 0.7\, f_{col}^{true}, 0.8\, b_{col}^{true}, 1.5\, E_{beam}^{true}, 0.8\, f_{beam}^{true}, 1.3\, b_{beam}^{true} \right]^T \in \mathbb{R}^{6 \times 1}$. For the unknown input excitations, the initial estimate is assumed equal to $\hat{\ddot{\mathbf{s}}}_{0|0} = \left[0.01, 0.01 \right]^T \in \mathbb{R}^{2 \times 1}$. The

initial estimate of the covariance matrix $\hat{\mathbf{P}}_{0|0}^{\mathbf{xx}}$ is assumed to be diagonal, i.e., initial estimates of the modeling parameters and unknown input excitation are statistically uncorrelated. The terms related to the modeling parameters and to the unknown input excitation are computed assuming a coefficient of variation of 10% of the initial estimate of the mean $\hat{\mathbf{x}}_{0|0}$, i.e., the diagonal entries of $\hat{\mathbf{P}}_{0|0}^{\mathbf{xx}}$ are computed as $(p \times \hat{x}_{0|0}^{i})^2$ where $i = 1, \ldots, n_x$ and $p = 0.10$. It is noted that at time step $(k+1)$ the *a priori* standard deviation of the last n_s components of $\mathbf{x}$ (which corresponds to unknown input excitation at that time step, $\ddot{\mathbf{s}}_{k+1}^{k+1}$), are taken equal to $(p \times \hat{\ddot{\mathbf{s}}}_{k|k}^{k})^2$, while other components of $\hat{\mathbf{P}}_{k+1|k}^{\mathbf{xx}}$ are obtained from the corresponding elements of the *a posteriori* covariance at previous time step ($\hat{\mathbf{P}}_{k|k}^{\mathbf{xx}}$). It is noteworthy that in the filtering stage the modeling parameters are normalized by their corresponding true values and the acceleration time histories are in the unit of m/s^2. This implies that all the variables involved in the filtering have comparable amplitudes, which make the estimation problem better conditioned.

The framework shown in Figure 10.1 is used to estimate the unknown modeling parameters and the time history of both unknown input excitations. The number of SPs required at each time step is $2n_x + 1 = 2 \times \left[6 + 2\min\left(k+1, L\right)\right] + 1$. This means that $\left[13 + 4\min\left(k+1, L\right)\right]$ nonlinear FE models (one for each SP) need to be run when estimating the modeling parameters and input excitations at time step $(k+1)$. Different values of the memory factor (L) are considered, namely L=10, 20, 30, 50, and 600. It is noteworthy that in the case L=600, when estimating the modeling parameters and

unknown inputs at time step $t_k = k\Delta t$ ($k = 1,...N$) the input excitations from $t_1 = \Delta t = 0.02\,\text{sec}$ to $t_k = k\Delta t$ are included in the augmented unknown vector [see Equation (10.5)]. It is noted that in the case of noiseless output response measurements, only the case of L=10 is shown here, because the other values of L provide almost identical results.

Figure 10.5 shows the time history of the *a posteriori* estimate of the modeling parameters obtained with the noiseless acceleration-only output response measurements and L=10. Similarly, Figure 10.6 shows the time history of the estimates obtained with the noisy acceleration-only output response measurement and L=20 and L=50. Table 10.1 reports the final estimates of the modeling parameters, $\hat{\boldsymbol{\theta}}_{N|N}$, normalized by their corresponding true parameter values for the two levels of output measurement noise considered. In the case of noiseless acceleration-only output response measurements with L=10 (Figure 10.5 and Table 10.1), the estimate of the modeling parameters converge to their corresponding true values with relative errors lower than 4%, i.e., the proposed estimation framework accurately estimates the unknown modeling parameters. In the case of noisy acceleration-only output response measurements (Figure 10.6 and Table 10.1), the estimate of both modulus of elasticity for columns and beams (E_{col} and E_{beam}) is accurate with relative error lower than 2% for all values of memory factor L. Estimation of yield strength of fibers in columns and beams (f_{col} and f_{beam}) is accurate for all values of L with relative error less than or equal to 4% and 5%, respectively. The error in the estimation of the yield strengths decreases as L increases. Errors associated to the estimation of strain-hardening ratios (post-yield parameters), b_{col} and b_{beam}, are the

highest, and they decrease as L increases, reaching errors of 0% and 5% for L=600, respectively. It is noted that strain-hardening ratios (b_{col} and b_{beam}) influence the response of the nonlinear FE model when the strain ductility demand of enough steel fibers increases sufficiently and, as will be discussed later in Section 10.3.5, the acceleration output response measurements are not very sensitive to these parameters. As will be discussed later, fibers of columns experience more hysteretic cycles and larger excursions in the nonlinear range of the material constitutive law compared to fibers of beams. As a result of this, output response measurements contain more information about b_{col} than b_{beam}, which implies a better estimation of the former. On the other hand, acceleration output response measurements are very sensitive to the moduli of elasticity (E_{col} and E_{beam}) from the beginning of the response, because before the strong motion part, the response of the structure is linear elastic and therefore sensitive to the initial elastic stiffness of the structure. When some fibers start to yield at around 2.5 sec, the measured response start to contain information about yield strengths (f_{col} and f_{beam}) and strain-hardening ratios.

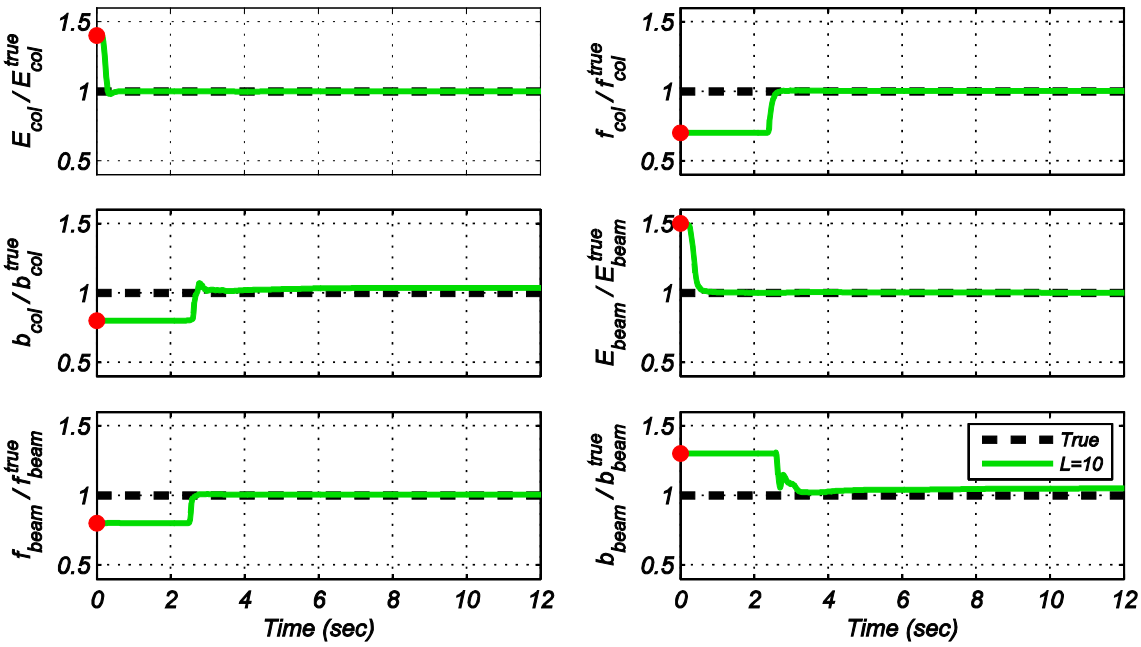

Figure 10.5: Time history of the *a posteriori* estimates of the modeling parameters of the steel frame in the case of noiseless acceleration-only output response measurements with L=10.

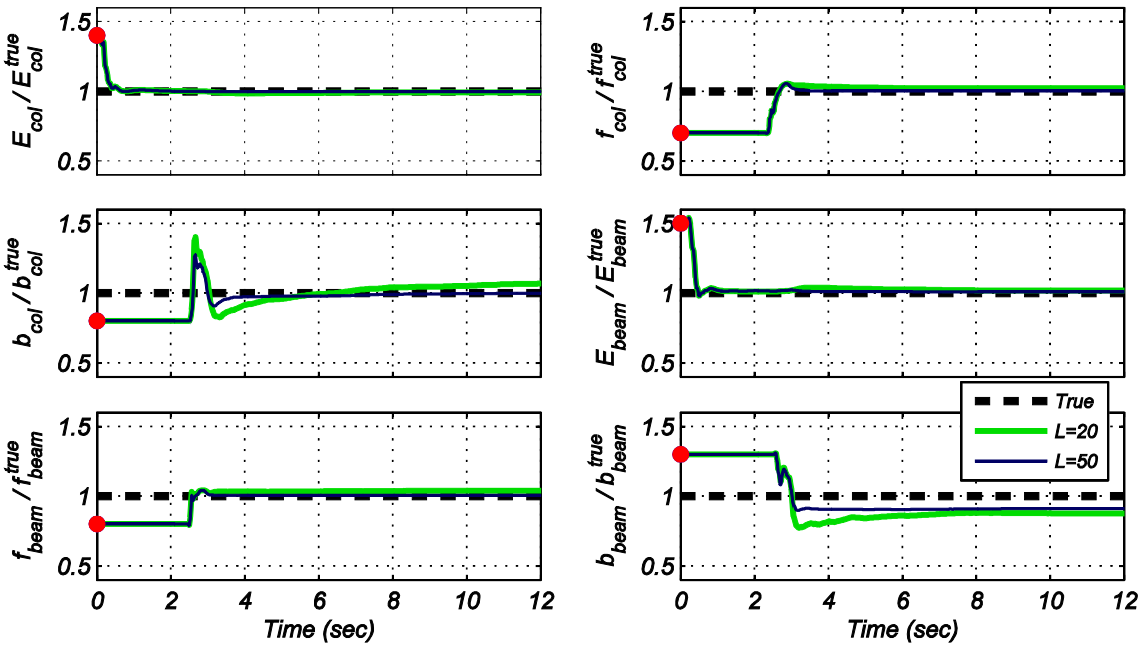

Figure 10.6: Time history of the *a posteriori* estimates of the modeling parameters of the steel frame in the case of noisy acceleration-only output response measurements with L=20 and L=50.

Table 10.1: Final estimates of the modeling parameters of the steel frame in the case of acceleration-only output response measurements.

Output noise (%g RMS)	Memory factor (L)	Modeling parameter					
		$\frac{E_{col}}{E_{col}^{true}}$	$\frac{f_{col}}{f_{col}^{true}}$	$\frac{b_{col}}{b_{col}^{true}}$	$\frac{E_{beam}}{E_{beam}^{true}}$	$\frac{f_{beam}}{f_{beam}^{true}}$	$\frac{b_{beam}}{b_{beam}^{true}}$
0.0	10	1.00	1.00	1.03	1.00	1.00	1.04
0.5	10	0.99	1.04	1.23	1.02	1.05	1.11
	20	0.99	1.02	1.07	1.02	1.04	0.87
	30	1.00	1.01	1.00	1.01	1.02	0.84
	50	1.00	1.00	1.00	1.01	1.01	0.91
	600	1.00	1.00	1.00	1.00	1.00	0.95

Figure 10.7 shows the time histories of the true and estimated input excitations (i.e., both translational components recorded at the Sylmar station during the 1994 Northridge earthquake) in the case of noisy acceleration-only output response measurements with L=20. Figure 10.7a shows the comparison between the true and actual estimate (unfiltered) of the unknown input time histories. It is observed that estimated time histories include a low-frequency component inducing a permanent drift in the estimation, effect that has been already detected in previous studies (e.g. Zhang et al. 2011, Sun and Betti 2013, Naets et al. 2015). Because the formulation proposed in this chapter is intended to be used in an off-line fashion, the permanent drift can be eliminated using a high-pass filter (HPF). An infinite impulse response (IIR) Butterworth filter of order 7 with cut-off frequency at 0.15 Hz is used here. Figure 10.7b shows the comparison between the true and the estimated input time histories after application of the HPF. The permanent drift is eliminated after the application of the HPF and consequently the match between the true and estimated input acceleration time histories improves considerably.

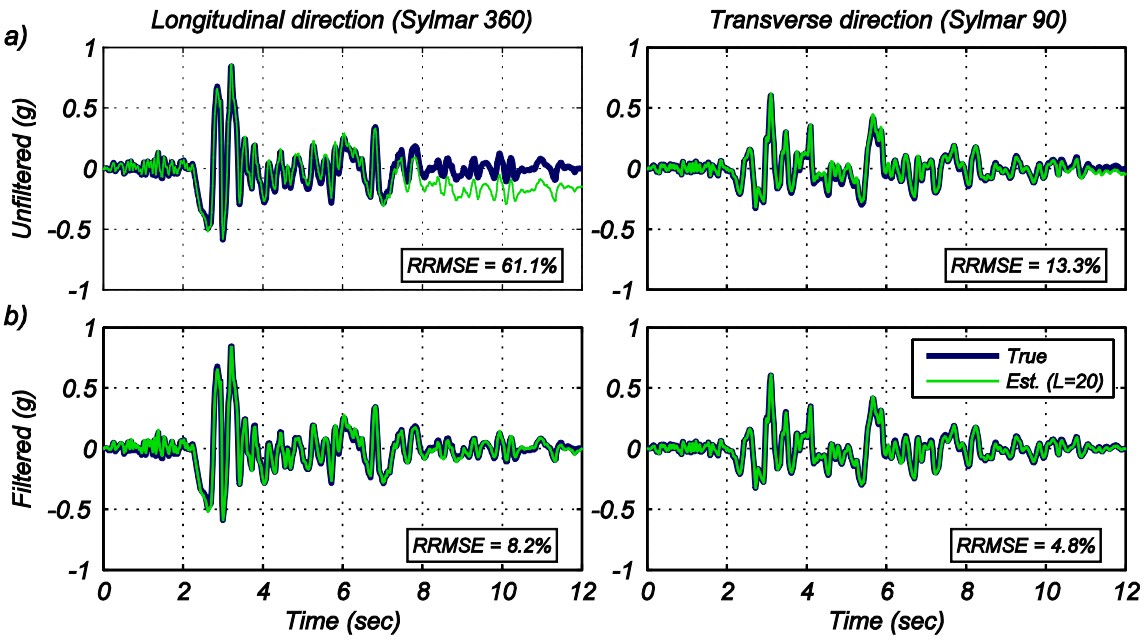

Figure 10.7: Comparison of the true and estimated input time histories to the steel frame in the case of noisy acceleration-only output response measurements with L=20. (a) Unfiltered estimations, (b) Filtered estimations.

Table 10.2 summarizes the relative RMS error (*RRMSE*) between the true and estimated input excitations, for both unfiltered and filtered cases. Note that the *RRMSE* between two signals $\mathbf{z}^1$ (reference) and $\mathbf{z}^2$ is compute as $RRMSE[\%] = \sqrt{\left[1/Nt \sum_{k=1}^{Nt} \left(z_k^1 - z_k^2\right)^2\right]} \Big/ \sqrt{\left[1/Nt \sum_{k=1}^{Nt} \left(z_k^1\right)^2\right]} \times 100$, where Nt is the total number of data samples. In the case of noiseless output response measurements, no permanent drift in the estimate of the unknown input excitations occurs. In this case, the estimation of the input excitations is very accurate, with *RRMSE* lower than 3%. In the case of noisy acceleration-only output response measurements the *RRMSE* decrease as L increases, consistently with the results obtained in the estimation of modeling parameters (Table 10.1). Based on the results shown in Table 10.2, it can be concluded that the estimation of the unknown input excitations is accurate, with *RRMSE* lower than 8.2%

when the estimates of the input excitations are low-pass filtered to remove the permanent drift. It is noted that the presence of spurious low-frequency components in the estimated input excitations are caused by the numerical integration of the noisy output response measurements and because no responses sensitive to long-period forces are considered in the output response measurements.

Table 10.2: *RRMSE*s (in %) between the true and estimated input excitations to the steel frame in the case of acceleration-only output response measurements.

Output noise (%*g* RMS)	Memory factor (*L*)	*RRMSE* (%) – Input excitation			
		Sylmar 360°		Sylmar 90°	
		Unfiltered	Filtered	Unfiltered	Filtered
0.0	10	1.6	1.4	3.1	2.0
0.5	10	117.5	7.5	38.0	6.6
	20	61.1	8.2	13.3	4.8
	30	23.2	4.4	5.4	3.4
	50	17.0	3.7	3.2	3.1
	600	11.9	3.2	2.4	2.3

To further verify that the process to jointly estimate the unknown modeling parameters and input excitations given only the output response measured by the sparse accelerometer array is successful, the discrepancy between the true and estimated output response measurements is studied. The *RRMSE* between the true responses and the corresponding responses computed using the final estimates of the modeling parameters and estimated input excitations are computed (Table 10.3). It is noted that the unfiltered estimate of the input excitations are used here to compute the estimated response. In Table 10.3, the output measurement $\mathbf{a}_{ij}$ represents the absolute acceleration time history response at level i in direction j, where $l =$ longitudinal and $t =$ transverse directions, respectively. In the case of noiseless output response measurements, the *RRMSE* are less than or equal to 0.6% indicating the excellent agreement between the true and estimated

output response measurements. In the case of noisy measurement, the *RRMSE* between true and estimated output responses decrease as L increases, which is expected based on the results from Table 10.1 and Table 10.2. In the case of L=10, the *RRMSE*s are less than or equal to 8%, and for higher values of L, the *RRMSE*s are lower than 4%, which together with the results presented in Table 10.1 and Table 10.2 confirms the successful performance of the proposed framework to estimate the modeling parameters and input excitations given only the output response measurements.

Figure 10.8 compares the true and estimated acceleration time histories used as output response measurements in the case of noisy measurements with L=20. The excellent agreement between the true and estimated responses is clearly observed, with *RRMSE*s lower than 5.1%. This confirms the minor effect that the low-frequency components in the estimated input excitations have in the measured acceleration responses.

Table 10.3: *RRMSE*s (in %) between the true measured responses of the steel frame and their corresponding estimated responses based on the final estimate of the modeling parameters and the estimated input excitations (unfiltered) in the case of acceleration-only output response measurements.

Output noise (%g RMS)	Memory factor (L)	*RRMSE* (%) – Output response measurement							
		$\mathbf{a}_{2l}$	$\mathbf{a}_{3l}$	$\mathbf{a}_{4l}$	$\mathbf{a}_{5l}$	$\mathbf{a}_{2t}$	$\mathbf{a}_{3t}$	$\mathbf{a}_{4t}$	$\mathbf{a}_{5t}$
0.0	10	0.3	0.3	0.3	0.4	0.6	0.5	0.5	0.6
0.5	10	7.4	7.6	6.7	6.1	6.8	6.5	6.0	6.4
	20	3.2	3.2	2.9	2.6	3.8	3.6	3.6	3.4
	30	1.5	1.5	1.3	1.1	1.9	1.9	2.2	1.5
	50	1.4	1.4	1.2	1.0	1.6	1.6	1.8	1.3
	600	1.3	1.3	1.1	0.9	1.5	1.5	1.7	1.2

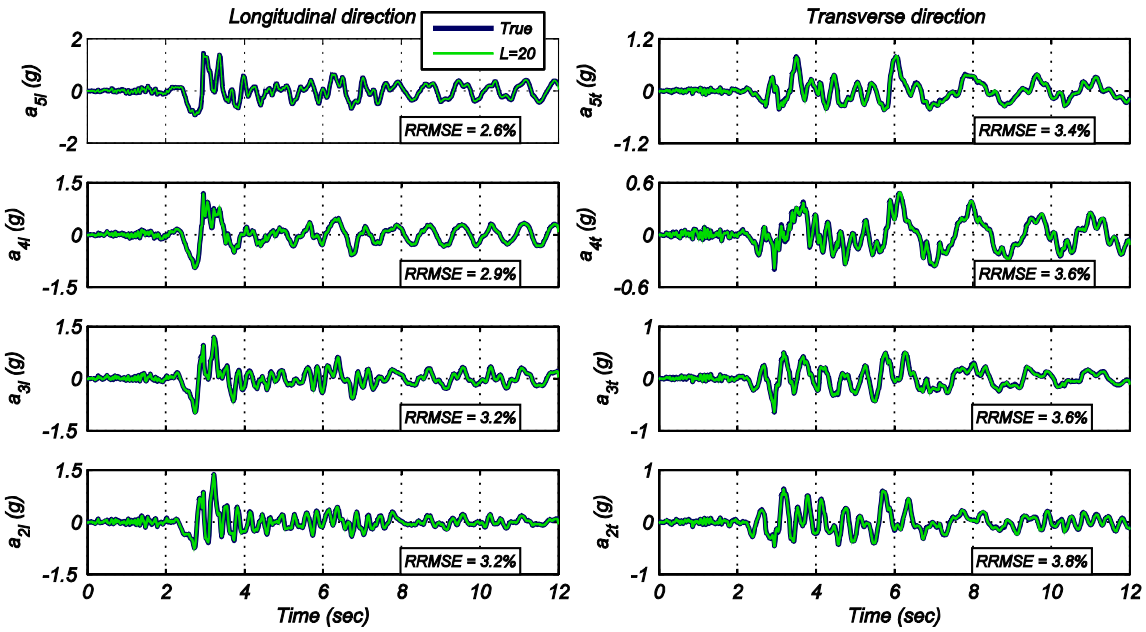

Figure 10.8: Comparison of the true measured and estimated acceleration response of the steel frame based on estimated input (unfiltered) and final estimate of modeling parameters in the case of noisy acceleration-only output response measurements with L=20.

To compare unobserved response quantities, Figure 10.9 shows different global and local responses predicted from the FE model based on the true input excitations and true values of the modeling parameters (true responses) and their counterparts obtained using the final estimates of the modeling parameters and estimated input excitations (filtered). Global responses consist of the roof drift ratio (relative displacement of the top of the building normalized by its total height) time history in the longitudinal direction (RDR^x) and base shear time history in the transverse direction normalized by the total weight of the building (V_b^z/W). Section level responses consist of the moment (M) versus curvature (κ) at the base of a column (section 4 – 4 in Figure 10.3a) and at the end of a longitudinal beam (section 5 – 5 in Figure 10.3a). Finally, fiber level responses comprise the stress (σ) versus strain (ε) response of a corner steel fiber (see Figure 10.3c)

at the bottom of a column (section 4 – 4 in Figure 10.3a) and at the end of a transverse beam (section 6 – 6 in Figure 10.3a). The results show that the agreement between true and estimated unobserved global response quantities is excellent with both L=20 and L=50. At the section level the match is very good and the case with L=50 outperforms the case with L=20. For the fiber responses, the agreement between the true and estimated responses is also very good, and it is slightly better for the column's fiber compared to the beam's fiber with both L=20 and L=50. From the fiber responses, it is observed that the fibers of the columns experienced more and larger excursions in the post-yield zone of the stress-strain constitutive law, which suggests that the output response measurements contain more information about the post-yield behavior of columns' fibers than about beams' fibers. This observation is in agreement with the results in Table 10.1.

The good agreement between different true and estimated unobserved global and local response quantities confirm the very good performance of the proposed methodology and its capabilities for damage identification purposes. Using the estimated modeling parameters and input excitations, the updated nonlinear FE model can be interrogated to detect, localize, classify, and assess the damage in the structure, from global to local resolution levels.

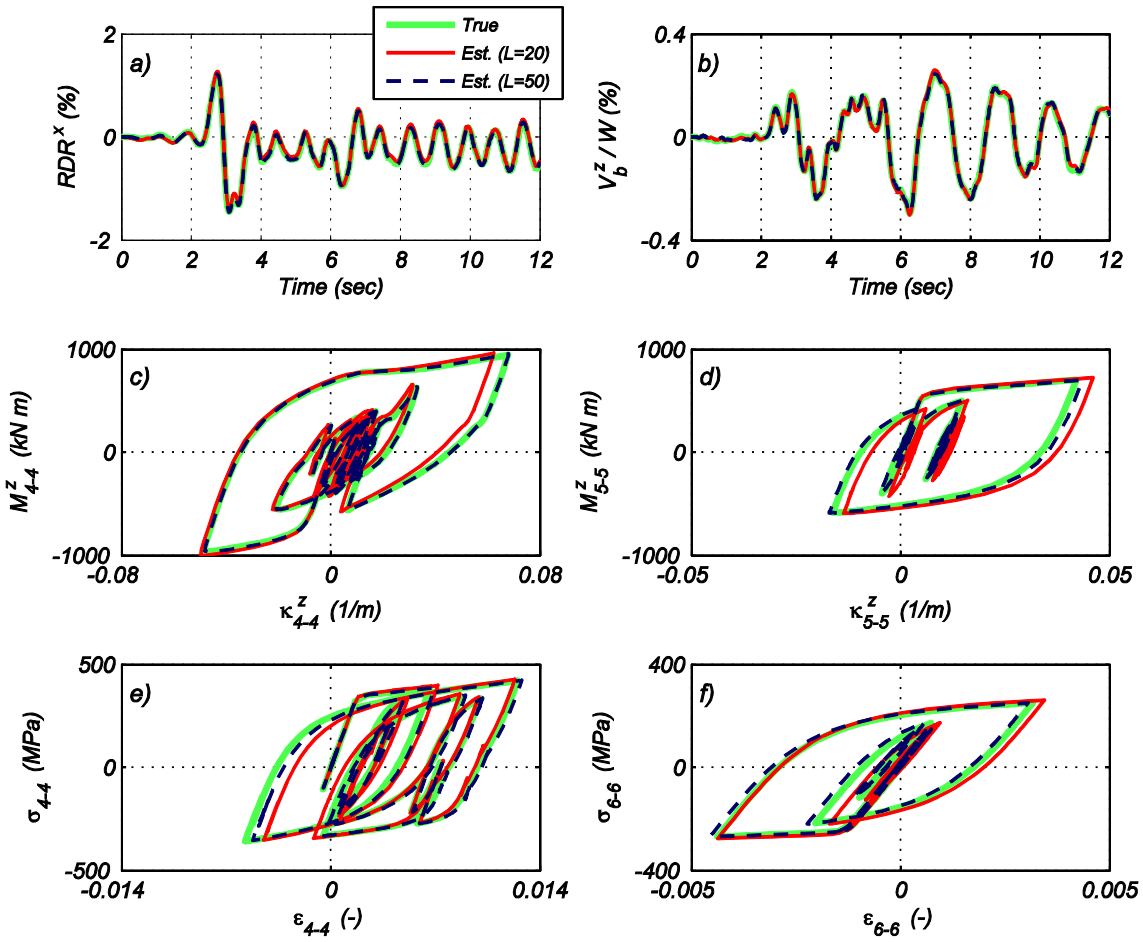

Figure 10.9: Comparison of the true unobserved responses and estimated unobserved responses of the steel frame based on estimated input and final estimate of modeling parameters. Case of noisy acceleration-only output response measurements with L=20 and L=50. (a) roof drift ratio time history in the longitudinal (X) direction, (b) normalized base shear time history in the transverse (Z) direction, (c) moment versus curvature at the base of a column (section 4 − 4 in Figure 10.3a), (d) moment versus curvature at the end of a longitudinal beam (section 5 − 5 in Figure 10.3a), (e) stress versus strain in a corner steel fiber at the base of a column (section 4 − 4 in Figure 10.3a), (f) stress versus strain in a corner steel fiber at the end of a transverse beam (section 6 − 6 in Figure 10.3a).

The results exhibited in this section show the good performance of the proposed methodology to estimate unknown modeling parameters of nonlinear FE models and unknown input excitations. In the case of noisy acceleration-only output response measurements, a permanent drift due to a spurious low-frequency component arise in the estimation of the input excitations. These low-frequency components in the input

excitations do not affect the acceleration response measurements, which are non-sensitive to long-period force excitations. Because the proposed methodology works in an offline fashion, a HPF is applied to the estimated input excitations to remove the low-frequency components. The use of the final estimates of the modeling parameters and the low-pass filtered estimated input excitations allow to predict global and local unobserved response quantities with excellent accuracy.

10.3.3.2. Effect of heterogeneous response measurements

The effect of considering heterogeneous output response measurements is studied in this section. In a previous study, Astroza et al. (2015) concluded that the use of different type of measurements improves the identifiability of unknown modeling parameters in the case of known input excitation. In this section, the effect of considering displacement and strain response measurements, in addition to acceleration response measurements, is investigated. Because results presented in Section 10.3.1 showed that the case of noiseless output response measurements provides excellent estimation results for modeling parameters and input excitations with acceleration-only output response measurements, in this section only the case of noisy heterogeneous output response measurements is considered.

To pollute the true responses, $2.0\,mm$ and $0.5\,mm/m$ RMS zero-mean white Gaussian noises are added, after completion of the response simulation phase, to the each true relative displacement and strain response measurements, respectively. This means that the actual noise covariance of each displacement and strain response measurement is $4.0\,mm^2$ and $0.25\,(mm/m)^2$, respectively. Statistically uncorrelated realizations of noise

are assumed to contaminate the different true output response measurements. Three cases of heterogeneous output response measurements are analyzed and in all of them it is assumed that the eight acceleration response measurements considered in Section 10.3.3.1 are also available. In a first case, four relative displacements corresponding to both translational components at fourth and roof levels (see green circles in Figure 10.3a) are also assumed to be measured, i.e., $\mathbf{y}_{k+1} \in \mathbb{R}^{12\times 1}$. A second case considers that strains in three corner steel fibers located at specific cross-sections (see red lines in Figure 10.3a) are measured in addition to the acceleration responses, i.e., $\mathbf{y}_{k+1} \in \mathbb{R}^{11\times 1}$. Finally, a third case assumes that accelerations, displacements, and strains previously described are measured, i.e., $\mathbf{y}_{k+1} \in \mathbb{R}^{15\times 1}$. For each case, the polluted output response measurements ($\mathbf{y}$) are employed to estimate the unknown modeling parameters of the nonlinear FE model and the unknown time histories of both components of the earthquake input excitation. As explained in Section 10.3.3.1, in the estimation process the values of the variances to construct the output measurement noise covariance matrix ($\mathbf{R}$) are taken different to the ones used to pollute the responses. Noise covariances of $2.25\,mm^2$ and $0.09\,(mm/m)^2$ are assumed for the displacement and strain response measurements, respectively, i.e. standard deviation (or RMS) of $1.5\,mm$ and $0.3\,mm/m$ are considered in $\mathbf{R}$. Similarly to the acceleration-only output response measurements case, time-invariant second order statistics with zero-mean and covariance matrix $\mathbf{Q}_k = \mathbf{Q}$, are assumed for the process noise $\boldsymbol{\gamma}_k$, with diagonal entries of $\mathbf{Q}$ taken as $(q \times \hat{x}_0^i)^2$ where $i = 1,\ldots,n_x = 6+2L$ and $q = 1\times 10^{-5}$. The same initial values of the unknown augmented

state vector ($\hat{\mathbf{x}}_{0|0}$) (which includes both modeling parameters, $\hat{\boldsymbol{\theta}}_{0|0}$, and unknown input excitations, $\hat{\hat{\mathbf{s}}}_{0|0}$) and initial estimate of the covariance matrix ($\hat{\mathbf{P}}_{0|0}^{\mathbf{xx}}$) as described in Section 10.3.1 are assumed. The same values of the memory factor (L) are studied in the case of heterogeneous output response measurements.

Figure 10.10 shows the time history of the *a posteriori* estimates of the modeling parameters (normalized by their true values) in the case of noisy heterogeneous output response measurements with L=50. It is observed that inclusion of displacement and strain response measurements improves the accuracy in the estimation of the modeling parameters, especially for post-yield parameters b_{col} and b_{beam}. Table 10.4 summarizes the final estimates of the modeling parameters normalized by their corresponding true values. Accurate estimation of E_{col}, E_{beam}, f_{col}, and f_{beam} is obtained in the different cases of heterogeneous output response measurements and with different values of L, and their estimation accuracy slightly improves compared to the case of acceleration-only measurements (see Table 10.1). Moreover, the accuracy in the estimation of b_{col} and b_{beam} significantly improve when heterogeneous output responses are measured, especially when both displacements and strains are considered and $L \geq 20$. This is due to the fact that displacement and strain responses are more sensitive with respect to post-yield parameters than acceleration response measurements.

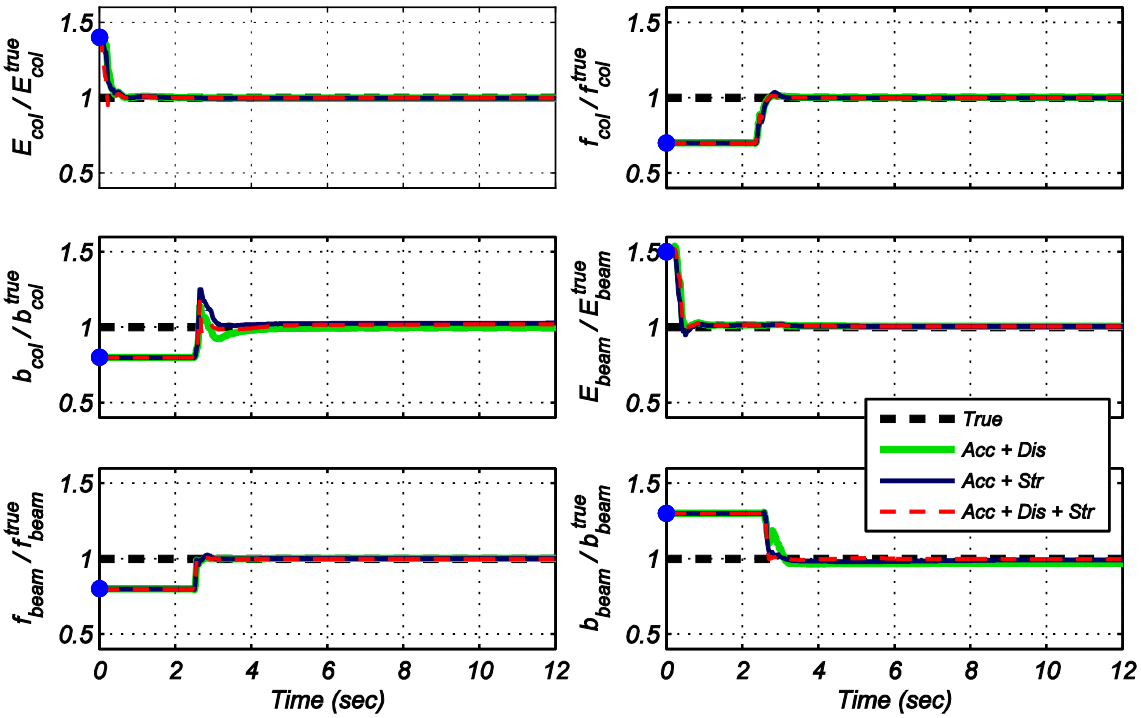

Figure 10.10: Time history of the *a posteriori* estimates of the modeling parameters of the steel frame in the case of noisy heterogeneous output response measurements with L=50.

Figure 10.11 shows the time histories of the true and estimated input excitations in the case of noisy heterogeneous output response measurements with L=50. Figure 10.11a shows the comparison between the true and actual estimate (unfiltered) of the unknown inputs. It is observed that the spurious low-frequency component in the estimated input excitations is negligible. When displacement response measurements are considered, the spurious low-frequency components in the estimated input excitations are eliminated because displacement responses, contrary to acceleration responses, are sensitive to long-period force excitations. Figure 10.11b shows the comparison between the true and the high-pass filtered estimated input time histories. The agreements of the filtered and unfiltered versions of the estimated input time histories with respect to the true input excitations are practically identical.

Table 10.4: Final estimates of the modeling parameters of the steel frame in the case of noisy heterogeneous output response measurements.

Type of response measurement	Memory factor (L)	Modeling parameter					
		$\frac{E_{col}}{E_{col}^{true}}$	$\frac{f_{col}}{f_{col}^{true}}$	$\frac{b_{col}}{b_{col}^{true}}$	$\frac{E_{beam}}{E_{beam}^{true}}$	$\frac{f_{beam}}{f_{beam}^{true}}$	$\frac{b_{beam}}{b_{beam}^{true}}$
Case 1: Acceleration and Displacement	10	0.99	1.02	1.31	1.03	1.07	1.13
	20	0.99	1.01	0.97	1.01	1.01	0.94
	30	1.00	1.00	0.99	1.01	1.00	0.97
	50	1.00	1.00	1.00	1.00	1.00	0.97
	600	1.00	1.00	1.01	1.00	1.00	0.98
Case 2: Acceleration and Strain	10	1.00	1.01	1.54	1.01	1.06	1.33
	20	0.99	1.02	1.16	1.02	1.03	1.13
	30	1.00	1.00	1.06	1.01	1.01	1.01
	50	1.00	1.00	1.03	1.00	1.00	0.99
	600	1.00	1.00	1.01	1.00	1.00	1.00
Case 3: Acceleration, Displacement, and Strain	10	0.98	1.03	1.14	1.03	1.07	1.11
	20	1.00	1.01	1.02	1.01	1.01	0.99
	30	1.00	1.00	1.02	1.01	1.00	1.00
	50	1.00	1.00	1.01	1.00	1.00	1.00
	600	1.00	1.00	1.02	1.00	1.00	1.00

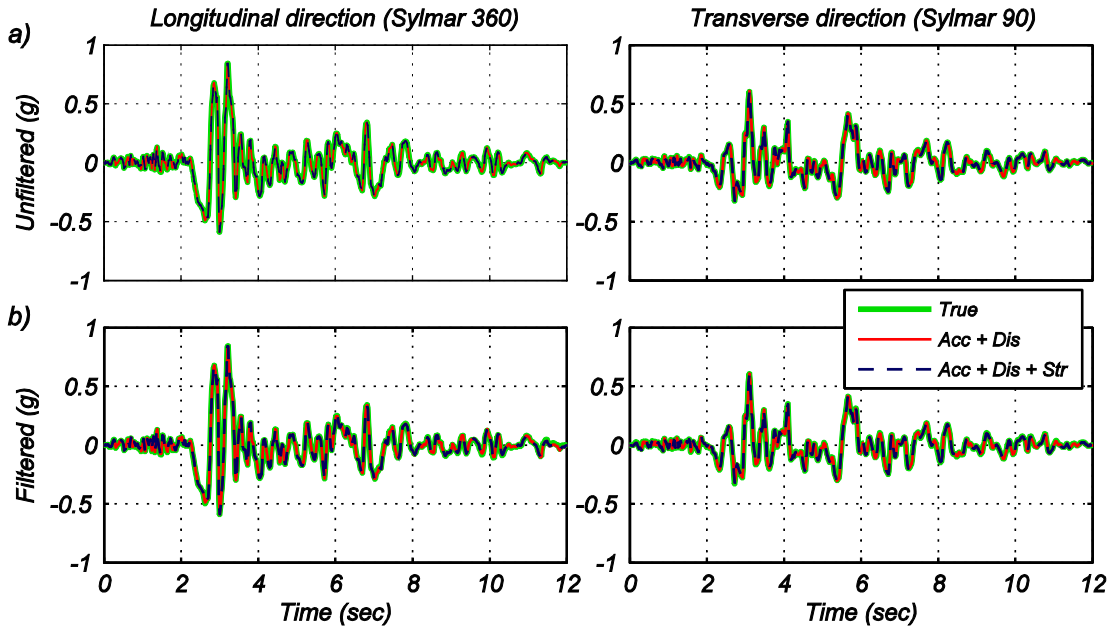

Figure 10.11: Comparison of the true and estimated input time histories to the steel frame in the case of noisy heterogeneous output response measurements with L=50. (a) Unfiltered estimations, (b) Filtered estimations.

Table 10.5 summarizes the *RRMSE* between the true and estimated input excitations, for both unfiltered and filtered cases. It is clearly observed that the spurious

low-frequency component is minimized when displacement output response measurements are considered because the *RRSME* for unfiltered and filtered cases are very similar. Consistently with results shown in Section 10.3.3.1, *RRMSE*s decrease as L increases. Comparing Table 10.5 and Table 10.2, it is concluded that a better estimation of the unknown input excitations is obtained when displacement output response measurements are considered.

Table 10.5: *RRMSE*s (in %) between the true and estimated input excitation to the steel frame in the case of noisy heterogeneous output response measurements.

Type of response measurement	Memory factor (L)	*RRMSE* (%) – Input excitation			
		Sylmar 360°		Sylmar 90°	
		Unfiltered	Filtered	Unfiltered	Filtered
Case 1: Acceleration and Displacement	10	14.9	12.2	7.3	6.6
	20	2.3	2.3	3.6	3.1
	30	1.6	1.2	2.2	1.9
	50	1.6	1.1	2.1	1.9
	600	1.5	1.1	2.1	1.9
Case 2: Acceleration and Strain	10	45.6	9.2	22.6	6.5
	20	34.5	7.8	17.7	4.4
	30	7.7	4.8	4.3	3.6
	50	5.0	4.0	2.5	2.1
	600	2.9	2.6	2.3	2.1
Case 3: Acceleration, Displacement, and Strain	10	15.9	13.6	7.2	6.6
	20	2.3	1.7	2.3	2.0
	30	1.6	1.4	2.1	1.9
	50	1.6	1.4	2.1	1.9
	600	1.5	1.4	2.1	1.9

Table 10.6 summarizes the *RRMSE* between the true heterogeneous output response measurements and the corresponding responses computed using the final estimates of the modeling parameters and estimated input excitations (unfiltered). In this table, $\mathbf{a}_{ij}$ and $\mathbf{d}_{ij}$ stand for the absolute acceleration and relative displacement time history response at level i in direction j, respectively, where l = longitudinal and t = transverse directions, and $\boldsymbol{\varepsilon}_c$, $\boldsymbol{\varepsilon}_{bx}$, and $\boldsymbol{\varepsilon}_{bz}$ are the strain time histories measured in the

corner fiber of the cross-section of column, longitudinal beam, and transverse beam as shown in Figure 10.3a. When accelerations and displacements (Case 1) and accelerations, displacements, and strain (Case 3) are measured, the *RRMSE*s are small (most of them lower than 10%) and they decrease as L increases. In the case that accelerations and strains (Case 2) are measured, low *RRMSE*s are obtained for the acceleration responses but larger *RRMSE*s are obtained for the strain responses, especially when $L \leq 20$. This is due to the fact that spurious low-frequency components in the estimated input excitations are present with important effects when accelerations and strains responses (no displacements included) are considered. These low-frequency components in the estimated input excitations affect the responses of the structure that are sensitive to quasi-static forces, such as displacements, curvatures, and strains.

Table 10.6: *RRMSE*s (in %) between the true response and the estimated response of the steel frame based on the final estimate of the modeling parameters and the estimated input excitation in the case of noisy heterogeneous output response measurements.

Type of response measurement	Memory factor (L)	*RRMSE* (%) – Output response measurement														
		$\mathbf{a}_{2l}$	$\mathbf{a}_{3l}$	$\mathbf{a}_{4l}$	$\mathbf{a}_{5l}$	$\mathbf{a}_{2t}$	$\mathbf{a}_{3t}$	$\mathbf{a}_{4t}$	$\mathbf{a}_{5t}$	$\mathbf{d}_{4l}$	$\mathbf{d}_{5l}$	$\mathbf{d}_{4t}$	$\mathbf{d}_{5t}$	$\boldsymbol{\varepsilon}_{c}$	$\boldsymbol{\varepsilon}_{bx}$	$\boldsymbol{\varepsilon}_{bz}$
Case 1: Acceleration and Displacement	10	3.4	3.3	2.7	3.5	4.9	4.2	4.1	4.5	7.5	7.4	5.0	5.1	–	–	–
	20	1.3	1.3	1.2	1.0	1.8	1.8	1.8	1.5	1.1	1.0	0.8	0.8	–	–	–
	30	1.2	1.2	1.1	0.9	1.6	1.6	1.7	1.2	0.6	0.6	0.3	0.3	–	–	–
	50	1.2	1.1	1.0	0.8	1.5	1.5	1.6	1.2	0.5	0.5	0.2	0.2	–	–	–
	600	1.2	1.1	1.0	0.8	1.5	1.5	1.6	1.1	0.5	0.5	0.2	0.2	–	–	–
Case 2: Acceleration and Strain	10	4.3	4.1	3.2	4.0	5.5	5.0	5.0	5.2	–	–	–	–	22.7	21.7	20.0
	20	2.1	2.0	1.8	1.9	3.3	3.3	3.4	2.8	–	–	–	–	13.4	19.2	24.4
	30	1.3	1.2	1.1	1.0	1.9	1.8	2.0	1.5	–	–	–	–	4.4	4.8	3.9
	50	1.2	1.1	1.0	0.8	1.5	1.6	1.7	1.2	–	–	–	–	2.2	2.1	2.0
	600	1.2	1.1	1.0	0.8	1.5	1.5	1.7	1.2	–	–	–	–	1.4	1.1	0.7
Case 3: Acceleration, Displacement, and Strain	10	3.3	3.2	2.7	3.5	5.3	4.6	4.3	4.8	8.5	8.4	4.7	4.8	10.1	13.3	9.2
	20	1.3	1.3	1.2	1.0	1.8	1.7	1.8	1.4	1.1	1.1	0.8	0.8	1.1	1.8	0.9
	30	1.2	1.2	1.0	0.9	1.6	1.5	1.7	1.2	0.6	0.5	0.3	0.3	0.9	0.6	0.6
	50	1.2	1.1	1.0	0.8	1.5	1.5	1.6	1.2	0.5	0.5	0.2	0.2	0.8	0.5	0.3
	600	1.2	1.1	1.0	0.8	1.5	1.5	1.6	1.2	0.5	0.5	0.2	0.2	0.8	0.4	0.2

Figure 10.12 and Figure 10.13 compares the true and estimated time histories used as output responses in the case of noisy acceleration/displacement and acceleration/displacement/strain measurements with L=50, respectively. An excellent agreement between the true and estimated responses is observed in both cases, with *RRMSE*s lower than 2% for all measured responses. Because the estimated responses are obtained using the estimated input excitations (unfiltered), it is confirmed that the spurious low-frequency components in the estimated inputs are practically eliminated when displacement response measurements are considered. Recall that displacement and strain responses are sensitive to low-frequency components in the input excitations.

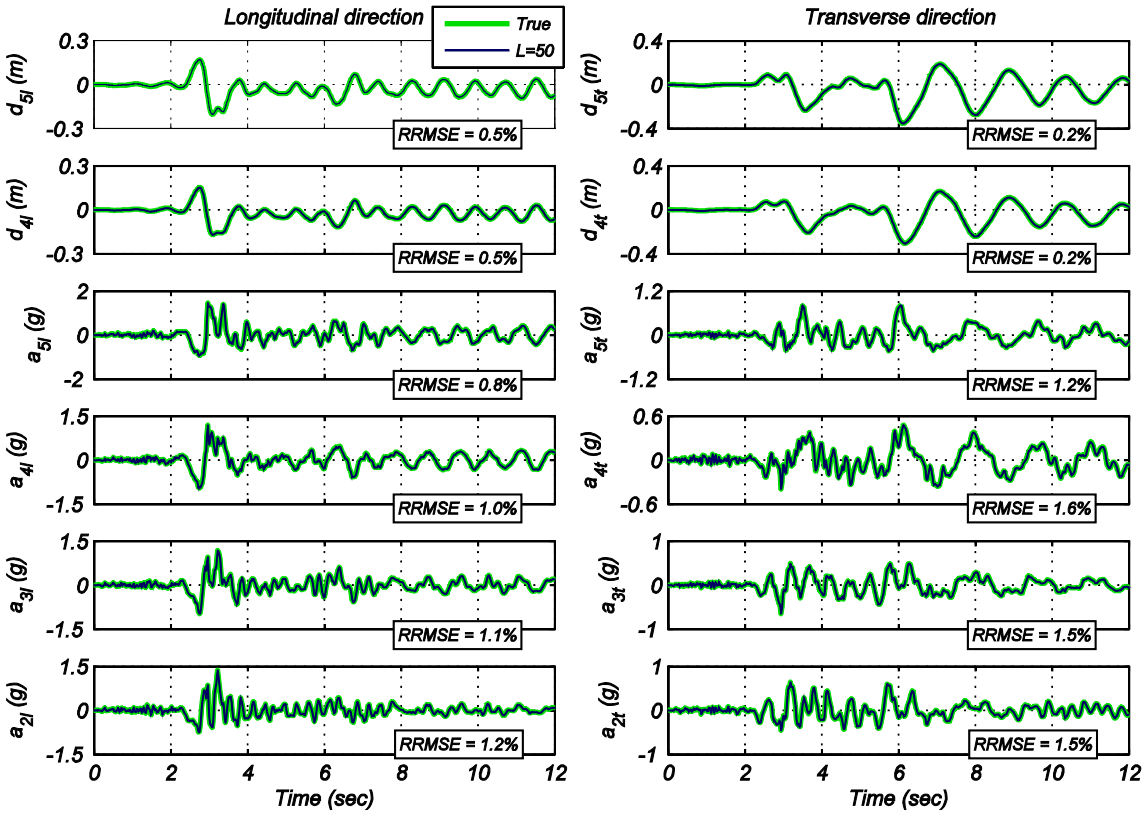

Figure 10.12: Comparison of the true measured and estimated acceleration response of the steel frame based on estimated input and final estimate of modeling parameters in the case of noisy acceleration and displacement response measurements with L=50.

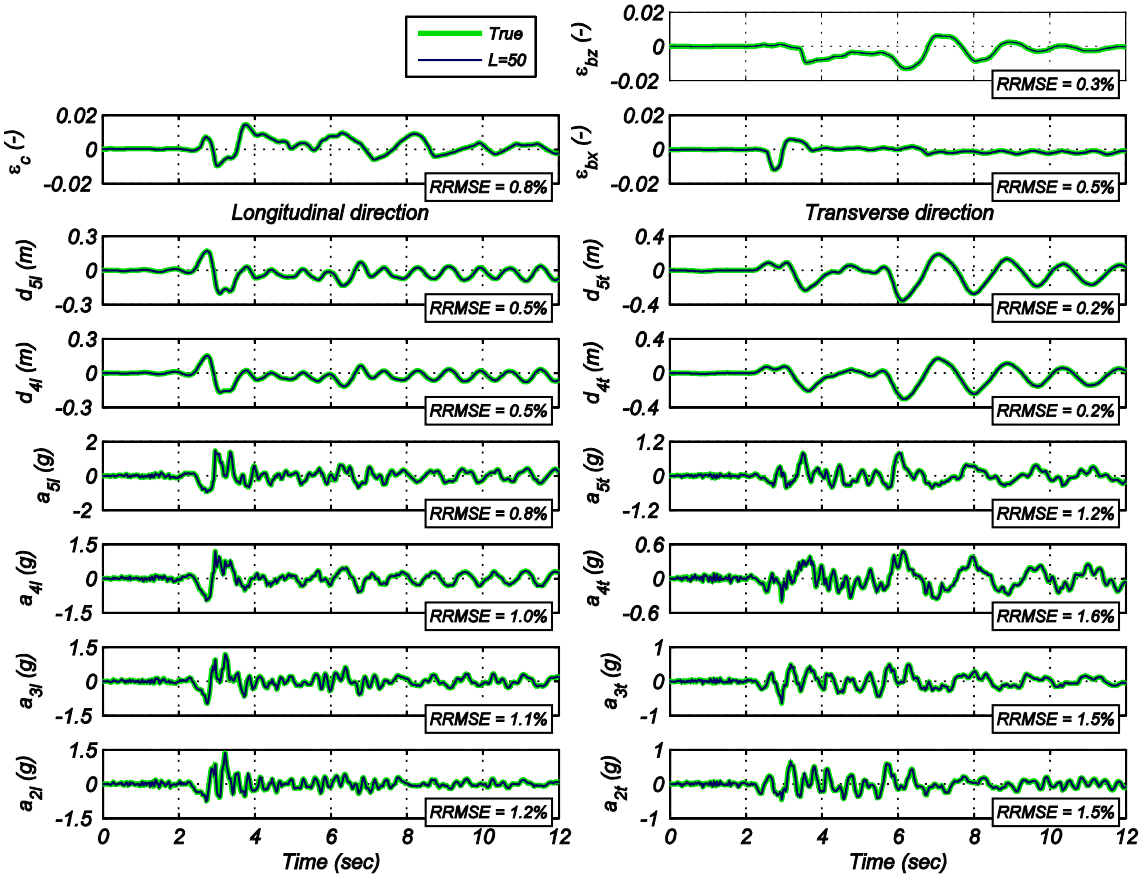

Figure 10.13: Comparison of the true measured and estimated acceleration response of the steel frame based on estimated input and final estimate of modeling parameters in the case of noisy acceleration, displacement, and strain response measurements with L=50.

Figure 10.14 compares different global and local unobserved response quantities of the FE model based on the true input excitations and true values of the modeling parameters (true responses) and the corresponding responses based on the final estimates of the modeling parameters and estimated input excitations (filtered) with L=50. As in Section 10.3.3.1, global responses consist of the RDR^x and V_b^z/W, section level responses consist of the M–κ at the base of a column (section 4 – 4 in Figure 10.3a) and at the end of a longitudinal beam (section 5 – 5 in Figure 10.3a), and fiber level responses comprise σ–ε of a corner steel fiber (see Figure 10.3c) at the bottom of a column (section

4 – 4 in Figure 10.3a) and at the end of a transverse beam (section 6 – 6 in Figure 10.3a). An excellent agreement for all the responses is observed when acceleration/displacement (Case 1) and acceleration/displacement/strain (Case 3) are considered in the output response measurements.

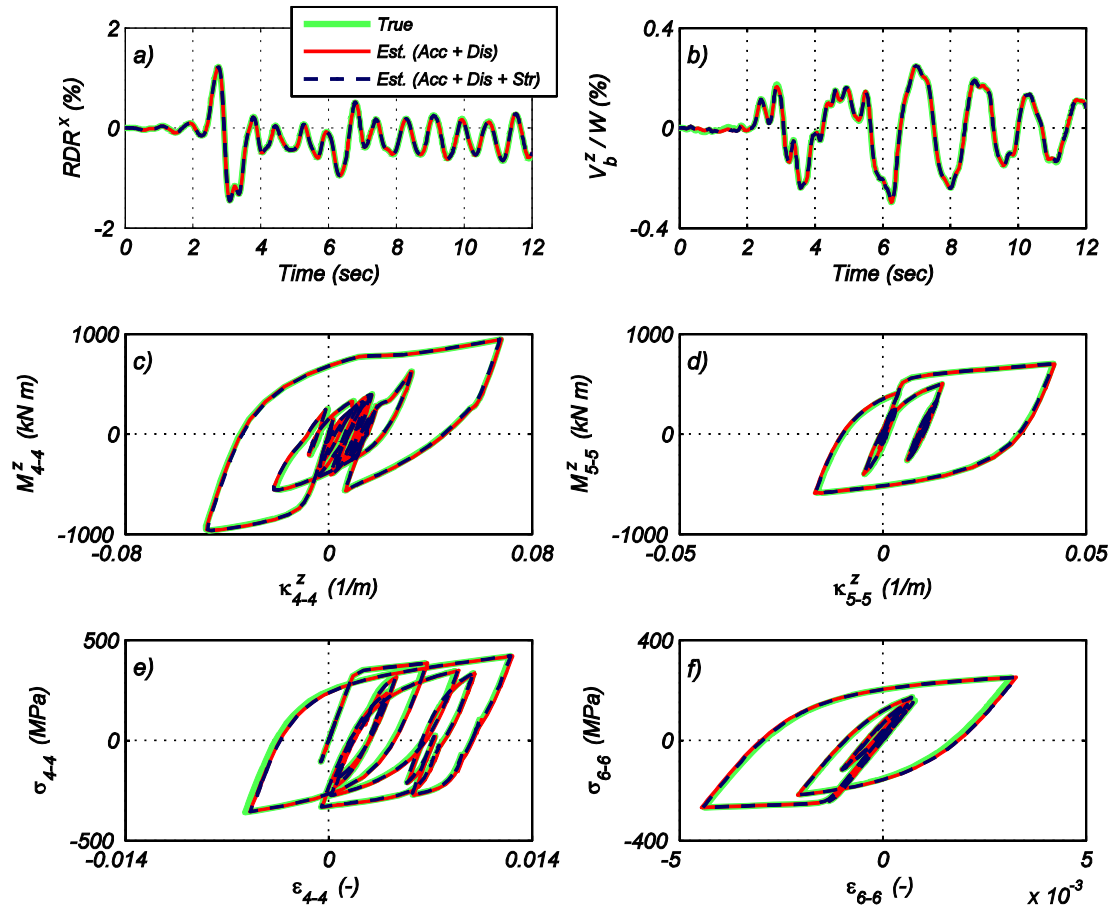

Figure 10.14: Comparison of the true unobserved responses and estimated unobserved responses of the steel frame based on estimated input and final estimate of modeling parameters. Case of noisy heterogeneous output response measurements with L=50. (a) roof drift ratio time history in the longitudinal (X) direction, (b) normalized base shear time history in the transverse (Z) direction, (c) moment versus curvature at the base of a column (section 4 − 4 in Figure 10.3a), (d) moment versus curvature at the end of a longitudinal beam (section 5 − 5 in Figure 10.3a), (e) stress versus strain in a corner steel fiber at the base of a column (section 4 − 4 in Figure 10.3a), (f) stress versus strain in a corner steel fiber at the end of a transverse beam (section 6 − 6 in Figure 10.3a).

The excellent estimation results of the modeling parameters and input excitations and excellent agreement between different true and estimated unobserved response quantities when considering heterogeneous measurements verify the excellent performance of the proposed methodology. In addition, the flexibility of the methodology to incorporate measurements collected using different types of sensors and its capabilities for damage identification purposes even in the case of unknown input excitations are confirmed.

10.3.3.3. Computational costs

An important objective of the proposed framework is to provide a tool for rapid condition assessment of structures subjected to unknown input excitations after potentially damage-inducing earthquake events. Therefore, the computational cost and time required to conduct the estimation are important variables that must be considered, especially when considering the importance of the period of time following a disastrous event. The computational cost of the proposed algorithm is evaluated in terms of process time required to complete the estimation. All the results presented in this section were obtained using a desktop workstation with an Intel Xeon CPU E5-2630 2.6-GHz processor and 32-GB random-access memory. Table 10.7 shows the computational cost associated to the estimation process in the case of noisy heterogeneous output response measurements (accelerations, displacements, and strains) for different values of the memory factor (L). It is observed that the computational cost increases considerably as L increases. Recall that the UKF requires to run $\left[13+4\min\left(k+1,L\right)\right]$ nonlinear FE models (number of SPs) when estimating the modeling parameters and input excitations at time

step $(k+1)$. Based on these results it is concluded that the application of the proposed framework for detailed damage diagnosis of realistic civil structures (like the 3D steel frame building considered in this application example) is feasible, and a description of the state of the structure can be obtained within a fraction of a day to a few days after the occurrence of the damaging-event.

Table 10.7: Computational cost of the estimation process in Case 3 of the steel frame (noisy acceleration, displacement, and strain response measurements) for different values of L.

Type of response measurement	Memory factor (L)	Process time (hr)
Case 3: Acceleration, Displacement, and Strain	10	8.2
	20	14.3
	30	20.5
	50	31.2
	600	137.5

10.3.3.4. Performance of the proposed framework in the presence of high output measurement noise

Results presented in Section 10.3.3.1 and 10.3.3.2 assumed a level of output measurement noise moderately higher than the ones expected in real world applications. In this section, the performance of the proposed joint input-parameter estimation framework in the presence of level of noises much larger than those expected from current sensors available for earthquake engineering applications is investigated. A memory factor $L=30$ is considered for the cases of acceleration-only, acceleration and displacement, and acceleration, displacement, and strain response measurements.

To pollute the true responses, $1.5\%g$, $5.0\,mm$ and $1.0\,mm/m$ RMS zero-mean white Gaussian noises are added, after completion of the structural response simulation,

to each true absolute acceleration, displacement, and strain response. In the estimation phase, standard deviations (or RMS) of 1.0%g, $3.0\,mm$, and $0.5\,mm/m$ are assumed in matrix **R** for acceleration, displacement, and strain measurements, respectively, i.e., noise covariances of $9.62\times10^{-3}\left(m/s^2\right)^2$, $9.0mm^2$, and $0.25\left(mm/m\right)^2$ are considered, respectively.

Table 10.8 summarizes the final estimates of the modeling parameters normalized by their corresponding true values. Accurate estimation of E_{col}, E_{beam}, f_{col}, and f_{beam} is obtained in the different cases of heterogeneous output response measurements in the case of high measurement noise. The accuracy in the estimation of b_{col} and b_{beam} significantly improve when heterogeneous output responses are measured, especially when both displacements and strains are considered.

Table 10.8: Final estimates of the modeling parameters of the steel frame in the case of high output measurement noise with $L=30$.

Type of response measurement	Modeling parameter					
	$\frac{E_{col}}{E_{col}^{true}}$	$\frac{f_{col}}{f_{col}^{true}}$	$\frac{b_{col}}{b_{col}^{true}}$	$\frac{E_{beam}}{E_{beam}^{true}}$	$\frac{f_{beam}}{f_{beam}^{true}}$	$\frac{b_{beam}}{b_{beam}^{true}}$
Acceleration-only	0.99	1.02	1.00	1.04	1.04	0.62
Acceleration and displacement	0.99	1.01	0.98	1.03	1.01	0.93
Acceleration and strain	0.99	1.02	1.10	1.02	1.02	0.99
Acceleration, displacement, and strain	0.99	1.01	1.06	1.03	1.01	0.99

Table 10.9 summarizes the *RRMSE* between the true and estimated input excitations, for both unfiltered and filtered cases. Similar results to those presented for moderate level of output measurement noise in Sections 10.3.3.1 and 10.3.3.2 are

observed. The spurious low-frequency component is detected when only acceleration measurement are considered, while it is significantly reduced when displacement measurements are included.

Table 10.9: *RRMSE*s (in %) between the true and estimated input excitation to the steel frame in the case of high output measurement noise with $L = 30$.

Type of response measurement	*RRMSE* (%) – Input excitation			
	Sylmar 360°		Sylmar 90°	
	Unfiltered	Filtered	Unfiltered	Filtered
Acceleration-only	80.0	10.3	12.9	8.7
Acceleration and displacement	4.7	4.4	6.4	6.2
Acceleration and strain	23.4	13.9	9.1	8.9
Acceleration, displacement, and strain	4.8	4.4	6.3	6.2

Table 10.10 presents the *RRMSE* between the true and estimated (computed using the final estimates of the modeling parameters and the unfiltered estimated input excitations) output response measurements. The same nomenclature as described in Section 10.3.3.2 is used here. Low *RRMSE*s between true and estimated output response measurements confirm the successful performance of the joint input-parameter estimation framework proposed, even for the case of high output measurement noise.

Table 10.10: *RRMSE*s (in %) between the true response and the estimated response of the steel frame based on the final estimate of the modeling parameters and the estimated input excitation in the case of high output measurement noise with $L = 30$.

Type of response measurement	*RRMSE* (%) – Output response measurement														
	$\mathbf{a}_{2l}$	$\mathbf{a}_{3l}$	$\mathbf{a}_{4l}$	$\mathbf{a}_{5l}$	$\mathbf{a}_{2t}$	$\mathbf{a}_{3t}$	$\mathbf{a}_{4t}$	$\mathbf{a}_{5t}$	$\mathbf{d}_{4l}$	$\mathbf{d}_{5l}$	$\mathbf{d}_{4t}$	$\mathbf{d}_{5t}$	$\boldsymbol{\varepsilon}_{c}$	$\boldsymbol{\varepsilon}_{bx}$	$\boldsymbol{\varepsilon}_{bz}$
Acceleration-only	5.0	4.9	4.4	3.6	5.7	5.6	6.4	4.5	–	–	–	–	–	–	–
Acceleration and displacement	3.6	3.5	3.1	2.6	4.8	4.7	5.0	3.7	1.4	1.4	0.6	0.6	–	–	–
Acceleration and strain	3.7	3.6	3.3	2.8	5.8	5.6	5.9	4.9	–	–	–	–	8.1	8.6	5.5
Acceleration, displacement, and strain	3.7	3.5	3.2	2.6	4.8	4.6	4.9	3.7	1.4	1.4	0.6	0.6	1.9	2.4	1.0

10.3.4. Estimation of unknown modeling parameters in the case of known input excitation

In this section is assumed that the input excitation is known and only the modeling parameters are estimated using the UKF as originally proposed by Astroza et al. (2014). The same level of output measurement noises as considered in Section 10.3.3 are used here. Cases of acceleration–only, acceleration+displacement, acceleration+strain, and acceleration+displacement+strain using the same sensor arrays are considered for comparison purposes. Figure 10.15 shows the time histories of the normalized *a posteriori* estimates of the modeling parameters for three instrumentation arrays. It is observed that the modeling parameters converge to their true values in all cases. Table 10.11 summarizes the final estimated of the modeling parameters in the case of known input excitation. For all instrumentation arrays, estimation of E_{col}, E_{beam}, f_{col}, and f_{beam} is excellent, however, even in the case of known input excitation estimation of b_{col} and b_{beam} (post-yield parameters) exhibits small relative errors. In the case of acceleration–only measurements, estimation of post-yield parameters has relative errors of 3%. These errors decrease as heterogeneous sensors arrays are considered, which is in agreement with the results obtained by Astroza et al. (2015) for a three-dimensional reinforced concrete (RC) building. By comparing these results with those obtained in Section 10.3.3, it can be concluded that the methodology to updated nonlinear FE model subjected to unknown input has an excellent performance in terms of accuracy, and robustness, with results comparable to those achieved when the input excitation is known.

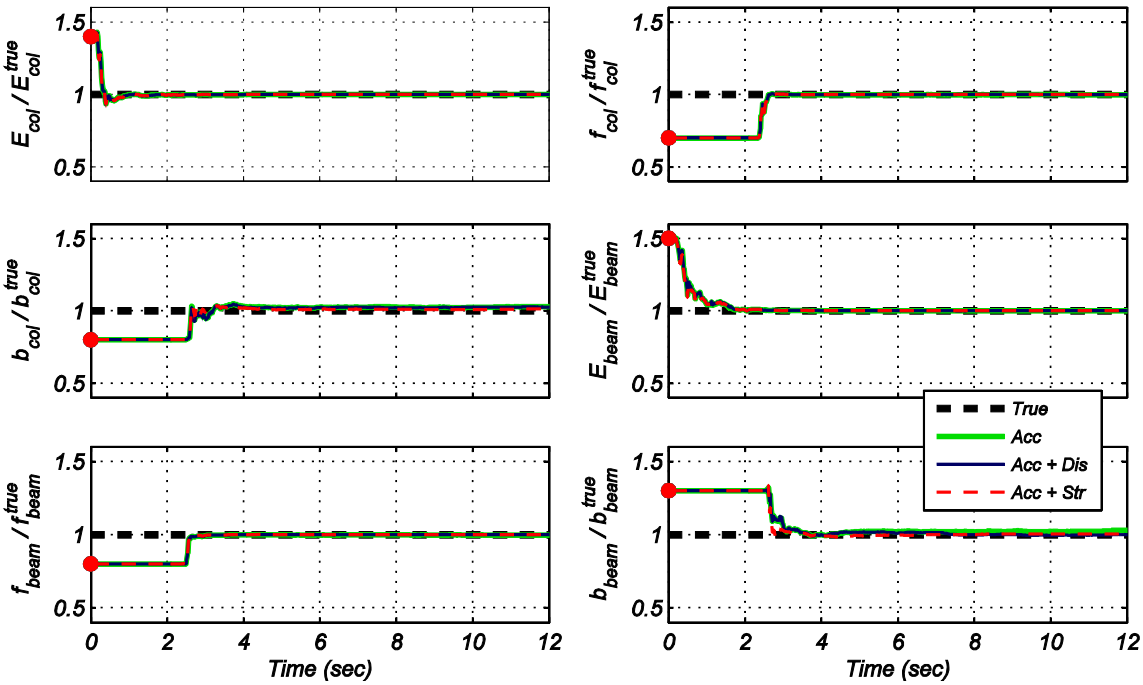

Figure 10.15: Time history of the *a posteriori* estimates of the modeling parameters of the steel frame in the case of known input and noisy heterogeneous output response measurements.

Table 10.11: Final estimates of the modeling parameters of the steel frame in the case of known input and noisy heterogeneous output response measurements.

Type of response measurement	Modeling parameter					
	$\frac{E_{col}}{E_{col}^{true}}$	$\frac{f_{col}}{f_{col}^{true}}$	$\frac{b_{col}}{b_{col}^{true}}$	$\frac{E_{beam}}{E_{beam}^{true}}$	$\frac{f_{beam}}{f_{beam}^{true}}$	$\frac{b_{beam}}{b_{beam}^{true}}$
Acceleration–only	1.00	1.00	1.03	1.00	1.00	1.03
Acceleration and displacement	1.00	1.00	1.01	1.00	1.00	1.00
Acceleration and strain	1.00	1.00	1.01	1.00	1.00	1.00
Acceleration, displacement, and strain	1.00	1.00	1.01	1.00	1.00	1.00

10.3.5. Modeling parameter sensitivity

In order to analyze the sensitivity of the different output response measurements considered (accelerations, displacements, and strains) with respect to the six modeling

parameters to be estimated (jointly with the unknown input excitations), Figure 10.16 shows the envelopes of three response quantities (acceleration at level 5 in longitudinal direction $\mathbf{a}_{5l}$, displacement at level 5 in longitudinal direction $\mathbf{d}_{5l}$, and strain of a corner steel fiber at the bottom of a column ε_c – section 1−1 in Figure 10.3a) when the modeling parameters take values of 0.5, 1.0, and 2.0 times their true values. It is observed that acceleration and displacement responses are very sensitive to $E_{col}, f_{col}, E_{beam}$, and f_{beam}, because variation in these modeling parameters induce significant variation in those responses. Contrarily, acceleration responses are almost insensitive with respect to b_{col} and b_{beam}, since variation in these modeling parameters induce negligible changes in those responses. However, displacement responses show sensitivity with respect to b_{col} and b_{beam} around the largest displacement demand imposed by the earthquake excitation in the longitudinal direction (~3.0 sec). This time instant matches the time at which the post-yield parameters start to update (see Figure 10.10 and Figure 10.15). In the case of strain response measurements, they are sensitive to all modeling parameters. In particular, strain measured in a corner fiber at the bottom of a column (Figure 10.16) is sensitive to all modeling parameters except b_{beam}. Similarly, strains measured in corner fibers at the end of beams (sections 2−2 and 3−3 in Figure 10.3a) are sensitive to all modeling parameters except b_{col}. It is noteworthy that the fifteen output response measurements (eight accelerations, four displacements, and three strains) were analyzed and all the results are consistent with those discussed above, however, results for only three output response measurements are shown here due to space limitations.

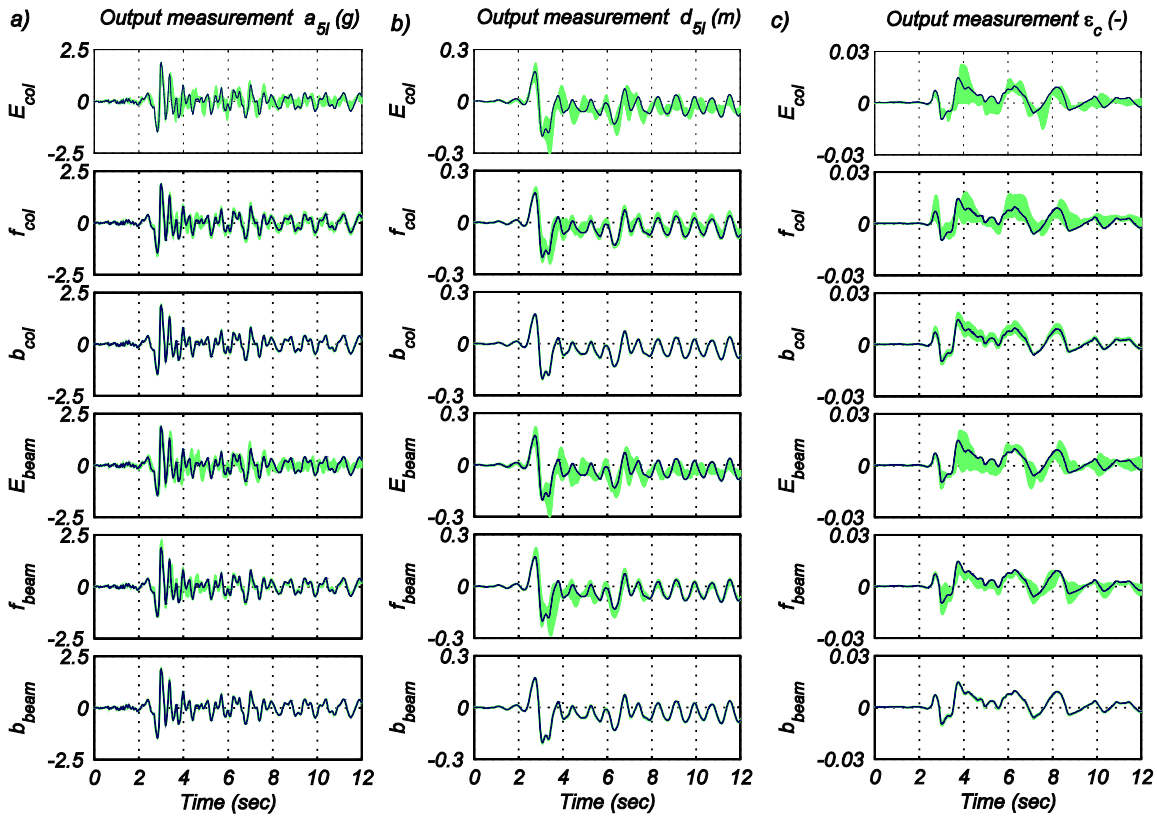

Figure 10.16: Sensitivities of output response quantities of the steel frame with respect to modeling parameters. (a) Roof longitudinal acceleration, (b) Roof longitudinal displacement, (c) Strain in a corner steel fiber at the base of a column (section 1−1 in Figure 10.3a). Blue line: true response. Green area: envelope of responses for $0.5\theta^{true}$, $1.0\theta^{true}$, and $2.0\theta^{true}$.

10.4. Numerical application 2: 3D RC frame

10.4.1. Finite element model and earthquake input excitation

The second application example consists of the 3D 5-story 2-by-1 bay RC frame building presented in Chapter 9 of this dissertation. Details of design, FE model, and characteristics of the building can be found in Section 9.5.1.

The same procedure as described in Section 10.3.1. is followed. First, the nonlinear seismic response of the structure is simulated using the nonlinear FE model

with fiber beam-column elements. In this application example, only the strong motion portions of translation components 360° and 90° of ground acceleration recorded at the Sylmar County Hospital during the 1994 Northridge earthquake are considered as base excitation in the longitudinal and transverse direction of the building, respectively (Figure 10.17). The same sampling rate (50 Hz) and PGAs (0.84*g* and 0.60*g*) as described in Section 10.3.1 are still valid for the input excitation used in the second application example.

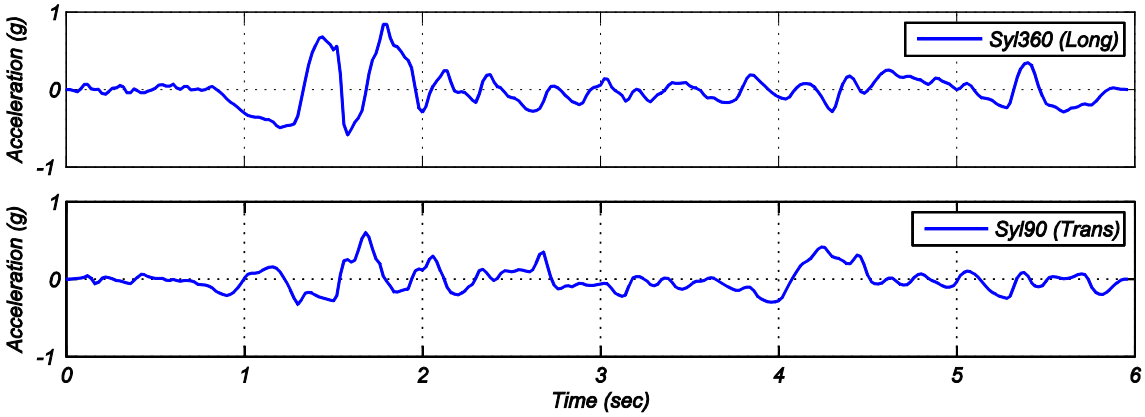

Figure 10.17: Acceleration time history of the input seismic motion for the 3D RC frame.

10.4.2. Response simulation

The true modeling parameter vector of the RC frame is $\boldsymbol{\theta}^{true} = \left[E_{s-col}^{true}, f_{y-col}^{true}, b_{col}^{true}, E_{s-beam}^{true}, f_{y-beam}^{true}, b_{beam}^{true}, E_c^{true}, f_c^{true}, \varepsilon_c^{true} \right]^T \in \mathbb{R}^{9\times 1}$, $E_{s-col}^{true} = 200\ GPa$, $f_{y-col}^{true} = 517\ MPa$, $b_{col}^{true} = 0.01$, $E_{s-beam}^{true} = 200\ GPa$, $f_{y-beam}^{true} = 414\ MPa$, $b_{beam}^{true} = 0.05$, $E_c^{true} = 27600\ MPa$, $f_c^{true} = 40\ MPa$, and $\varepsilon_c^{true} = 0.0035$. The FE model described in Section 9.5.1. with the true modeling parameters' values ($\boldsymbol{\theta}^{true}$) is used to simulate the

response of the RC building to the ground acceleration time histories shown in Figure 10.17 (true response).

10.4.3. Estimation of modeling parameters and unknown input

The true (simulated) responses of the structure are polluted by AWGN and used as output response measurements in the estimation phase. Here, three cases of heterogeneous response measurements are considered. First, absolute acceleration-only response time histories in both translational directions at 3rd, 5th, and roof floors of the building are considered. Second, relative displacement response time histories in both translational directions at the 4th and roof levels are considered in addition to acceleration responses of previous case. Third, strain response time histories of reinforcing steel and cover concrete at the bottom of a corner column and end of a longitudinal beam are assumed to be recorded in addition to absolute accelerations and relative displacements described above. The location of the accelerometers, GPS, and strain gauges used to measured different output response quantities are shown by blue arrows, green circles, and red lines, respectively, in Figure 10.18.

Both translational components of ground acceleration time histories used as input excitation and the nine modeling parameters describing the constitutive laws of reinforcing steel and concrete fibers in beams and columns are considered as unknown in the estimation phase. Nine material parameters define the unknown modeling parameter vector $\boldsymbol{\theta} = \left[E_{s-col}, f_{y-col}, b_{col}, E_{s-beam}, f_{y-beam}, b_{beam}, E_c, f_c, \varepsilon_c \right]^T \in \mathbb{R}^{9\times 1}$ and the unknown input ground acceleration time histories define the unknown input $\ddot{\mathbf{s}}_{1:300} \in \mathbb{R}^{2\times 300}$. Note that in

this application example $n_s = 2$ and $N = 300$. As in application example 1, model uncertainty is not accounted for.

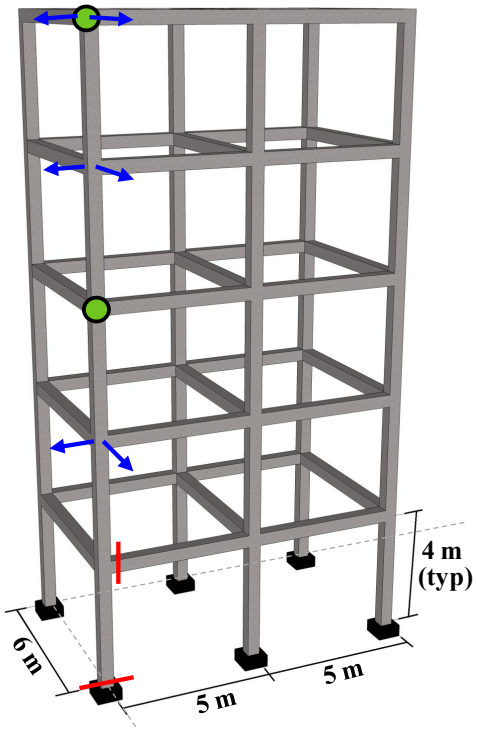

Figure 10.18: RC frame building. Blue arrows indicate acceleration measurements, Green circles indicate displacement measurements, and Red lines indicate location of strain measurements.

After completion of the structural response simulation, zero-mean AWGN is used to pollute the true responses. Noises with RMS amplitudes of $0.5\%g$, $2.0\,mm$, and $0.5\,mm/m$ are added to the true absolute acceleration, relative displacement, and strain responses, respectively. As abovementioned, based on the characteristics of sensors currently used in earthquake engineering, these levels of noise are slightly higher than those expected in real-world applications. In the estimation phase, zero-mean and standard deviation (or RMS) of $0.3\%g$, $1.5\,mm$, and $0.3\,mm/m$ are considered to

construct the covariance matrix of the output measurement noise of absolute acceleration, relative displacement, and strain response quantities, respectively.

Time-invariant second order statistics with zero-mean and covariance matrix $\mathbf{Q}_k = \mathbf{Q} \in \mathbb{R}^{n_x \times n_x}$, where $n_x = n_\theta + n_s \min(k+1, L) = 9 + 2\min(k+1, L)$, are assumed for the process noise $\boldsymbol{\gamma}_k$. The diagonal entries of $\mathbf{Q}$ are assumed equal to $(q \times \hat{x}_{0|0}^i)^2$ where $i = 1, \ldots, n_x$ and $q = 1 \times 10^{-5}$, i.e., the process noise covariance matrix is constructed assuming a coefficient of variation of 1×10^{-5} of the initial estimate of the modeling parameters and unknown input excitations.

The initial unknown augmented vector is equal to $\hat{\mathbf{x}}_{0|0} = \left[\hat{\boldsymbol{\theta}}_{0|0}^T, \hat{\ddot{\mathbf{s}}}_{0|0}^T\right]^T \in \mathbb{R}^{11\times 1}$. For the modeling parameters ($\hat{\boldsymbol{\theta}}$), the initial estimate is assumed as $\hat{\boldsymbol{\theta}}_{0|0} = \left[0.7E_{s-col}^{true}, 1.3f_{y-col}^{true}, 1.25b_{col}^{true}, 1.3E_{s-beam}^{true}, 0.8f_{y-beam}^{true}, 0.75b_{beam}^{true}, 1.2E_c^{true}, 0.85f_c^{true}, 0.9\varepsilon_c^{true}\right]^T$. For the unknown input excitations, the initial estimate is assumed equal to $\hat{\ddot{\mathbf{s}}}_{0|0} = [0.01, 0.01]^T \in \mathbb{R}^{2\times 1}$. The initial estimate of the covariance matrix $\hat{\mathbf{P}}_{0|0}^{\mathbf{xx}}$ is assumed to be diagonal. The terms related to the modeling parameters and to the unknown input excitation are computed assuming a coefficient of variation of 10% of the initial estimate of the mean $\hat{\mathbf{x}}_{0|0}$, i.e., the diagonal entries of $\hat{\mathbf{P}}_{0|0}^{\mathbf{xx}}$ are computed as $(p \times \hat{x}_{0|0}^i)^2$ where $i = 1, \ldots, n_x$ and $p = 0.10$. As in application example 1, at time step $(k+1)$ the *a priori* standard deviation of the last n_s components of $\mathbf{x}$ (which corresponds to unknown input excitation at that time step, $\ddot{\mathbf{s}}_{k+1}^{k+1}$), are taken equal to $(p \times \hat{\ddot{\mathbf{s}}}_{k|k}^k)^2$, while other components

of $\hat{\mathbf{P}}^{\mathbf{xx}}_{k+1|k}$ are obtained from the corresponding elements of the *a posteriori* covariance at previous time step ($\hat{\mathbf{P}}^{\mathbf{xx}}_{k|k}$). All the variables involved in the estimation have comparable amplitudes, because the modeling parameters are normalized by their corresponding true values and the acceleration time histories are in the unit of m/s^2.

Using the framework shown in Figure 10.1, the unknown modeling parameters and the time history of both unknown input excitations are estimated. The number of SPs required at each time step is $2n_x+1=2\times\left[9+2\min\left(k+1,L\right)\right]+1$. This means that $\left[19+4\min\left(k+1,L\right)\right]$ nonlinear FE models (one for each SP) need to be run when estimating the modeling parameters and input excitations at time step $\left(k+1\right)$. Only the value $L=30$ is considered for the memory factor in this application example.

Figure 10.19 shows the time history of the estimates obtained with the noisy output response measurements and *L*=30. Table 10.12 reports the final estimates of the modeling parameters, $\hat{\boldsymbol{\theta}}_{N|N}$, normalized by their corresponding true parameter values for the different cases of response measurements. In all cases, excellent estimation results are obtained for stiffness-related modeling parameters (E_{s-col}, E_{s-beam}, and E_c), parameters related to yield of reinforcing steel (f_{y-col} and f_{y-beam}), post-yield parameter of reinforcing steel in beams (b_{beam}). For these modeling parameters relative errors between estimated and true values less than or equal to 3% are obtained. Moreover, the additional information contained in the displacement and strain responses for modeling parameters b_{col}, f_c, and ε_c compared to the case of acceleration-only response measurements is

clearly observed. The estimation of these three modeling parameters improves significantly as displacement and strain response measurements are considered.

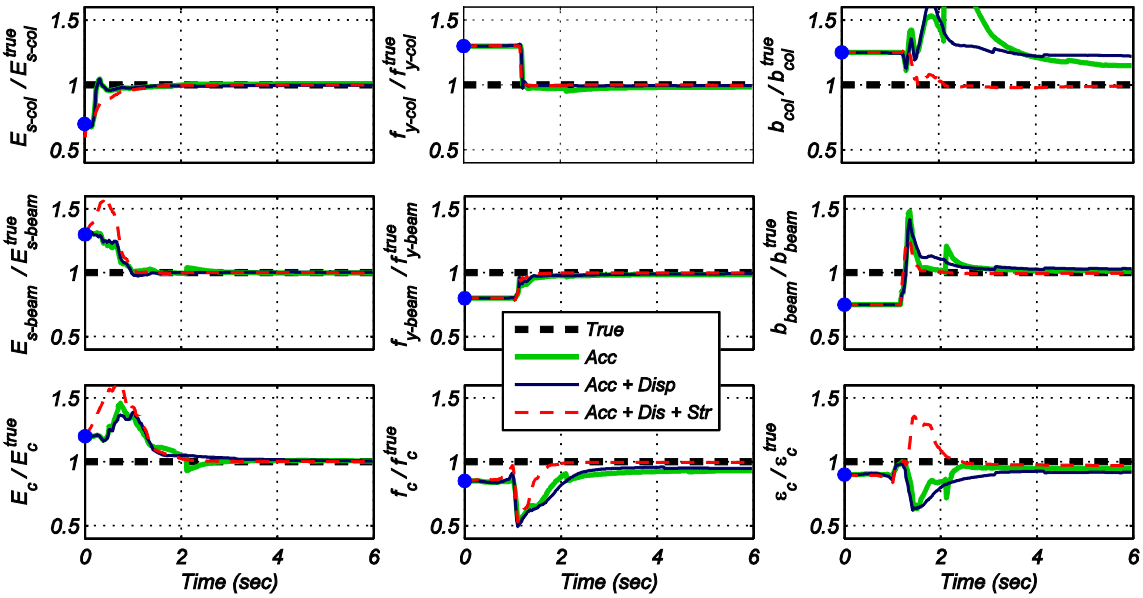

Figure 10.19: Time history of the *a posteriori* estimates of the modeling parameters of the RC frame in the case of noisy output response measurements with L=30.

Table 10.12: Final estimates of the modeling parameters of the RC frame in the case of noisy output response measurements with L=30.

Type of response measurement	Modeling parameter								
	$\frac{E_{s-col}}{E_{s-col}^{true}}$	$\frac{f_{y-col}}{f_{y-col}^{true}}$	$\frac{b_{col}}{b_{col}^{true}}$	$\frac{E_{s-beam}}{E_{s-beam}^{true}}$	$\frac{f_{y-beam}}{f_{y-beam}^{true}}$	$\frac{b_{beam}}{b_{beam}^{true}}$	$\frac{E_c}{E_c^{true}}$	$\frac{f_c}{f_c^{true}}$	$\frac{\varepsilon_c}{\varepsilon_c^{true}}$
Acceleration	1.01	0.98	1.15	1.00	0.98	1.01	1.01	0.93	0.95
Acceleration and displacement	1.00	0.99	1.22	1.00	0.99	1.03	1.01	0.95	0.92
Acceleration, displacement, and strain	1.00	1.00	0.99	1.00	1.00	0.99	1.00	1.00	0.97

Figure 10.20 shows the time histories of the true and estimated (unfiltered) input excitations (i.e., both translational components recorded at the Sylmar station during the 1994 Northridge earthquake) in the case of noisy acceleration-only output response measurements with L=30. Table 10.13 summarizes the *RRMSE* between the true and

estimated input excitations (unfiltered) for the different cases of response measurements. The estimated input excitations are very accurate for both components, with *RRMSE* lower than 3%. Contrary to the results obtained for the steel frame, where a spurious low-frequency component appears in the estimation after the strong motion part of the input excitation, no spurious low frequency component is detected in the estimated input with acceleration-only output response measurements. This is because in the case of the RC frame, only the strong motion part of the excitation is considered.

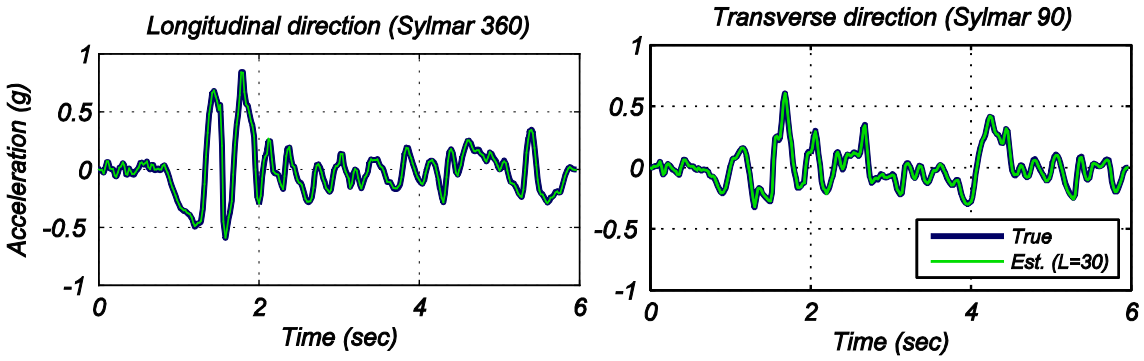

Figure 10.20: Comparison of the true and estimated input time histories to the RC frame in the case of noisy acceleration-only output response measurements with L=30.

Table 10.13: *RRMSE*s (in %) between the true and estimated (unfiltered) input excitation to the RC frame in the case of noisy output response measurements with L=30.

Type of response measurement	*RRMSE* (%) – Input excitation (unfiltered)	
	Sylmar 360°	Sylmar 90°
Acceleration	2.4	2.6
Acceleration and displacement	1.6	2.1
Acceleration, displacement, and strain	1.3	1.8

Table 10.14 presents the *RRMSE* between the true and estimated (computed using the final estimates of the modeling parameters and the unfiltered estimated input excitations) output response measurements. In this table, $\mathbf{a}_{ij}$ and $\mathbf{d}_{ij}$ stand for the

absolute acceleration and relative displacement time history response at level i in direction j, respectively, where l = longitudinal and t = transverse directions, and $\boldsymbol{\varepsilon}_{i-j}$ denotes the strain time history measured in the corner fiber of the cross-section of member element i (where c = column and bx = longitudinal beam) and material j (where s = reinforcing steel and c = concrete). The location of the output response measurements are shown in Figure 10.18. An excellent agreement between true and estimated response is observed, with *RRMSE*s lower than or equal to 2.1%.

Table 10.14: *RRMSE*s (in %) between the true response and the estimated response of the RC frame based on the final estimate of the modeling parameters and the estimated input excitation in the case of noisy output response measurements with L=30.

Type of response measurement	*RRMSE* (%) – Output response measurement													
	$\mathbf{a}_{3l}$	$\mathbf{a}_{5l}$	$\mathbf{a}_{6l}$	$\mathbf{a}_{3t}$	$\mathbf{a}_{5t}$	$\mathbf{a}_{6t}$	$\mathbf{d}_{4l}$	$\mathbf{d}_{6l}$	$\mathbf{d}_{4t}$	$\mathbf{d}_{6t}$	$\boldsymbol{\varepsilon}_{c-s}$	$\boldsymbol{\varepsilon}_{c-c}$	$\boldsymbol{\varepsilon}_{bx-s}$	$\boldsymbol{\varepsilon}_{bx-c}$
Acceleration	1.7	2.0	1.5	1.6	2.1	1.8	–	–	–	–	–	–	–	–
Acceleration and displacement	1.6	1.4	1.0	1.2	1.6	1.3	0.0	0.0	0.2	0.2	–	–	–	–
Acceleration, displacement, and strain	1.0	1.1	0.9	0.9	1.3	1.0	0.0	0.0	0.2	0.2	0.2	0.2	0.4	0.5

10.5. Conclusions

This chapter proposed and verified a methodology to update mechanics-based nonlinear structural FE models subjected to unknown input excitation. The framework uses recorded output response data to estimate unknown modeling parameters of the FE model and unknown input excitation using the UKF as estimation tool. The updated FE model and the estimated input excitation allow to accurately evaluate the state of damage of the structure, including loss of stiffness, strength degradation, and ductility capacity.

The performance of the methodology was analyzed in terms of convergence, accuracy, robustness, and computational cost using numerically simulated response data of realistic three-dimensional building structures, including a 4-story 2-by-1 bay steel frame building and a 5-story 2-by-1 bay reinforced concrete (RC) frame building, both subjected to bi-directional earthquake excitation. Six and nine modeling parameters for the steel and RC buildings, respectively, characterizing the nonlinear material constitutive models and samples of both input acceleration time histories were successfully estimated when limited response data were recorded. The use of heterogeneous sensor arrays, including acceleration, displacement, and strain measurements, was investigated and its effects on the estimation results were highlighted. It was observed that the use of heterogeneous sensor arrays improves considerably the accuracy of the estimation results, especially for post-yield material parameters.

When noisy acceleration-only output response measurements were considered, the estimation of the input excitations after the strong motion part contained a permanent drift due to a spurious low-frequency component, which does not affect the absolute acceleration response measurements. This spurious low-frequency component is eliminated using a high-pass filter. When displacement response measurements were considered, the spurious components in the estimated input excitations were automatically eliminated because displacement responses are sensitive to long-period force excitations.

Different true and estimated unobserved global and local response quantities were compared and they were found to be in very good agreement. This further confirms the

excellent performance of the proposed methodology and its capabilities for damage identification at different resolution levels, from global to the local levels.

10.6. Acknowledgements

Part of Chapter 10 is a reprint of the material that is currently being prepared for submission for publication “Bayesian nonlinear structural FE model updating for damage identification of civil structures subjected to unknown inputs” in *Structural Safety*, Astroza, Rodrigo; Ebrahimian, H.; and Conte, J.P. The dissertation author was the primary investigator and author of this paper.

References

Al-Hussein, A. and Haldar, A. (2015a). "Novel unscented Kalman filter for health assessment of structural systems with unknown input." *Journal of Engineering Mechanics ASCE*, 10.1061/(ASCE)EM.1943-7889.0000926, 04015012.

Al-Hussein, A. and Haldar, A. (2015b). "Unscented Kalman filter with unknown input and weighted global iteration for health assessment of large structural systems." *Structural Control and Health Monitoring*, In Press.

Astroza, R., Ebrahimian, H., and Conte, J. P. (2014). "Material parameter identification in distributed plasticity FE models of frame-type structures using nonlinear stochastic filtering." *Journal of Engineering Mechanics ASCE*, In press.

Astroza, R., Ebrahimian, H., and Conte. J.P. (2015). "Nonlinear system identification for health monitoring of civil structures." To be submitted to *Computers and Structures*.

Chen, J. and Li, J. (2004). "Simultaneous identification of structural parameters and input time history from output-only measurements" *Computational Mechanics*, 33(5), 365-374.

Ching, J., Beck, J. L., Porter, K. A., and Shaikhutdinov, R. (2006). "Bayesian state estimation method for nonlinear systems and its application to recorded seismic response." *Journal of Engineering Mechanics ASCE*, 132 (4), 396–410.

Distefano, N. and Pena-Pardo, B. (1976). "System identification of frames under seismic loads." *Journal of the Engineering Mechanics Division*, 102(EM2), 313–330.

Ebrahimian, H., Astroza, R., and Conte, J. P. (2015). "Extended Kalman filter for material parameter estimation in nonlinear structural finite element models using direct differentiation method." *Earthquake Engineering & Structural Dynamics*, In press.

Ebrahimian, H., Astroza, R., Conte, J.P., Restrepo, J.I, and Hutchinson, T.C. (2014). "Experimental validation of dynamic nonlinear FE model of full-scale five-story reinforced concrete building." *Ninth International Conference on Structural Dynamics* (*EURODYN 2014*), Porto, Portugal.

Eftekhar Azam, S., Chatzi, E., and Papadimitriou, C. (2015). "A dual Kalman filter approach for state estimation via output-only acceleration measurements." *Mechanical Systems and Signal Processing*, In press.

Filippou, F.C., and Fenves, G.L. (2004). "Methods of analysis for earthquake-resistant structures." Chapter 6, *Earthquake engineering: From engineering seismology to performance-based engineering*, CRC Press, Boca Raton, FL.

Filippou, F.C., Popov, E.P., and Bertero, V.V. (1983). "Effects of bond deterioration on hysteretic behavior of reinforced concrete joints." *Report EERC 83–19, Earthquake Engineering Research Center* (*EERC*), University of California, Berkeley.

Hsieh, C.S. (2011). "Optimal filtering for systems with unknown inputs via the descriptor Kalman filtering method." *Automatica*, 47(10), 2313–2318.

Huang, H., Yang, J.N., and Zhou, L. (2010). "Adaptive quadratic sum-squares error for structural damage identification." *Journal of Engineering Mechanics ASCE*, 135(2), 67–77.

Huang, H., Yang, J.N., and Zhou, L. (2010). "Adaptive quadratic sum-squares error with unknown inputs for damage identification of structures" *Structural Control and Health Monitoring*, 17(4), 404–426.

International Code Council (ICC). (2006). *International Building Code*. Falls Church, VA.

Julier, S.J. and Uhlmann, J.K. (1997). "A new extension of the Kalman filter to nonlinear systems." The *11th International Symposium on Aerospace/Defense Sensing, Simulation and Controls*, Orlando, FL.

Kitanidis, P.K. (1987). "Unbiased minimum-variance linear state estimation." *Automatica*, 23(6), 775–778.

Liu, P. and Au, S-K. (2013). "Bayesian parameter identification of hysteretic behavior of composite walls." *Probabilistic Engineering Mechanics*, 34, 101–109.

Lourens, E., Papadimitriou, C., Gillinjs, S., Reynders, E., De Roeck, G., and Lombaert, G. (2012). "Joint input-response estimation for structural systems based on reduced-order models and vibration data from a limited number of sensors." *Mechanical Systems and Signal Processing*, 29, 310–327.

Martinelli, P. and Filippou, F.C. (2009). "Simulation of the shaking table test of a seven-story shear wall building." *Earthquake Engineering and Structural Dynamics*, 38(5), 587–607.

Mazzoni, S., McKenna, F., and Fenves, G.L. (2005). *Opensees command language manual*. http://opensees.berkeley.edu/. Pacific Earthquake Engineering Research.

Mottershead, J.E. and Friswell, M.I. (1993). "Model updating in structural dynamics: A survey." *Journal of Sound and Vibration*, 167(2), 347–375.

Naets, F., Cuadrado, J., and Desmet, W. (2015). "Stable force identification in structural dynamics using Kalman filtering and dummy-measurements." *Mechanical Systems and Signal Processing*, 50-51, 235–248.

Omrani, R., Hudson, R., and Taciroglu, E. (2013). "Parametric identification of non-degrading hysteresis in a laterally-torsionally coupled building using an unscented Kalman filter." *Journal of Engineering Mechanics ASCE*, 139(4), 452–468.

Radhika, B and Manohar, CS. (2013). "Dynamic state estimation for identifying earthquake support motions in instrumented structures." *Earthquakes and Structures*, 5 (3), 359-378.

Ren, W. X., and De Roeck, G. (2002). "Structural damage identification using modal data. II: Test verification." *Journal of Structural Engineering ASCE*, 128(1), 96–104.

Ribeiro, F., Barbosa, A., Scott, M., and Neves, L. (2014). "Deterioration modeling of steel moment resisting frames using finite-length plastic hinge force-based beam-column elements." *Journal of Structural Engineering ASCE*, In Press.

Simoen, E., Moaveni, B., Conte, J.P., and Lombaert, G. (2013). "Uncertainty quantification in the assessment of progressive damage in a seven-story full-scale building slice." *Journal of Engineering Mechanics ASCE*, 139(12), 1818–1830.

Sun, H. and Betti, R. (2013). "Simultaneous identification of structural parameters and dynamic input with incomplete output-only measurements" *Structural Control and Health Monitoring*, 21(6), 868–889.

Taucer, F.F., Spacone, E., and Filippou, F.C. (1991). "A fiber beam-column element for seismic response analysis of reinforced concrete structures." *Report 91/17, EERC, Earthquake Engineering Research Center* (*EERC*), University of California, Berkeley.

Teughels, A. and De Roeck, G. (2004). "Structural damage identification of the highway bridge Z24 by FE model updating." *Journal of Sound and Vibration*, 278 (3), 589–610.

Uriz, P., Filippou, F., and Mahin, S. (2008). "Model for cyclic inelastic buckling of steel braces." *Journal of Structural Engineering ASCE*, 134(4), 619–628.

Wan, E.A. and van der Merwe, R. (2000). "The unscented Kalman filter for nonlinear estimation." *IEEE 2000 Adaptive Systems for Signal Processing, Communications, and Control Symposium*, Lake Louise, AB, Canada.

Wang, D. and Haldar, A. (1997). "System identification with limited observations and without input". *Journal of Engineering Mechanics ASCE*, 123(5), 504-511.

Yang, J.N. and Huang, H. (2007). "Sequential non-linear least-square estimation for damage identification of structures with unknown inputs and unknown outputs" *International Journal of Non-Linear Mechanics*, 42(5), 789–801.

Yang, J.N., Pan, S., and Huang, H. (2006). "An adaptive extended Kalman filter for structural damage identifications II: Unknown inputs." *Structural Control and Health Monitoring*, 14(3), 497–521.

Zhang, K., Li, H., Duan, Z., and Law, S.S. (2011). "A probabilistic damage identification approach for structures with uncertainties under unknown input." *Mechanical Systems and Signal Processing*, 25(4), 1126–1145.

CHAPTER 11

CONCLUDING REMARKS

11.1. Summary of the dissertation

This dissertation presents linear and nonlinear system and damage identification studies on civil structures. First, system identification (SID) of a linear elastic viscously damped model of a full-scale five-story reinforced concrete (RC) building built and tested on the NEES@UCSD shake table is conducted. Five different state-of-the-art methods of SID, including output-only and input-output methods, are used to estimate the modal properties (natural frequencies, damping ratios, and mode shapes) of the building and the SID results obtained are compared. Evolution of the modal properties during the construction process and effects of nonstructural components and systems (NCSs), amplitude of the excitation, environmental conditions, isolation system, and structural and nonstructural damage on the identified dynamic characteristics are investigated. Second, new frameworks for system and damage identification of nonlinear structural systems are developed and validated through numerical simulation. The proposed frameworks integrate high-fidelity mechanics-based nonlinear finite element (FE) structural modeling and analysis with Bayesian inference methods. The methodologies

can be employed for rapid damage identification (detection, localization, classification, and assessment) of civil structures.

11.2. Summary of major findings and novel contributions

The research work presented in this dissertation contributes to the research areas of: (1) system identification of full-scale structures with real-world complexities using input-output and output-only SID methods based on dynamic test data; (2) damage identification of real-world structures subjected to progressive damage induced by a realistic source of dynamic excitation based on the modal parameters identified from dynamic test data; (3) investigation of the effects of the construction process, nonstructural components and systems (NCSs), amplitude of the excitation, and changing environmental conditions on the identified modal parameters; (4) nonlinear system and damage identification of civil structures; (5) mechanics-based nonlinear finite element (FE) model updating for damage identification of civil structures.

The main contributions and major findings of this dissertation are summarized as follows:

1. The evolution of the modal properties (natural frequencies, damping ratios, and mode shapes) of a full-scale five-story RC building (BNCS building) during the construction process and placement of major NCSs was investigated. A sequence of dynamic tests was performed on the building, including ambient vibrations (AVs) that were recorded daily and shock (free vibration) and forced vibration tests (low-amplitude white noise and seismic base excitations) that were conducted at different stages of construction.

Different state-of-the-art SID methods, including three output-only and two input-output methods, were used to estimate the modal properties of the building. The results obtained allowed to investigate in detail the effects of the construction process and NCSs on the dynamic parameters of this building system and to compare the modal properties identified from different methods, as well as the performance of these methods. It was found that placement of the concrete to build the main structural elements (slabs, columns, and walls) reduces the natural frequencies because of the additional mass (without stiffness contribution) incorporated to the structure. The effect of concrete hardening and corresponding stiffness gain during the curing process was detected through gradual increase in the natural frequencies. Some NCSs had a significant effect on the identified natural frequencies and damping ratios of the building. The precast cladding induced abrupt reductions in the natural frequencies due to their significant mass (without significant stiffness) added to the building. The interior partition walls increased significantly the initial lateral stiffness of the building and consequently decreased its natural frequencies. Furthermore, they slightly increased the identified damping ratios of the building. The installation of the NCSs decreased the natural frequency (identified from ambient vibration data) of some modes (by up to 9%) and increased that of others (by up to 18%), while the identified damping ratios increased by 15 to 191% for all the modes from the bare building structure to the complete building, due to the additional sources of energy dissipation provided by the NCSs themselves and their

interaction with the structural frame. Using the white noise (WN) base excitation test data, the effect of cracking in the concrete and corresponding loss of stiffness during the WN tests performed on both the bare structure and the complete building was clearly observed from the natural frequencies identified. It was observed that the low amplitude of structural vibration induced by AV was not sufficient to exercise (re-open) the majority of the cracks developed during the WN base excitation tests performed and, therefore, to identify the corresponding loss of stiffness of the structure.

2. Using vibration data recorded from the BNCS building while fixed at its base, a comprehensive comparative study of five state-of-the-art system identification methods was conducted. The building fixed at its base was tested on the NEES@UCSD shake table and subjected to a sequence of earthquake motions selected to progressively damage the structure and NCSs. Between seismic tests, AV response was recorded. Additionally, low-amplitude WN base excitation tests were conducted at key stages during the test protocol. Using the vibration data recorded, five state-of-the-art SID methods are employed to estimate the modal properties of an equivalent linear elastic viscously-damped time-invariant model of the building at different levels of damage and the results obtained are compared. The results showed that modal properties identified from different methods are in good agreement and that the estimated modal parameters are affected by the amplitude of the excitation and the level of structural/nonstructural damage. The natural frequencies and mode shapes identified by different methods were found in

very good and good agreement, respectively, whereas the identified damping ratios show much larger method-to-method variability than the natural frequencies and mode shapes. Detailed visual inspections of the damage conducted between the seismic tests permitted to correlate the identified modal parameters and global and story-level responses of the building with the actual level of damage. Distribution of damage over the height of the building observed from visual inspections was found in good agreement with the loss of apparent story stiffness inferred from the recorded floor acceleration data. Using the WN base excitation test data, the ratio between the natural frequencies of the building in its damage states (after the first WN test) and its reference state (first WN test) was computed from the apparent global structural stiffnesses and from the identified natural frequencies of the longitudinal modes of the building. The ratio obtained from the apparent global structural stiffnesses was found in excellent agreement with the ratio of the identified natural frequency of the first longitudinal mode (1-L), suggesting that the global response of the building (total base shear versus roof drift) during the low-amplitude WN base excitation tests was dominated by mode 1-L. Identified natural frequencies of other modes (2-L to 5-L) also decreased as damage progressed, but less (in relative terms) than that of mode 1-L. The modal contributions to the absolute acceleration response were also studied. As the damage in the building progressed, the relative contributions of the higher modes (2-L, 3-L, and 4-L) increased drastically as compared to

the reference state of the building (DS0), whereas the relative contribution of the fundamental mode (1-L) decreased considerably.

3. Using vibration data recorded in the BNCS building isolated at its base, the effects of the isolation system in elongating the predominant period of the building, concentrating the deformation in the isolation layer, and augmenting the energy dissipation capacity of the system were investigated. For the base isolated (BI) configuration of the building, a sequence of seven seismic tests was designed and applied to the BNCS building to progressively increase the seismic demand on the structure and NCSs. The effectiveness of the isolation in reducing the floor acceleration and interstory drift demands was demonstrated. The dependency of the secant stiffness and effective damping ratio on the shear deformation in the isolators was investigated using data from quality control (component), WN base excitation, and seismic tests. Before and after each seismic test, low-amplitude WN base excitation tests with three different nominal amplitudes were carried out and AV data were recorded continuously for approximately sixteen days. Because of the low intensity of these excitations, a quasi-linear response of the system was assumed and the modal parameters of an equivalent viscously-damped linear elastic time invariant model were estimated using vibration data recorded during AV and WN tests. Using the structural vibration data recorded by twenty six accelerometers, five system identification methods, including three output-only (SSI-DATA, NExT-ERA, and EFDD) and two input-output (OKID-ERA and DSI), were used to estimate the modal properties of the

base-isolated building. An automated SID process using the SSI-DATA and NExT-ERA methods and based on the stabilization diagram was applied to the continuously-recorded AV data to identify the modal properties of the BI building under small amplitude excitations. Eight dominant modes were identified using the AV data, with the first three corresponding mainly to the deformation of the isolation layer, i.e., isolation modes, and the higher modes corresponding to structural modes mostly involving deformation of the superstructure. With the WN base excitation test data, ten modes were identified, with the first three corresponding to the isolation modes. Results show that the identified modal parameters obtained by different methods are in good agreement and that the natural frequencies and damping ratios have the lowest and highest method-to-method variability, respectively. Natural frequencies of the isolation modes identified with WN test data are larger than those identified using AV data because of the reduction of the effective lateral stiffness of the isolation layer. However, the differences between natural frequencies of structural modes identified from WN and AV data were much smaller, suggesting that the structure itself experienced a linear elastic response during the WN tests. Damping ratios of the isolation modes were considerably higher than those of the structural modes, especially when identified from the WN test data. This is because more intense excitations induced larger deformations in the isolators increasing the energy dissipated through hysteretic behavior of the bearings, which is identified as equivalent viscous damping because of the underlying mathematical model assumed by

the SID methods used. The identified damping ratios correlated well with the effective damping ratios computed from the hysteretic response of the bearings. The effects of the amplitude of the excitation, seismic excitations, and environmental conditions (wind speed and temperature) were clearly shown via the changes induced on the estimated modal parameters of the building.

4. A comprehensive statistical analysis was performed on the identified modal properties of the BNCS building fixed at its base and at different damage states. Two state-of-the-art methods of operational modal analysis were used to automatically identify the modal properties of the fixed-base building at different damage states using AV data recorded continuously for about fifteen days. A statistical analysis of the identified modal parameters was performed to investigate the statistical variability and accuracy of the system identification results. The variability of the identified modal parameters due to environmental conditions was also investigated.
5. A novel framework was proposed that combines high-fidelity mechanics-based nonlinear (hysteretic) FE models and a nonlinear stochastic filtering method, referred to as the unscented Kalman filter, to estimate unknown material parameters in frame-type structures from input-output dynamic data. The identification framework updates nonlinear FE models using spatially-limited noisy measurement data and it can be further used for damage identification (DID) purposes. The effectiveness, robustness, and accuracy of the framework were validated using numerically simulated data from realistic

nonlinear FE models of structures of increasing complexity: a cantilever steel column representing a bridge pier and a two-dimensional steel frame. Both structures were modeled using beam-column elements with distributed plasticity and are subjected to a suite of earthquake ground motions of varying intensity. The results indicated that the material parameters of the nonlinear finite element models are accurately estimated, provided that: (i) the loading intensity is sufficient to exercise the parts (branches) of the nonlinear material model which are governed by the material parameters to be identified, and (ii) the measured response quantities are sufficiently sensitive to the material parameters to be identified, especially when a limited number of measurements is considered.

6. The framework for updating mechanics-based nonlinear FE models was extended and its performance and robustness were analyzed when limited response data from a realistic nonlinear FE model of a realistic three-dimensional five-story two-by-one bay RC frame building subjected to bi-directional horizontal earthquake excitation were available. Parameters characterizing the nonlinear material constitutive laws and Rayleigh damping characteristics of the FE model were successfully estimated when limited response data (6 acceleration time histories) were available. Excellent results were obtained for two different earthquake excitations and two initial estimates of the expected value of the modeling parameters. To alleviate the computational burden of the proposed methodology, three non-sequential updating approaches were presented and examined. The proposed non-

sequential approaches reduced the computational cost by about 70–80% as compared to the sequential updating approach initially proposed. Accurate estimation results were achieved with cumulative innovation and time-window approaches, while the non-cumulative approach required a small updating step parameter (D) to properly estimate the modeling parameters. The effects of using data from heterogeneous sensor arrays on the identifiability of the modeling parameters and updating of the nonlinear FE model were also investigated. Fusion of acceleration, displacement and strain response data improved considerable the accuracy of the parameter estimation results because sensitivity of different types of recorded responses to modeling parameters may vary significantly, and consequently, heterogeneous sensor data may be more informative than acceleration-only data. An adaptive filtering approach based on a covariance matching technique was proposed to estimate the measurement noise covariance in addition to the time-invariant modeling parameters. Favorable effects of the proposed adaptive filtering approach were observed, especially when the initial guesses of the standard deviations of the output measurement noises are far from the actual level of measurement noise and only acceleration outputs were recorded. Finally, effects of input measurement noise on the estimation results were studied. It was concluded that the proposed framework is very robust to input noise, achieving good estimation results even for unrealistically high levels of input measurement noise.

7. A comprehensive comparison of the performance of different Kalman-based filters for nonlinear structural FE model updating was conducted. The Extended Kalman filter (EKF), Unscented Kalman filter (UKF), and iterated Extended Kalman filter (IEKF) were studied and their performances in terms of convergence, accuracy, robustness, and computational requirements were investigated and compared. Numerically simulated response data from a three-dimensional five-story two-by-one bay RC building subjected to bi-directional horizontal earthquake excitation were used for an application example. The FE response sensitivities with respect to eleven modeling parameter describing the nonlinear constitutive law of the materials (reinforcing steel and concrete) were analyzed. Based on the obtained results, only nine parameters were found to significantly influence the output measured response, and were therefore chosen as unknown parameters to be estimated. Excellent estimation results of these modeling parameters were obtained using the UKF, EKF, and IEKF. Because of the analytical linearization used in the EKF and IEKF, abrupt and large jumps in the estimates of the modeling parameters were observed when using these filters, which may lead to problems of convergence of the nonlinear FE response simulation. The UKF slightly outperformed the EKF and IEKF and prevents large and abrupt changes in the estimates of the modeling parameters because it does not use analytical linearization of the nonlinear FE model; however, the UKF has a slightly higher computational cost. The non-sequential estimation procedure previously proposed for the UKF was also implemented for the EKF and

IEKF. The capability of the non-sequential scheme to reduce the computational cost, while maintaining accurate and robust estimation results, was demonstrated. The non-sequential procedure alleviated the problems related to abrupt and large jumps in the estimates of the modeling parameters when using the EKF and IEKF. Because of its iterative nature, the IEKF outperformed the UKF and EKF when the non-sequential updating procedure was used, but at a higher computational cost.

8. A methodology to update mechanics-based nonlinear structural FE models subjected to unknown input excitation was proposed. The approach allows to jointly estimate unknown time-invariant modeling parameters of a nonlinear FE model of the structure and the unknown time histories of input excitations using spatially-sparse output response measurements recorded during a damage-inducing earthquake event. The updated FE model and the estimated input excitation allowed to accurately evaluate the state of damage of the structure, including loss of stiffness, strength degradation, and loss of ductility capacity. The UKF, which avoids the computation of FE response sensitivities with respect to the unknown modeling parameters and the unknown input excitations, was employed as estimation tool. The performance of the methodology was analyzed in terms of convergence, accuracy, robustness, and computational cost using numerically simulated response data from a realistic nonlinear FE model of a realistic three-dimensional four-story two-by-one bay steel frame building with six unknown modeling parameters subjected to unknown bi-directional horizontal earthquake excitation and of a realistic

three-dimensional five-story two-by-one bay RC frame building with nine unknown modeling parameters subjected to unknown bi-directional horizontal earthquake excitation. The use of heterogeneous sensor arrays, including acceleration, displacement, and strain measurements was investigated. The results showed the excellent performance and robustness of the proposed algorithm to jointly estimate unknown modeling parameters and unknown input excitations. It was observed that the use of measurement data from a heterogeneous sensor array improves considerably the accuracy of the estimation results, especially for post-yield material parameters. When noisy acceleration-only output response measurements were considered, the estimation of the input excitations contained a permanent drift due to a spurious low-frequency component, which did not affect the absolute acceleration response measurements. This spurious low-frequency component can be artificially eliminated using a high-pass filter. When displacement response measurements were added to the acceleration response measurements, the spurious low frequency components in the estimated input excitations were automatically eliminated because displacement responses are sensitive to low-frequency dynamic excitations.

11.3. Recommendations for future work

Based on the research work performed and presented in this dissertation, several research topics have been identified and deserve further investigation in future work.

1. Quantification and propagation of uncertainty in the linear SID results of the BNCS building.
2. Correlation between identified modal properties and measured environmental conditions.
3. Separation of changes in modal properties due to structural damage and those due to other sources such as changes in environmental conditions.
4. Deterministic and probabilistic (Bayesian) linear FE model updating of the BNCS building (fixed and isolated at its base) using the identified modal properties.
5. Deterministic and probabilistic (Bayesian) linear FE model updating of the BNCS building (fixed and isolated at its base) using recorded response time histories
6. Investigation of the effects of modeling errors on the methodologies proposed to update mechanics-based nonlinear FE models and extension of the framework to account for modeling errors.
7. Validation of the proposed methodologies to update mechanics-based nonlinear FE models using experimental dynamic/quasi-static data recorded from large/full-scale physical specimens.
8. Extension of the work presented in this dissertation for the purpose of damage prognosis.

APPENDIX A: STATE-SPACE MODELS FOR MULTIPLE-INPUT MULTIPLE-OUTPUT DYNAMICAL SYSTEMS

This appendix presents the formulation of state-space models for multiple-input multiple-output (MIMO) systems in structural dynamics. First the derivation of the state and measurements equations in continuous-time is introduced. Modal analysis of non-proportionally damped systems and modal decomposition of continuous-time state-space models are then presented. The state-space model in discrete time is derived and its relationship with the continuous-time state-space model is studied. The expressions relating the modal properties of the structural system and the state-space matrices are revisited. State equations of MIMO problems are derived, including formulations for multiple support excitation and 2-D and 3-D shear buildings models with translational and rotational input excitations. Finally, a summary and flowcharts of the five state-of-the-art system identification methods used in this chapter are presented.

A.1. Derivation of state and measurement equations in continuous-time

The equation of dynamic equilibrium of a linear-elastic structure can be expressed as

$$\mathbf{M}\,\ddot{\mathbf{q}}(t)+\mathbf{C}\,\dot{\mathbf{q}}(t)+\mathbf{K}\,\mathbf{q}(t)=\mathbf{f}(t) \tag{A.1}$$

where $\mathbf{M} \in \mathbb{R}^{n \times n}$ = mass matrix, $\mathbf{C} \in \mathbb{R}^{n \times n}$ = viscous-damping matrix, $\mathbf{K} \in \mathbb{R}^{n \times n}$ = stiffness matrix, $\mathbf{f}(t) \in \mathbb{R}^{n}$ = vector of external excitation, $\mathbf{q}(t) \in \mathbb{R}^{n}$ = vector of displacement response, $\dot{\mathbf{q}}(t) \in \mathbb{R}^{n}$ = vector of velocity response, and $\ddot{\mathbf{q}}(t) \in \mathbb{R}^{n}$ = vector of acceleration response.

Using the additional equation $\mathbf{M}\dot{\mathbf{q}}(t) - \mathbf{M}\dot{\mathbf{q}}(t) = \mathbf{0}$, the following extended version of the equation (A.1) can be written

$$\mathbf{P}\,\dot{\mathbf{x}}(t) + \mathbf{Q}\,\mathbf{x}(t) = \begin{bmatrix} \mathbf{f}(t) \\ \mathbf{0} \end{bmatrix} \tag{A.2}$$

where

$$\mathbf{x}(t) = \begin{bmatrix} \mathbf{q}(t) \\ \dot{\mathbf{q}}(t) \end{bmatrix} \in \mathbb{R}^{2n} \text{ = state vector}$$

$$\mathbf{P} = \begin{bmatrix} \mathbf{C} & \mathbf{M} \\ \mathbf{M} & \mathbf{0} \end{bmatrix} \in \mathbb{R}^{2n \times 2n} \tag{A.3}$$

$$\mathbf{Q} = \begin{bmatrix} \mathbf{K} & \mathbf{0} \\ \mathbf{0} & -\mathbf{M} \end{bmatrix} \in \mathbb{R}^{2n \times 2n}$$

Moreover, the external excitation can be written as a function of the input motion as

$$\mathbf{f}(t) = \mathbf{E}\,\mathbf{u}(t) \tag{A.4}$$

in which $\mathbf{E} \in \mathbb{R}^{n \times m}$ = matrix defining the location of the inputs and $\mathbf{u}(t) \in \mathbb{R}^{m}$ = inputs to the system (displacement, velocity, and/or acceleration).

Then, from (A.2) and (A.4) the following expression is obtained,

$$\dot{\mathbf{x}}(t) = \mathbf{A_c}\,\mathbf{x}(t) + \mathbf{B_c}\,\mathbf{u}(t) \tag{A.5}$$

where

$$\begin{aligned} \mathbf{A_c} &= -\mathbf{P}^{-1}\,\mathbf{Q} = \begin{bmatrix} \mathbf{0} & \mathbf{I} \\ -\mathbf{M}^{-1}\,\mathbf{K} & -\mathbf{M}^{-1}\,\mathbf{C} \end{bmatrix} \in \mathbb{R}^{2n\times 2n} \\ \mathbf{B_c} &= \mathbf{P}^{-1}\begin{bmatrix} \mathbf{E} \\ \mathbf{0} \end{bmatrix} = \begin{bmatrix} \mathbf{0} \\ \mathbf{M}^{-1}\,\mathbf{E} \end{bmatrix} \in \mathbb{R}^{2n\times m} \end{aligned} \tag{A.6}$$

Equation (A.5) is known as the state equation and matrices $\mathbf{A_c}$ and $\mathbf{B_c}$ are the state (dynamical system matrix) and input matrices, respectively.

Now, let's consider

$$\mathbf{y}(t) = \mathbf{C_{ac}}\,\ddot{\mathbf{q}}(t) + \mathbf{C_{ve}}\,\dot{\mathbf{q}}(t) + \mathbf{C_{di}}\,\mathbf{q}(t) \tag{A.7}$$

where $\mathbf{y}(t) \in \mathbb{R}^l$ = measured outputs (observed responses) and $\mathbf{C_{ac}}, \mathbf{C_{ve}}, \mathbf{C_{di}} \in \mathbb{R}^{l\times n}$ = Boolean matrices indicating the position of the outputs. Pre-multiplying (A.1) by $\mathbf{C_{ac}}^{-1}\,\mathbf{M}^{-1}$ and using (A.4),

$$\Rightarrow \mathbf{C_{ac}}\,\mathbf{M}^{-1}\,\mathbf{M}\,\ddot{\mathbf{q}}(t) + \mathbf{C_{ac}}\,\mathbf{M}^{-1}\,\mathbf{C}\,\dot{\mathbf{q}}(t) + \mathbf{C_{ac}}\,\mathbf{M}^{-1}\,\mathbf{K}\,\mathbf{q}(t) = \mathbf{C_{ac}}\,\mathbf{M}^{-1}\,\mathbf{E}\,\mathbf{u}(t)$$

$$\Rightarrow -\mathbf{C_{ac}}\,\mathbf{M}^{-1}\,\mathbf{K}\,\mathbf{q}(t) - \mathbf{C_{ac}}\,\mathbf{M}^{-1}\,\mathbf{C}\,\dot{\mathbf{q}}(t) + \mathbf{C_{ac}}\,\mathbf{M}^{-1}\,\mathbf{E}\,\mathbf{u}(t) = \mathbf{C_{ac}}\,\ddot{\mathbf{q}}(t)$$

$$\begin{aligned} \Rightarrow\ & \mathbf{C_{di}}\,\mathbf{q}(t) - \mathbf{C_{ac}}\,\mathbf{M}^{-1}\,\mathbf{K}\,\mathbf{q}(t) + \mathbf{C_{ve}}\,\dot{\mathbf{q}}(t) - \mathbf{C_{ac}}\,\mathbf{M}^{-1}\,\mathbf{C}\,\dot{\mathbf{q}}(t) + \mathbf{C_{ac}}\,\mathbf{M}^{-1}\,\mathbf{E}\,\mathbf{u}(t) = \\ & \mathbf{C_{ac}}\,\ddot{\mathbf{q}}(t) + \mathbf{C_{ve}}\,\dot{\mathbf{q}}(t) + \mathbf{C_{di}}\,\mathbf{q}(t) \end{aligned}$$

$$\Rightarrow \left(\mathbf{C_{di}} - \mathbf{C_{ac}}\,\mathbf{M}^{-1}\,\mathbf{K}\right)\mathbf{q}(t) + \left(\mathbf{C_{ve}} - \mathbf{C_{ac}}\,\mathbf{M}^{-1}\,\mathbf{C}\right)\dot{\mathbf{q}}(t) + \left(\mathbf{C_{ac}}\,\mathbf{M}^{-1}\,\mathbf{E}\right)\mathbf{u}(t) = \mathbf{y}(t)$$

$$\Rightarrow \begin{bmatrix} \mathbf{C_{di}} - \mathbf{C_{ac}}\,\mathbf{M}^{-1}\,\mathbf{K} & \mathbf{C_{ve}} - \mathbf{C_{ac}}\,\mathbf{M}^{-1}\,\mathbf{C} \end{bmatrix}\begin{bmatrix} \mathbf{q}(t) \\ \dot{\mathbf{q}}(t) \end{bmatrix} + \left(\mathbf{C_{ac}}\,\mathbf{M}^{-1}\,\mathbf{E}\right)\mathbf{u}(t) = \mathbf{y}(t)$$

$$\mathbf{y}(t) = \mathbf{C_c}\ \mathbf{x}(t) + \mathbf{D_c}\ \mathbf{u}(t) \tag{A.8}$$

where

$$\mathbf{C_c} = \left[\mathbf{C_{di}} - \mathbf{C_{ac}}\ \mathbf{M}^{-1} \cdot \mathbf{K} \ \vdots\ \mathbf{C_{ve}} - \mathbf{C_{ac}}\ \mathbf{M}^{-1}\ \mathbf{C}\right] \in \mathbb{R}^{l \times 2n}$$
$$\mathbf{D_c} = \mathbf{C_{ac}}\ \mathbf{M}^{-1}\ \mathbf{E} \in \mathbb{R}^{l \times m} \tag{A.9}$$

Equation (A.8) is known as the measurement equation and $\mathbf{C_c}$ and $\mathbf{D_c}$ are the output and direct feed-through matrices, respectively.

Equations (A.5) and (A.8) define the state-space model of a multiple input - multiple output (MIMO) linear time-invariant system in continuous time, which is summarized in the following equation:

$$\begin{cases} \dot{\mathbf{x}}(t) = \mathbf{A_c}\ \mathbf{x}(t) + \mathbf{B_c}\ \mathbf{u}(t) \\ \mathbf{y}(t) = \mathbf{C_c}\ \mathbf{x}(t) + \mathbf{D_c}\ \mathbf{u}(t) \end{cases} \tag{A.10}$$

A.2. Modal analysis of non-proportionally damped systems

From (A.2) and (A.4),

$$\mathbf{P}\ \dot{\mathbf{x}}(t) + \mathbf{Q}\ \mathbf{x}(t) = \begin{bmatrix} \mathbf{E} \\ \mathbf{0} \end{bmatrix} \mathbf{u}(t) \tag{A.11}$$

Let's assume a solution for (A.1) of the form

$$\mathbf{q}(t) = \sum_i \mathbf{\Theta}_i\ G\ e^{\lambda_i t} \ \text{ and } \ \mathbf{q}_i(t) = \mathbf{\Theta}_i\ G\ e^{\lambda_i t} \tag{A.12}$$

where $\mathbf{\Theta}_i$ is the i-th eigenvector of the original second order equation (A.1). Then,

$$\dot{\mathbf{q}}_i(t) = \lambda_i\ \mathbf{q}_i(t) \ \text{ and } \ \ddot{\mathbf{q}}_i(t) = \lambda_i\ \dot{\mathbf{q}}_i(t) \tag{A.13}$$

Let's define the matrix $[\mathbf{\Lambda_c}]$, which contains the $2n$ complex eigenvalues of the system, as

$$\mathbf{\Lambda_c} = \begin{bmatrix} \ddots & & \\ & \lambda_i & \\ & & \ddots \end{bmatrix} \in \mathbb{C}^{2n \times 2n} \tag{A.14}$$

and the vector $\mathbf{\Psi}_i$ as

$$\mathbf{\Psi}_i = \begin{bmatrix} \mathbf{\Theta}_i \\ \lambda_i \cdot \mathbf{\Theta}_i \end{bmatrix} \tag{A.15}$$

Using (A.15) and the definition of the state vector from (A.3), it is obtained that

$$\mathbf{x}_i(t) = \begin{bmatrix} \mathbf{q}_i(t) \\ \dot{\mathbf{q}}_i(t) \end{bmatrix} = \begin{bmatrix} \mathbf{\Theta}_i \, G \, e^{\lambda_i t} \\ \lambda_i \, \mathbf{\Theta}_i \, G \, e^{\lambda_i t} \end{bmatrix} = \mathbf{\Psi}_i \, G \, e^{\lambda_i t} \tag{A.16}$$

Replacing (A.16) in the homogeneous version of (A.11), for each i the following expression can be written

$$\mathbf{P} \, \lambda_i \, \mathbf{\Psi}_i \, G \, e^{\lambda_i t} + \mathbf{Q} \, \mathbf{\Psi}_i \, G \, e^{\lambda_i t} = \mathbf{0} \tag{A.17}$$

Then,

$$\mathbf{P} \, \mathbf{\Psi} \, \mathbf{\Lambda_c} + \mathbf{Q} \, \mathbf{\Psi} = \mathbf{0} \tag{A.18}$$

where $\mathbf{\Psi} \in \mathbb{R}^{2n \times 2n}$ contains the complex eigenvectors in the columns of the matrix. Previous equation corresponds to a generalized eigenvalue problem, in which $\mathbf{\Psi}_i$ is the eigenvector corresponding to the eigenvalue λ_i.

Since matrices $\mathbf{P}$ and $\mathbf{Q}$ are symmetric but are not positive-definite, the eigenvalues and eigenvectors come as complex conjugate pairs. Therefore, the eigenvalues and eigenvectors can be written in the form

$$\boldsymbol{\Lambda}_c = \begin{bmatrix} \boldsymbol{\Lambda} & \mathbf{0} \\ \mathbf{0} & \boldsymbol{\Lambda}^* \end{bmatrix}$$
$$\boldsymbol{\Psi} = \begin{bmatrix} \boldsymbol{\Theta} & \boldsymbol{\Theta}^* \\ \boldsymbol{\Lambda}\,\boldsymbol{\Theta} & \boldsymbol{\Lambda}^*\,\boldsymbol{\Theta}^* \end{bmatrix} \tag{A.19}$$

From the first equation of (A.18) and using (A.19),

$$\mathbf{M}\,\boldsymbol{\Theta}\,\boldsymbol{\Lambda}^2 + \mathbf{C}\,\boldsymbol{\Theta}\,\boldsymbol{\Lambda} + \mathbf{K}\,\boldsymbol{\Theta} = \mathbf{0} \tag{A.20}$$

Now, it is possible to prove the orthogonality property of the matrices $\mathbf{P}$ and $\mathbf{Q}$. Pre-multiplying (A.17) by $\boldsymbol{\Psi}_j^{\,T}$,

$$\begin{aligned} &\Rightarrow \boldsymbol{\Psi}_j^{\,T}\,\mathbf{P}\,\lambda_i\,\boldsymbol{\Psi}_i + \boldsymbol{\Psi}_j^{\,T}\,\mathbf{Q}\,\boldsymbol{\Psi}_i = 0 \\ &\Rightarrow -\boldsymbol{\Psi}_j^{\,T}\,\mathbf{P}\,\lambda_i \cdot \boldsymbol{\Psi}_i = \boldsymbol{\Psi}_j^{\,T}\,\mathbf{Q}\,\boldsymbol{\Psi}_i \end{aligned} \tag{A.21}$$

But, because of the symmetry of $\mathbf{Q}$

$$\Rightarrow -\boldsymbol{\Psi}_j^{\,T}\,\mathbf{P}\,\lambda_i\,\boldsymbol{\Psi}_j = \left(\mathbf{Q}\,\boldsymbol{\Psi}_j\right)^T\,\boldsymbol{\Psi}_i \tag{A.22}$$

From (A.17), $-\mathbf{P}\,\lambda_j\,\boldsymbol{\Psi}_j = \mathbf{Q}\,\boldsymbol{\Psi}_j$. Using this expression and (A.22),

$$\begin{aligned} &\Rightarrow -\boldsymbol{\Psi}_j^{\,T}\,\mathbf{P}\,\lambda_i\,\boldsymbol{\Psi}_i = \left(-\mathbf{P}\,\boldsymbol{\Psi}_j\,\lambda_j\right)^T\,\boldsymbol{\Psi}_i \\ &\Rightarrow \boldsymbol{\Psi}_j^{\,T}\,\mathbf{P}\,\boldsymbol{\Psi}_i\,\lambda_i = \lambda_j\,\boldsymbol{\Psi}_j^{\,T}\,\mathbf{P}^T\,\boldsymbol{\Psi}_i \\ &\Rightarrow \boldsymbol{\Psi}_j^{\,T}\,\mathbf{P}\,\boldsymbol{\Psi}_i\,\lambda_i = \lambda_j\,\boldsymbol{\Psi}_j^{\,T}\,\mathbf{P}\,\boldsymbol{\Psi}_i \end{aligned} \tag{A.23}$$

Using the symmetry of $\mathbf{P}$ $\Rightarrow \left(\lambda_i - \lambda_j\right)\left(\boldsymbol{\Psi}_j^{\,T}\,\mathbf{P}\,\boldsymbol{\Psi}_i\right) = 0$

Then, if $i \neq j$

$$\left(\boldsymbol{\Psi}_j^{\,T}\,\mathbf{P}\,\boldsymbol{\Psi}_i\right) = 0 \tag{A.24}$$

The last equation proves the orthogonality property of the matrix $\mathbf{P}$, which in matrix form can be written as

$$\boldsymbol{\Psi}^T \, \mathbf{P} \, \boldsymbol{\Psi} = \begin{bmatrix} \ddots & & \\ & a_i & \\ & & \ddots \end{bmatrix} \tag{A.25}$$

where $a_i = \boldsymbol{\Psi}_i^T \, \mathbf{P} \, \boldsymbol{\Psi}_i$.

A similar procedure can be follow for matrix $\mathbf{Q}$. From (A.22) and considering the symmetry of $\mathbf{P}$,

$$-\left(\mathbf{P} \, \boldsymbol{\Psi}_j\right)^T \boldsymbol{\Psi}_i \, \lambda_i = \boldsymbol{\Psi}_j^T \, \mathbf{Q} \, \boldsymbol{\Psi}_i \tag{A.26}$$

From (A.17), $\mathbf{P} \, \boldsymbol{\Psi}_j = -\frac{1}{\lambda_j} \mathbf{Q} \, \boldsymbol{\Psi}_j$. Using this expression and (A.26),

$$\begin{aligned}
&\Rightarrow -\left(-\frac{1}{\lambda_j} \mathbf{Q} \, \boldsymbol{\Psi}_j\right)^T \boldsymbol{\Psi}_i \, \lambda_i = \boldsymbol{\Psi}_j^T \, \mathbf{Q} \, \boldsymbol{\Psi}_i \\
&\Rightarrow \frac{1}{\lambda_j} \boldsymbol{\Psi}_j^T \, \mathbf{Q} \, \boldsymbol{\Psi}_i \, \lambda_i = \boldsymbol{\Psi}_j^T \, \mathbf{Q} \, \boldsymbol{\Psi}_i \\
&\Rightarrow \frac{\lambda_i}{\lambda_j} \boldsymbol{\Psi}_j^T \, \mathbf{Q}^T \, \boldsymbol{\Psi}_i = \boldsymbol{\Psi}_j^T \, \mathbf{Q} \, \boldsymbol{\Psi}_i \\
&\Rightarrow \left(\frac{\lambda_i - \lambda_j}{\lambda_j}\right) \boldsymbol{\Psi}_j^T \, \mathbf{Q} \, \boldsymbol{\Psi}_i = 0
\end{aligned} \tag{A.27}$$

Then, if $i \neq j$,

$$\left(\boldsymbol{\Psi}_j^T \, \mathbf{Q} \, \boldsymbol{\Psi}_i\right) = 0 \tag{A.28}$$

The last equation proves the orthogonality property of the matrix $\mathbf{Q}$, which can be written in matrix form as

$$\boldsymbol{\Psi}^T \, \mathbf{Q} \, \boldsymbol{\Psi} = \begin{bmatrix} \ddots & & \\ & b_i & \\ & & \ddots \end{bmatrix} \tag{A.29}$$

where $b_i = \boldsymbol{\Psi}_i^T \, \mathbf{Q} \, \boldsymbol{\Psi}_i$.

Replacing equation (A.25) and (A.29) in (A.18) pre-multiplied by $\boldsymbol{\Psi}^T$ follows

$$
\begin{aligned}
&\Rightarrow \boldsymbol{\Psi}^T\ \mathbf{P}\ \boldsymbol{\Psi}\ \boldsymbol{\Lambda}_\mathbf{c} + \boldsymbol{\Psi}^T\ \mathbf{Q}\ \boldsymbol{\Psi} = \mathbf{0} \\
&\Rightarrow \begin{bmatrix} \ddots & \\ & a_i \end{bmatrix} \boldsymbol{\Lambda}_\mathbf{c} + \begin{bmatrix} \ddots & \\ & b_i \end{bmatrix} = \mathbf{0} \\
&\Rightarrow \boldsymbol{\Lambda}_\mathbf{c} = \begin{bmatrix} \ddots & \\ & \lambda_i \end{bmatrix} = -\begin{bmatrix} \ddots & \\ & 1/a_i \end{bmatrix} \begin{bmatrix} \ddots & \\ & b_i \end{bmatrix} = -\begin{bmatrix} \ddots & \\ & b_i/a_i \end{bmatrix}
\end{aligned}
\tag{A.30}
$$

From (A.25),

$$
\begin{aligned}
&\Rightarrow \mathbf{P} = \left(\boldsymbol{\Psi}^T\right)^{-1} \begin{bmatrix} \ddots & \\ & a_i \end{bmatrix} \boldsymbol{\Psi}^{-1} \\
&\Rightarrow \left(\boldsymbol{\Psi}^T\right)^{-1} \begin{bmatrix} \ddots & \\ & a_i \end{bmatrix} \boldsymbol{\Psi}^{-1}\ \mathbf{P}^{-1} = \mathbf{I} \\
&\Rightarrow \begin{bmatrix} \ddots & \\ & a_i \end{bmatrix} \boldsymbol{\Psi}^{-1}\ \mathbf{P}^{-1} = \boldsymbol{\Psi}^T \\
&\Rightarrow \boldsymbol{\Psi}^{-1}\ \mathbf{P}^{-1} = \begin{bmatrix} \ddots & \\ & 1/a_i \end{bmatrix} \boldsymbol{\Psi}^T \\
&\Rightarrow \mathbf{P}^{-1} = \boldsymbol{\Psi} \begin{bmatrix} \ddots & \\ & 1/a_i \end{bmatrix} \boldsymbol{\Psi}^T
\end{aligned}
\tag{A.31}
$$

From (A.29),

$$
\Rightarrow \mathbf{Q} = \left(\boldsymbol{\Psi}^T\right)^{-1} \begin{bmatrix} \ddots & \\ & b_i \end{bmatrix} \boldsymbol{\Psi}^{-1}
\tag{A.32}
$$

Replacing the last expression of (A.31) and (A.32) in (A.6), it is obtained

$$
\begin{aligned}
&\Rightarrow \mathbf{A}_\mathbf{c} = -\mathbf{P}^{-1}\ \mathbf{Q} = -\boldsymbol{\Psi} \begin{bmatrix} \ddots & \\ & 1/a_i \end{bmatrix} \boldsymbol{\Psi} \left(\boldsymbol{\Psi}^T\right)^{-1} \begin{bmatrix} \ddots & \\ & b_i \end{bmatrix} \cdot \boldsymbol{\Psi}^{-1} \\
&\Rightarrow \mathbf{A}_\mathbf{c} = -\boldsymbol{\Psi} \begin{bmatrix} \ddots & \\ & 1/a_i \end{bmatrix} \begin{bmatrix} \ddots & \\ & b_i \end{bmatrix} \boldsymbol{\Psi}^{-1} \\
&\Rightarrow \mathbf{A}_\mathbf{c} = -\boldsymbol{\Psi} \begin{bmatrix} \ddots & \\ & b_i/a_i \end{bmatrix} \boldsymbol{\Psi}^{-1}
\end{aligned}
\tag{A.33}
$$

Using the last expression of (A.30),

$$\begin{aligned} &\Rightarrow \mathbf{A_c} = \boldsymbol{\Psi}\, \boldsymbol{\Lambda_c}\, \boldsymbol{\Psi}^{-1} \\ &\Rightarrow \mathbf{A_c}\, \boldsymbol{\Psi} = \boldsymbol{\Psi}\, \boldsymbol{\Lambda_c} \end{aligned} \tag{A.34}$$

(A.34) represents a generalized eigenvalue problem and implies that $\boldsymbol{\Lambda_c}$ and $\boldsymbol{\Psi}$ correspond to the eigenvalues and eigenvectors of the matrix $\mathbf{A_c}$, respectively.

A.3. Modal decomposition of continuous-time state-space models

A.3.1. Relationship with conventional modal analysis

In conventional modal analysis the system response can be obtained as the sum of the contribution of all modes as

$$\mathbf{x}(t) = \boldsymbol{\Psi}\, \mathbf{x_m}(t) \tag{A.35}$$

where $\mathbf{x_m}(t) \in \mathbb{C}^n$.

Replacing (A.35) in (A.5), using $\boldsymbol{\Lambda_c} = \boldsymbol{\Psi}^{-1}\, \mathbf{A_c}\, \boldsymbol{\Psi}$ from (A.34) and pre-multiplying by $\boldsymbol{\Psi}^{-1}$,

$$\dot{\mathbf{x}}_\mathbf{m}(t) = \boldsymbol{\Lambda_c}\, \mathbf{x_m}(t) + \mathbf{L_c}^T\, \mathbf{u}(t) \tag{A.36}$$

where $\mathbf{L_c}^T$ is the modal participation matrix defined by

$$\mathbf{L_c}^T = \boldsymbol{\Psi}^{-1}\, \mathbf{B_c} \tag{A.37}$$

However, from (A.25) $\boldsymbol{\Psi}^{-1} = \begin{bmatrix} \ddots & & \\ & 1/a_i & \\ & & \ddots \end{bmatrix} \boldsymbol{\Psi}^T\, \mathbf{P}$, and using (A.6) and (A.19),

$$
\begin{aligned}
\Rightarrow \mathbf{L_c}^T &= \begin{bmatrix} \ddots & & \\ & 1/a_i & \\ & & \ddots \end{bmatrix} \boldsymbol{\Psi}^T \, \mathbf{P} \, \mathbf{B_c} \\
\Rightarrow \mathbf{L_c}^T &= \begin{bmatrix} \ddots & & \\ & \dfrac{1}{a_i} & \\ & & \ddots \end{bmatrix} \boldsymbol{\Psi}^T \, \mathbf{P} \, \mathbf{P}^{-1} \begin{bmatrix} \mathbf{E} \\ \mathbf{0} \end{bmatrix} \\
\Rightarrow \mathbf{L_c}^T &= \begin{bmatrix} \ddots & & \\ & \dfrac{1}{a_i} & \\ & & \ddots \end{bmatrix} \begin{bmatrix} \boldsymbol{\Theta} & \boldsymbol{\Theta}^* \\ \boldsymbol{\Lambda} \cdot \boldsymbol{\Theta} & \boldsymbol{\Lambda}^* \cdot \boldsymbol{\Theta}^* \end{bmatrix}^T \begin{bmatrix} \mathbf{E} \\ \mathbf{0} \end{bmatrix} \\
\Rightarrow \mathbf{L_c}^T &= \begin{bmatrix} \ddots & & \\ & \dfrac{1}{a_i} & \\ & & \ddots \end{bmatrix} \begin{bmatrix} \boldsymbol{\Theta}^T \\ \boldsymbol{\Theta}^{*T} \end{bmatrix} \mathbf{E}
\end{aligned}
\tag{A.38}
$$

Replacing (A.35) in (A.8),

$$
\mathbf{y}(t) = \mathbf{V_c} \, \mathbf{x_m}(t) + \mathbf{D_c} \, \mathbf{u}(t) \tag{A.39}
$$

where

$$
\mathbf{V_c} = \mathbf{C_c} \, \boldsymbol{\Psi}
$$

$$
\Rightarrow \mathbf{V_c} = \left[\mathbf{C_{di}} - \mathbf{C_{ac}} \, \mathbf{M}^{-1} \, \mathbf{K} \;\; \vdots \;\; \mathbf{C_{ve}} - \mathbf{C_{ac}} \, \mathbf{M}^{-1} \, \mathbf{C} \right] \begin{bmatrix} \boldsymbol{\Theta} & \boldsymbol{\Theta}^* \\ \boldsymbol{\Lambda} \, \boldsymbol{\Theta} & \boldsymbol{\Lambda}^* \, \boldsymbol{\Theta}^* \end{bmatrix} \tag{A.40}
$$

Making use (A.20), the following special cases are highlighted,

i. Only accelerations are measured: $\mathbf{C_{di}} = \mathbf{C_{ve}} = \mathbf{0}$

$$
\Rightarrow \mathbf{V_c} = \mathbf{C_{ac}} \begin{bmatrix} \boldsymbol{\Theta} \, \boldsymbol{\Lambda}^2 & \boldsymbol{\Theta}^* \, \boldsymbol{\Lambda}^{*2} \end{bmatrix}
$$

ii. Only velocities are measured: $\mathbf{C_{di}} = \mathbf{C_{ac}} = \mathbf{0}$

$$
\Rightarrow \mathbf{V_c} = \mathbf{C_v} \begin{bmatrix} \boldsymbol{\Theta} \, \boldsymbol{\Lambda} & \boldsymbol{\Theta}^* \, \boldsymbol{\Lambda}^* \end{bmatrix}
$$

iii. Only displacements are measured: $\mathbf{C_{ve}} = \mathbf{C_{ac}} = \mathbf{0}$

$$
\Rightarrow \mathbf{V_c} = \mathbf{C_{di}} \begin{bmatrix} \boldsymbol{\Theta} & \boldsymbol{\Theta}^* \end{bmatrix}
$$

Summarizing, the continuous-time state-space model is described by

$$\begin{cases} \dot{\mathbf{x}}_{\mathbf{m}}(t) = \boldsymbol{\Lambda}_{\mathbf{c}}\, \mathbf{x}_{\mathbf{m}}(t) + \mathbf{L}_{\mathbf{c}}{}^{T}\, \mathbf{u}(t) \\ \mathbf{y}(t) = \mathbf{V}_{\mathbf{c}}\, \mathbf{x}_{\mathbf{m}}(t) + \mathbf{D}_{\mathbf{c}}\, \mathbf{u}(t) \end{cases} \tag{A.41}$$

A.3.2. Modal decomposition of the continuous-time state-space model

To fully decompose the continuous-time state-space mode, a modal decomposition of matrix $\mathbf{D}_{\mathbf{c}}$ is required. Using (A.9) and (A.6),

$$\begin{aligned} &\mathbf{C}_{\mathbf{c}} \cdot \mathbf{A}_{\mathbf{c}}{}^{-1} \cdot \mathbf{B}_{\mathbf{c}} = \\ &\left(\mathbf{C}_{\mathbf{di}} - \mathbf{C}_{\mathbf{ac}} \cdot \mathbf{M}^{-1} \cdot \mathbf{K} \qquad \mathbf{C}_{\mathbf{ve}} - \mathbf{C}_{\mathbf{ac}} \cdot \mathbf{M}^{-1} \cdot \mathbf{C}\right) \cdot \left(-\mathbf{Q}^{-1} \cdot \mathbf{P}\right) \cdot \mathbf{P}^{-1} \cdot \begin{bmatrix} \mathbf{E} \\ \mathbf{0} \end{bmatrix} \end{aligned} \tag{A.42}$$

Replacing $\mathbf{Q}^{-1} = \begin{bmatrix} \mathbf{K}^{-1} & \mathbf{0} \\ \mathbf{0} & -\mathbf{M}^{-1} \end{bmatrix}$ from (A.3) in (A.42),

$$\begin{aligned} &\Rightarrow \mathbf{C}_{\mathbf{c}}\, \mathbf{A}_{\mathbf{c}}{}^{-1}\, \mathbf{B}_{\mathbf{c}} = \left(\mathbf{C}_{\mathbf{di}} - \mathbf{C}_{\mathbf{ac}}\, \mathbf{M}^{-1}\, \mathbf{K} \qquad \mathbf{C}_{\mathbf{ve}} - \mathbf{C}_{\mathbf{ac}}\, \mathbf{M}^{-1}\, \mathbf{C}\right) \begin{bmatrix} -\mathbf{K}^{-1} & \mathbf{0} \\ \mathbf{0} & \mathbf{M}^{-1} \end{bmatrix} \begin{bmatrix} \mathbf{E} \\ \mathbf{0} \end{bmatrix} \\ &\Rightarrow \mathbf{C}_{\mathbf{c}}\, \mathbf{A}_{\mathbf{c}}{}^{-1}\, \mathbf{B}_{\mathbf{c}} = \left(\mathbf{C}_{\mathbf{di}} - \mathbf{C}_{\mathbf{ac}}\, \mathbf{M}^{-1}\, \mathbf{K} \qquad \mathbf{C}_{\mathbf{ve}} - \mathbf{C}_{\mathbf{ac}}\, \mathbf{M}^{-1}\, \mathbf{C}\right) \begin{bmatrix} -\mathbf{K}^{-1}\, \mathbf{E} \\ \mathbf{0} \end{bmatrix} \\ &\Rightarrow \mathbf{C}_{\mathbf{c}}\, \mathbf{A}_{\mathbf{c}}{}^{-1}\, \mathbf{B}_{\mathbf{c}} = -\mathbf{C}_{\mathbf{di}}\, \mathbf{K}^{-1}\, \mathbf{E} + \mathbf{C}_{\mathbf{ac}}\, \mathbf{M}^{-1}\, \mathbf{E} \end{aligned} \tag{A.43}$$

If $\mathbf{C}_{\mathbf{di}} = \mathbf{0}$, i.e., no displacement are measured, and using (A.9),

$$\Rightarrow \mathbf{C}_{\mathbf{c}}\, \mathbf{A}_{\mathbf{c}}{}^{-1}\, \mathbf{B}_{\mathbf{c}} = \mathbf{C}_{\mathbf{ac}}\, \mathbf{M}^{-1}\, \mathbf{E} = \mathbf{D}_{\mathbf{c}} \tag{A.44}$$

So, the feed-through matrix can be expressed in terms of the matrices $\mathbf{A}_{\mathbf{c}}$, $\mathbf{B}_{\mathbf{c}}$, and $\mathbf{C}_{\mathbf{c}}$ as

$$\Rightarrow \mathbf{D}_{\mathbf{c}} = \mathbf{C}_{\mathbf{c}}\, \mathbf{A}_{\mathbf{c}}{}^{-1}\, \mathbf{B}_{\mathbf{c}} = \mathbf{V}_{\mathbf{c}}\, \boldsymbol{\Lambda}_{\mathbf{c}}{}^{-1}\, \mathbf{L}_{\mathbf{c}}{}^{T} = \sum_{i=1}^{n} \frac{1}{\lambda_i}\, \mathbf{v}_{\mathbf{ci}}\, \mathbf{l}_{\mathbf{ci}}{}^{T} \tag{A.45}$$

Finally, it is concluded that the output vector corresponds to the sum of modal contributions,

$$\Rightarrow \mathbf{y}(t) = \sum_{i=1}^{n} \mathbf{y_i}(t) \tag{A.46}$$

where each vector $\mathbf{y_i}(t)$ corresponds to the response of a continuous-time state-space model of first order

$$\begin{cases} \dot{x}_m^{(i)}(t) = \lambda_i \; x_m^{(i)}(t) + \mathbf{l_{ci}}^T \; \mathbf{u}(t) \\ \mathbf{y_i}(t) = \mathbf{v_{ci}} \; x_m^{(i)}(t) + \dfrac{1}{\lambda_i} \mathbf{v_{ci}} \; \mathbf{l_{ci}}^T \; \mathbf{u}(t) \end{cases} \tag{A.47}$$

where the complex scalar $x_m^{(i)}(t)$ corresponds to the i-th component of the state vector.

A.4. Discrete-time state-space model

The solution of the Equation (A.5) is given by (Jeffrey and Dai 2008)

$$\mathbf{x}(t) = e^{\mathbf{A_c}(t-t_0)} \; \mathbf{x}(t_0) + e^{\mathbf{A_c}\,t} \int_{t_0}^{t} e^{-\mathbf{A_c}\,\tau} \; \mathbf{B_c} \; \mathbf{u}(\tau) \, d\tau \tag{A.48}$$

Then, (A.48) can be converted to discrete time assuming that $t = k\Delta t$ with $k \in \mathbb{N}$,

$$\Rightarrow \mathbf{x}_{k+1} = e^{\mathbf{A_c}(t_{k+1}-t_k)} \; \mathbf{x}_k + \int_{t_k}^{t_{k+1}} e^{\mathbf{A_c}(t_{k+1}-\tau)} \; \mathbf{B_c} \; \mathbf{u}(\tau) \, d\tau \tag{A.49}$$

i. *Solution 1 - Zero Order Hold (ZOH)*: Constant input between two consecutive time samples.

$$\Rightarrow \mathbf{u}(\tau) = \mathbf{u}_k = constant \qquad \tau \in [t_k, t_{k+1}] \tag{A.50}$$

Then, the integral in (A.49) can be solved as

$$\Rightarrow \int_{t_k}^{t_{k+1}} e^{\mathbf{A_c}\,(t_{k+1}-\tau)}\,\mathbf{B_c}\,\mathbf{u}(\tau)\,d\tau = \mathbf{B_c}\,\mathbf{u}_k\,e^{\mathbf{A_c}\,t_{k+1}} \int_{t_k}^{t_{k+1}} e^{-\mathbf{A_c}\,\tau}\,d\tau$$

$$= \mathbf{B_c}\,\mathbf{u}_k\,e^{\mathbf{A_c}\,t_{k+1}} - \mathbf{A_c}^{-1}\,e^{-\mathbf{A_c}\,\tau}\Big|_{t_k}^{t_{k+1}}$$

$$= -\mathbf{B_c}\,\mathbf{u}_k\,e^{\mathbf{A_c}\,t_{k+1}}\,\mathbf{A_c}^{-1}\left[e^{-\mathbf{A_c}\,t_{k+1}} - e^{-\mathbf{A_c}\,t_k}\right] \qquad \text{(A.51)}$$

$$= \mathbf{A_c}^{-1}\left[e^{-\mathbf{A_c}\,\Delta t} - \mathbf{I}\right]\mathbf{B_c}\,\mathbf{u}_k$$

Replacing (A.51) in (A.49)

$$\Rightarrow \mathbf{x}_{k+1} = e^{\mathbf{A_c}\,\Delta t}\,\mathbf{x}_k + \mathbf{A_c}^{-1}\left(e^{\mathbf{A_c}\,\Delta t} - \mathbf{I}\right)\mathbf{B_c}\,\mathbf{u}_k \qquad \text{(A.52)}$$

Defining

$$\mathbf{A_d} = e^{\mathbf{A_c}\,\Delta t}$$
$$\mathbf{B_d} = \mathbf{A_c}^{-1}\left[\mathbf{A_d} - \mathbf{I}\right]\mathbf{B_c} \qquad \text{(A.53)}$$

the state-space model in discrete-time can be expressed as

$$\begin{cases} \mathbf{x_{k+1}} = \mathbf{A_d}\,\mathbf{x_k} + \mathbf{B_d}\,\mathbf{u_k} \\ \mathbf{y_k} = \mathbf{C_d}\,\mathbf{x_k} + \mathbf{D_d}\,\mathbf{u_k} \end{cases} \qquad \text{(A.54)}$$

where $\mathbf{A_d}$ = discrete state matrix (dynamical system matrix), $\mathbf{B_d}$ = discrete input matrix, $\mathbf{C_d} \equiv \mathbf{C_c}$ = discrete output matrix, $\mathbf{D_d} \equiv \mathbf{D_c}$ = discrete direct feed-through matrix. Since $\mathbf{C_d}$ and $\mathbf{D_d}$ are dependent of the location of the outputs and of the matrices $\mathbf{M}$ and $\mathbf{K}$, which are time invariant in the linear case, then $\mathbf{C_d} \equiv \mathbf{C_c}$ and $\mathbf{D_d} \equiv \mathbf{D_c}$.

ii. *Solution 2 - First Order Hold (FOH)*: Linear variation of input between consecutive time samples.

$$\Rightarrow \mathbf{u}(\tau) = \mathbf{u}_k + \frac{\mathbf{u}_{k+1} - \mathbf{u}_k}{\Delta t}(\tau - t_k) \qquad \tau \in [t_k, t_{k+1}] \qquad \text{(A.55)}$$

Then, the state vector in (A.49) can be expressed as

$$\Rightarrow \mathbf{x}_{k+1} = e^{\mathbf{A_c}\,\Delta t}\,\mathbf{x}_k + \int_{t_k}^{t_{k+1}} e^{\mathbf{A_c}\,\Delta t}\,\mathbf{B_c}\,\mathbf{u_k}\,\delta(\tau - t_k)\,\Delta t\,d\tau$$
$$\Rightarrow \mathbf{x}_{k+1} = e^{\mathbf{A_c}\,\Delta t}\,\mathbf{x}_k + e^{\mathbf{A_c}\,\Delta t}\,\Delta t\,\mathbf{B_c}\,\mathbf{u_k} \tag{A.56}$$

Defining

$$\mathbf{A_d} = e^{\mathbf{A_c}\,\Delta t}$$
$$\mathbf{B_d} = \Delta t\,e^{\mathbf{A_c}\,\Delta t}\,\mathbf{B_c} \tag{A.57}$$

the state-space model in discrete-time can be expressed as

$$\begin{cases} \mathbf{x_{k+1}} = \mathbf{A_d}\,\mathbf{x_k} + \mathbf{B_d}\,\mathbf{u_k} \\ \mathbf{y_k} = \mathbf{C_d}\,\mathbf{x_k} + \mathbf{D_d}\,\mathbf{u_k} \end{cases} \tag{A.58}$$

where $\mathbf{A_d}$ = discrete state matrix (dynamical system matrix), $\mathbf{B_d}$ = discrete input matrix, $\mathbf{C_d} \equiv \mathbf{C_c}$ = discrete output matrix, $\mathbf{D_d} \equiv \mathbf{D_c}$ = discrete direct feed-through matrix. Since $\mathbf{C_d}$ and $\mathbf{D_d}$ are dependent of the location of the outputs and of the matrices $\mathbf{M}$ and $\mathbf{K}$, which are time invariant in the linear case, then $\mathbf{C_d} \equiv \mathbf{C_c}$ and $\mathbf{D_d} \equiv \mathbf{D_c}$.

iii. *Observation 1*: the choice of inter-sample behavior of the input does not affect the derivation of matrices $\mathbf{A_d}$ (state matrix) and $\mathbf{C_d}$ (output matrix), consequently the relationship between the poles of the continuous and discrete models is invariant for any discretization used for the input. (A.53) and (A.57) represent two special choices for the discrete-time state-space model.

iv. *Observation 2*: Let's define a new state vector such that $\mathbf{x} = \mathbf{T}\,\mathbf{z}$ where $\mathbf{T}$ is a non-singular square matrix. Then, replacing this equation in (A.58) yields $\mathbf{z}_{k+1} = \mathbf{T}^{-1}\,\mathbf{A}\,\mathbf{T}\,\mathbf{z}_k + \mathbf{T}^{-1}\,\mathbf{B}\,\mathbf{u}_k$ and $\mathbf{y}_k = \mathbf{C}\,\mathbf{T}\,\mathbf{z}_k + \mathbf{D}\,\mathbf{u}_k$, thus the matrices $\mathbf{T}^{-1}\,\mathbf{A}\,\mathbf{T}$, $\mathbf{T}^{-1}\,\mathbf{B}$, $\mathbf{C}\,\mathbf{T}$, and $\mathbf{D}$ describe the same input-output relationships as matrices $\mathbf{A}$, $\mathbf{B}$,

$\mathbf{C}$, and $\mathbf{D}$ and therefore there are infinite number of state-space representations that produce the same input-output description. This implies that the physical matrices $\mathbf{M}$, $\mathbf{K}$, and $\mathbf{C}$ cannot be uniquely recovered from the system matrices $\mathbf{A}$, $\mathbf{B}$, $\mathbf{C}$, and $\mathbf{D}$.

A.5. Relationships between continuous-time and discrete-time state space models

Using the definition of the matrix exponential (Jeffrey and Dai 2008)

$$e^{\mathbf{A}\,z} = \sum_{r=0}^{\infty} \frac{1}{r!}\,\mathbf{A}^r\,z^r \tag{A.59}$$

where $\mathbf{A}$ is a square matrix and z is a complex number, the state matrix in discrete-time can be expressed as

$$\mathbf{A_d} = e^{\mathbf{A_c}\,\Delta t} = \mathbf{I} + \mathbf{A_c}\,\Delta t + \frac{1}{2!}\left(\mathbf{A_c}\,\Delta t\right)^2 + \ldots + \frac{1}{k!}\left(\mathbf{A_c}\,\Delta t\right)^k \tag{A.60}$$

But, from (A.34) the continuous state matrix can be written as $\mathbf{A_c} = \mathbf{\Psi}\,\mathbf{\Lambda_c}\,\mathbf{\Psi}^{-1}$, then,

$$\begin{aligned}
&\Rightarrow e^{\mathbf{A_c}\,\Delta t} = \mathbf{I} + \mathbf{\Psi}\,\mathbf{\Lambda_c}\,\mathbf{\Psi}^{-1}\,\Delta t + \frac{1}{2!}\left(\mathbf{\Psi}\,\mathbf{\Lambda_c}\,\mathbf{\Psi}^{-1}\,\Delta t\right)^2 + \ldots + \frac{1}{k!}\left(\mathbf{\Psi}\,\mathbf{\Lambda_c}\,\mathbf{\Psi}^{-1}\,\Delta t\right)^k \\
&\Rightarrow e^{\mathbf{A_c}\,\Delta t} = \mathbf{I} + \mathbf{\Psi}\,\mathbf{\Lambda_c}\,\mathbf{\Psi}^{-1}\,\Delta t + \frac{1}{2!}\left(\mathbf{\Psi}\,\mathbf{\Lambda_c}^2\,\mathbf{\Psi}^{-1}\,\Delta t^2\right) + \ldots + \frac{1}{k!}\left(\mathbf{\Psi}\,\mathbf{\Lambda_c}^k\,\mathbf{\Psi}^{-1}\,\Delta t^k\right) \\
&\Rightarrow e^{\mathbf{A_c}\,\Delta t} = \mathbf{\Psi}\,e^{\mathbf{\Lambda_c}\,\Delta t}\,\mathbf{\Psi}^{-1}
\end{aligned} \tag{A.61}$$

Next, the following equation can be established

$$\Rightarrow \mathbf{A_d} = e^{\mathbf{A_c}\,\Delta t} = e^{\mathbf{\Psi}\,\mathbf{\Lambda_c}\,\mathbf{\Psi}^{-1}\,\Delta t} = \mathbf{\Psi}\,e^{\mathbf{\Lambda_c}\,\Delta t}\,\mathbf{\Psi}^{-1} = \mathbf{\Psi}\,\mathbf{\Lambda_d}\,\mathbf{\Psi}^{-1} = \mathbf{\Psi}\begin{bmatrix} \ddots & & \\ & \mu_i & \\ & & \ddots \end{bmatrix}\mathbf{\Psi}^{-1} \tag{A.62}$$

where $\mathbf{\Lambda_d} = e^{\mathbf{\Lambda_c}\,\Delta t} = \begin{bmatrix} \ddots & & \\ & \mu_i & \\ & & \ddots \end{bmatrix}$ is the matrix of the discrete eigenvalues. Therefore, the continuous and discrete eigenvectors are identical and the continuous and discrete eigenvalues (λ_i and μ_i, respectively) satisfy the condition:

$$\mu_i = e^{\lambda_i \Delta t} \Rightarrow \lambda_i = \frac{\ln(\mu_i)}{\Delta t} \tag{A.63}$$

Also, the discrete modal participation matrix, equivalently to (A.37), and the modal vectors as follow, equivalently to (A.40), can be expressed as:

$$\begin{aligned} \mathbf{L_d}^T &= \mathbf{\Psi}^{-1}\,\mathbf{B_d} \\ \mathbf{V_d} &= \mathbf{C_d}\,\mathbf{\Psi} \end{aligned} \tag{A.64}$$

A.6. Relationship between state-space matrices and modal parameters of the system

From (A.34), (A.61), (A.60), and (A.62) the following relations hold,

$$\Lambda_c = \mathbf{\Psi}\,\mathbf{\Lambda_c}\,\mathbf{\Psi}^{-1} \tag{A.65}$$

$$e^{\mathbf{A_c}\,\Delta t} = \mathbf{\Psi}\,e^{\mathbf{\Lambda_c}\,\Delta t}\,\mathbf{\Psi}^{-1} \tag{A.66}$$

$$\mathbf{A_d} = e^{\mathbf{A_c}\,\Delta t} \tag{A.67}$$

$$\mathbf{A_d} = \mathbf{\Psi}\,\mathbf{\Lambda_d}\,\mathbf{\Psi}^{-1} = \mathbf{\Psi}\begin{bmatrix} \ddots & & \\ & \mu_i & \\ & & \ddots \end{bmatrix}\mathbf{\Psi}^{-1} \tag{A.68}$$

Also, from (A.6),

$$\mathbf{A_c} = \begin{bmatrix} \mathbf{0} & \mathbf{I} \\ -\mathbf{M}^{-1}\,\mathbf{K} & -\mathbf{M}^{-1}\,\mathbf{C} \end{bmatrix} \tag{A.69}$$

From (A.34):

$$\begin{aligned} &\Rightarrow \mathbf{A_c}\ \boldsymbol{\Psi} = \boldsymbol{\Psi}\ \boldsymbol{\Lambda_c} \\ &\Rightarrow \mathbf{A_c}\ \boldsymbol{\psi_i} = \lambda_i\ \boldsymbol{\psi_i} \end{aligned} \tag{A.70}$$

If $\boldsymbol{\psi_i} = \begin{bmatrix} \phi_i^{\mathbf{1}} \\ \phi_i^{\mathbf{2}} \end{bmatrix}$,

$$\Rightarrow \begin{bmatrix} \mathbf{0} & \mathbf{I} \\ -\mathbf{M}^{-1}\ \mathbf{K} & -\mathbf{M}^{-1}\ \mathbf{C} \end{bmatrix} \begin{bmatrix} \phi_i^{\mathbf{1}} \\ \phi_i^{\mathbf{2}} \end{bmatrix} = \lambda_i \begin{bmatrix} \phi_i^{\mathbf{1}} \\ \phi_i^{\mathbf{2}} \end{bmatrix} \tag{A.71}$$

The first equation of (A.71) implies $\phi_i^{\mathbf{2}} = \lambda_i\ \phi_i^{\mathbf{1}}$, then

$$\Rightarrow \boldsymbol{\psi_i} = \begin{bmatrix} \phi_i \\ \lambda_i\ \phi_i \end{bmatrix} \tag{A.72}$$

The second equation of (E.33) implies

$$\left(\lambda_i^{\,2}\ \mathbf{M} + \lambda_i\ \mathbf{C} + \mathbf{K}\right)\phi_i = \mathbf{0} \tag{A.73}$$

Then, $\left(\lambda_i^{\,2} + 2\,\xi_i\,\lambda_i + \omega_i^2\right) = 0$ and the poles of continuous-time state-space model can be obtained as

$$\Rightarrow \lambda_i, \lambda_i^* = -\xi_i\ \omega_i \pm i\ \omega_i\ \sqrt{1-\xi_i^2} \tag{A.74}$$

(A.72) and (A.74) show that the modal parameters of the structural system can be obtained from the eigenvalues and eigenvectors of the state dynamic matrix $\mathbf{A_c}$. Since in practice the data are recorded in discrete-time, the modal frequencies, modal damping and mode shapes of the structural system can be obtained using the relationships between discrete-time and continuous-time state-space models, (A.63) and (A.64),

$$\Rightarrow \omega_i = \sqrt{\lambda_i \, \lambda_i^*} = \left|\lambda_i\right| \text{ with } \lambda_i = \frac{\ln\left(\mu_i\right)}{\Delta t} \tag{A.75}$$

$$\Rightarrow \xi_i = -\frac{\left(\lambda_i + \lambda_i^*\right)}{2\sqrt{\lambda_i \, \lambda_i^*}} = -\frac{\mathrm{Re}\left(\lambda_i\right)}{\left|\lambda_i\right|} \tag{A.76}$$

$$\Rightarrow \mathbf{\Phi} = \mathbf{C_d} \, \mathbf{\Psi} \tag{A.77}$$

where ω_i, ξ_i $(i = 1,...,n)$, and $\mathbf{\Phi}$ are the natural frequencies, damping ratios, and mode shapes of the structural system.

A.7. State equations for multiple-input multiple-output problems

A.7.1. Multiple-support excitation problems

For a linear system, the equation of dynamic equilibrium can be written in the following partitioned form (Chopra 2012)

$$\begin{bmatrix} \mathbf{M}_{ff} & \mathbf{M}_{fs} \\ \mathbf{M}_{sf} & \mathbf{M}_{ss} \end{bmatrix} \begin{bmatrix} \ddot{\mathbf{u}}_f^t \\ \ddot{\mathbf{u}}_g \end{bmatrix} + \begin{bmatrix} \mathbf{C}_{ff} & \mathbf{C}_{fs} \\ \mathbf{C}_{sf} & \mathbf{C}_{ss} \end{bmatrix} \begin{bmatrix} \dot{\mathbf{u}}_f^t \\ \dot{\mathbf{u}}_g \end{bmatrix} + \begin{bmatrix} \mathbf{K}_{ff} & \mathbf{K}_{fs} \\ \mathbf{K}_{sf} & \mathbf{K}_{ss} \end{bmatrix} \begin{bmatrix} \mathbf{u}_f^t \\ \mathbf{u}_g \end{bmatrix} = \begin{bmatrix} \mathbf{0} \\ \mathbf{p}_g \end{bmatrix} \tag{A.78}$$

where f = free nodes (superstructure), $\mathbf{u}_f^t$: absolute displacement of the free nodes, s = support nodes, $\mathbf{u}_g$ = absolute displacement of the supports, $\mathbf{p}_g$ = support forces, $\mathbf{M}_{ff}$, $\mathbf{C}_{ff}$, and $\mathbf{K}_{ff}$ = mass, damping and stiffness matrices of the superstructure, $\mathbf{M}_{ss}$, $\mathbf{C}_{ss}$, and $\mathbf{K}_{ss}$ = mass, damping and stiffness matrices of the supports, $\mathbf{M}_{fs}$, $\mathbf{C}_{fs}$, and $\mathbf{K}_{fs}$ = mass, damping and stiffness coupling matrices. The unknowns of the problem described in (A.78) are $\mathbf{u}_f^t$ and $\mathbf{p}_g$.

Since the system is linear, the principle of superposition can be applied. Then,

$$\begin{bmatrix} \mathbf{u}_f^t \\ \mathbf{u}_g \end{bmatrix} = \begin{bmatrix} \mathbf{u}_f^s \\ \mathbf{u}_g \end{bmatrix} + \begin{bmatrix} \mathbf{u} \\ \mathbf{0} \end{bmatrix} \tag{A.79}$$

$$\uparrow \qquad \uparrow \qquad \uparrow$$

total pseudostatic dynamic

where $\mathbf{u}_f^s$ are the displacements due to static application of the prescribed support displacements $\mathbf{u}_g$ at each time.

Also, from the static equilibrium

$$\begin{bmatrix} \mathbf{K}_{ff} & \mathbf{K}_{fs} \\ \mathbf{K}_{sf} & \mathbf{K}_{ss} \end{bmatrix} \begin{bmatrix} \mathbf{u}_f^s \\ \mathbf{u}_g \end{bmatrix} = \begin{bmatrix} \mathbf{0} \\ \mathbf{p}_g^s \end{bmatrix} \tag{A.80}$$

where $\mathbf{p}_g^s$ are the support forces required to statically impose displacements $\mathbf{u}_g$ at each time. From the first equation of (A.78), it follows

$$\mathbf{M}_{ff}\,\ddot{\mathbf{u}}_f^t + \mathbf{M}_{fs}\,\ddot{\mathbf{u}}_g + \mathbf{C}_{ff}\,\dot{\mathbf{u}}_f^t + \mathbf{C}_{fs}\,\dot{\mathbf{u}}_g + \mathbf{K}_{ff}\,\mathbf{u}_f^t + \mathbf{K}_{fs}\,\mathbf{u}_g = \mathbf{0} \tag{A.81}$$

Replacing (A.79) in (A.81),

$$\begin{aligned} \mathbf{M}_{ff}\,\ddot{\mathbf{u}}_f + \mathbf{C}_{ff}\,\dot{\mathbf{u}}_f + \mathbf{K}_{ff}\,\mathbf{u}_f = &-\left(\mathbf{M}_{ff}\,\ddot{\mathbf{u}}_f^s + \mathbf{M}_{fs}\,\ddot{\mathbf{u}}_g\right) - \left(\mathbf{C}_{ff}\,\dot{\mathbf{u}}_f^s + \mathbf{C}_{fs}\,\dot{\mathbf{u}}_g\right) \\ &- \cancel{\left(\mathbf{K}_{ff}\,\mathbf{u}_f^s + \mathbf{K}_{fs}\,\mathbf{u}_g\right)} \end{aligned} \tag{A.82}$$

From (A.80),

$$\mathbf{u}_f^s = \mathbf{R}_s\,\mathbf{u}_g \tag{A.83}$$

where, $\mathbf{R}_s$ is the pseudo-static influence matrix defined by

$$\mathbf{R}_s = -\mathbf{K}_{ff}^{-1}\,\mathbf{K}_{fs} \tag{A.84}$$

Then,

$$\mathbf{M}_{ff}\,\ddot{\mathbf{u}}_f + \mathbf{C}_{ff}\,\dot{\mathbf{u}}_f + \mathbf{K}_{ff}\,\mathbf{u}_f = -\left(\mathbf{M}_{ff}\,\mathbf{R}_s + \mathbf{M}_{fs}\right)\ddot{\mathbf{u}}_g - \left(\mathbf{C}_{ff}\,\mathbf{R}_s + \mathbf{C}_{fs}\right)\dot{\mathbf{u}}_g \tag{A.85}$$

Notes:

- If damping matrices are proportional to stiffness matrices, then the damping term in (A.85) is equal to $\mathbf{0}$, which is usually an unrealistic assumption.
- Usually, the damping term is neglected because it is small compared to the inertia term.
- For lumped mass models: $\mathbf{M}_{fs} = \mathbf{0}$
- N_s : # of DOF of supports N : # of DOF of the superstructure

From (A.85),

$$\begin{aligned}\ddot{\mathbf{u}}_f = &-\mathbf{M}_{ff}^{-1}\,\mathbf{K}_{ff}\,\mathbf{u}_f - \mathbf{M}_{ff}^{-1}\,\mathbf{C}_{ff}\,\dot{\mathbf{u}}_f - \mathbf{M}_{ff}^{-1}\left(\mathbf{M}_{ff}\,\mathbf{R}_s + \mathbf{M}_{fs}\right)\ddot{\mathbf{u}}_g \\ &- \mathbf{M}_{ff}^{-1}\left(\mathbf{C}_{ff}\,\mathbf{R}_s + \mathbf{C}_{fs}\right)\dot{\mathbf{u}}_g\end{aligned} \tag{A.86}$$

Then,

$$\begin{aligned}\begin{bmatrix}\dot{\mathbf{u}}_f \\ \ddot{\mathbf{u}}_f\end{bmatrix} = &\begin{bmatrix}\mathbf{0} & \mathbf{I} \\ -\mathbf{M}_{ff}^{-1}\,\mathbf{K}_{ff} & -\mathbf{M}_{ff}^{-1}\,\mathbf{C}_{ff}\end{bmatrix}\begin{bmatrix}\mathbf{u}_f \\ \dot{\mathbf{u}}_f\end{bmatrix} \\ &+\begin{bmatrix}\mathbf{0} & \mathbf{0} \\ -\mathbf{M}_{ff}^{-1}\left(\mathbf{M}_{ff}\,\mathbf{R}_s + \mathbf{M}_{fs}\right) & -\mathbf{M}_{ff}^{-1}\left(\mathbf{C}_{ff}\,\mathbf{R}_s + \mathbf{C}_{fs}\right)\end{bmatrix}\begin{bmatrix}\ddot{\mathbf{u}}_g \\ \dot{\mathbf{u}}_g\end{bmatrix}\end{aligned} \tag{A.87}$$

Defining

$$\mathbf{x} = \begin{bmatrix}\mathbf{u}_f \\ \dot{\mathbf{u}}_f\end{bmatrix}$$

$$\mathbf{A}_\mathbf{c} = \begin{bmatrix}\mathbf{0} & \mathbf{I} \\ -\mathbf{M}_{ff}^{-1}\,\mathbf{K}_{ff} & -\mathbf{M}_{ff}^{-1}\,\mathbf{C}_{ff}\end{bmatrix} \tag{A.88}$$

$$\mathbf{B}_\mathbf{c} = \begin{bmatrix}\mathbf{0} & \mathbf{0} \\ -\mathbf{M}_{ff}^{-1}\left(\mathbf{M}_{ff}\,\mathbf{R}_s + \mathbf{M}_{fs}\right) & -\mathbf{M}_{ff}^{-1}\left(\mathbf{C}_{ff}\,\mathbf{R}_s + \mathbf{C}_{fs}\right)\end{bmatrix}$$

$$\mathbf{u} = \begin{bmatrix} \ddot{\mathbf{u}}_g \\ \dot{\mathbf{u}}_g \end{bmatrix}$$

, the equation of dynamic equilibrium of a linear system subjected to multiple support excitations can be expressed in state-space form as

$$\dot{\mathbf{x}}(t) = \mathbf{A_c}\, \mathbf{x}(t) + \mathbf{B_c}\, \mathbf{u}(t) \tag{A.89}$$

A.7.2. Two-dimensional shear building model with translational and rotational input excitations

The equation of motion can be expressed as

$$\mathbf{M}\, \ddot{\mathbf{q}}^t + \mathbf{C}\, \dot{\mathbf{q}} + \mathbf{K}\, \mathbf{q} = \mathbf{0} \tag{A.90}$$

where $\mathbf{M} \in \mathbb{R}^{n\times n}$, $\mathbf{C} \in \mathbb{R}^{n\times n}$, and $\mathbf{K} \in \mathbb{R}^{n\times n}$ = mass, damping, and stiffness matrices of the structure, $\mathbf{q} \in \mathbb{R}^n$, $\dot{\mathbf{q}} \in \mathbb{R}^n$, and $\ddot{\mathbf{q}} \in \mathbb{R}^n$ = displacement, velocity, and acceleration response of the structure.

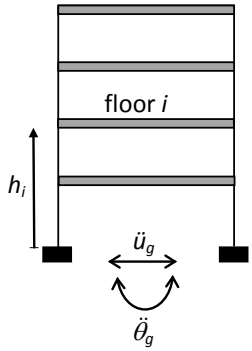

But $\ddot{\mathbf{q}}^t = \ddot{\mathbf{q}} + \ell_1\, \ddot{u}_g + \ell_2\, \ddot{\theta}_g$ with $\ell_1 = \begin{bmatrix} 1 & \dots & 1 \end{bmatrix}^T \in \mathbb{R}^{n\times 1}$ and $\ell_2 = \begin{bmatrix} h_1 & \dots & h_n \end{bmatrix}^T \in \mathbb{R}^{n\times 1}$ $\ell_2 = \begin{bmatrix} h_1 & \dots & h_n \end{bmatrix}^T \in \mathbb{R}^{n\times 1}$. Then,

$$\mathbf{M}\, \ddot{\mathbf{q}} + \mathbf{C}\, \dot{\mathbf{q}} + \mathbf{K}\, \mathbf{q} = -\mathbf{M}\, \ell_1\, \ddot{u}_g - \mathbf{M}\, \ell_2\, \ddot{\theta}_g \tag{A.91}$$

$$\Rightarrow \begin{bmatrix} \mathbf{C} & \mathbf{M} \\ \mathbf{M} & \mathbf{0} \end{bmatrix} \begin{bmatrix} \dot{\mathbf{q}} \\ \ddot{\mathbf{q}} \end{bmatrix} + \begin{bmatrix} \mathbf{K} & \mathbf{0} \\ \mathbf{0} & -\mathbf{M} \end{bmatrix} \begin{bmatrix} \mathbf{q} \\ \dot{\mathbf{q}} \end{bmatrix} = \begin{bmatrix} -\mathbf{M}\, \ell_1\, \ddot{u}_g - \mathbf{M}\, \ell_2\, \ddot{\theta}_g \\ \mathbf{0} \end{bmatrix} = \begin{bmatrix} \mathbf{E}_{n\times 2} \\ \mathbf{0}_{n\times 2} \end{bmatrix} \begin{bmatrix} \ddot{u}_g \\ \ddot{\theta}_g \end{bmatrix}_{2\times 1} \tag{A.92}$$

where $\mathbf{E} = \begin{bmatrix} -\mathbf{M}\,\ell_1 & -\mathbf{M}\,\ell_2 \end{bmatrix}$. From (A.92) the following first order differential equation can be written

$$\begin{aligned} &\Rightarrow \mathbf{P}\,\dot{\mathbf{x}} + \mathbf{Q}\,\mathbf{x} = \begin{bmatrix} \mathbf{E} \\ \mathbf{0} \end{bmatrix} \mathbf{u} \\ &\Rightarrow \dot{\mathbf{x}} = -\mathbf{P}^{-1}\,\mathbf{Q}\,\mathbf{x} + \mathbf{P}^{-1} \begin{bmatrix} \mathbf{E} \\ \mathbf{0} \end{bmatrix} \mathbf{u} \\ &\Rightarrow \dot{\mathbf{x}} = \mathbf{A}_c\,\mathbf{x} + \mathbf{B}_c\,\mathbf{u} \end{aligned} \tag{A.93}$$

where $\mathbf{x} = \begin{bmatrix} \mathbf{q} \\ \dot{\mathbf{q}} \end{bmatrix}$

$$\mathbf{A_c} = -\mathbf{P}^{-1}\,\mathbf{Q} = \begin{bmatrix} \mathbf{0} & \mathbf{I} \\ -\mathbf{M}^{-1}\,\mathbf{K} & -\mathbf{M}^{-1}\,\mathbf{C} \end{bmatrix} \in \mathbb{R}^{2n \times 2n}$$

$$\mathbf{B_c} = \mathbf{P}^{-1} \begin{Bmatrix} \mathbf{E} \\ \mathbf{0} \end{Bmatrix} = \begin{bmatrix} \mathbf{0} \\ \mathbf{M}^{-1}\,\mathbf{E} \end{bmatrix} = \begin{bmatrix} \mathbf{0}_{n\times 2} \\ \mathbf{M}^{-1} \begin{bmatrix} -\mathbf{M}\,\ell_1 & -\mathbf{M}\,\ell_2 \end{bmatrix} \end{bmatrix} = -\begin{bmatrix} \mathbf{0}_{n\times 2} \\ \begin{bmatrix} \ell_1 & \ell_2 \end{bmatrix} \end{bmatrix} \in \mathbb{R}^{2n \times 2}$$

$$\mathbf{u} = \begin{bmatrix} \ddot{u}_g \\ \ddot{\theta}_g \end{bmatrix}_{2\times 1}$$

A.7.3. Three-dimensional shear building model with translational excitations

The equation of motion can be expressed as

$$\mathbf{M}\,\ddot{\mathbf{q}}^t + \mathbf{C}\,\dot{\mathbf{q}} + \mathbf{K}\,\mathbf{q} = \mathbf{0} \tag{A.94}$$

where $\mathbf{M} \in \mathbb{R}^{3n\times 3n}$, $\mathbf{C} \in \mathbb{R}^{3n\times 3n}$, and $\mathbf{K} \in \mathbb{R}^{3n\times 3n}$ = mass, damping, and stiffness matrices of the structure, $\mathbf{q} \in \mathbb{R}^{3n}$, $\dot{\mathbf{q}} \in \mathbb{R}^{3n}$, and $\ddot{\mathbf{q}} \in \mathbb{R}^{3n}$ = displacement, velocity, and acceleration response of the structure, and n = number of stories of the building.

For a shear building model, the mass and stiffness matrices can be expressed as

$$\mathbf{M}=\begin{bmatrix} \mathbf{m_t} & \mathbf{0} & \mathbf{0} \\ \mathbf{0} & \mathbf{m_t} & \mathbf{0} \\ \mathbf{0} & \mathbf{0} & \mathbf{I_m} \end{bmatrix} \qquad \mathbf{K}=\begin{bmatrix} \mathbf{k_{xx}} & \mathbf{k_{xy}} & \mathbf{k_{x\theta}} \\ \mathbf{k_{yx}} & \mathbf{k_{yy}} & \mathbf{k_{y\theta}} \\ \mathbf{k_{\theta x}} & \mathbf{k_{\theta y}} & \mathbf{k_{\theta\theta}} \end{bmatrix} \tag{A.95}$$

But $\ddot{\mathbf{q}}^t = \ddot{\mathbf{q}} + \ddot{\mathbf{U}}_g \Rightarrow \mathbf{M}\,\ddot{\mathbf{q}} + \mathbf{C}\,\dot{\mathbf{q}} + \mathbf{K}\,\mathbf{q} = -\mathbf{M}\,\ddot{\mathbf{U}}_g$, where

$$\mathbf{q}=\begin{bmatrix} \mathbf{q_x} \\ \mathbf{q_y} \\ \mathbf{q_\theta} \end{bmatrix}_{3n\times 1} \qquad \ddot{\mathbf{U}}_{\mathbf{g}}=\begin{bmatrix} \ddot{\mathbf{U}}_{\mathbf{gx}} \\ \ddot{\mathbf{U}}_{\mathbf{gy}} \\ \mathbf{0} \end{bmatrix}_{3n\times 1}=\begin{bmatrix} \ell_1\,\ddot{\mathbf{u}}_{\mathbf{gx}} \\ \ell_2\,\ddot{\mathbf{u}}_{\mathbf{gy}} \\ \mathbf{0} \end{bmatrix}_{3n\times 1} \qquad \ell_1 = \ell_2 = \begin{bmatrix} 1 & \dots & 1 \end{bmatrix}^T \in \mathbb{R}^{n\times 1}$$

Then, the following first order differential equation can be written

$$\Rightarrow \dot{\mathbf{x}} = \mathbf{A}_c\,\mathbf{x} + \mathbf{B}_c\,\mathbf{u} \tag{A.96}$$

where $\mathbf{x}=\begin{bmatrix} \mathbf{q} \\ \dot{\mathbf{q}} \end{bmatrix}_{6n\times 1}$

$$\mathbf{E}=-\mathbf{M}\begin{bmatrix} \ell_1 & \mathbf{0} \\ \mathbf{0} & \ell_2 \\ \mathbf{0} & \mathbf{0} \end{bmatrix}_{3n\times 2}$$

$$\mathbf{u}=\begin{bmatrix} \ddot{\mathbf{u}}_{\mathbf{gx}} \\ \ddot{\mathbf{u}}_{\mathbf{gy}} \end{bmatrix}_{2\times 1}$$

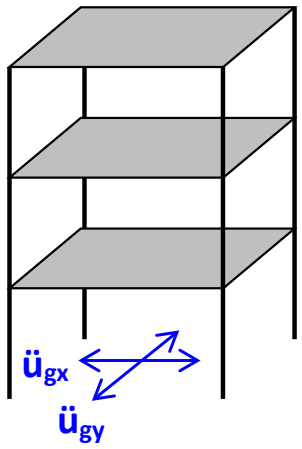

$$\mathbf{A_c}=\begin{bmatrix} \mathbf{0} & \mathbf{I} \\ -\mathbf{M}^{-1}\,\mathbf{K} & -\mathbf{M}^{-1}\,\mathbf{C} \end{bmatrix}_{6n\times 6n}$$

$$\mathbf{B_c}=\mathbf{P}^{-1}\begin{Bmatrix} \mathbf{E} \\ \mathbf{0} \end{Bmatrix}=\begin{bmatrix} \mathbf{0} \\ \mathbf{M}^{-1}\,\mathbf{E} \end{bmatrix}=-\begin{bmatrix} \mathbf{0}_{3n\times 2} \\ \begin{bmatrix} \ell_1 & \mathbf{0} \\ \mathbf{0} & \ell_1 \\ \mathbf{0} & \mathbf{0} \end{bmatrix} \end{bmatrix}_{6n\times 2}$$

A.7.4. Three-dimensional shear building model with translational and rocking excitations

The equation of motion can be expressed as

$$\mathbf{M}\,\ddot{\mathbf{q}}^{t} + \mathbf{C}\,\dot{\mathbf{q}} + \mathbf{K}\,\mathbf{q} = \mathbf{0} \tag{A.97}$$

where $\mathbf{M} \in \mathbb{R}^{3n\times 3n}$, $\mathbf{C} \in \mathbb{R}^{3n\times 3n}$, and $\mathbf{K} \in \mathbb{R}^{3n\times 3n}$ = mass, damping, and stiffness matrices of the structure, $\mathbf{q} \in \mathbb{R}^{3n}$, $\dot{\mathbf{q}} \in \mathbb{R}^{3n}$, and $\ddot{\mathbf{q}} \in \mathbb{R}^{3n}$ = displacement, velocity, and acceleration response of the structure, and n = number of stories of the building.

For a shear building model, the displacement vector, mass and stiffness matrices can be expressed as

$$\mathbf{q} = \begin{bmatrix} \mathbf{q_x} \\ \mathbf{q_y} \\ \mathbf{q_\theta} \end{bmatrix}_{3n\times 1} \qquad \ddot{\mathbf{q}}^{t} = \ddot{\mathbf{q}} + \ddot{\mathbf{U}}_{\mathbf{g}} + \ddot{\mathbf{\Theta}}_{\mathbf{g}}$$

$$\mathbf{M} = \begin{bmatrix} \mathbf{m_t} & \mathbf{0} & \mathbf{0} \\ \mathbf{0} & \mathbf{m_t} & \mathbf{0} \\ \mathbf{0} & \mathbf{0} & \mathbf{I_m} \end{bmatrix} \qquad \mathbf{K} = \begin{bmatrix} \mathbf{k_{xx}} & \mathbf{k_{xy}} & \mathbf{k_{x\theta}} \\ \mathbf{k_{yx}} & \mathbf{k_{yy}} & \mathbf{k_{y\theta}} \\ \mathbf{k_{\theta x}} & \mathbf{k_{\theta y}} & \mathbf{k_{\theta\theta}} \end{bmatrix} \tag{A.98}$$

where

$$\ddot{\mathbf{U}}_{\mathbf{g}} = \begin{bmatrix} \ddot{\mathbf{U}}_{\mathbf{gx}} \\ \ddot{\mathbf{U}}_{\mathbf{gy}} \end{bmatrix} = \begin{bmatrix} [1 \quad \dots \quad 1]^{T}\ \ddot{u}_{gx} \\ [1 \quad \dots \quad 1]^{T}\ \ddot{u}_{gy} \end{bmatrix} = \begin{bmatrix} \ell_1\,\ddot{u}_{gx} \\ \ell_2\,\ddot{u}_{gy} \end{bmatrix}$$

$$\ddot{\mathbf{\Theta}}_{\mathbf{g}} = \begin{bmatrix} \ddot{\mathbf{\Theta}}_{\mathbf{gx}} \\ \ddot{\mathbf{\Theta}}_{\mathbf{gy}} \end{bmatrix} = \begin{bmatrix} [h_1 \quad \dots \quad h_n]^{T}\ \ddot{\theta}_{gx} \\ [h_1 \quad \dots \quad h_n]^{T}\ \ddot{\theta}_{gy} \end{bmatrix} = \begin{bmatrix} \ell_3\,\ddot{\theta}_{gx} \\ \ell_4\,\ddot{\theta}_{gy} \end{bmatrix}$$

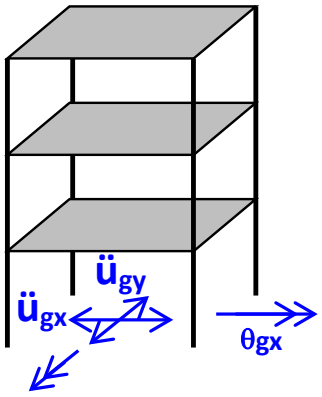

Then,

$$\begin{aligned} &\Rightarrow \mathbf{M}\,\ddot{\mathbf{q}} + \mathbf{C}\,\dot{\mathbf{q}} + \mathbf{K}\,\mathbf{q} = -\mathbf{M}\left(\ddot{\mathbf{U}}_{\mathbf{g}} + \ddot{\boldsymbol{\Theta}}_{\mathbf{g}}\right) \\ &\Rightarrow \mathbf{M}\,\ddot{\mathbf{q}} + \mathbf{C}\,\dot{\mathbf{q}} + \mathbf{K}\,\mathbf{q} = \mathbf{E}\,\mathbf{u} \\ &\Rightarrow \dot{\mathbf{x}} = \mathbf{A}_c\,\mathbf{x} + \mathbf{B}_c\,\mathbf{u} \end{aligned} \tag{A.99}$$

where $\mathbf{x} = \begin{bmatrix} \mathbf{q} \\ \dot{\mathbf{q}} \end{bmatrix}_{6n\times 1}$

$$\mathbf{E} = -\mathbf{M}\cdot\begin{bmatrix} \ell_1 & \mathbf{0} & \ell_3 & \mathbf{0} \\ \mathbf{0} & \ell_2 & \mathbf{0} & \ell_4 \\ \mathbf{0} & \mathbf{0} & \mathbf{0} & \mathbf{0} \end{bmatrix}_{3n\times 4}$$

$$\mathbf{u} = \begin{bmatrix} \ddot{\mathbf{u}}_{\mathbf{gx}} \\ \ddot{\mathbf{u}}_{\mathbf{gy}} \\ \ddot{\boldsymbol{\theta}}_{\mathbf{gx}} \\ \ddot{\boldsymbol{\theta}}_{\mathbf{gy}} \end{bmatrix}_{4\times 1}$$

$$\mathbf{A}_{\mathbf{c}} = \begin{bmatrix} \mathbf{0} & \mathbf{I} \\ -\mathbf{M}^{-1}\,\mathbf{K} & -\mathbf{M}^{-1}\,\mathbf{C} \end{bmatrix}_{6n\times 6n}$$

$$\mathbf{B}_{\mathbf{c}} = \mathbf{P}^{-1}\begin{bmatrix} \mathbf{E} \\ \mathbf{0} \end{bmatrix} = \begin{bmatrix} \mathbf{0} \\ \mathbf{M}^{-1}\,\mathbf{E} \end{bmatrix} = -\begin{bmatrix} \mathbf{0}_{3n\times 4} \\ \begin{bmatrix} \ell_1 & \mathbf{0} & \ell_3 & \mathbf{0} \\ \mathbf{0} & \ell_2 & \mathbf{0} & \ell_4 \\ \mathbf{0} & \mathbf{0} & \mathbf{0} & \mathbf{0} \end{bmatrix} \end{bmatrix}_{6n\times 4}$$

References.

Jeffrey, A. and Dai, H.H. (2008). *Handbook of mathematical formulas and integrals*. Academic Press, 4th edition, Burlington, MA.

Chopra, A.K. (2012). *Dynamics of structures: Theory and applications to earthquake engineering*. 4th Edition, Prentice Hall, Englewood Cliffs, NJ.

APPENDIX B: BAYESIAN INFERENCE FOR NONLINEAR STATE-SPACE MODELS

B.1. Nonlinear state-space model of dynamical systems

Consider the following general discrete-time nonlinear state-space model

$$\begin{aligned} \mathbf{x}_k &= \mathbf{f}_{k-1}\left(\mathbf{x}_{k-1}, \mathbf{u}_{k-1}, \mathbf{w}_{k-1}\right) \\ \mathbf{y}_k &= \mathbf{h}_k\left(\mathbf{x}_k, \mathbf{u}_k, \mathbf{v}_k\right) \\ \mathbf{w}_{k-1} &\sim \left(\mathbf{0}, \mathbf{Q}_{k-1}\right) \quad ; \quad \mathbf{v}_k \sim \left(\mathbf{0}, \mathbf{R}_k\right) \end{aligned} \tag{B.1}$$

where the first and second equations are called state (or process) and measurement (or observation) equations, respectively. $\mathbf{x}$, $\mathbf{u}$, and $\mathbf{y}$ are the state, input, and output vectors, respectively. $\mathbf{f}$ and $\mathbf{h}$ are the system and measurement nonlinear functions. $\mathbf{w}$ and $\mathbf{v}$ are the process and measurement noises, respectively, and the subscript denotes the time step. In the case of additive noises, previous model can be written as

$$\begin{aligned} \mathbf{x}_k &= \mathbf{f}_{k-1}\left(\mathbf{x}_{k-1}, \mathbf{u}_{k-1}\right) + \mathbf{w}_{k-1} \\ \mathbf{y}_k &= \mathbf{h}_k\left(\mathbf{x}_k, \mathbf{u}_k\right) + \mathbf{v}_k \\ \mathbf{w}_{k-1} &\sim \left(\mathbf{0}, \mathbf{Q}_{k-1}\right) \quad ; \quad \mathbf{v}_k \sim \left(\mathbf{0}, \mathbf{R}_k\right) \end{aligned} \tag{B.2}$$

B.2. Bayesian approach

The goal of the Bayesian approach is to determine estimates of at least the first two statistical moments of $\mathbf{x}_k$ based on the sequence of all available input and

measurements up to time k ($\mathbf{u}_{1:k}$ and $\mathbf{y}_{1:k}$). Construction of the posterior PDF $p(\mathbf{x}_k|\mathbf{u}_{1:k},\mathbf{y}_{1:k})$ is required assuming prior distribution $p(\mathbf{x}_0)$ known and that $p(\mathbf{x}_{k-1}|\mathbf{u}_{1:k-1},\mathbf{y}_{1:k-1})$. For the sake of notation simplicity, the deterministic input $\mathbf{u}_k$ will be omitted from now on.

Prior probability: Chapman-Kolmogorov (CK) equation

$$\begin{aligned} p(\mathbf{x}_k|\mathbf{y}_{1:k-1}) &= \int p\left[(\mathbf{x}_k,\mathbf{x}_{k-1})|\mathbf{y}_{1:k-1}\right] d\mathbf{x}_{k-1} \\ &= \int p\left[\mathbf{x}_k|(\mathbf{x}_{k-1},\mathbf{y}_{1:k-1})\right] p(\mathbf{x}_{k-1}|\mathbf{y}_{1:k-1})\, d\mathbf{x}_{k-1} \\ &= \int p(\mathbf{x}_k|\mathbf{x}_{k-1})\, p(\mathbf{x}_{k-1}|\mathbf{y}_{1:k-1})\, d\mathbf{x}_{k-1} \end{aligned} \tag{B.3}$$

$p(\mathbf{x}_k|\mathbf{x}_{k-1})$ is available from process equation $\mathbf{f}_k(\cdot)$ and the PDF of the noise $\mathbf{w}_k$ and $p(\mathbf{x}_{k-1}|\mathbf{y}_{1:k-1})$ available from the previous time step.

Posterior probability: Bayes theorem

$$\begin{aligned} p(\mathbf{x}_k|\mathbf{y}_{1:k}) &= p(\mathbf{x}_k|\mathbf{y}_k,\mathbf{y}_{1:k-1}) \\ &= \frac{p(\mathbf{y}_k|\mathbf{x}_k)\, p(\mathbf{x}_k|\mathbf{y}_{1:k-1})}{p(\mathbf{y}_k|\mathbf{y}_{1:k-1})} \\ &= \frac{p(\mathbf{y}_k|\mathbf{x}_k)\, p(\mathbf{x}_k|\mathbf{y}_{1:k-1})}{\int p(\mathbf{y}_k|\mathbf{x}_k)\, p(\mathbf{x}_k|\mathbf{y}_{1:k-1})\, d\mathbf{x}_k} \end{aligned} \tag{B.4}$$

$p(\mathbf{y}_k|\mathbf{x}_k)$ is the likelihood function and is obtained from $\mathbf{h}_k(\cdot)$ and PDF of $\mathbf{v}_k$, $p(\mathbf{x}_k|\mathbf{y}_{1:k-1})$ available from CK equation, and

$$\begin{aligned} p(\mathbf{y}_k|\mathbf{y}_{1:k-1}) &= \int p\left[(\mathbf{y}_k,\mathbf{x}_k)|\mathbf{y}_{1:k-1}\right] d\mathbf{x}_k \\ &= \int p\left[\mathbf{y}_k|(\mathbf{x}_k,\mathbf{y}_{1:k-1})\right] p\left[\mathbf{x}_k|\mathbf{y}_{1:k-1}\right] d\mathbf{x}_k \\ &= \int p(\mathbf{y}_k|\mathbf{x}_k)\, p(\mathbf{x}_k|\mathbf{y}_{1:k-1})\, d\mathbf{x}_k \end{aligned} \tag{B.5}$$

B.3. Bayesian approach for Gaussian approximation

Consider the case of additive and Gaussian noises, i.e.,

$$\begin{aligned}\mathbf{x}_k &= \mathbf{f}_{k-1}\left(\mathbf{x}_{k-1}, \mathbf{u}_{k-1}\right) + \mathbf{w}_{k-1} \\ \mathbf{y}_k &= \mathbf{h}_k\left(\mathbf{x}_k, \mathbf{u}_k\right) + \mathbf{v}_k \\ \mathbf{w}_k &\sim \mathcal{N}\left(\mathbf{0}, \mathbf{Q}_k\right) \\ \mathbf{v}_k &\sim \mathcal{N}\left(\mathbf{0}, \mathbf{R}_k\right)\end{aligned} \tag{B.6}$$

with $\mathbf{v}_k$, $\mathbf{w}_k$ independent processes and $\mathbf{x}_0 \sim \mathcal{N}\left(\hat{\mathbf{x}}_0, \mathbf{P}_0^{\mathbf{xx}}\right)$ independent of $\mathbf{v}_k$ and $\mathbf{w}_k$.

Assuming that the posterior PDF of the state at time t_{k-1} can be approximated by a Gaussian density,

$$\mathbf{p}\left(\mathbf{x}_{k-1} \middle| \mathbf{y}_{1:k-1}\right) = \mathcal{N}\left(\mathbf{x}_{k-1}; \hat{\mathbf{x}}_{k-1|k-1}, \mathbf{P}_{k-1|k-1}^{\mathbf{xx}}\right) \tag{B.7}$$

Replacing (B.7) in (B.3),

$$\begin{aligned}p\left(\mathbf{x}_k \middle| \mathbf{y}_{1:k-1}\right) &= \int p\left(\mathbf{x}_k \middle| \mathbf{x}_{k-1}\right) p\left(\mathbf{x}_{k\text{-}1} \middle| \mathbf{y}_{1:k\text{-}1}\right) \mathbf{dx}_{k-1} \\ &= \int p\left(\mathbf{x}_k \middle| \mathbf{x}_{k-1}\right) \mathcal{N}\left(\mathbf{x}_{k-1}; \hat{\mathbf{x}}_{k-1|k-1}, \mathbf{P}_{k-1|k-1}^{\mathbf{xx}}\right) \cdot \mathbf{dx}_{k-1}\end{aligned} \tag{B.8}$$

If $\mathbf{f}_k(\cdot)$ and $\mathbf{h}_k(\cdot)$ are deterministic, from the first equation in (B.6):

$$p\left(\mathbf{x}_k \middle| \mathbf{x}_{k-1}\right) = \mathcal{N}\left(\mathbf{x}_k; \mathbf{f}_k\left(\mathbf{x}_{k-1}, \mathbf{u}_{k-1}\right), \mathbf{Q}_{k-1}\right) \tag{B.9}$$

Then,

$$\begin{aligned}p\left(\mathbf{x}_k \middle| \mathbf{y}_{1:k-1}\right) &= \int p\left(\mathbf{x}_k \middle| \mathbf{x}_{k-1}\right) p\left(\mathbf{x}_{k\text{-}1} \middle| \mathbf{y}_{1:k\text{-}1}\right) \mathbf{dx}_{k-1} \\ &= \int \mathcal{N}\left(\mathbf{x}_k; \mathbf{f}_k\left(\mathbf{x}_{k-1}, \mathbf{u}_{k-1}\right), \mathbf{Q}_{k-1}\right) p\left(\mathbf{x}_{k-1} \middle| \mathbf{y}_{1:k-1}\right) \mathbf{dx}_{k-1}\end{aligned} \tag{B.10}$$

But,

$$E\{\mathbf{t}\} = \int \mathbf{t}\, \mathcal{N}\left(\mathbf{t}; \mathbf{f}(\mathbf{s}), \boldsymbol{\Sigma}\right) \mathbf{dt} = \mathbf{f}(\mathbf{s}) \tag{B.11}$$

$$\Rightarrow E\left\{\mathbf{x}_k \middle| \mathbf{y}_{1:k-1}\right\} = \int \mathbf{x}_k \; p\left(\mathbf{x}_k \middle| \mathbf{y}_{1:k\text{-}1}\right) \mathbf{dx}_k$$

$$= \int \mathbf{x}_k \left[\int \mathcal{N}^{\circledcirc}\left(\mathbf{x}_k ; \mathbf{f}_k\left(\mathbf{x}_{k-1}, \mathbf{u}_{k-1}\right), \mathbf{Q}_{k-1}\right) p\left(\mathbf{x}_{k-1} \middle| \mathbf{y}_{1:k\text{-}1}\right) \mathbf{dx}_{k-1} \right] \mathbf{dx}_k$$

$$= \int \left[\int \mathbf{x}_k \, \mathcal{N}^{\circledcirc}\left(\mathbf{x}_k ; \mathbf{f}_k\left(\mathbf{x}_{k-1}, \mathbf{u}_{k-1}\right), \mathbf{Q}_{k-1}\right) \mathbf{dx}_k \right] \mathbf{p}\left(\mathbf{x}_{k-1} \middle| \mathbf{y}_{1:k\text{-}1}\right) \mathbf{dx}_{k-1} \qquad \text{(B.12)}$$

$$= \int \mathbf{f}_k\left(\mathbf{x}_{k-1}, \mathbf{u}_{k-1}\right) p\left(\mathbf{x}_{k-1} \middle| \mathbf{y}_{1:k\text{-}1}\right) \mathbf{dx}_{k-1}$$

$$= \int \mathbf{f}_k\left(\mathbf{x}_{k-1}, \mathbf{u}_{k-1}\right) \mathcal{N}^{\circledcirc}\left(\mathbf{x}_{k-1} ; \hat{\mathbf{x}}_{k-1|k-1}, \mathbf{P}^{\mathbf{xx}}_{k-1|k-1}\right) \mathbf{dx}_{k-1}$$

$$\Rightarrow \hat{\mathbf{x}}_{k|k-1} = \int \mathbf{f}_k\left(\mathbf{x}_{k-1}, \mathbf{u}_{k-1}\right) \mathcal{N}^{\circledcirc}\left(\mathbf{x}_{k-1} ; \hat{\mathbf{x}}_{k-1|k-1}, \mathbf{P}^{\mathbf{xx}}_{k-1|k-1}\right) \mathbf{dx}_{k-1} \qquad \text{(B.13)}$$

Also,

$$\mathbf{P}^{\mathbf{xx}}_{k|k-1} = E\left\{ \left(\mathbf{x}_k - \hat{\mathbf{x}}_{k|k-1}\right) \left(\mathbf{x}_k - \hat{\mathbf{x}}_{k|k-1}\right)^T \right\}$$

$$\Rightarrow \mathbf{P}^{\mathbf{xx}}_{k|k-1} = \int \left(\mathbf{x}_k - \hat{\mathbf{x}}_{k|k-1}\right) \left(\mathbf{x}_k - \hat{\mathbf{x}}_{k|k-1}\right)^T p\left(\mathbf{x}_k \middle| \mathbf{y}_{1:k\text{-}1}\right) \mathbf{dx}_k \qquad \text{(B.14)}$$

$$\Rightarrow \mathbf{P}^{\mathbf{xx}}_{k|k-1} = \int \mathbf{x}_k \, \mathbf{x}_k^T \, p\left(\mathbf{x}_k \middle| \mathbf{y}_{1:k-1}\right) \mathbf{dx}_k - \hat{\mathbf{x}}_{k|k-1} \, \hat{\mathbf{x}}^T_{k|k-1}$$

$$\Rightarrow \mathbf{P}^{\mathbf{xx}}_{k|k-1} = \int \mathbf{f}\left(\mathbf{x}_{k-1}, \mathbf{u}_{k-1}\right) \mathbf{f}_k^T\left(\mathbf{x}_{k-1}, \mathbf{u}_{k-1}\right) \mathcal{N}^{\circledcirc}\left(\mathbf{x}_{k-1} ; \hat{\mathbf{x}}_{k-1|k-1}, \mathbf{P}^{\mathbf{xx}}_{k-1|k-1}\right) \mathbf{dx}_{k-1} - \hat{\mathbf{x}}_{k|k-1} \, \hat{\mathbf{x}}^T_{k|k-1} + \mathbf{Q}_{k-1} \qquad \text{(B.15)}$$

Now, considering a Gaussian approximation for $p\left(\mathbf{x}_k \middle| \mathbf{y}_{1:k-1}\right)$

$$p\left(\mathbf{x}_k \middle| \mathbf{y}_{1:k\text{-}1}\right) = \mathcal{N}^{\circledcirc}\left(\mathbf{x}_k ; \hat{\mathbf{x}}_{k|k-1}, \mathbf{P}^{\mathbf{xx}}_{k|k-1}\right) \qquad \text{(B.16)}$$

Also,

$$\mathbf{y}_k = \mathbf{h}_k\left(\mathbf{x}_k, \mathbf{u}_k\right) + \mathbf{v}_k \qquad \text{(B.17)}$$

Notin that

$$p\left(\mathbf{y}_k \middle| \mathbf{y}_{1:k-1}\right) = \int p\left(\mathbf{x}_k, \mathbf{y}_k \middle| \mathbf{y}_{1:k-1}\right) \mathbf{dx}_k$$

$$= \int p\left(\mathbf{y}_k \middle| \mathbf{x}_k\right) p\left(\mathbf{x}_k \middle| \mathbf{y}_{1:k-1}\right) \mathbf{dx}_k$$

$$\begin{aligned}\Rightarrow E\left\{\mathbf{y}_k \middle| \mathbf{x}_k, \mathbf{y}_{1:k-1}\right\} &= \int \mathbf{y}_k \, p\left(\mathbf{y}_k \middle| \mathbf{y}_{1:k-1}\right) d\mathbf{y}_k \\ &= \int \mathbf{y}_k \left[\int p\left(\mathbf{y}_k \middle| \mathbf{x}_k\right) p\left(\mathbf{x}_k \middle| \mathbf{y}_{1:k-1}\right) d\mathbf{x}_k\right] d\mathbf{y}_k \\ &= \int \left[\int \mathbf{y}_k \, p\left(\mathbf{y}_k \middle| \mathbf{x}_k\right) d\mathbf{y}_k\right] p\left(\mathbf{x}_k \middle| \mathbf{y}_{1:k-1}\right) d\mathbf{x}_k \\ &= \int \mathbf{h}_k\left(\mathbf{x}_k, \mathbf{u}_k\right) p\left(\mathbf{x}_k \middle| \mathbf{y}_{1:k-1}\right) d\mathbf{x}_k\end{aligned} \tag{B.18}$$

$$\Rightarrow \hat{\mathbf{y}}_{k|k-1} = \int \mathbf{h}_k\left(\mathbf{x}_k, \mathbf{u}_k\right) \mathcal{N}\left(\mathbf{x}_k; \hat{\mathbf{x}}_{k|k-1}, \mathbf{P}^{\mathbf{xx}}_{k|k-1}\right) d\mathbf{x}_k \tag{B.19}$$

Defining

$$e^{\mathbf{y}}_{k|k-1} = \mathbf{h}_k\left(\mathbf{x}_k, \mathbf{u}_k\right) - \hat{\mathbf{y}}_{k|k-1} \tag{B.20}$$

$$\begin{aligned}\Rightarrow \mathbf{P}^{\mathbf{yy}}_{k|k-1} &= E\left\{e^{\mathbf{y}}_{k|k-1}\left(e^{\mathbf{y}}_{k|k-1}\right)^T\right\} \\ &= E\left\{\left[\mathbf{h}_k\left(\mathbf{x}_k, \mathbf{u}_k\right) - \hat{\mathbf{y}}_{k|k-1}\right]\left[\mathbf{h}_k\left(\mathbf{x}_k, \mathbf{u}_k\right) - \hat{\mathbf{y}}_{k|k-1}\right]^T\right\}\end{aligned} \tag{B.21}$$

$$\Rightarrow \mathbf{P}^{\mathbf{yy}}_{k|k-1} = \int \left(\mathbf{h}_k\left(\mathbf{x}_k, \mathbf{u}_k\right) - \hat{\mathbf{y}}_{k|k-1}\right)\left(\mathbf{h}_k\left(\mathbf{x}_k, \mathbf{u}_k\right) - \hat{\mathbf{y}}_{k|k-1}\right)^T p\left(\mathbf{y}_k \middle| \mathbf{y}_{1:k-1}\right) d\mathbf{y}_k \tag{B.22}$$

$$\Rightarrow \mathbf{P}^{\mathbf{yy}}_{k|k-1} = \int \mathbf{h}_k\left(\mathbf{x}_k, \mathbf{u}_k\right) \mathbf{h}_k^T\left(\mathbf{x}_k, \mathbf{u}_k\right) \mathcal{N}\left(\mathbf{x}_k; \hat{\mathbf{x}}_{k|k-1}, \mathbf{P}^{\mathbf{xx}}_{k|k-1}\right) d\mathbf{x}_k - \hat{\mathbf{y}}_{k|k-1} \hat{\mathbf{y}}^T_{k|k-1} + \mathbf{R}_k \tag{B.23}$$

Similarly,

$$\mathbf{P}^{\mathbf{xy}}_{k|k-1} = E\left\{\left(\mathbf{x}_k - \hat{\mathbf{x}}_{k|k-1}\right)\left(e^{\mathbf{y}}_{k|k-1}\right)^T\right\} \tag{B.24}$$

$$\Rightarrow \mathbf{P}^{\mathbf{yy}}_{k|k-1} = \int\int \left(\mathbf{x}_k - \hat{\mathbf{x}}_{k|k-1}\right)\left(\mathbf{h}_k\left(\mathbf{x}_k, \mathbf{u}_k\right) - \hat{\mathbf{y}}_{k|k-1}\right)^T p\left(\mathbf{x}_k, \mathbf{y}_k \middle| \mathbf{y}_{1:k-1}\right) d\mathbf{x}_k d\mathbf{y}_k \tag{B.25}$$

$$\Rightarrow \mathbf{P}^{\mathbf{xy}}_{k|k-1} = \int \mathbf{x}_k \mathbf{h}_k^T\left(\mathbf{x}_k, \mathbf{u}_k\right) \mathcal{N}\left(\mathbf{x}_k; \hat{\mathbf{x}}_{k|k-1}, \mathbf{P}^{\mathbf{xx}}_{k|k-1}\right) d\mathbf{x}_k - \hat{\mathbf{x}}_{k|k-1} \hat{\mathbf{y}}^T_{k|k-1} \tag{B.26}$$

Then,

$$p\left(\mathbf{x}_k \middle| \mathbf{y}_{1:k}\right) = \mathcal{N}\left(\mathbf{x}_k; \hat{\mathbf{x}}_{k|k}, \mathbf{P}^{\mathbf{xx}}_{k|k}\right) \tag{B.27}$$

where

$$\begin{aligned}\hat{\mathbf{x}}_{k|k} &= \hat{\mathbf{x}}_{k|k-1} + \mathbf{K}_k\left(\mathbf{y}_k - \hat{\mathbf{y}}_{k|k-1}\right)\\ \mathbf{P}^{\mathbf{xx}}_{k|k} &= \mathbf{P}^{\mathbf{xx}}_{k|k} - \mathbf{K}_k\mathbf{P}^{\mathbf{yy}}_{k|k-1}\mathbf{K}_k^T\\ \mathbf{K}_k &= \mathbf{P}^{\mathbf{xy}}_{k|k-1}\left(\mathbf{P}^{\mathbf{yy}}_{k|k-1}\right)^{-1}\end{aligned} \tag{B.28}$$

B.4. Kalman-based filters for nonlinear Gaussian processes

The posterior PDF of $\mathbf{x}_k$ given $\mathbf{y}_{1:k}$ can be written as:

$$p\left(\mathbf{x}_k\middle|\mathbf{y}_{1:k}\right) = \frac{p\left(\mathbf{x}_k,\mathbf{y}_{1:k}\right)}{p\left(\mathbf{y}_{1:k}\right)} \propto p\left(\mathbf{x}_k,\mathbf{y}_{1:k}\right) \tag{B.29}$$

where it is assumed that $p\left(\mathbf{y}_{1:k}\right)$ can be ignored because it is a normalization PDF. Now, we can approximate the joint PDF $p\left(\mathbf{x}_k,\mathbf{y}_{1:k}\right)$ by the predictive PDF:

$$p\left(\mathbf{x}_k\middle|\mathbf{y}_{1:k}\right) \approx p\left(\mathbf{x}_k,\mathbf{y}_k\middle|\mathbf{x}_{k-1},\mathbf{y}_{1:k-1}\right) \tag{B.30}$$

Let,

$$\hat{\mathbf{x}} = \hat{\mathbf{x}}_{k|k} = E\left\{\mathbf{x}_k\middle|\mathbf{y}_{1:k}\right\} \tag{B.31}$$

$$\mathbf{P}^{\hat{\mathbf{x}}\hat{\mathbf{x}}} = \mathbf{P}^{\mathbf{xx}}_{k|k} = E\left\{\left(\mathbf{x}_k - \hat{\mathbf{x}}\right)\left(\mathbf{x}_k - \hat{\mathbf{x}}\right)^T\middle|\mathbf{y}_{1:k}\right\} \tag{B.32}$$

The Gaussian posterior can be written as:

$$\begin{aligned}p\left(\mathbf{x}_k\middle|\mathbf{y}_{1:k}\right) &= \mathcal{N}\left(\hat{\mathbf{x}},\mathbf{P}^{\hat{\mathbf{x}}\hat{\mathbf{x}}}\right)\\ &= \frac{1}{\left(2\pi\right)^{N_x/2}\left|\mathbf{P}^{\hat{\mathbf{x}}\hat{\mathbf{x}}}\right|^{1/2}}\exp\left\{-\frac{1}{2}\mathbf{A}\right\}\end{aligned} \tag{B.33}$$

where

$$\begin{aligned}\mathbf{A} &= \left(\mathbf{x}_k - \hat{\mathbf{x}}\right)^T \left(\mathbf{P}^{\hat{\mathbf{x}}\hat{\mathbf{x}}}\right)^{-1} \left(\mathbf{x}_k - \hat{\mathbf{x}}\right) \\ &= \mathbf{x}_k^T \left(\mathbf{P}^{\hat{\mathbf{x}}\hat{\mathbf{x}}}\right)^{-1} \mathbf{x}_k - \mathbf{x}_k^T \left(\mathbf{P}^{\hat{\mathbf{x}}\hat{\mathbf{x}}}\right)^{-1} \hat{\mathbf{x}} - \hat{\mathbf{x}}^T \left(\mathbf{P}^{\hat{\mathbf{x}}\hat{\mathbf{x}}}\right)^{-1} \mathbf{x}_k + \hat{\mathbf{x}}^T \left(\mathbf{P}^{\hat{\mathbf{x}}\hat{\mathbf{x}}}\right)^{-1} \hat{\mathbf{x}}\end{aligned} \tag{B.34}$$

Let,

$$\mathbf{z}_k = \begin{bmatrix} \mathbf{x}_k \\ \mathbf{y}_k \end{bmatrix} \tag{B.35}$$

Assuming that the joint PDF is Gaussian:

$$p\left(\mathbf{z}_k\right) = \mathcal{N}\left(\overline{\mathbf{z}}_k, \mathbf{P}^{\mathbf{zz}}\right) \tag{B.36}$$

where

$$\overline{\mathbf{z}}_k = \begin{bmatrix} \overline{\mathbf{x}}_k \\ \overline{\mathbf{y}}_k \end{bmatrix} = E\left\{ \begin{bmatrix} \mathbf{x}_k \\ \mathbf{y}_k \end{bmatrix} \middle| \mathbf{x}_{k-1}, \mathbf{y}_{1:k-1} \right\} = \begin{bmatrix} \hat{\mathbf{x}}_{k|k-1} \\ \hat{\mathbf{y}}_{k|k-1} \end{bmatrix} \tag{B.37}$$

$$\mathbf{P}^{\mathbf{zz}} = E\left\{ \left(\mathbf{z}_k - \overline{\mathbf{z}}_k\right)\left(\mathbf{z}_k - \overline{\mathbf{z}}_k\right)^T \middle| \mathbf{x}_{k-1}, \mathbf{y}_{1:k-1} \right\} = \begin{bmatrix} \mathbf{P}^{\mathbf{xx}} & \mathbf{P}^{\mathbf{xy}} \\ \mathbf{P}^{\mathbf{yx}} & \mathbf{P}^{\mathbf{yy}} \end{bmatrix} = \begin{bmatrix} \mathbf{P}^{\mathbf{xx}}_{k|k-1} & \mathbf{P}^{\mathbf{xy}}_{k|k-1} \\ \mathbf{P}^{\mathbf{yx}}_{k|k-1} & \mathbf{P}^{\mathbf{yy}}_{k|k-1} \end{bmatrix} \tag{B.38}$$

From the matrix inversion lemma:

$$\left(\mathbf{P}^{\mathbf{zz}}\right)^{-1} = \begin{bmatrix} \mathbf{C}_{11} & \mathbf{C}_{12} \\ \mathbf{C}_{21} & \mathbf{C}_{22} \end{bmatrix} \tag{B.39}$$

where

$$\begin{aligned} \mathbf{C}_{11} &= \left[\mathbf{P}^{\mathbf{xx}}_{k|k-1} - \mathbf{P}^{\mathbf{xy}}_{k|k-1} \left(\mathbf{P}^{\mathbf{yy}}_{k|k-1}\right)^{-1} \mathbf{P}^{\mathbf{yx}}_{k|k-1} \right]^{-1} \\ \mathbf{C}_{12} &= -\mathbf{C}_{11} \mathbf{P}^{\mathbf{xy}}_{k|k-1} \left(\mathbf{P}^{\mathbf{yy}}_{k|k-1}\right)^{-1} \\ \mathbf{C}_{12} &= -\mathbf{C}_{22} \mathbf{P}^{\mathbf{yx}}_{k|k-1} \left(\mathbf{P}^{\mathbf{yy}}_{k|k-1}\right)^{-1} \end{aligned} \tag{B.40}$$

$$\mathbf{C}_{22} = \left[\mathbf{P}^{\mathbf{yy}}_{k|k-1} - \mathbf{P}^{\mathbf{yx}}_{k|k-1} \left(\mathbf{P}^{\mathbf{xx}}_{k|k-1} \right)^{-1} \mathbf{P}^{\mathbf{xy}}_{k|k-1} \right]^{-1}$$

Then, the Gaussian joint PDF can be written:

$$\begin{aligned} p(\mathbf{z}_k) &= \mathcal{N}^{\circ}\left(\overline{\mathbf{z}}_k, \mathbf{P}^{\mathbf{zz}}_k \right) \\ &= \frac{1}{(2\pi)^{(N_x+N_y)/2} \left| \mathbf{P}^{\mathbf{zz}}_k \right|^{1/2}} \exp\left\{ -\frac{1}{2}\mathbf{B} \right\} \end{aligned} \tag{B.41}$$

where

$$\begin{aligned} \mathbf{B} &= \left[(\mathbf{x}_k - \overline{\mathbf{x}}_k) \ \vdots \ (\mathbf{y}_k - \overline{\mathbf{y}}_k) \right]^T \left(\mathbf{P}^{\mathbf{zz}}_k \right)^{-1} \left[(\mathbf{x}_k - \overline{\mathbf{x}}_k) \ \vdots \ (\mathbf{y}_k - \overline{\mathbf{y}}_k) \right] \\ &= (\mathbf{x}_k - \overline{\mathbf{x}}_k)^T \mathbf{C}_{11} (\mathbf{x}_k - \overline{\mathbf{x}}_k) + (\mathbf{x}_k - \overline{\mathbf{x}}_k)^T \mathbf{C}_{12} (\mathbf{y}_k - \overline{\mathbf{y}}_k) \\ &\quad + (\mathbf{y}_k - \overline{\mathbf{y}}_k)^T \mathbf{C}_{21} (\mathbf{x}_k - \overline{\mathbf{x}}_k) + (\mathbf{y}_k - \overline{\mathbf{y}}_k)^T \mathbf{C}_{12} (\mathbf{y}_k - \overline{\mathbf{y}}_k) \\ &= \mathbf{x}_k{}^T \mathbf{C}_{11} \mathbf{x}_k + \mathbf{x}_k{}^T \left[-\mathbf{C}_{11} \overline{\mathbf{x}}_k + \mathbf{C}_{12} (\mathbf{y}_k - \overline{\mathbf{y}}_k) \right] + \ldots \end{aligned} \tag{B.42}$$

Comparing (B.42) and (B.34):

$$\left(\mathbf{P}^{\hat{\mathbf{x}}\hat{\mathbf{x}}} \right)^{-1} = \mathbf{C}_{11} = \left[\mathbf{P}^{\mathbf{xx}}_{k|k-1} - \mathbf{P}^{\mathbf{xy}}_{k|k-1} \left(\mathbf{P}^{\mathbf{yy}}_{k|k-1} \right)^{-1} \mathbf{P}^{\mathbf{yx}}_{k|k-1} \right]^{-1} \tag{B.43}$$

$$\Rightarrow \mathbf{P}^{\hat{\mathbf{x}}\hat{\mathbf{x}}} = \mathbf{P}^{\mathbf{xx}}_{k|k-1} - \mathbf{P}^{\mathbf{xy}}_{k|k-1} \left(\mathbf{P}^{\mathbf{yy}}_{k|k-1} \right)^{-1} \mathbf{P}^{\mathbf{yx}}_{k|k-1} \tag{B.44}$$

$$\begin{aligned} \left(\mathbf{P}^{\hat{\mathbf{x}}\hat{\mathbf{x}}} \right)^{-1} \hat{\mathbf{x}} &= \mathbf{C}_{11} \overline{\mathbf{x}}_k - \mathbf{C}_{12} (\mathbf{y}_k - \overline{\mathbf{y}}_k) \\ &= \left[\mathbf{P}^{\mathbf{xx}}_{k|k-1} - \mathbf{P}^{\mathbf{xy}}_{k|k-1} \left(\mathbf{P}^{\mathbf{yy}}_{k|k-1} \right)^{-1} \mathbf{P}^{\mathbf{yx}}_{k|k-1} \right]^{-1} \overline{\mathbf{x}}_k \\ &\quad + \left[\mathbf{P}^{\mathbf{xx}}_{k|k-1} - \mathbf{P}^{\mathbf{xy}}_{k|k-1} \left(\mathbf{P}^{\mathbf{yy}}_{k|k-1} \right)^{-1} \mathbf{P}^{\mathbf{yx}}_{k|k-1} \right]^{-1} \mathbf{P}^{\mathbf{xy}}_{k|k-1} \left(\mathbf{P}^{\mathbf{yy}}_{k|k-1} \right)^{-1} (\mathbf{y}_k - \overline{\mathbf{y}}_k) \end{aligned} \tag{B.45}$$

Solving for $\hat{\mathbf{x}}$ from (B.45) and using (B.44):

$$\hat{\mathbf{x}} = \overline{\mathbf{x}}_k + \mathbf{P}^{\mathbf{xy}}_{k|k-1} \left(\mathbf{P}^{\mathbf{yy}}_{k|k-1} \right)^{-1} (\mathbf{y}_k - \overline{\mathbf{y}}_k) \tag{B.46}$$

Defining the Kalman gain as

$$\mathbf{K}_k = \mathbf{P}^{\mathbf{xy}}_{k|k-1}\left(\mathbf{P}^{\mathbf{yy}}_{k|k-1}\right)^{-1} \tag{B.47}$$

Using (B.44), (B.46), and (B.47):

$$\begin{aligned} \Rightarrow \hat{\mathbf{x}}_{k|k} &= \hat{\mathbf{x}}_{k|k-1} + \mathbf{K}_k\left(\mathbf{y}_k - \hat{\mathbf{y}}_{k|k-1}\right) \\ \mathbf{P}^{\mathbf{xx}}_{k|k} &= \mathbf{P}^{\mathbf{xx}}_{k|k} - \mathbf{K}_k\mathbf{P}^{\mathbf{yy}}_{k|k-1}\mathbf{K}_k^T \end{aligned} \tag{B.48}$$

where

$$\mathbf{P}^{\mathbf{xx}}_{k|k-1} = E\left\{\left[\mathbf{x}_{k|k-1} - \hat{\mathbf{x}}_{k|k-1}\right]\left[\mathbf{x}_{k|k-1} - \hat{\mathbf{x}}_{k|k-1}\right]^T\right\}$$

$$\mathbf{P}^{\mathbf{xy}}_{k|k-1} = E\left\{\left[\mathbf{x}_{k|k-1} - \hat{\mathbf{x}}_{k|k-1}\right]\left[\mathbf{y}_{k|k-1} - \hat{\mathbf{y}}_{k|k-1}\right]^T\right\} \tag{B.49}$$

$$\mathbf{P}^{\mathbf{yy}}_{k|k-1} = E\left\{\left[\mathbf{y}_{k|k-1} - \hat{\mathbf{y}}_{k|k-1}\right]\left[\mathbf{y}_{k|k-1} - \hat{\mathbf{y}}_{k|k-1}\right]^T\right\}$$

B.5. Kalman Filter for linear systems

Consider the following linear state-space model

$$\begin{aligned} \mathbf{x}_k &= \mathbf{F}_{k-1}\mathbf{x}_{k-1} + \mathbf{G}_{k-1}\mathbf{u}_{k-1} + \mathbf{w}_{k-1} \\ \mathbf{y}_k &= \mathbf{H}_k\mathbf{x}_k + \mathbf{v}_k \end{aligned} \tag{B.50}$$

where the noise processes $\mathbf{w}_k$ and $\mathbf{v}_k$ are white, zero-mean, uncorrelated, and have covariance matrices $\mathbf{Q}_k$ and $\mathbf{R}_k$ respectively, i.e.,

$$\begin{aligned} &\mathbf{w}_k \sim (\mathbf{0}, \mathbf{Q}_k) \qquad \mathbf{v}_k \sim (\mathbf{0}, \mathbf{R}_k) \\ &E\left[\mathbf{w}_k\mathbf{w}_j^T\right] = \mathbf{Q}_k\delta_{k-j} \qquad E\left[\mathbf{v}_k\mathbf{v}_j^T\right] = \mathbf{R}_k\delta_{k-j} \\ &E\left[\mathbf{v}_k\mathbf{w}_j^T\right] = \mathbf{0} \end{aligned} \tag{B.51}$$

Time-update step

From the state equation,

$$\begin{aligned}\Rightarrow\ \hat{\mathbf{x}}_{k|k-1} &= E\left[\mathbf{x}_k \mid \mathbf{y}_{1:k-1}\right] \\ &= E\left[\mathbf{F}_{k-1}\mathbf{x}_{k-1} + \mathbf{G}_{k-1}\mathbf{u}_{k-1} + \mathbf{w}_{k-1}\right] \\ &= \mathbf{F}_{k-1}E\left[\mathbf{x}_{k-1}\right] + \mathbf{G}_{k-1}\mathbf{u}_{k-1} \\ &= \mathbf{F}_{k-1}\hat{\mathbf{x}}_{k-1|k-1} + \mathbf{G}_{k-1}\mathbf{u}_{k-1}\end{aligned} \tag{B.52}$$

$$\Rightarrow\ \hat{\mathbf{x}}_{k|k-1} = \mathbf{F}_{k-1}\hat{\mathbf{x}}_{k-1|k-1} + \mathbf{G}_{k-1}\mathbf{u}_{k-1}$$

Similarly,

$$\begin{aligned}\mathbf{P}_{k|k-1} &= E\left[\left(\mathbf{x}_k - \hat{\mathbf{x}}_{k|k-1}\right)\left(\mathbf{x}_k - \hat{\mathbf{x}}_{k|k-1}\right)^T\right] \\ &= E\left[\left(\mathbf{F}_{k-1}\mathbf{x}_{k-1} + \mathbf{G}_{k-1}\mathbf{u}_{k-1} + \mathbf{w}_{k-1} - \mathbf{F}_{k-1}\hat{\mathbf{x}}_{k-1|k-1} - \mathbf{G}_{k-1}\mathbf{u}_{k-1}\right)(\cdots)^T\right] \\ &= E\left[\left(\mathbf{F}_{k-1}\left(\mathbf{x}_{k-1} - \hat{\mathbf{x}}_{k-1|k-1}\right) + \mathbf{w}_{k-1}\right)\left(\mathbf{F}_{k-1}\left(\mathbf{x}_{k-1} - \hat{\mathbf{x}}_{k-1|k-1}\right) + \mathbf{w}_{k-1}\right)^T\right] \\ &= \mathbf{F}_{k-1}E\left[\left(\mathbf{x}_{k-1} - \hat{\mathbf{x}}_{k-1|k-1}\right)\left(\mathbf{x}_{k-1} - \hat{\mathbf{x}}_{k-1|k-1}\right)^T\right]\mathbf{F}_{k-1}^T + E\left[\mathbf{w}_{k-1}\mathbf{w}_{k-1}^T\right] + \\ &\quad \mathbf{F}_{k-1}E\left[\left(\mathbf{x}_{k-1} - \hat{\mathbf{x}}_{k-1|k-1}\right)\mathbf{w}_{k-1}^T\right] + E\left[\mathbf{w}_{k-1}\left(\mathbf{x}_{k-1} - \hat{\mathbf{x}}_{k-1|k-1}\right)\right]\mathbf{F}_{k-1}^T\end{aligned} \tag{B.53}$$

but $\left(\mathbf{x}_{k-1} - \hat{\mathbf{x}}_{k-1|k-1}\right)$ is uncorrelated with $\mathbf{w}_{k-1}$

$$\Rightarrow \mathbf{P}_{k|k-1} = \mathbf{F}_{k-1}\mathbf{P}_{k-1|k-1}\mathbf{F}_{k-1}^T + \mathbf{Q}_{k-1} \tag{B.54}$$

Equation (B.54) is known as Discrete-time Lyapunov equation or Stein equation.

Measurement-update step

A linear estimator of $\mathbf{x}_k$ when the measurement $\mathbf{y}_k$ is recorded can be written as

$$\hat{\mathbf{x}}_{k|k} = \mathbf{K}_{k,x}\hat{\mathbf{x}}_{k|k-1} + \mathbf{K}_k\mathbf{y}_k \tag{B.55}$$

Then,

$$\begin{aligned}E\left[\hat{\mathbf{x}}_{k|k} - \mathbf{x}_k\right] &= \mathbf{K}_{k,x}E\left[\hat{\mathbf{x}}_{k|k-1}\right] + \mathbf{K}_k E\left[\mathbf{H}_k\mathbf{x}_k + \mathbf{v}_k\right] - E\left[\mathbf{x}_k\right] \\ &= \mathbf{K}_{k,x}E\left[\hat{\mathbf{x}}_{k|k-1}\right] + \left(\mathbf{K}_k\mathbf{H}_k - \mathbf{I}\right)E\left[\mathbf{x}_k\right] + \mathbf{K}_k E\left[\mathbf{v}_k\right]\end{aligned} \tag{B.56}$$

If the estimator is unbiased, $E\left[\hat{\mathbf{x}}_{k|k} - \mathbf{x}_k\right] = \mathbf{0}$, and then

$$\mathbf{K}_{k,x} = \mathbf{I} - \mathbf{K}_k \mathbf{H}_k \tag{B.57}$$

$$\Rightarrow \hat{\mathbf{x}}_{k|k} = \hat{\mathbf{x}}_{k|k-1} + \mathbf{K}_k \left(\mathbf{y}_k - \mathbf{H}_k \hat{\mathbf{x}}_{k|k-1} \right) \tag{B.58}$$

The expected value of the estimation error can be expressed as

$$\begin{aligned} E\left[\in_{x,k} \right] &= E\left[\left(\mathbf{x}_k - \hat{\mathbf{x}}_{k|k} \right) \right] = E\left[\mathbf{x}_k - \hat{\mathbf{x}}_{k|k-1} - \mathbf{K}_k \left(\mathbf{y}_k - \mathbf{H}_k \hat{\mathbf{x}}_{k|k-1} \right) \right] \\ &= E\left[\mathbf{x}_k - \hat{\mathbf{x}}_{k|k-1} - \mathbf{K}_k \left(\mathbf{H}_k \mathbf{x}_k + \mathbf{v}_k - \mathbf{H}_k \hat{\mathbf{x}}_{k|k-1} \right) \right] \\ &= E\left[\in_{x,k-1} - \mathbf{K}_k \mathbf{H}_k \left(\mathbf{x}_k - \hat{\mathbf{x}}_{k|k-1} \right) - \mathbf{K}_k \mathbf{v}_k \right] \\ &= \left(\mathbf{I} - \mathbf{K}_k \mathbf{H}_k \right) E\left[\in_{x,k-1} \right] - \mathbf{K}_k E\left[\mathbf{v}_k \right] \end{aligned} \tag{B.59}$$

and its covariance matrix as

$$\begin{aligned} \Rightarrow \mathbf{P}_{k|k} &= E\left[\in_{x,k} \in_{x,k}^T \right] = E\left[\left(\mathbf{x}_k - \hat{\mathbf{x}}_{k|k} \right) \left(\mathbf{x}_k - \hat{\mathbf{x}}_{k|k} \right)^T \right] \\ &= E\left[\left\{ \left(\mathbf{I} - \mathbf{K}_k \mathbf{H}_k \right) E\left[\in_{x,k-1} \right] - \mathbf{K}_k \mathbf{E}\left[v_k \right] \right\} \left\{ \cdots \right\}^T \right] \\ &= \left(\mathbf{I} - \mathbf{K}_k \mathbf{H}_k \right) E\left[\in_{x,k-1} \in_{x,k-1}^T \right] \left(\mathbf{I} - \mathbf{K}_k \mathbf{H}_k \right)^T - \mathbf{K}_k E\left[\mathbf{v}_k \in_{x,k-1}^T \right] \left(\mathbf{I} - \mathbf{K}_k \mathbf{H}_k \right)^T - \\ &\quad \left(\mathbf{I} - \mathbf{K}_k \mathbf{H}_k \right) E\left[\in_{x,k-1} v_k^T \right] \mathbf{K}_k^T + \mathbf{K}_k E\left[\mathbf{v}_k \mathbf{v}_k^T \right] \mathbf{K}_k^T \end{aligned} \tag{B.60}$$

But $\in_{x,k-1}$ is independent of $\mathbf{v}_k$, then

$$E\left[\mathbf{v}_k \in_{x,k-1}^T \right] = E\left[\mathbf{v}_k \right] E\left[\in_{x,k-1}^T \right] = 0 \tag{B.61}$$

and the following expression for $\mathbf{P}_{k|k}$ is obtained

$$\begin{aligned} \Rightarrow \mathbf{P}_{k|k} &= \left(\mathbf{I} - \mathbf{K}_k \mathbf{H}_k \right) \mathbf{P}_{k|k-1} \left(\mathbf{I} - \mathbf{K}_k \mathbf{H}_k \right)^T + \mathbf{K}_k \mathbf{R}_k \mathbf{K}_k^T \\ &= \left[\left(\mathbf{P}_{k|k-1} \right)^{-1} + \mathbf{H}_k^T \mathbf{R}_k^{-1} \mathbf{H}_k \right]^{-1} \\ &= \left(\mathbf{I} - \mathbf{K}_k \mathbf{H}_k \right) \mathbf{P}_{k|k-1} \end{aligned} \tag{B.62}$$

Optimality condition of the Kalman gain

Let,

$$J_k = E\left[\epsilon_{x,k}^{+\,T}\epsilon_{x,k}^{+}\right] = E\left[tr\left(\epsilon_{x,k}^{+}\epsilon_{x,k}^{+\,T}\right)\right] = tr\left(\mathbf{P}_{k|k}\right) \tag{B.63}$$

but

$$\begin{aligned}&\mathbf{P}_{k|k} = \mathbf{P}_{k|k-1} - \mathbf{K}_k\mathbf{H}_k\mathbf{P}_{k|k-1} - \mathbf{P}_{k|k-1}\mathbf{H}_k^T\mathbf{K}_k^T + \mathbf{K}_k\left(\mathbf{H}_k\mathbf{P}_{k|k-1}\mathbf{H}_k^T + \mathbf{R}_k\right)\mathbf{K}_k^T \\ &\Rightarrow \frac{\partial J_k}{\partial \mathbf{K}_k} = \mathbf{0} \Rightarrow -2\mathbf{P}_{k|k-1}\mathbf{H}_k^T + 2\mathbf{K}_k\left(\mathbf{H}_k\mathbf{P}_{k|k-1}\mathbf{H}_k^T + \mathbf{R}_k\right) = \mathbf{0}\end{aligned} \tag{B.64}$$

$$\begin{aligned}\Rightarrow \mathbf{K}_k &= \mathbf{P}_{k|k-1}\mathbf{H}_k^T\left(\mathbf{H}_k\mathbf{P}_{k|k-1}\mathbf{H}_k^T + \mathbf{R}_k\right)^{-1} \\ &= \mathbf{P}_{k|k}\mathbf{H}_k^T\mathbf{R}_k^{-1}\end{aligned} \tag{B.65}$$

B.6. Numerical integration: Gauss-Hermite and Unscented transformation

In the Bayesian approach for Gaussian approximation (Section B.3), integrals of the form $\mathbf{I} = \int \mathbf{g}(\mathbf{x})\mathcal{N}\left(\mathbf{x};\hat{\mathbf{x}},\mathbf{P}^{xx}\right)d\mathbf{x}$ need to be solved. Note that

$$\mathbf{I} = \int \mathbf{g}(\mathbf{x})\frac{1}{\left[(2\pi)^n\left\|\boldsymbol{\Sigma}\right\|\right]^{1/2}}\exp\left[-\frac{1}{2}\left(\mathbf{x}-\hat{\mathbf{x}}\right)\boldsymbol{\Sigma}^{-1}\left(\mathbf{x}-\hat{\mathbf{x}}\right)^T\right]d\mathbf{x} \tag{B.66}$$

Let $\boldsymbol{\Sigma} = \mathbf{S}^T\mathbf{S}$ and $\mathbf{z} = \frac{1}{\sqrt{2}}\mathbf{S}^{-1}\left(\mathbf{x}-\hat{\mathbf{x}}\right)$, then

$$\Rightarrow \mathbf{I} = \frac{\sqrt{2}}{(2\pi)^{n/2}}\int \mathbf{g}(\mathbf{z})\mathrm{e}^{-\mathbf{z}^T\mathbf{z}}\,d\mathbf{z} \tag{B.67}$$

For n=1 (univariate Gaussian PDF) $\mathbf{z} = \frac{\mathbf{x}-\hat{\mathbf{x}}}{\sigma\sqrt{2}}$, then

$$\Rightarrow I_1 = \pi^{-1/2} \int_{-\infty}^{\infty} f(z) e^{-z^2} dz \tag{B.68}$$

But $\int_{-\infty}^{\infty} f(z) e^{-z^2} dz \approx \sum_{i=1}^{M} w_i \, f(z_i)$: Gauss-Hermite (GH) quadrature.

Let's generate a set of orthonormal polynomials $H_j(z)$,

$$\begin{aligned} &H_{-1}(z) = 0 \qquad H_0(z) = \frac{1}{\pi^{1/4}} \\ &H_{j+1}(z) = z\sqrt{\frac{2}{j+1}} H_j(z) - \sqrt{\frac{j}{j+1}} H_{j-1}(z) \qquad j=0,...,M \end{aligned} \tag{B.69}$$

Let $\beta_j = \sqrt{j/2} \Rightarrow z H_j(z) = \beta_j H_{j-1}(z) + \beta_{j+1} H_{j+1}(z)$

In matrix form:

$$z\mathbf{h}(z) = \mathbf{J}_M \mathbf{h}(z) + \beta_M H_M(z) \mathbf{e}_M \tag{B.70}$$

where $\mathbf{h}(z) = \left[H_0(z), ..., H_{M-1}(z) \right]^T \qquad (M \times 1)$

$$\mathbf{e}_M = [0, 0, ..., 1]^T \qquad (M \times 1)$$

$$\mathbf{J}_M = \begin{bmatrix} 0 & \beta_1 & & & \\ \beta_1 & 0 & \beta_2 & \mathbf{0} & \\ & \beta_2 & \ddots & \ddots & \\ & \mathbf{0} & \ddots & 0 & \beta_{M-1} \\ & & & \beta_{M-1} & 0 \end{bmatrix} \text{ tridiagonal}$$

If (B.70) is evaluated for values of z such that $H_M(z) = 0 \Rightarrow z\mathbf{h}(z) = \mathbf{J}_M \mathbf{h}(z)$

$\Rightarrow \mathbf{h}(z)$ is an eigenvector of $\mathbf{J}_M$ if $H_M(z) = 0$.

These eigenvectors are: $v_j^i = \frac{H_j(z_i)}{\sqrt{W_i}}$ where $W_i = \sum_{j=0}^{M-1} \left[H_j(z_i) \right]^2$

The ortoghonality condition of the eigenvectors is

$$\sum_{j=0}^{M-1} v_j^i v_j^k = \delta_{ik} \tag{B.71}$$

The completeness condition of the eigenvectors is given by

$$\sum_{j=0}^{M} v_j^i v_l^i = \sum_{j=0}^{M} \frac{H_j(z_i) H_l(z_i)}{W_i} = \delta_{jl} \tag{B.72}$$

The ortoghonality condition of the Hermite polynomials is

$$\int_{-\infty}^{\infty} dz\, w(z)\, H_j(z) H_l(z) = \delta_{jl} \tag{B.73}$$

Then, the continuous-time versus discrete-time versions can be compared

Continuous-time	Discrete-time
$\int_{-\infty}^{\infty}$	$\sum_{i=1}^{M}$
$dz\, w(z)$	$1/W_i$

Notes:

- For products of polynomials up to order M, this quadrature gives exact results.
- $\int_{-\infty}^{\infty} H_M(z) H_{M-1}(z) w(z)\, dz = 0$ since $H_M(z) = 0$ on the nodes.
- Any polynomial of order $(2M-2)$ can be written as a sum of products of pairs of polynomials up to order $(M-1)$ $\rightarrow$ for any polynomial of order $(2M-1)$ or less, the quadrature is exact.

The previous formulation is one dimension. For the multivariate case, it must be applied sequentially (one variable at a time).

Example 1: $M = 3$ and n-dimensional vector

$$\begin{aligned} \Rightarrow \mathbf{I} &= \frac{\sqrt{2}}{(2\pi)^{n/2}} \int \mathbf{g}(\mathbf{z}) \mathrm{e}^{-\mathbf{z}^T \mathbf{z}} \, d\mathbf{z} \\ &= \sqrt{2} \sum_{i_1=1}^{3} \cdots \sum_{i_n=1}^{3} \mathbf{g}\left(x_{i_1}, \ldots, x_{i_n}\right) p_{i_1} \cdots p_{i_n} \end{aligned} \tag{B.74}$$

where $p_{i_n} = \dfrac{q_{i_n}}{\sqrt{2}}$

Example 2: $M = 3$ and univariate vector

$$\Rightarrow I_1 = \pi^{-1/2} \int_{-\infty}^{\infty} f(z) e^{-z^2} dz \approx \sum_{i=1}^{3} q_i \, f(x_i) = \sum_{j=0}^{2} q_j \, f(x_j) \tag{B.75}$$

where $z = \begin{bmatrix} -\sqrt{3}/2 \\ 0 \\ \sqrt{3}/2 \end{bmatrix}$, $q = \pi^{-1} w = \begin{bmatrix} 1/6 \\ 2/3 \\ 1/6 \end{bmatrix}$, $x_i = \hat{x} + \sqrt{2} z_i \sigma$

When $\mathbf{g}(\mathbf{z}) = 1$ in (B.74): $I = 1 \Rightarrow \tilde{p}_{j_i} = \dfrac{p_{j_i}}{\sqrt{2} \sum \cdots \sum p_{j_1} \cdots p_{j_n}}$

For a 2-D vector: $I_2 = \sum_{j=0}^{8} \mathbf{g}(\mathbf{x}_j) \alpha_j$

For a n-D vector: $I_n = \sum_{j=0}^{M^n - 1} \mathbf{g}(\mathbf{x}_j) \alpha_j$

where

$$\begin{aligned} \mathbf{x}_0 &= \hat{\mathbf{x}} \\ \mathbf{x}_j &= \hat{\mathbf{x}} + \sqrt{3} \left(\boldsymbol{\Sigma}^{1/2}\right)_j \qquad j=1,\ldots,n \\ \mathbf{x}_j &= \hat{\mathbf{x}} - \sqrt{3} \left(\boldsymbol{\Sigma}^{1/2}\right)_{j-n} \qquad j=n+1,\ldots,2n \\ \mathbf{x}_j &= \hat{\mathbf{x}} + H.O.T. \qquad j=2n+1,\ldots,M^n\text{-}1 \end{aligned}$$

The unscented transformation (UT) is a modified version that uses the first $(2n+1)$ terms of the GH quadrature,

$$\begin{aligned}
\mathbf{x}_0 &= \hat{\mathbf{x}} \\
\mathbf{x}_j &= \hat{\mathbf{x}} + \sqrt{\frac{n}{1-w_0}}\left(\boldsymbol{\Sigma}^{1/2}\right)_j \qquad j=1,\ldots,n \\
\mathbf{x}_j &= \hat{\mathbf{x}} - \sqrt{\frac{n}{1-w_0}}\left(\boldsymbol{\Sigma}^{1/2}\right)_j \qquad j=n+1,\ldots,2n
\end{aligned} \tag{B.76}$$

where $w_j = \dfrac{1-w_0}{2n} \qquad j=1,\ldots,2n$

In the GH the number of operations on each iteration is $\mathcal{O}\left(M^n\right)$ while in the UT the number of operations on each iteration is $\mathcal{O}(2n+1)$.

B.7. The Unscented transformation

In this section, the accuracy of the UT is investigated.

B.7.1. Taylor series expansion and notation

Let $\mathbf{x} \in \mathbb{R}^n$ and $\mathbf{g}(\mathbf{x})$ a vector-valued function:

$$\begin{aligned}
\mathbf{g}(\mathbf{x}) = \mathbf{g}(\bar{\mathbf{x}}) &+ \left[\left(x_1-\bar{x}_1\right)\frac{\partial}{\partial x_1} + \ldots + \left(x_n-\bar{x}_n\right)\frac{\partial}{\partial x_n}\right]^1 \mathbf{g}\big|_{\bar{\mathbf{x}}} \\
&+ \frac{1}{2!}\left[\left(x_1-\bar{x}_1\right)\frac{\partial}{\partial x_1} + \ldots + \left(x_n-\bar{x}_n\right)\frac{\partial}{\partial x_n}\right]^2 \mathbf{g}\big|_{\bar{\mathbf{x}}} + \ldots
\end{aligned} \tag{B.77}$$

Defining $\tilde{x}_i = x_i - \bar{x}_i$ where $\bar{x}_i = E[x_i]$

$$\mathbf{g}(\mathbf{x}) = \mathbf{g}(\bar{\mathbf{x}}) + \left[\tilde{x}_1 \frac{\partial}{\partial x_1} + \ldots + \tilde{x}_n \frac{\partial}{\partial x_n} \right]^1 \mathbf{g}\big|_{\bar{\mathbf{x}}} + \frac{1}{2!}\left[\tilde{x}_1 \frac{\partial}{\partial x_1} + \ldots + \tilde{x}_n \frac{\partial}{\partial x_n} \right]^2 \mathbf{g}\big|_{\bar{\mathbf{x}}} + \ldots \tag{B.78}$$

Defining the operator $D^k_{\tilde{\mathbf{x}}}\mathbf{g} = \left(\sum_{i=1}^{n} \tilde{x}_i \frac{\partial}{\partial x_i} \right)^k \mathbf{g}(\mathbf{x})\big|_{\bar{\mathbf{x}}}$

$$\Rightarrow \mathbf{g}(\mathbf{x}) = \mathbf{g}(\bar{\mathbf{x}}) + D^1_{\tilde{\mathbf{x}}}\mathbf{g} + \frac{1}{2!}D^2_{\tilde{\mathbf{x}}}\mathbf{g} + \frac{1}{3!}D^3_{\tilde{\mathbf{x}}}\mathbf{g} + \ldots \tag{B.79}$$

B.7.2. Nonlinear transformation of a random vector

Consider a nonlinear function $\mathbf{y} = \mathbf{h}(\mathbf{x})$ where $\mathbf{x}$ is a random vector and $\mathbf{h}$ is a vector-valued function.

Then, the Taylor series expansion of $\mathbf{y} = \mathbf{h}(\mathbf{x})$ around $\bar{\mathbf{x}}$ is

$$\mathbf{y} = \mathbf{h}(\mathbf{x}) = \mathbf{h}(\bar{\mathbf{x}}) + D^1_{\tilde{\mathbf{x}}}\mathbf{h} + \frac{1}{2!}D^2_{\tilde{\mathbf{x}}}\mathbf{h} + \frac{1}{3!}D^3_{\tilde{\mathbf{x}}}\mathbf{h} + \ldots \tag{B.80}$$

where $\tilde{\mathbf{x}} = \mathbf{x} - \bar{\mathbf{x}}$.

i. True (exact) mean of y

$$\begin{aligned} \bar{\mathbf{y}} &= E\left[\mathbf{h}(\mathbf{x})\right] = E\left[\mathbf{h}(\bar{\mathbf{x}}) + D^1_{\tilde{\mathbf{x}}}\mathbf{h} + \frac{1}{2!}D^2_{\tilde{\mathbf{x}}}\mathbf{h} + \frac{1}{3!}D^3_{\tilde{\mathbf{x}}}\mathbf{h} + \ldots \right] \\ \Rightarrow \bar{\mathbf{y}} &= \mathbf{h}(\bar{\mathbf{x}}) + E\left[D^1_{\tilde{\mathbf{x}}}\mathbf{h} + \frac{1}{2!}D^2_{\tilde{\mathbf{x}}}\mathbf{h} + \frac{1}{3!}D^3_{\tilde{\mathbf{x}}}\mathbf{h} + \ldots \right] \end{aligned} \tag{B.81}$$

But $E\left[D^1_{\tilde{\mathbf{x}}}\mathbf{h}\right] = E\left[\sum_{i=1}^{n} \tilde{x}_i \frac{\partial}{\partial x_i}\mathbf{h}(\mathbf{x})\big|_{\bar{\mathbf{x}}} \right] = \sum_{i=1}^{n} E\left[\tilde{x}_i\right] \frac{\partial}{\partial x_i}\mathbf{h}(\mathbf{x})\big|_{\bar{\mathbf{x}}} = \mathbf{0}$. Similarly,

$E\left[D^3_{\tilde{\mathbf{x}}}\mathbf{h}\right] = E\left[\left(\sum_{i=1}^{n} \tilde{x}_i \frac{\partial}{\partial x_i} \right)^3 \mathbf{h}(\mathbf{x})\big|_{\bar{\mathbf{x}}} \right]$.

i.1. For a random vector $\mathbf{x}$ with zero mean and symmetric PDF ($\mathbf{f}_{\mathbf{x}}(\mathbf{x}) = \mathbf{f}_{\mathbf{x}}(-\mathbf{x})$)

$$\Rightarrow \mathbf{m}_k = E\left[\mathbf{x}^k\right] = \int_{-\infty}^{\infty} \mathbf{x}^k \, \mathbf{f}_{\mathbf{x}}(\mathbf{x}) d\mathbf{x} = \int_{-\infty}^{0} \mathbf{x}^k \, \mathbf{f}_{\mathbf{x}}(\mathbf{x}) d\mathbf{x} + \int_{0}^{\infty} \mathbf{x}^k \, \mathbf{f}_{\mathbf{x}}(\mathbf{x}) d\mathbf{x} \tag{B.82}$$

If k is odd $\mathbf{x}^k = -(-\mathbf{x}^k)$, then

$$\begin{aligned} \mathbf{m}_k = E\left[\mathbf{x}^k\right] &= \int_{-\infty}^{0} \mathbf{x}^k \, \mathbf{f}_{\mathbf{x}}(\mathbf{x}) d\mathbf{x} + \int_{0}^{\infty} \mathbf{x}^k \, \mathbf{f}_{\mathbf{x}}(\mathbf{x}) d\mathbf{x} \\ &= \int_{0}^{\infty} (-\mathbf{x})^k \, \mathbf{f}_{\mathbf{x}}(-\mathbf{x}) d\mathbf{x} + \int_{0}^{\infty} \mathbf{x}^k \, \mathbf{f}_{\mathbf{x}}(\mathbf{x}) d\mathbf{x} \\ &= -\int_{-\infty}^{0} \mathbf{x}^k \, \mathbf{f}_{\mathbf{x}}(\mathbf{x}) d\mathbf{x} + \int_{0}^{\infty} \mathbf{x}^k \, \mathbf{f}_{\mathbf{x}}(\mathbf{x}) d\mathbf{x} = 0 \end{aligned} \tag{B.83}$$

It can be observed that $E\left[D_{\tilde{\mathbf{x}}}^3 \mathbf{h}\right] = 0$ because in the sum there are only 3rd order terms ($E\left[\tilde{x}_1^3\right], E\left[\tilde{x}_1^2 \tilde{x}_2\right], \ldots$). Similarly, $E\left[D_{\tilde{\mathbf{x}}}^m \mathbf{h}\right] = 0 \quad \forall\, m$ odd.

Therefore, the true mean of a random vector with zero mean and symmetric PDF can be expressed as

$$\Rightarrow \bar{\mathbf{y}} = E\left[\mathbf{h}(\mathbf{x})\right] = \mathbf{h}(\bar{\mathbf{x}}) + \frac{1}{2!} E\left[D_{\tilde{\mathbf{x}}}^2 \mathbf{h}\right] + \frac{1}{4!} E\left[D_{\tilde{\mathbf{x}}}^4 \mathbf{h}\right] + \ldots \tag{B.84}$$

But

$$\begin{aligned} \frac{1}{2!} E\left[D_{\tilde{\mathbf{x}}}^2 \mathbf{h}\right] &= \frac{1}{2!} E\left[\left(\sum_{i=1}^{n} \tilde{x}_i \frac{\partial}{\partial x_i}\right)^2 \mathbf{h}(\mathbf{x})\Big|_{\mathbf{x}=\bar{\mathbf{x}}}\right] = \frac{1}{2!} E\left[\left(\sum_{i,j=1}^{n} \tilde{x}_i \tilde{x}_j \frac{\partial^2 \mathbf{h}}{\partial x_i \, \partial x_j}\Big|_{\mathbf{x}=\bar{\mathbf{x}}}\right)\right] \\ &= \frac{1}{2!} \sum_{i,j=1}^{n} E\left[\tilde{x}_i \tilde{x}_j\right] \frac{\partial^2 \mathbf{h}}{\partial x_i \, \partial x_j}\Big|_{\mathbf{x}=\bar{\mathbf{x}}} = \frac{1}{2} \sum_{i,j=1}^{n} \mathbf{P}_{ij} \frac{\partial^2 \mathbf{h}}{\partial x_i \, \partial x_j}\Big|_{\mathbf{x}=\bar{\mathbf{x}}} \end{aligned} \tag{B.85}$$

Therefore, the true mean is given by

$$\bar{\mathbf{y}} = E\left[\mathbf{h}\left(\mathbf{x}\right)\right] = \mathbf{h}\left(\bar{\mathbf{x}}\right) + \frac{1}{2}\sum_{i,j=1}^{n} \mathbf{P}_{ij} \left.\frac{\partial^2 \mathbf{h}}{\partial x_i \, \partial x_j}\right|_{\mathbf{x}=\bar{\mathbf{x}}} + \frac{1}{4!} E\left[D_{\tilde{\mathbf{x}}}^4 \mathbf{h}\right] + \ldots \tag{B.86}$$

ii. True (exact) covariance matrix of $\mathbf{y}$

$$\mathbf{P}_{\mathbf{y}} = E\left[\left(\mathbf{y}-\bar{\mathbf{y}}\right)\left(\mathbf{y}-\bar{\mathbf{y}}\right)^T\right] \tag{B.87}$$

But

$$\begin{aligned}
\left(\mathbf{y}-\bar{\mathbf{y}}\right) &= \left(\mathbf{h}\left(\bar{\mathbf{x}}\right) + D_{\tilde{\mathbf{x}}}^1 \mathbf{h} + \frac{1}{2!} D_{\tilde{\mathbf{x}}}^2 \mathbf{h} + \frac{1}{3!} D_{\tilde{\mathbf{x}}}^3 \mathbf{h} + \ldots\right) - \\
&\quad \left(\mathbf{h}\left(\bar{\mathbf{x}}\right) + E\left[D_{\tilde{\mathbf{x}}}^1 \mathbf{h}\right] + \frac{1}{2!} E\left[D_{\tilde{\mathbf{x}}}^2 \mathbf{h}\right] + \frac{1}{3!} E\left[D_{\tilde{\mathbf{x}}}^3 \mathbf{h}\right] + \ldots\right) \\
\Rightarrow \left(\mathbf{y}-\bar{\mathbf{y}}\right) &= \left(D_{\tilde{\mathbf{x}}}^1 \mathbf{h} + \frac{1}{2!} D_{\tilde{\mathbf{x}}}^2 \mathbf{h} + \frac{1}{3!} D_{\tilde{\mathbf{x}}}^3 \mathbf{h} + \ldots\right) - \\
&\quad \left(E\left[D_{\tilde{\mathbf{x}}}^1 \mathbf{h}\right] + \frac{1}{2!} E\left[D_{\tilde{\mathbf{x}}}^2 \mathbf{h}\right] + \frac{1}{3!} E\left[D_{\tilde{\mathbf{x}}}^3 \mathbf{h}\right] + \ldots\right)
\end{aligned} \tag{B.88}$$

ii.1. For a random vector $\mathbf{x}$ with zero mean and symmetric PDF ($\mathbf{f}_{\mathbf{x}}\left(\mathbf{x}\right) = \mathbf{f}_{\mathbf{x}}\left(-\mathbf{x}\right)$)

$$\Rightarrow \left(\mathbf{y}-\bar{\mathbf{y}}\right) = \left(D_{\tilde{\mathbf{x}}}^1 \mathbf{h} + \frac{1}{2!} D_{\tilde{\mathbf{x}}}^2 \mathbf{h} + \frac{1}{3!} D_{\tilde{\mathbf{x}}}^3 \mathbf{h} + \ldots\right) - \left(\frac{1}{2!} E\left[D_{\tilde{\mathbf{x}}}^2 \mathbf{h}\right] + \frac{1}{4!} E\left[D_{\tilde{\mathbf{x}}}^4 \mathbf{h}\right] + \ldots\right) \tag{B.89}$$

$$\Rightarrow \mathbf{P}_{\mathbf{y}} = E\left[\left\{\left(D_{\tilde{\mathbf{x}}}^1 \mathbf{h} + \frac{1}{2!} D_{\tilde{\mathbf{x}}}^2 \mathbf{h} + \ldots\right) - \left(\frac{1}{2!} E\left[D_{\tilde{\mathbf{x}}}^2 \mathbf{h}\right] + \frac{1}{4!} E\left[D_{\tilde{\mathbf{x}}}^4 \mathbf{h}\right] + \ldots\right)\right\}\left\{\cdots\right\}^T\right] \tag{B.90}$$

If the PDF is symmetric and $\tilde{\mathbf{x}} = \mathbf{x} - \bar{\mathbf{x}}$ is zero-mean, all the odd powered terms will be zero. Then,

$$\begin{aligned}
\Rightarrow \mathbf{P}_{\mathbf{y}} &= E\left[D_{\tilde{\mathbf{x}}}^1 \mathbf{h}\left(D_{\tilde{\mathbf{x}}}^1 \mathbf{h}\right)^T\right] + E\left[\frac{D_{\tilde{\mathbf{x}}}^1 \mathbf{h}\left(D_{\tilde{\mathbf{x}}}^3 \mathbf{h}\right)^T}{3!} + \frac{D_{\tilde{\mathbf{x}}}^2 \mathbf{h}\left(D_{\tilde{\mathbf{x}}}^2 \mathbf{h}\right)^T}{2!\,2!} + \frac{D_{\tilde{\mathbf{x}}}^3 \mathbf{h}\left(D_{\tilde{\mathbf{x}}}^1 \mathbf{h}\right)^T}{3!}\right] + \\
&\quad E\left[\frac{D_{\tilde{\mathbf{x}}}^2 \mathbf{h}}{2!}\right] E\left[\frac{\left(D_{\tilde{\mathbf{x}}}^2 \mathbf{h}\right)^T}{2!}\right] + \ldots
\end{aligned} \tag{B.91}$$

Note that

$$
\begin{aligned}
E\left[D_{\tilde{\mathbf{x}}}^{1}\mathbf{h}\left(D_{\tilde{\mathbf{x}}}^{1}\mathbf{h}\right)^{T}\right] &= E\left[\left(\sum_{i=1}^{n}\tilde{x}_i\left.\frac{\partial\mathbf{h}}{\partial x_i}\right|_{\bar{\mathbf{x}}}\right)\left(\sum_{i=1}^{n}\tilde{x}_i\left.\frac{\partial\mathbf{h}}{\partial x_i}\right|_{\bar{\mathbf{x}}}\right)^{T}\right] \\
&= E\left[\sum_{i,j=1}^{n}\tilde{x}_i\left.\frac{\partial\mathbf{h}}{\partial x_i}\right|_{\bar{\mathbf{x}}}\left.\frac{\partial\mathbf{h}^{T}}{\partial x_j}\right|_{\bar{\mathbf{x}}}\tilde{x}_j\right] \\
&= \sum_{i,j=1}^{n}\mathbf{H}_i\,E\left[\tilde{x}_i\tilde{x}_j\right]\mathbf{H}_j \\
&= \sum_{i,j=1}^{n}\mathbf{H}_i\,\mathbf{P}_{ij}\,\mathbf{H}_j
\end{aligned}
\tag{B.92}
$$

where $\mathbf{H}_i = \left.\frac{\partial\mathbf{h}}{\partial x_i}\right|_{\bar{\mathbf{x}}}$.

Therefore, the true covariance matrix of a random vector with symmetric PDF can be expressed as

$$
\begin{aligned}
\Rightarrow \mathbf{P}_{\mathbf{y}} = \mathbf{H}\mathbf{P}\mathbf{H}^{T} + E\left[\frac{D_{\tilde{\mathbf{x}}}^{1}\mathbf{h}\left(D_{\tilde{\mathbf{x}}}^{3}\mathbf{h}\right)^{T}}{3!} + \frac{D_{\tilde{\mathbf{x}}}^{2}\mathbf{h}\left(D_{\tilde{\mathbf{x}}}^{2}\mathbf{h}\right)^{T}}{2!\,2!} + \frac{D_{\tilde{\mathbf{x}}}^{3}\mathbf{h}\left(D_{\tilde{\mathbf{x}}}^{1}\mathbf{h}\right)^{T}}{3!}\right] + \\
E\left[\frac{D_{\tilde{\mathbf{x}}}^{2}\mathbf{h}}{2!}\right]E\left[\frac{\left(D_{\tilde{\mathbf{x}}}^{2}\mathbf{h}\right)^{T}}{2!}\right] + \ldots
\end{aligned}
\tag{B.93}
$$

iii. Unscented transformation

Premises:

1. It is easy to perform a nonlinear transformation on a single point (rather than an entire PDF).
2. It is not too hard to find a set of individual points in state-space whose sample PDF approximates the true PDF of a state vector.

Idea:

1. Find a set of deterministic vectors (sigma points) whose ensemble mean and ensemble covariance are equal to the mean and covariance of a vector **x**.
2. Apply the known nonlinear function $\mathbf{y}=\mathbf{h}(\mathbf{x})$ to each sigma point to obtain transformed vectors.
3. Compute the ensemble mean and covariance of the transformed vectors which are an estimate of the true mean and covariance of **y**.

iii.1. Basic Unscented transformation

Sigma points (SPs):

$$\begin{aligned}
&\boldsymbol{\chi}^{(i)}=\bar{\mathbf{x}}+\tilde{\mathbf{x}}^{(i)} \quad i=1,\ldots,2n\\
&\tilde{\mathbf{x}}^{(i)}=\left(\sqrt{n\mathbf{P}}\right)_i^T \quad i=1,\ldots,n\\
&\tilde{\mathbf{x}}^{(n+i)}=-\left(\sqrt{n\mathbf{P}}\right)_i^T \quad i=1,\ldots,n\\
&\text{Weights}: W_c^{(i)}=W_m^{(i)}=\frac{1}{2n}
\end{aligned} \tag{B.94}$$

where $\left(\sqrt{n\mathbf{P}}\right)^T\sqrt{n\mathbf{P}}=n\mathbf{P}$ (square-root matrix) and $\left(\sqrt{n\mathbf{P}}\right)_i$: ith row of $\sqrt{n\mathbf{P}}$

- ✓ Sample mean of the sigma points:

$$\frac{1}{2n}\sum_{i=1}^{2n}\boldsymbol{\chi}^{(i)}=\frac{1}{2n}\left[n\bar{\mathbf{x}}+\sum_{i=1}^{n}\left(\sqrt{n\mathbf{P}}\right)_i^T+n\bar{\mathbf{x}}-\sum_{i=n+1}^{2n}\left(\sqrt{n\mathbf{P}}\right)_{i-n}^T\right]=\frac{1}{2n}\left(2n\bar{\mathbf{x}}\right)=\bar{\mathbf{x}} \tag{B.95}$$

- ✓ Sample covariance of the sigma points: (maximum likelihood estimation for Gaussian distribution)

$$\frac{1}{2n}\sum_{i=1}^{2n}\left(\boldsymbol{\chi}^{(i)}-\bar{\mathbf{x}}\right)\left(\boldsymbol{\chi}^{(i)}-\bar{\mathbf{x}}\right)^{T}=\frac{1}{2n}\sum_{i=1}^{2n}\left(\tilde{\mathbf{x}}^{(i)}\right)\left(\tilde{\mathbf{x}}^{(i)}\right)^{T}=\frac{1}{2n}\left(\sum_{i=1}^{2n}\left(\sqrt{n\mathbf{P}}\right)_{i}^{T}\left(\sqrt{n\mathbf{P}}\right)_{i}\right)$$
$$=\frac{1}{2n}\left(\sum_{i=1}^{n}\left(\sqrt{n\mathbf{P}}\right)_{i}^{T}\left(\sqrt{n\mathbf{P}}\right)_{i}+\sum_{i=n+1}^{2n}\left(\sqrt{n\mathbf{P}}\right)_{i-n}^{T}\left(\sqrt{n\mathbf{P}}\right)_{i-n}\right)=\frac{1}{2n}\left(n\mathbf{P}+n\mathbf{P}\right)=\mathbf{P} \tag{B.96}$$

✓ Mean approximation: The SPs are propagated through the nonlinear function

$$\boldsymbol{\mathcal{Y}}^{(i)}=\mathbf{h}\left(\boldsymbol{\chi}^{(i)}\right) \tag{B.97}$$

with $i=1,...,2n$. Then,

$$\bar{\mathbf{y}}_{u}=\sum_{i=1}^{2n}W_{m}^{(i)}\boldsymbol{\mathcal{Y}}^{(i)}=\frac{1}{2n}\sum_{i=1}^{2n}\boldsymbol{\mathcal{Y}}^{(i)}=\frac{1}{2n}\sum_{i=1}^{2n}\left(\mathbf{h}\left(\bar{\mathbf{x}}\right)+D_{\tilde{\mathbf{x}}^{(i)}}^{1}\mathbf{h}+\frac{1}{2!}D_{\tilde{\mathbf{x}}^{(i)}}^{2}\mathbf{h}+\frac{1}{3!}D_{\tilde{\mathbf{x}}^{(i)}}^{3}\mathbf{h}+....\right)$$
$$=\mathbf{h}\left(\bar{\mathbf{x}}\right)+\frac{1}{2n}\sum_{i=1}^{2n}\left(D_{\tilde{\mathbf{x}}^{(i)}}^{1}\mathbf{h}+\frac{1}{2!}D_{\tilde{\mathbf{x}}^{(i)}}^{2}\mathbf{h}+\frac{1}{3!}D_{\tilde{\mathbf{x}}^{(i)}}^{3}\mathbf{h}+....\right) \tag{B.98}$$

For an integer $k\geq 0$:

$$\sum_{j=1}^{2n}D_{\tilde{\mathbf{x}}^{(j)}}^{2k+1}\mathbf{h}=\sum_{j=1}^{2n}\left[\left(\sum_{i=1}^{n}\tilde{x}_{i}^{(j)}\frac{\partial}{\partial x_{i}}\right)^{2k+1}\mathbf{h}\left(\mathbf{x}\right)\Big|_{\mathbf{x}=\bar{\mathbf{x}}}\right]$$
$$=\sum_{j=1}^{2n}\left[\left(\sum_{i=1}^{n}\tilde{x}_{i}^{(j)}\right)^{2k+1}\frac{\partial^{2k+1}\mathbf{h}\left(\mathbf{x}\right)}{\partial x_{i}^{2k+1}}\Big|_{\mathbf{x}=\bar{\mathbf{x}}}\right] \tag{B.99}$$
$$=\sum_{i=1}^{n}\left[\left(\sum_{j=1}^{2n}\tilde{x}_{i}^{(j)}\right)^{2k+1}\frac{\partial^{2k+1}\mathbf{h}\left(\mathbf{x}\right)}{\partial x_{i}^{2k+1}}\Big|_{\mathbf{x}=\bar{\mathbf{x}}}\right]$$

But, $\tilde{\mathbf{x}}^{(j)}=-\tilde{\mathbf{x}}^{(n+j)}\quad j=1,...,n$

$$\Rightarrow\sum_{j=1}^{2n}D_{\tilde{\mathbf{x}}^{(j)}}^{2k+1}\mathbf{h}=\sum_{i=1}^{n}\left[\left(\sum_{j=1}^{n}\tilde{x}_{i}^{(j)}\right)^{2k+1}\frac{\partial^{2k+1}\mathbf{h}\left(\mathbf{x}\right)}{\partial x_{i}^{2k+1}}\Big|_{\mathbf{x}=\bar{\mathbf{x}}}-\left(\sum_{j=1}^{n}\tilde{x}_{i}^{(j)}\right)^{2k+1}\frac{\partial^{2k+1}\mathbf{h}\left(\mathbf{x}\right)}{\partial x_{i}^{2k+1}}\Big|_{\mathbf{x}=\bar{\mathbf{x}}}\right] \tag{B.100}$$
$$\Rightarrow\sum_{j=1}^{2n}D_{\tilde{\mathbf{x}}^{(j)}}^{2k+1}\mathbf{h}=0$$

$\therefore$ all odd terms are equal to zero in equation (B.98) for $\bar{\mathbf{y}}_u$.

$$\begin{aligned}\Rightarrow \bar{\mathbf{y}}_u &= \mathbf{h}(\bar{\mathbf{x}}) + \frac{1}{2n}\sum_{i=1}^{2n}\left(\frac{1}{2!}D^2_{\tilde{\mathbf{x}}^{(i)}}\mathbf{h} + \frac{1}{4!}D^4_{\tilde{\mathbf{x}}^{(i)}}\mathbf{h} + ...\right) \\ &= \mathbf{h}(\bar{\mathbf{x}}) + \frac{1}{2n}\sum_{i=1}^{2n}\frac{1}{2!}D^2_{\tilde{\mathbf{x}}^{(i)}}\mathbf{h} + \frac{1}{2n}\sum_{i=1}^{2n}\left(\frac{1}{4!}D^4_{\tilde{\mathbf{x}}^{(i)}}\mathbf{h} + \frac{1}{6!}D^6_{\tilde{\mathbf{x}}^{(i)}}\mathbf{h} + ...\right)\end{aligned} \tag{B.101}$$

In addition,

$$\begin{aligned}\frac{1}{2n}\sum_{i=1}^{2n}\frac{1}{2!}D^2_{\tilde{\mathbf{x}}^{(i)}}\mathbf{h} &= \frac{1}{2n}\sum_{k=1}^{2n}\frac{1}{2!}\left(\sum_{i=1}^{2n}\tilde{x}_i^{(k)}\frac{\partial}{\partial x_i}\right)^2\mathbf{h}(\mathbf{x})\Big|_{\mathbf{x}=\bar{\mathbf{x}}} \\ &= \frac{1}{4n}\sum_{k=1}^{2n}\sum_{i,j=1}^{2n}\tilde{x}_i^{(k)}\tilde{x}_j^{(k)}\frac{\partial^2\mathbf{h}(\mathbf{x})}{\partial x_i\partial x_j}\Big|_{\mathbf{x}=\bar{\mathbf{x}}} \\ &= \frac{1}{4n}\sum_{i,j=1}^{2n}\sum_{k=1}^{2n}\tilde{x}_i^{(k)}\tilde{x}_j^{(k)}\frac{\partial^2\mathbf{h}(\mathbf{x})}{\partial x_i\partial x_j}\Big|_{\mathbf{x}=\bar{\mathbf{x}}} \\ &= \frac{1}{2n}\sum_{i,j=1}^{n}\sum_{k=1}^{n}\tilde{x}_i^{(k)}\tilde{x}_j^{(k)}\frac{\partial^2\mathbf{h}(\mathbf{x})}{\partial x_i\partial x_j}\Big|_{\mathbf{x}=\bar{\mathbf{x}}} \quad \text{since } \tilde{x}_i^{(k)} = -\tilde{x}_i^{(k+n)} \quad k = 1,...,n \\ &= \frac{1}{2n}\sum_{i,j=1}^{n}\sum_{k=1}^{n}\left(\sqrt{n\mathbf{P}}\right)_{ki}\left(\sqrt{n\mathbf{P}}\right)_{kj}\frac{\partial^2\mathbf{h}(\mathbf{x})}{\partial x_i\partial x_j}\Big|_{\mathbf{x}=\bar{\mathbf{x}}} \\ &= \frac{1}{2n}\sum_{i,j=1}^{n}n\,\mathbf{P}_{ij}\frac{\partial^2\mathbf{h}(\mathbf{x})}{\partial x_i\partial x_j}\Big|_{\mathbf{x}=\bar{\mathbf{x}}} \\ &= \frac{1}{2}\sum_{i,j=1}^{n}\mathbf{P}_{ij}\frac{\partial^2\mathbf{h}(\mathbf{x})}{\partial x_i\partial x_j}\Big|_{\mathbf{x}=\bar{\mathbf{x}}}\end{aligned} \tag{B.102}$$

Then, the approximated mean can be expressed as

$$\Rightarrow \bar{\mathbf{y}}_u = \mathbf{h}\left(\bar{\mathbf{x}}\right) + \frac{1}{2}\sum_{i,j=1}^{n} \mathbf{P}_{ij} \left.\frac{\partial^2 \mathbf{h}\left(\mathbf{x}\right)}{\partial x_i \partial x_j}\right|_{\mathbf{x}=\bar{\mathbf{x}}} + \frac{1}{2n}\sum_{i=1}^{2n}\left(\frac{1}{4!}D^4_{\tilde{\mathbf{x}}^{(i)}}\mathbf{h} + \frac{1}{6!}D^6_{\tilde{\mathbf{x}}^{(i)}}\mathbf{h} + \ldots\right) \tag{B.103}$$

Comparing (B.86) and (B.103) it is concluded that the approximated mean, $\bar{\mathbf{y}}_u$, matches the true mean up to the third order of the Taylor Series expansion if $\mathbf{x}$ has zero-mean and a symmetric PDF.

✓ Covariance approximation:

$$\mathbf{P}_u = \sum_{i=1}^{2n} W_c^{(i)} \left(\mathcal{Y}^{(i)} - \mathbf{y}_u\right)\left(\mathcal{Y}^{(i)} - \mathbf{y}_u\right)^T = \sum_{i=1}^{2n} W_c^{(i)} \left(\mathbf{h}\left(\mathcal{X}^{(i)}\right) - \mathbf{y}_u\right)\left(\mathbf{h}\left(\mathcal{X}^{(i)}\right) - \mathbf{y}_u\right)^T$$

$$\mathbf{P}_u = \frac{1}{2n}\sum_{i=1}^{2n}\left[\begin{array}{l} \mathbf{h}\left(\bar{\mathbf{x}}\right) + D^1_{\tilde{\mathbf{x}}^{(i)}}\mathbf{h} + \frac{1}{2!}D^2_{\tilde{\mathbf{x}}^{(i)}}\mathbf{h} + \frac{1}{3!}D^3_{\tilde{\mathbf{x}}^{(i)}}\mathbf{h} + ... - \mathbf{h}\left(\bar{\mathbf{x}}\right) - \\ \frac{1}{2n}\sum_{j=1}^{2n}\left(\frac{1}{2!}D^2_{\tilde{\mathbf{x}}^{(j)}}\mathbf{h} + \frac{1}{4!}D^4_{\tilde{\mathbf{x}}^{(j)}}\mathbf{h} + ...\right) \end{array}\right]\left[\ldots\right]^T$$

$$\begin{aligned} \mathbf{P}_u = \frac{1}{2n}\sum_{i=1}^{2n}\Bigg\{ & \left(D^1_{\tilde{\mathbf{x}}^{(i)}}\mathbf{h}\right)\left(D^1_{\tilde{\mathbf{x}}^{(i)}}\mathbf{h}\right)^T + \cancel{\left[\frac{1}{2}\left(D^1_{\tilde{\mathbf{x}}^{(i)}}\mathbf{h}\right)\left(D^2_{\tilde{\mathbf{x}}^{(i)}}\mathbf{h}\right)^T\right]} + \cancel{\left[\frac{1}{2}\left(D^1_{\tilde{\mathbf{x}}^{(i)}}\mathbf{h}\right)\left(D^2_{\tilde{\mathbf{x}}^{(i)}}\mathbf{h}\right)^T\right]^T} + \\ & \frac{1}{4}\left(D^2_{\tilde{\mathbf{x}}^{(i)}}\mathbf{h}\right)\left(D^2_{\tilde{\mathbf{x}}^{(i)}}\mathbf{h}\right)^T - \cancel{\left(D^1_{\tilde{\mathbf{x}}^{(i)}}\mathbf{h}\right)\left(\frac{1}{2n}\sum_{j=1}^{2n}\frac{1}{2}D^2_{\tilde{\mathbf{x}}^{(j)}}\mathbf{h}\right)^T} - \cancel{\left[\left(D^1_{\tilde{\mathbf{x}}^{(i)}}\mathbf{h}\right)\left(\frac{1}{2n}\sum_{j=1}^{2n}\frac{1}{2}D^2_{\tilde{\mathbf{x}}^{(j)}}\mathbf{h}\right)^T\right]^T} + \\ & \frac{1}{4n^2}\left(\sum_{j=1}^{2n}\frac{1}{2}D^2_{\tilde{\mathbf{x}}^{(j)}}\mathbf{h}\right)\left(\sum_{k=1}^{2n}\frac{1}{2}D^2_{\tilde{\mathbf{x}}^{(k)}}\mathbf{h}\right)^T - \left[\frac{1}{4n}\left(D^2_{\tilde{\mathbf{x}}^{(i)}}\mathbf{h}\right)\left(\sum_{j=1}^{2n}\frac{1}{2}D^2_{\tilde{\mathbf{x}}^{(j)}}\mathbf{h}\right)^T\right] - \\ & \left[\frac{1}{4n}\left(D^2_{\tilde{\mathbf{x}}^{(i)}}\mathbf{h}\right)\left(\sum_{j=1}^{2n}\frac{1}{2}D^2_{\tilde{\mathbf{x}}^{(j)}}\mathbf{h}\right)^T\right]^T + \left[\left(D^1_{\tilde{\mathbf{x}}^{(i)}}\mathbf{h}\right)\left(\frac{1}{3!}D^3_{\tilde{\mathbf{x}}^{(i)}}\mathbf{h}\right)^T\right] + \left[\left(D^1_{\tilde{\mathbf{x}}^{(i)}}\mathbf{h}\right)\left(\frac{1}{3!}D^3_{\tilde{\mathbf{x}}^{(i)}}\mathbf{h}\right)^T\right]^T + \ldots \end{aligned} \tag{B.104}$$

But $\tilde{\mathbf{x}}^{(i)} = -\tilde{\mathbf{x}}^{(n+i)}$ i=1,...,n, therefore all odd powered terms are zero. Then,

$$\Rightarrow \mathbf{P}_u = \frac{1}{2n}\sum_{i=1}^{2n}\left(D^1_{\tilde{\mathbf{x}}^{(i)}}\mathbf{h}\right)\left(D^1_{\tilde{\mathbf{x}}^{(i)}}\mathbf{h}\right)^T + H.O.T. \tag{B.105}$$

where $H.O.T.$ are terms of order 4 and higher.

$$\Rightarrow \mathbf{P}_u = \frac{1}{2n}\sum_{i=1}^{2n}\sum_{j,k=1}^{n}\left(\tilde{x}_j^{(i)}\left.\frac{\partial \mathbf{h}}{\partial x_j}\right|_{\mathbf{x}=\bar{\mathbf{x}}}\right)\left(\tilde{x}_k^{(i)}\left.\frac{\partial \mathbf{h}}{\partial x_k}\right|_{\mathbf{x}=\bar{\mathbf{x}}}\right)^T + H.O.T. \tag{B.106}$$

But $\tilde{\mathbf{x}}_j^{(i)} = -\tilde{\mathbf{x}}_j^{(i+n)}$ *and* $\tilde{\mathbf{x}}_k^{(i)} = -\tilde{\mathbf{x}}_k^{(i+n)}$ $\quad i=1,\ldots,n$

$$\Rightarrow \mathbf{P}_u = \frac{1}{n}\sum_{i=1}^{n}\sum_{j,k=1}^{n}\left(\tilde{x}_j^{(i)}\left.\frac{\partial \mathbf{h}}{\partial x_j}\right|_{\mathbf{x}=\bar{\mathbf{x}}}\right)\left(\tilde{x}_k^{(i)}\left.\frac{\partial \mathbf{h}}{\partial x_k}\right|_{\mathbf{x}=\bar{\mathbf{x}}}\right)^T + H.O.T.$$

$$\Rightarrow \mathbf{P}_u = \frac{1}{n}\sum_{j,k=1}^{n}\sum_{i=1}^{n}\tilde{x}_j^{(i)}\left(\tilde{x}_k^{(i)}\right)^T\left.\frac{\partial \mathbf{h}}{\partial x_j}\right|_{\mathbf{x}=\bar{\mathbf{x}}}\left(\left.\frac{\partial \mathbf{h}}{\partial x_k}\right|_{\mathbf{x}=\bar{\mathbf{x}}}\right)^T + H.O.T. \tag{B.107}$$

$$\Rightarrow \mathbf{P}_u = \sum_{j,k=1}^{n}\mathbf{P}_{jk}\left.\frac{\partial \mathbf{h}}{\partial x_j}\right|_{\mathbf{x}=\bar{\mathbf{x}}}\left(\left.\frac{\partial \mathbf{h}}{\partial x_k}\right|_{\mathbf{x}=\bar{\mathbf{x}}}\right)^T + H.O.T.$$

Then, the approximated covariance can be expressed as

$$\Rightarrow \mathbf{P}_u = \mathbf{H}\mathbf{P}\mathbf{H}^T + H.O.T. \tag{B.108}$$

where $H.O.T.$ are terms of order 4 and higher.

Comparing (B.93) and (B.108) it is concluded that the approximated covariance matrix, $\mathbf{P}_u$, matches the true covariance of $\mathbf{y}$ up to the third order of the Taylor Series expansion if $\mathbf{x}$ has zero-mean and a symmetric PDF.

- ✓ Note: In the case that the PDF of $\mathbf{x}$ is not symmetric, the odd-powered terms are different to 0, and in particular terms of power 3 are not zero anymore. Then, the approximations of the mean and covariance match the true mean and covariance up to order 2.

B.8. The Scaled Unscented transformation

Let $\mathbf{x} \in \mathbb{R}^n$ a random vector with mean $\bar{\mathbf{x}}$ and covariance matrix $\mathbf{P}_{\mathbf{xx}}$. Let $\mathbf{x} = \bar{\mathbf{x}} + \boldsymbol{\delta}\mathbf{x}$ where $\boldsymbol{\delta}\mathbf{x}$ is a zero-mean random vector with covariance matrix $\mathbf{P}_{\mathbf{xx}}$. Then, a second random vector is defined by

$$\mathbf{y} = \mathbf{h}(\mathbf{x}) \tag{B.109}$$

Then,

$$\begin{aligned} \mathbf{y} = \mathbf{h}(\mathbf{x}) = \mathbf{h}(\bar{\mathbf{x}} + \boldsymbol{\delta}\mathbf{x}) &= \mathbf{h}(\bar{\mathbf{x}}) + \boldsymbol{\delta}\mathbf{x}\frac{\partial \mathbf{h}}{\partial \mathbf{x}}\bigg|_{\mathbf{x}=\bar{\mathbf{x}}} + \frac{1}{2!}\boldsymbol{\delta}\mathbf{x}^2\frac{\partial^2 \mathbf{h}}{\partial \mathbf{x}^2}\bigg|_{\mathbf{x}=\bar{\mathbf{x}}} + \frac{1}{3!}\boldsymbol{\delta}\mathbf{x}^3\frac{\partial^3 \mathbf{h}}{\partial \mathbf{x}^3}\bigg|_{\mathbf{x}=\bar{\mathbf{x}}} + \ldots \\ \mathbf{y} &= \mathbf{h}(\bar{\mathbf{x}}) + \nabla\mathbf{h}\,\boldsymbol{\delta}\mathbf{x} + \frac{1}{2!}\nabla^2\mathbf{h}\,\boldsymbol{\delta}\mathbf{x}^2 + \frac{1}{3!}\nabla^3\mathbf{h}\,\boldsymbol{\delta}\mathbf{x}^3 + \ldots \end{aligned} \tag{B.110}$$

Noting that $\boldsymbol{\delta}\mathbf{x}^j\frac{\partial^j \mathbf{h}}{\partial \mathbf{x}^j}\bigg|_{\mathbf{x}=\bar{\mathbf{x}}} = \nabla^j\mathbf{h}\,\boldsymbol{\delta}\mathbf{x}^j = \left[(x_1 - \bar{x}_1)\frac{\partial}{\partial x_1} + \ldots + (x_n - \bar{x}_n)\frac{\partial}{\partial x_n}\right]^j \mathbf{h}\big|_{\mathbf{x}=\bar{\mathbf{x}}}$, the mean and covariance matrix of $\mathbf{y}$ can be expressed as

$$\bar{\mathbf{y}} = \mathbf{h}(\bar{\mathbf{x}}) + \frac{1}{2!}\nabla^2\mathbf{h}\,\mathbf{P}_{\mathbf{xx}} + \frac{1}{3!}\nabla^3\mathbf{h}\,E\left[\boldsymbol{\delta}\mathbf{x}^3\right] + \ldots \tag{B.111}$$

$$\mathbf{P}_{\mathbf{yy}} = E\left[(\mathbf{y} - \bar{\mathbf{y}})(\mathbf{y} - \bar{\mathbf{y}})^T\right] \tag{B.112}$$

But,

$$\begin{aligned} (\mathbf{y} - \bar{\mathbf{y}}) = &\left(\mathbf{h}(\bar{\mathbf{x}}) + \nabla\mathbf{h}\,\boldsymbol{\delta}\mathbf{x} + \frac{1}{2!}\nabla^2\mathbf{h}\,\boldsymbol{\delta}\mathbf{x}^2 + \frac{1}{3!}\nabla^3\mathbf{h}\,\boldsymbol{\delta}\mathbf{x}^3 + \ldots\right) - \\ &\left(\mathbf{h}(\bar{\mathbf{x}}) + \frac{1}{2!}\nabla^2\mathbf{h}\,\mathbf{P}_{\mathbf{xx}} + \frac{1}{3!}\nabla^3\mathbf{h}\,E\left[\boldsymbol{\delta}\mathbf{x}^3\right] + \ldots\right) \end{aligned} \tag{B.113}$$

$$\Rightarrow \left(\mathbf{y}-\bar{\mathbf{y}}\right)=\nabla\mathbf{h}\,\boldsymbol{\delta}\mathbf{x}+\frac{1}{2!}\nabla^2\mathbf{h}\,\boldsymbol{\delta}\mathbf{x}^2+\frac{1}{3!}\nabla^3\mathbf{h}\,\boldsymbol{\delta}\mathbf{x}^3+\ldots-\frac{1}{2!}\nabla^2\mathbf{h}\,\mathbf{P}_{\mathbf{xx}}-\frac{1}{3!}\nabla^3\mathbf{h}\,E\left[\boldsymbol{\delta}\mathbf{x}^3\right]-\ldots \quad \text{(B.114)}$$

$$\Rightarrow \left(\mathbf{y}-\bar{\mathbf{y}}\right)=\nabla\mathbf{h}\,\boldsymbol{\delta}\mathbf{x}+\frac{1}{2!}\nabla^2\mathbf{h}\,\boldsymbol{\delta}\mathbf{x}^2-\frac{1}{2!}\nabla^2\mathbf{h}\,\mathbf{P}_{\mathbf{xx}}+\frac{1}{3!}\nabla^3\mathbf{h}\,\boldsymbol{\delta}\mathbf{x}^3-\frac{1}{3!}\nabla^3\mathbf{h}\,E\left[\boldsymbol{\delta}\mathbf{x}^3\right]+\ldots \quad \text{(B.115)}$$

and

$$\begin{aligned}\Rightarrow \mathbf{P}_{\mathbf{yy}}=&\nabla\mathbf{h}\,\mathbf{P}_{\mathbf{xx}}\left(\nabla\mathbf{h}\right)^T+\frac{1}{2!}\nabla\mathbf{h}\,E\left[\boldsymbol{\delta}\mathbf{x}^3\right]\left(\nabla^2\mathbf{h}\right)^T-\frac{1}{2!}\nabla\mathbf{h}\,E\left[\boldsymbol{\delta}\mathbf{x}\,\mathbf{P}_{\mathbf{xx}}\right]\left(\nabla^2\mathbf{h}\right)^T+\frac{1}{3!}\nabla\mathbf{h}\,E\left[\boldsymbol{\delta}\mathbf{x}^4\right]\left(\nabla^3\mathbf{h}\right)^T\\&-\frac{1}{3!}\nabla\mathbf{h}\,E\left[\boldsymbol{\delta}\mathbf{x}\right]E\left[\boldsymbol{\delta}^3\mathbf{x}\right]\left(\nabla^3\mathbf{h}\right)^T+\frac{1}{2!}\nabla^2\mathbf{h}\,E\left[\boldsymbol{\delta}\mathbf{x}^3\right]\left(\nabla\mathbf{h}\right)^T+\frac{1}{4}\nabla^2\mathbf{h}\,E\left[\boldsymbol{\delta}\mathbf{x}^4\right]\left(\nabla^2\mathbf{h}\right)^T\\&-\frac{1}{4}\nabla^2\mathbf{h}\,E\left[\boldsymbol{\delta}\mathbf{x}^2\,\mathbf{P}_{\mathbf{xx}}\right]\left(\nabla^2\mathbf{h}\right)^T+\frac{1}{2\times 3!}\nabla^2\mathbf{h}\,E\left[\boldsymbol{\delta}\mathbf{x}^5\right]\left(\nabla^3\mathbf{h}\right)^T-\frac{1}{2\times 3!}\nabla^2\mathbf{h}\,E\left[\boldsymbol{\delta}\mathbf{x}^2\right]E\left[\boldsymbol{\delta}\mathbf{x}^3\right]\left(\nabla^3\mathbf{h}\right)^T\\&-\frac{1}{2!}\nabla^2\mathbf{h}\,E\left[\mathbf{P}_{\mathbf{xx}}\,\boldsymbol{\delta}\mathbf{x}\right]\left(\nabla\mathbf{h}\right)^T-\frac{1}{4}\nabla^2\mathbf{h}\,E\left[\mathbf{P}_{\mathbf{xx}}\,\boldsymbol{\delta}\mathbf{x}^2\right]\left(\nabla^2\mathbf{h}\right)^T+\frac{1}{4}\nabla^2\mathbf{h}\,E\left[\mathbf{P}_{\mathbf{xx}}^2\right]\left(\nabla^2\mathbf{h}\right)^T\\&-\frac{1}{3!}\nabla^3\mathbf{h}\,E\left[\boldsymbol{\delta}\mathbf{x}^4\right]\left(\nabla\mathbf{h}\right)^T-\frac{1}{2\times 3!}\nabla^3\mathbf{h}\,E\left[\boldsymbol{\delta}\mathbf{x}^5\right]\left(\nabla^2\mathbf{h}\right)^T+\ldots\end{aligned} \quad \text{(B.116)}$$

$$\begin{aligned}\Rightarrow \mathbf{P}_{\mathbf{yy}}=&\nabla\mathbf{h}\,\mathbf{P}_{\mathbf{xx}}\left(\nabla\mathbf{h}\right)^T+\frac{1}{2}\nabla^2\mathbf{h}\,E\left[\boldsymbol{\delta}\mathbf{x}^3\right]\left(\nabla\mathbf{h}\right)^T+\frac{1}{2}\nabla\mathbf{h}\,E\left[\boldsymbol{\delta}\mathbf{x}^3\right]\left(\nabla^2\mathbf{h}\right)^T\\&+\frac{1}{4}\nabla^2\mathbf{h}\left\{E\left[\boldsymbol{\delta}\mathbf{x}^4\right]-E\left[\boldsymbol{\delta}\mathbf{x}^2\,\mathbf{P}_{\mathbf{xx}}\right]-E\left[\mathbf{P}_{\mathbf{xx}}\,\boldsymbol{\delta}\mathbf{x}^2\right]+\mathbf{P}_{\mathbf{xx}}^2\right\}\left(\nabla^2\mathbf{h}\right)^T\\&+\frac{1}{3!}\nabla^3\mathbf{h}\,E\left[\boldsymbol{\delta}\mathbf{x}^4\right]\left(\nabla\mathbf{h}\right)^T+\frac{1}{3!}\nabla\mathbf{h}\,E\left[\boldsymbol{\delta}\mathbf{x}^4\right]\left(\nabla^3\mathbf{h}\right)^T+\ldots\end{aligned} \quad \text{(B.117)}$$

The Unscented transformation choose a set of $(p+1)$ sigma points $\mathcal{S}=\{\mathcal{W},\mathcal{X}\}$, such that $\sum_{i=0}^{p}W_i=1$, such that they reflect certain properties of **x**. The first two statistical moments of **y** can be computed from the sigma points propagated trough the nonlinear function **h** as follows

$$\bar{\mathbf{y}}=\sum_{i=0}^{p}W_i\,\mathcal{Y}_i \quad \text{(B.118)}$$

where $\mathcal{Y}_i=\mathbf{h}\left(\mathcal{X}_i\right)$, and

$$\mathbf{P}_{\mathbf{yy}} = \sum_{i=0}^{p} W_i \{\mathcal{Y}_i - \bar{\mathbf{y}}\}\{\mathcal{Y}_i - \bar{\mathbf{y}}\}^T \tag{B.119}$$

The SPs scaling methods attempt to overcome dimensional scaling effects by calculating the transformation of a scaled set of SPs of the form

$$\mathcal{X}_i' = \mathcal{X}_0 + \alpha\left(\mathcal{X}_i - \mathcal{X}_0\right) \tag{B.120}$$

where $0 < \alpha < 1$ (intended to minimize higher order effects).

Any formulation should meet:

i. $\mathbf{P}_{\mathbf{yy}}$ is positive-definite $\forall\alpha$

ii. Second order accuracy in $\bar{\mathbf{y}}$ and $\mathbf{P}_{\mathbf{yy}}$.

Two formulations achieving these requirements are described below.

a. Auxiliary random variable

We consider the problem of estimating the mean $\bar{\mathbf{z}}$ and covariance $\mathbf{P}_{\mathbf{zz}}$ of the auxiliary random vector **z**. It is related to **x** through the nonlinear equation:

$$\mathbf{g}\left(\mathbf{x}, \bar{\mathbf{x}}, \alpha, \mu\right) = \frac{\mathbf{h}\left(\bar{\mathbf{x}} + \alpha\left(\mathbf{x} - \bar{\mathbf{x}}\right)\right) - \mathbf{h}\left(\bar{\mathbf{x}}\right)}{\mu} + \mathbf{h}\left(\mathbf{x}\right) \tag{B.121}$$

where α is a point scaling parameter and μ is a is a normalization term which scales the transformed point about $\mathbf{h}\left(\bar{\mathbf{x}}\right)$ to the offset the effects of α. Because all SPs are propagated through the term $\mathbf{h}\left(\bar{\mathbf{x}} + \alpha\left(\mathbf{x} - \bar{\mathbf{x}}\right)\right)$, the scaling effect of (B.120) is implicitly

achieved. To prove the second order accuracy of this form, we consider the role played by α and μ. Taking a Taylor Series expansion of $\mathbf{g}(\cdot,\cdot,\cdot,\cdot)$ about $\bar{\mathbf{x}}$,

$$\mathbf{g}(\mathbf{x},\bar{\mathbf{x}},\alpha,\mu)=\mathbf{h}(\bar{\mathbf{x}})+\nabla\mathbf{h}\frac{\alpha}{\mu}\boldsymbol{\delta}\mathbf{x}+\frac{1}{2}\nabla^2\mathbf{h}\frac{\alpha^2}{\mu}\boldsymbol{\delta}\mathbf{x}^2+\frac{1}{3!}\nabla^3\mathbf{h}\frac{\alpha^3}{\mu}\boldsymbol{\delta}\mathbf{x}^3+\ldots \tag{B.122}$$

Then,

$$\bar{\mathbf{z}}=E\left[\mathbf{g}(\mathbf{x},\bar{\mathbf{x}},\alpha,\mu)\right]=\mathbf{h}(\bar{\mathbf{x}})+\frac{1}{2}\nabla^2\mathbf{h}\frac{\alpha^2}{\mu}\mathbf{P}_{\mathbf{xx}}+\frac{1}{3!}\nabla^3\mathbf{h}\frac{\alpha^3}{\mu}E\left[\boldsymbol{\delta}\mathbf{x}^3\right]+\ldots \tag{B.123}$$

These terms can be related directly to those of the Taylor Series expansion of $\mathbf{y}$. If $\mu=\alpha^2$, the expressions for $\bar{\mathbf{y}}$ and $\bar{\mathbf{z}}$ agree up to the second order. The ratio of the third and higher order terms of $\bar{\mathbf{z}}$ against $\bar{\mathbf{y}}$ scale geometrically with a common ratio of α. Since α only affects the third and higher orders, its value can be chosen so that the scaling effects in the higher order terms are minimized. With a sufficiently small value of α, the same mean can be calculated as with the modified form of the unscented transformation.

A similar result holds for the covariance. Let $\mathbf{P}^*_{\mathbf{zz}}=\mu\mathbf{P}_{\mathbf{yy}}$. Taking expectations,

$$\begin{aligned}\mathbf{P}^*_{\mathbf{zz}}=&\frac{\alpha^2}{\mu}\nabla\mathbf{h}\,\mathbf{P}_{\mathbf{xx}}\left(\nabla\mathbf{h}\right)^T+\frac{\alpha^3}{\mu}\frac{1}{2}\nabla^2\mathbf{h}\,E\left[\boldsymbol{\delta}\mathbf{x}^3\right]\left(\nabla\mathbf{h}\right)^T\\&+\frac{\alpha^4}{\mu^2}\frac{1}{4}\nabla^2\mathbf{h}\left\{E\left[\boldsymbol{\delta}\mathbf{x}^4\right]-E\left[\boldsymbol{\delta}\mathbf{x}^2\,\mathbf{P}_{\mathbf{xx}}\right]-E\left[\mathbf{P}_{\mathbf{xx}}\,\boldsymbol{\delta}\mathbf{x}^2\right]+\mathbf{P}_{\mathbf{xx}}^2\right\}\left(\nabla^2\mathbf{h}\right)^T\\&+\frac{\alpha^4}{\mu}\frac{1}{3!}\nabla^3\mathbf{h}\,E\left[\boldsymbol{\delta}\mathbf{x}^4\right]\left(\nabla\mathbf{h}\right)^T+\frac{\alpha^4}{\mu}\frac{1}{3!}\nabla\mathbf{h}\,E\left[\boldsymbol{\delta}\mathbf{x}^4\right]\left(\nabla^3\mathbf{h}\right)^T+\ldots\end{aligned} \tag{B.124}$$

When $\mu = \alpha^2$, the expansion of $\mathbf{P}_{zz}^*$ agrees with $\mathbf{P}_{yy}$ up to the second order and the third and higher order terms scale with α.

The auxiliary form of the unscented transformation simply applies the unscented transformation to the problem of estimating the mean and covariance of the auxiliary random variable. Given an *n*-dimensional random variable $\mathbf{x}$ with mean $\bar{\mathbf{x}}$ and covariance $\mathbf{P}_{xx}$, a set of $(p+1)$ SPs are chosen such that the mean and covariance of those points are $\bar{\mathbf{x}}$ and $\mathbf{P}_{xx}$ respectively. The unscented transformation is then

$$\mathcal{Z}_i = \frac{\mathbf{h}\left(\bar{\mathbf{x}} + \alpha\left(\mathcal{X} - \bar{\mathbf{x}}\right)\right) - \mathbf{h}\left(\bar{\mathbf{x}}\right)}{\alpha^2} + \mathbf{h}\left(\mathbf{x}\right) \tag{B.125}$$

with

$$\begin{aligned} \bar{\mathbf{z}} &= \sum_{i=0}^{p} \mathcal{W}_i' \mathcal{Z}_i \\ \mathbf{P}_{zz}^* &= \alpha^2 \sum_{i=0}^{p} \mathcal{W}_i' \left\{\mathcal{Z}_i - \bar{\mathbf{z}}\right\}\left\{\mathcal{Z}_i - \bar{\mathbf{z}}\right\}^T \end{aligned} \tag{B.126}$$

The auxiliary form is able to meet the requirements set out at the beginning of this section. However, it requires a change in the fundamental transformation system itself. We now show that it is possible to leave the original problem in place but apply a transformation to the sigma points themselves.

b. The Scaled Unscented Transform

The scaled unscented transform yields the same results as the auxiliary form, but without the need to modify the transformation (B.109). Rather, an initial set of points are

chosen using a normal sigma point selection algorithm. A specific transformation is applied to these points. The mean and covariance are calculated using (B.118) and (B.119). A final term is added to offset the initial transformation which was applied to the sigma points.

Suppose a set of sigma points $\mathcal{S} = \{W, \mathcal{X}\}$ have been constructed with mean $\bar{\mathbf{x}}$ and covariance and a positive scaling parameter $\alpha > 0$ has been chosen. These points are transformed to a new set $\mathcal{S}' = \{W', \mathcal{X}'\}$ which has the same mean and covariance as $\mathcal{S}$ but the points now obey the condition of (B.120). As a result, the weights of this transformed sequence are

$$W_i' = \begin{cases} \frac{W_0}{\alpha^2} + \left(1 - \frac{1}{\alpha^2}\right) & i = 0 \\ \frac{W_i}{\alpha^2} & i \neq 0 \end{cases} \tag{B.127}$$

Proof:

Normalization and covariance conditions of $\mathcal{S}$:

$$\sum_{i=0}^{p} W_i = 1 \qquad \mathbf{P}_{\mathbf{xx}} = \sum_{i=1}^{p} W_i \{\mathcal{X}_i - \bar{\mathbf{x}}\}\{\mathcal{X}_i - \bar{\mathbf{x}}\}^T \qquad (\mathcal{X}_0 = \bar{\mathbf{x}}) \tag{B.128}$$

Normalization and covariance conditions of $\mathcal{S}'$:

$$\sum_{i=0}^{p} W_i' = 1 \qquad \mathbf{P}_{\mathbf{xx}} = \sum_{i=1}^{p} W_i' \{\mathcal{X}_i' - \bar{\mathbf{x}}\}\{\mathcal{X}_i' - \bar{\mathbf{x}}\}^T \qquad (\mathcal{X}_0' = \bar{\mathbf{x}}) \tag{B.129}$$

But $\mathcal{X}_i' = \mathcal{X}_0 + \alpha(\mathcal{X}_i - \mathcal{X}_0) = \bar{\mathbf{x}} + \alpha(\mathcal{X}_i - \bar{\mathbf{x}})$. Then the covariance conditions imply

$$\Rightarrow \sum_{i=1}^{p} W_i^{'} \left\{ \bar{\mathbf{x}} + \alpha\left(\mathcal{X}_i - \bar{\mathbf{x}}\right) - \bar{\mathbf{x}} \right\} \left\{ \bar{\mathbf{x}} + \alpha\left(\mathcal{X}_i - \bar{\mathbf{x}}\right) - \bar{\mathbf{x}} \right\}^T = \sum_{i=1}^{p} W_i \left\{ \mathfrak{X}_i - \bar{\mathbf{x}} \right\} \left\{ \mathfrak{X}_i - \bar{\mathbf{x}} \right\}^T$$

$$\Rightarrow \sum_{i=1}^{p} W_i^{'} \alpha^2 \left(\mathcal{X}_i - \bar{\mathbf{x}}\right)\left(\mathcal{X}_i - \bar{\mathbf{x}}\right)^T = \sum_{i=1}^{p} W_i \left\{ \mathfrak{X}_i - \bar{\mathbf{x}} \right\} \left\{ \mathfrak{X}_i - \bar{\mathbf{x}} \right\}^T \tag{B.130}$$

$$\Rightarrow W_i^{'} = \frac{W}{\alpha^2} \qquad i > 0$$

and the normalization conditions yield

$$\sum_{i=0}^{p} W_i = 1 = \sum_{i=1}^{p} W_i + W_0 = W_0 + \alpha^2 \sum_{i=1}^{p} W_i^{'} \tag{B.131}$$

but

$$\sum_{i=0}^{p} W_i^{'} = 1 = W_0^{'} + \sum_{i=1}^{p} W_i^{'} \Rightarrow \sum_{i=1}^{p} W_i^{'} = 1 - W_0^{'} \tag{B.132}$$

then,

$$\begin{aligned} \Rightarrow 1 &= W_0 + \alpha^2 \left(1 - W_0^{'}\right) \\ \Rightarrow W_0^{'} &= \frac{W_0}{\alpha^2} + 1 - \frac{1}{\alpha^2} \end{aligned} \tag{B.133}$$

Because $\mathcal{S}'$ is, itself, a sigma point set, it is possible with some selection algorithms to implicitly combine the scaling directly with the original sigma point selection. Given this set of points, the scaled unscented transform calculates its statistics as follows

$$\mathcal{Y}_i^{'} = \mathbf{h}\left(\mathcal{X}_i^{'}\right) \tag{B.134}$$

$$\bar{\mathbf{y}}' = \sum_{i=0}^{p} W_i' \mathcal{Y}_i' \tag{B.135}$$

$$\mathbf{P}_{\mathbf{yy}}' = \sum_{i=0}^{p} W_i' \left\{\mathcal{Y}_i' - \bar{\mathbf{y}}'\right\}\left\{\mathcal{Y}_i' - \bar{\mathbf{y}}'\right\}^T + \left(1-\alpha^2\right)\left\{\mathcal{Y}_0' - \bar{\mathbf{y}}'\right\}\left\{\mathcal{Y}_0' - \bar{\mathbf{y}}'\right\}^T \tag{B.136}$$

But $\bar{\mathbf{y}}' = \bar{\mathbf{z}}$ and $\mathbf{P}_{\mathbf{yy}}' = \mathbf{P}_{\mathbf{zz}}^*$ when $\mu = \alpha^2$. This has a number of important consequences. First, the scaled unscented transformation possesses all of the properties of the auxillary form. The predicted mean and covariance are accurate to the second order and $\mathbf{P}_{\mathbf{yy}}'$ is guaranteed to be positive semidefinite if all of the untransformed weights are non-negative. Second, the numerical costs of this form are the same as with the unscaled unscented transform. Comparing (B.136) to (B.119), the only difference is that a term $\left(1-\alpha^2\right)$ is added to the weight on the zero-*th* sigma point. Finally this form provides a very simple interpretation for α. When $\alpha = 1$, (B.119) is recovered.

c. Incorporating Higher Order Information

Although the SPs in the general case only capture the first two moments of the sigma points (and so the first two moments of the Taylor Series expansion), the scaled unscented can be extended to include partial higher order information of the fourth order term in the Taylor Series expansion of the covariance. The fourth order term of (B.117) is

$$\begin{aligned}\mathbf{A} = &\frac{1}{4}\nabla^2\mathbf{h}\left\{E\left[\boldsymbol{\delta}\mathbf{x}^4\right] - E\left[\boldsymbol{\delta}\mathbf{x}^2\,\mathbf{P}_{\mathbf{xx}}\right] - E\left[\mathbf{P}_{\mathbf{xx}}\,\boldsymbol{\delta}\mathbf{x}^2\right] + \mathbf{P}_{\mathbf{xx}}^2\right\}\left(\nabla^2\mathbf{h}\right)^T \\ &+ \frac{1}{3!}\nabla^3\mathbf{h}\,E\left[\boldsymbol{\delta}\mathbf{x}^4\right]\left(\nabla\mathbf{h}\right)^T\end{aligned} \tag{B.137}$$

The term $\nabla^2\mathbf{h}\mathbf{P}_{\mathbf{xx}}^2\left(\nabla^2\mathbf{h}\right)^T$ can be calculated from the same set of sigma points which match the mean and covariance. From (B.110),

$$\mathcal{Y}_0 - \bar{\mathbf{y}} = \frac{1}{2}\nabla^2\mathbf{h}\,\mathbf{P}_{\mathbf{xx}} + \frac{1}{6}\nabla^3\mathbf{h}E\left[\delta\mathbf{x}^3\right] + \ldots \tag{B.138}$$

Taking outer products:

$$\left(\mathcal{Y}_0 - \bar{\mathbf{y}}\right)\left(\mathcal{Y}_0 - \bar{\mathbf{y}}\right)^T = \frac{1}{4}\nabla^2\mathbf{h}\,\mathbf{P}_{\mathbf{xx}}^2\left(\nabla^2\mathbf{h}\right)^T + \ldots \tag{B.139}$$

Therefore, adding extra weighting to the contribution of the zero-*th* point, further higher order effects can be incorporated at no additional computational cost by rewriting (B.136) as

$$\mathbf{P}_{\mathbf{yy}}' = \sum_{i=0}^{p} W_i'\left\{\mathcal{Y}_i' - \bar{\mathbf{y}}'\right\}\left\{\mathcal{Y}_i' - \bar{\mathbf{y}}'\right\}^T + \left(\beta + 1 - \alpha^2\right)\left\{\mathcal{Y}_0' - \bar{\mathbf{y}}'\right\}\left\{\mathcal{Y}_0' - \bar{\mathbf{y}}'\right\}^T \tag{B.140}$$

In this form,

$$\begin{aligned}\Delta\mathbf{A} = {} & \frac{1}{4}\nabla^2\mathbf{h}\left\{E\left[\delta\mathbf{x}^4\right] - E\left[\delta\mathbf{x}^2\,\mathbf{P}_{\mathbf{xx}}\right] - E\left[\mathbf{P}_{\mathbf{xx}}\,\delta\mathbf{x}^2\right] + \left(1-\beta\right)\mathbf{P}_{\mathbf{xx}}^2\right\}\left(\nabla^2\mathbf{h}\right)^T \\ & + \frac{1}{3!}\nabla^3\mathbf{h}\,E\left[\delta\mathbf{x}^4\right]\left(\nabla\mathbf{h}\right)^T\end{aligned} \tag{B.141}$$

In the case that $\mathbf{x}$ is Gaussian, $E\left[\delta\mathbf{x}^4\right] = 3\mathbf{P}_{\mathbf{xx}}^2$ and then the error is

$$\Delta\mathbf{A} = \left(2-\beta\right)\nabla^2\mathbf{h}\,\mathbf{P}_{\mathbf{xx}}^2\left(\nabla^2\mathbf{h}\right)^T + \frac{1}{3!}\nabla^3\mathbf{h}\,E\left[\delta\mathbf{x}^4\right]\left(\nabla\mathbf{h}\right)^T \tag{B.142}$$

Under the assumption that no information about $\mathbf{h}(\cdot)$ is used, this term is minimized when $\beta = 2$.

APPENDIX C: LINEAR REGRESSION KALMAN FILTERS

The so-called Linear Regression Kalman Filters (LRKFs) linearize the process and measurement equations of the nonlinear state-space model by statistical linear regression of the functions through a number of regression points in state-space. These filters define the uncertainty due to linearization errors on the linearized process or measurement function as the sample covariance matrix of the deviations between the function values of the nonlinear and the linearized function in the regression points.

C.1. Statistical linear regression

Let's consider a nonlinear vector function $\mathbf{y} = \mathbf{g}(\mathbf{x})$ evaluated in r points ($\boldsymbol{x}^{(j)}, \boldsymbol{y}^{(j)}$, $j = 1,...,r$) where $\boldsymbol{y}^{(j)} = \mathbf{g}\left(\boldsymbol{x}^{(j)}\right)$. Define the following weighted sample means

$$\bar{\boldsymbol{x}} = \sum_{j=1}^{r} W_m^{(j)} \boldsymbol{x}^{(j)} \tag{C.1}$$

$$\bar{\boldsymbol{y}} = \sum_{j=1}^{r} W_m^{(j)} \boldsymbol{y}^{(j)} \tag{C.2}$$

where $W_m^{(j)} =$ mean weighting coefficient for point j, and the weighted sample covariance matrices

$$\mathbf{P}_{\mathbf{xx}} = \sum_{j=1}^{r} W_c^{(j)} \left(\boldsymbol{x}^{(j)} - \bar{\boldsymbol{x}}\right)\left(\boldsymbol{x}^{(j)} - \bar{\boldsymbol{x}}\right)^T \tag{C.3}$$

$$\mathbf{P}_{\mathbf{xy}} = \sum_{j=1}^{r} W_c^{(j)} \left(\boldsymbol{x}^{(j)} - \bar{\boldsymbol{x}}\right)\left(\boldsymbol{y}^{(j)} - \bar{\boldsymbol{y}}\right)^T \tag{C.4}$$

$$\mathbf{P}_{\mathbf{yy}} = \sum_{j=1}^{r} W_c^{(j)} \left(\boldsymbol{y}^{(j)} - \bar{\boldsymbol{y}}\right)\left(\boldsymbol{y}^{(j)} - \bar{\boldsymbol{y}}\right)^T \tag{C.5}$$

where $W_c^{(j)} =$ covariance weighting coefficient for point j.

A linear regression for y can be expressed by $\mathbf{y} = \mathbf{A}_{lr}\mathbf{x} + \mathbf{b}_{lr}$ such that it minimizes the sum of the squared errors between the function values of the nonlinear and linearized functions in the regression points

$$\left(\mathbf{A}_{lr}, \mathbf{b}_{lr},\right) = \arg\min_{(\mathbf{A},\mathbf{b})} \sum_{j=1}^{r} \mathbf{e}_j^T \mathbf{e}_j \tag{C.6}$$

in which

$$\mathbf{e}_j = \boldsymbol{y}^{(j)} - \left(\mathbf{A}\boldsymbol{x}^{(j)} + \mathbf{b}\right) \tag{C.7}$$

The solution of (C.6) is given by

$$\mathbf{A}_{lr} = \mathbf{P}_{\mathbf{xy}}^T \mathbf{P}_{\mathbf{yy}}^{-1} = \mathbf{P}_{\mathbf{yx}} \mathbf{P}_{\mathbf{yy}}^{-1} \qquad ; \qquad \mathbf{b}_{lr} = \bar{\boldsymbol{y}} - \mathbf{A}_{lr}\bar{\boldsymbol{x}} \tag{C.8}$$

The sample covariance matrix of the deviations $\mathbf{e}_j$ is

$$\begin{aligned}
\mathbf{P}_{\mathbf{ee}} &= \sum_{j=1}^{r} W_c^{(j)} \mathbf{e}_j \mathbf{e}_j^T \\
&= \sum_{j=1}^{r} \left[\left(\boldsymbol{y}^{(j)} - \bar{\boldsymbol{y}}\right) - \mathbf{A}_{lr}\left(\boldsymbol{x}^{(j)} - \bar{\boldsymbol{x}}\right)\right]\left[\left(\boldsymbol{y}^{(j)} - \bar{\boldsymbol{y}}\right) - \mathbf{A}_{lr}\left(\boldsymbol{x}^{(j)} - \bar{\boldsymbol{x}}\right)\right]^T \\
&= \mathbf{P}_{\mathbf{yy}} - \mathbf{A}_{lr}\mathbf{P}_{\mathbf{xy}} - \mathbf{P}_{\mathbf{yx}}\mathbf{A}_{lr}^T + \mathbf{A}_{lr}\mathbf{P}_{\mathbf{xx}}\mathbf{A}_{lr}^T \\
\mathbf{P}_{\mathbf{ee}} &= \mathbf{P}_{\mathbf{yy}} - \mathbf{A}_{lr}\mathbf{P}_{\mathbf{xx}}\mathbf{A}_{lr}^T
\end{aligned} \tag{C.9}$$

C.2. Nonlinear state-space model

A nonlinear state-space model with additive white Gaussian noise can be written as

$$\begin{aligned}\mathbf{x}_{k+1} &= \mathbf{f}_k\left(\mathbf{x}_k\right) + \mathbf{w}_k \\ \mathbf{y}_{k+1} &= \mathbf{h}_{k+1}\left(\mathbf{x}_{k+1}\right) + \mathbf{v}_{k+1}\end{aligned} \tag{C.10}$$

with $\mathbf{w}_k \sim \mathcal{N}\left(\mathbf{0}, \mathbf{Q}_k\right)$ and $\mathbf{v}_{k+1} \sim \mathcal{N}\left(\mathbf{0}, \mathbf{R}_{k+1}\right)$

C.3. Process update using LRKF

LRKFs use the function values of r regression points, $\boldsymbol{\chi}_{k|k}^{j}$ ($j = 1,...,r$), in state space to model the behavior of the process function in the "uncertainty region" around the updated state estimate $\hat{\mathbf{x}}_{k|k}$. The regression points are chosen such that their weighted sample mean and weighted covariance matrix equal the state estimate $\hat{\mathbf{x}}_{k|k}$ and its covariance matrix $\mathbf{P}_{k|k}$

$$\hat{\mathbf{x}}_{k|k} = \overline{\boldsymbol{\chi}}_{k|k} = \sum_{j=1}^{r} W_m^{(j)} \boldsymbol{\chi}_{k|k}^{(j)} : \text{weighted sample mean} \tag{C.11}$$

$$\mathbf{P}_{k|k} = \sum_{j=1}^{r} W_c^{(j)} \left(\boldsymbol{\chi}_{k|k}^{(j)} - \hat{\mathbf{x}}_{k|k}\right)\left(\boldsymbol{\chi}_{k|k}^{(j)} - \hat{\mathbf{x}}_{k|k}\right)^T : \text{weighted sample covariance} \tag{C.12}$$

The function values of the regression points are

$$\boldsymbol{\chi}_{k+1|k}^{(j)} = \mathbf{f}_k\left(\boldsymbol{\chi}_{k|k}^{(j)}\right) \tag{C.13}$$

Using the results from Section C.1 (Statistical linear regression) and considering the following analogy

Section C.1.	This section
$\mathbf{x}$	$\mathbf{x}_k$
$\mathbf{y}$	$\mathbf{x}_{k+1}$
$\mathbf{g}$	$\mathbf{f}_k$
$\mathbf{A}_{lr}$	$\mathbf{F}_k$
$\mathbf{b}_{lr}$	$\mathbf{b}_k$
$\boldsymbol{\chi}^j$	$\boldsymbol{\chi}_{k\|k}^{(j)}$
$\boldsymbol{\gamma}^j$	$\boldsymbol{\chi}_{k+1\|k}^{(j)}$
$\mathbf{P}_{\mathbf{ee}}$	$\mathbf{Q}_k^*$

we have

$$\mathbf{F}_k = \left[\sum_{j=1}^{r} W_c^{(j)} \left(\boldsymbol{\chi}_{k+1|k}^{(j)} - \overline{\boldsymbol{\chi}}_{k+1|k}\right)\left(\boldsymbol{\chi}_{k|k}^{(j)} - \overline{\boldsymbol{\chi}}_{k|k}\right)^T\right]\left[\sum_{j=1}^{r} W_c^{(j)} \left(\boldsymbol{\chi}_{k|k}^{(j)} - \overline{\boldsymbol{\chi}}_{k|k}\right)\left(\boldsymbol{\chi}_{k|k}^{(j)} - \overline{\boldsymbol{\chi}}_{k|k}\right)^T\right]^{-1}$$

$$\Rightarrow \mathbf{F}_k = \left[\sum_{j=1}^{r} W_c^{(j)} \left(\boldsymbol{\chi}_{k+1|k}^{(j)} - \overline{\boldsymbol{\chi}}_{k+1|k}\right)\left(\boldsymbol{\chi}_{k|k}^{(j)} - \hat{\mathbf{x}}_{k|k}\right)^T\right]\mathbf{P}_{k|k}^{-1} \tag{C.14}$$

$$\mathbf{b}_k = \overline{\boldsymbol{\chi}}_{k+1|k} - \mathbf{F}_k \overline{\boldsymbol{\chi}}_{k|k} = \sum_{j=1}^{r} W_m^{(j)} \boldsymbol{\chi}_{k+1|k}^{(j)} - \mathbf{F}_k \hat{\mathbf{x}}_{k|k} \tag{C.15}$$

$$\mathbf{Q}_k^* = \sum_{j=1}^{r} W_c^{(j)} \left(\boldsymbol{\chi}_{k+1|k}^{(j)} - \overline{\boldsymbol{\chi}}_{k+1|k}\right)\left(\boldsymbol{\chi}_{k+1|k}^{(j)} - \overline{\boldsymbol{\chi}}_{k+1|k}\right)^T - \mathbf{F}_k \left[\sum_{j=1}^{r} W_c^{(j)} \left(\boldsymbol{\chi}_{k|k}^{(j)} - \overline{\boldsymbol{\chi}}_{k|k}\right)\left(\boldsymbol{\chi}_{k|k}^{(j)} - \overline{\boldsymbol{\chi}}_{k|k}\right)^T\right]\mathbf{F}_k^T$$

$$\Rightarrow \mathbf{Q}_k^* = \sum_{j=1}^{r} W_c^{(j)} \left(\boldsymbol{\chi}_{k+1|k}^{(j)} - \overline{\boldsymbol{\chi}}_{k+1|k}\right)\left(\boldsymbol{\chi}_{k+1|k}^{(j)} - \overline{\boldsymbol{\chi}}_{k+1|k}\right)^T - \mathbf{F}_k \mathbf{P}_{k|k} \mathbf{F}_k^T \tag{C.16}$$

Then, process update equations of LRKFs follow the linear KF equations (prediction step):

$$\hat{\mathbf{x}}_{k+1|k} = \mathbf{F}_k \hat{\mathbf{x}}_{k|k} + \mathbf{b}_k = \mathbf{F}_k \hat{\mathbf{x}}_{k|k} + \sum_{j=1}^{r} W_m^{(j)} \boldsymbol{\chi}_{k+1|k}^{(j)} - \mathbf{F}_k \hat{\mathbf{x}}_{k|k} = \sum_{j=1}^{r} W_m^{(j)} \boldsymbol{\chi}_{k+1|k}^{(j)} \tag{C.17}$$

$$\mathbf{P}_{k+1|k} = \mathbf{F}_k \mathbf{P}_{k|k} \mathbf{F}_k^T + \mathbf{Q}_k^* + \mathbf{Q}_k \tag{C.18}$$

$$\mathbf{P}_{k+1|k} = \mathbf{F}_k \mathbf{P}_{k|k} \mathbf{F}_k^T + \sum_{j=1}^{r} W_c^{(j)} \left(\boldsymbol{\chi}_{k+1|k}^{(j)} - \overline{\boldsymbol{\chi}}_{k+1|k} \right) \left(\boldsymbol{\chi}_{k+1|k}^{(j)} - \overline{\boldsymbol{\chi}}_{k+1|k} \right)^T - \mathbf{F}_k \mathbf{P}_{k|k} \mathbf{F}_k^T + \mathbf{Q}_k$$

$$\Rightarrow \mathbf{P}_{k+1|k} = \sum_{j=1}^{r} W_c^{(j)} \left(\boldsymbol{\chi}_{k+1|k}^{(j)} - \hat{\mathbf{x}}_{k+1|k} \right) \left(\boldsymbol{\chi}_{k+1|k}^{(j)} - \hat{\mathbf{x}}_{k+1|k} \right)^T + \mathbf{Q}_k$$

C.4. Measurement update using LRKF

The LRKF evaluates the measurement function in r regression points $\boldsymbol{\chi}_{k+1|k}^{(j)}$ in the "uncertainty region" around the predicted state estimate $\hat{\mathbf{x}}_{k+1|k}$. The $\boldsymbol{\chi}_{k+1|k}^{(j)}$ are chosen such that their weighted sample mean and weighted sample covariance matrix are equal to the predicted state estimate and its covariance:

$$\hat{\mathbf{x}}_{k+1|k} = \overline{\boldsymbol{\chi}}_{k+1|k} = \sum_{j=1}^{r} W_m^{(j)} \boldsymbol{\chi}_{k+1|k}^{(j)} \text{ : weighted sample mean} \tag{C.19}$$

$$\begin{aligned} \mathbf{P}_{k+1|k} &= \sum_{j=1}^{r} W_c^{(j)} \left(\boldsymbol{\chi}_{k+1|k}^{(j)} - \overline{\boldsymbol{\chi}}_{k+1|k} \right) \left(\boldsymbol{\chi}_{k+1|k}^{(j)} - \overline{\boldsymbol{\chi}}_{k+1|k} \right)^T \\ &= \sum_{j=1}^{r} W_c^{(j)} \left(\boldsymbol{\chi}_{k+1|k}^{(j)} - \hat{\mathbf{x}}_{k+1|k} \right) \left(\boldsymbol{\chi}_{k+1|k}^{(j)} - \hat{\mathbf{x}}_{k+1|k} \right)^T \end{aligned} \text{ : weighted sample covariance} \tag{C.20}$$

The function values of the regression points thought the nonlinear function are:

$$\boldsymbol{\gamma}_{k+1}^{(j)} = \mathbf{h}_{k+1} \left(\boldsymbol{\chi}_{k+1|k}^{(j)} \right) \tag{C.21}$$

$$\hat{\boldsymbol{\gamma}}_{k+1|k} = \sum_{j=1}^{r} W_m^{(j)} \boldsymbol{\gamma}_{k+1}^{(j)} \text{ : estimated response} \tag{C.22}$$

Using the results from Section C.1 (Statistical linear regression) and considering the following analogy

Section C.1.	This section
$\mathbf{x}$	$\mathbf{x}_{k+1}$
$\mathbf{y}$	$\mathbf{y}_{k+1}$
$\mathbf{g}$	$\mathbf{h}_{k+1}$
$\mathbf{A}_{lr}$	$\mathbf{H}_{k+1}$
$\mathbf{b}_{lr}$	$\mathbf{d}_{k+1}$
$\boldsymbol{\chi}^j$	$\boldsymbol{\chi}_{k+1\|k}^{(j)}$
$\boldsymbol{\gamma}^j$	$\boldsymbol{\gamma}_{k+1}^{(j)}$
$\mathbf{P}_{\mathbf{ee}}$	$\mathbf{R}_{k+1}^{*}$

we have

$$\mathbf{H}_{k+1} = \left[\sum_{j=1}^{r} W_c^{(j)} \left(\boldsymbol{\gamma}_{k+1}^{(j)} - \hat{\mathbf{y}}_{k+1|k}\right)\left(\boldsymbol{\chi}_{k+1|k}^{(j)} - \overline{\boldsymbol{\chi}}_{k+1|k}\right)^T\right] \left[\sum_{j=1}^{r} W_c^{(j)} \left(\boldsymbol{\chi}_{k+1|k}^{(j)} - \overline{\boldsymbol{\chi}}_{k+1|k}\right)\left(\boldsymbol{\chi}_{k+1|k}^{(j)} - \overline{\boldsymbol{\chi}}_{k+1|k}\right)^T\right]^{-1} \tag{C.23}$$

$$\mathbf{H}_{k+1} = \left[\sum_{j=1}^{r} W_c^{(j)} \left(\boldsymbol{\gamma}_{k+1}^{(j)} - \hat{\mathbf{y}}_{k+1|k}\right)\left(\boldsymbol{\chi}_{k+1|k}^{(j)} - \hat{\mathbf{x}}_{k+1|k}\right)^T\right] \mathbf{P}_{k+1|k}^{-1} \tag{C.24}$$

$$\mathbf{d}_{k+1} = \hat{\mathbf{y}}_{k+1|k} - \mathbf{H}_{k+1}\overline{\boldsymbol{\chi}}_{k+1|k} \tag{C.25}$$

$$\mathbf{d}_{k+1} = \sum_{j=1}^{r} W_m^{(j)} \boldsymbol{\gamma}_{k+1}^{(j)} - \mathbf{H}_{k+1}\hat{\mathbf{x}}_{k+1|k} \tag{C.26}$$

$$\mathbf{R}_{k+1}^{*} = \sum_{j=1}^{r} W_c^{(j)} \left(\boldsymbol{\gamma}_{k+1}^{(j)} - \hat{\mathbf{y}}_{k+1|k}\right)\left(\boldsymbol{\gamma}_{k+1}^{(j)} - \hat{\mathbf{y}}_{k+1|k}\right)^T - \mathbf{H}_{k+1} \left[\sum_{j=1}^{r} W_c^{(j)} \left(\boldsymbol{\chi}_{k+1|k}^{(j)} - \overline{\boldsymbol{\chi}}_{k+1|k}\right)\left(\boldsymbol{\chi}_{k+1|k}^{(j)} - \overline{\boldsymbol{\chi}}_{k+1|k}\right)^T\right] \mathbf{H}_{k+1}^T \tag{C.27}$$

$$\mathbf{R}_{k+1}^{*} = \sum_{j=1}^{r} W_c^{(j)} \left(\boldsymbol{\gamma}_{k+1}^{(j)} - \hat{\mathbf{y}}_{k+1|k}\right)\left(\boldsymbol{\gamma}_{k+1}^{(j)} - \hat{\mathbf{y}}_{k+1|k}\right)^T - \mathbf{H}_{k+1}\mathbf{P}_{k+1|k}^{-1}\mathbf{H}_{k+1}^T \tag{C.28}$$

Then, measurement update equations of LRKFs follow the linear KF equations (correction step):

$$\hat{\mathbf{x}}_{k+1|k+1} = \hat{\mathbf{x}}_{k+1|k} + \mathbf{K}_{k+1}\boldsymbol{\eta}_{k+1} \tag{C.29}$$

$$\mathbf{P}_{k+1|k+1} = \left(\mathbf{I}_{n\times n} - \mathbf{K}_{k+1}\mathbf{H}_{k+1}\right)\mathbf{P}_{k+1|k} \tag{C.30}$$

where

$$\begin{aligned}\boldsymbol{\eta}_{k+1} &= \mathbf{y}_{k+1} - \mathbf{H}_{k+1}\hat{\mathbf{x}}_{k+1|k} - \mathbf{d}_{k+1} \\ &= \mathbf{y}_{k+1} - \mathbf{H}_{k+1}\hat{\mathbf{x}}_{k+1|k} - \sum_{j=1}^{r} W_m^{(j)}\boldsymbol{\psi}_{k+1}^{(j)} + \mathbf{H}_{k+1}\hat{\mathbf{x}}_{k+1|k}\end{aligned} \tag{C.31}$$

$$\boldsymbol{\eta}_{k+1} = \mathbf{y}_{k+1} - \hat{\mathbf{y}}_{k+1|k} = \mathbf{y}_{k+1} - \sum_{j=1}^{r} W_m^{(j)}\boldsymbol{\psi}_{k+1}^{(j)} \tag{C.32}$$

$$\begin{aligned}\mathbf{S}_{k+1} &= \mathbf{R}_{k+1}^{*} + \mathbf{R}_{k+1} + \mathbf{H}_{k+1}\mathbf{P}_{k+1|k}\mathbf{H}_{k+1}^{T} \\ &= \sum_{j=1}^{r} W_c^{(j)}\left(\boldsymbol{\psi}_{k+1}^{(j)} - \hat{\mathbf{y}}_{k+1|k}\right)\left(\boldsymbol{\psi}_{k+1}^{(j)} - \hat{\mathbf{y}}_{k+1|k}\right)^{T} \\ &\quad - \mathbf{H}_{k+1}\mathbf{P}_{k+1|k}^{-1}\mathbf{H}_{k+1}^{T} + \mathbf{R}_{k+1} + \mathbf{H}_{k+1}\mathbf{P}_{k+1|k}\mathbf{H}_{k+1}^{T}\end{aligned} \tag{C.33}$$

$$\mathbf{S}_{k+1} = \sum_{j=1}^{r} W_c^{(j)}\left(\boldsymbol{\psi}_{k+1}^{(j)} - \hat{\mathbf{y}}_{k+1|k}\right)\left(\boldsymbol{\psi}_{k+1}^{(j)} - \hat{\mathbf{y}}_{k+1|k}\right)^{T} + \mathbf{R}_{k+1} \tag{C.34}$$

$$\begin{aligned}\mathbf{K}_{k+1} &= \mathbf{P}_{k+1|k}\mathbf{H}_{k+1}^{T}\mathbf{S}_{k+1}^{-1} \\ &= \mathbf{P}_{k+1|k}\mathbf{P}_{k+1|k}^{-1}\left[\sum_{j=1}^{r} W_c^{(j)}\left(\boldsymbol{\chi}_{k+1|k}^{(j)} - \hat{\mathbf{x}}_{k+1|k}\right)\left(\boldsymbol{\psi}_{k+1}^{(j)} - \hat{\mathbf{y}}_{k+1|k}\right)^{T}\right]\mathbf{S}_{k+1}^{-1}\end{aligned} \tag{C.35}$$

$$\mathbf{K}_{k+1} = \left[\sum_{j=1}^{r} W_c^{(j)}\left(\boldsymbol{\chi}_{k+1|k}^{(j)} - \hat{\mathbf{x}}_{k+1|k}\right)\left(\boldsymbol{\psi}_{k+1}^{(j)} - \hat{\mathbf{y}}_{k+1|k}\right)^{T}\right]\mathbf{S}_{k+1}^{-1} \tag{C.36}$$

Case of parameter estimation for mechanics-based nonlinear FE model updating

Nonlinear state-space model

$$\begin{aligned}\boldsymbol{\theta}_k &= \boldsymbol{\theta}_{k-1} + \mathbf{w}_{k-1} \\ \mathbf{y}_k &= \mathbf{h}_k\left(\mathbf{x}_k\right) + \mathbf{v}_k\end{aligned} \tag{C.37}$$

with

$$\mathbf{w}_{k-1} \sim \mathcal{N}\left(\mathbf{0}, \mathbf{Q}_{k-1}\right) \text{ and } \mathbf{v}_k \sim \mathcal{N}\left(\mathbf{0}, \mathbf{R}_k\right) \tag{C.38}$$

Process update

Since the process equation is $\boldsymbol{\theta}_k = \boldsymbol{\theta}_{k-1} + \mathbf{w}_{k-1}$:

$$\boldsymbol{\vartheta}_{k+1|k}^{(j)} = \boldsymbol{\vartheta}_{k|k}^{(j)} \text{: values of the regression points} \tag{C.39}$$

$$\hat{\boldsymbol{\theta}}_{k+1|k} = \hat{\boldsymbol{\theta}}_{k|k} \text{ : predicted parameter estimate} \tag{C.40}$$

$$\mathbf{P}_{k+1|k}^{\boldsymbol{\theta}\boldsymbol{\theta}} = \mathbf{P}_{k|k}^{\boldsymbol{\theta}\boldsymbol{\theta}} + \mathbf{Q}_k \text{: predicted covariance estimate} \tag{C.41}$$

Measurement update

The function values of the regression points thought the nonlinear function are:

$$\boldsymbol{\gamma}_{k+1}^{(j)} = \mathbf{h}_{k+1}\left(\boldsymbol{\vartheta}_{k+1|k}^{(j)}\right) \tag{C.42}$$

$$\mathbf{H}_{k+1} = \left[\sum_{j=1}^{r} W_c^{(j)}\left(\boldsymbol{\gamma}_{k+1}^{(j)} - \hat{\mathbf{y}}_{k+1|k}\right)\left(\boldsymbol{\vartheta}_{k+1|k}^{(j)} - \hat{\boldsymbol{\theta}}_{k+1|k}\right)^T\right]\mathbf{P}_{k+1|k}^{-1} = \left(\mathbf{P}_{k+1|k}^{\boldsymbol{\theta}\mathbf{y}}\right)^T\left(\mathbf{P}_{k+1|k}^{\boldsymbol{\theta}\boldsymbol{\theta}}\right)^{-1} \tag{C.43}$$

$$\mathbf{d}_{k+1} = \sum_{j=1}^{r} W_m^{(j)} \boldsymbol{\gamma}_{k+1}^{(j)} - \mathbf{H}_{k+1}\hat{\boldsymbol{\theta}}_{k+1|k} \tag{C.44}$$

$$\mathbf{R}_{k+1}^{*} = \sum_{j=1}^{r} W_c^{(j)} \left(\boldsymbol{\mathcal{Y}}_{k+1}^{(j)} - \hat{\mathbf{y}}_{k+1|k} \right) \left(\boldsymbol{\mathcal{Y}}_{k+1}^{(j)} - \hat{\mathbf{y}}_{k+1|k} \right)^T - \mathbf{H}_{k+1} \left(\mathbf{P}_{k+1|k}^{\boldsymbol{\theta}\boldsymbol{\theta}} \right)^{-1} \mathbf{H}_{k+1}^T \tag{C.45}$$

$$\hat{\boldsymbol{\theta}}_{k+1|k+1} = \hat{\boldsymbol{\theta}}_{k+1|k} + \mathbf{K}_{k+1} \boldsymbol{\eta}_{k+1} \tag{C.46}$$

$$\mathbf{P}_{k+1|k+1}^{\boldsymbol{\theta}\boldsymbol{\theta}} = \left(\mathbf{I}_{n \times n} - \mathbf{K}_{k+1} \mathbf{H}_{k+1} \right) \mathbf{P}_{k+1|k}^{\boldsymbol{\theta}\boldsymbol{\theta}} \tag{C.47}$$

where

$$\boldsymbol{\eta}_{k+1} = \mathbf{y}_{k+1} - \hat{\mathbf{y}}_{k+1|k} = \mathbf{y}_{k+1} - \sum_{j=1}^{r} W_m^{(j)} \boldsymbol{\mathcal{Y}}_{k+1}^{(j)} : \text{innovation} \tag{C.48}$$

$$\mathbf{S}_{k+1} = \sum_{j=1}^{r} W_c^{(j)} \left(\boldsymbol{\mathcal{Y}}_{k+1}^{(j)} - \hat{\mathbf{y}}_{k+1|k} \right) \left(\boldsymbol{\mathcal{Y}}_{k+1}^{(j)} - \hat{\mathbf{y}}_{k+1|k} \right)^T + \mathbf{R}_{k+1} \tag{C.49}$$

$$\mathbf{K}_{k+1} = \left[\sum_{j=1}^{r} W_c^{(j)} \left(\boldsymbol{\vartheta}_{k+1|k}^{(j)} - \hat{\boldsymbol{\theta}}_{k+1|k} \right) \left(\boldsymbol{\mathcal{Y}}_{k+1}^{(j)} - \hat{\mathbf{y}}_{k+1|k} \right)^T \right] \mathbf{S}_{k+1}^{-1} \tag{C.50}$$

APPENDIX D: KALMAN-BASED FILTERS FOR NONLINEAR SYSTEMS

D.1. Linear Kalman Filter for state estimation

Consider the linear state-space model

$$\begin{aligned} \mathbf{x}_{k+1} &= \mathbf{A}_k \mathbf{x}_k + \mathbf{B}_k \mathbf{u}_k + \mathbf{w}_k \\ \mathbf{y}_{k+1} &= \mathbf{C}_{k+1} \mathbf{x}_{k+1} + \mathbf{D}_{k+1} \mathbf{u}_{k+1} + \mathbf{v}_{k+1} \end{aligned} \tag{D.1}$$

Alternatively, the model can be expressed as

$$\begin{aligned} \mathbf{x}_{k+1} &= \mathbf{A}_k \mathbf{x}_k + \mathbf{b}_k + \mathbf{w}_k \\ \mathbf{y}_{k+1} &= \mathbf{C}_{k+1} \mathbf{x}_{k+1} + \tilde{\mathbf{d}}_{k+1} + \mathbf{v}_{k+1} \end{aligned} \tag{D.2}$$

where $\mathbf{b}_k = \mathbf{B}_k \mathbf{u}_k$ and $\tilde{\mathbf{d}}_{k+1} = \mathbf{D}_{k+1} \mathbf{u}_{k+1}$.

The prediction-correction algorithm of the Kalman filter can be summarized as follows

$$\hat{\mathbf{x}}_{k+1|k} = \mathbf{A}_k \hat{\mathbf{x}}_{k|k} + \mathbf{b}_k \;;\; \hat{\mathbf{P}}^{\mathbf{xx}}_{k+1|k} = \mathbf{A}_k \hat{\mathbf{P}}^{\mathbf{xx}}_{k|k} \mathbf{A}_k^T + \mathbf{Q}_k \tag{D.3}$$

$$\hat{\mathbf{x}}_{k+1|k+1} = \hat{\mathbf{x}}_{k+1|k} + \mathbf{K}_{k+1} \left(\mathbf{y}_{k+1} - \hat{\mathbf{y}}_{k+1|k} \right) \;;\; \hat{\mathbf{P}}^{\mathbf{xx}}_{k+1|k+1} = \hat{\mathbf{P}}^{\mathbf{xx}}_{k+1|k} - \mathbf{K}_{k+1} \hat{\mathbf{P}}^{\mathbf{yy}}_{k+1|k} \mathbf{K}_{k+1}^T \tag{D.4}$$

where

$$\hat{\mathbf{y}}_{k+1|k} = \mathbf{C}_{k+1} \hat{\mathbf{x}}_{k+1|k} + \tilde{\mathbf{d}}_{k+1} \tag{D.5}$$

$$\hat{\mathbf{P}}^{\mathbf{yy}}_{k+1|k} = \mathbf{C}_{k+1} \hat{\mathbf{P}}^{\mathbf{xx}}_{k+1|k} \mathbf{C}_{k+1}^T + \mathbf{R}_{k+1} \tag{D.6}$$

$$\hat{\mathbf{P}}^{\mathbf{xy}}_{k+1|k} = \hat{\mathbf{P}}^{\mathbf{xx}}_{k+1|k}\mathbf{C}^{T}_{k+1} \tag{D.7}$$

$$\mathbf{K}_{k+1} = \hat{\mathbf{P}}^{\mathbf{xy}}_{k+1|k}\left(\hat{\mathbf{P}}^{\mathbf{yy}}_{k+1|k}\right)^{-1} \tag{D.8}$$

D.2. Kalman-based filters for nonlinear systems

Consider the nonlinear state-space model used in parameter estimation problems of mechanics-based nonlinear FE models

$$\begin{aligned}\boldsymbol{\theta}_{k+1} &= \boldsymbol{\theta}_k + \mathbf{w}_k \\ \mathbf{y}_{k+1} &= \mathbf{h}_{k+1}\left(\boldsymbol{\theta}_{k+1}, \ddot{\mathbf{u}}^{g}_{1:k+1}\right) + \mathbf{v}_{k+1}\end{aligned} \tag{D.9}$$

A linearized version can be expressed by

$$\begin{aligned}\boldsymbol{\theta}_{k+1} &= \boldsymbol{\theta}_k + \mathbf{w}_k \\ \mathbf{y}_{k+1} &= \mathbf{H}_{k+1}\boldsymbol{\theta}_{k+1} + \mathbf{d}_{k+1} + \boldsymbol{\rho}_{k+1} + \mathbf{v}_{k+1}\end{aligned} \tag{D.10}$$

where $\mathbf{H}_{k+1}$, $\mathbf{d}_{k+1}$, and $\boldsymbol{\rho}_{k+1}$ vary depending on the linearization strategy.

The vector $\boldsymbol{\rho}_{k+1}$ represents errors related to the linearization of the measurement equation and this additional uncertainty is modeled by a zero-mean Gaussian distribution with covariance matrix $\mathbf{R}^{*}_{k+1}$. The linearized state-space model described by Eq. (D.10) is analogous to the linear state-space mode described by Eq. (D.2), and consequently can be solved using the KF algorithm presented in Section D.1.

Comparing Eqs. (D.2) and (D.10) it is noted that in the linearized parameter estimation problem, the following relationships are satisfied:

$$\mathbf{A}_k = \mathbf{I} \tag{D.11}$$

$$\mathbf{b}_k = \mathbf{0} \tag{D.12}$$

$$\mathbf{C}_{k+1} = \mathbf{H}_{k+1} \tag{D.13}$$

$$\tilde{\mathbf{d}}_{k+1} = \mathbf{d}_{k+1} \tag{D.14}$$

Extended Kalman filter (EKF)

In the EKF the nonlinear measurement equation in Eq. (D.9) is linearized around the latest predicted parameter estimate ($\hat{\boldsymbol{\theta}}_{k+1|k}$) using a first-order approximation of the Taylor series expansion of $\mathbf{h}_{k+1}\left(\boldsymbol{\theta}_{k+1}, \ddot{\mathbf{u}}^{g}_{1:k+1}\right)$, i.e. in the measurement equation of Eq. (D.10)

$$\mathbf{H}_{k+1} = \left.\frac{\partial \mathbf{h}_{k+1}\left(\boldsymbol{\theta}, \ddot{\mathbf{u}}^{g}_{1:k+1}\right)}{\partial \boldsymbol{\theta}^{T}}\right|_{\hat{\boldsymbol{\theta}}_{k+1|k}} \tag{D.15}$$

$$\mathbf{d}_{k+1} = \hat{\mathbf{y}}_{k+1|k} - \mathbf{H}_{k+1}\hat{\boldsymbol{\theta}}_{k+1|k} = \mathbf{h}_{k+1}\left(\hat{\boldsymbol{\theta}}_{k+1|k}, \ddot{\mathbf{u}}^{g}_{1:k+1}\right) - \mathbf{H}_{k+1}\hat{\boldsymbol{\theta}}_{k+1|k} \tag{D.16}$$

Then, the linearized version can be written as:

$$\begin{aligned}
\boldsymbol{\theta}_{k+1} &= \boldsymbol{\theta}_{k} + \mathbf{w}_{k} \\
\mathbf{y}_{k+1} &= \left.\frac{\partial \mathbf{h}_{k+1}\left(\boldsymbol{\theta}, \ddot{\mathbf{u}}^{g}_{1:k+1}\right)}{\partial \boldsymbol{\theta}^{T}}\right|_{\hat{\boldsymbol{\theta}}_{k+1|k}} \boldsymbol{\theta}_{k+1} + \mathbf{h}_{k+1}\left(\hat{\boldsymbol{\theta}}_{k+1|k}, \ddot{\mathbf{u}}^{g}_{1:k+1}\right) \\
&\quad - \left.\frac{\partial \mathbf{h}_{k+1}\left(\boldsymbol{\theta}, \ddot{\mathbf{u}}^{g}_{1:k+1}\right)}{\partial \boldsymbol{\theta}^{T}}\right|_{\hat{\boldsymbol{\theta}}_{k+1|k}} \hat{\boldsymbol{\theta}}_{k+1|k} + \mathbf{v}_{k+1}
\end{aligned} \tag{D.17}$$

Note that The EKF does not take into account the linearization errors, i.e., $\boldsymbol{\rho}_{k+1} = 0$.

Using the prediction-correction scheme [Eqs. (D.3) to (D.8)]) of the linear KF for the state-space model in Eq. (D.17):

$$\hat{\boldsymbol{\theta}}_{k+1|k} = \hat{\boldsymbol{\theta}}_{k|k} \;;\; \hat{\mathbf{P}}^{\boldsymbol{\theta}\boldsymbol{\theta}}_{k+1|k} = \hat{\mathbf{P}}^{\boldsymbol{\theta}\boldsymbol{\theta}}_{k|k} + \mathbf{Q}_k \tag{D.18}$$

$$\hat{\boldsymbol{\theta}}_{k+1|k+1} = \hat{\boldsymbol{\theta}}_{k+1|k} + \mathbf{K}_{k+1}\left(\mathbf{y}_{k+1} - \hat{\mathbf{y}}_{k+1|k}\right) \;;\; \hat{\mathbf{P}}^{\boldsymbol{\theta}\boldsymbol{\theta}}_{k+1|k+1} = \hat{\mathbf{P}}^{\boldsymbol{\theta}\boldsymbol{\theta}}_{k+1|k} - \mathbf{K}_{k+1}\hat{\mathbf{P}}^{\mathbf{yy}}_{k+1|k}\mathbf{K}^T_{k+1} \tag{D.19}$$

where

$$\begin{aligned}\hat{\mathbf{y}}_{k+1|k} &= \cancel{\mathbf{H}_{k+1}\hat{\boldsymbol{\theta}}_{k+1|k}} + \mathbf{h}_{k+1}\left(\hat{\boldsymbol{\theta}}_{k+1|k}, \ddot{\mathbf{u}}^g_{1:k+1}\right) - \cancel{\mathbf{H}_{k+1}\hat{\boldsymbol{\theta}}_{k+1|k}} \\ &= \mathbf{h}_{k+1}\left(\hat{\boldsymbol{\theta}}_{k+1|k}, \ddot{\mathbf{u}}^g_{1:k+1}\right)\end{aligned} \tag{D.20}$$

$$\hat{\mathbf{P}}^{\mathbf{yy}}_{k+1|k} = \mathbf{H}_{k+1}\hat{\mathbf{P}}^{\boldsymbol{\theta}\boldsymbol{\theta}}_{k+1|k}\mathbf{H}^T_{k+1} + \mathbf{R}_{k+1} \tag{D.21}$$

$$\hat{\mathbf{P}}^{\boldsymbol{\theta}\mathbf{y}}_{k+1|k} = \hat{\mathbf{P}}^{\boldsymbol{\theta}\boldsymbol{\theta}}_{k+1|k}\mathbf{H}^T_{k+1} \tag{D.22}$$

$$\mathbf{K}_{k+1} = \hat{\mathbf{P}}^{\boldsymbol{\theta}\mathbf{y}}_{k+1|k}\left(\hat{\mathbf{P}}^{\mathbf{yy}}_{k+1|k}\right)^{-1} \tag{D.23}$$

$$\mathbf{H}_{k+1} = \left.\frac{\partial \mathbf{h}_{k+1}\left(\boldsymbol{\theta}, \ddot{\mathbf{u}}^g_{1:k+1}\right)}{\partial \boldsymbol{\theta}^T}\right|_{\hat{\boldsymbol{\theta}}_{k+1|k}} \tag{D.24}$$

Iterated Extended Kalman filter (IEKF)

In the EKF $\mathbf{h}_{k+1}\left(\boldsymbol{\theta}_{k+1}, \ddot{\mathbf{U}}^g_{k+1}\right)$ is linearized around $\hat{\boldsymbol{\theta}}_{k+1|k}$, the best available estimate of $\boldsymbol{\theta}_{k+1}$ before $\mathbf{y}_{k+1}$ is taken into account. The IEKF linearizes $\mathbf{h}_{k+1}(\cdot,\cdot)$ around $\hat{\boldsymbol{\theta}}_{k+1|k+1}$, which is the corrected parameter estimate of $\boldsymbol{\theta}_{k+1}$ after $\mathbf{y}_{k+1}$ is assimilated. This is achieved by an iterative procedure. First, the filter linearizes $\mathbf{h}_{k+1}(\cdot,\cdot)$ around $\hat{\boldsymbol{\theta}}^0_{k+1|k+1}$ (where the superscript indicates the iteration number), usually assumed equals to $\hat{\boldsymbol{\theta}}_{k+1|k}$, and computes the updated parameter and parameter covariance estimates $\hat{\boldsymbol{\theta}}^1_{k+1|k+1}$ and $\hat{\mathbf{P}}^{\boldsymbol{\theta}\boldsymbol{\theta},1}_{k+1|k+1}$, respectively. Then, the filter linearizes $\mathbf{h}_{k+1}(\cdot,\cdot)$ around $\hat{\boldsymbol{\theta}}^1_{k+1|k+1}$ and computes a

new updated parameter and parameter covariance estimates $\hat{\boldsymbol{\theta}}^{2}_{k+1|k+1}$ and $\hat{\mathbf{P}}^{\boldsymbol{\theta\theta},2}_{k+1|k+1}$, respectively. The iterative process finishes when the difference between two consecutive updated parameter estimates is less than a defined threshold (e.g., $\left\|\hat{\boldsymbol{\theta}}^{i}_{k+1|k+1}-\hat{\boldsymbol{\theta}}^{i-1}_{k+1|k+1}\right\|\leq\varepsilon$) or after a maximum number of iterations (N_{iter}) is reached.

Therefore, on each iteration i, $\mathbf{H}^{i}_{k+1}$ and $\mathbf{d}^{i}_{k+1}$ in the measurement equation of Eq. (D.10) can be expressed as:

$$\mathbf{H}^{i}_{k+1}=\left.\frac{\partial\mathbf{h}_{k+1}\left(\boldsymbol{\theta},\ddot{\mathbf{u}}^{g}_{1:k+1}\right)}{\partial\boldsymbol{\theta}^{T}}\right|_{\hat{\boldsymbol{\theta}}^{i}_{k+1|k+1}} \tag{D.25}$$

$$\mathbf{d}^{i}_{k+1}=\hat{\mathbf{y}}^{i}_{k+1|k+1}-\mathbf{H}^{i}_{k+1}\hat{\boldsymbol{\theta}}^{i}_{k+1|k+1}=\mathbf{h}_{k+1}\left(\hat{\boldsymbol{\theta}}^{i}_{k+1|k+1},\ddot{\mathbf{u}}^{g}_{1:k+1}\right)-\mathbf{H}_{k+1}\hat{\boldsymbol{\theta}}^{i}_{k+1|k+1} \tag{D.26}$$

Following the same procedure as in the EKF, it is obtained that for each iteration i:

$$\hat{\boldsymbol{\theta}}_{k+1|k}=\hat{\boldsymbol{\theta}}_{k|k}\ ;\ \hat{\mathbf{P}}^{\boldsymbol{\theta\theta}}_{k+1|k}=\hat{\mathbf{P}}^{\boldsymbol{\theta\theta}}_{k|k}+\mathbf{Q}_{k} \tag{D.27}$$

$$\hat{\boldsymbol{\theta}}^{i+1}_{k+1|k+1}=\hat{\boldsymbol{\theta}}_{k+1|k}+\mathbf{K}^{i}_{k+1}\left(\mathbf{y}_{k+1}-\hat{\mathbf{y}}^{i}_{k+1|k+1}\right)\ ;\ \hat{\mathbf{P}}^{\boldsymbol{\theta\theta},i+1}_{k+1|k+1}=\hat{\mathbf{P}}^{\boldsymbol{\theta\theta}}_{k+1|k}-\mathbf{K}^{i}_{k+1}\hat{\mathbf{P}}^{\mathbf{yy},i}_{k+1|k+1}\left(\mathbf{K}^{i}_{k+1}\right)^{T} \tag{D.28}$$

where

$$\hat{\mathbf{y}}^{i}_{k+1|k+1}=\mathbf{h}_{k+1}\left(\hat{\boldsymbol{\theta}}^{i}_{k+1|k+1},\ddot{\mathbf{u}}^{g}_{1:k+1}\right) \tag{D.29}$$

$$\hat{\mathbf{P}}^{\mathbf{yy},i}_{k+1|k+1}=\mathbf{H}^{i}_{k+1}\hat{\mathbf{P}}^{\boldsymbol{\theta\theta},i}_{k+1|k+1}\left(\mathbf{H}^{i}_{k+1}\right)^{T}+\mathbf{R}_{k+1} \tag{D.30}$$

$$\hat{\mathbf{P}}^{\boldsymbol{\theta}\mathbf{y},i}_{k+1|k+1}=\hat{\mathbf{P}}^{\boldsymbol{\theta\theta},i}_{k+1|k+1}\left(\mathbf{H}^{i}_{k+1}\right)^{T} \tag{D.31}$$

$$\mathbf{K}^{i}_{k+1}=\hat{\mathbf{P}}^{\boldsymbol{\theta}\mathbf{y},i}_{k+1|k+1}\left(\hat{\mathbf{P}}^{\mathbf{yy},i}_{k+1|k+1}\right)^{-1} \tag{D.32}$$

$$\mathbf{H}_{k+1}^{i} = \left.\frac{\partial \mathbf{h}_{k+1}\left(\boldsymbol{\theta}, \ddot{\mathbf{u}}_{1:k+1}^{g}\right)}{\partial \boldsymbol{\theta}^{T}}\right|_{\hat{\boldsymbol{\theta}}_{k+1|k}^{i}} \tag{D.33}$$

Unscented Kalman filter (UKF)

The UKF evaluates the nonlinear measurement equation around the predicted parameter estimate $\hat{\boldsymbol{\theta}}_{k+1|k}$ in a set of $(2n_\theta + 1)$ regression points $\vartheta_{k+1|k}^{(i)}$ ($i = 1, \ldots, 2n_\theta + 1$), referred to as sigma points (SPs). The SPs are deterministically chosen such that their sample mean and covariance matrix are equal to the predicted parameter estimate ($\hat{\boldsymbol{\theta}}_{k+1|k}$) and the predicted parameter covariance matrix estimate ($\hat{\mathbf{P}}_{k+1|k}^{\boldsymbol{\theta}\boldsymbol{\theta}}$), respectively. The SPs are propagated through the nonlinear measurement function yielding:

$$\boldsymbol{\gamma}_{k+1}^{(i)} = \mathbf{h}_{k+1}\left(\vartheta_{k+1|k}^{(i)}, \ddot{\mathbf{u}}_{1:k+1}^{g}\right) \tag{D.34}$$

The UKF uses a linearized measurement equation with $\mathbf{H}_{k+1}$, $\mathbf{d}_{k+1}$, and $\boldsymbol{\rho}_{k+1}^{m}$ obtained by statistical linear regression (Lefebvre et al. 2005) though the pairs $\left(\vartheta_{k+1|k}^{(i)}, \boldsymbol{\gamma}_{k+1}^{(i)}\right)$, $i = 1, \ldots, 2n_\theta + 1$. This statistical linear regression is defined to minimize the difference ($\mathbf{e}_i$) between the nonlinear and linearized functions evaluated in the SPs in a least-squares sense:

$$\mathbf{e}_i = \boldsymbol{\gamma}_{k+1}^{(i)} - \left(\mathbf{H}\vartheta_{k+1|k}^{(i)} + \mathbf{d}\right) \tag{D.35}$$

$$\left(\mathbf{H}_{k+1}, \mathbf{d}_{k+1}\right) = \arg\min_{(\mathbf{H},\mathbf{d})} \sum_{i=1}^{2n_\theta+1} \mathbf{e}_i \mathbf{e}_i^{T} \tag{D.36}$$

The solution of Eq. (D.36) is (Lefebvre et al. 2005):

$$\mathbf{H}_{k+1} = \left(\hat{\mathbf{P}}^{\boldsymbol{\theta}\mathbf{y}}_{k+1|k}\right)^T \left(\hat{\mathbf{P}}^{\boldsymbol{\theta}\boldsymbol{\theta}}_{k+1|k}\right)^{-1} \tag{D.37}$$

$$\mathbf{d}_{k+1} = \hat{\mathbf{y}}_{k+1|k} - \mathbf{H}_{k+1}\hat{\boldsymbol{\theta}}_{k+1|k} \tag{D.38}$$

where $\hat{\mathbf{P}}^{\boldsymbol{\theta}\boldsymbol{\theta}}_{k+1|k}$ = predicted parameter covariance estimate computed as a weighted sample covariance of $\vartheta^{(i)}_{k+1|k}$, $\hat{\mathbf{P}}^{\boldsymbol{\theta}\mathbf{y}}_{k+1|k}$ = predicted cross-covariance estimate computed as the weighted sample covariance of $\vartheta^{(i)}_{k+1|k}$ and $\psi^{(i)}_{k+1}$, and $\hat{\boldsymbol{\theta}}_{k+1|k}$ = predicted parameter estimate computed as a weighted sample mean of $\vartheta^{(i)}_{k+1|k}$. The sample covariance of $\mathbf{e}_i$ provides a measure of the magnitude of the linearization errors:

$$\mathbf{R}^*_{k+1} = \hat{\mathbf{P}}^{\mathbf{yy}}_{k+1|k} - \mathbf{H}_{k+1}\hat{\mathbf{P}}^{\boldsymbol{\theta}\boldsymbol{\theta}}_{k+1|k}\mathbf{H}^T_{k+1} \tag{D.39}$$

in which $\hat{\mathbf{P}}^{\mathbf{yy}}_{k+1|k}$ = predicted output covariance estimate computed as a weighted sample covariance of $\psi^{(i)}_{k+1}$, $i = 1,\ldots,2n_\theta+1$. Further details on the mathematical derivation of the UKF as the solution of a statistical linearization problem can be found in Lefebvre et al. 2005.

Then, the linearized version can be written as:

$$\begin{aligned} \boldsymbol{\theta}_{k+1} &= \boldsymbol{\theta}_k + \mathbf{w}_k \\ \mathbf{y}_{k+1} &= \left(\hat{\mathbf{P}}^{\boldsymbol{\theta}\mathbf{y}}_{k+1|k}\right)^T \left(\hat{\mathbf{P}}^{\boldsymbol{\theta}\boldsymbol{\theta}}_{k+1|k}\right)^{-1} \boldsymbol{\theta}_{k+1} + \left(\hat{\mathbf{y}}_{k+1|k} - \mathbf{H}_{k+1}\hat{\boldsymbol{\theta}}_{k+1|k}\right) + \boldsymbol{\rho}_{k+1} + \mathbf{v}_{k+1} \end{aligned} \tag{D.40}$$

Using the prediction-correction scheme [Eqs. (D.3) to (D.8)] of the linear KF for the state-space model in Eq. (D.40):

$$\hat{\boldsymbol{\theta}}_{k+1|k} = \hat{\boldsymbol{\theta}}_{k|k} \;;\; \hat{\mathbf{P}}^{\boldsymbol{\theta}\boldsymbol{\theta}}_{k+1|k} = \hat{\mathbf{P}}^{\boldsymbol{\theta}\boldsymbol{\theta}}_{k|k} + \mathbf{Q}_k \tag{D.41}$$

$$\hat{\boldsymbol{\theta}}_{k+1|k+1} = \hat{\boldsymbol{\theta}}_{k+1|k} + \mathbf{K}_{k+1}\left(\mathbf{y}_{k+1} - \hat{\mathbf{y}}_{k+1|k}\right) \;;\; \hat{\mathbf{P}}^{\boldsymbol{\theta}\boldsymbol{\theta}}_{k+1|k+1} = \hat{\mathbf{P}}^{\boldsymbol{\theta}\boldsymbol{\theta}}_{k+1|k} - \mathbf{K}_{k+1}\hat{\mathbf{P}}^{\mathbf{yy}}_{k+1|k}\mathbf{K}^T_{k+1} \tag{D.42}$$

where

$$\begin{aligned}\hat{\mathbf{y}}_{k+1|k} &= \cancel{\mathbf{H}_{k+1}\hat{\boldsymbol{\theta}}_{k+1|k}} + \hat{\mathbf{y}}_{k+1|k} - \cancel{\mathbf{H}_{k+1}\hat{\boldsymbol{\theta}}_{k+1|k}} \\ &= \sum_{i=1}^{2n_\theta+1} W_m^{(i)} \boldsymbol{\mathcal{Y}}_{k+1}^{(i)}\end{aligned} \tag{D.43}$$

$$\begin{aligned}\hat{\mathbf{P}}_{k+1|k}^{\mathbf{yy}} &= \mathbf{H}_{k+1}\hat{\mathbf{P}}_{k+1|k}^{\boldsymbol{\theta\theta}}\mathbf{H}_{k+1}^T + \mathbf{R}_{k+1} + \mathbf{R}_{k+1}^* = \\ &= \cancel{\mathbf{H}_{k+1}\hat{\mathbf{P}}_{k+1|k}^{\boldsymbol{\theta\theta}}\mathbf{H}_{k+1}^T} + \mathbf{R}_{k+1} + \hat{\mathbf{P}}_{k+1|k}^{\mathbf{yy}} - \cancel{\mathbf{H}_{k+1}\hat{\mathbf{P}}_{k+1|k}^{\boldsymbol{\theta\theta}}\mathbf{H}_{k+1}^T} \\ &= \sum_{i=1}^{2n_\theta+1} W_c^{(i)}\left[\boldsymbol{\mathcal{Y}}_{k+1}^{(i)} - \hat{\mathbf{y}}_{k+1|k}\right]\left[\boldsymbol{\mathcal{Y}}_{k+1}^{(i)} - \hat{\mathbf{y}}_{k+1|k}\right]^T + \mathbf{R}_{k+1}\end{aligned} \tag{D.44}$$

$$\begin{aligned}\hat{\mathbf{P}}_{k+1|k}^{\boldsymbol{\theta}\mathbf{y}} &= \hat{\mathbf{P}}_{k+1|k}^{\boldsymbol{\theta\theta}}\left[\left(\hat{\mathbf{P}}_{k+1|k}^{\boldsymbol{\theta}\mathbf{y}}\right)^T\left(\hat{\mathbf{P}}_{k+1|k}^{\boldsymbol{\theta\theta}}\right)^{-1}\right]^T \\ &= \hat{\mathbf{P}}_{k+1|k}^{\boldsymbol{\theta}\mathbf{y}} \\ &= \sum_{i=1}^{2n_\theta+1} W_c^{(i)}\left[\boldsymbol{\vartheta}_{k+1|k}^{(i)} - \hat{\boldsymbol{\theta}}_{k+1|k}\right]\left[\boldsymbol{\mathcal{Y}}_{k+1}^{(i)} - \hat{\mathbf{y}}_{k+1|k}\right]^T\end{aligned} \tag{D.45}$$

$$\mathbf{K}_{k+1} = \hat{\mathbf{P}}_{k+1|k}^{\boldsymbol{\theta}\mathbf{y}}\left(\hat{\mathbf{P}}_{k+1|k}^{\mathbf{yy}}\right)^{-1} \tag{D.46}$$

References

Lefebvre, T., Bruyninckx, H., and de Schutter, J. (2005). *Nonlinear Kalman Filtering for Force-Controlled Robot Tasks*. Springer-Verlag Berlin, Germany.